Super-Resolution Microscopy of Sphingolipids and Protein Nanodomains

Hochaufgelöste Mikroskopie von Sphingolipiden und Protein Nanodomänen

JAN SCHLEGEL

AUS

FEUCHTWANGEN

WÜRZBURG, 2020

Eingereicht am: ....

Mitglieder des Promotionskomitees:

Vorsitzender: Prof. Dr. Jörg Schultz

1. Betreuer: Prof. Dr. Markus Sauer

2. Betreuer: Dr. Ulrich Terpitz

3. Betreuer: Prof. Dr. Christian Wegener

4. Betreuer: Prof. Dr. Katrin Heinze

Tag des Promotionskolloquiums: ....

Doktorurkunden ausgehändigt am: ....

"Imagination is more important than knowledge. Knowledge is limited."

Albert Einstein

Abstract

The development of cellular life on earth is coupled to the formation of lipid-based biological membranes. Although many tools to analyze their biophysical properties already exist, their variety and number is still relatively small compared to the field of protein studies. One reason for this, is their small size and complex assembly into an asymmetric tightly packed lipid bilayer showing characteristics of a two-dimensional heterogenous fluid. Since membranes are capable to form dynamic, nanoscopic domains, enriched in sphingolipids and cholesterol, their detailed investigation is limited to techniques which access information below the diffraction limit of light.

In this work, I aimed to extend, optimize and compare three different labeling approaches for sphingolipids and their subsequent analysis by the single-molecule localization microscopy (SMLM) technique *direct* stochastic optical reconstruction microscopy (*d*STORM). First, I applied classical immunofluorescence by immunoglobulin G (IgG) antibody labeling to detect and quantify sphingolipid nanodomains in the plasma membrane of eukaryotic cells. I was able to identify and characterize ceramide-rich platforms (CRPs) with a size of $\approx 75\,nm$ on the basal and apical membrane of different cell lines.

Next, I used click-chemistry to characterize sphingolipid analogs in living and fixed cells. By using a combination of fluorescence microscopy and anisotropy experiments, I analyzed their accessibility and configuration in the plasma membrane, respectively. Azide-modified, short fatty acid side chains, were accessible to membrane impermeable dyes and localized outside the hydrophobic membrane core. In contrast, azide moieties at the end of longer fatty acid side chains were less accessible and conjugated dyes localized deeper within the plasma membrane. By introducing photo-crosslinkable diazirine groups or chemically addressable amine groups, I developed methods to improve their immobilization required for *d*STORM.

Finally, I harnessed the specific binding characteristics of non-toxic shiga toxin B subunits (STxBs) and cholera toxin B subunits (CTxBs) to label and quantify glycosphingolipid nanodomains in the context of *Neisseria meningitidis* infection. Under pyhsiological conditions, these glycosphingolipids were distributed homogenously in the plasma membrane but upon bacterial infection CTxB detectable gangliosides accumulated around invasive *Neisseria meningitidis*. I was able to highlight the importance of cell cycle dependent glycosphingolipid expression for the invasion process. Blocking membrane accessible sugar headgroups by pretreatment with CTxB significantly reduced the number of invasive bacteria which confirmed the importance of gangliosides for bacterial uptake into cells.

Based on my results, it can be concluded that labeling of sphingolipids should be carefully optimized depending on the research question and applied microscopy technique. In particular, I was able to develop new tools and protocols which enable the characterization of sphingolipid nanodomains by dSTORM for all three labeling approaches.

Zusammenfassung

Die Entwicklung von zellulären Lebensformen auf der Erde basiert auf der Entstehung biologischer Lipid-Membranen. Obwohl viele Techniken zur Verfügung stehen, welche es erlauben deren biophysikalische Eigenschaften zu untersuchen, sind die Möglichkeiten, verglichen mit der Analyse von Proteinen, eher eingeschränkt. Ein Grund hierfür, ist die geringe Größe von Lipiden und deren komplexe Zusammenlagerung in eine asymmetrische dicht gepackte Lipiddoppelschicht, welche sich wie eine heterogene zweidimensionale Flüssigkeit verhält. Durch die lokale Anreicherung von Sphingolipiden und Cholesterol sind Membranen in der Lage dynamische, nanoskopische Domänen auszubilden, welche lediglich mit Techniken, welche die optische Auflösungsgrenze umgehen, detailliert untersucht werden können.

Ein wesentliches Ziel meiner Arbeit war es, drei Färbeverfahren für Sphingolipide zu vergleichen, erweitern und optimieren, um eine anschliessende Untersuchung mit Hilfe der einzelmolekülsensitiven Technik dSTORM ($direct$ stochastic optical reconstruction microscopy) zu ermöglichen. Zunächst verwendete ich das klassische Färbeverfahren der Immunfluoreszenz, um Sphingolipid-Nanodomänen auf eukaryotischen Zellen mit Hilfe von Farbstoff-gekoppelten Antikörpern zu detektieren und quantifizieren. Dieses Vorgehen ermöglichte es mir, Ceramid-angereicherte Plattformen mit einer Größe von $\approx 75\,nm$ auf der basalen und apikalen Membran verschiedener Zell-Linien zu identifizieren und charakterisieren.

Als nächstes Verfahren verwendete ich die Klick-Chemie, um Sphingolipid-Analoge in lebenden und fixierten Zellen zu untersuchen. Eine Kombination aus Fluoreszenz-Mikroskopie und Anisotropie-Messungen erlaubte es mir Rückschlüsse über deren Zugänglichkeit und Konfiguration innerhalb der Plasmamembran zu ziehen. Hierbei lokalisierten Azid-Gruppen am Ende kurzkettiger Fettsäurereste außerhalb des hydrophoben Membrankerns, wodurch sie mittels membran-undurchlässige Farbstoffe angeklickt werden konnten. Im Gegensatz dazu, waren Azide an längeren Fettsäureresten weniger zugänglich und konjugierte Farbstoffe tauchten tiefer in die Plasmamembran ein. Durch die Einführung photoreaktiver Diazirin-Gruppen oder chemisch modifizierbarer Amin-Gruppen wurden Wege geschaffen, welche eine Immobilisierung und anschließende Analyse mit Hilfe von dSTORM ermöglichen.

Schließlich nutzte ich das spezifische Bindeverhalten der nicht toxischen B Untereinheiten von Shiga- (STxB) und Cholera-Toxin (CTxB) aus, um Glycosphingolipid Nanodomänen im Kontext einer $Neisseria\ meningitidis$ Infektion zu untersuchen. Unter physiologischen Bedingungen waren diese homogen in der Plasmamembran verteilt, jedoch reicherten sich CTxB-detektierbare Ganglioside um eindringende Bakterien an. Darüber hinaus konnte ich einen Zusammenhang zwischen der zellzyklusabhängigen Expression von Glycosphingolipiden und dem Eindringen der Bakterien herstellen. Eine Absättigung der Zucker an der äußeren Membran durch

CTxB-Vorbehandlung reduzierte die Anzahl von invasiven Bakterien signifikant und bestätigte die Schlüsselrolle von Gangliosiden bei der Aufnahme von Bakterien.

Meine Ergebnisse legen Nahe, dass das Färbeverfahren für Sphingolipide an die jeweilige Fragestellung und Mikroskopietechnik angepasst werden sollte. Im Rahmen dieser Arbeit konnten neue Werkzeuge und Protokolle geschaffen werden, die die Charakterisierung von Sphingolipid-Nanodomänen mittels dSTORM für alle drei Färbeverfahren ermöglichen.

Contents

1   Introduction

1.1   Cell and Plasma Membrane Organization

The cell represents the essential and minimal unit of life on earth and is characterized by the highly coordinated arrangement of molecules into a micrometer sized entity. It was first discovered and named by Robert Hooke in his work „*Micrographia, or, Some physiological descriptions of minute bodies made by magnifying glasses: With observations and inquiries thereupon*“ published in 1665 [1]. The porous, honeycomb-like structures he initially investigated under the microscope were actually dead plant cell walls from cork which are quite different to living cells. Several years later in 1674, the Dutch scientist and co-inventor of the light microscope Antoni van Leeuwenhoek described the algae *Spirogyra* and saw bacteria and sperm cells. Nevertheless, it took more than 150 years until Matthias Jakob Schleiden and Theodor Schwann layed the cornerstone of modern cell theory in 1838. They proposed, that all living organisms are composed of one or more cells and that the cell is the most basic unit of life. However, their third assumption of free cell formation through crystallization was wrong and could be corrected in the 1850s by Robert Remak, Rudolf Virchow and Albert Kolliker. Since then, the tenet *Omnis cellula e cellula* which means all cells arise only from pre-existing cells is a fundamental part of modern cell theory. In the following years Moritz Traube formulated the concept of a semi-permeable membrane surrounding every living cell, although it was not clear which material it represented.

The lipid nature of the plasma membrane was first postulated by Georg Quincke, who mentioned in 1888 that a cell behaves as oil when broken in half and described it as a fluid layer of fat less than $100\,\mathrm{nm}$ thin [2, 3]. The discovery of Hans Horst Meyer and Ernest Overton that anesthetics can only cross the membrane which are soluble in both, oil and water, supported the concept of a lipid membrane. Moreover, they concluded it might consist of phopshatidylcholine (PC) and cholesterol which turned out to be in principle true. The final evidence of a plasma membrane with distinct biophysical properties went hand in hand with the development of microinjection [4], electrophysiological [5, 6] and electron microscopy techniques [7, 8]. In 1925, Gorter and Grendel measured the total surface area from extracted erythrocyte lipids at the air water interface and inferred a ratio of 2:1 between monolayer area and cell surface area. They reasoned that „[i]t is clear that all our results fit in well with the supposition that the chromocytes are covered by a layer of fatty substances that is two molecules thick“[9] and were among the first scientists to present conclusive data of the lipid bilayer nature.

With the discovery and description of the nucleus in 1833 by Robert Brown, scientists started to realize that cells contain individual compartments with distinct underlying

functions. The following section 1.1.1 will give an overview about the consequences and importance of cellular compartmentalization through lipid membranes.

1.1.1 Cellular Compartmentalization

Hallmark of the cell is the separation into different organelles and compartments which allow to pursue its manifold tasks under appopriate reaction conditions (see Figure 1).
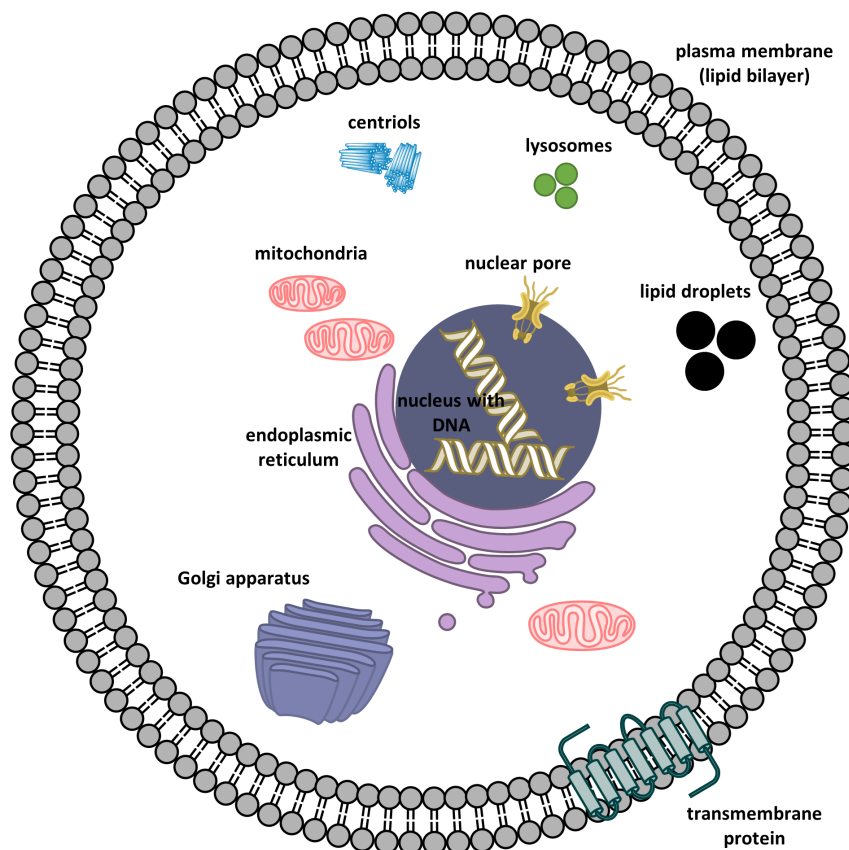
Figure 1: Scheme of a model eukaryotic cell. The plasma membrane (gray) separates the extracellular environment from the intracellular cytosol and consists of a tightly packed lipid bilayer. Transmembrane proteins (turquoise) enable signaling and transport through the membrane and allow to respond to environmental changes. The cell nucleus (dark blue) contains the genetic information as deoxyribonucleid acid (DNA) and molecule im- and export is mediated by nuclear pore complexes (NPCs) located within the nuclear envelope. Lipid *de novo* synthesis occurs at the endoplasmic reticulum (ER) (pink) and maturation of proteins and lipids is performed by the Golgi apparatus (blue). This model is not drawn to scale and not complete. Created with *ChemDraw Professional*[10]

The outermost boundary is represented by the plasma membrane, consisting of an inner and outer leaflet of tightly packed lipids, to allow semipermeable transport between the extracellular environment into the intracellular cytosol and *vice versa*. Manifold transmembrane proteins located within the plasma membrane catalyze the transport of otherwise membrane impermeable molecules and transfer signals between the extracellular and intracellular space. The most prominent structure within an eukaryotic cell is probably

the nucleus which harbors the genetic information in the form of DNA packed as chromatin forming individual chromosomes. DNA is transcribed into ribonucleic acid (RNA) by RNA polymerases and mature messenger RNA (mRNA) transported through NPCs into the cytosol of the cell. Subsequently, translation of mRNAs into proteins occurs at free ribosomes or ER residing ribosomes with the help of transfer RNAs (tRNAs). Of note, the ER constitutes approximately half of the total cell membrane area and is the major site for lipid and transmembrane protein synthesis. Although simplified in Figure 1, it establishes contact with almost every other organelle in the cell to sense its lipid composition and to react towards imbalances. Moreover, it serves as important calcium (Ca^{2+}) storage and ER dysfunction can be correlated with many neurologic disorders. The detailed mechanism of lipid synthesis will be discussed in the following section 1.1.2 on page 5. Many lipids and proteins synthesized at the ER are transported via vesicles to the Golgi apparatus, an organelle consisting of many disc-like compartments called *Golgi cisternae.* Upon arrival, the vesicles fuse with the cis Golgi network (CGN) and the molecules are processed and finally released at the trans Golgi network (TGN). Subsequently, some vesicles will fuse with lysosomes in order to supply them with enzymes required for degradation of proteins and lipids. Continous replenishment of transmembrane proteins within the plasma membrane is maintained by fusion of another set of Golgi derived vesicles which are directed from the TGN to the plasma membrane. In addition, the Golgi apparatus assembles sectretory vesicles to secrete important metabolites such as insuline into the extracellular space.

In contrast to the nuclear membrane, ER membrane, plasma membrane and mitochondrial membrane which are all lipid bilayers, the membrane of lipid droplets consists of a phospholipid monolayer. Lipid droplets were first discovered by Richard Altmann in 1890 in liver tissue of the frog *Rana esculenta* [11] and serve as important cellular energy stores because they are densely packed with triacylglycerol (TAG) and cholesterol [12, 13]. They are generated at the ER membrane and assembly is dependent on several proteins such as seipin and lipid droplet assembly factor 1 (LDAF1) [14]. To maintain cellular homeostasis a lot of chemical energy is produced in the form of adenosine triphosphate (ATP) from mitochondria, also termed the powerhouse of the cell. These double membrane enclosed organelles are derived from bacteria via endosymbiosis and have their own circular mitochondrial DNA (mtDNA) coding for only 13 proteins [15]. As in gram-negative bacteria, the outer membrane is approximately 7 nm thick and contains many pore forming integral membrane proteins called porins which offer passive permeability towards small hydrophilic molecules. In distance of ≈ 20 nm [16] the inner membrane houses all required proteins for energy production and therefore has an extraordinary high protein to lipid ratio of 3:1 by weight [17]. In addition, the inner mitochondrial membrane contains high amounts of the unusual phospholipid cardiolipin (see Figure 2) which is also abundant in most bacterial membranes. The two phosphates within the
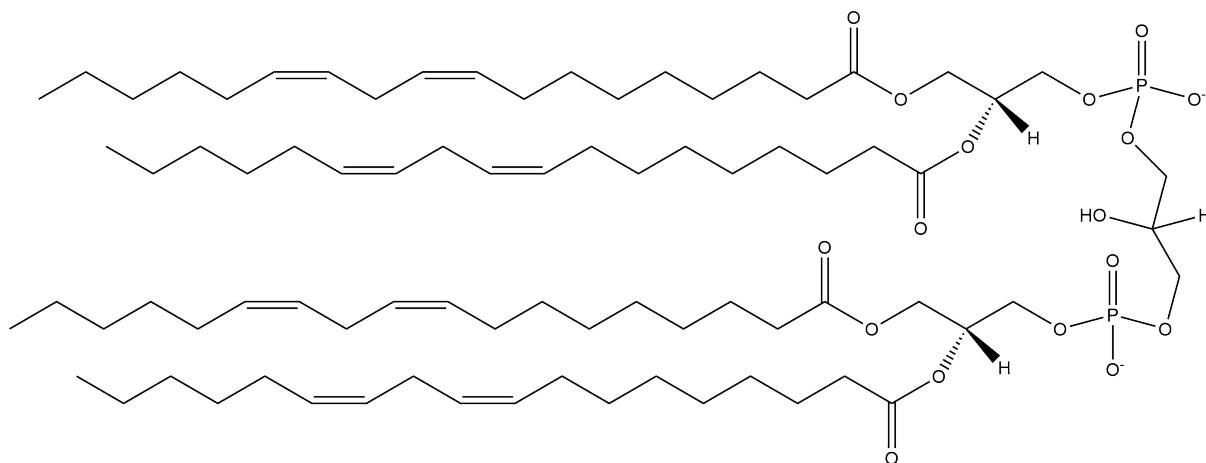
Figure 2: Chemical structure of the most abundant (18:2-18:2)-(18:2-18:2) cardiolipin molecular species found in animals. Its structure resembles a kind of diphosphatidylglycerol with two potentially negative charged phosphate headgroups and four alkyl chains. Cardiolipin is essential component of the inner mitochondrial membrane and bacterial membranes. Structure was created with *ChemDraw Professional*[10]

headgroup improve the ability to trap protons and support the process of oxidative phosphorylation [18]. Due to the four alkyl chains cardiolipin could theoretically exist in many different configurations but the most abundant molecular species in rat liver and bovine heart is the symmetrical (18:2-18:2)-(18:2-18:2) species with 18 carbon atoms and 2 double bonds per fatty acid chain [19]. The development of autoantibodies against cardiolipin concomitants the autoimmune disease antiphospholipid antibody syndrome (APLS) [20] and inappropriate acylation of cardiolipin due to mutations in tafazzin cause infantile death during Barth syndrome [21]. Moreover, cardiolipin dysfunction is linked to many clinical relevant diseases such as Parkinson's [22], nonalcoholic fatty liver [23], diabetes [24], syphilis [25], cancer [26] and Tangier disease [27]. An important additional organelle found in most multicellular eukaryotic cells, except for fungi and plants, is the centrosome. It is composed of two rectangular arranged centriols each composed of 9 sets of triplet microtubules and embedded in an amorphous protein matrix termed pericentriolar material (PCM). The centrosome serves as microtubule organizing center (MTOC) where microtubule nucleation begins at γ-tubulin ring complexes and their plus ends extend into the cytoplasm to perform manifold tasks.

1.1.2   Lipid Synthesis and Composition of Cellular Membranes

As illustrated in Figure 3, sphingolipids, cholesterol and phosphoglycerides represent the three major lipid types of mammalian cellular membranes. They are predominantly synthesized within the ER membrane via complex synthesis pathways and are mainly held together via noncovalent interactions to form biological membranes. Since I focused on the visualization of sphingolipids, the biosynthetic pathways of cholesterol and phosphoglycerides will be only briefly discussed.
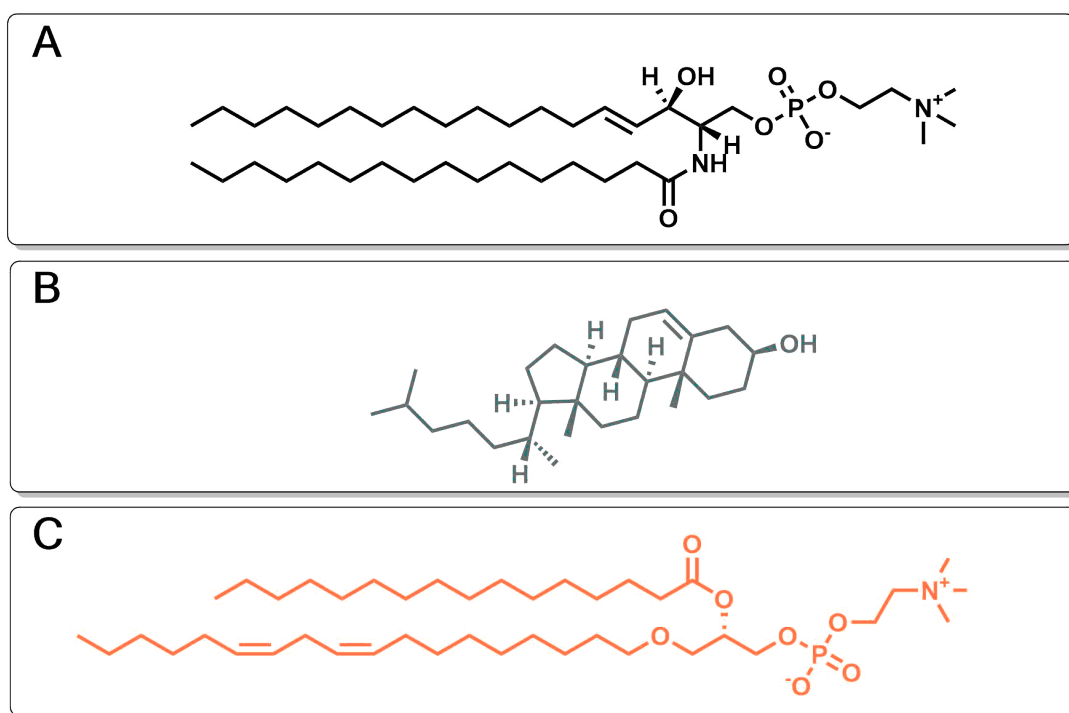
Figure 3: Example chemical structures of the major lipid classes found in eukaryotic membranes. (A) Example chemical structure of 18:1/16:0 sphingomyelin. (B) Example structure of the sterol cholesterol. (C) Example structure of PC. Structures were drawn with *ChemDraw Professional*[10]

Cholesterol is probably the best-known lipid for its disadvantageous participation in human cardiovascular diseases and often attributed with negative properties. But the mere reduction of this sterol to a harmful molecule is in conflict with its important role in the evolution of multicellular organisms. Sterol-based molecules play an essential role in eukaryotic organisms and have evolved to a repertoire of similiar molecules with minor changes. For example, fungi synthesize ergosterol and plants a variety of phytosterols, which differ mostly in the number of double bonds and the number of carbons on the side chain. In the plasma mebrane of human erythrocytes an average cholesterol content of $\approx 30 - 40\,mol\,\%$ is found and an approximately equal distribution within both leaflets is assumed from simulations [28]. Due to their rigid ring structure they align in the plasma membrane with their polar hydroxyl group in proximity to the polar headgroups of phosphoglycerides and their nonpolar hydrocarbon chain within the hydrophobic membrane

core. For this reason, cholesterol can fill up gaps within the bilayer and reinforces the membrane which reduces overall permeability. Of note, cholesterol is found in distinct pools which can be investigated by cholesterol binding proteins with varying specificities [29]. When the plasma membrane concentration of cholesterol decreases below a threshold of $\approx 30\,mol\,\%$ it is sequestered by sphingomyelin and inaccessible to binding of the cholesterol binding protein perfringolysin O (PFO) [30]. Above this threshold, free cholesterol is transported to the ER to inhibit the activity of sterol-regulatory element binding proteins (SREBPs) which are transcription factors required for cholesterol synthesis and uptake. Since the overall concentration of cholesterol in the ER is much lower as compared to the plasma membrane, it is able to sense small cholesterol changes. Below a threshold of $\approx 5\,mol\,\%$ SREBPs are transported via coat protein complex II (COPII) coated vesicles to the Golgi apparatus where transcription factors are released into the cytosol to enter the nucleus and drive cholesterol-synthesizing genes [31]. The biosynthetic pathway of cholesterol starts with acetyl coenzyme A (acetyl-CoA) and involves more than 20 enzymes [32]. Despite *de novo* synthesis, cells can take up cholesterol from the extracellular environment via low-density lipoprotein (LDL) receptors to ensure continuous supply. Since lipoproteins are not able to cross the blood-brain barrier, this cholesterol rich organ has to generate all its cholesterol via *de novo* synthesis. In addition to its structural function in membrane organization, it is the building block for many important bile acids, steroid hormones, including estrogens, glucocorticoids and testosterone and oxysterols.

In contrast, phosphoglycerides are synthesized from a three carbon glycerol backbone whereas esterification of two hydroxy groups with fatty acids produces the hydrophobic tails extending in the plasma membrane. Typically, one fatty acid tail comprises several cis-double bonds (unsaturated) whereas the other tail is saturated and the length varies between 12 to 26 carbon atoms. An ester bond with the third carbon atom connects a charged phosphate group representing the polar head group of the lipid which is aligned towards the water filled extracellular or intracellular environment. As depicted in Figure 4, structural variations in the polar head group discriminate the main cellular phosphoglycerides into PC, phosphatidylethanolamine (PE), phosphatidylserine (PS), phosphatidylglycerol (PG) and phosphatidylinositol (PI). In addition to the great variability in fatty acid side chain length and degree of saturation a myriad of modifications such as phosphorylations, glcosylations and usage of ether linkages instead of ester linkages may produce an enormous set of different phosphoglycerides.
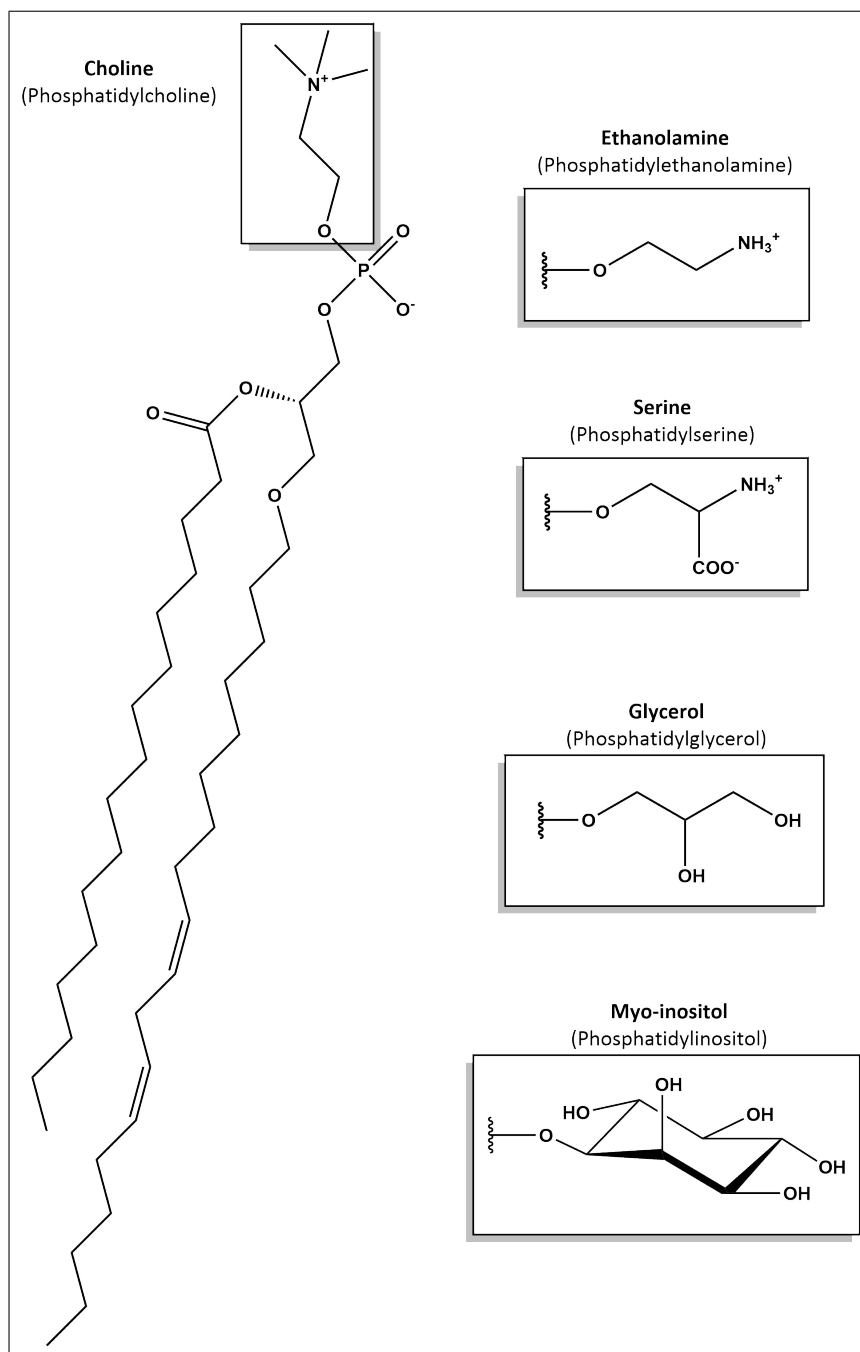
Figure 4: Example chemical structures of the major phosphoglycerides found in eukaryotic membranes. Variations in the polar head group (boxed region) discriminate phosphoglycerides into PC, PE, PS, PG and PI. Adapted from [32] structures were drawn with *ChemDraw Professional*[10]

The third major class of cellular membrane lipids and focus of this thesis are sphingolipids. These lipids were first described by the German biochemist Johann Ludwig Wilhelm Thudichum in his 1884 published book "*A treatise on the chemical constitution of the brain: Based throughout upon original researches*" [33]. In contrast to the already known phosphoglycerides, Thudichum recognized their different composition and according to their enigmatic behaviour he named them after the greek mythical creature the Sphinx. Sphingolipids are essential part of all eukaryotic cells ranging from fungi and plants to mammals

but are also rarely present in some bacteria and viruses [34]. In interplay with cholesterol, sphingolipids are thought to play a decisive role in membrane signaling and trafficking through the formation of small, heterogenous and highly dynamic plasma membrane lipid rafts [35, 36]. Besides their tremendous structural role in plasma membrane subcompartmentalization, recent data also shows that sphingolipids can serve as receptor ligands and second messengers [37]. Like glycerophospholipids they are amphipathic molecules with hydrophobic hydrocarbon chains and a hydrophilic head group.

Biosynthetic *de novo* synthesis starts with the condensation of the amino acid L-serine with acetyl-CoA via serine-palmitoyl transferase (SPT) in the ER (see Figure 5) to form 3-ketosphinganine (3KS). Of note, SPT is also capable to use C14 (myristoyl) and C18 (stearoyl) CoA acyl chains as substrates [38] and the amino acids alanine and glycine [39, 40] instead of serine. In fact, mutations in the active site of SPT can increase its specificity towards alanine which is the underlying pathomechanism of the rare genetic disease hereditary sensory neuropathy type I (HSAN1) [41] and leads to generation of neurotoxic 1-deoxysphinganine. Oral administration of L-serine mitigates HSAN1 symptoms and reduces the accumulation of deoxysphingolipids in mice and humans [42]. SPT activity can be inhibited by the non-proteinogenic amino acid myriocin which leads to total sphingolipid depletion in cells [43] and is a useful tool to investigate the impact of sphingolipids. Enzymatic catalysis of 3KS by SPT is the first and rate-limiting step of sphingolipid *de novo* synthesis. The second step in sphingolipid *de novo* synthesis is catalyzed by 3-ketosphinganine reductase (KDSR) and results in the reduction of 3KS to generate sphinganine. Subsequently, one of six different ceramide synthase (CerS) catalyzes N-acylation of sphinganine with acyl CoA chains of different length to build dihydroceramide (dhCer). The six human CerS are located on different chromosomes and are highly specific towards the length of the hydrocarbon chain which are attached to sphinganine[44]. Mammals synthesize sphingolipids with fatty acid side chain lengths ranging from C14 to C32 which are predominantly saturated [32]. For example, CerS1 specifically catalyzes the addition of C18 CoA [45] and CerS5 of C16 CoA acyl chains [46] to sphinganine. In addition, the enzymatic activity of different CerS may be dependent on each other and mRNA expression does not correlate *per se* with the observed sphingolipid composition of the tissue [47]. For this reason, CerS crosstalk and signaling within the ER raises many questions which have to be adressed in future studies.

Following dhCer generation, dihydroceramide desaturase (DEGS) introduces a conserved and characteristic 4,5-trans double bond to generate ceramide which is released at the ER mebrane. A recent study could show, that inhibition of DEGS and downstream generation of dihydro sphingolipids resolves hepatic steatosis and insulin resistance in adult mice [48] although embryonal ablation of DEGS is lethal [49]. Thus, under physiological condition, most cellular sphingolipids exhibit this conserved double bond but a minor set

gives rise to complex dihydrosphingolipids with non-overlapping function and different biophysical characteristics [50].

After synthesis of ceramides on the cytosolic ER surface, generation of more complex sphingolipids by head group modifications is initiated. Indeed, most mammalian ceramides are converted to sphingomyelin (SM) by sphingomyelin synthase (SMS) at the inner leaflet of the Golgi apparatus [51]. How unmodified ceramides are transported from the ER to the Golgi apparatus was of great interest and different mechanism were discussed. Surprisingly, it turned out, that SM is almost exclusively generated from ceramides transported by ceramide transport protein (CERT) [52] in a non-vesicular fashion from the ER to the Golgi apparatus. CERT consists of different domains required for efficient and directed ceramide transport. An N-terminal pleckstrin homology (PH) domain facilitates attachment with phosphatidylinositol-4-phosphate (PI-4P) localized at the trans Golgi apparatus. At the C-terminal side, a steroidogenic acute regulatory protein-related lipid transfer (START) domain serves as amphiphilic cavity which buries one (dihydro)ceramide molecule with fatty acid length C14 to C20. Due to the limited space within the hydrophobic part of the cavity, (dihydro)ceramides with longer chains cannot be transported [53]. In addition, a two phenylalanines in an acidic tract (FFAT) motif mediates interaction with two membrane proteins of the ER, vesicle-associated membrane protein-associated protein (VAP)-A and VAP-B which is required to tether CERT at the cytosolic surface of the ER. Finally, ceramide is released at the Golgi apparatus and SM is formed by SMS through transfer of the phosphorylcholine head group from PC to ceramide. The product diacylglycerol (DAG) serves as important second messenger and is involved in diverse cellular processes [54, 55]. In addition to non-vesicular transport, vesicular transport of ceramides [56] and transport at organelle membrane contact sites [57] play important roles to ensure proper sphingolipid distribution in the cell.

Depending on the linkage and type of sugars attached at the head group, glycosphingolipids are categorized into the globo-, isoglobo-, lacto-, neolacto- and ganglio-series. The complexity and plethora of enzymes gives rise to tens of thousands different possible subspecies [58] which play major roles in the different human blood group systems [59]. In addition, dysfunction of enzymes relevant for degradation of sphingolipids lead to complex human diseases, the lysosomal storage disorders or sphingolipidoses [60]. The two most frequent ones are *Morbus Gaucher* (Gaucher's disease) and *Morbus Fabry* (Fabry disease) with impaired lysosomal degradation of glycosylceramides and globotriaosylceramide (Gb3), respectively.
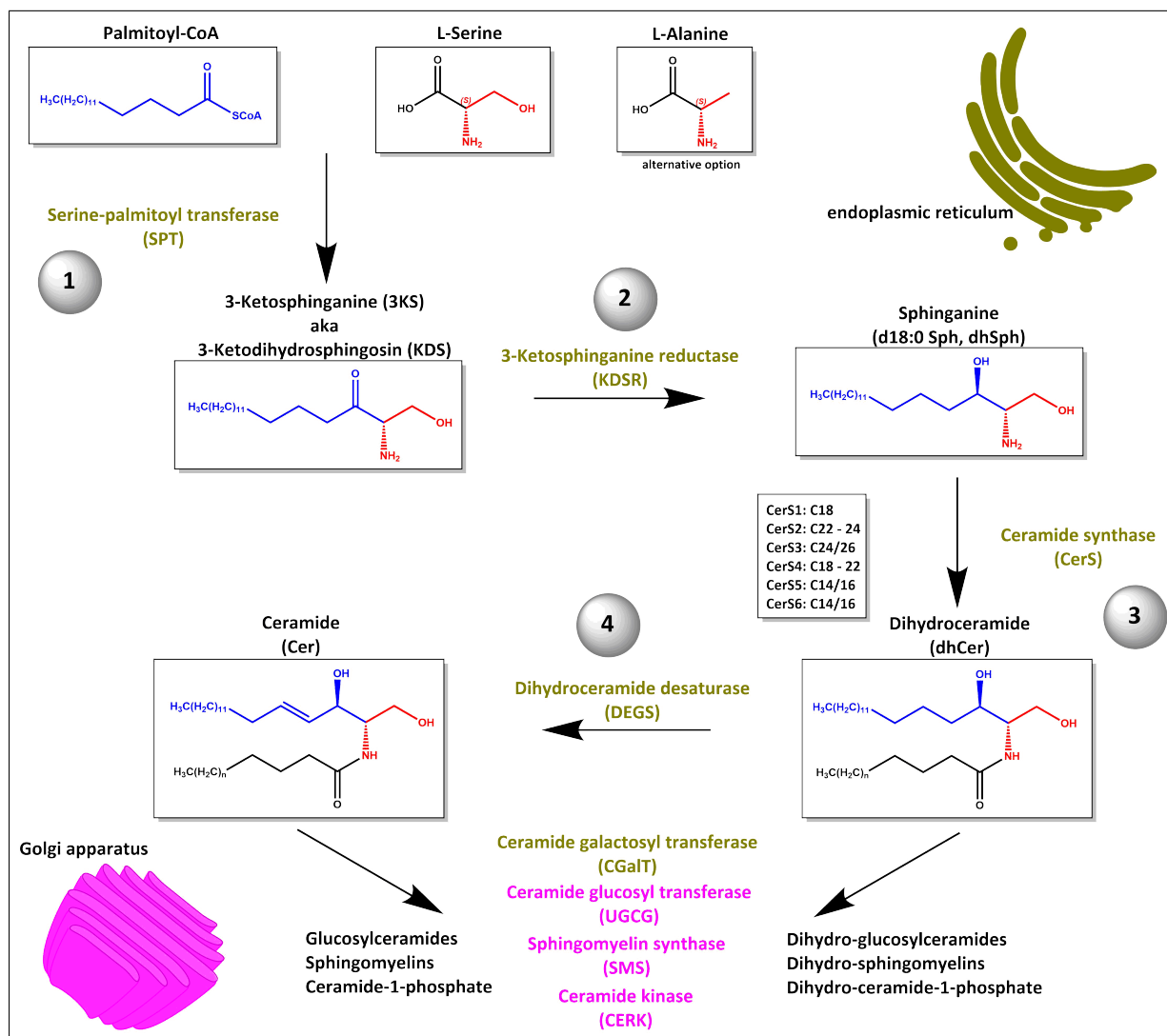
Figure 5: Biosynthetic *de novo* synthesis of sphingolipids is compartmentalized between ER (olive) and Golgi apparatus (magenta). ① *De novo* synthesis of sphingolipids is initiated by condensation of L-serine with acetyl-CoA through SPT in the ER membrane. ② Subsequently, 3KS is reduced by KDSR to produce sphinganine. ③ One of six different CerS attaches a fatty acide with distinct chain length via an amide bond. ④ A characteristic and conserved 4,5-trans double bond is introduced by DEGS and ceramides are transported to the Golgi apparatus for complex head group modifications. Adapted from [61] structures were drawn with *ChemDraw Professional*[10]

1.2 Tools to Study Membrane Organization

1.2.1 Fluorescence and Super-Resolution Microscopy

As introduced in section 1.1, the discovery and characterization of cellular membranes went hand in hand with the development of microscopy techniques. In particular, to use the phenomenon of fluorescence was a milestone for several reasons. Fluorescence was first described by Sir Frederik Herschel who observed a "vivid and beautiful celestial blue color" in a solution of quinine illuminated with sunlight [62]. Shortly after, Sir George Stokes investigated this phenomenon in more detail [63] and laid the foundation of the nowadays well-known Stokes shift which describes the difference in absorption and emission spectrum of a fluorophore. In contrast to its absorption, fluorophores typically emit fluorescence at longer and thus less energetic wavelengths. The theoretical foundation for this observation can be visualized by a so called Jablonski diagram. Here, Professor Alexander Jablonski, known as the father of modern fluorescence spectroscopy, described and illustrated the processes that occur upon absorption of light. As depicted in Figure 6, following absorption of light ($h\nu_A$) the fluorophore is excited from the singlet ground state (S_0) to a higher vibrational/rotational level $(0, 1, 2)$ of the first (S_1) or second (S_2) electronic state. In most instances, rapid internal conversion to the lowest vibrational level of S_1 occurs which is followed by return to an excited vibrational ground state and emission of fluorescence ($h\nu_F$). For this reason, the energy of the emission is usually less, than that of absorption, explaining the Stokes shift. On the other hand, that process takes place in the time regime of several nanoseconds, resembling typical fluorescence lifetime values of fluorophores. In addition, excited fluorophores in S_1 can also undergo intersystem crossing by conversion to the first triplet state T_1 which can lead to emission by phosphorescence ($h\nu_P$). The phosphorescence causing processes occur on time scales several orders of magnitude greater than that for fluorescence and are, for example, exploited by "glow-in-the-dark" toys. As observed by Sir George Stokes and visualized by Professor Alexander Jablonski, the emission light is red-shifted with respect to absorption and this discrimination can be advantageously used in fluorescence microscopy. By filtering perturbing excitation light from the emission path of a microscope, researchers are able to visualize the structure of interest at high signal-to-noise ratio (SNR). With the beginning of the 20th century, companies such as Carl Reichert and Carl Zeiss built the first commercial fluorescence microscopes [64, 65].

Although the advent of fluorescence microscopy represented an important step in understanding the molecular principles of life, certain limitations hindered the observation of cellular processes in more detail. In particular, the physical diffraction limit of light
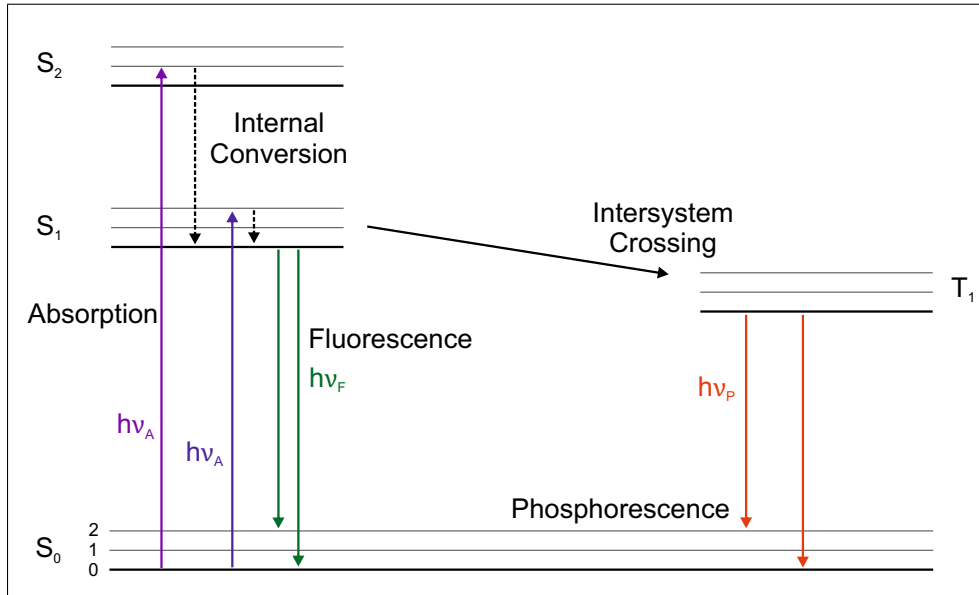
Figure 6: Jablonski diagram showing the processes between light absorption and emission and the involved transitions in energetic and vibrational/rotational states. Absorption of light ($h\nu_A$) excites the fluorophre from the singlet ground state (S_0) to a higher vibrational/rotational level (thin lines; $1, 2$) of the first (S_1) or second (S_2) electronic state (fat lines). Rapid internal conversion followed by return to the ground state can result in the emission of fluorescence ($h\nu_F$). Intersystem crossing to the semi-stable triplet state T_1 by spin conversion may shift the fluorophore to a long-lived dark state which is used by some super-resolution microscopy techniques. Image adapted from *Principles of fluorescence spectroscopy*[66].

described by Ernst Abbe in 1873 prohibited the visualization of two lines in a grating closer than a minimum resolvable distance d. The diffraction limit according to Abbe is depicted in the following equation 1:

$$\mathbf{d = \frac{\lambda}{2n * \sin\alpha} = \frac{\lambda}{2NA}} \tag{1}$$

The equation states, that the minimal resolvable distance d is dependent on the wavelength of light λ divided by 2 times the refractive index multiplied with the sine of the half-angular width α of the objective. The denominator can also be described as two times the numerical aperture (NA) of the objective. A typical value for the NA of modern immersion objectives is 1.4 which limits the resolution to the wavelength divided by 2.8. According to the heuristic Rayleigh criterion for self-emitting fluorescent objects the following equation 2 should be applied:

$$\mathbf{d = \frac{1.22}{2} * \frac{\lambda}{NA} = \frac{0.61\lambda}{NA}} \tag{2}$$

The equation was derived by Rayleigh's assumption, that two point emitters are resolvable if their distance is equal or larger than the distance from the central maximum to the first minimum of the airy disc. Of note, several other concepts of defining an optical

resolution limit exist (e.g. Sparrow resolution limit, Dawes' limit), and modern methods to estimate the resolution rely on Fourier ring correlation [67, 68] or decorrelation analysis [69]. Speaking in practical terms, it is hard to resolve any structures which are closer than 200 nm apart by conventional wide field fluorescence microscopy. Nevertheless, many interesting cellular processes occur at the nanometer scale and were not accessible until the development of new techniques circumventing the diffraction limit of light.

Considering the formal relationship between wavelength and resolution, it seems obvious, that improved resolution can be obtained by the use of decreased excitation wavelengths. Indeed, one of the first approaches to resolve structures below 200 nm was the development of electron microscopy. Here, electron beams with 100 000 times shorter wavelength as compared to visible light are used as excitation source. The first electromagnetic lens was built in 1926 by Hans Busch and in the following years, Ernst Ruska and Max Knoll developed the first prototype of an electron microscope for which Ernst Ruska was awarded the physics nobel prize in 1986 [70]. Several different types of electron microscopes were developed and in particular scanning electron microscopy (SEM) and transmission electron microscopy (TEM) have the potential to resolve structures below 1 Å. For the first time, the lipid double-layer could be observed by eye [71] and correctly interpreted as bilayer structure by J. David Robertson [72, 73]. Besides the huge increase in resolution, electron microscopy also has several disadvantages as compared to conventional fluorescence microscopy. In particular, electron microscopy has to be performed under high vacuum to prohibit scattering of the electron beams with air molecules and such require elaborate sample fixation protocols. Moreover, contrast is represented by differences in electron densities within the image plane which are generated by the use of heavy metals such as uranium and lead and additional fixation with osmium tetroxide. By using solely electron microscopy, it is hard to visualize a protein or lipid of interest and differentiate it from the other present molecules in the sample.

Here, fluorescence microscopy is at an advantage due to many available different labeling techniques which are highly specific for the molecule of interest. One of the major breakthroughs in the life sciences was the development of fluorescence microscopy techniques that offer resolution below the diffraction limit of light. The first demonstration of resolving structures below the diffraction limit of light in the far field, goes back into 1966 [74] by using structured light. Nevertheless, it was the concept of detecting and separating single molecule emission patterns [75–77] which revolutionized the field and led to the development of single-molecule localization microscopy (SMLM) techniques. In SMLM, the emission patterns of single molecules are separated and detected over time which enables the reconstruction of a super-resolved image with typical resolution of $\approx 20\,\text{nm}$, but at the expense of longer acquisition times and the need for sophisticated reconstruction algorithms. In principle, two different types of SMLM exist which differ in the type of flu-

orophores and switching mechanisms used. One type relies on the use of photoactivatable fluorescent proteins, termed photoactivated localization microscopy (PALM) [78, 79], and is linked to the discovery [80] cloning [81] characterization [82] and modification [83] of green fluorescent protein (GFP). On the other hand, synthetic organic fluorophores are used in *direct* stochastic optical reconstruction microscopy (*d*STORM) [84] and STORM [85].

In addition, deterministic methods such as stimulated emission depletion (STED) [86, 87] and structured illumination microscopy (SIM) [88, 89] also have the potential to circumvent the diffraction limit of light. STED is an adaption of confocal laser scanning microscopy (CLSM) where in addition to the excitation beam an overlaying doughnut shaped depletion beam is used to narrow the emission area via stimulated emission. Twofold lateral improvement beyond the resolution limit can be achieved by SIM which relies on the use of structured illumination in a wide field fluorescence microscope and reconstruction of an image with increased spatial resolution.

The constant improvement of microscopic techniques and sample preparation tools to circumvent Abbe's diffraction limit of light also required the development of new labeling techniques. Classical immunofluorescence relies on the use of antibody labeling which was introduced in 1942 by Coons et al. [90]. The size of an immunoglobulin G (IgG) antibody is between 10-15 nm and classical immunofluorescence displaces the fluorophores from the target of interest which may lead to erroneous images if the resolution is good enough. For example, microtubules have an actual diameter of 25 nm but labeling with primary and secondary antibodies causes a displacement of 10 nm on either side and they appear as 45 nm thick structures when visualized by SMLM [91]. In contrast, GFP and its derivatives are much smaller (see Figure 7) and have the dimensions of a cylinder 4.2 nm long and 2.4 nm in diameter [82]. Moreover, genetic encoding has the advantage of a strict 1:1 stoichiometry which may facilitate quantification of target molecules. However, often probes carrying organic fluorophores are preferred due to their increased brightness and photostability.
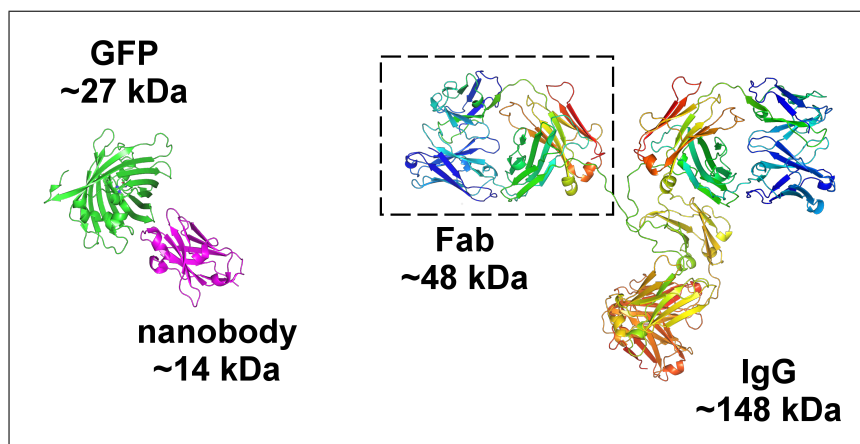
Figure 7: Scheme showing the crystal structures of GFP bound to a nanobody (6LR7)[92] in contrast to a full length IgG (1IGT)[93].

In order to decrease the labeling size, it is possible to purify only the antigen-binding fragments (F(ab)$_2$) or its monovalent part (Fab) by cleavage of IgGs with the enzyme pepsin or papain, respectively. Single-domain antibodies, also termed nanobodies, consist of a single monomeric variable antibody domain derived from "heavy chain only anti-bodies" found in camelids or cartilaginous fishes. With a size of approximately 3 nm they are one of the smallest probes available for targeting endogenous epitopes and have broad applications in biotechnology and therapeutics. Unfortunately, many labeling tech-niques available for proteins are not well suited for the detetction of lipids because of their different biosynthetic pathway and biophysical properties. The next section 1.2.2 will give an overview of a technique convenient for studying exogenously added lipids, termed bioorthogonal click-chemistry.

1.2.2   Bioorthogonal Click-Chemistry

Due to their small size and amphiphilic character, labeling of lipids poses a special challenge. In 2003, the concept of bioorthogonal labeling was introduced by Carolyn R. Bertozzi and her team [94] which implies the following characteristics. The exogenously introduced reaction partners should exclusively react with each other under physiological condition and not perturb cellular homeostasis. In addition, the size of the reactive groups should be small in order to decrease any perturbations of the biological function of the molecules. The following Figure 8 depicts three common bioorthogonal click-chemistry reactions:
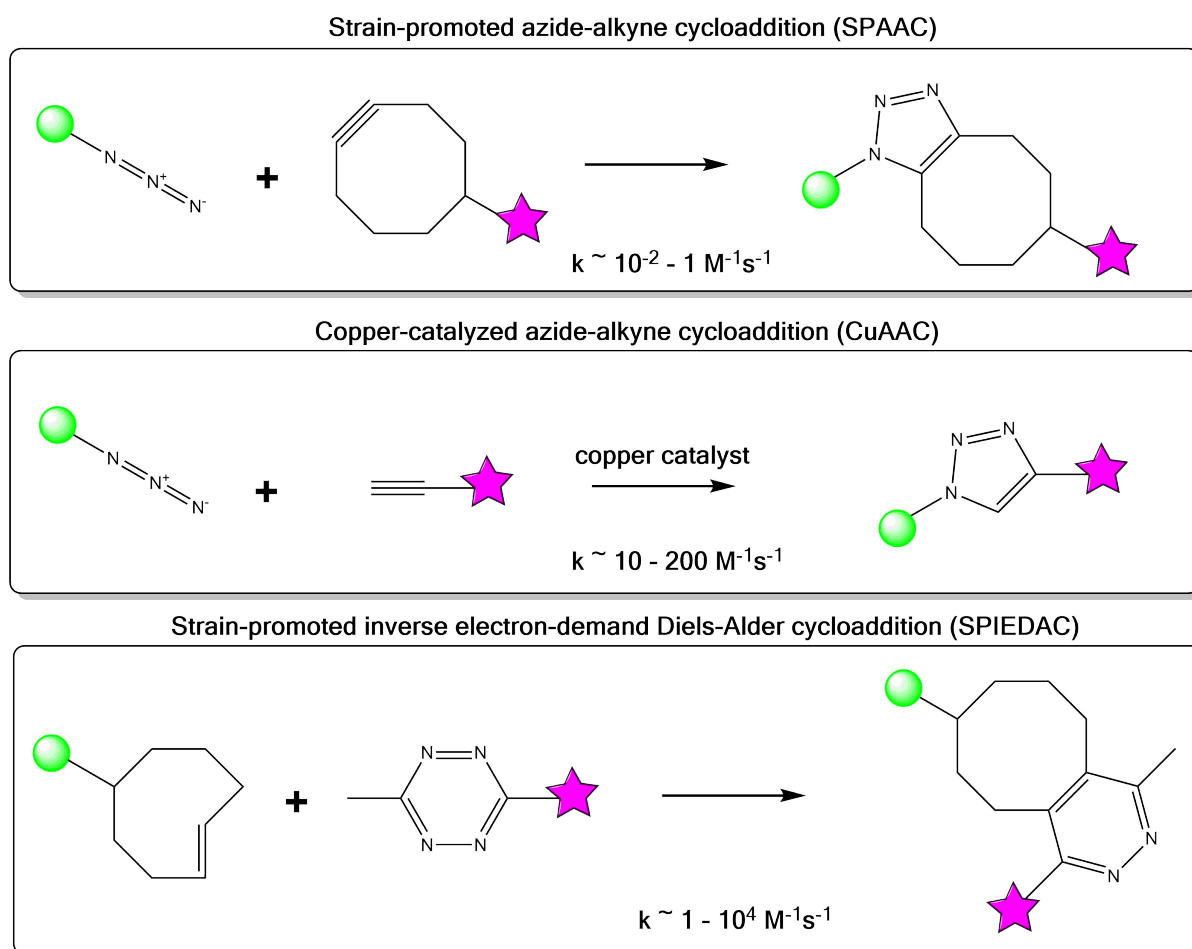
Figure 8: Overview of three common click-chemistry reactions and characteristic rate constants. Green circle represents a biomolecule of interest and magenta star any functional moiety, for example a fluorophore, although the reactive groups are interchangeable with each other. Note the ring strain of dibenzocyclooctin (DBCO) and trans-cyclooctene (TCO) which increases the reaction kinetics. Scheme was adapted from [95] and drawn with *ChemDraw Professional*[10]

In this work, mostly strain-promoted azide-alkyne cycloaddition (SPAAC) was used as bioorthogonal click-chemistry reaction because the azide group is one of the smallest reactive groups available for click-chemistry. In contrast to copper-catalyzed azide-alkyne cycloaddition (CuAAC), SPAAC is appropriate for live-cell labeling and rate constants are reasonable when DBCO is used as reaction partner [96, 97]. Of note, SPAAC and

strain-promoted inverse electron-demand Diels-Alder cycloaddition (SPIEDAC) can be applied simultaneously for multitarget imaging [97].

1.2.3   Optogenetics

One of the most powerful techniques to control and manipulate membrane properties with high spatial and temporal resolution is optogenetics. According to Ernst Bamberg, optogenetics can be defined as "[...] the use of genetically encoded light-activated proteins for manipulation of cells in an almost noninvasive way by light" [98]. As depicted in Figure 9, the history and development of optogenetic tools is closely linked to the characterization of rhodopsins.
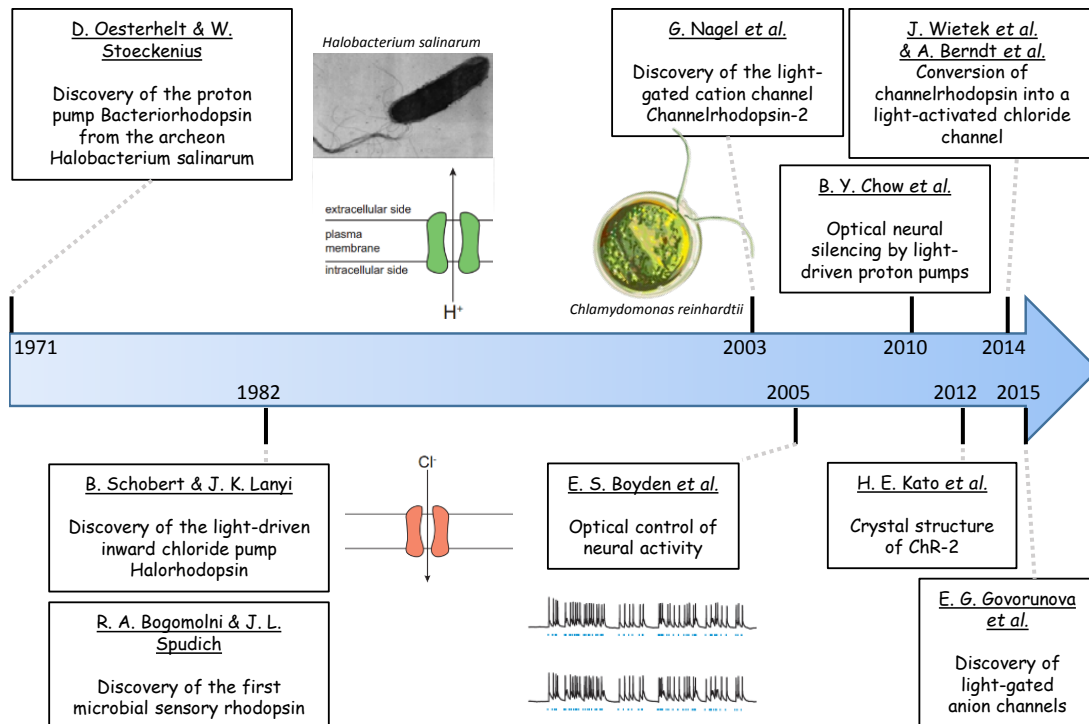
Figure 9: Schematic representation of important discoveries in rhodopsin-based optogenetics until 2015. Image taken with permission from [99].

A milestone was certainly the discovery of the ligh-gated cation channel channelrhodopsin-2 (ChR-2) in 2003 by Nagel et al. [100]. Here, the authors already reasoned that "heterologous expression of ChR-2 should become a useful tool to manipulate intracellular Ca^{2+} concentration or membrane potential, especially in mammalian cells" [100]. In the following years, numerous examples confirmed this hypothesis [101–105] and paved the way for non-invasive control of neuronal behaviour. The initial discovery and characterization was awarded with several prizes, most notably the Brain Prize in 2013 [106] and the Shaw Prize in 2020 [107]. In this thesis, I developed a chimeric tandem protein consisting of the G protein-coupled receptor (GPCR) CXCR4 (CD184) and the calcium translocating ChR-2 mutation L132C. Upon stimulation of CXCR4 with its *bona fide* ligand stromal cell-derived factor 1 (SDF-1) clathrin-mediated internalization of the tandem protein is induced. We investigated the capacity of the internalized tandem protein to release Ca^{2+} from the endolysosomal system by light stimulation.

2   Material & Methods

2.1   General Labeling Procedure

Although the detailed labeling procedure is described in the respective Materials and Methods section of each manuscript, I would like to describe a general labeling procedure. Typically, cells of interest were seeded onto cleaned high precision cover slips or similar chambered cover glass systems. The glass was cleaned with a solution of $1\,$M KOH for $30\,$minutes and washed thoroughly with sterile ultrapure water and dried under a flow of sterile air. Adherent cells were directly seeded onto the glass surface but less adherent cell lines required an additional coating with $0.01\,\%\,(\frac{w}{v})$ poly-D-lysine or $0.2\,\%\,(\frac{w}{v})$ glycine solution. Coating was performed for 30 to 60 minutes at $37\,°$C and followed by an additional wash step with sterile ultrapure water. Live-cell labeling of cells was usually performed at $4\,°$C and antibodies or dyes diluted in Hank's Balanced Salt Solution (HBSS) or medium. Cells were fixed by a combination of $2\,\%\,(\frac{v}{v})$ formaldehyde and $0.2\,\%\,(\frac{v}{v})$ glutaraldehyde diluted in HBSS or medium without fetal calf serum (FCS). Immunofluorescence of cytoskeletal structures was performed according to Small et al. [108] (see Table 1). When SIM was performed samples were mounted in curing mountant to reduce photobleaching and to match the refractive index of the coverglass and immersion oil. For single color dSTORM the structures of interest were labeled with Alexa Fluor 647 or Cy5 and imaging performed in switching buffer. The switching buffer consisted of $100\,$mM cysteamine in phosphate-buffered solution (PBS) with a pH value of 7.7 which was adjusted with KOH.

Cytoskeleton Buffer:	
$10\,$mM MES ($195.24\frac{g}{mol}$), pH 6.1, $150\,$mM NaCl ($58.44\frac{g}{mol}$), $5\,$mM EGTA ($380.35\frac{g}{mol}$), $5\,$mM MgCl$_2$ ($203.3\frac{g}{mol}$)	
Small Buffer #1:	
$0.3\,\%\,(\frac{v}{v})$ glutaraldehyde and $0.25\,\%\,(\frac{v}{v})$ Triton X-100 in **Cytoskeleton Buffer** ($37\,°$C)	
Small Buffer #2:	
$2\,\%\,(\frac{v}{v})$ glutaraldehyde in **Cytoskeleton Buffer** ($37\,°$C)	
1$^{\text{st}}$	Wash sample with PBS (1x, $37\,°$C)
2$^{\text{nd}}$	Fixation: 1-2 min with **Small Buffer #1** ($37\,°$C)
3$^{\text{rd}}$	Permeabilization: 10 min with **Small Buffer #2** ($37\,°$C)
4$^{\text{th}}$	Background reduction: 7 min with $0.1\,\%\,(\frac{w}{v})$ NaBH$_4$ in PBS (optional)
5$^{\text{th}}$	Wash 3x 10 min with PBS
6$^{\text{th}}$	Labeling: phalloidin ($\approx 66\,nM$) in PBS for 24 h at $4\,°$C
7$^{\text{th}}$	Wash 3x PBS + $0.05\,\%$ Tween and immediately measure

Table 1: Buffers and protocol for labeling cytoskeletal elements according to Small et al. [108]

2.2   List of Materials

Reagent	Company
Cholera Toxin B subunit	Sigma-Aldrich (C9903)
Cytochalasin D	Sigma-Aldrich (C8273)
DBCO-amine	Sigma-Aldrich (761540)
Hoechst 34580	Sigma-Aldrich (63493)
Myriocin	Sigma-Aldrich (M1177)
Methyl-β-cyclodextrin	Sigma Aldrich (332615)
Acryloyl-X, SE	Thermo Fischer (A20770)
Alexa Fluor 555 NHS-Ester	Thermo Fischer (A20009)
Alexa Fluor 488 Phalloidin	Thermo Fischer (A12379)
Lipofectamine 2000	Thermo Fischer (11668030)
ProLong Glass Antifade	Thermo Fischer (P36980)
FluoroBrite DMEM	Thermo Fischer (A1896701)
2-Mercaptoethanol	Thermo Fischer (31350010)
F(ab)$_2$ Goat anti-Rabbit IgG (H+L) Secondary Antibody Qdot 655	Thermo Fischer (Q-11421MP)
ER-Tracker Red	Thermo Fischer (E34250)
NucleoBond Xtra Midi EF	Macherey-Nagel
DBCO-AF555	Jena Bioscience (CLK-0931-1)
DBCO-PEG$_4$-FL-BDP	Jena Bioscience (CLK-040-05)
DBCO-PEG$_4$-5/6-Carboxyrhodamine 110	Jena Bioscience (CLK-A127-1)
DBCO-AF647	Jena Bioscience (CLK-1302-1)
DBCO-Sulfo-Cy5	Jena Bioscience (CLK-A130-1)
DBCO-AF488	Jena Bioscience (CLK-1278-1)
BamHI-HF	New England BioLabs (R3136S)
NotI-HF	New England BioLabs (R3189S)
Gb3 (Ceramide trihexoside)	Biotrend (1067)
GM1-Ganglioside sodium	Biosynth Carbosynth (OG03918)
mouse monoclonal MEM-M6/6 CD147	Abcam (ab119114)
mouse monoclonal MEM-M6/6 CD147	Abcam (ab666)
DBCO-PEG$_3$-TCO	Conju-Probe (CP-2043-25MG)
HMSiR-NHS	MoBiTec (A208-01)
16 % paraformaldehyde solution	Science Services (E15710)

3   Results

3.1   Optochemokine Tandem for Light-Control of Intracellular Calcium

Abstract

"An optochemokine tandem was developed to control the release of calcium from endosomes into the cytosol by light and to analyze the internalization kinetics of G-protein coupled receptors (GPCRs) by electrophysiology. A previously constructed rhodopsin tandem was re-engineered to combine the light-gated Ca^{2+}-permeable cation channel Channelrhodopsin-2(L132C), CatCh, with the chemokine receptor CXCR4 in a functional tandem protein tCXCR4/CatCh. The GPCR was used as a shuttle protein to displace CatCh from the plasma membrane into intracellular areas. As shown by patch-clamp measurements and confocal laser scanning microscopy, heterologously expressed tCXCR4/CatCh was internalized via the endocytic SDF1/CXCR4 signaling pathway. The kinetics of internalization could be followed electrophysiologically via the amplitude of the CatCh signal. The lightinduced release of Ca^{2+} by tandem endosomes into the cytosol via CatCh was visualized using the Ca^{2+}-sensitive dyes rhod2 and rhod2-AM showing an increase of intracellular Ca^{2+} in response to light." [109]

The following manuscript was published on October 21st, 2016 in PLOS ONE and permission for legal second publication within this thesis was kindly granted from both the publishers and the co-authors.

RESEARCH ARTICLE

Optochemokine Tandem for Light-Control of Intracellular Ca²⁺

Katrin Feldbauer[1☯], Jan Schlegel[2☯], Juliane Weissbecker[1], Frank Sauer[2¤], Phillip G. Wood[1], Ernst Bamberg[1,3], Ulrich Terpitz[2]*

1 Department of Biophysical Chemistry, Max-Planck-Institute of Biophysics, Frankfurt am Main, Germany, **2** Department of Biotechnology and Biophysics, Biocenter, Julius Maximilian University, Würzburg, Germany, **3** Chemical and Pharmaceutical Sciences Department, Johann Wolfgang Goethe University, Frankfurt am Main, Germany

☯ These authors contributed equally to this work.
¤ Current address: Biological Physics Division, Institute for Experimental Physics I, University of Leipzig, Leipzig, Germany
* ulrich.terpitz@uni-wuerzburg.de

Abstract

An optochemokine tandem was developed to control the release of calcium from endosomes into the cytosol by light and to analyze the internalization kinetics of G-protein coupled receptors (GPCRs) by electrophysiology. A previously constructed rhodopsin tandem was re-engineered to combine the light-gated Ca²⁺-permeable cation channel Channelrhodopsin-2(L132C), CatCh, with the chemokine receptor CXCR4 in a functional tandem protein tCXCR4/CatCh. The GPCR was used as a shuttle protein to displace CatCh from the plasma membrane into intracellular areas. As shown by patch-clamp measurements and confocal laser scanning microscopy, heterologously expressed tCXCR4/CatCh was internalized via the endocytic SDF1/CXCR4 signaling pathway. The kinetics of internalization could be followed electrophysiologically via the amplitude of the CatCh signal. The light-induced release of Ca²⁺ by tandem endosomes into the cytosol via CatCh was visualized using the Ca²⁺-sensitive dyes rhod2 and rhod2-AM showing an increase of intracellular Ca²⁺ in response to light.

Introduction

In the last decade, optogenetics emerged as a technique that allows the manipulation of cells by light in a broad range of topics such as the restoration of vision after retina degeneration [1], T-cell migration [2], and cell death [3]. Optogenetics has the potential to contribute to or even substitute traditional drug-based therapies in the future [4]. Recently, optogenetic approaches for the generation of Ca²⁺ signals were described, where light-switchable ligands or customized light-gated Ca²⁺ channels were used to generate Ca²⁺ influx through the plasma membrane upon light activation [5–7], but to date, there is no report on intracellularly acting light-gated calcium switches.

Ca²⁺ is a key signal in cell regulation, modulating the activity of a plenitude of sensitive proteins. Ca²⁺ regulation is involved in many fundamental processes such as egg-fertilization, cell

cycle, cell-cell contacts, generation of action potentials, motility, hormonal regulation, and programmed cell death via activation of caspases [8]. Prerequisite for accurate signaling is the exact buffering of Ca^{2+} concentrations within the cell. Ca^{2+} ions entering the cell from the environment are either rapidly buffered by Ca^{2+}-binding proteins like calmodulin in the sub-second time scale [9] or removed to the extracellular lumen or into intracellular calcium-stores by membrane bound proteins like Ca^{2+}-ATPases [8]. The steep Ca^{2+} gradients between the cytosol (100 nM), endosomes (4–40 μM), lysosomes (~500 μM), and the extracellular lumen (~1 mM) allow for the generation of fast, spatially and temporally modulated Ca^{2+} signals [10]. The non-invasive triggering of this universal signal would enable the manipulation of cell behavior. In consequence, detailed insights into the physiology of the cell might be obtained.

The microbial rhodopsin Channelrhodopsin-2 (ChR2) [11] is a light-gated, inwardly rectifying cation channel from the green alga *Chlamydomonas reinhardtii* located in the plasma membrane. In CatCh, a ChR2 mutant, a single amino acid exchange from *Leu* to *Cys* in position 132 leads to 6-fold increased Ca^{2+} permeability in comparison to the wild type [12]. As Ca^{2+} ions are quickly sequestered or exported into the cell environment, the CatCh-mediated signal is expected to arise mainly in the direct neighborhood of the plasma membrane. Distinct light-triggered, intracellular Ca^{2+} signals would require CatCh to be localized in the membrane of organelles that provide higher Ca^{2+} content than the cytosol. In 2011, we described a gene cassette that, once expressed, combines different rhodopsins in one functional protein thereby ensuring stoichiometric expression of both membrane proteins [13]. In order to optically trigger Ca^{2+} signals inside the cell, a tandem combining the light-gated CatCh with a protein providing distinct intracellular trafficking could be used.

Microbial rhodopsins and G-Protein coupled receptors (GPCRs) are members of the same protein super-family. Both exhibit a 7-transmembrane domain structure, making them suitable for the tandem cassette [13]. GPCRs represent the most ubiquitous family of membrane receptors, play a distinct role in cell regulation, and are important drug targets [14]. A subgroup of GPCRs, the chemokine receptors are activated upon external stimuli by their specific agonists, the chemokines. The activation is then followed by the internalization of the membrane-bound receptor protein via clathrin-mediated endocytosis to transfer the signal into the cell. In the early step of vesicle formation, mediated by the adaptor molecules β-arrestin and clathrin [15], the lumen contains the extracellular liquid. After internalization endosomes are acidified to enable ligand displacement, dephosphorylation, and receptor recycling [16], while Ca^{2+} is released from the endosome into the cytosol through TRPML channels, members of the transient receptor potential (TRP) superfamily of ion channels. In early endosomes the Ca^{2+} concentration is already reduced to 3–40 μM in contrast to about 1 mM in the extracellular environment [10].

The Cxc-motive-chemokine receptor 4 (CXCR4) is an important regulatory protein, of high medical relevance, and strongly involved in cell migration of cancers with poor prognosis, metastasis formation, and virulence of the human immunodeficiency virus [17,18]. Once its endogenous ligand, the stromal derived factor 1 (SDF1), binds to CXCR4, the receptor undergoes a conformational change. The signal is then transferred to the cytoplasmic heterotrimeric G_i protein, leading to further downstream signaling cascades [19]. Binding of SDF1 to CXCR4 can be impaired by the antagonist AMD3100 (plerixafor) [20]. After internalization, CXCR4 will either be recycled back into the cell membrane or degraded according to the corresponding cellular pathway [15]. Recently, a photoactivatable version of CXCR4 was used to control chemokine receptor signaling and T-cell migration by light [2].

In the present study we combined CXCR4 with CatCh [12] in one functional tandem protein (Fig 1) which in the following is referred to as the optochemokine tandem tCXCR4/CatCh. tCXCR4/CatCh was overexpressed in the hybrid mouse neuroblastoma × rat glioma cell line

23

NG108-15 and in the human embryonic kidney cell line HEK293. The function of the light-gated cation channel and the internalization of the construct via the endocytotic SDF1/CXCR4 signaling pathway were investigated by patch-clamp measurements and confocal laser scanning microscopy (CLSM). To explore the function of tCXCR4/CatCh the Ca^{2+}-sensitive dyes rhod2 or rhod2-AM were used as reporter for changes of the endosomal or intracellular Ca^{2+} concentration, respectively.

Materials and Methods

Molecular biology

All constructs and the tandem cassette (Fig 1), which was described in detail before [13], were cloned into pcDNA3.1(-) plasmids (Invitrogen, Carlsbad, USA) under control of the strong human cytomegalovirus (CMV) promoter suitable for mammalian cell transfection. *hcxcr*4 was synthesized (Sloning BioTechnology, Puching, Germany) and introduced into the original tandem cassette (*hvChR1-mKateA-β-hChR2*) via *BamH*I and *Sac*II restriction sites to form *hCXCR4-mKateA-β-hChR2*. *mKateA* (Evrogen-TagFP635) was then replaced by *eyfp* (*Sbf*I & *Sac*II). Furthermore, a fluorescent variant of hCXCR4 was produced by introducing the construct into a plasmid containing the *eyfp* gene. pcDNA3.1(-)-*hchr2*::*eyfp* and pcDNA3.1(-)-*catch*::*eyfp* were described in an earlier study [12]. DNA sequences of ChR2 and CXCR4 were adapted to human codon usage, to improve recombinant expression in mammalian cells. Plasmids were purified using an endotoxin free purification kit (Nucleobond Xtra Midi EF (Macherey & Nagel, Düren, Germany) or Qiagen Endofree Plasmid Maxi (Qiagen, Hilden, Germany). For establishment of the stable HEK293 Flp-In™T-Rex™ (Invitrogen, Darmstadt, Germany) cell lines, the tandem cassette and *hcxcr4*::*eyfp* were cloned into pcDNA5/FRT/TO using the In-Fusion® HD Cloning Kit (Clontech, Mountainview, USA). DNA constructs are available from the corresponding author upon request.

Cell culture and Transfection

NG108-15 cells (fused mouse N18TG2 neuroblastoma and rat C6BU1 glioma) were obtained from ATCC. HEK293 Flp-In™T-Rex™ was obtained from Invitrogen. Cells were cultured at 37°C and 5% CO_2 in Dulbecco's Modified Eagle's Medium (DMEM) supplemented with 4500 mg/l glucose, 10% fetal calf serum (FCS), 2 mM L-glutamine, 100 U/ml penicillin, and 100 μg/ml streptomycin (enriched DMEM). HEK293 Flp-In™T-Rex™ cells were selected using 15 μg/ml blasticidin and 100 μg/ml zeocin before transfection, whereas after transfection zeocin was replaced by 100 μg/ml hygromycin. Sub-confluent cultures (70–90% confluency) were passaged twice a week in a ratio of 1:5 to 1:10 and detached either mechanically or by means of 0.05% trypsin in presence of 0.53 mM EDTA (2 min, RT). G1-Subpopulations were excluded by FACS analysis (S1 Fig). Occurrence of mycoplasms in the cell culture was excluded by frequent PCR-based analysis (LookOut®Mycoplasma PCR Detection Kit, Sigma-Aldrich, Germany) of the growth medium and microscopic control.

For recombinant expression of our constructs, NG108-15 cells were seeded either on glass-coverslips (diameter 12 mm) in 24-well plates or in 8-well labtek II (Nunc, Wiesbaden, Germany or Sarstedt, Nümbrecht, Germany) coated with 0.01% Poly-D-lysine and transfected at a cell confluence of 50–80% by means of Lipofectamine® 2000 (Invitrogen, Darmstadt, Germany) in OptiMEM (Invitrogen) medium according to the supplier's instructions. After a minimum incubation period of 5 h, the medium was exchanged with enriched DMEM including 1 μM *all-trans* retinal (atr). Appropriate protein expression was achieved after 12 to 24 hours.

For generation of stable HEK293 Flp-In™T-Rex™ cell lines of CXCR4::YFP and the tandem construct, cells were transfected using effectene (Qiagen, Hilden, Germany) with the respective
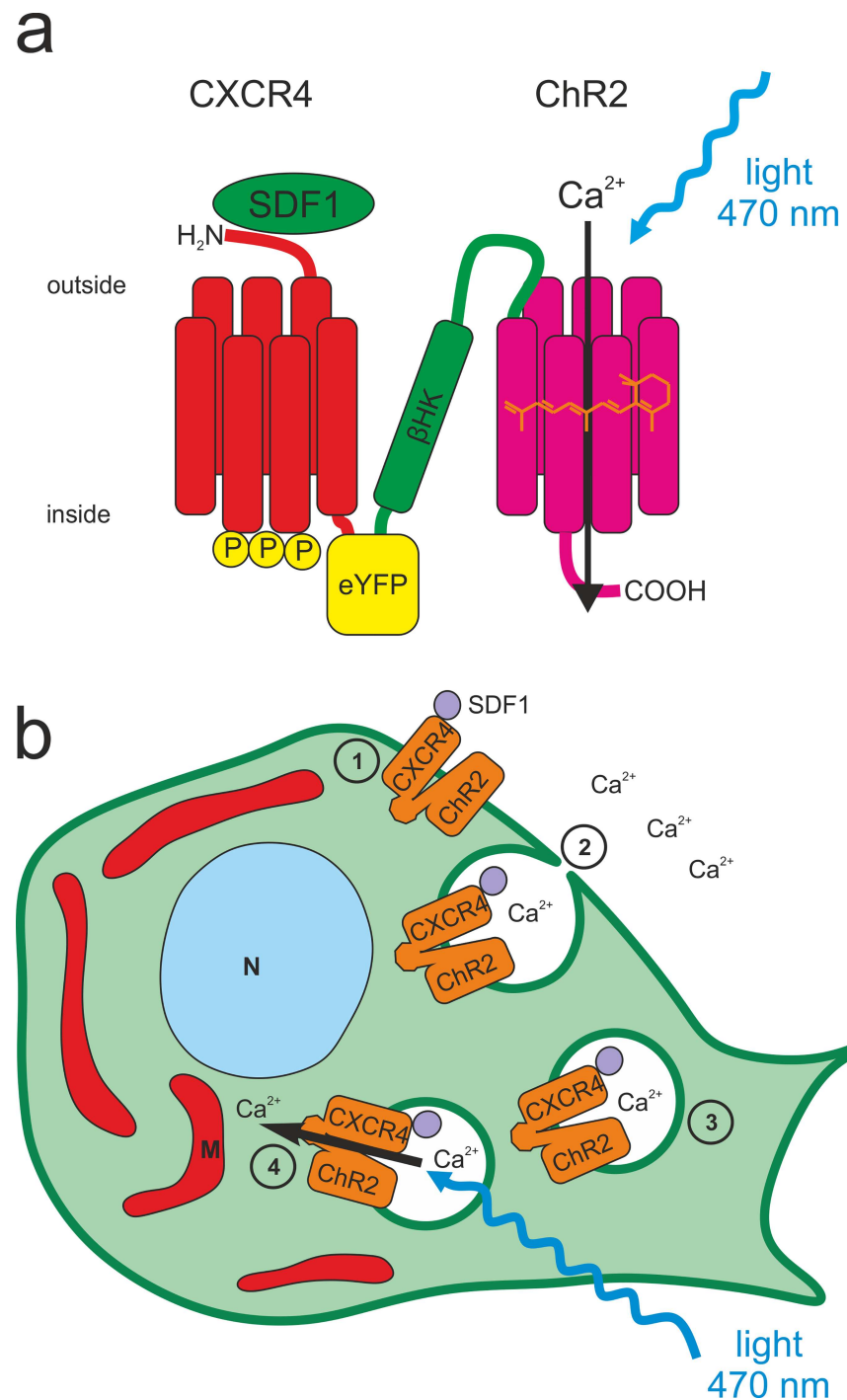
Fig 1. Structure and function of the optochemokine tandem tCXCR4/CatCh. This optophysiological tool combines two features in one functional unit, the internalization after the binding of stromal cell-derived factor 1 (SDF1) and the light-gated influx of cations, including Ca^{2+}, via CatCh upon illumination. **a.** The CXCR4-protein was placed at the N-terminus, followed C-terminally by eYFP and the β-subunit of the rat HK-ATPase, to combine the intracellular C-terminus of eYFP with the extracellular N-terminus of ChR2 (aa 1–309). **b.** Schematic overview of the light-induced intracellular Ca^{2+} signaling mediated by tCXCR4/CatCh in an eukaryotic cell. In this optogenetic application the SDF1/CXCR4 signaling pathway (1–4) is used to induce internalization of tCXCR4/CatCh in endosomes. **1.** tCXCR4/CatCh is expressed heterologously in the mammalian cell and trafficked towards and integrated into the plasma membrane. There, the chemokine

receptor CXCR4 will be activated by its endogenous ligand SDF1. **2.** Upon SDF1-activation tCXCR4/CatCh is internalized. As the Ca^{2+} concentration in the cell environment is four magnitudes higher than within the cell, also the calcium concentration in these endosomes is considerably higher than in the cytosol. **3.** The endosome is trafficked into intracellular areas of the cell. **4.** Upon illumination with blue light, CatCh will open and release Ca^{2+} ions into the cytosol, resulting in a local intracellular increase of Ca^{2+}. This transient Ca^{2+} signal might be used for triggering Ca^{2+}-dependent physiological processes by light. N = nucleus, M = mitochondrion.

doi:10.1371/journal.pone.0165344.g001

pcDNA5/FRT/TO-construct and pOG44 in relation 1:10. The cell line expressing Catch::YFP was available from earlier studies [12].

Western blot

Membrane proteins (CXCR4::eYFP; tCXCR4/CatCh tandem) were extracted from NG108-15 cells using the Mem-PER Plus Membrane Protein Exctraction Kit (Thermo Scientific, Braunschweig, Germany) 24 to 48h after transient transfection (Lipofectamine® 2000). Before the protein concentration was determined (Quick Start™ Bradford 1x Dye Reagent, BioRad, Munich, Germany; according to manual), membrane protein samples were concentrated (Amicon® Ultracel® 50K, Merck Milipore, Cork, Ireland). Reduced Protein samples (prepared with NuPage LDS Sample Buffer and NuPage Sample Reduction Agent) were separated using Gel electrophoresis (NuPage 10% Bis-Tris Gels) in a XCell SureLock® Mini Cell Chamber (all Invitrogen, Darmstadt, Germany) using Page Ruler Prestained Protein Ladder (Thermo Scientific, Waltham, USA) as a marker. Gels were blotted in an iBlot™ Dry Blotting System (Invitrogen, Darmstadt, Germany) onto a nitrocellulose membrane (Novex iBlot® Gel Transfer Stacks, Invitrogen, Darmstadt, Germany, 23 V, 6 minutes) and blocked overnight at 4°C (dry milk). Primary antibodies and secondary antibodies were incubated for 1 h each: Anti-Mouse CD184(CXCR4) (1:1000, #14-9991-82, eBioscience, Frankfurt, Germany) and Rabbit Anti Rat IgG HRP (1:1000, #PA1-28573, Pierce/Thermo Fisher Scientific). Blots were developed using SuperSignal™ West Pico Substrate (Thermo Scientific, Waltham, USA), Amersham Hyperfilm™ ECL (GE Healthcare, Freiburg, Germany) and a Curix 60 Tabletop Processor (Agfa Health-Care, Bonn, Germany).

Microscopy

Unless otherwise specified, generally, for fluorescence microscopy 8-well labtek II chambers were used (see cell culture and transfection). Confocal laser scanning microscopy (CLSM) was either performed with a Leica SP2 (Wetzlar, Germany) or a Carl Zeiss LSM 700 (Jena, Germany) microscope. Images were subsequently processed using either LAS AF Lite (v2.6.3., Leica, Wetzlar, Germany) or ZEN 10 (Zeiss, Jena, Germany), and Fiji [21].

The internalization of CXCR4::eYFP and the optochemokine tandem was analyzed after treatment with either 50 nM SDF1α (recombinant human SDF1α; Invitrogen) or 50 nM SDF1α and 10 µM AMD3100 for 40 min *in vivo* or after fixation (10 min; 4% paraformaldehyde) in phosphate buffered saline (PBS, pH 7.4). The anti-mouse CD184 (CXCR4) PE-eFluor® 610 (eBioscience) was added at a ratio of 1:500 (V/V) for 30 min and washed twice with enriched DMEM before measurements. Alexa-647 labelled transferrin was purchased from Thermo Fisher Scientific (Molecular Probes Invitrogen, Darmstadt, Germany) and the staining procedure was performed as recommended by the supplier's protocol. Early endosomes were visualized using CellLight® Early Endosomes-RFP BacMam 2.0 kit (life technologies—molecular probes) in a concentration of 10 to 50 particles per cell. Cells were imaged after an incubation period of 20 hours.

In order to improve the signal, calcium imaging was performed with tCXCR4/CatCh (D156C) containing the ChR2 L132C-D156C mutant. This mutant exhibits slower kinetics as well as better expression which was beneficial for calcium imaging conditions. tCXCR4/CatCh (D156C) was heterologously expressed in NG108-15 cells. 24 to 48 hours after Lipofecta-mine® 2000 transfection, the internalization and dye loading were performed under physio-logical condition (1.8 mM Ca^{2+}) in DMEM without serum supplemented with 50 nM SDF1α and 2 µM rhod2-AM or 5 µM rhod2 for 1 hour. In order to remove extracellular Ca^{2+} and to detect only intracellular signals, the cells were washed 2 min with chelator solution (10 mM glucose, 10 mM EGTA, 110 mM NaCl, 10 mM HEPES, pH 7.4). Calcium imaging was then performed in calcium-free solution (130 mM NaCl, 10 mM HEPES, 2 mM $MgCl_2$, 30 mM glu-cose, pH 7.2) supplemented with 10 µM AMD3100. The cells were simultaneously excited with two laser lines (488 nm 10 mW 2%, 555 nm 10 mW 1%) at the confocal microscope (LSM700) at a frequency of 0.5 Hz in order to activate ChR2 and to detect YFP fluorescence and the rhod2 signal at the same time. All parameters (area, light intensity, photomultiplier, pin hole etc.) were kept constant in all measurements. Time series were analyzed with Fiji [21].

For cell death analysis long-term time-lapse imaging experiments were performed. Cells were seeded on coverslips, treated with 50 nM SDF1α for 45 min, and transferred into a cus-tom-built cell chamber (Nikon BioStation IM). Cells were exposed to enriched DMEM at 37°C, 5% CO_2, and 95% air humidity and illuminated for 20 min by means of a blue LUXEON Rebel light-emitting diode (470 nm, Phillips, San Jose, USA; 5 mW/mm^2). In a time span of 60 min fluorescence and phase contrast pictures (illumination with red light) were taken every five minutes with a cooled charge-coupled device (CCD) camera. Data was analyzed with the Bios-tation IM software (Nikon) and GIMP 2.8.10. Cell death ratios after 60 min were estimated by morphological criteria and compared between the different genetic constructs by means of two-tailed student's t-test (p = 0.05).

Patch clamp

Patch-clamp experiments were performed at two different setups that were described in detail before [22,23], both were equipped with a 473 nm-DPSS laser (Pusch optotech, Baden Baden, Germany) for the activation of Channelrhodopsin-2. For internalization experiments laser light was coupled into a 0.5 mm diameter fiber and measurements were performed at laser intensities in the sample of >10 mW/mm^2. Experiments were performed with pipette resis-tances of 1–2 MΩ (cell attached) or 3–5 MΩ (whole cell; GB150F-8P, Scientific-Instruments, Hofheim, Germany) in a temperature controlled patch-chamber [22] allowing for patch clamp experiments at 34°C. The membrane potential was held at -100 mV and cells were illuminated for 100 ms. Once a gigaseal was established, photocurrents were recorded every 2 min for a maximal duration of 30 min. Cell-attached or whole-cell currents were low-pass filtered at 5 kHz and digitized at a sampling rate of 100 kHz. Data recordings were controlled by the Soft-ware Clampex 8.2 or 10.3 (Molecular Devices Co.). Data analysis was performed using Clamp-fit 10.3 (Molecular Devices Co.) and Origin (OriginLab Corporation, Northampton, USA). All data was normalized to the stationary photocurrent at t_0 (time = 0).

In cell-attached measurements the standard bath solution (140 mM NaCl, 2 mM $MgCl_2$, 2 mM $CaCl_2$, and 10 mM HEPES pH7.4) was also applied in the pipette but supplemented either with SDF1α, SDF1β or the inhibitor AMD3100. In whole-cell measurements a pipette solution consisting of 110 mM NaCl, 2 mM $MgCl_2$, 10 mM EGTA, and 10 mM HEPES pH 7.4 and the standard bath solution were used.

Cell capacitance measurements in native cells were carried out as described before [24]. Briefly, the capacitive currents during the voltage step were used to define the charges required

27
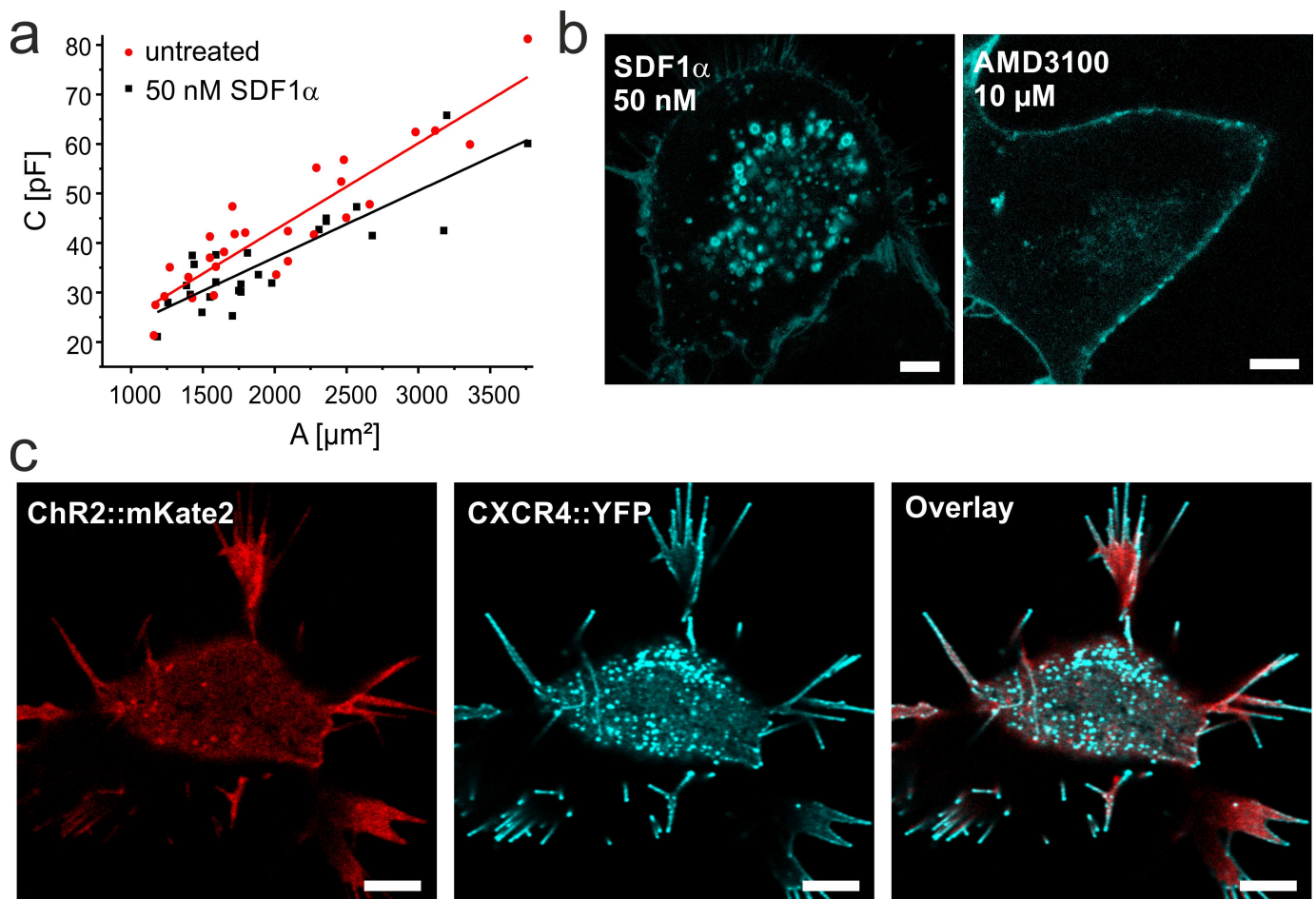
Fig 2. SDF1-mediated CXCR4-internalization in NG108-15 cells. a. Plot of cell capacitance (including stray capacitance) measured in whole cell configuration by patch-clamp technique against the membrane area. Cells were either not treated (red) or treated with 50 nM SDF1α (black) for >40 min. The membrane area was calculated from the measured cell diameter assuming a spherical shape of the cell. The specific cell capacitance (slope of the linear fit) decreases in presence of SDF1α. **b.** Confocal laser scanning micrographs of NG108-15 cells expressing CXCR4::eYFP in the presence of the inhibitor AMD3100 or the agonist SDF1α as indicated. While strong internalization is observed with SDF1α, only few vesicles are observed in presence of the inhibitor. **c.** Co-expression of CatCh::mKateA (red) and CXCR4::eYFP (cyan) in presence of 50 nM SDF1α. Note that after binding of SDF1α CXCR4 is internalized while CatCh mainly remains in the plasma membrane and is not directly affected by this growth factor (S3 Fig). Scale bars represent 5 µm.

doi:10.1371/journal.pone.0165344.g002

for the repolarization of the membrane and plotted against the membrane potential. The slope represents the sum of cell and stray capacitance (Fig 2(A)). The membrane surface of each cell was estimated by calculation from the radius assuming a spherical shape. The cell capacitance was plotted against the membrane area and fitted using linear regression. The slope represents the area-specific membrane capacitance.

Results

CXCR4::eYFP is internalized in NG-108-15 cells and HEK293 cells

For the functional characterization of tCXCR4/CatCh we chose the NG108-15 cell line, as it is suitable for patch clamp experiments and was successfully used in previous experiments with tandem proteins [13]. NG108-15 cells express endogenous CXCR4 [25] and SDF1-dependent internalization was investigated by capacitance measurements of native cells in whole cell

patch-clamp experiments (Fig 2(A)). The membrane capacitance of untreated NG108-15 cells and cells exposed to 50 nM SDF1α was compared. To determine the area-specific membrane capacitance, the respective cell surface was calculated from the radius assuming spherical cell shape. While the area-specific membrane capacitance was $1.72 \pm 0.14 \, \mu F/cm^2$ (n = 28) for untreated cells, the cell capacitance significantly ($\alpha < 0.05$, two-tailed student t-test) decreased to $1.35 \pm 0.16 \, \mu F/cm^2$ (n = 25) after incubation with 50 nM SDF1α for >40 min. The folding factor φ [26] describes the folding state of the membrane, reflecting microvilli and other membrane substructures. Thus, φ is expected to be higher when no internalization takes place. Indeed, assuming a specific membrane capacitance of $0.8 \, \mu F/cm^2$ φ values of 2.15 for untreated and 1.69 for treated cells were calculated. A similar, significant reduction of membrane capacitance was also observed in electrorotation experiments (S2 Fig) confirming our results.

CXCR4 is translocated via the clathrin-mediated endocytic pathway [17]. To visualize the SDF1α-induced internalization process, the NG108-15 cells were transiently transfected with CXCR4 tagged with yellow fluorescent protein (CXCR4::eYFP) and investigated by CLSM. Intense fluorescence in the membrane clearly indicated the successful expression of CXCR4::eYFP in NG108-15 cells (Fig 2(B) and 2(C)). After treatment with 50 nM SDF1α for 40 min, CXCR4::eYFP was partly internalized into small vesicles with diameters of 300–1500 nm (Fig 2 (B)). In contrast, when cells were treated with 10 μM of the antagonist AMD3100, the internalization was strongly reduced, indicating a functional CXCR4 internalization system in NG108-15 cells. Similar results could be obtained using HEK293 cells overexpressing CXCR4::eYFP (see Material and Methods; S4 Fig) as an alternative cell system.

The high activity of SDF1α-mediated internalization might lead to unspecific displacement of other membrane proteins. If the specificity of CXCR4 cargo selection in clathrin-coated pits could be impaired by overexpression of the membrane-bound light-gated cation channel Channelrhodopsin-2 (ChR2) it would eventually result in translocation of both proteins into endosomes and thus provide a strategy to localize ChR2 in intracellular vesicles. To test this hypothesis, fluorescently tagged ChR2 (CatCh::mKateA) was co-expressed together with CXCR4::eYFP in NG108-15 cells. As can be seen in the CLSM images, CatCh::mKateA is not substantially internalized upon addition of SDF1α (Fig 2(C); see also S3 Fig) but mainly remains in the membrane, while internalization of CXCR4::eYFP is not affected by the presence of CatCh.

The optochemokine tandem tCXCR4/CatCh is internalized in presence of SDF1α via clathrin-mediated endocytosis

In order to realize mutual internalization of CatCh and CXCR4, both proteins were combined in one functional tandem entity. The optochemokine tandem tCXCR4/CatCh (Fig 1(A)) was either expressed in NG108-15 (Fig 3) or HEK293 cells (S5 Fig). Similarly to earlier investigations of tandem proteins [13], the protein was expressed in one entity and not fragmented during the expression/trafficking process. This was shown by Western blot analysis of membrane proteins isolated from NG108-15 cells expressing tCXCR4/CatCh stained with anti-CXCR4 antibodies (S6 Fig). In agreement with the Western blot results we observed robust expression and localization of the YFP fluorescence in the cytoplasmic membrane for both mammalian cell types.

For our strategy it is fundamental that both 7TM-proteins preserve their function even when combined in one tandem protein. Thus, the functional tandem proteins should be internalized while CatCh should have unaltered kinetics and channel characteristics. The ability of the tandem to be internalized upon addition of SDF1α was shown in transiently transfected NG108-15 cells treated either with 50 nM SDF1 only, or with 10 μM AMD3100. CLSM images
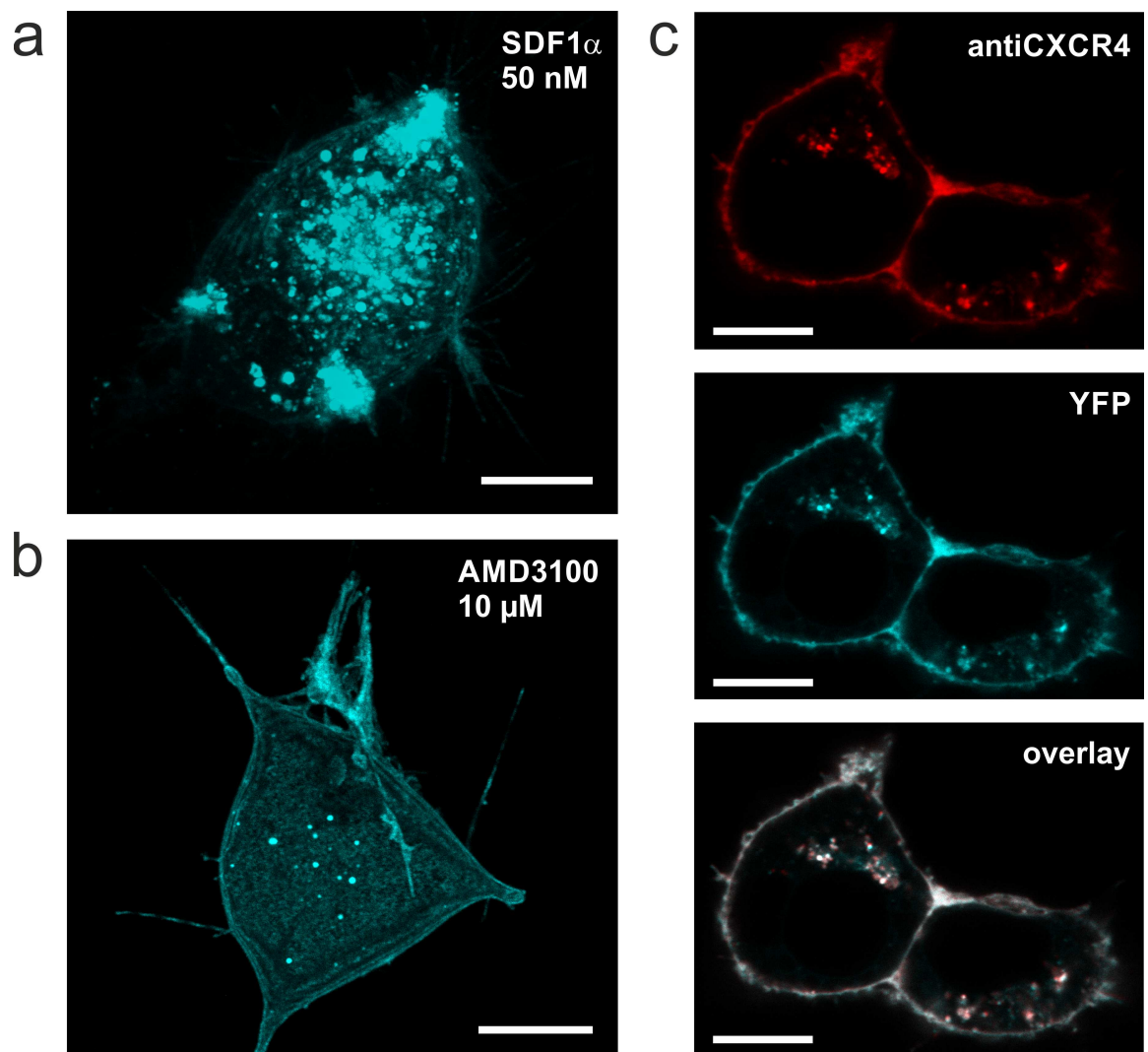
Fig 3. Confocal laser scanning micrographs of tCXCR4/CatCh protein in NG108-15 cells. a,b. Z-stack overlay of a typical tCXCR4/CatCh cell either treated with 50 nM SDF1α for 45 min (a) or with AMD3100 (b). The tandem construct is internalized by the action of SDF1α (similar to CXCR4 shown in Fig 2). **c.** Internalization of anti-CXCR4 antibody after immunoreaction with tCXCR4/CatCh in cells exposed to 50 nM SDF1α. The fluorescence signal of anti-CXCR4 (top, red) and tCXCR4/CatCh (middle, cyan) co-localize to a great extend as can be seen from white areas in the overlay (bottom). Scale bars represent 10 μm.

doi:10.1371/journal.pone.0165344.g003

clearly showed that after 40 min in presence of SDF1α the majority of tCXCR4/CatCh proteins was located in intracellular vesicles (Fig 3(A)), putative endosomes. The number of vesicles was strongly reduced when cells were treated with the antagonist AMD3100 (Fig 3(B)). Thus, in tCXCR4/CatCh the internalization feature of CXCR4 was not impaired by the additional C-terminally fused CatCh. In average the tCXCR4/CatCh vesicles were bigger (up to 4–5 μm) than CXCR4::eYFP vesicles (<2 μm).

To support our assumption that the vesicles represent endosomes internalized from the membrane, we used a functional CXCR4 specific antibody labelled with red-fluorescent dye (Anti-Mouse CD184 PE-eFluor 610; eBioscience). Immediately after the treatment, immuno-labeled CXCR4 was only found in the cytoplasmic membrane. After several hours of

incubation it was also localized in a number of intracellularly located vesicles. These vesicles exhibited both red and green fluorescence indicating successful translocation of the tandem protein from the plasma membrane (Fig 3(C)). Strikingly, the antibody did not show any immunoreaction with endogenous NG108-15 and HEK293 CXCR4 neither in microscopic analyses nor in Western blot experiments (S6 Fig) thus allowing for specific detection of the heterologous CXCR4 constructs. The *in vivo* immunostaining of heterologous CXCR4 showed that the majority of the intracellular, green-fluorescent vesicles originated from the cytoplasmic membrane (Fig 3(C)), further supporting the assumption that these intracellular vesicles represent endosomes.

To verify this, NG108-15 tCXCR4/CatCh cells were transfected with fluorescent early-endosome marker Rab5a-RFP [27,28]. Indeed, vesicles that exhibited green and red fluorescence could be observed indicating the internalization of tCXCR4/CatCh into endosomes (data not shown). However, the overall transduction efficiency of the baculovirus Rab5a-RFP construct in NG108-15 cells was very low. Therefore, a similar experiment was performed in stable HEK293 FlpIn-T-Rex™ (Invitrogen) cell lines expressing either CXCR4::eYFP or the tCXCR4/CatCh tandem. Rab5a-RFP colocalized with either CXCR4::eYFP or the tCXCR4/CatCh tandem (S7 Fig), confirming the results in NG108-15 cells. Also alexa647-labeled transferrin, a compound known to be internalized in endosomes [29], was observed to cluster in the same regions as the tandem constructs or Rab5a, hence giving more evidence that the optochemokine tandem is internalized via clathrin-mediated endocytosis into early endosomes (S7 Fig).

CatCh is functional in tCXCR4/CatCh

Once tCXCR4/CatCh is internalized into the cell, it is designed to release cations upon illumination. In order to assess whether CatCh is fully functional in tCXCR4/CatCh, patch-clamp experiments using NG108-15 cells expressing either tCXCR4/CatCh or CatCh::eYFP were performed. After illumination (diode pumped solid-state laser; 473 nm; saturating conditions: >10 mW/mm^2) we observed the typical CatCh signal [12] in both proteins (Fig 4(A)): A short transient peak, which was followed by a stationary current that decayed with a time constant of 16 ± 3 ms (S8 Fig) indicating unchanged kinetics of CatCh in the tandem protein. The mean current density at -100 mV measured in whole cell conditions in NG108-15 cells was -67 pA/pF (tCXCR4/CatCh; n = 11, s.e.m = 6) and -125 pA/pF (CatCh; n = 14, s.e.m. = 8). Thus, we conclude that CatCh is functionally expressed in the optochemokine tandem and that the expression level of the tandem construct is slightly reduced in comparison to CatCh only.

The functional expression of CatCh allowed us to electrophysiologically monitor the internalization process of tCXCR4/CatCh. In order to avoid possible negative effects of cytosol replacement by pipette solution on the internalization process, the cell attached patch-clamp mode was used ensuring the complete preservation of the cytosol. In these experiments the pipette solution was identical with the extracellular solution supplemented either with 50 nM SDF1α only or in addition to 10 μM AMD3100. The light-triggered channel response was measured every 2 min within a time course of 30 min at about 34°C (Fig 4(B)).

In the presence of SDF1α the signal recorded from tCXCR4/CatCh cells decreased by about 60% within half an hour. In contrast, when the action of SDF1α was impaired by its antagonist AMD3100 the signal decreased only by about 30%. In accordance, cells expressing CatCh::eYFP showed only an initial signal reduction by 15–20% and not further reduction. Thus, also the electrophysiological data clearly indicate functional SDF1 dependent internalization of the optochemokine tandem. We investigated the role of SDF1 splicing variant [30] and the agonist concentration on the internalization behavior of tCXCR4/CatCh. However, no significant

PLOS ONE

a

b
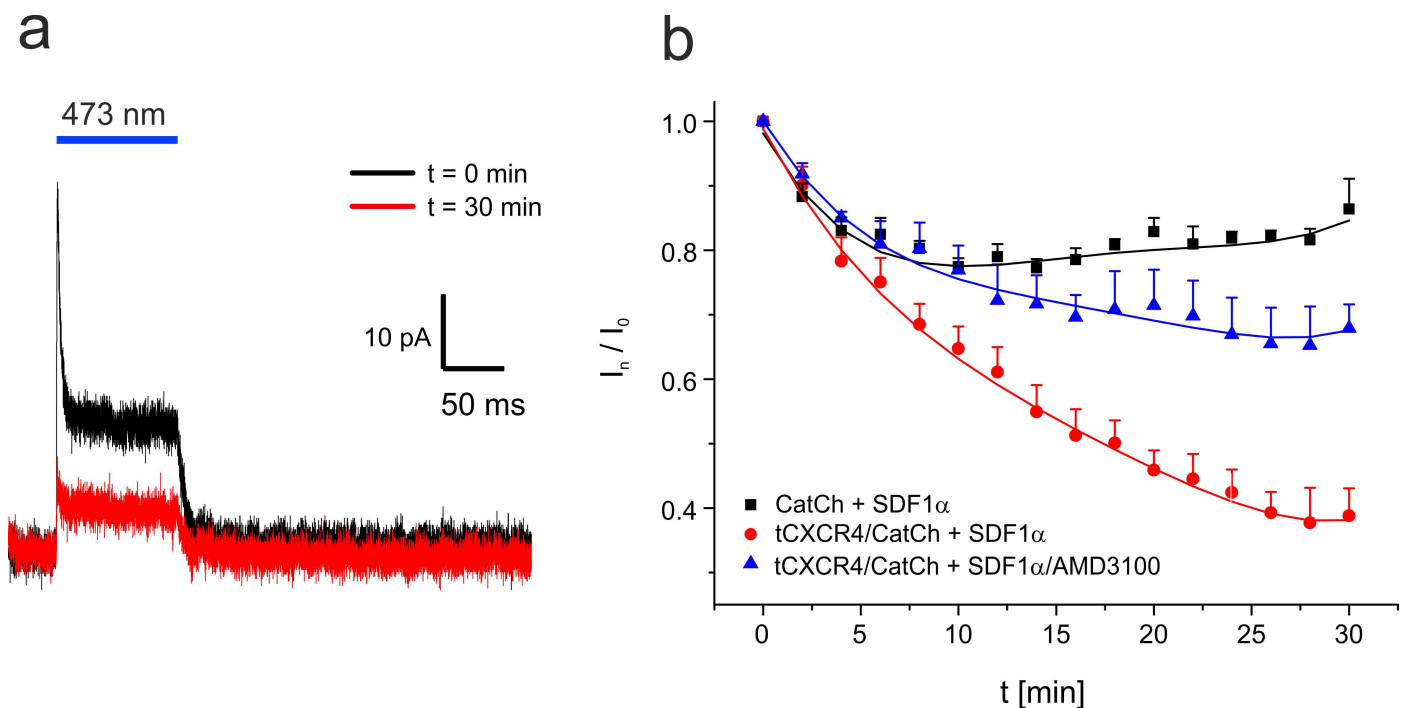
Fig 4. Patch-clamp investigation of the optochemokine tandem in cell attached configuration at 34°C. The pipette solution was supplemented with 50 nM SDF1α. **a.** Typical current trace recorded at an applied membrane potential of -100 mV. Light-dependent signal of tCXCR4/CatCh directly after the sealing process and 30 min later. During that time the cell was illuminated every two minutes for 100 ms. **b.** Time course of the relative tCXCR4/CatCh current in presence of SDF1α (square, 5 cells) or SDF1α and the inhibitor AMD3100 (triangle, 3 cells), and CatCh in presence of SDF1α (circle, 4 cells). Mean values are given, bars represent the standard error.

doi:10.1371/journal.pone.0165344.g004

differences in internalization kinetics between SDF1β and SDF1β or 50 nM and 100 nM SDF1α, respectively, could be observed (S9 Fig).

Optochemokine tandem endosomes release calcium into the cytosol upon illumination

Upon SDF1α incubation and illumination of tCXCR4/CatCh expressing cells we expect intracellular Ca^{2+} signals to be generated by ion efflux from endosomes. In order to gain more information on the Ca^{2+} transfer inside the cells, we performed Ca^{2+} imaging experiments. In these experiments we used a variant of tCXCR4/CatCh, in the following referred to as tCXCR4/CatCh(D156C), in which *Asp*156 of CatCh was mutated to *Cys*. This mutation alters the gating behavior of the channel [31] and was recently used in optogenetic experiments with *Drosophila*, renamed as ChR2-XXL due to its prolonged open state and improved expression [32]. These advantages were also observed in NG108-15 cells and allowed us to trigger tCXCR4/CatCh(D156C) with very short light pulses with a scanning laser during CLSM measurements.

NG108-15 cells either expressing CXCR4::eYFP or tCXCR4/CatCh(D156C) tandem were exposed to 5 μM rhod2 (not membrane permeable) and 50 nM SDF1α in the presence of physiological extracellular Ca^{2+} and subsequently analyzed using CLSM in absence of extracellular Ca^{2+} (Fig 5(A) and 5(B)). Within 60 s after illumination (488 nm laser) the red fluorescence of the tCXCR4/CatCh(D156C) endosomes decreased much faster and in a non-linear fashion compared to endosomes expressing CXCR4 only (Fig 5(C); significant difference after 8s). This observation indicates an accelerated reduction of the endosomal Ca^{2+} concentration mediated

32
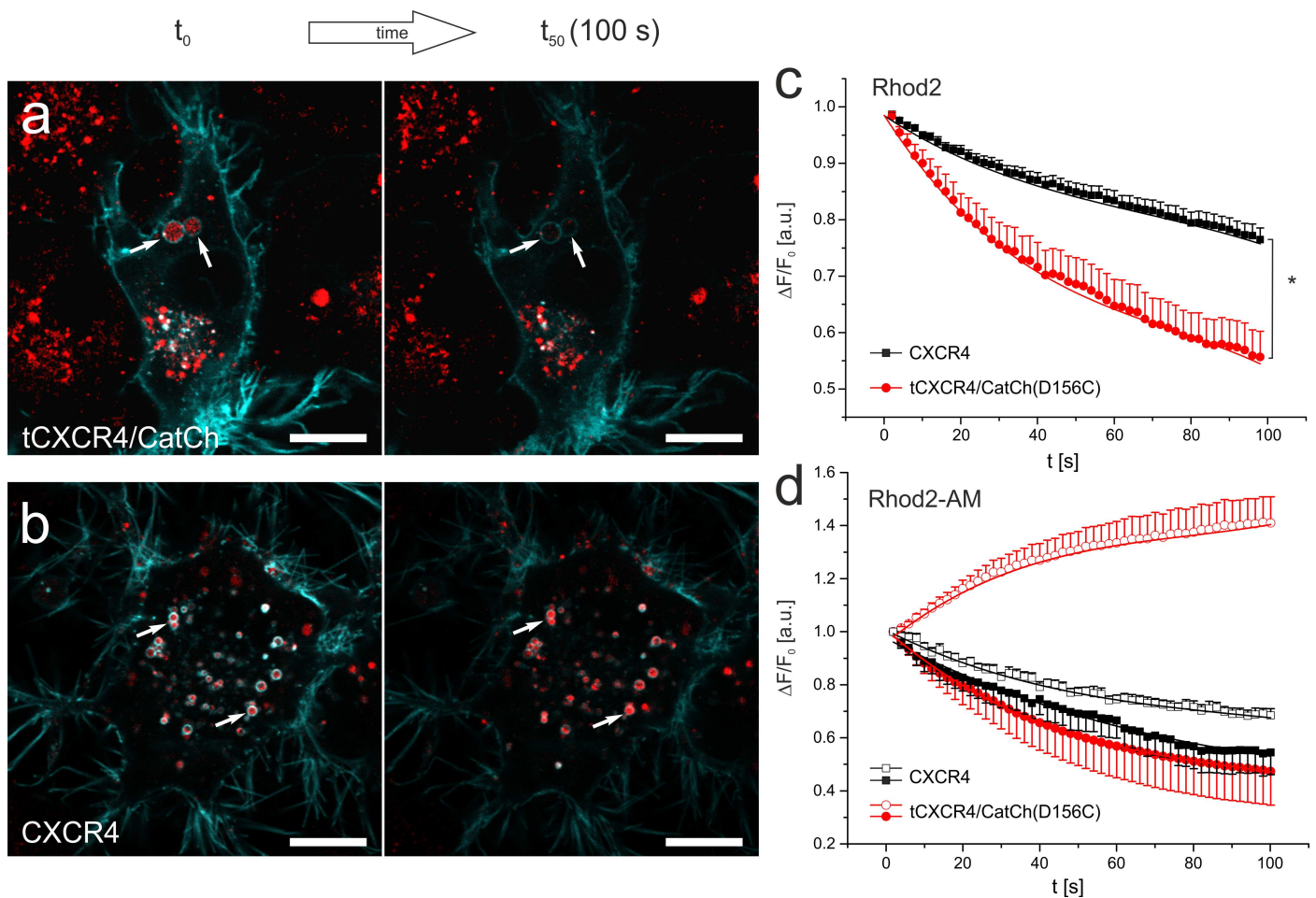
Fig 5. Intracellular, light-induced Ca^{2+}-signaling mediated by optochemokine tandem-endosomes. a,b. CLSM micrographs of NG108-15 expressing the tCXCR4/CatCh(D156C) (a, cyan) or CXCR4::eYFP (b, cyan) stained with rhod2 (red). White arrows highlight such endosomes that express the respective membrane protein and are loaded with rhod2. Note that the rhod2 intensity decreases in tCXCR4/CatCh(D156C) to a larger extent than in CXCR4::eYFP endosomes. **c.** Time course of the rhod2 fluorescence of endosomes exhibiting tCXCR4/CatCh(D156C) (17 cells, mean s.e.m) or CXCR4 (21 cells) as identified by their fluorescence. Upon blue light activation rhod2-fluorescence non-linearly decreases in endosomes with tandem construct, while endosomes containing CXCR4 in their membrane show only moderate, nearly linear decrease of rhod2 fluorescence. **d.** Time course of rhod2 fluorescence in endosomes (filled symbols) and nuclei (empty symbols) as a measure for small changes in the cytosolic Ca^{2+} [33] of cells loaded with the membrane permeable rhod2AM-derivate (See also S11 Fig). Note that in tCXCR4/CatCh(D156C) cells (red, n = 7, mean + s.e.m) an increase in cytosolic Ca^{2+} concentration was observed while only fluorescence decrease was observed in CXCR4-expressing cells (black, n = 8, mean + s.e.m.). All rhod2-experiments were performed in absence of extracellular Ca^{2+}. Scale bars represent 10 µm.

doi:10.1371/journal.pone.0165344.g005

by the action of CatCh in the tandem construct. In accordance with this assumption we did not observe any difference when CatCh was illuminated with 640 nm laser (no excitation of CatCh; S10 Fig). In order to discover whether a release of Ca^{2+} from the endosomes could notably change the Ca^{2+} concentration in the cytosol, we performed imaging experiments with cells loaded with 2 µM rhod2-AM. In each cell the fluorescence intensity within one representative endosome and the nucleus (as a measure for small changes in the cytosolic Ca^{2+} concentration [33]) were compared over time (Fig 5(D); S11 Fig). Indeed, in tCXCR4/CatCh(D156C) endosomes we observed a decrease of fluorescence while the fluorescence in the nucleus increased. In contrast, the CXCR4 cells exhibited a decrease of fluorescence in nucleus as well as endosomes.

33

Discussion

To date there is no report about functional expression of intracellularly acting, light-controlled Ca^{2+} regulators. This is due to the absence of suitable strategies for the intracellular expression of light-switchable membrane-transport proteins. The light-induced release of Ca^{2+} from intracellular calcium stores would enable the precise regulation of physiological processes and thus are expected to be of extreme interest for cell biologists.

Herein, we established a novel approach for the light-controlled, intracellular manipulation of the second messenger Ca^{2+} by re-engineering our previous invention, a gene cassette for stoichiometric expression of two rhodopsins [13]. The novel optochemokine tandem was designed to shuttle the tool from the plasma membrane into intracellular organelles by ligand-induced endocytosis, to monitor the displacement by decreasing ion-channel activity, and to generate intracellular Ca^{2+} elevation by light. N-terminally the chemokine receptor CXCR4 was set to take advantage of the well-known clathrin-mediated endocytosis [17,30] and to traffic the optochemokine tandem into intracellular organelles in a SDF1-dependent manner. As optogenetic actuator the CatCh mutant of the light-gated cation channel ChR2 was placed c-terminally. This mutant holds an about 6-fold enhanced Ca^{2+} permeability [12] compared to the wild type protein. In addition, the light-sensitivity of this actuator was further improved by the point mutation D156C [31,32], which exhibits extra high expression and a long open state.

Two mammalian cell lines were selected for the characterization of this novel optophysiological tool after testing for the SDF1-dependent internalization of CXCR4 by capacitance measurements and fluorescence microscopy (Fig 2 and S4 Fig). Our data clearly shows that tCXCR4/CatCh was functionally expressed in NG108-15 and HEK293 cells, that the activation of CXCR4 by SDF1 in tCXCR4/CatCh led to the internalization of the whole tandem construct by endocytosis via the clathrin-mediated endosome pathway, and that the optophysiological tool could generate intracellular Ca^{2+}-elevation upon light-induced channel opening. In contrast, co-expressed single fluorescent CXCR4 and CatCh constructs did not lead to any substantial internalization of the cation channel.

Similar to other rhodopsin-tandem proteins [13] tCXCR4/CatCh was expressed as one single fluorescent entity (S6 Fig). From the whole-cell patch-clamp data we conclude that the opotchemokine tandem in contrast to other previous tandems was expressed to a similar extent as CatCh::eYFP. tCXCR4/CatCh located both in the plasma membrane and in intracellular vesicles. By immune-labeling with a red-fluorescent CXCR4-specific antibody we identified the majority of intracellular vesicles as tCXCR4/CatCh endosomes, which had been internalized from the plasma membrane within several hours after staining of the plasma membrane (Fig 3 (C)). Thus, internalization behavior of tCXCR4/CatCh was similar as in the pure CXCR4::eYFP constructs (Fig 2(B)). The internalization process could, to a great extent, be inhibited by the specific antagonist AMD3100 which blocks SDF1-binding [20]. In addition, our experiments with the endosome markers Rab5 and transferrin clearly showed that the internalization process is realized via the well-conserved clathrin-pathway [34] (S7 Fig).

Also the kinetics of the internalization process observed in patch clamp experiments analyzing the photocurrent over time was in accordance with previously published data measured in other cell types [35,36]. Interestingly, with this sensitive method we could not detect any significant difference between the splicing variant alpha or beta of the SDF1 ligand [30] (S9 Fig), suggesting successful activation of the tool by both variants. SDF1-specificity of endocytosis was further supported by the fact that in presence of the antagonist AMD3100 the internalization was strongly reduced (CatCh-signal decrease of ~30%). As in CatCh alone a similar decrease (~20%) was observed but no displacement was observed in the imaging data (S3 Fig), we assume that the major part of the slight current decrease of tCXCR4/CatCh most likely

corresponded to run-down effects in CatCh. Such initial current decrease can frequently be noticed in patch-clamp experiments under saturating light conditions.

Once internalized, the tCXCR4/CatCh endosomes migrate into the cell and serve as Ca^{2+} stores that can release Ca^{2+} into the cytosol upon blue light illumination. Assuming a mean radius of 500 nm for endosomes (Figs 2(B), 5(A) and 5(B)), the single channel conductance of CatCh of 140 fS [12], and a mean number [24] of 500 channel proteins per μm^2 we can estimate the amount of Ca^{2+} ions released by each endosome. During the endocytosis process a substantial amount of Ca^{2+} can enter the cell and the vesicles are filled with extracellular medium. Once internalized, Ca^{2+} is quickly released from the endosome, which in turn is acidified [16,37]. The Ca^{2+} concentrations measured inside the endosomes differ strongly [38–40]. Assuming a Ca^{2+} concentration of 40 μM [10] the endosome contains around 12600 Ca^{2+} ions which could be released with a maximal rate of $7^{*}10^{6}$ s^{-1} (see complete calculation in S1 Text). It has to be taken into account that, though CatCh provides increased permeability for Ca^{2+}, other cations as sodium and protons have higher permeability and therefore might interfere with the Ca^{2+} signal. During endosome maturation the Ca^{2+} content increases again [39], thus allowing for an intensified light-induced Ca^{2+} signal by late endosomes. Though Albrecht et al. [39] postulate a minor role of endosomes in Ca^{2+} signal shaping, in comparison to mitochondria and ER, our theoretical considerations and experiments suggest endosomes as potential Ca^{2+} source for optophysiological experiments.

In accordance with our estimates, in intra-endosomal Ca^{2+} measurements (Fig 5A–5C) a non-linear decrease in rhod2 fluorescence was observed upon blue-light illumination in tCXCR4/CatCh endosomes, suggesting a release of Ca^{2+} ions into the cytosol, while only a slight linear decrease was observed in endosomes with CXCR4 alone. Indeed, measurements with rhod2-AM further supported the finding that the release of Ca^{2+} from the endosomes leads to an increase of cytosolic Ca^{2+} (Fig 5(D)) as the effect of tCXCR4/CatCh was quite pronounced though it was measured in absence of extracellular Ca^{2+}. These measurements were performed in the presence of the CXCR4 antagonist AMD3100 in order to reduce the native signaling activity of CXCR4. Stimulation of CXCR4 will activate heterotrimeric G_i protein pathways and thus might affect the phosphorylation status of proteins or even influence the activity of Ca^{2+} channels [41–43]. Therefore, one is obligated to perform accurate control measurements deciphering the signals potentially induced by CXCR4 from those induced by Ca^{2+} elevation via the optochemokine tandem. This is especially important as due to the expression of the optochemokine tandem the number of CXCR4 copies in the cell increases. Further work is needed to optimize the tandem function for its use in a certain physiological process, e.g. by substituting CXCR4 by other class A GPCRs or by introducing mutations that affect the GPCRs function [44]. Furthermore, cell specific calcium release would require fine tuning of the tandem-signal activation process for the cell type used. Nevertheless, in our study the increment of cytosolic Ca^{2+} after illumination of the optochemokine tandem was clearly dependent on blue light (activation of ChR2) while with red light (no ChR2 activity) no difference was observed when compared with cells expressing CXCR4 only (S10 Fig).

Conclusions

Summarizing our findings, the novel optophysiological tool combines two different features in one functional protein. First, the internalization pattern of distinct GPCRs can be followed up by the activity of CatCh in patch-clamp experiments. Thus, combining unknown or less investigated GPCRs with ChR2 in the tandem cassette would provide new insights into their internalization characteristics. Second, the intracellular Ca^{2+} concentration can be manipulate by light-triggered Ca^{2+} release from endosomes. In this respect it is important to emphasize that

the tCXCR4/CatCh approach could be extended to combine different GPCRs with other (e.g. red-light sensitive) channelrhodopsins or even with various light-gated ion pumps suited for the modulation of intracellular pH, as recently done in synapses [45]. Time-resolved modulation of the Ca^{2+} concentration by light could be used to induce Ca^{2+}-dependent processes like gating of Ca^{2+}-activated Ca^{2+} channels, membrane fusion, secretion, induction of gene expression, and cell proliferation [8,46] or even cell death [47,48]. Indeed, in tCXCR4/CatCh expressing NG108-15 cells, as shown in S12 Fig, cell death was induced under physiological conditions by blue light reflecting its potential usefulness in the treatment of solid tumors. This topic will be subject of ensuing study to unravel a potential role of this optophysiological tool as a strategy for the induction of cell death of cancer cells upon light irradiation.

Supporting Information

S1 Fig. Cell cycle analysis of NG108-15 cells determined by flow cytometry. Illustration of the characteristic distribution of cells across the cell cycle suggesting absence of any chromosomal aberrant subpopulations. Experiments were performed with a BD FACSCanto™ II (BD Biosciences). The cells were detached by trypsination and centrifuged at 20°C and 400 g for 5 min. $5 \cdot 10^5$ cells were resuspended in DNA-buffer (100 mM Tris pH7.4, 154 mM NaCl, 1 mM $CaCl_2$, 0.5 mM $MgCl_2$, 0.2% BSA, 0.1% NP40, RNase A 100 U/ml and propidium iodide 10 μg/ ml) and incubated for one hour at 4°C in the dark. Excitation of propidium iodide was performed with the 488 nm laser line. Data analysis and visualisation was performed with Flowing Software (version 2.5.1 Turku Centre for Biotechnology).
(PDF)

S2 Fig. Electrorotation data of NG108-15 cells before (red) and after (black) treatment with SDF1α. C_m was calculated to be 2.46 ± 0.19 μF/cm^2 (untreated cells, n = 366) and 1.89 ± 0.08 μF/cm^2 (treated, n = 345), reflecting a significant decrease of the specific membrane capacitance upon addition of SDF1 (two tailed student t-test, alpha<0.5). Due to methodical reasons the absolute C_m values are slightly higher than in patch-clamp experiments (Fig 2), whereas the relative decrease is similar in both methods.
(PDF)

S3 Fig. Confocal laser scanning micrographs of NG108-15 cells expressing ChR2::eYFP. Cells were imaged in presence of the CXCR4 inhibitor AMD3100 (left) or the activator SDF1α (right). Note that upon addition of SDF1 no substantial internalization of ChR2 could be observed. Scale bar represents 10 μm.
(PDF)

S4 Fig. HEK293 CXCR4::eYFP cell line. Cells were incubated for 24 hours in media supplemented with either 10 μM AMD3100 (left) or 50 nM SDF1α (right). Strong internalization was observed in presence of the agonist but not the antagonist. Scale bar represents 20 μm.
(PDF)

S5 Fig. HEK293 FlipIn-T-Rex tCXCR4/CatCh cell line. a. Confocal laser scanning micrographs showing co localisation of tCXCR4/CatCh (cyan) and antiCXCR4 antibody (red) after treatment with 50 nM SDF1α. White bar represents 5 μm. **b.** Patch-clamp experiments. Voltage step protocol in whole cell mode, showing full functionality of the CatCh-Protein in tCXCR4/CatCh.
(PDF)

S6 Fig. Western blot analysis with anti-CXCR4 antibody. Membrane fragments were isolated from NG108-15 cells expressing either CXCR4::YFP, tCXCR4/CatCh, or no heterologous

protein (control) as indicated.
(PDF)

S7 Fig. CLSM analysis of endocytosis in HEK293 cells expressing tCXCR4/CatCh. a. Coexpression of tCXCR4/CatCh (cyan) and the endosome marker Rab5-RFP. **b.** Cells were exposed to Alexa647-transferrin (red) which is internalised into endosomes via clathrin-mediated endocytosis. Note, that both proteins colocalize with tCXCR4/CatCh indicating the endosome-nature of the observed intracellular vesicles. Scale bars represent 10 μm.
(PDF)

S8 Fig. Time course of the closing kinetics of CatCh (black) and tCXCR4/CatCh (red). Patch-clamp experiments were performed at -100 mV membrane potential after blue light (473 nm; 200 ms) illumination in cell attached mode in presence of 50 nm SDF1α at 34–36°C. Mean τ_{off} and standard error of up to 10 cells (CatCh) and up to 14 cells (tCXCR4/CatCh) are given. There was no significant difference observable in the behavior of CatCh in the tandem construct compared to the protein alone. Note, that time constant differs from the published [12] value of 16 ms due to higher temperatures.
(PDF)

S9 Fig. Dependency of the tCXCR4/CatCh internalization on concentration (a) and splicing variant (b) of the chemokine ligand. Data were obtained in cell attached Patch-clamp measurements of NG108-15 cells expressing tCXCR4/CatCh protein. **a.** When supplying 100 nM SDF1α instead of 50 nM the internalization efficiency did not significantly increase. Therefore, in our experiments we used 50 nM SDF1α. Mean values and standard error of 5 cells (50 nM SDF1α) and 3 cells (100 nM SDF1α) are given. **b.** No significant difference was observed between SDF1α (black) and SDF1β (red). Mean values and standard error of 5 cells (SDF1α) and 3 cells (SDF1β) are given.
(PDF)

S10 Fig. Control experiment showing the time course of rhod2 fluorescence in endosomes exhibiting tCXCR4/CatCh(D156C) (7 cells, mean s.e.m) or CXCR4 (10 cells) upon red light illumination. The conditions were similar to the experiment depicted in Fig 5C but repetitive red light illumination (639 nm 5mW 4%) was used instead of blue light to avoid activation of CatCh.
(PDF)

S11 Fig. Calcium-imaging of NG108-15 cells loaded with the calcium-dye rhod2-AM. Cells were transfected with tCXCR4/CatCh(D156C) (upper row, cyan) or CXCR4::eYFP (lower row, cyan) and pre-incubated with 50 nM SDF1α 24 h after expression before they were additionally loaded with the dye. Images were acquired by cLSM in absence of extracellular Ca^{2+}. Each figure shows the fluorescence intensity of rhod2-AM (red) in ROIs containing either endosomes (white) or nucleus (magenta). Scale bars represent 10 μm. The graph below each photograph represents the time course of normalised fluorescence intensity $\Delta F/F_0$ within the respective ROIs as indicated. Averaged data of 5 cells are given in main document Fig 5D. See also S1 Movie.
(PDF)

S12 Fig. Light-induced cell death in NG108-15 cells expressing tCXCR4/CatCh or CXCR4. **a.** Obvious changes in cell morphology were taken as criterion to distinguish dead and alive fluorescent cells. While healthy viable cell did not lose their membrane integrity, dead cells were recognized by membrane blebbing, cell shrinkage, and lose of cellular material (red arrows). **b.** Cells were illuminated with a light intensity of about 5 mW/ mm^2 for 20 min

37

followed by a subsequent dark exposure time of 40 min and the ratio of dead cells was followed over the time **c.** After 60 min the tCXCR4/CatCh cells showed a significant increase (two tailed student t-test, a$<$0.05) in the number of dead cells upon illumination as compared with CXCR4-expressing cells.
(PDF)

S1 Movie. Intracellular, light-induced Ca^{2+}-signaling. Ca^{2+} signals were mediated in NG108-15 cells by tCXCR4/CatCh (green) endosomes visualized by the calcium sensitive dye Rhod-d2-AM (red) and recorded with a confocal laser scanning microscope. In order to improve the signal to noise ratio of the rhod2 channel, the images were subjected to the Fiji mean filter (value = 1) and rhod2 intensity values are depicted on a logarithmic scale.
(MP4)

S1 Text. Estimation of endosomal Ca^{2+} content and release rate.
(PDF)

Acknowledgments

Author Contributions

Conceptualization: PGW EB UT FS.

Data curation: JS KF JW PGW UT.

Formal analysis: KF JS JW UT.

Funding acquisition: EB.

Investigation: KF JS JW FS UT.

Methodology: JS KF PGW UT.

Project administration: UT.

Resources: EB UT.

Software: JS FS.

Supervision: EB UT.

Validation: KF JS JW FS UT.

Visualization: UT FS.

Writing – original draft: UT.

Writing – review & editing: EB KF JW FS JS PGW UT.

References

1. Busskamp V, Picaud S, Sahel JA, Roska B. Optogenetic therapy for retinitis pigmentosa. Gene Ther. 2011; 19: 169–175. doi: 10.1038/gt.2011.155 PMID: 21993174

2. Xu Y, Hyun YM, Lim K, Lee H, Cummings RJ, Gerber SA, et al. Optogenetic control of chemokine receptor signal and T-cell migration. Proc Natl Acad Sci U S A. 2014; 111: 6371–6376. doi: 10.1073/pnas.1319296111 PMID: 24733886

3. Chernet BT, Adams DS, Lobikin M, Levin M. Use of genetically encoded, light-gated ion translocators to control tumorigenesis. Oncotarget. 2016; 7: 19575–19588. doi: 10.18632/oncotarget.8036 PMID: 26988909

4. Adamantidis AR, Arber S, Bains JS, Bamberg E, Bonci A, Buzsáki G, et al. Optogenetics: 10 years after ChR2 in neurons—views from the community. Nat Neurosci. 2015; 18: 1202–1212. doi: 10.1038/nn.4106 PMID: 26308981

5. Ishii T, Sato K, Kakumoto T, Miura S, Touhara K, Takeuchi S, et al. Light generation of intracellular Ca^{2+} signals by a genetically encoded protein BACCS. Nat Commun. 2015; 6: 8021. doi: 10.1038/ncomms9021 PMID: 26282514

6. Kyung T, Lee S, Kim JE, Cho T, Park H, Jeong Y-M, et al. Optogenetic control of endogenous Ca^{2+} channels in vivo. Nat Biotechnol. 2015; 33: 1092–1096. doi: 10.1038/nbt.3350 PMID: 26368050

7. Li D, Hérault K, Isacoff EY, Oheim M, Ropert N. Optogenetic activation of LiGluR-expressing astrocytes evokes anion channel-mediated glutamate release. J Physiol. 2012; 590: 855–873. doi: 10.1113/jphysiol.2011.219345 PMID: 22219341

8. Brini M, Calì T, Ottolini D, Carafoli E, Cali T, Ottolini D, et al. Intracellular calcium homeostasis and signaling. Met Ions Life Sci. 2013; 12: 119–168. doi: 10.1007/978-94-007-5561-1_5 PMID: 23595672

9. Gilabert JA. Cytoplasmic calcium buffering. Adv Exp Med Biol. 2012; 740: 483–498. doi: 10.1007/978-94-007-2888-2_20 PMID: 22453955

10. Lloyd-Evans E, Waller-Evans H, Peterneva K, Platt FM. Endolysosomal calcium regulation and disease. Biochem Soc Trans. 2010; 38: 1458–1464. doi: 10.1042/BST0381458 PMID: 21118107

11. Nagel G, Szellas T, Huhn W, Kateriya S, Adeishvili N, Berthold P, et al. Channelrhodopsin-2, a directly light-gated cation-selective membrane channel. Proc Natl Acad Sci U S A. 2003; 100: 13940–13945. doi: 10.1073/pnas.1936192100 PMID: 14615590

12. Kleinlogel S, Feldbauer K, Dempski RE, Fotis H, Wood PG, Bamann C, et al. Ultra light-sensitive and fast neuronal activation with the Ca^{2+}-permeable channelrhodopsin CatCh. Nat Neurosci. 2011; 14: 513–518. doi: 10.1038/nn.2776 PMID: 21399632

13. Kleinlogel S, Terpitz U, Legrum B, Gökbuget D, Boyden ES, Bamann C, et al. A gene-fusion strategy for stoichiometric and co-localized expression of light-gated membrane proteins. Nat Methods. 2011; 8: 1083–1088. doi: 10.1038/nmeth.1766 PMID: 22056675

14. Lundstrom K. An overview on GPCRs and drug discovery: structure-based drug design and structural biology on GPCRs. Methods Mol Biol. 2009; 552: 51–66. doi: 10.1007/978-1-60327-317-6_4 PMID: 19513641

15. Marchese A. Endocytic trafficking of chemokine receptors. Curr Opin Cell Biol. 2014; 27: 72–77. doi: 10.1016/j.ceb.2013.11.011 PMID: 24680433

16. Andersen CBF, Moestrup SK. How calcium makes endocytic receptors attractive. Trends Biochem Sci. Elsevier Ltd; 2014; 39: 82–90. doi: 10.1016/j.tibs.2013.12.003 PMID: 24393667

17. Furusato B, Mohamed A, Uhlén M, Rhim JS. CXCR4 and cancer. Pathol Int. 2010; 60: 497–505. doi: 10.1111/j.1440-1827.2010.02548.x PMID: 20594270

18. Arnolds KL, Spencer J V. CXCR4: a virus's best friend? Infect Genet Evol. 2014; 25: 146–156. doi: 10.1016/j.meegid.2014.04.018 PMID: 24793563

19. Dorsam RT, Gutkind JS. G-protein-coupled receptors and cancer. Nat Rev Cancer. 2007; 7: 79–94. doi: 10.1038/nrc2069 PMID: 17251915

20. Hatse S, Princen K, Bridger G, De Clercq E, Schols D. Chemokine receptor inhibition by AMD3100 is strictly confined to CXCR4. FEBS Lett. 2002; 527: 255–262. doi: 10.1016/S0014-5793(02)03143-5 PMID: 12220670

21. Schindelin J, Arganda-Carreras I, Frise E, Kaynig V, Longair M, Pietzsch T, et al. Fiji: an open-source platform for biological-image analysis. Nat Methods. 2012; 9: 676–682. doi: 10.1038/nmeth.2019 PMID: 22743772

22. Feldbauer K, Zimmermann D, Pintschovius V, Spitz J, Bamann C, Bamberg E. Channelrhodopsin-2 is a leaky proton pump. Proc Natl Acad Sci U S A. 2009; 106: 12317–12322. doi: 10.1073/pnas.0905852106 PMID: 19590013

23. García-Martínez J, Brunk M, Avalos J, Terpitz U. The CarO rhodopsin of the fungus *Fusarium fujikuroi* is a light-driven proton pump that retards spore germination. Sci Rep. 2015; 5: 7798. doi: 10.1038/srep07798 PMID: 25589426

39

24. Zimmermann D, Zhou A, Kiesel M, Feldbauer K, Terpitz U, Haase W, et al. Effects on capacitance by overexpression of membrane proteins. Biochem Biophys Res Commun. 2008; 369: 1022–1026. doi: 10.1016/j.bbrc.2008.02.153 PMID: 18331832

25. Ronjat M, Kiyonaka S, Barbado M, De Waard M, Mori Y. Nuclear life of the voltage-gated Cacnb4 sub-unit and its role in gene transcription regulation. Channels. 2013; 7: 119–125. doi: 10.4161/chan.23895 PMID: 23511121

26. Gascoyne PRC, Shim S, Noshari J, Becker FF, Stemke-Hale K. Correlations between the dielectric properties and exterior morphology of cells revealed by dielectrophoretic field-flow fractionation. Electrophoresis. 2013; 34: 1042–1050. doi: 10.1002/elps.201200496 PMID: 23172680

27. Zerial M, McBride H. Rab proteins as membrane organizers. Nat Rev Mol Cell Biol. 2001; 2: 107–117. doi: 10.1038/35052055 PMID: 11252952

28. Seachrist JL, Ferguson SSG. Regulation of G protein-coupled receptor endocytosis and trafficking by Rab GTPases. Life Sci. 2003; 74: 225–235. doi: 10.1016/j.lfs.2003.09.009 PMID: 14607250

29. Aisen P. Transferrin receptor 1. Int J Biochem Cell Biol. 2004; 36: 2137–2143. doi: 10.1016/j.biocel.2004.02.007 PMID: 15313461

30. Janowski M. Functional diversity of SDF-1 splicing variants. Cell Adh Migr. 2009; 3: 243–249. doi: 10.4161/cam.3.3.8260 PMID: 19287206

31. Scholz F, Bamberg E, Bamann C, Wachtveitl J. Tuning the Primary Reaction of Channelrhodopsin-2 by Imidazole, pH, and Site-Specific Mutations. Biophys J. 2012; 102: 2649–2657. doi: 10.1016/j.bpj.2012.04.034 PMID: 22713581

32. Dawydow A, Gueta R, Ljaschenko D, Ullrich S, Hermann M, Ehmann N, et al. Channelrhodopsin-2-XXL, a powerful optogenetic tool for low-light applications. Proc Natl Acad Sci U S A. 2014; 111: 13972–13977. doi: 10.1073/pnas.1408269111 PMID: 25201989

33. Al-Mohanna FA, Caddy KW, Bolsover SR. The nucleus is insulated from large cytosolic calcium ion changes. Nature. 1994; 367: 745–50. doi: 10.1038/367745a0 PMID: 7993399

34. Huotari J, Helenius A. Endosome maturation. EMBO J. 2011; 30: 3481–3500. doi: 10.1038/emboj.2011.286 PMID: 21878991

35. Hesselgesser J, Liang M, Hoxie J, Greenberg M, Brass LF, Orsini MJ, et al. Identification and characterization of the CXCR4 chemokine receptor in human T cell lines: ligand binding, biological activity, and HIV-1 infectivity. J Immunol. 1998; 160: 877–883. Available: http://www.ncbi.nlm.nih.gov/pubmed/9551924 PMID: 9551924

36. Tilton B, Ho L, Oberlin E, Loetscher P, Baleux F, Clark-Lewis I, et al. Signal transduction by CXC chemokine receptor 4. Stromal cell-derived factor 1 stimulates prolonged protein kinase B and extracellular signal-regulated kinase 2 activation in T lymphocytes. J Exp Med. 2000; 192: 313–324. doi: 10.1084/jem.192.3.313 PMID: 10934220

37. Abe K, Puertollano R. Role of TRP Channels in the Regulation of the Endosomal Pathway. Physiology. 2011; 26: 14–22. doi: 10.1152/physiol.00048.2010 PMID: 21357899

38. Gerasimenko J V, Tepikin A V, Petersen OH, Gerasimenko O V. Calcium uptake via endocytosis with rapid release from acidifying endosomes. Curr Biol. 1998; 8: 1335–1338. doi: 10.1016/S0960-9822(07)00565-9 PMID: 9843688

39. Albrecht T, Zhao Y, Hai T, Campbell RE, Johnson JD. Fluorescent biosensors illuminate calcium levels within defined beta-cell endosome subpopulations. Cell Calcium. Elsevier Ltd; 2015; 57: 263–274. doi: 10.1016/j.ceca.2015.01.008 PMID: 25682167

40. Swanson SJ, Choi W-G, Chanoca A, Gilroy S. In Vivo Imaging of Ca^{2+}, pH, and Reactive Oxygen Species Using Fluorescent Probes in Plants. Annu Rev Plant Biol. 2011; 62: 273–297. doi: 10.1146/annurev-arplant-042110-103832 PMID: 21370977

41. Teicher BA, Fricker SP. CXCL12 (SDF-1)/CXCR4 pathway in cancer. Clin Cancer Res. 2010; 16: 2927–2931. doi: 10.1158/1078-0432.CCR-09-2329 PMID: 20484021

42. Obukhov AG, Harteneck C, Zobel A, Harhammer R, Kalkbrenner F, Leopoldt D, et al. Direct activation of trpl cation channels by G alpha11 subunits. Embo J. 1996; 15: 5833–5838. Available: http://www.ncbi.nlm.nih.gov/pubmed/8918461 PMID: 8918461

43. Maghazachi AA. Role of the Heterotrimeric G Proteins in Stromal-Derived Factor-1α-Induced Natural Killer Cell Chemotaxis and Calcium Mobilization. Biochem Biophys Res Commun. 1997; 236: 270–274. doi: 10.1006/bbrc.1997.6937 PMID: 9240423

44. Wescott MP, Kufareva I, Paes C, Goodman JR, Thaker Y, Puffer BA, et al. Signal transmission through the CXC chemokine receptor 4 (CXCR4) transmembrane helices. Proc Natl Acad Sci U S A. 2016; 113: 9928–9933. doi: 10.1073/pnas.1601278113 PMID: 27543332

40

45. Rost BR, Schneider F, Grauel MK, Wozny C, G Bentz C, Blessing A, et al. Optogenetic acidification of synaptic vesicles and lysosomes. Nat Neurosci. Nature Publishing Group; 2015; 18: 1845–1852. doi: 10.1038/nn.4161 PMID: 26551543

46. Dupont G, Combettes L, Dupont G, Combettes L. Fine tuning of cytosolic Ca^{2+} oscillations. F1000Research. 2016; 5: 2036. doi: 10.12688/f1000research.8438.1 PMID: 27630768

47. Mattson MP, Chan SL. Calcium orchestrates apoptosis. Nat Cell Biol. 2003; 5: 1041–1043. doi: 10.1038/ncb1203-1041 PMID: 14647298

48. Li G-Y, Fan B, Zheng Y-C. Calcium overload is a critical step in programmed necrosis of ARPE-19 cells induced by high-concentration H_2O_2. Biomed Environ Sci. 2010; 23: 371–7. doi: 10.1016/S0895-3988(10)60078-5 PMID: 21112485

41

3.2   Characterization of Plasma Membrane Ceramides by Super-Resolution Microscopy

Abstract

"The sphingolipid ceramide regulates cellular processes such as differentiation, proliferation, growth arrest, and apoptosis. Ceramide-rich membrane areas promote structural changes within the plasma membrane that segregate membrane receptors and affect membrane curvature and vesicle formation, fusion, and trafficking. Ceramides were labeled by immunocytochemistry to visualize their distribution on the plasma membrane of different cells with virtually molecular resolution by *direct* stochastic optical reconstruction microscopy (*d*STORM). Super-resolution images show that independent of labeling conditions and cell type 50–60% of all membrane ceramides are located in ceramide-rich platforms (CRPs) with a size of about 75 nm that are composed of at least about 20 ceramides. Treatment of cells with *Bacillus cereus* sphingomyelinase (bSMase) increases the overall ceramide concentration in the plasma membrane, the quantity of CRPs, and their size. Simultaneously, the ceramide concentration in CRPs increases approximately twofold." [110]

Characterization of Plasma Membrane Ceramides by Super-Resolution Microscopy

Anne Burgert, Jan Schlegel, Jérôme Bécam, Sören Doose, Erhard Bieberich, Alexandra Schubert-Unkmeir, and Markus Sauer*

Abstract: *The sphingolipid ceramide regulates cellular processes such as differentiation, proliferation, growth arrest, and apoptosis. Ceramide-rich membrane areas promote structural changes within the plasma membrane that segregate membrane receptors and affect membrane curvature and vesicle formation, fusion, and trafficking. Ceramides were labeled by immunocytochemistry to visualize their distribution on the plasma membrane of different cells with virtually molecular resolution by direct stochastic optical reconstruction microscopy (dSTORM). Super-resolution images show that independent of labeling conditions and cell type 50–60 % of all membrane ceramides are located in ceramide-rich platforms (CRPs) with a size of about 75 nm that are composed of at least about 20 ceramides. Treatment of cells with Bacillus cereus sphingomyelinase (bSMase) increases the overall ceramide concentration in the plasma membrane, the quantity of CRPs, and their size. Simultaneously, the ceramide concentration in CRPs increases approximately twofold.*

The plasma membrane is mainly composed of glycerophospholipids, sphingolipids, and cholesterol. Sphingolipids are natural lipids comprised of the sphingoid base backbone sphingosine, which when *N*-acylated with fatty acids forms ceramide, a central molecule in sphingolipid biology. De novo synthesis of ceramide occurs in the endoplasmatic reticulum followed by conversion into complex sphingolipids in the Golgi apparatus. Furthermore, sphingomyelinases (SMases) can generate ceramide from sphingomyelin in the plasma membrane.[1,2] Interactions of sphingolipids with one another and with cholesterol typically result in membrane microdomains or rafts that segregate membrane-associated proteins and compartmentalize signaling components within the plasma membrane.[3–6] Activation of SMases by cellular stress

or ligation of receptors results in ceramide synthesis and subsequent self-association within the plasma membrane, resulting in ceramide-rich platforms (CRPs).[7,8] The formation of CRPs rearranges the organization of the plasma membrane including clustering of diverse receptors and facilitates vesicle formation and fusion.[8,9] These changes induce differentiation, proliferation, growth arrest, and cell death.[1,2]

Moreover, SMases and ceramides have been shown to be critically involved in the internalization of pathogens.[10–15] The recent observation, that CRP formation is essential in controlling the metabolic activity of regulatory T cells demonstrates that ceramides play also an essential role in regulating immune functions and inflammation.[16,17] However, despite these important roles the molecular organization of ceramides in the plasma membrane remains elusive. Hitherto, CRPs have been studied extensively in artificial membranes by biochemical and biophysical approaches[3,4,18–20] and in fixed cells by immunocytochemistry.[21–23] CRPs have been visualized by electron microscopy and fluorescence microscopy in the plasma membrane of cells as macrodomains with diameters of 200 nm up to several micrometers.[7,24,25]

To fully understand ceramide biology, we have to develop refined methods to study their distribution in the plasma membrane, ideally quantitatively with molecular resolution. The limited knowledge about the distribution of sphingolipids in plasma membranes is mainly due to experimental hurdles. First, the analysis of interactions among distinct molecular lipid species is complicated due to the fact that classical spectroscopic approaches using fluorescent membrane lipid analogs are hampered by structural and physical alterations induced by the fluorescent molecules.[26–28] Second, standard fluorescence imaging methods exhibit only a spatial resolution of half of the wavelength of the light used to image the structure and cannot resolve internal architecture and distribution of sphingolipids in nanodomains or clusters with a size of 2–300 nm.[29,30] Recently, the distribution of sphingolipids in the plasma membrane of cells has been investigated by super-resolution microscopy.[31,32] Furthermore, high-resolution imaging mass spectrometry has been used to map the distribution of ^{15}N-enriched ions from metabolically labeled ^{15}N-sphingolipids with about 50 nm lateral resolution and an analysis depth of < 5 nm to ensure the selective investigation of membrane sphingolipids.[33] The study revealed the existence of micrometer-scale sphingolipid platforms with a mean diameter of about 200 nm, independent of fixation conditions and temperature.

[*] A. Burgert, J. Schlegel, Dr. S. Doose, Prof. Dr. M. Sauer
Department of Biotechnology and Biophysics
Julius Maximilian University Würzburg
Am Hubland, 97074 Würzburg (Germany)
E-mail: m.sauer@uni-wuerzburg.de

J. Bécam, Prof. Dr. A. Schubert-Unkmeir
Institute of Hygiene and Microbiology
Julius Maximilian University Würzburg
97080 Würzburg (Germany)

Prof. Dr. E. Bieberich
Department of Neuroscience and Regenerative Medicine
Medical College of Georgia, Augusta University
Augusta, GA 30912 (USA)

43

Herein, we used rabbit anti-C18 and anti-C16/24 ceramide IgG antibodies for specific labeling and Alexa Fluor 647 labeled secondary antibodies[23] in different cell lines before and after SMase treatment to visualize ceramides with high spatial resolution by *d*STORM.[34,35] However, when using immunolabeling for visualization of membrane components, crosslinking of antibodies can induce clustering artifacts. Furthermore, the fixation procedure can alter the distribution of molecules in the plasma membrane. Even after fixation with 4% formaldehyde (FA) and 0.3% glutaraldehyde (GA), residual post-fixation diffusion of membrane sphingolipids in combination with antibody crosslinking can potentially lead to clustering artifacts.[8,36,37] Therefore, in first experiments we investigated the influence of different live and fixed cell labeling conditions on the distribution of plasma membrane ceramides in U2OS cells (Supporting Information, Figure S1)). In accordance with previous experiments,[33] our results demonstrate that independent of the labeling conditions, for example, live-cell, or formaldehyde and glutaraldehyde fixation, respectively, ceramides form CRPs with similar distribution and size (Supporting Information, Figure S1). Therefore, we fixed different cells after labeling with 4% FA and 0.3% GA for 30 min in the following super-resolution imaging experiments.

*d*STORM images clearly reveal non-random distributions of ceramides in HBMEC, Jurkat, and U2OS cells for both IgG antibodies (Figure 1; Supporting Information, Figures S2, S3). Recently,[38] it has been demonstrated that high emitter densities in combination with inappropriate photoswitching rates can give rise to the appearance of artificial membrane clusters or nanodomains in single-molecule localization

microscopy images of membrane molecules. To exclude reconstruction artifacts of overlapping point-spread-functions (PSFs), we carefully examined the emitter density in our data. The recorded single-molecule movies show spatially well-resolved PSFs of individual emitters and thus affirm the existence of CRPs in the plasma membrane (Supporting Information, Video S1).

To describe the distribution of membrane ceramides, we first calculated Ripley's K-function of several regions of interest (ROI) of the plasma membranes with a size of $2 \times 2 \, \mu m^2$ (Supporting Information, Figure S4).[39] Here, it is important to consider that the maximum of Ripley's K-function (r_{Max}) is located between the actual cluster radius and diameter and gives only an estimate of the average cluster size. To obtain detailed information about cluster size and localizations per cluster, we used a morphological cluster analysis.[40] Based on the results of Ripley's K-function, we analyzed those clusters that have a radius between r_{Max} and $r_{Max}/2$ (for a detailed description, see the Supporting Information, Materials and Methods). Morphological cluster analysis demonstrates that CRP diameters vary between 72 ± 8 nm (median $\pm$ MAD; MAD: median absolute deviation) and 78 ± 11 nm (median $\pm$ MAD) measured on the basal membranes of U2OS cells and HBMEC, and the apical membrane of Jurkat cells, respectively (Table 1). The number of CRPs per μm^2 differs between the different cell lines, from about 1.8 per μm^2 for HBMEC, about 2.4 per μm^2 for U2OS cells, to about 3.6 per μm^2 for Jurkat cells (Table 1). Independent of the cell line 50–60% of all localizations are part of CRPs whereas the remaining localizations are detected outside of CRPs (Figure 1, Table 1, Supporting Information, Figure S3). Our results demonstrate that the size, shape, and composition of CRPs is identical in the upper (apical) and lower (basal) plasma membrane (Figure 1; Supporting Information, Figure S3).

Furthermore, our data show that the plasma membrane of Jurkat cells exhibits the highest density of ceramides, with 700–1100 localizations per μm^2, followed by U2OS cells with 400–500 localizations per μm^2 and HBMEC with 250–370 localizations per μm^2 (Table 1). To estimate the number of localizations typically detected per primary/secondary Alexa Fluor 647 labeled antibody complex, we proceeded as recently introduced for super-resolution imaging of plasma membrane glycans[41] and grouped repeated localizations using the tracking function of rapi*d*STORM[42] and extracted 5.4 ± 0.2 (median $\pm$ MAD) localizations per isolated fluorescent
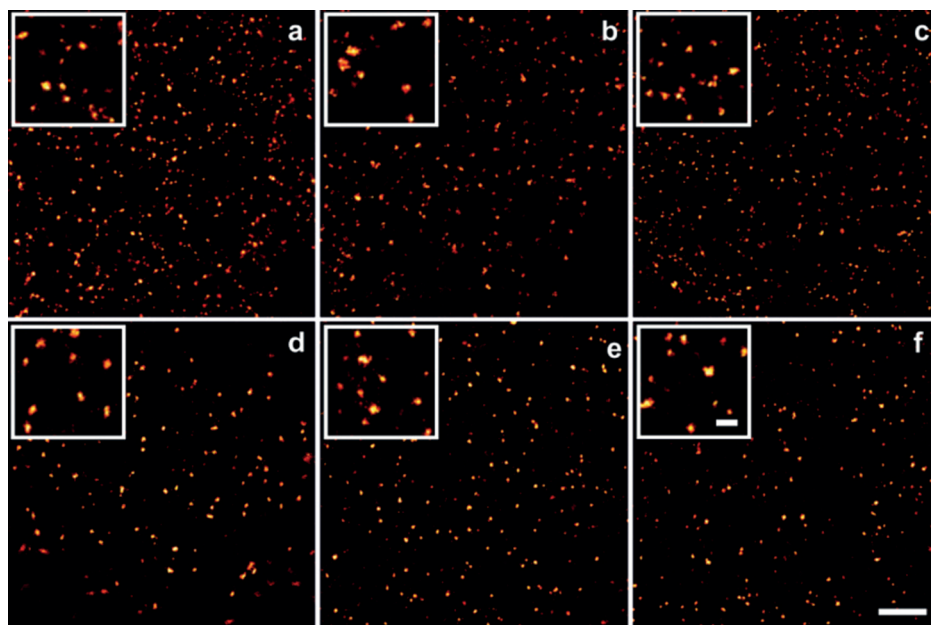
Figure 1. Ceramides form CRPs in the plasma membrane. Jurkat (a, d), U2OS (b, e), and HBME (c, f) cells were fixed and stained with IgG antibodies against C16/24 ceramides and Alexa Fluor 647 labeled secondary antibodies. *d*STORM imaging of the basal (a–c) and apical (d–f) plasma membrane reveals a non-random distribution of ceramides. Individual CPRs with diameters < 100 nm can be detected in the plasma membrane of all cell lines at the apical and basal membrane. Insets show enlarged regions of the respective *d*STORM image. Scale bars: 1 μm (a–f) and 200 nm (insets).

GDCh

3 RESULTS

Communications

Angewandte
International Edition
Chemie

Table 1: Characteristics of plasma membrane ceramides.[a]

	D [nm]	Loc/CRP	Cer/CRP	CRPs [μm^{-2}]	Loc [μm^{-2}]	Cer [μm^{-2}]
Jurkat basal	76 ± 10	97 ± 33	18 ± 6	3.5 ± 0.5	1048 ± 88	194 ± 16
Jurkat apical	78 ± 11	112 ± 43	21 ± 8	3.7 ± 0.5	749 ± 106	139 ± 20
U2OS basal	72 ± 8	92 ± 28	17 ± 5	2.5 ± 0.2	433 ± 39	80 ± 7
U2OS apical	74 ± 9	121 ± 42	22 ± 8	2.2 ± 0.2	472 ± 40	87 ± 7
HBMEC basal	72 ± 8	85 ± 26	16 ± 5	1.7 ± 0.2	259 ± 21	48 ± 4
HBMEC apical	74 ± 9	93 ± 29	17 ± 5	1.9 ± 0.2	334 ± 35	62 ± 6

[a] Data were derived from *d*STORM measurements of the basal and apical plasma membrane of cells stained with C16/24 antibodies. Diameter, D [nm] and localizations per ceramide-rich platform (CRP) are results of morphological cluster analysis based on Ripley's $H(r)$ function. Molecule numbers were calculated by dividing the number of localizations by a factor of 5.4. Diameter (D), localizations per CRP (Loc/CRP), and ceramides per CRP (Cer/CRP) are presented as median $\pm$ MAD. CRPs per μm^2 (CRPs/μm^2), localizations per μm^2 (Loc/μm^2), and ceramides per μm^2 (Cer/μm^2) are presented as mean $\pm$ s.e.m.

spot (primary/secondary antibody complex; Supporting Information, Figure S5). Using the value of 5.4 localizations per isolated fluorescent spot, we can now estimate the number of primary antibodies bound to C16/24 ceramides in the plasma membrane to approximately 139–194 (Jurkat cells), 80–87 (U2OS cells), and 48–62 (HBMEC) per μm^2 (Table 1). Under the assumption of identical ceramide approachability (perceptibility and specific orientation of the binding side) inside and outside of CRPs we can directly translate the estimated ceramide numbers to CRP composition. Hence, CRPs exhibit an average diameter of about 75 nm and contain approximately 16-22 C16/24 ceramides independent of the cell type (Table 1).

Apart from the de novo synthesis, ceramides can also arise from the hydrolysis of sphingomyelin by the activation of sphingomyelinases (SMases).[1,2,6–9] To study the influence of SMases on the distribution of ceramides in the plasma membrane, we incubated HBMEC with exogenous *Bacillus cereus* sphingomyelinase (bSMase) before imaging (Figure 2). First, we performed flow cytometry measurements of HBMEC incubated with different concentrations of bSMase before staining with anti-ceramide antibodies. Here, the highest ceramide concentration in the plasma membrane is visible with 150 mU bSMase during a 40 min incubation period (Supporting Information, Figure S7). Super-resolution imaging measurements applying the same bSMase concentration (Figure 2) clearly show non-

random ceramide distributions in bSMase treated cells (Figure 2 a–c).

However, treatment with bSMase increases ceramide concentration in the plasma membrane about 3.3 fold, that is, the number of localizations increases from 259 ± 21 (mean $\pm$ s.e.m.; s.e.m.: standard error of the mean) localizations per μm^2 in untreated to 867 ± 55 (mean $\pm$ s.e.m.) localizations per μm^2 in bSMase-treated HBMEC (Figure 2 d). 60 % of the localizations in untreated cells and 72 % in treated cells are found in CRPs. Simultaneously, more CRPs with slightly larger diameter (Figure 2 c and e) and more localizations (Figure 2 f) appear after bSMase treatment. Furthermore, the quantity of CRPs increases from 1.8 ± 0.3 to 3.6 ± 0.7 per μm^2 plasma membrane.

To conclude, we imaged two types of ceramides using two specific IgG antibodies directed against ceramides with different fatty acids chains (C18 and C16/24).[23] Lipid-ELISAs have shown that the C18 antibody predominantly recognizes C16:0 and C18:0, and C18:1 ceramide, while the C16/C24 antibody recognizes a broad spectrum of ceramides from C16:0 to C24:1 ceramide.[23] Therefore, our data are representative of the composition of
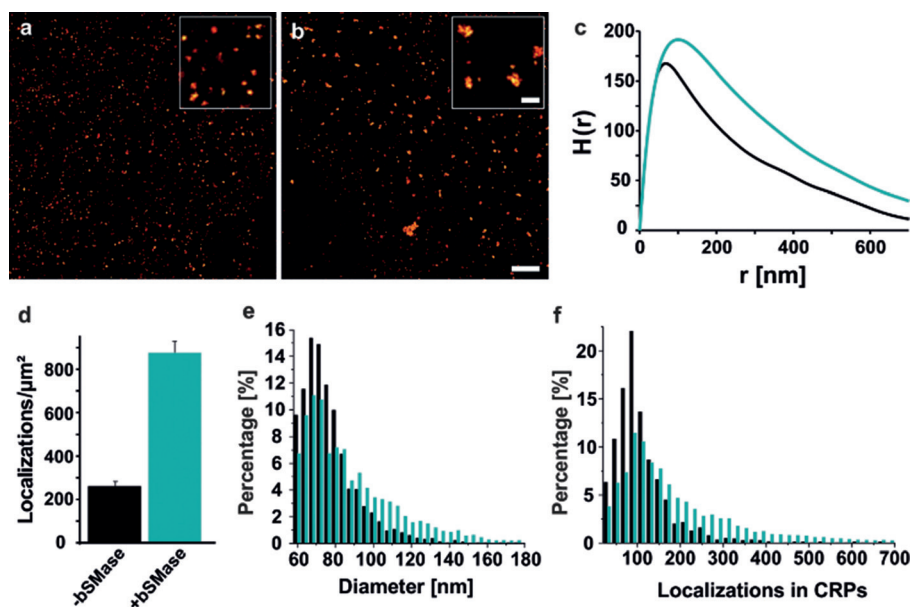
Figure 2. bSMase treatment of HBMEC increases ceramide concentration and size of CRPs. HBMEC were incubated without (a) or with (b) 150 mU bSMase for 40 min and plasma membrane C16/24 ceramides were stained by indirect immunocytochemistry with Alexa Fluor 647. bSMase-treated cells imaged by *d*STORM reveal larger clusters of C16/24 ceramides than untreated cells. Insets show enlarged regions of the respective *d*STORM image. c) The normalized Ripley's K-functions, $H(r)$, indicate non-random distributions of ceramides and exhibit maxima of clustering at $r = 68 \pm 1$ nm (mean $\pm$ s.e.m., 44 regions (2×2 μm) of 11 cells) for untreated cells (black) and $r = 105 \pm 5$ nm (mean $\pm$ s.e.m., 113 regions (2×2 μm) of 18 cells) for bSMase-treated cells (cyan). d) Calculation of all localizations/area inside and outside of CRPs results in 259 ± 21 localizations/μm^2 (mean $\pm$ s.e.m) for untreated cells and 867 ± 55 localizations/μm^2 (mean $\pm$ s.e.m.) for bSMase-treated cells. The percentage of CRPs with a diameter between 60–220 nm was calculated using morphological cluster analysis.[38] e) Compared to untreated cells, more CRPs with larger diameters were found in bSMase-treated cells. f) bSMase-treated cells show more CPRs that contain on average more localizations. 3543 CPRs of untreated and 9379 of treated cells were analyzed. Scale bars: 1 μm (a, b) and 200 nm (insets).

45

ceramide in the cell membrane. To further rule out effects of residual mobility of sphingolipids in the plasma membrane after fixation and antibody-induced crosslinking effects, we performed *d*STORM experiments at various antibody concentrations (Supporting Information, Figure S8).[43] Here, the diameter and number of CRPs detected remain virtually unaffected by the concentration of primary antibodies used over a broad range of antibody concentrations, from 3.1 ± 0.3 CRPs μm^{-2} (20 $\mu g\,mL^{-1}$) to 3.0 ± 0.2 CRPs μm^{-2} (10 $\mu g\,mL^{-1}$) and 2.5 ± 0.2 CRPs μm^{-2} (5 $\mu g\,mL^{-1}$) (Supporting Information, Figure S8).[43] Only for the lowest primary antibody concentration used (0.5 $\mu g\,mL^{-1}$) the number of CRPs μm^{-2} decreased to 1.1 ± 0.2 (Supporting Information, Figure S8). Furthermore, we measured the residual mobility of ceramides in the plasma membrane after fixation with 4% FA (Supporting Information, Figure S9). The data clearly corroborate our finding that residual mobility of ceramides after fixation does not permit the formation of artificial CRPs. Together these results confirm the existence of CRPs in the plasma membrane independent of the cell type and imply that segregation of sphingolipids into CRPS with a size of about 75 nm is a universal characteristic of cell membranes essential for cellular function. The finding that actin depolymerization by treatment of cells with latrunculin A eliminates the sphingolipid domains on the plasma membrane[33] demonstrates that antibody-induced crosslinking effects can be neglected and indicates that the cytoskeleton and its associated membrane proteins confine ceramides within CRPs in the plasma membrane.

The estimation of 16-22 C16/24 ceramides per CRP (Table 1) is certainly a lower limit. It also has to be considered that quantification experiments have been performed with a primary antibody concentration of 5 $\mu g\,mL^{-1}$. However, even under saturation conditions (20 $\mu g\,mL^{-1}$ primary antibody) the number of localizations detected per μm^2 in CRPs increases only slightly (1.2 fold; Supporting Information, Figure S8) corroborating the result that each CRP contains at least about 20 ceramides.

Finally, our data demonstrate that not only the number of ceramides (Figure 2d) (from 259 ± 21 (s.e.m.) to 967 ± 55 (s.e.m.) localizations per μm^2) and quantity of CRPs (1.8 ± 0.3 to 3.6 ± 0.7 per μm^2) and their dimension increase (Figure 2e) but similarly the density of ceramides in CRPs increases almost twofold after bSMase treatment (Figure 2f). Hence, the increased ceramide concentration in CRPs and quantity of platforms after bSMase treatment might very well change the solubility of membrane components and thus influence partitioning of proteins in the plasma membrane. The accumulation of ceramides in CRPs can likewise promote local interactions with other membrane components and potentially change the reactivity of protein receptors.

Conflict of interest

The authors declare no conflict of interest.

[1] Y. A. Hannun, L. M. Obeid, *J. Biol. Chem.* **2002**, *277*, 25847–25850.

[2] E. Gulbins, P. L. Li, *Am. J. Physiol.* **2006**, *290*, R11–R26.

[3] F. M. Goñi, J. Sot, A. Alonso, *Biochem. Soc. Trans.* **2014**, *42*, 1401–1408.

[4] B. M. Castro, L. C. Silva, A. Fedorov, R. F. de Almeida, M. Petro, *J. Biol. Chem.* **2009**, *284*, 22978–22987.

[5] K. Simons, E. Ikonen, *Nature* **1997**, *387*, 569–572.

[6] E. B. Babiychuk, K. Monastryrskaya, A. Draeger, *Traffic* **2008**, *9*, 1757–1775.

[7] B. Stancevic, R. Kolesnick, *FEBS Lett.* **2010**, *584*, 1728–1740.

[8] M. L. Kraft, *Front. Cell Dev. Biol.* **2017**, *4*, 154.

[9] C. R. Bollinger, V. Teichgräber, E. Gulbins, *Biochim. Biophys. Acta Mol. Cell Res.* **2005**, *1746*, 284–294.

[10] S. Luisoni, et al., *Cell Host Microbe* **2015**, *18*, 75–85.

[11] M. C. Fernandes, M. Cortez, A. R. Flannery, C. Tam, R. A. Mortara, N. W. Andrews, *J. Exp. Med.* **2011**, *208*, 909–921.

[12] A. Simonis, S. Hebling, E. Gulbins, S. Schnedier-Schaulies, A. Schubert-Unkmeir, *PLoS Pathog.* **2014**, *10*, e1004160.

[13] M. Faulstich, E. Avota, V. Kozjak-Paplovic, A. C. Winkler, Y. Xian, S. Schneider-Schaulies, T. Rudel, *Cell. Microbiol.* **2015**, *17*, 241–253.

[14] M. E. Miller, S. Adhikary, A. A. Kolokoltsov, R. A. Davey, *J. Virol.* **2012**, *86*, 7473–7483.

[15] M. Nagahama, M. Takehara, T. Takagishi, S. Seike, K. Miyamoto, K. Kobayashi, *Infect. Immun.* **2017**, DOI: 10.1128/IAI.00966-16. [Epub ahead of print].

[16] N. Beyersdorf, N. Müller, *Biol. Chem.* **2015**, *396*, 749–758.

[17] S. A. Apostolidis, N. Rodriguez-Rodriguez, A. Suarez-Fueyo, N. Dioufa, E. Ozcan, J. C. Crispin, M. G. Tsokos, G. C. Tsokos, *Nat. Immunol.* **2016**, *17*, 556–564.

[18] J. M. Holopainen, M. Subramanian, P. K. Kinnunen, *Biochemistry* **1998**, *37*, 17562–17570.

[19] S. Chiantia, N. Kahya, P. Schwille, *Langmuir* **2007**, *23*, 7659–7665.

[20] A. Björkbom, et al., *Biophys. J.* **2010**, *99*, 3300–3308.

[21] Ira, L. J. Johnston, *Biochim. Biophys. Acta Biomembr.* **2008**, *1778*, 185–197.

[22] A. B. Abdel Shakor, K. Kwiatkowska, A. Sobota, *J. Biol. Chem.* **2004**, *279*, 36778–36787.

[23] K. Krishnamurthy, S. Dasgupta, E. Bieberich, *J. Lipid Res.* **2007**, *48*, 968–975.

[24] A. E. Cremesti, F. M. Goni, R. Kolesnick, *FEBS Lett.* **2002**, *531*, 47–53.

[25] Ira, S. Zou, D. M. Ramirez, S. Vanderlip, W. Ogilvie, Z. J. Jakubek, L. J. Johnston, *J. Struct. Biol.* **2009**, *168*, 78–89.

[26] L. Kuerschner, C. S. Ejsing, K. Ekroos, A. Shevchenko, K. I. Anderson, C. Thiele, *Nat. Methods* **2005**, *2*, 39–45.

[27] S. Mukherjee, H. Raghuraman, S. Dasgupta, A. Chattopadhyay, *Chem. Phys. Lipids* **2004**, *127*, 91–101.

[28] J. E. Shaw, R. F. Epand, R. M. Epand, Z. Li, R. Bittmann, C. M. Yip, *Biophys. J.* **2006**, *90*, 2170–2178.

[29] K. Simons, M. J. Gerl, *Nat. Rev. Mol. Cell Biol.* **2010**, *11*, 688–699.

[30] A. Kusumi, T. K. Fujiwara, R. Chadda, M. Xie, T. A. Tsunoyama, Z. Kalay, R. S. Kasai, K. G. N. Suzuki, *Annual Rev. Cell Develop. Biol.* **2012**, *28*, 215–250.

[31] H. Mizuno, et al., *Chem. Sci.* **2011**, *2*, 1548–1553.

[32] V. Mueller, et al., *Biophys. J.* **2011**, *101*, 1651–1660.

[33] J. F. Frisz, et al., *Proc. Natl. Acad. Sci. USA* **2013**, *110*, E613-E622.

[34] M. Heilemann, S. van de Linde, M. Schüttpelz, R. Kasper, B. Seefeldt, A. Mukherjee, P. Tinnefeld, M. Sauer, *Angew. Chem. Int. Ed.* **2008**, *47*, 6172–6176; *Angew. Chem.* **2008**, *120*, 6266–6271.

[35] S. van de Linde, A. Löschberger, T. Klein, M. Heidbreder, S. Wolter, M. Heilemann, M. Sauer, *Nat. Protoc.* **2011**, *6*, 991–1009.

[36] K. A. K. Tanaka, et al., *Nat. Methods* **2010**, *7*, 865–866.

[37] T. A. Stanly, M. Fritzsche, S. Banerji, E. Garc, J. B. de la Serna, D. G. Jackson, C. Eggeling, *Biol. Open* **2016**, *5*, 1343–1350.

[38] A. Burgert, S. Letschert, S. Doose, M. Sauer, *Histochem. Cell Biol.* **2015**, *144*, 123–131.

[39] B. D. Ripley, *J. R. Statist. Soc.* **1977**, *39*, 172–212.

[40] S. Malkusch, M. Heilemann, *Sci. Rep.* **2016**, *6*, 34486.

[41] S. Letschert, A. Göhler, C. Franke, N. Bertleff-Zieschang, E. Memmel, S. Doose, J. Seibel, M. Sauer, *Angew. Chem. Int. Ed.* **2014**, *53*, 10921–10924; *Angew. Chem.* **2014**, *126*, 11101–11104.

[42] S. Wolter, A. Löschberger, T. Holm, S. Aufmkolk, M. C. Dabauvalle, S. van de Linde, M. Sauer, *Nat. Methods* **2012**, *9*, 1040–1041.

[43] F. Baumgart, A. M. Arnold, K. Leskovar, K. Staszek, M. Fölser, J. Weghuber, H. Stockinger, G. J. Schütz, *Nat. Methods* **2016**, *13*, 661–664.

47

3.3   Incorporation Studies of Clickable Ceramides in Jurkat Cell Plasma Membranes

Abstract

"The incorporation properties of ceramide analogues for click chemistry in Jurkat T cells were investigated. The analogues varied in the acyl chain length and the position of the functional group for click chemistry. Fluorescence microscopy studies including anisotropy and quenching experiments showed significant differences in the accessibility of the functional group indicating different incorporation properties into the plasma membrane."
[111]

The following manuscript was published on May 31$^{\text{st}}$, 2017 in Chemical Communications and permission for legal second publication within this thesis was kindly granted from both the publishers and the co-authors.

ChemComm

View Article Online

View Journal | View Issue

Check for updates

Incorporation studies of clickable ceramides in Jurkat cell plasma membranes†

T. Walter, [ID] ‡[a] J. Schlegel, [ID] ‡[b] A. Burgert,[b] A. Kurz,[b] J. Seibel*[a] and M. Sauer*[b]

The incorporation properties of ceramide analogues for click chemistry in Jurkat T cells were investigated. The analogues varied in the acyl chain length and the position of the functional group for click chemistry. Fluorescence microscopy studies including anisotropy and quenching experiments showed significant differences in the accessibility of the functional group indicating different incorporation properties into the plasma membrane.

Sphingolipid ceramides regulate cellular processes such as differentiation, proliferation, growth arrest and apoptosis. Ceramide-rich membrane areas promote structural changes within the plasma membrane which segregate membrane receptors and affect the membrane curvature and vesicle formation, fusion and trafficking.[1–4] In addition, ceramides play an essential role in the control of viral and bacterial infections.[5,6]

A powerful tool to study the signalling pathways and improve our current understanding of the sphingolipid function, especially with respect to cell signalling during infection, is fluorescence microscopy. In a pioneering work, Pagano *et al.* used NBD-C6-ceramide as a Golgi marker in 1985.[7,8] Since then different fluorescent sphingolipids have been developed, most of them with the fluorescent capabilities were derived from the acylated chain like BODIPY modified C5-DMB-Cer[9] and the corresponding glycolipid analogs.[9,10] A fluorescent probe with limited structural alterations is obtained by acylation of the polyunsaturated fatty acids,[11] albeit the resulting probe exhibits a rather stiff hydrophobic moiety and limited spectral qualities compared to other fluorescent dyes. Later on NBD linked to the end of the sphingosine chain has been successfully used to assess the binding of potential ligands to the CERT transfer protein.[12] More recently it has been indicated that the ceramide

analogue azido-*N*-oleoyl serinol can be transported into the Golgi without cytotoxic effects.[9] An alternative tool to localize ceramides in the plasma membrane of cells by fluorescence microscopy is the use of specific IgG antibodies.[13,14] However, when using immunolabeling for visualization of membrane components, cross-linking of antibodies can induce clustering artifacts and the fixation procedure can alter the distribution of molecules in the plasma membrane.

A new and efficient approach to visualize ceramides in cells is the use of bioorthogonal click chemistry.[15] It exploits the tolerance of cells to biomolecules with small modifications. By introducing a small bioorthogonal linker, the structure of ceramide analogues differs only slightly from the natural compounds (Fig. 1). After incorporation into the membrane, it can be linked covalently to its counterpart (*e.g.* DBCO Sulfo Cy5), in a selective and efficient way. With its counterpart linked to a fluorophore it can be used advantageously for fluorescence microscopic investigations.[16–21]

Here, we used various azide-functionalized ceramides (Fig. 1) and studied their incorporation efficiency into the plasma membrane of Jurkat cells and their accessibility in fluorescence anisotropy and quenching experiments.

First, we synthesized the functionalized azides CerC6ω, CerC6α, CerC16ω, and CerC16α (Fig. 1) which can be conjugated with DBCO-Sulfo-Cy5 *via* the [3+2] strain-promoted azide–alkyne cycloaddition[15–21] either before (preclicked) or after (postclicked) incubation with living human cells. The incorporation efficiency

[a] *Institute for Organic Chemistry, Julius-Maximilians University Würzburg, Am Hubland C1, 97074 Würzburg, Germany. E-mail: seibel@chemie.uni-wuerzburg.de*

[b] *Department of Biotechnology and Biophysics, Julius-Maximilians-University Würzburg, 97074 Würzburg, Germany. E-mail: m.sauer@uni-wuerzburg.de*

‡ The authors contributed equally to this work.
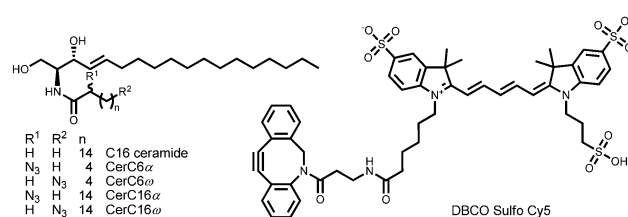
Fig. 1 Molecular structures of the biorthogonal click system azido functionalized ceramide analogue and alkyne fluorescent dye DBCO Sulfo Cy5 used in this study.

Communication

ChemComm

Fig. 2 Confocal laser scanning microscopy (LSM) images of Jurkat cells with azido-functionalized ceramides incorporated into their plasma membrane. (A–D) Postclicked ceramides. Cells were incubated with 25 μM (A) CerC6α, (B) CerC6ω, (C) CerC16α or (D) CerC16ω for 30 min and then clicked with 25 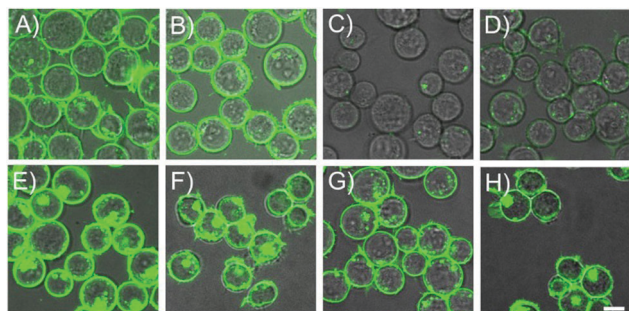μM of DBCO-Cy5 for 7 min. Cells fed with CerC6α (A) and CerC6ω (B) show high fluorescence intensities in the plasma membrane whereas only a weak fluorescence signal is detected for CerC16α (C) and CerC16ω (D) incubated cells (CerC16α < CerC16ω). Control experiments in the absence of azido-functionalized ceramides but with incubation with 25 μM of DBCO-Cy5 show no fluorescence signal comparable to postclicked CerC16α (Fig. S1, ESI†). (E–H) Preclicked ceramides. Jurkat cells fed with 25 μM (E) Cy5-CerC6α, (F) Cy5-CerC6ω, (G) Cy5-CerC16α or (H) Cy5-CerC16ω for 30 min show stronger fluorescence signals independent of the ceramide structure. Green colour is used to show the fluorescence signal at 650 nm to enhance the contrast. Scale bars: 10 μm.

was then investigated by confocal laser scanning microscopy (LSM) (Fig. 2).

Both ceramide analogues CerC6ω and CerC6α show strong fluorescence signals predominantly from the plasma membrane after postclicking with DBCO-Cy5 (Fig. 2A and B). Incubation of cells with preclicked CerC6ω and CerC6α analogues results in slightly higher fluorescence signals (Fig. 2E and F). In addition, the preclicked ceramide analogues show a higher tendency to accumulate in intracellular vesicular structures. In contrast, the long chain ceramide analogues CerC16ω and CerC16α exhibit different incorporation and/or fluorescence labelling efficiencies. While the preclicked compounds show a high fluorescence signal on the plasma membrane and in the intracellular structures (Fig. 2G and H), a weaker fluorescence intensity is seen in the LSM images of cells postclicked with CerC16ω (Fig. 2D). The LSM images of postclicked CerC16α (Fig. 2C) show almost no plasma membrane fluorescence intensity similar to untreated Jurkat cells after addition of DBCO-Cy5 (Fig. S1, ESI†).

In previous studies, we have shown using mass spectrometry that the azide-functionalized ceramide analogues are generally well incorporated into the cells.[21,22] This suggests that the click reaction proceeds with different efficiencies. If the chemical reactivities of the azides in the alpha positions of CerC6 and CerC16 and in the omega positions of CerC6 and CerC16 are similar, respectively (Fig. 1), then the accessibility of the reaction partners represents the limiting factor determining the click reaction efficiency. Since penetration of DBCO-Cy5 through the cell membrane is inefficient,[17] the ceramide analogues can only react if the azide-functionalized side chain directs outside the membrane. To verify this hypothesis, we performed fluorescence anisotropy measurements of preclicked and postclicked

ceramide analogues. Fluorescence anisotropy experiments provide information about fluorescence depolarization, *i.e.* information about the rotational mobility of the fluorophore. If the fluorophore is conjugated to the ceramide, then the rotational mobility of the fluorophore can be used as a measure of the interaction efficiency of the fluorophore with the membrane and the ceramide structure. In these experiments, cells were incubated with 25 μM solutions of the different ceramide compounds for 30 min at 37 °C, washed and then either directly measured or postlabelled with Cy5 for 7 min (see the ESI†). Time-dependent postlabeling and LSM fluorescence experiments demonstrate that the clickable ceramide concentration on the plasma membrane remains constant during the first 24 min after washing and does not decrease due to internalization of ceramides (Fig. S2, ESI†). This result corroborates the finding that preclicked ceramides are integrated more efficiently into the plasma membrane (Fig. 2).

The steady-state anisotropy of free Cy5 and preclicked ceramides in aqueous buffer is ∼0.16 (Fig. S3, ESI†). Incorporated into the plasma membrane of Jurkat cells, Cy5-CerC6α shows higher steady-state anisotropy values of 0.27–0.28 independent of the labelling sequence indicating hindered rotational mobility of the dye (Fig. 3). Together with the fluorescence intensity data (Fig. 2) our results indicate that Cy5-labeled and unlabelled CerC6α is incorporated in a similar way albeit the incorporation efficiency is higher for the preclicked compound (compare Fig. 2A and E). Independent of the labelling conditions the fluorophore reveals hindered rotational mobility due to at least partial sticking into or interacting with the plasma membrane of Jurkat cells.
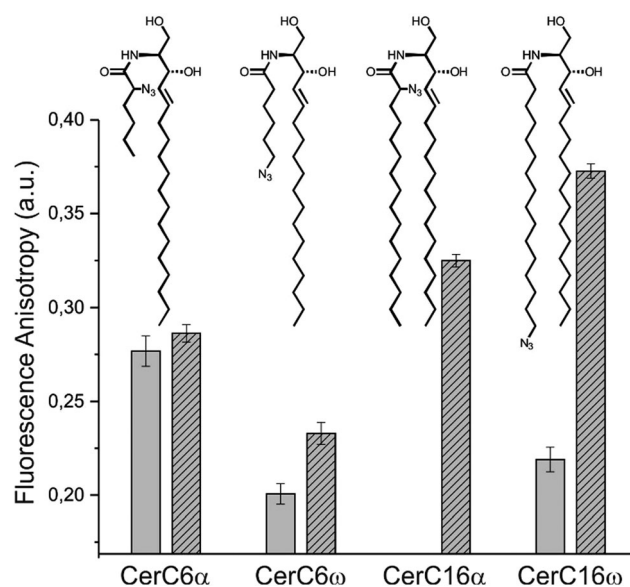
Fig. 3 Steady-state fluorescence anisotropy azido-ceramides incorporated into Jurkat cells. Jurkat cells were fed with 25 μM CerC6α, CerC6ω, CerC16α, or CerC16ω for 30 min, washed and then either directly measured (preclicked; grey bars) or postclicked with DBCO-Cy5 (striped bars). The data represent the mean values with standard errors of two independent experiments with five measurements each. The steady-state anisotropy measured for free Cy5 and pre-clicked ceramides in Hank's buffered salt solution (HBSS) of ∼0.16 (ESI†, Fig. S1) is set as a lower level.

50

On the other hand, the steady-state anisotropy values of postclicked and preclicked Cy5-CerC6ω of ~0.20 and ~0.23, respectively, indicate only slightly hindered rotational mobility. This finding implies that the C6 ω-chain sticks out of the plasma membrane most of the time, enabling more or less unhindered rotational mobility of the fluorophore. Only for preclicked Cy5-CerC6ω the dye tends to stick slightly more into the membrane. That is, the azide group of CerC6ω sticks out of the plasma membrane most of the time, where it is accessible for postclicking with DBCO-Cy5 (Fig. 2B). In the case of the preclicked compound, the polymethine dye structure itself might well promote the incorporation efficiency of the C6 ceramide chain resulting in a higher steady-state anisotropy.

To rule out corruption of the measured steady-state fluorescence anisotropy values by homo-FRET between the fluorophores[23] we performed control experiments at different ceramide concentrations. However, steady-state anisotropy values measured for cells labelled with preclicked Cy5-CerC6ω are constant in the concentration range of 2.5–25 μM. This result demonstrates that the reduced anisotropy values measured for CerC6ω are not caused by homo-FRET between identical fluorophores.

The low fluorescence intensities recorded for postclicked CerC16α and CerC16ω indicate that the azide groups are shielded in the plasma membrane most of the time and are thus inaccessible for clicking with DBCO-Cy5 (Fig. 2). Only for postclicked CerC16ω (Fig. 2D) the labelling efficiency is good enough to enable anisotropy experiments (Fig. 3). The measured steady-state anisotropy of ~0.24 supports the idea that clicking with DBCO-Cy5 succeeds only for those ceramides where the alkyl chain with the azide group sticks out of the membrane. Consequently, the resulting anisotropy indicates only slightly hindered rotational mobility of the fluorophore.

On the other hand, preclicked CerC16α and CerC16ω are well incorporated and exhibit steady-state fluorescence anisotropy values of 0.32 and 0.37, respectively (Fig. 3). This implies that the fluorophores are embedded in the plasma membrane most of the time and exhibit at least in the case of CerC16ω an almost stationary emission dipole moment.

To verify the obtained information about the positons of the fluorophores and their resulting rotational mobility, we performed additional fluorescence quenching experiments of Cy5-ceramides incorporated into Jurkat cells with the reductant tris(2-carboxyethyl) phosphine (TCEP) (Fig. S4, ESI†). TCEP does not penetrate into the plasma membrane and reacts with cyanine dyes spontaneously to form a non-fluorescent adduct by 1,4-addition to the γ-carbon on the polymethine bridge of cyanine dyes.[24] Thus, the measured quenching efficiency ideally directly reflects the accessibility of the fluorophore for collisions with the quencher TECP. The obtained results (Fig. S5, ESI†), however, are more difficult to interpret. They demonstrate that the postclicked ceramides CerC6α and CerC6ω show higher quenching efficiencies than the preclicked compounds (Fig. S5, ESI†) most probably because they are easier to access by the quencher. The fact that the lowest quenching efficiency is measured for the fluorophore attached to the ω-azide in the preclicked ceramides Cy5-CerC6ω and
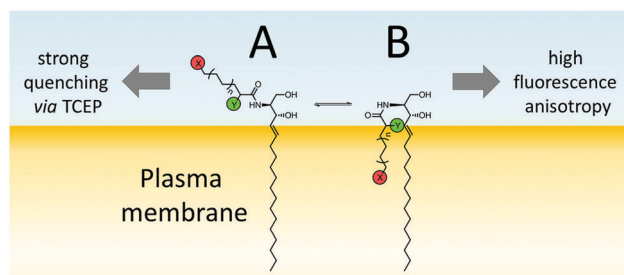
Fig. 4   Incorporation scheme of ceramide analogues in cell membranes, explaining the varying accessibility of the azide group for postclicking with DBCO-Cy5. Only if the alkyl chain sticks out of the membrane (A) the azide group can be clicked by explaining the higher rotational mobility and the quenching efficiency of postclicked ceramides (Fig. 3).

Cy5-CerC16ω is in agreement with the steady-state anisotropy measured for Cy5-CerC16ω but, unfortunately, it is in contrast to the value measured for CerC16ω (Fig. 3). The reason for this discrepancy has to be clarified in future experiments.

To summarize, our fluorescence imaging and steady-state anisotropy data demonstrate that preclicked ceramides are all very efficiently incorporated into the plasma membrane of Jurkat cells. In addition, especially preclicked analogues tend to accumulate in intracellular vesicular structures (Fig. 2). Furthermore, the preclicked ceramides exhibit a higher steady-state anisotropy in Jurkat cells than the corresponding postclicked molecules. This implies that depending on the chain length and the position of the coupling group the fluorophore sticks onto or into the plasma membrane, which is reflected in a moderate to high rotational immobility and accessibility of external quenchers (Fig. 4).

On the other hand, experiments with the corresponding unlabelled ceramides demonstrate that the azide group of the two CerC16 compounds is most of the time inaccessible for clicking with DBCO-Cy5 independent of the position of the functional group (Fig. 2). Both the α and ω azide groups in the two CerC6 derivatives can be labelled efficiently after incorporation demonstrating that they stick out of the membrane most of the time (Fig. 4).

Our studies highlight the differences in the cell membrane incorporation properties and efficiencies of ceramide analogues and their biorthogonal chemical reactions with fluorescent probes. Our results also show that the equilibria between the inserted and outside directed side chains of sphingolipids in cell membranes can be followed by combining click chemistry, fluorescence microscopy, fluorescence anisotropy and fluorescence quenching experiments.

Notes and references

1   Y. A. Hannun and L. M. Obeid, *J. Biol. Chem.*, 2002, **277**, 25847–25850.
2   F. M. Goni, J. Sot and A. Alonso, *Biochem. Soc. Trans.*, 2014, **52**, 1401–1408.
3   B. M. Castro, L. C. Silva, A. Fedorov, R. F. de Almeida and M. Petro, *J. Biol. Chem.*, 2009, **284**, 22978–22987.

51

4 L. M. Kraft, *Front. Cell Dev. Biol.*, 2017, **4**, 154.

5 H. Grassme, J. Riethmüller and E. Gulbins, *Prog. Lipid Res.*, 2007, **46**, 161–170.

6 E. Gulbins, S. Dreschers, B. Wilker and H. Grassme, *J. Mol. Med.*, 2004, **82**, 357–363.

7 N. G. Lipsky and R. E. Pagano, *Science*, 1985, **228**, 745–747.

8 N. G. Lipsky and R. E. Pagano, *J. Cell Biol.*, 1985, **100**, 27–34.

9 R. E. Pagano, O. C. Martin, H. C. Kang and R. P. Haugland, *J. Cell Biol.*, 1991, **113**, 1267–1279.

10 S.-H. Son, S. Daikoku, A. Ohtake, K. Suzuki, K. Kabayama, Y. Ito and O. Kanie, *Chem. Commun.*, 2014, **50**, 3010–3013.

11 L. Kuerschner, C. S. Ejsing, K. Ekroos, A. Shevchenko, K. I. Anderson and C. Thiele, *Nat. Methods*, 2005, **2**, 39–45.

12 S. Combemale, C. Santos, F. Rodriguez, V. Garcia, C. Galaup, C. Frongia, V. Lobjois, T. Levade, C. Baudoin-Dehoux, S. Ballereau and Y. Genisson, *RSC Adv.*, 2013, **3**, 18970–18984.

13 K. Krishnamurthy, S. Dasgupta and E. Bieberich, *J. Lipid Res.*, 2007, **48**, 968–975.

14 A. Burgert, J. Schlegel, J. Bécam, S. Doose, E. Bieberich, A. Schubert-Unkmeir and M. Sauer, *Angew. Chem., Int. Ed.*, 2017, **56**, 6131–6135.

15 J. A. Prescher and C. R. Bertozzi, *Nat. Chem. Biol.*, 2005, **1**, 13–21.

16 A. Mertsch, S. Letschert, E. Memmel, M. Sauer and J. Seibel, *Z. Naturforsch., C*, 2016, **71**, 347–354.

17 A. Homann, R.-u. Qamar, S. Serim, P. Dersch and J. Seibel, *Beilstein J. Org. Chem.*, 2010, **6**, 24.

18 M. J. Gerl, V. Bittl, S. Kirchner, T. Sachsenheimer, H. L. Brunner, C. Luechtenborg, C. Oezbalci, H. Wiedemann, S. Wegehingel, W. Nickel, P. Haberkant, C. Schultz, M. Krueger and B. Bruegge, *PLoS One*, 2016, **11**, 1–25.

19 E. M. Sletten, H. Nakamura, J. C. Jewett and C. R. Bertozzi, *J. Am. Chem. Soc.*, 2010, **132**, 11799–11805.

20 (*a*) N. E. Mbua, J. Guo, M. A. Wolfert, R. Steet and G. J. Boons, *ChemBioChem*, 2011, **12**, 1912–1921; (*b*) S. Letschert, A. Gohler, C. Franke, N. Bertleff-Zieschang, E. Memmel, S. Doose, J. Seibel and M. Sauer, *Angew. Chem., Int. Ed.*, 2014, **53**, 10921–10924.

21 L. Collenburg, T. Walter, A. Burgert, N. Müller, J. Seibel, L. Japtok, B. Kleuser, M. Sauer and S. Schneider-Schaulies, *J. Immunol.*, 2016, **196**, 3951–3962.

22 T. Walter, L. Collenburg, L. Japtok, B. Kleuser, S. Schneider-Schaulies, N. Müller, J. Becam, A. Schubert-Unkmeir, J. N. Kong, E. Bieberich and J. Seibel, *Chem. Commun.*, 2016, **52**, 8612–8614.

23 J. R. Lakowicz, *Principles of Fluorescence Spectroscopy*, Springer Science Business Media, New York, 2006.

24 J. C. Vaughan, G. T. Dempsey, E. Sun and X. Zhuang, *J. Am. Chem. Soc.*, 2013, **135**, 1197–1200.

3.4   CD56 is a Pathogen Recognition Receptor on Human Natural Killer Cells

Abstract

"*Aspergillus (A.) fumigatus* is an opportunistic fungal mold inducing invasive aspergillosis (IA) in immunocompromised patients. Although antifungal activity of human natural killer (NK) cells was shown in previous studies, the underlying cellular mechanisms and pathogen recognition receptors (PRRs) are still unknown. Using flow cytometry we were able to show that the fluorescence positivity of the surface receptor CD56 significantly decreased upon fungal contact. To visualize the interaction site of NK cells and *A. fumigatus* we used SEM, CLSM and *d*STORM techniques, which clearly demonstrated that NK cells directly interact with *A. fumigatus* via CD56 and that CD56 is re-organized and accumulated at this interaction site time-dependently. The inhibition of the cytoskeleton showed that the receptor re-organization was an active process dependent on actin re-arrangements. Furthermore, we could show that CD56 plays a role in the fungus mediated NK cell activation, since blocking of CD56 surface receptor reduced fungal mediated NK cell activation and reduced cytokine secretion. These results confirmed the direct interaction of NK cells and *A. fumigatus*, leading to the conclusion that CD56 is a pathogen recognition receptor. These findings give new insights into the functional role of CD56 in the pathogen recognition during the innate immune response." [112]

SCIENTIFIC REPORTS

OPEN

CD56 Is a Pathogen Recognition Receptor on Human Natural Killer Cells

Sabrina Ziegler[1], Esther Weiss[1], Anna-Lena Schmitt[1], Jan Schlegel [2], Anne Burgert[2], Ulrich Terpitz [2], Markus Sauer[2], Lorenzo Moretta[3], Simona Sivori [4], Ines Leonhardt[5], Oliver Kurzai[5], Hermann Einsele[1] & Juergen Loeffler[1]

Aspergillus (*A*.) *fumigatus* is an opportunistic fungal mold inducing invasive aspergillosis (IA) in immunocompromised patients. Although antifungal activity of human natural killer (NK) cells was shown in previous studies, the underlying cellular mechanisms and pathogen recognition receptors (PRRs) are still unknown. Using flow cytometry we were able to show that the fluorescence positivity of the surface receptor CD56 significantly decreased upon fungal contact. To visualize the interaction site of NK cells and *A. fumigatus* we used SEM, CLSM and *d*STORM techniques, which clearly demonstrated that NK cells directly interact with *A. fumigatus* via CD56 and that CD56 is re-organized and accumulated at this interaction site time-dependently. The inhibition of the cytoskeleton showed that the receptor re-organization was an active process dependent on actin re-arrangements. Furthermore, we could show that CD56 plays a role in the fungus mediated NK cell activation, since blocking of CD56 surface receptor reduced fungal mediated NK cell activation and reduced cytokine secretion. These results confirmed the direct interaction of NK cells and *A. fumigatus*, leading to the conclusion that CD56 is a pathogen recognition receptor. These findings give new insights into the functional role of CD56 in the pathogen recognition during the innate immune response.

Invasive aspergillosis (IA), primarily caused by the mold *Aspergillus fumigatus*, is a devastating disease in immunocompromised patients suffering from hematological malignancies or undergoing allogeneic hematopoietic stem cell transplantation (HSCT)[1]. The mortality rate of HSCT patients diagnosed with IA ranges from 60–90%[2] and the prognosis for long-term survival is extremely poor[3]. Recently, it was shown that HSCT patients with probable/proven IA had a delayed reconstitution of natural killer (NK) cells for more than a year post HSCT[4]. In addition, patients with severe IA were found to have a lower NK cell count compared to patients with well-controlled IA, suggesting that NK cells play a critical role in immunity to IA.

NK cells comprise 5–15% of the peripheral blood mononuclear cells (PBMCs) in healthy individuals and belong to the innate immune system[5]. Upon activation, NK cells release immune regulatory cytokines to stimulate other immune cells and display cytotoxicity directed against tumor or virus-infected cells by granule release[5]. NK cells are defined as CD56 positive and CD3 negative cells and can be distinguished into CD3−CD56dimCD16+ and CD3−CD56brightCD16− cells. While CD56dim cells are more cytotoxic, CD56bright cells produce high levels of cytokines such as IFNγ and TNFα[6]. The function of NK cells is induced by the interplay of inhibitory and activating receptors[7], leading to cytotoxicity directed against tumors and virus-infected cells. Besides the recognition of these cells, NK cells also recognize other infectious pathogens, become activated, and as a response induce either lysis of these pathogens or trigger activation of other immune cells by cytokine release[8–10]. Consequently, an important role of NK cells in the response to several fungal pathogens, including *A. fumigatus*, *Candida albicans*, *Cryptococcus neoformans* and *Mucorales* has been demonstrated[8, 11–16].

[1]Department of Internal Medicine II, WÜ4i, University Hospital Wuerzburg, Wuerzburg, Germany. [2]Department of Biotechnology and Biophysics, Biocenter, Julius-Maximilian-University Wuerzburg, Wuerzburg, Germany. [3]Immunology Area, Pediatric Hospital Bambino Gesù, Rome, Italy. [4]Dipartimento di Medicina Sperimentale (DIMES) and Centro di Eccellenza per la Ricerca Biomedica, Universita' di Genova, Genova, Italy. [5]Septomics Research Centre, Friedrich Schiller University and Leibniz Institute for Natural Product Research and Infection Biology–Hans Knoell Institute, Jena, Germany. Sabrina Ziegler and Esther Weiss contributed equally to this work. Hermann Einsele and Juergen Loeffler jointly supervised this work. Correspondence and requests for materials should be addressed to J.L. (email: Loeffler_J@ukw.de)

Previous studies demonstrated that NK cells are activated by direct interaction with *A. fumigatus* germ tubes and hyphae[11, 14]. Upon activation NK cells release cytotoxic granules containing granzyme and perforin, which damage *A. fumigatus* hyphae[14]. Direct contact with *A. fumigatus* germ tubes induces IFNγ release of NK cells which interferes with fungal metabolic activity and growth[11]. Furthermore, studies in a neutropenic IA mouse model demonstrated that NK cell recruitment is essential for the clearance of the fungal infection and that IFNγ release by NK cells is critical for the immune defense during IA[17, 18]. Although NK cells have been shown to play a crucial role in host - pathogen interaction during *A. fumigatus* infection, the underlying mechanism and the NK cell recognition receptors have not been identified to date.

In this study, we examined the NK cell-*A. fumigatus* interaction to determine the PRR responsible for *A. fumigatus* recognition. None of the tested NK cell activating receptors demonstrated any changes in their expression levels on the cell surface when exposed to *A. fumigatus*. However, a significant reduction of CD56 fluorescence positivity of NK cells was observed upon contact with *A. fumigatus* germ tubes. Scanning electron microscopy (SEM), confocal laser scanning microscopy (CLSM) and *direct* stochastic optical reconstruction microscopy (*d*STORM)[19, 20] were used to visualize the direct interaction of NK cells with *A. fumigatus* hyphae. We were able to demonstrate that CD56 was accumulating at the direct interaction site of NK cells with the fungus and that this re-organization of CD56 was dependent on the actin-cytoskeleton re-arrangement. Furthermore, we showed that blocking of CD56 reduced NK cell activation and partially restored CD56 fluorescence positivity of NK cells suggesting that CD56 is one recognition receptor for *A. fumigatus*.

Results

NK cell receptors are not altered in their expression while CD56 fluorescence positivity is significantly decreased upon fungal contact.

To identify possible NK cell PRRs, the expression of several NK cell activating receptors and of the *A. fumigatus* PRRs TLR-2, TLR-4 and Dectin-1[21–23] were analyzed in the presence of *A. fumigatus* after different incubation times using flow cytometry. Importantly, no difference in the expression of the mentioned receptors was noticed (Supplementary Fig. 1). Even so, NKp30 has been described as a PRR for fungal pathogens[8, 24], no significant changes were detected in the presence of *A. fumigatus* (Supplementary Fig. 1).

CD56 used in combination with CD3 is a well-known characterization marker to distinguish NK cells from other immune cells such as T-cells or monocytes[25, 26]. Surprisingly, we detected a prominent reduction of CD56 fluorescence positivity of NK cells after co-cultivation with *A. fumigatus* germ tubes compared to control NK cells (Fig. 1a and Supplementary Fig. 2). Additionally, NK cells were observed to upregulate the CD69 receptor (Fig. 1b) upon fungal contact, indicating NK cell activation[27]. Interestingly, reduction of CD56 fluorescence positivity of NK cells started as early as 2 h post incubation (Fig. 1c).

To evaluate whether this effect was dependent on the fungal MOI, we investigated the decrease of CD56 fluorescence positivity of NK cells at different MOIs 6 h after co-cultivation. A significant decrease of CD56 fluorescence positivity of NK cells (71.9%) was observed at a MOI of 0.1 compared to control NK cells (97%) (Fig. 1d).

A potential mechanism that could provoke down-regulation of protein expression on the cell surface is apoptosis. Mycotoxins produced by *A. fumigatus* are not only able to inhibit DNA and RNA synthesis in affected cells, but can also induce apoptosis by cell membrane alterations[28]. To investigate whether the reduction of CD56 fluorescence positivity of NK cells was caused by the induction of apoptosis, NK cells were stained with Annexin V to identify apoptotic NK cells. NK cells confronted with *A. fumigatus* germ tubes for 9 h showed a reduction of CD56 fluorescence positivity (Fig. 2a), while only a few NK cells were both, CD56 negative and Annexin V positive. However, the CD56 negative NK cells were mostly negative for Annexin V (54.6%), indicating that apoptosis is not induced in these cells (Fig. 2a).

To better understand the mechanism of CD56 reduction, we determined CD56 gene expression in NK cells confronted with *A. fumigatus* germ tubes for different incubation times. In the control experiments the expression of CD56 mRNA was time-dependently increased after treatment with IL-15 and IL-2 (Fig. 2b) whereas the expression of CD56 mRNA in NK cells co-cultivated with *A. fumigatus* was not altered (Fig. 2b). These results indicated that gene expression was not differentially regulated by exposure to *A. fumigatus* and that a different mechanism is responsible for the reduction of CD56 positive NK cells.

To study potential CD56 shedding upon contact of NK cells with *A. fumigatus*, cell culture supernatants were collected from co-cultures after 3, 6, 9 and 12 h and the supernatants were tested for CD56 by ELISA. The level of CD56 in the supernatant was observed to be equal or below the smallest standard for all samples and no significant changes in CD56 levels were detected at any of the incubation times of the co-culture experiments (Fig. 2c). Thus, CD56 shedding from the cell surface during NK cell-*A. fumigatus* interaction could be excluded as a possible mechanism.

To investigate whether CD56 was internalized upon contact with *A. fumigatus*, NK cells were co-cultured with *A. fumigatus* germ tubes for 6 h before CD56 was surface- and intracellularly-labeled. CD56 on the cell surface of NK cells cultured with germ tubes was significantly reduced compared to control NK cells while the intracellular CD56 signal did not change (Fig. 2d). Even when intracellular CD56 signal was measured after preceding trypsination of surface receptors, CD56 levels did not change (Supplementary Fig. 4). The protein concentration of CD56 was evaluated to investigate whether CD56 protein was degraded or protein synthesis was inhibited in NK cells exposed to *A. fumigatus* potentially due to the release of mycotoxins[28]. Cells were harvested after co-culture with *A. fumigatus* for 4 h, and protein lysates were subsequently prepared for western blot analysis. The signal of the CD56 protein in *A. fumigatus* treated NK cells was comparable to the one of control NK cells (Fig. 2e, Supplementary Fig. 3). Since we detected a decrease in CD56 fluorescence positivity of NK cells but not by western blotting, we concluded that this effect might be the consequence of fewer antigen-antibody interactions due to sterical problems.
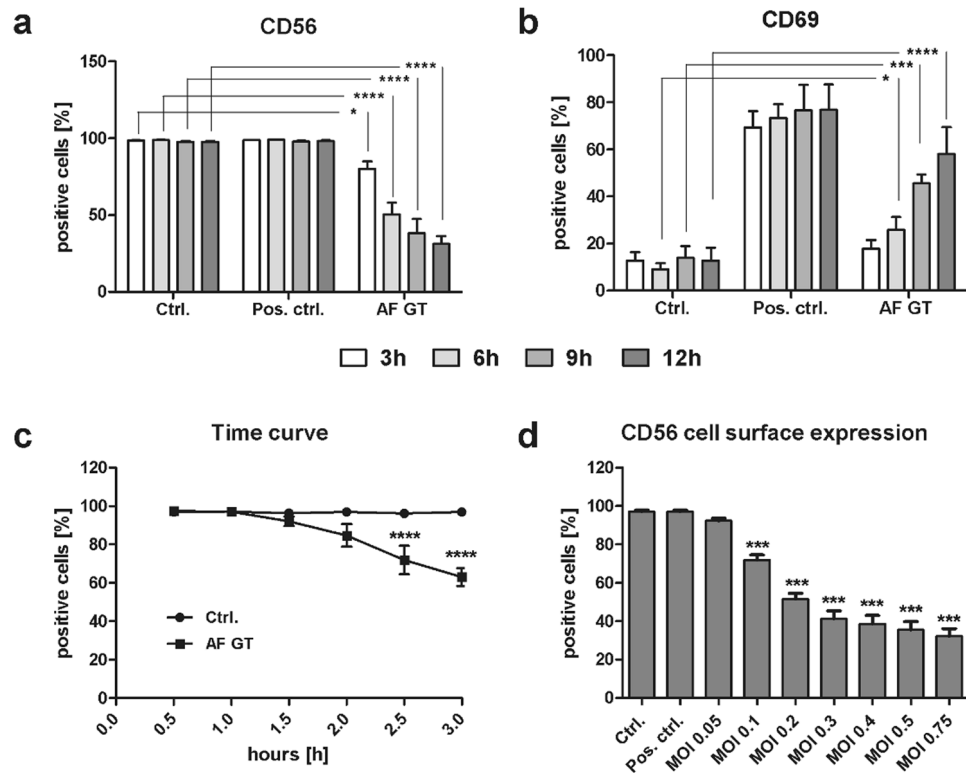
Figure 1. Reduction in CD56 positivity after fungal contact. NK cells were treated with 500 U/ml IL-15 and IL-2 (Pos. Ctrl.), with *A. fumigatus* germ tubes (AF GT, MOI 0.5) or left untreated (Ctrl.) for different periods of time. Flow cytometry was performed to analyze (**a**) CD56 expression (n = 4), (**b**) CD69 expression (n = 5), (**c**) time dependent down-regulation of CD56 (n = 5) and (**d**) CD56 expression after treatment with different MOIs of *A. fumigatus* germ tubes (AF GT, n = 3). NK cells were incubated for 3, 6, 9 and 12 h to determine (**a**) CD56 and (**b**) CD69 expression. To determine the time dependent down-regulation of CD56 NK cells were incubated for 0.5, 1, 1.5, 2, 2.5 and 3 h (**c**). To assess the effect of different fungal MOIs NK cells were incubated for 6 h (**d**). NK cells were defined as NKp46$^+$CD3$^-$. Data are represented as mean + SEM. Significant differences were are marked with an asterisk (*p < 0.05, ***p < 0.005, ****p < 0.001).

NK cells directly interact with live *A. fumigatus* and CD56 is re-organized to the interaction site via actin filaments. NK cells were shown to release IFNγ and perforin upon direct contact with *A. fumigatus*[11, 14], thus we investigated the role of direct contact on the reduction of CD56 fluorescence positivity of NK cells.

Co-cultures were prepared, separating NK cells and *A. fumigatus* germ tubes with transwell permeable membranes. The membranes were small enough to prohibit the contact of cells and *A. fumigatus* but large enough for molecules such as cytokines or mycotoxins to diffuse into the lower compartment. Expression of CD56 and CD69 on the surface of NK cells was determined after a 6 h cultivation. As a positive control, IL-15 and IL-2 were added to the transmembrane system to activate NK cells (Fig. 3a). Separation of *A. fumigatus* germ tubes and NK cells by the transwell membrane did not induce NK cell activation, nor was CD56 fluorescence positivity of NK cells reduced (Fig. 3a). These results demonstrate that the reduction of CD56 fluorescence positivity of NK cells was not mediated via a fungal-derived soluble factor but was depended on direct contact with *A. fumigatus*.

To determine whether the decrease of CD56 fluorescence positivity of NK cells was regulated by the interaction with live germ tubes, NK cells were co-cultivated with inactivated *A. fumigatus* germ tubes, inactivated *C. albicans*, and live *A. fumigatus* germ tubes. NK cells exhibit cytotoxicity against tumor cells and become activated upon contact with these cells[29], therefore NK cells cultivated in the presence of the cancer cell line K562 served as a positive control. Cells were incubated for 12 h with the different targets. Then, CD56 and CD69 fluorescence positive cells were determined. K562 cells induced a significant activation of NK cells that was comparable to the activation of NK cells treated with IL-15 and IL-2, but showed no decrease of CD56 (Fig. 3b). Inactivated *C. albicans* and *A. fumigatus* did not induce the reduction of CD56 fluorescence positivity nor activate NK cells (Fig. 3b). Live *A. fumigatus* germ tubes activated NK cells and significantly reduced the number of CD56 fluorescence positive NK cells (Fig. 3b), suggesting that the decrease of CD56 fluorescence positivity of NK cells was only induced by live *A. fumigatus*.

From these experiments we hypothesized that CD56 interacts as a recognition receptor with *A. fumigatus*.

A further potential mechanism hypothesized for the reduction of CD56 fluorescence positivity of NK cells upon contact with *A. fumigatus* germ tubes is that CD56 acts as an interaction receptor for *A. fumigatus*. SEM, CLSM and *d*STORM microscopy were used to determine whether or not human NK cells interact directly with *A. fumigatus* hyphae and if CD56 is re-located during this interaction. NK cells were cultured alone or in the

56
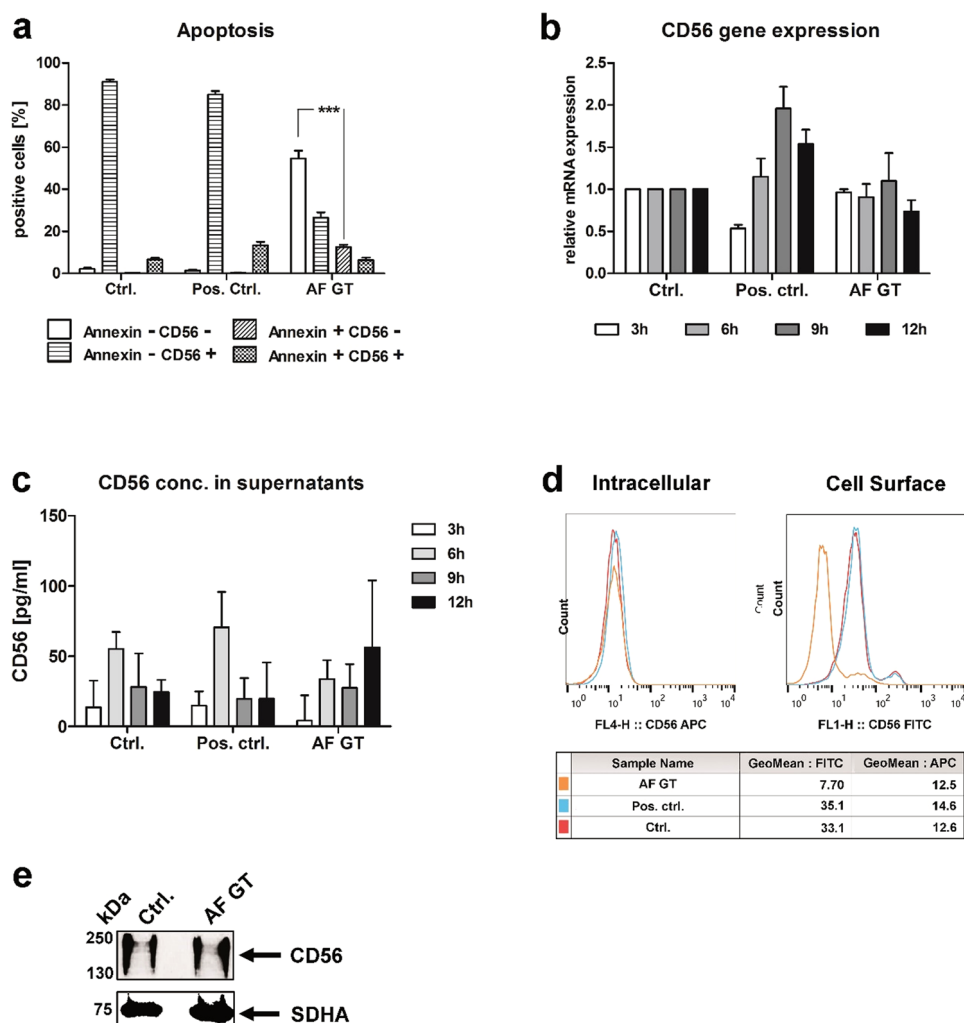
Figure 2. CD56 reduction is not induced by apoptosis, deregulation of protein and gene expression. NK cells were either treated with 500 U/ml IL-15 and IL-2 (Pos. ctrl.), with *A. fumigatus* germ tubes (AF GT, MOI 0.5) or left untreated (Ctrl.). (**a**) Induction of apoptosis was determined 9 h after co-cultivation and (**b**) mRNA/transcript expression after different incubation times was quantified by real-time RT-qPCR. (**c**) CD56 withdrawal was analysed by ELISA. (**d**) Intracellular and membranous CD56 expression was analysed by flow cytometry 6 h after co-cultivation, representative data of three independent experiments. Red line: NK cells (Ctrl.); blue line: NK cells treated with IL-15 and Proleukine (Pos. ctrl.); orange line: NK cells treated with *A. fumigatus* (AF GT). (**e**) Protein concentrations were visualized by western blot analyses 4 h after co-cultivation. Blots were cropped and image processing was performed by Adobe Photoshop software. Representative data of five independent experiments. Data of (**a**–**c**) are represented as mean + SEM for (**a**) n =, (**b**) n = and (**c**) n = 3). Significant differences are marked with an asterisk (***p < 0.005).

presence of *A. fumigatus* germ tubes for 3 h and SEM pictures were taken from NK-*A. fumigatus* co-cultures. In fact, NK cells were observed interacting directly with *A. fumigatus*, and the interaction site was mostly at the hyphal part of the fungus (Fig. 4). We observed a close interaction of NK cells with *A. fumigatus* suggesting that NK cells recognize the fungus via specific receptors.

To further confirm this observation and the possibility that CD56 is a recognition receptor we performed CLSM and super-resolution *d*STORM microscopy. After the cultivation of NK cells in the presence of *A. fumigatus* for different incubation times, CD56 localization was determined. Indeed, NK cells incubated with *A. fumigatus* revealed a strong CD56 signal at the contact site whereas other parts of the plasma membrane exhibited only a weak signal (Fig. 5b,d–f). In contrast, the CD56 fluorescence signal in control NK cells was homogenously distributed on the plasma membrane (Fig. 5a,c). 3D-*d*STORM analysis revealed a concentration of CD56 fluorescence at the interaction site and in lanes surrounding the interaction site (Fig. 5e,f; Video 1). We further observed that CD56 relocalization occurs in a time dependent manner (Fig. 6a). At 3 h and 6 h after initiation of co-culture, CD56 signal is observed at the fungal interface and still ubiquitously distributed in the remaining NK cell membrane which is not interacting with the fungus. At 9 h and 12 h, the CD56 signal is detected at the fungal interface but not in the remaining NK cell membrane anymore (Fig. 6a). To proof the result that the interaction site is increasing time dependently, we measured the length and amount of CD56 stained interaction sites after

57
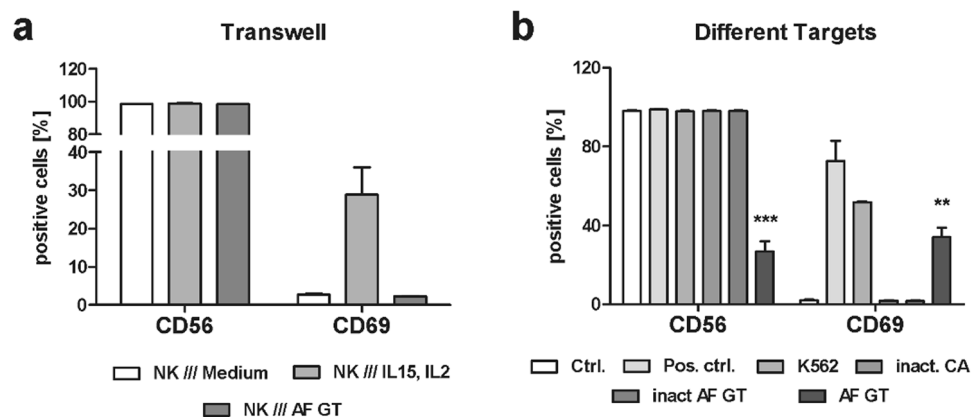
Figure 3. Reduction of CD56 is a result of the direct fungal contact. (**a**) NK cells were separated from fungal germ tubes (AF GT, MOI 0.5), medium supplemented with 500 U/ml IL-15 and IL-2 (Pos. ctrl) or medium (Ctrl.) by a transwell membrane (n = 3). (**b**) NK cells were cultured alone (Ctrl.), with 500 U/ml IL-15 and IL-2 (Pos. ctrl.), with K562 at an effector to target ratio of 5:1 (K562), with inactivated *C. albicans* (inact. CA, MOI 0.5) and with live and inactivated *A. fumigatus* germ tubes (AF GT, inact. AF GT, MOI 0.5, n = 6). Data are represented as mean ± SEM. Significant differences are marked with an asterisk (**p < 0.01, ***p < 0.005).
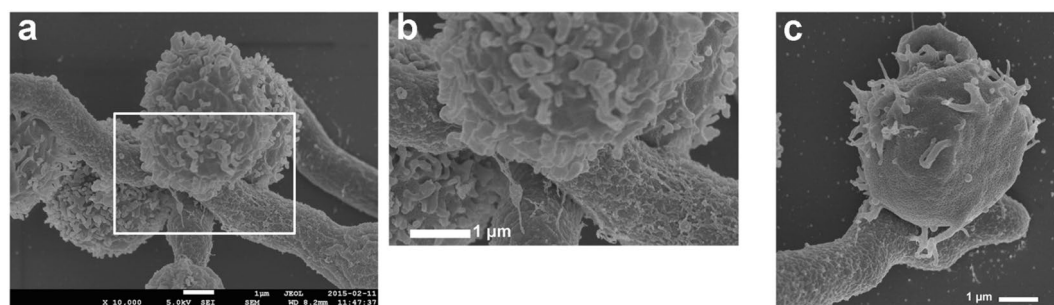
Figure 4. Direct contact with *A. fumigatus* hyphae. NK cells-*A. fumigatus* 3 h co-culture specimens were inspected with a field emission SEM using a detector for secondary electrons at 5 kV and a magnification of ×10,000. Representative result of two independent experiments performed in duplicates. Picture (**b**) is a zoom in of (**a**), illustrating the interaction site of NK cells with *A. fumigatus* hyphae. Scale bar for (**a–c**): 1 μm.

3, 6, 9, and 12 h of co-culture, respectively. Indeed, the highest counts and the greatest lengths of interaction sites were detectable after 12 h of co-cultivation (Supplementary Fig. 5), confirming that CD56 is re-localized to the fungal interface in a time dependent manner. To elucidate whether CD56 is directly interacting with the fungus or if CD56 accumulation at the fungal interface is mediated by indirect mechanisms, we co-cultured live *A. fumigatus* germ tubes with different concentrations of soluble CD56 protein for 6 h and afterwards stained the samples with a fluorescent anti-CD56 antibody (Fig. 6b). As a control, *A. fumigatus* germ tubes were cultured alone and were stained with fluorescent anti-CD56 antibody to exclude the possibility of unspecific antibody binding to the fungus (Fig. 6b). In contrast to the negative control, incubation of *A. fumigatus* with soluble CD56 resulted in a staining of fungal structures after incubation with anti-CD56 antibody (Fig. 6b). These experiments showed that CD56 is time-dependently relocalized to the fungal interface and directly binds the fungus.

It is well known that NK cells encounter the cytoskeleton when they recognize and lyse target cells[30]. While the actin cytoskeleton plays a role in the early recognition of target cells and enables receptor reorganization[30], cell lysis occurs to later time points and is mediated by the transport of lytic granules to the target interface via microtubules[30]. To investigate whether the actin or the microtubule cytoskeleton plays a role in the re-organization of CD56, we treated NK cells with either actin or microtubules inhibiting agents and then co-cultured NK cells with *A. fumigatus* germ tubes for 0, 3, 6, and 9 h, respectively. Cytochalasin D is preventing actin polymerization and elongation by binding to existing actin filaments[31], whereas colchicine binds to soluble tubulin dimers and thereby inhibits microtubule polymerization[32] and thus prevents the transport of granules to the membrane[33]. NK cells treated with cytochalasin D compared to control NK cells did not show any differences in the CD56 fluorescence positivity of NK cells (Fig. 7a). However, when NK cells were challenged with the fungus we detected significantly less CD56 reduction of fluorescence positivity in cytochalasin D treated samples compared to controls, concluding that relocalization of CD56 is inhibited (Fig. 7a).

In contrast, treatment with colchicine did not result in any increase of the CD56 fluorescence positivity of NK cells in the presence of fungus compared to untreated NK cells (Fig. 7b).

58

cLSM   2D-dSTORM   3D-dSTORM
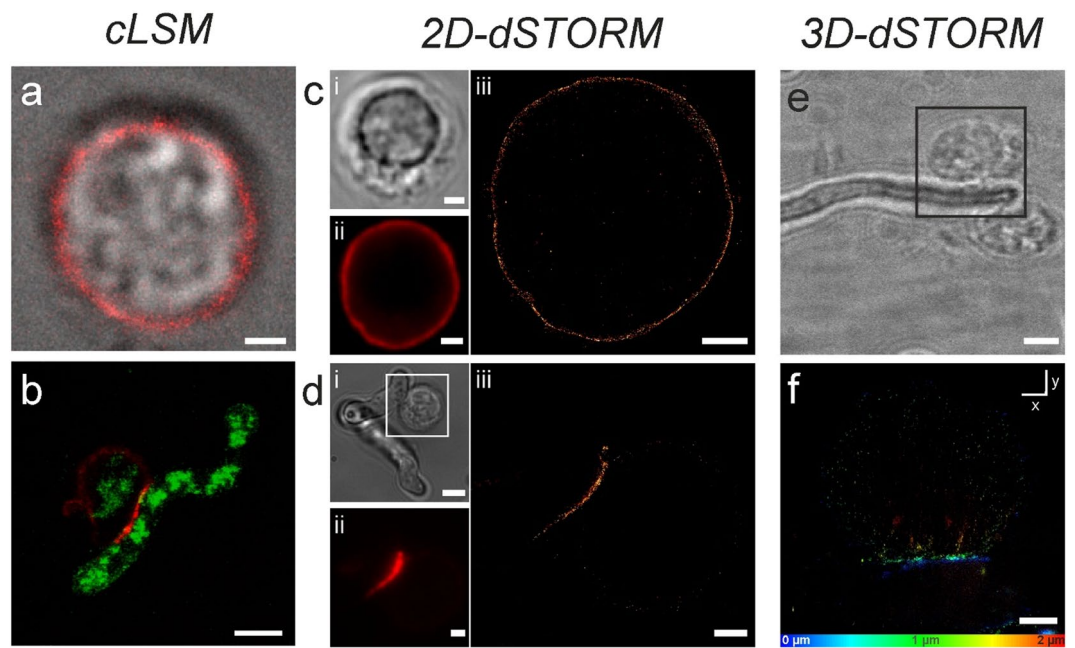
Figure 5. CD56 re-organization to the interaction site. NK cells and NK cells-*A. fumigatus* co-cultures were visualized with (**a,b**) CLSM, (**c,d**) 2D *d*STORM, and (**e,f**) 3D *d*STORM after staining with anti-CD56. NK cells were either left untreated (**a,c**) or incubated with *A. fumigatus* germ tubes (MOI 0.5) for 3 h (**b,d–f**). (**b**) Auto fluorescence was recorded to visualize NK cell-*A. fumigatus* interaction. Transmitted light pictures (ci, di), (**e**), widefield fluorescence images (cii, dii), and *d*STORM images (ciii, diii) of the interaction site were compared. In (**f**) the x-y projection of a reconstructed 3D dSTORM image is given which is color coded in z. (**e**) The transmitted light picture is a zoom out of (**f**) illustrating two NK cells which interact with *A. fumigatus*. Scale bars: 1.5 μm (**c**, dii,iii), 2 μm (**b,f**), 3 μm (**a,e**), 4 μm (di), and 5 μm (**b**). 3D stack showing interaction site of NK cell *and A. fumigatus* (**e,f**). NK cells were incubated for 3 h with *A. fumigatus*, thereafter stained with anti CD56-Alexa Fluor 647, and visualized in 3D.

Consequently, inhibition of actin polymerization but not inhibition of the microtubules impaired CD56 re-localization to the fungal interaction site concluding that CD56 plays a role in the early fungal recognition.

To further functionally analyze the role of CD56, we blocked CD56 on the NK cell surface using an anti-CD56 blocking antibody before co-cultivation of NK cells with *A. fumigatus* germ tubes for 9 h (Fig. 7c). The blocked CD56 receptor was still recognized by the flow cytometric antibody directed against CD56, since NK cells treated with the blocking antibody displayed the same percentage of CD56 positivity as unblocked NK cells (Fig. 7c). In the presence of the fungus, CD56 blocking restored the number of CD56 fluorescence positive NK cells to 55% after fungal co-culture compared to 20% when CD56 was not blocked (Fig. 7c). Interestingly, treatment with CD56 blocking antibody significantly decreased the fungal-induced activation of NK cells (13.3%) compared to NK cells on which CD56 was not blocked (18.5%) (Fig. 7c).

To further characterize the effects on CD56 blocking in the NK cell response to the fungus, culture supernatants from CD56 blocked and unblocked NK cells were analyzed by multiplex immunoassay (Fig. 7d–f). Challenging unblocked NK cells with *A. fumigatus* provoked a significant induction in the secretion of macrophage inflammatory protein (MIP)-1α (CCL3) and RANTES (CCL5) while MIP-1β showed a tendency (p = 0.067) to be higher secreted after fungal stimulation (Fig. 7d–f). This fungal mediated cytokine secretion was reduced when CD56 was blocked on the NK cell surface compared to the unblocked NK cells in the presence of the fungus. We detected no significant differences between CD56 blocked NK cells with and without fungal stimulation (Fig. 7d–f). Indeed, we further observed a significant reduction for MIP-1α secretion in CD56 blocked NK cells challenged with the fungus compared to unblocked NK cells in the presence of the fungus (Fig. 7d). These blocking experiments verified the functional role of CD56 confirming that CD56 is a recognition receptor for *A. fumigatus*.

Reduction of CD56 fluorescence positivity is detectable in the presence of other *Aspergillus* species.

To investigate whether CD56 fluorescence positivity of NK cells was also reduced in the presence of other *Aspergillus* species, pre-stimulated NK cells were cultured with *A. niger*, *A. clavatus*, *A. flavus* and *A. fumigatus* germ tubes for 6 h. Expression of CD56 and CD69 was then determined using flow cytometry. All *Aspergillus* species tested induced a reduction of CD56 (Fig. 8a). However, NK cells confronted with *A. fumigatus* germ tubes displayed a significantly higher decrease of CD56 fluorescence positivity of NK cells compared to *A. niger*, *A. flavus* and *A. clavatus* (Fig. 8a). NK cells co-cultivated with *A. fumigatus*, *A. flavus* and *A. clavatus* displayed an increase in the CD69 expression indicating NK cell activation whereas NK cells treated with *A. niger* showed a

59
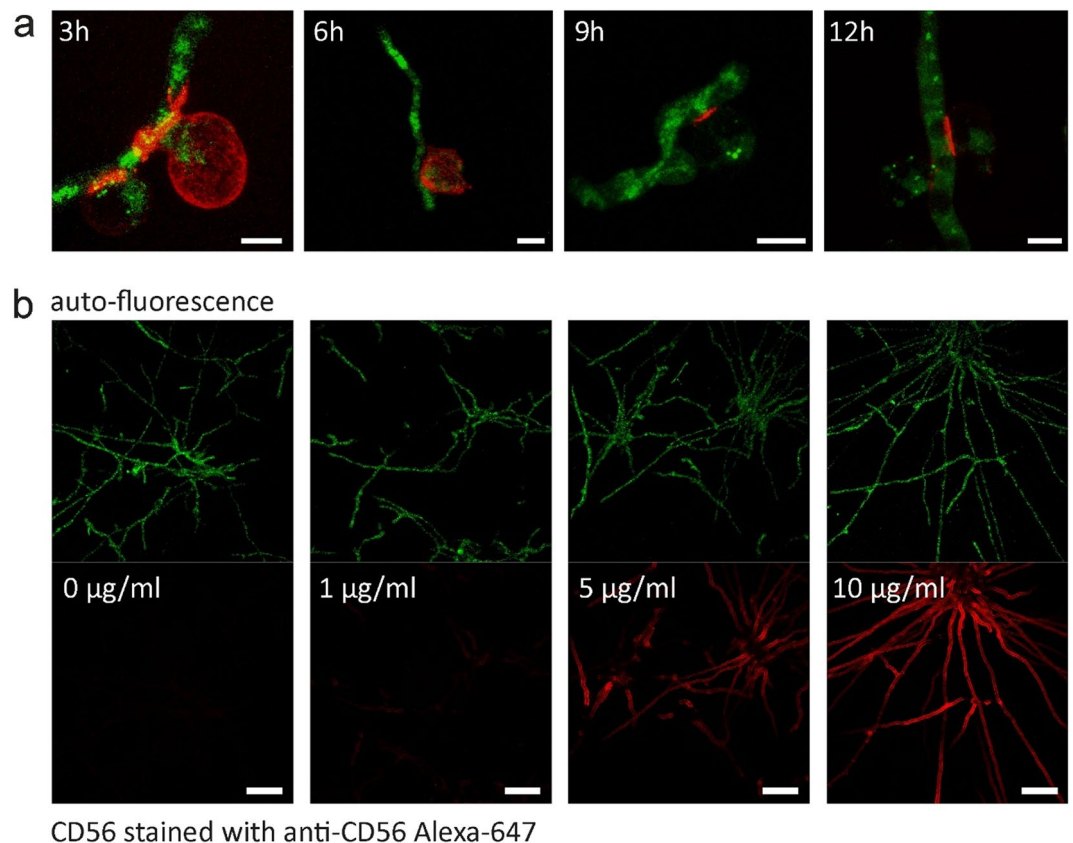
Figure 6. Time course of the NK cell-*A. fumigatus* interaction and direct binding of CD56 to the fungus. (**a**) NK cells were cultured with *A. fumigatus germ tubes* (MOI 0.5) for 3, 6, 9 and 12 h. CLSM pictures were taken from these co-cultures. (**b**) Fungal hyphae were incubated for 6 h with 0, 1, 5, and 10 μg/ml soluble CD56 and were afterwards stained with anti-CD56 antibody. Alexa 647-labeled anti-CD56 antibody was used to visualize the distribution of CD56, while germ tubes could be detected via their auto fluorescence. Scale bars represent 5 μm (**a**) and 30 μm (**b**).

decrease in CD69 expression compared to control NK cells (Fig. 8b). These results suggest that *Aspergillus* species express a specific molecule on their surface recognized by CD56 on NK cells.

Discussion

This study is the first to visualize the direct interaction of NK cells and *A. fumigatus* and to show that CD56 has a functional role during fungal recognition. NK cells can recognize fungal pathogens and induce their lysis[8–10, 12]. Besides their antifungal activity towards *C. albicans*, *C. neoformans*, *Paracoccidioides brasiliensis*[34] and *Coccidioides immitis*[35], it was shown that NK cells recognize *A. fumigatus* and display antifungal activity directed against the hyphae[11, 14]. However, the mechanism of this interaction is still poorly understood.

Previous studies demonstrated that NK cells form direct conjugates with *C. neoformans*[35, 36] and that NKp30 and NKp46 act as fungal PRR[8, 24]. These publications and our previous studies[11] suggested that the interaction of NK cells and *A. fumigatus* is mediated by a PRR. Unexpectedly, neither experimentally tested NK cell activating receptors nor the known fungal recognizing receptor NKp30 were modulated upon co-culture with *A. fumigatus*. Surprisingly, we observed a striking decrease of CD56 fluorescence positivity on the NK cell surface upon exposure to the fungus. By quantifying the NCAM/CD56 protein concentration in the supernatant of NK cells-*A. fumigatus* co-cultures, we could exclude that NCAM/CD56 was neither shed from the cell surface nor was the secreted isoform of NCAM/CD56 expressed.

Mycotoxins have an impact on the mRNA and protein expression of host cells but our analyses clearly showed that the secreted mycotoxins have no influence on the expression level of CD56 on transcriptome and protein level of NK cells.

On neuronal cells, NCAM/CD56 can be endocytosed and is then mostly recycled to the cell surface whereas a minority of the endocytosed NCAM/CD56 is degraded[37]. Analyses showed that NCAM/CD56 was not internalized upon contact with *A. fumigatus*. Thus, we speculated about a potential binding of CD56 to the fungus that is masking the molecule as it was seen as well for NKp30 in the studies of Li *et al.*[8]. Indeed, we were able to show a direct interaction of NK cells with live *A. fumigatus* by SEM, CLSM and super-resolution *d*STORM microscopy, which showed that NCAM/CD56 distribution on the NK cell surface markedly changed after fungal contact. In addition, NCAM/CD56 re-location was observed until the complete CD56 signal was detected at the fungal interaction site and the lengths and amounts of the interaction site increased over time (Supplemetary Fig. 4).

60
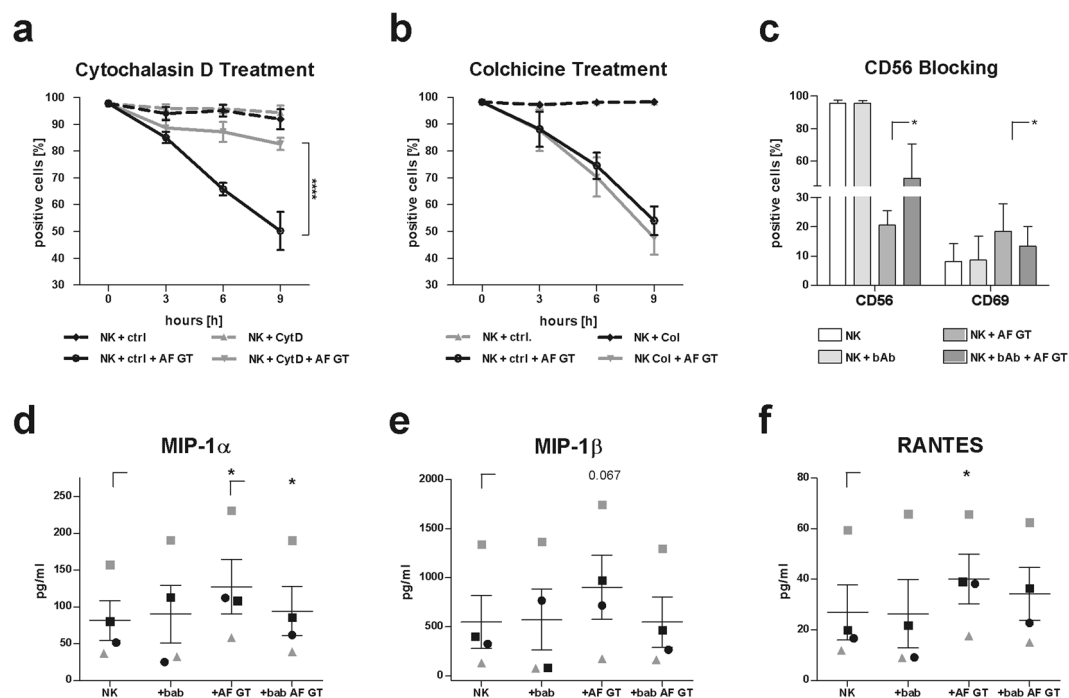
Figure 7. CD56 mediated fungal recognition is dependent on actin and CD56 blocking inhibits NK cell function. NK cells were incubated with (**a**) cytochalasin D (Cyt. D, n = 4), (**b**) colchicine (Col., n = 3) and (**c**) CD56 blocking antibody (bAb, n = 4) prior to co-cultivation with the fungus (AF GT). Percentage of CD56 positive cells was determined after an incubation with the fungus for 0, 3, 6, and 9 h. A paired student's t-test was performed to compare NK + ctrl + AF GT against NK + CytD + AF GT or NK + Col + AF GT (**a,b**). Control samples were cultured in the presence of the corresponding control solution. Percentage of CD56 and CD69 positive cells was assessed after a co-cultivation for 9 h. CD56 and CD69 expression was analysed using flow cytometry. NK cells were defined as NKp46$^+$CD3$^-$. Supernatants derived from CD56 blocking experiments were analysed by ProcartaPlex^{TM} multiplex immunoassays (n = 4, **d–f**). The concentration of (**d**) MIP-1α, (**e**) MIP-1β and (**f**) RANTES detectable in supernatants is displayed in pg/ml. A paired student's t-test was performed to compare (**c**) NK + AF GT against NK + bAb + AF GT and (**d–f**) NK against + AF GT and + AF GT against + bAb AF GT. Data are represented as mean ± SEM. Significant differences are indicated by an asterisk (*p < 0.05, ****p < 0.001).
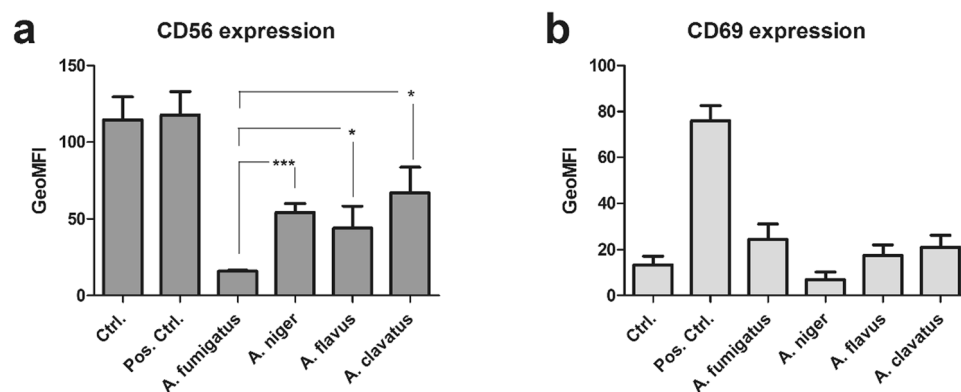
Figure 8. The reduction of CD56 is not as stringent for other Aspergillus species as it is for *A. fumigatus*. Primary NK cells were pre-treated overnight with IL-2 (1000 U/ml). Pre-treated NK cells were cultured in the presence of germ tubes of *A. fumigatus*, *A. niger*, *A. flavus* or *A. clavatus* at MOI 0.5, or were left untreated (Ctrl.) for 6 h. NK cells treated with 500 U/ml IL-15 and IL-2 served as control for NK cell activation (Pos. ctrl.). The expression of CD56 (**a**) and CD69 (**b**) was analysed using flow cytometry. NK cells were defined as NKp46$^+$CD3$^-$. Data are represented as mean of the geometric mean fluorescence intensity (GeoMFI) + SEM of n = 4 independent experiments. Significant differences between AF GT treated NK cells and NK cells treated with the other *Aspergilli* are indicated by an asterisk (*p < 0.05; **p < 0.01; ***p < 0.005; ****p < 0.001).

Furthermore, we could exclude that CD56 is shed from the NK cell surface and bound to *A. fumigatus* by CLSM microscopy. In NK cells-*A. fumigatus* co-cultures we were not able to detect any CD56 outside of the interaction site with NK cells. NCAM/CD56 positive NK cells were also decreased in the presence of other *Aspergillus* species but less when compared to *A. fumigatus* suggesting that *A. fumigatus* is expressing a CD56 ligand with a higher abundance.

CD56 was identified as the 140 kDa isoform of the human neural-cell adhesion molecule (NCAM)[25]. Two isoforms (140 kD and 180 kD) of NCAM show transmembrane binding and have intracellular domains while the 120 kD isoform has a glycosyl-phosphatidylinositol membrane anchor but no intracellular domains[38]. While the three isoforms have different C-termini, the N-terminal extracellular domains are identical in all three isoforms[39]. Therefore, we used the 120 kD isoform to test whether CD56 is directly interacting with *A. fumigatus*. By microscopy, we showed that soluble CD56 directly binds in a concentration dependent manner to growing *A. fumigatus* structures, confirming our previous observations and hypothesis.

Blocking of CD56 did not only reduce fungal mediated NK cell activation but further inhibited the amount of secreted cytokines. Chemokines like MIP-1α (CCL3), MIP-1β (CCL4), and RANTES (CCL5) are secreted by human blood NK cells[40, 41]. CCL3, 4, and 5 modulate the migratory behavior of leukocytes and their importance in cryptococcal infections was highlighted by the study from Huffnagle and McNeil (1999)[42]. Huffnagle and McNeil showed that depletion of either MIP-1α or the common MIP-1α, MIP-1β and RANTES receptor CCR5 conferred to a higher fungal burden and inhibited leukocyte recruitment in the central nervous system of knockout mice[42]. The role of the CCR5 ligands CCL3, 4, and 5 was also highlighted in another study that reported an abolished NK cell accumulation at sites of infection in CCR5$^{-/-}$ mice[43]. Detection of fewer levels of MIP-1α, MIP-1β, and RANTES in supernatants derived from samples in which NK cells were blocked with CD56 and challenged with the fungus compared to co-cultures in which CD56 was not blocked is suggesting a crucial role for these chemokines and NK cells in the immune response directed against the fungus.

Based on these results and the previous publications we conclude that CD56 is involved in the secretion of CCL3, 4, and 5 to recruit further leukocytes such as NK cells, monocytes and neutrophils to sites of *A. fumigatus* infections.

Recently, Mace *et al*. demonstrated that CD56 is accumulated at the developmental synapse which is formed at stromal cells and that CD56 is co-localized with F-actin[44]. Showing that CD56 re-localization is dependent on the actin cytoskeleton, we could confirm the findings of Mace *et al*.[44] leading to the suggestion that CD56 plays a crucial role in the recognition of pathogens.

A recent study published by Voigt *et al*. demonstrated a decrease of NCAM/CD56 expression in the presence of live *C. albicans*[16]. In addition, it was shown that the surface protein gp63 of *Leishmania* further reduces CD56 fluorescence positivity, indicating that NCAM/CD56 plays a functional role in the recognition of eukaryotic and prokaryotic pathogens expressing a specific molecule on their cell surface. These publications further strengthen our hypothesis that NCAM/CD56 is a pathogen recognition receptor[45].

The functional role of NCAM/CD56 expressed by NK cells referring to NK cell cytotoxicity against tumor cells has been controversially discussed. It was observed that NCAM/CD56 had no impact on the lysis effect of target cells[46, 47] whereas on the other hand, other reports demonstrated that the cytotoxicity of NK cells interacting with NCAM-expressing target cells is enhanced by NCAM/CD56[48, 49]. These reports suggested a functional role of NCAM/CD56 in the recognition of target cells and in the induction of cytotoxicity. These observations and our findings suggest that NCAM/CD56 is a pathogen recognition receptor and plays a functional role for the NK cell cytotoxicity in the innate immune response. Our study provides novel insights in the interaction of NK cells and *A. fumigatus* as well as in NK cell biology.

Methods

Cell culture. Human PBMCs were isolated from fresh blood of healthy volunteers giving written consent by a Ficoll standard density gradient centrifugation (Biochrom AG). Usage of the human blood specimens was approved by the Ethical Committee of the University Hospital Wuerzburg. NK cells were isolated from PBMCs using MACS NK negative selection kit (Miltenyi Biotec) and were cultured in RPMI 1640 (Invitrogen) supplemented with 10% heat-inactivated fetal bovine serum (FBS) and 120 µg/ml gentamicin (Refobacin; Merck) at 37 °C and 5% CO$_2$. K562 cells were cultured under the same conditions as human NK cells. NK cells were stimulated overnight with 1000 U/ml recombinant human (rh) IL-2 (Proleukin, Novartis).

Infection conditions. *A. fumigatus* (ATCC 46645), *A. flavus* (CBS 625.66) and *A. clavatus* (CBS 114.48) conidia and germ tubes were prepared as described previously[50]. *A. niger* (CBS 553.65) germ tubes were prepared in RPMI with 10% FCS overnight. NK cells were incubated with live *A. fumigatus* germ tubes at a multiplicity of infection (MOI) of 0.5 at 37 °C for 3, 6, 9 or 12 h. For one experimental setup NK cells were incubated with *A. fumigatus* germ tubes and *C. albicans* (Wildtype SC5314) hyphae that were inactivated as previously described[51].

Flow Cytometry. The purity of isolated NK cells (>95%) and expression of surface receptors were determined by flow cytometry using a FACSCalibur (BD-Biosciences). NK cell population was defined as NKp46$^+$CD3$^-$ cells.

Changes in the expression of NK cell receptors were examined using the following antibodies: anti-NKp30 PE (Biolegend), anti-NKp44 PE (Biolegend), anti-NKG2D PE (BD-Biosciences), anti-CD16 FITC (Miltenyi Biotec), anti-CD56 FITC and APC (BD-Biosciences), anti-2B4 FITC (Biolegend), anti-NTB-A PE (Biolegend), anti-Dectin-1 PE, anti-TLR-2 PE and anti-TLR-4 PE (BD-Biosciences). Apoptotic NK cells were assessed after an incubation time of 9 h using Annexin V FITC (BD-Biosciences) after staining cells with the surface marker antibodies anti-NKp46 PE, anti-CD3 PerCP and anti-CD56 APC. Intracellular expression of CD56 after incubation with germ tubes for 6 h was investigated by firstly staining CD56 on the cell surface with anti-CD56 FITC (BD-Biosciences). Then, cells were fixed (4% formaldehyde), permeabilized (Wash Perm, BD-Biosciences) and

intracellular CD56 was stained using anti-CD56 APC (BD-Biosciences). To remove surface markers, NK cells were incubated in 0.5% trypsin-EDTA (Sigma) for 30 min at 37 °C before samples were stained. All data were analyzed with FlowJo software (Tree Star Inc.).

Western Blot Analysis. NK cells were incubated for 4 h either alone or with *A. fumigatus* germ tubes at MOI 0.5 under standard culture conditions, before a total crude protein extraction was performed[52]. Proteins were separated on 12% SDS-PAGE gels, blotted onto nitrocellulose membrane and CD56 was detected using an anti-CD56 antibody (Cell Signaling, clone 123C3). Succinate dehydrogenase complex, subunit A (SDHA) served as a loading control (Cell Signaling).

Enzyme Linked Immunosorbent Assay (ELISA) and multiplex immunoassay. To quantify the CD56 concentration in co-culture supernatants, an ELISA assay was performed according to the manufacturer's instructions (Abcam). Secretion of cytokines and other proteins released by NK cells were assessed in cell-free supernatants using the ProcartaPlex™ multiplex immunoassay from Affymetrix eBioscience. The analyses were performed according to the manufacturer's instructions using the Bio-Plex 200 System from Bio-Rad. CCL 3 ELISA (MIP-1α, R&D), CCL 4 ELISA (MIP-1β, R&D), and CCL 5 ELISA (RANTES, Biolegend) were performed as described in the manufacture's manual. The ELISA was performed according to the manufacture's manual using the NanoQuant (infinite M200 Pro, Tecan).

Transwell experiments. 600 μl RPMI containing 0.6×10^6 NK cells were seeded in 24-well plates, then a transwell membrane insert (Corning) with a pore size of 0.4 μm was inserted into each well and 100 μl RPMI were added per transwell. Depending on the condition, the 100 μl RPMI were either pure, supplemented with 500 U/ml IL-15 and IL-2, or enriched with *A. fumigatus* germ tubes MOI 0.5. After 6 h, NK cells were harvested and receptor expression of CD56 and CD69 was monitored by flow cytometry.

CD56 blocking. A GPR165 (IgG2a) monoclonal blocking antibody was kindly provided by Daniela Pende and Alessandro Moretta and CD56 was blocked as previously described[53]. NK cells (4×10^6 cells/ml) were incubated in CD56 blocking antibody (10.9 μg/ml) or IgG2a isotype control (Biolegend, 10.9 μg/ml) diluted in RPMI + FCS for 30 min at 37 °C. Afterwards, NK cells were cultured alone or in co-culture with *A. fumigatus* germ tubes (MOI 0.5) at a NK cell concentration of 1×10^6 cells/ml. CD56 blocking antibody and isotype control were 4 fold diluted during culture. After 9 h, cells were harvested and CD56 and CD69 expression was evaluated by flow cytometry. Supernatants of co-cultures were stored at −20 °C until a ProcartaPlex™ or ELISA was performed.

Soluble CD56 protein binding. Different concentrations (0, 1, 5, 10 μg/ml) of soluble CD56 (120 kD, R&D) were incubated with live *A. fumigatus* germ tubes (0.5×10^6 cells/ml) on poly-D-lysine coated 8-well Lab-Tek coverglass chambers (Thermo Fisher Scientific) for 6 h at 37 °C. Samples were prepared and stained with mAB CD56 mouse-anti-human Alexa Fluor 647 as described in the section "*Fluorescence microscopy*". Confocal laser scanning microscopy (CLSM) images of the CD56 -*A. fumigatus* interaction were acquired as described in the section "*Fluorescence microscopy*".

Cytochalasin D and colchicine treatment. NK cells were treated with 10 μM cytochalasin D (Sigma), 10 μM colchicine or the perspective DMSO and ethanole control for 30 min at 37 °C. NK cells were cultured alone or with *A. fumigatus* germ tubes (MOI 0.5) for 0, 3, 6 and 9 h in the presence of 5 μM cytochalasin D or colchicine or the perspective DMSO or ethanol controls. Expression of CD56 was determined using flow cytometry.

Length and amount of CD56 fluorescent interaction sites. NK cell-*A. fumigatus* co-cultures were prepared on Lab-Tek coverglass chambers as described under the section "*Fluorescence microscopy*". In order to evaluate the volume of the CD56 – *A. fumigatus* interaction site, image stacks were recorded from four different time points of co-incubation by CLSM. The number and length of CD56 interaction sites after 3, 6, 9, and 12 h were determined by Fiji and the 3D object counter plugin[54].

Scanning electron microscopy (SEM). NK cells were seeded alone or with *A. fumigatus* germ tubes (MOI 0.5) on microscopic cover slips (10 mm, Hartenstein) coated with poly-D-lysine (Sigma Aldrich). 3 h post incubation, samples were washed with PBS and were fixed for 12–18 h at 4 °C in a solution of 2.5% glutaraldehyde (Merck), 2.5 mM $MgCl_2$, 50 mM KCl, and 50 mM cacodylic acid, pH 7.2. Afterwards, samples were washed with 50 mM cacodylic acid, pH 7.2 and then, dehydrated stepwise with acetone, critical point dried (critical point dryer: BAL-TEC CPD 030) and metal coated (sputter coater BAL-TEC SCD 005) with gold-palladium. Specimens were examined with a field emission scanning electron microscope (JEOL JSM-7500F) using a detector for secondary electrons (SEI detector) at 5 kV and a magnification of ×10,000.

Fluorescence microscopy. NK cells were cultured alone or with *A. fumigatus* (MOI 0.5) on poly-D-lysine coated 8-well Lab-Tek coverglass chambers for 3, 6, 9 or 12 h. Then, samples were fixed in 0.67% formaldehyde for 30 min. After blocking with 5% BSA in HBSS for 30 min, samples were stained with mAB CD56 mouse-anti-human Alexa Fluor 647 (1:50, Biolegend) and fixed in 2% formaldehyde for 20 min. CLSM images of the NK-*Aspergillus* interaction were acquired with a LSM700 system (Carl Zeiss) with a plan-apochromat 63 ×/1.40 oil immersion objective. *D*STORM imaging of *A. fumigatus* incubated NK cells and control NK cells was performed in photoswitching buffer (100 mM mercaptoethylamine in PBS pH 7.4). 2D measurements were conducted on an inverted wide-field fluorescence microscope (IX-71; Olympus) as described previously[20, 55, 56]. For each measurement 15,000 images with an exposure time of 20 ms and irradiation intensity of ~7 kW/cm² were recorded using highly inclined and laminated optical sheet (HILO) illumination.

63

For 3D *d*STORM measurements[57] an Axio Observer.Z1 (Carl Zeiss Microscopy) equipped with a water-immersion objective (LD C-Apochromat 63×/1.15 W Corr M27; Carl Zeiss Microscopy) was used. Fluorophores were excited with a 150 mW 640 nm laser (iBeam Smart 640-S; Toptica) which was spectrally cleaned (MaxDiode LD01-640/8; Semrock). Emission and excitation light was separated using a dichroic mirror (BrightLine Di01-R405/466/532/635-25 × 36; Semrock) and a bandpass filter (ZET405/488/532/642 m, Chroma) and the wavelength range of the emitted light was specified further with a single bandpass filter (E700/75 m; Chroma). Astigmatism of the point spread function (PSF) was introduced by a 250 mm achromatic cylindrical lens (Thorlabs). Fluorophores were detected by an EMCCD camera (iXon Ultra DU897U-CSO; Andor). At least 30,000 frames at a frame rate of 54 Hz were collected for each 3D measurement. The open source rapi*d*STORM[58], version 3.3.1 software was used to reconstruct *d*STORM images from the recorded 2D and 3D image stacks.

Statistical analysis. A two-way ANOVA or a two-tailed, paired Student's t-test was used to evaluate statistical significance. *P*-values < 0.05 were considered statistically significant. Statistics were calculated using GraphPad Prism 5 software.

Ethics approval. All methods were performed in accordance with the relevant guidelines and regulations. Informed consent has been obtained for study participation and for publication of information, as requested by the Ethics Committee of the University Hospital of Wuerzburg (permit #302/15).

References

1. Segal, B. H. A. *The New England journal of medicine* **360**, 1870–1884, doi:10.1056/NEJMra0808853 (2009).
2. Singh, N. & Paterson, D. L. Aspergillus infections in transplant recipients. *Clinical microbiology reviews* **18**, 44–69, doi:10.1128/CMR.18.1.44-69.2005 (2005).
3. Salmeron, G. *et al.* Persistent poor long-term prognosis of allogeneic hematopoietic stem cell transplant recipients surviving invasive aspergillosis. *Haematologica* **97**, 1357–1363, doi:10.3324/haematol.2011.058255 (2012).
4. Stuehler, C. *et al.* Immune Reconstitution After Allogeneic Hematopoietic Stem Cell Transplantation and Association With Occurrence and Outcome of Invasive Aspergillosis. *The Journal of infectious diseases* **212**, 959–967, doi:10.1093/infdis/jiv143 (2015).
5. Robertson, M. J. & Ritz, J. Biology and clinical relevance of human natural killer cells. *Blood* **76**, 2421–2438 (1990).
6. Cooper, M. A., Fehniger, T. A. & Caligiuri, M. A. The biology of human natural killer-cell subsets. *Trends in immunology* **22**, 633–640 (2001).
7. Lanier, L. L. Up on the tightrope: natural killer cell activation and inhibition. *Nat Immunol* **9**, 495–502, doi:10.1038/ni1581 (2008).
8. Li, S. S. *et al.* The NK receptor NKp30 mediates direct fungal recognition and killing and is diminished in NK cells from HIV-infected patients. *Cell host & microbe* **14**, 387–397, doi:10.1016/j.chom.2013.09.007 (2013).
9. Lieke, T., Graefe, S. E., Klauenberg, U., Fleischer, B. & Jacobs, T. NK cells contribute to the control of Trypanosoma cruzi infection by killing free parasites by perforin-independent mechanisms. *Infection and immunity* **72**, 6817–6825, doi:10.1128/IAI.72.12.6817-6825.2004 (2004).
10. Small, C. L. *et al.* NK cells play a critical protective role in host defense against acute extracellular Staphylococcus aureus bacterial infection in the lung. *J Immunol* **180**, 5558–5568 (2008).
11. Bouzani, M. *et al.* Human NK cells display important antifungal activity against Aspergillus fumigatus, which is directly mediated by IFN-gamma release. *J Immunol* **187**, 1369–1376, doi:10.4049/jimmunol.1003593 (2011).
12. Mavoungou, E., Held, J., Mewono, L. & Kremsner, P. G. A Duffy binding-like domain is involved in the NKp30-mediated recognition of Plasmodium falciparum-parasitized erythrocytes by natural killer cells. *The Journal of infectious diseases* **195**, 1521–1531, doi:10.1086/515579 (2007).
13. Schmidt, S., Schneider, A., Demir, A., Lass-Florl, C. & Lehrnbecher, T. Natural killer cell-mediated damage of clinical isolates of mucormycetes. *Mycoses* **59**, 34–38, doi:10.1111/myc.12431 (2016).
14. Schmidt, S. *et al.* Human natural killer cells exhibit direct activity against Aspergillus fumigatus hyphae, but not against resting conidia. *J Infect Dis* **203**, 430–435, doi:10.1093/infdis/jiq062 (2011).
15. Schmidt, S. *et al.* Rhizopus oryzae hyphae are damaged by human natural killer (NK) cells, but suppress NK cell mediated immunity. *Immunobiology* **218**, 939–944, doi:10.1016/j.imbio.2012.10.013 (2013).
16. Voigt, J. *et al.* Human natural killer cells acting as phagocytes against Candida albicans and mounting an inflammatory response that modulates neutrophil antifungal activity. *The Journal of infectious diseases* **209**, 616–626, doi:10.1093/infdis/jit574 (2014).
17. Morrison, B. E., Park, S. J., Mooney, J. M. & Mehrad, B. Chemokine-mediated recruitment of NK cells is a critical host defense mechanism in invasive aspergillosis. *The Journal of clinical investigation* **112**, 1862–1870, doi:10.1172/JCI18125 (2003).
18. Park, S. J., Hughes, M. A., Burdick, M., Strieter, R. M. & Mehrad, B. Early NK cell-derived IFN-{gamma} is essential to host defense in neutropenic invasive aspergillosis. *J Immunol* **182**, 4306–4312, doi:10.4049/jimmunol.0803462 (2009).
19. Heilemann, M. *et al.* Subdiffraction-resolution fluorescence imaging with conventional fluorescent probes. *Angew Chem Int Ed Engl* **47**, 6172–6176, doi:10.1002/anie.200802376 (2008).
20. van de Linde, S. *et al.* Direct stochastic optical reconstruction microscopy with standard fluorescent probes. *Nature protocols* **6**, 991–1009, doi:10.1038/nprot.2011.336 (2011).
21. Braedel, S. *et al.* Aspergillus fumigatus antigens activate innate immune cells via toll-like receptors 2 and 4. *British journal of haematology* **125**, 392–399, doi:10.1111/j.1365-2141.2004.04922.x (2004).
22. Meier, A. *et al.* Toll-like receptor (TLR) 2 and TLR4 are essential for Aspergillus-induced activation of murine macrophages. *Cellular microbiology* **5**, 561–570 (2003).
23. Steele, C. *et al.* The beta-glucan receptor dectin-1 recognizes specific morphologies of Aspergillus fumigatus. *PLoS Pathog* **1**, e42, doi:10.1371/journal.ppat.0010042 (2005).
24. Vitenshtein, A. *et al.* NK Cell Recognition of Candida glabrata through Binding of NKp46 and NCR1 to Fungal Ligands Epa1, Epa6, and Epa7. *Cell host & microbe* **20**, 527–534, doi:10.1016/j.chom.2016.09.008 (2016).
25. Lanier, L. L., Testi, R., Bindl, J. & Phillips, J. H. Identity of Leu-19 (CD56) leukocyte differentiation antigen and neural cell adhesion molecule. *The Journal of experimental medicine* **169**, 2233–2238 (1989).
26. Ritz, J., Schmidt, R. E., Michon, J., Hercend, T. & Schlossman, S. F. Characterization of functional surface structures on human natural killer cells. *Advances in immunology* **42**, 181–211 (1988).
27. Borrego, F., Pena, J. & Solana, R. Regulation of CD69 expression on human natural killer cells: differential involvement of protein kinase C and protein tyrosine kinases. *European journal of immunology* **23**, 1039–1043, doi:10.1002/eji.1830230509 (1993).
28. Abad, A. *et al.* What makes Aspergillus fumigatus a successful pathogen? Genes and molecules involved in invasive aspergillosis. *Revista iberoamericana de micologia* **27**, 155–182, doi:10.1016/j.riam.2010.10.003 (2010).
29. Lozzio, B. B. & Lozzio, C. B. Properties and usefulness of the original K-562 human myelogenous leukemia cell line. *Leukemia Research* **3**, 363–370 (1979).

64

30. Orange, J. S. Formation and function of the lytic NK-cell immunological synapse. *Nat Rev Immunol.* **8**, 713–725 (2008).
31. Mortensen, K. & Larsson, L. I. Effects of cytochalasin D on the actin cytoskeleton: association of neoformed actin aggregates with proteins involved in signaling and endocytosis. *Cellular and molecular life sciences: CMLS* **60**, 1007–1012, doi:10.1007/s00018-003-3022-x (2003).
32. Margolis, R. L. & Wilson, L. Addition of colchicine–tubulin complex to microtubule ends: the mechanism of substoichiometric colchicine poisoning. *Proceedings of the National Academy of Sciences of the United States of America* **74**, 3466–3470 (1977).
33. Orange, J. S. *et al.* The mature activating natural killer cell immunologic synapse is formed in distinct stages. *Proceedings of the National Academy of Sciences of the United States of America* **100**, 14151–14156, doi:10.1073/pnas.1835830100 (2003).
34. Jimenez, B. E. & Murphy, J. W. *In vitro* effects of natural killer cells against Paracoccidioides brasiliensis yeast phase. *Infection and immunity* **46**, 552–558 (1984).
35. Petkus, A. F. & Baum, L. L. Natural killer cell inhibition of young spherules and endospores of Coccidioides immitis. *J Immunol* **139**, 3107–3111 (1987).
36. Levitz, S. M., Dupont, M. P. & Smail, E. H. Direct activity of human T lymphocytes and natural killer cells against Cryptococcus neoformans. *Infection and immunity* **62**, 194–202 (1994).
37. Diestel, S., Schaefer, D., Cremer, H. & Schmitz, B. NCAM is ubiquitylated, endocytosed and recycled in neurons. *Journal of cell science* **120**, 4035–4049, doi:10.1242/jcs.019729 (2007).
38. Nybroe, O. & Bock, E. Structure and function of the neural cell adhesion molecules NCAM and L1. *Advances in experimental medicine and biology* **265**, 185–196 (1990).
39. Leshchyns'ka, I. & Sytnyk, V. Intracellular transport and cell surface delivery of the neural cell adhesion molecule (NCAM). *Bioarchitecture* **5**, 54–60, doi:10.1080/19490992.2015.1118194 (2015).
40. Nieto, M. *et al.* Roles of Chemokines and Receptor Polarization in NK-Target Cell Interactions. *The Journal of Immunology* **161**, 3330–3339 (1998).
41. Fehniger, T. A. *et al.* Natural Killer Cells from HIV-1+ Patients Produce C-C Chemokines and Inhibit HIV-1 Infection. *The Journal of Immunology* **161**, 6433–6438 (1998).
42. McNeil, G. B. H. A. L. K. Dissemination of C. neoformans to the central nervous system: role of chemokines, Th1 immunity and leukocyte recruitment. *Journal of NeuroVirology* **5**, 76–81 (1999).
43. Bonfa, G. *et al.* CCR5 controls immune and metabolic functions during Toxoplasma gondii infection. *PloS one* **9**, e104736, doi:10.1371/journal.pone.0104736 (2014).
44. Mace, E. M., Gunesch, J. T., Dixon, A. & Orange, J. S. Human NK cell development requires CD56-mediated motility and formation of the developmental synapse. *Nature communications* **7**, 12171, doi:10.1038/ncomms12171 (2016).
45. Lieke, T. *et al.* Leishmania surface protein gp63 binds directly to human natural killer cells and inhibits proliferation. *Clinical and experimental immunology* **153**, 221–230, doi:10.1111/j.1365-2249.2008.03687.x (2008).
46. Lanier, L. L. *et al.* Molecular and functional analysis of human natural killer cell-associated neural cell adhesion molecule (N-CAM/CD56). *J Immunol* **146**, 4421–4426 (1991).
47. Pandolfi, F. *et al.* Expression of cell adhesion molecules in human melanoma cell lines and their role in cytotoxicity mediated by tumor-infiltrating lymphocytes. *Cancer* **69**, 1165–1173 (1992).
48. Nitta, T., Yagita, H., Sato, K. & Okumura, K. Involvement of CD56 (NKH-1/Leu-19 antigen) as an adhesion molecule in natural killer-target cell interaction. *The Journal of experimental medicine* **170**, 1757–1761 (1989).
49. Takasaki, S., Hayashida, K., Morita, C., Ishibashi, H. & Niho, Y. CD56 directly interacts in the process of NCAM-positive target cell-killing by NK cells. *Cell biology international* **24**, 101–108, doi:10.1006/cbir.1999.0457 (2000).
50. Morton, C. O. *et al.* Gene expression profiles of human dendritic cells interacting with Aspergillus fumigatus in a bilayer model of the alveolar epithelium/endothelium interface. *PloS one* **9**, e98279, doi:10.1371/journal.pone.0098279 (2014).
51. Semmlinger, A. *et al.* Fever-range temperature modulates activation and function of human dendritic cells stimulated with the pathogenic mould Aspergillus fumigatus. *Med Mycol* **52**, 438–444, doi:10.1093/mmy/myu005 (2014).
52. Fliesser, M. *et al.* Hypoxia-inducible factor 1alpha modulates metabolic activity and cytokine release in anti-Aspergillus fumigatus immune responses initiated by human dendritic cells. *International journal of medical microbiology: IJMM* **305**, 865–873, doi:10.1016/j.ijmm.2015.08.036 (2015).
53. Valgardsdottir, R. *et al.* Direct involvement of CD56 in cytokine-induced killer-mediated lysis of CD56+ hematopoietic target cells. *Experimental hematology* **42**, 1013–1021, e1011, doi:10.1016/j.exphem.2014.08.005 (2014).
54. Cordelières, S. B. F. P. A guided tour into subcellular colocalization analysis in light microscopy. *Journal of Microscopy* **224**, 213–232 (2006).
55. Burgert, A., Letschert, S., Doose, S. & Sauer, M. Artifacts in single-molecule localization microscopy. *Histochemistry and cell biology* **144**, 123–131, doi:10.1007/s00418-015-1340-4 (2015).
56. Letschert, S. *et al.* Super-resolution imaging of plasma membrane glycans. *Angew Chem Int Ed Engl* **53**, 10921–10924, doi:10.1002/anie.201406045 (2014).
57. Proppert, S. *et al.* Cubic B-spline calibration for 3D super-resolution measurements using astigmatic imaging. *Optics express* **22**, 10304–10316, doi:10.1364/OE.22.010304 (2014).
58. Wolter, S. *et al.* rapidSTORM: accurate, fast open-source software for localization microscopy. *Nature methods* **9**, 1040–1041, doi:10.1038/nmeth.2224 (2012).

Acknowledgements

Author Contributions

S.Z. and E.W. developed concepts, designed the overall study, performed experiments, performed data analyses and wrote the manuscript. A.-L.S and I.L. performed experiments. U.T., A.B., J.S., M.S. performed the dSTORM and CLSM pictures, analyzed the data and contributed to the manuscript. L.M., S.S. and O.K. provided discussions, technical assistance and contributed to the manuscript. H.E. and J.L. developed concepts, supervised the study and wrote the manuscript.

65

Additional Information

Supplementary information accompanies this paper at doi:10.1038/s41598-017-06238-4

Competing Interests: The authors declare that they have no competing interests.

Publisher's note: Springer Nature remains neutral with regard to jurisdictional claims in published maps and institutional affiliations.

66

3.5   Antibacterial Activity of Ceramide and Ceramide Analogs Against Pathogenic Neisseria

Abstract

"Certain fatty acids and sphingoid bases found at mucosal surfaces are known to have antibacterial activity and are thought to play a more direct role in innate immunity against bacterial infections. Herein, we analysed the antibacterial activity of sphingolipids, including the sphingoid base sphingosine as well as short-chain C6 and long-chain C16-ceramides and azido-functionalized ceramide analogs against pathogenic *Neisseriae*. Determination of the minimal inhibitory concentration (MIC) and minimal bactericidal concentration (MBC) demonstrated that short-chain ceramides and a ω-azidofunctionalized C6-ceramide were active against *Neisseria meningitidis* and *N. gonorrhoeae*, whereas they were inactive against *Escherichia coli* and *Staphylococcus aureus*. Kinetic assays showed that killing of *N. meningitidis* occurred within 2 h with ω–azido-C6-ceramide at 1 X the MIC. Of note, at a bactericidal concentration, ω–azido-C6-ceramide had no significant toxic effect on host cells. Moreover, lipid uptake and localization was studied by flow cytometry and confocal laser scanning microscopy (CLSM) and revealed a rapid uptake by bacteria within 5 min. CLSM and super-resolution fluorescence imaging by *direct* stochastic optical reconstruction microscopy demonstrated homogeneous distribution of ceramide analogs in the bacterial membrane. Taken together, these data demonstrate the potent bactericidal activity of sphingosine and synthetic short-chain ceramide analogs against pathogenic *Neisseriae*." [113]

SCIENTIFIC REP🞅RTS

OPEN

Antibacterial activity of ceramide and ceramide analogs against pathogenic *Neisseria*

Jérôme Becam[1], Tim Walter [2], Anne Burgert[3], Jan Schlegel [3], Markus Sauer[3], Jürgen Seibel[2] & Alexandra Schubert-Unkmeir[1]

Certain fatty acids and sphingoid bases found at mucosal surfaces are known to have antibacterial activity and are thought to play a more direct role in innate immunity against bacterial infections. Herein, we analysed the antibacterial activity of sphingolipids, including the sphingoid base sphingosine as well as short-chain C_6 and long-chain C_{16}-ceramides and azido-functionalized ceramide analogs against pathogenic *Neisseriae*. Determination of the minimal inhibitory concentration (MIC) and minimal bactericidal concentration (MBC) demonstrated that short-chain ceramides and a ω-azido-functionalized C_6-ceramide were active against *Neisseria meningitidis* and *N. gonorrhoeae*, whereas they were inactive against *Escherichia coli* and *Staphylococcus aureus*. Kinetic assays showed that killing of *N. meningitidis* occurred within 2 h with ω–azido-C_6-ceramide at 1 X the MIC. Of note, at a bactericidal concentration, ω–azido-C_6-ceramide had no significant toxic effect on host cells. Moreover, lipid uptake and localization was studied by flow cytometry and confocal laser scanning microscopy (CLSM) and revealed a rapid uptake by bacteria within 5 min. CLSM and super-resolution fluorescence imaging by *direct* stochastic optical reconstruction microscopy demonstrated homogeneous distribution of ceramide analogs in the bacterial membrane. Taken together, these data demonstrate the potent bactericidal activity of sphingosine and synthetic short-chain ceramide analogs against pathogenic *Neisseriae*.

Sphingolipids are composed of a structurally related family of backbones termed sphingoid bases, which are sometimes referred to as 'long-chain bases' or 'sphingosines'. The long chain (sphingoid) bases are aliphatic amines, containing two or three hydroxyl groups, and often a distinctive trans-double bond in position 4. The most abundant sphingoid base in animal tissues is sphingosine ((2 S,3 R,4E)-2-amino-4-octadecen-1,3-diol) with a C18 aliphatic chain, hydroxyl groups in positions 1 and 3 and an amine group in position 2 (see also Fig. 1). If the amine group of a sphingoid base is *N*-acylated with a fatty acid moiety, a ceramide molecule is formed. Ceramides consist of a long-chain or sphingoid base linked to a fatty acid via an amide bond. They are formed as the key intermediates in the biosynthesis of all complex sphingolipids. Fatty acids within ceramide molecules may vary in chain length[1] and are usually saturated, or with a single double bond or an α-hydroxyl group. Natural sphingolipids can be further chemically modified, resulting in derivatives that possess new properties. For example, sphingosine can be coupled with phenethyl isothiocyanatecan (PEITC) which leads to a significant increase of its antitumour activity towards human leukaemia cell growth as compared to sphingosine or PEITC alone[2].

Interestingly, many of the naturally occurring and synthetic sphingoid bases are cytotoxic for cancer cells and some have been recognized to exert antibacterial activity against pathogenic microorganisms[3–5]. So far, growth inhibitory activity has been shown against Gram-positive and Gram-negative bacteria, fungi and microalgae[6–10]. Interestingly, recent studies demonstrated that the sphingoid base sphingosine is also an important first-line defence of healthy airways against *Pseudomonas aeruginosa*[11]. Recently, a series of ceramide analogs was synthesized and analysed for the growth inhibitory effect on *Chlamydia trachomatis*[12]. Moreover, several synthetic dihydrosphingosine analogs have been demonstrated to be active against multi-drug resistant strains of *Mycobacterium tuberculosis*[13].

[1]Institute of Hygiene and Microbiology, Julius-Maximilian University Wuerzburg, Wuerzburg, Germany. [2]Institute for Organic Chemistry, Julius-Maximilian University Wuerzburg, Wuerzburg, Germany. [3]Department of Biotechnology and Biophysics, Julius-Maximilian University Wuerzburg, Wuerzburg, Germany. Correspondence and requests for materials should be addressed to A.S.-U. (email: aunkmeir@hygiene.uni-wuerzburg.de)
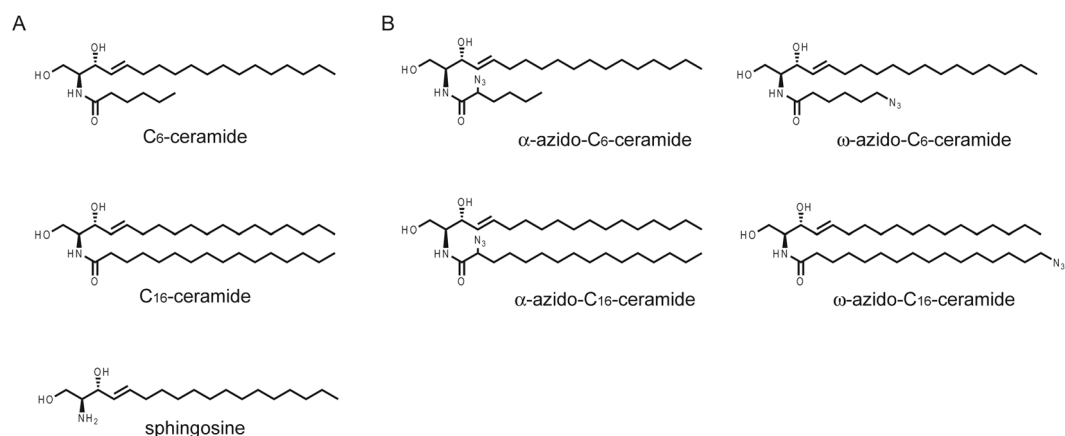
Figure 1. (**A**) Chemical structures of commercial available unmodified short-chain C_6-ceramide (d18:1/6:0) and long-chain C_{16}-ceramides (d18:1/16:0) and D-*erythro*-Sphingosine. (**B**) Chemical structures of α-azido-C_6-ceramide, ω-azido-C_6-ceramide, α-azido-C_{16}-ceramide and ω-azido-C_{16}-ceramide.

The inhibitory activity of sphingolipids towards microorganisms is thought to be a result of their ability to interact with the microbial cell wall[14], however the exact mechanism is still not known. As a result the leakage of cellular content and consequently microbial death occurs. Alternatively, lipids may penetrate and accumulate in the cytoplasm and may interfere with cell metabolism.

The present study details the antimicrobial activity of sphingolipids, focussing on sphingosines, ceramides and chemically modified ceramide-analogs against pathogenic *Neisseriae*. As an exclusive human pathogen, *Neisseria meningitidis* colonizes the upper respiratory tract of approximately 10–40% of the healthy population[15,16]. In rare cases, the bacteria can cause devastating invasive infections, resulting in sepsis and meningitis, mostly in young infants and toddlers. *N. gonorrhoeae* is a human pathogen responsible for genital tract infection (gonorrhoea). Occasionally, the organism can disseminate as a bloodstream infection. During the last years *N. gonorrhoeae* has evolved into a superbug with resistance to previously and currently recommended antimicrobials for treatment of gonorrhoea[17]. Herein, we demonstrate that a synthetic short-chain ceramide analog showed antimicrobial activity against pathogenic *Neisseriae*, and preliminary data indicate that this analog caused dissipation of the membrane potential. Broth microdilution assays were performed to determine the minimum inhibitory concentration (MIC) and the minimum bactericidal concentration (MBC) of sphingolipids against both species. *Escherichia coli* and the Gram-positive bacterium *Staphylococcus aureus* were included as positive controls. In addition, the bactericidal activity against *N. meningitidis* was studied in time-killing assays. In this context, we aimed to analyse the mechanism of lipid antimicrobial activity and applied "click-chemistry" to ceramides, which were equipped with an azide group in the acyl-side chain[18]. The influence of substitution of one hydroxyl group by an azide on the antimicrobial activity was assessed and modified ceramide analogs were used to study uptake and localization of functionalized ceramide analogs within the *N. meningitidis* membrane by confocal laser scanning (CLSM) and at subdiffraction resolution by *direct* stochastic optical reconstruction microscopy (*d*STORM)[19,20].

Results

Previous studies have demonstrated that numerous sphingoid bases and fatty acids act as antibacterial agents against a variety of Gram-positive and Gram-negative bacteria[6]. Among these is the long chain base sphingosine[7]. We first estimated MIC and MBC values for sphingosine for the Gram-negative organism *N. meningitidis* and the closely related species *N. gonorrhoeae* by broth microdilution assays. MIC, MIC_{50} and MBC values of 4 μg/ml, 1.97 μg/ml and 4 μg/ml, respectively, for *N. meningitidis* MC58 and 4 μg/ml (MIC), 1.25 μg/ml (MIC_{50}) and 8 μg/ml (MBC) for *N. gonorrhoeae* FA1090 were determined (Table 1). *E. coli* and the Gram-positive organism *S. aureus* were included as control organisms and MIC, MIC_{50} and MBC values of 16 μg/ml, 8.39 μg/ml and 16 μg/ml and 8 μg/ml, 1.22 μg/ml and >64 μg/ml, respectively, were estimated (Table 1). MIC_{50} values of 8.39 μg/ml and 1.22 μg/ml are in agreement with recently published data[6].

We next tested the antibacterial activity of ceramides, including short-chain C_6 and long-chain C_{16}-ceramides, and estimated MIC and MBC values as before. Interestingly, while long-chain C_{16}-ceramides were not active against *N. meningitidis* and *N. gonorrhoeae* (Table 1), short-chain C_6-ceramides displayed significant antimicrobial activity against both species: MIC, MIC_{50} and MBC values of 2 μg/ml, 0.69 μg/ml and 64 μg/ml, respectively, for *N. meningitidis* MC58 and 1 μg/ml (MIC), 0.18 μg/ml (MIC_{50}) and ≥64 μg/ml (MBC) for *N. gonorrhoeae* FA1090 were determined (Table 1).

We next made use of recently synthesized azido-functionalized ceramide analogs[21,22] allowing bio-orthogonal click–reactions[18] in order to follow uptake and transport of fluorescently labelled ceramides in *N. meningitidis*. Four different ceramide analogs were synthesized, including α–azido-C_6-ceramide, ω–azido-C_6-ceramide, α–azido-C_{16}-ceramide and ω–azido-C_{16}-ceramide (see Fig. 1) and first analysed for their antibacterial activity. Interestingly, when an additional azido group was added at the ω-position of the fatty acid chain of C_6-ceramide, the antibacterial activity was even increased: the ω–azido-C_6-ceramide analog displayed a MIC value of 2 μg/ml, MIC_{50} value of 0.8 μg/ml and MBC value of 4 μg/ml for *N. meningitidis* and a MIC value of 2 μg/ml, MIC_{50} value

Compound	N. meningitidis (MC58)			N. gonorrhoeae (FA1090)		
	[a]*MIC	**$MIC_{>50}$	#MBC	*MIC	**$MIC_{>50}$	#MBC
sphingosine	4	1.97	4	4	1.25	8
C_6-ceramide	2	0.69	64	1	0.18	>64
α-C_6-ceramide	>64	—	>64	>64	—	>64
ω-C_6-ceramide	2	0.8	4	2	0.8	4
C_{16}-ceramide	16	8.39	>64	>64	—	>64
α-C_{16}-ceramide	64	16.4	64	32	21	64
ω-C_{16}-ceramide	>64	—	>64	>64	—	>64
Compound	E. coli ATCC 25922			S. aureus ATCC 29213		
	[a]*MIC	**$MIC_{>50}$	#MBC	*MIC	**$MIC_{>50}$	#MBC
sphingosine	16	8.39	16	8	1.22	>64
C_6-ceramide	>64	—	>64	>64	—	>64
α-C_6-ceramide	>64	—	>64	>64	—	>64
ω-C_6-ceramide	>64	—	>64	>64	—	>64
C_{16}-ceramide	>64	—	>64	>64	—	>64
α-C_{16}-ceramide	>64	—	>64	>64	—	>64
ω-C_{16}-ceramide	>64	—	>64	>64	—	>64

Table 1. MICs and MBCs of sphingosine, short-chain C_6-ceramide, long-chain C_{16}-ceramide and C_6/C_{16}-ceramide analogs against N. meningitidis, N. gonorrhoeae, E. coli and S. aureus. [a]MIC and MBC (µg/ml) *MIC is defined as the lowest concentration of lipid that reduced growth by more than 95% **$MIC_{>50}$ is defined as the lowest concentration of lipid that reduced growth by more than 50% #MBC is defined as the lowest concentration of lipid that prevented growth.

Compound	N. meningitidis (MC58)			N. gonorrhoeae (FA1090)		
	[a]*MIC	**$MIC_{>50}$	#MBC	*MIC	**$MIC_{>50}$	#MBC
sphingosine	4	1.58	4	2	1.19	4
C_6-ceramide	4	2.32	8	8	2.01	32
α-C_6-ceramide	>64	—	>64	>64	—	>64
ω-C_6-ceramide	4	2.03	>64	4	1.46	16
C_{16}-ceramide	16	7.64	16	16	8.63	32
α-C_{16}-ceramide	32	17.6	32	32	20.4	64
ω-C_{16}-ceramide	>64	—	>64	>64	—	>64

Table 2. MICs and MBCs of sphingosine, short-chain C_6-ceramide, long-chain C_{16}-ceramide and C_6/C_{16}-ceramide analogs against N. meningitidis and N. gonorrhoeae determined in Graver-Wade medium. [a]MIC and MBC (µg/ml) *MIC is defined as the lowest concentration of lipid that reduced growth by more than 95% **$MIC_{>50}$ is defined as the lowest concentration of lipid that reduced growth by more than 50% #MBC is defined as the lowest concentration of lipid that prevented growth.

of 0.8 µg/ml and MBC value of 4 µg/ml for N. gonorrhoeae (Table 1). In contrast, modification at the α-position of the fatty acid chain of C_6-ceramide showed no significant activity against N. meningitidis (MIC and MBC value ≥64 µg/ml) or against N. gonorrhoeae FA1090 (MIC and MBC values ≥64 µg/ml). For E. coli ATCC 25922 and S. aureus ATCC 29213 the short-chain C_6-ceramide MIC/MBC values were ≥64 µg/ml, and antibacterial activity did not increase after modification of the fatty acid chain neither at the α- or ω-position (Table 1).

Effect of media on MIC and MBCs. It is well known that the inoculum size, the type of growth medium, the incubation time and the inoculum preparation method can influence MIC values. Many fastidious bacterial species including N. meningitidis and N gonorrhoeae do not grow satisfactorily using standard in vitro suscepti-bility testing approaches with unsupplemented media. For example, standard clinical laboratory broths, e.g. brain hart infusion or cation-adjusted Mueller-Hinton broth, allow multiplication of meningococci and gonococci only from large inocula. Recently a chemically defined liquid medium (Graver-Wade medium (GW)) was described, which permits growth of N. meningitidis and N. gonorrhoeae from low inocula[23]. We therefore next tested the antibacterial activity of ceramides by broth microdilution assays using GW medium. As shown in Table 2 the MIC values of sphingosine, C_6-ceramide and ω–azido-C_6-ceramide in GW medium shifted within 1 to 2 dilutions of the MIC tested in proteose peptone medium as shown in Table 1.

Time-killing studies. Next, time-killing studies for sphingosine, the unmodified C_6-ceramide from Avanti Polar and ω–azido-C_6-ceramide were performed on N. meningitidis. Both sphingosine and ω–azido-C_6-ceramide decreased the number of CFU/ml over the 0- to 24-h time period against N. meningitidis using 1 X MIC (Fig. 2). Kinetic assays showed that killing of N. meningitidis with sphingosine and ω–azido-C_6-ceramide occurred
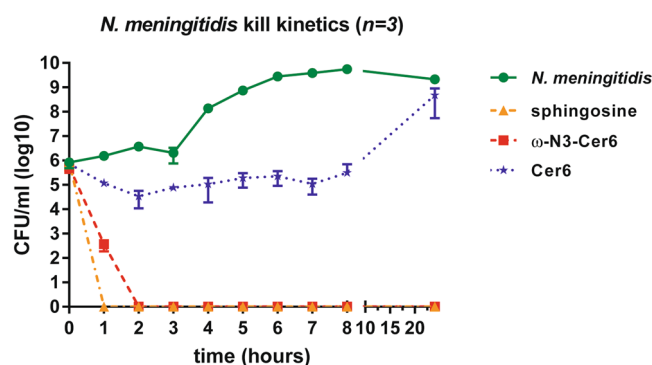
Figure 2. Kinetic killing of *N. meningitidis* with lipid treatment (sphingosine, unmodified C_6-ceramide and ω-azido-C_6-ceramide) at 1 time the MIC. Where no bacteria were recovered, +1 was added to the zero values before log transformation of the data. A geometric mean of $n = 3$ is shown for each data point. The error bars show mean $\pm$ SD of triplicate experiments.

	N. meningitides alone	Treatment with		
		C_6-ceramide	sphingosine	ω–C_6-ceramide
AUC	215.54	154.27	2.95	5.44
Trapezoidal-area significance probability[b,c] (P value)		0.039792	<0.0001	<0.0001

Table 3. Comparison of the trapezoideal-AUC significance probabilities[a]. [a]AUC for *N. meningitidis* was compared across lipid treatment as a summary measure of viability over the time course. AUC was calculated from time T_{0h} to the last sampling point (T_{24h}). The significance probabilities are shown. [b]Significance probability associated with the exact nonparametric Kruskal-Wallis test of the null hypothesis that the distribution of the trapezoidal area is the same across all treatment groups. [c]Significance level 0.05.

within 1 h and 2 h, respectively (Fig. 2), whereas killing of *N. meningitidis* with the unmodified C_6-ceramide was more gradual: *N. meningitidis* had at least a 1.3-$\log_{10}$ decrease in the number of CFU/ml with treatment with the unmodified C_6-ceramide at 2 h post treatment, never showing a greater than 1.3 log reduction from the initial inoculum. Moreover, a slight degree of regrowth was seen for *N. meningitidis* at the 24-h time point for the unmodified C_6-ceramide (Fig. 2). Treatment of the bacterial culture with ω–azido-C_6-ceramide at 1 X MIC caused at least a 2.4-$\log_{10}$ reduction in the number of CFU/ml at 1 h and a 5.8-$\log_{10}$ decrease in the number of CFU/ml at 2 h. Thus, sphingosine and ω–azido-C6-ceramide demonstrated potent *in vitro* bactericidal activity against *N. meningitidis* at concentrations 1 x the MIC, while a bacteriostatic activity was observed for unmodified C_6-ceramide against *N. meningitidis* at concentrations 1 x the MIC. Exact Kruskal-Wallis tests confirmed highly significant differences among non-treated and sphingosine (p < 0.0001) or ω–azido-C_6-ceramide (p < 0.0001) treated *N. meningitidis* (Table 3). Comparison of the trapezoidal area under the curves (AUCs) also showed significant differences after treatment with sphingosine and ω–azido-C_6-ceramide (Table 3).

Toxicity testing. We next tested the cytotoxicity induced by the unmodified and the functionalized ceramides in human brain microvascular endothelial cells (HBMEC), human embryonic kidney (HEK293T) cell line or the human hepatocellular carcinoma cell line HepG2 overnight using a concentration of 5 μM corresponding to the observed MIC values (2 μg/ml) determined for *N. meningitidis* and *N. gonorrhoeae*. Overnight treatment of the three different mammalian cells with staurosporine (1 μM) was used as a positive control. Notably, no significant cytotoxic effects neither on HBMEC, nor on HEK293T cells or HepG2 cells were observed for the concentration used in this study (Fig. 3).

Uptake of functionalized ceramide analogs by bacteria. Little is known about the exact mechanism of lipid antimicrobial activity. In previous studies it has been shown that the bioorthogonal strain-promoted $3 + 2$ cyloaddition between cyclooctyne and azide derivatives allow the conjugation between a biomolecule and a fluorescent dye[24–27]. In order to get insight into the mechanism we aimed at analysing the transport and localisation of the synthesized azido-functionalized ceramides in *N. meningitidis*. We therefore first established the incorporation kinetics of the functionalized ceramides in bacteria with different treatment times varying from 5 min to 30 min followed by fluorophore coupling. DBCO-Sulfo-Cy5 was selected as suitable dye for bio-orthogonal click reaction and the dye was coupled under copper-free conditions (Fig. 4A)[24]. Using flow cytometry analysis, we compared the uptake of α–azido-C_6-, ω–azido-C_6-, α–azido-C_{16}- and ω–azido-C_{16}-ceramide treated bacteria showing that both short-chain ceramide analogs efficiently accumulated in bacteria with a maximum peak at 15 min (Fig. 4B). Uptake levels of ω–azido-C_{16}- and α–azido-C_{16}-ceramide at 5 μM were substantially lower than that of the short-chain ceramide analogs. Flow cytometry data suggested that the long-chain ceramide analogs are less efficiently incorporated within this time interval. To confirm uptake levels, bacteria were treated with
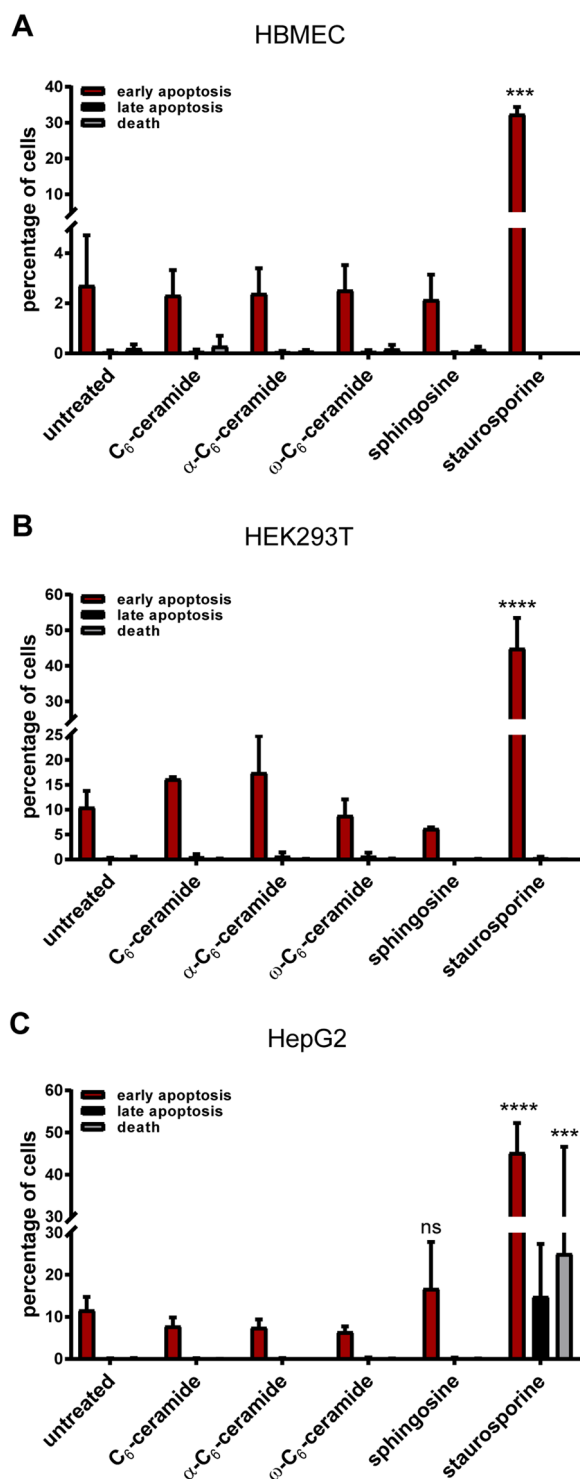
Figure 3. Effects of unmodified short-chain C_6-ceramide (C_6-ceramide), ω-azido-C_6-ceramide, α-azido-C_6-ceramide and sphingosine on (**A**) HBMEC, (**B**) HEK293T and (**C**) HepG2 cell apoptosis. Cells were left untreated or were treated with 5 μM of the compounds overnight. Staurosporine in a concentration of 1 μM was used as a positive control. Apoptosis was quantified using flow cytometry after staining with annexin V (AnnV)/PI. Percentage of early (AnnV+/PI−), late apoptotic cells (AnnV+/PI+) and dead cells (AnnV−/PI+) are shown. Data are presented as the mean ± SD of triplicate experiments. ***$P < 0.001$ in Students t-test relative to untreated cells.

ceramide analogs as described above followed by 15 min fluorophore coupling and subsequent CLSM analyses. CLSM images of labelled bacteria confirmed that all clickable ceramides were efficiently incorporated into bacteria (Fig. 4C).

72
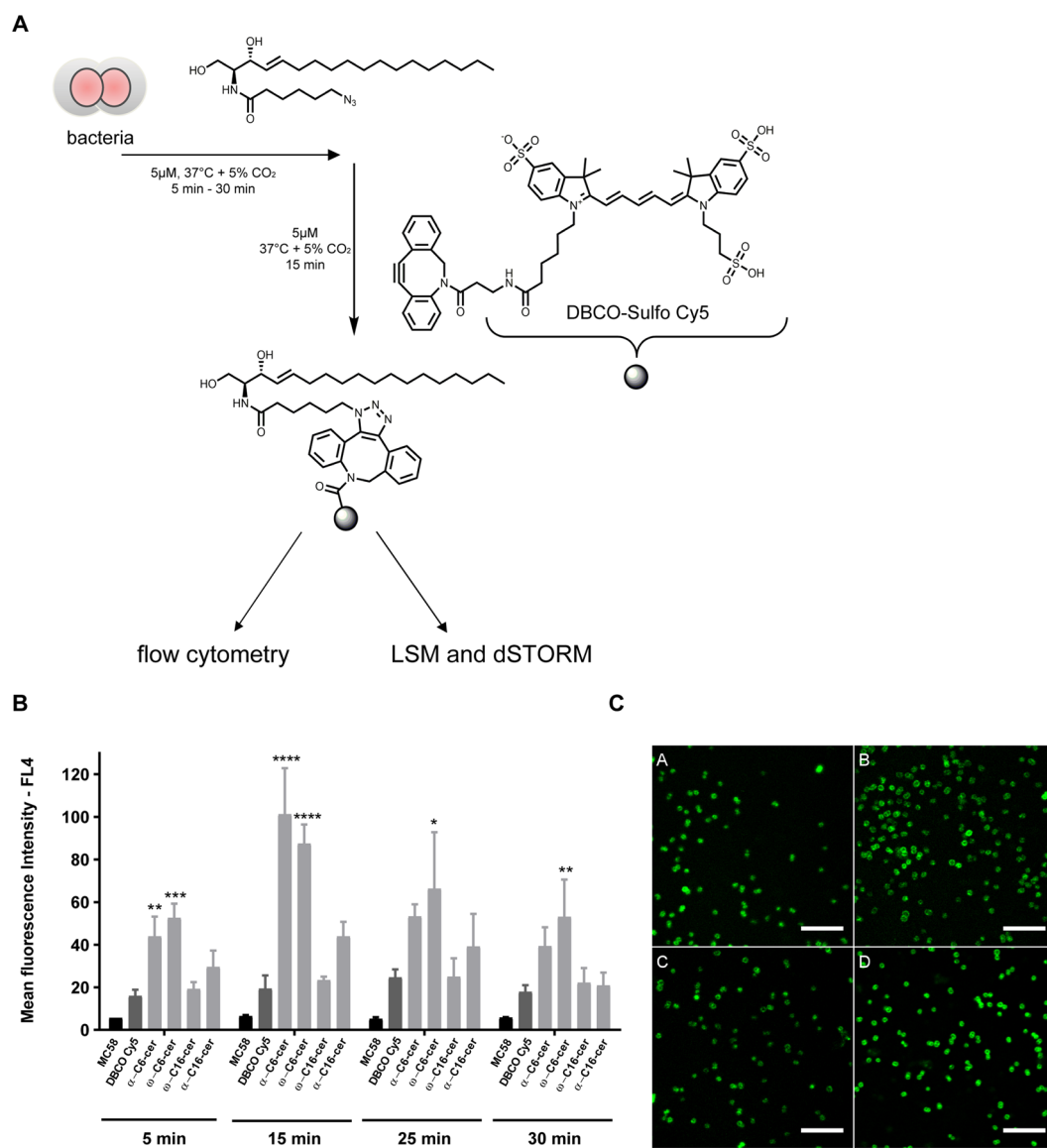
Figure 4. (**A**) Schematic of bacteria treated with ceramide analogs, followed by click reaction with DCBO-Sulfo-Cy5. (**B**) Azido-modified ceramides are rapidly incorporated into *N. meningitidis*. Bacteria were treated with 5 μM of α-azido-C_6-ceramide (α-C6-cer), ω-azido-C_6-ceramide (ω-C6-cer), α-azido-C_{16}-ceramide (α-C16-cer) and ω-azido-C_{16}-ceramide (ω-C16-cer), or DBCO-sulfo-Cy5 (DBCO Cy5) for indicated time points, washed, and ceramide incorporation levels were detected after 15 min DBCO-sulfo-Cy5-clicking and flow cytometry analysis. Three independent experiments with SD are shown. *, **, ***, ****$P < 0.05$, 0.01, 0.001, 0.0001 in one-way ANOVA and Tukey post hoc test relative to dye control (DCBO-sulfo-Cy5). (**C**) LSM images of *N. meningitidis* after incorporation of (**A**) α–azido-C_6-ceramide, (**B**) ω–azido-C_6-ceramide, (**C**) α–azido-C_{16}-ceramide, and (**D**) ω–azido-C_{16}-ceramide and clicking with DBCO-Sulfo-Cy5 by copper-free biorthogonal click chemistry. For visualization the contrast was adjusted for each image individually. Scale bar, 10 μm.

Visualization of ceramide uptake in N. meningitidis (dSTORM). In order to visualize the distribution of ceramides in *N. meningitidis* in more detail we used super-resolution imaging by *d*STORM, a single-molecule based localization microscopy technique that achieves virtually molecular resolution[28] and has been already successfully used to image the distribution of clickable glycans and proteins in the plasma membrane of eukaryotes[24,29]. *d*STORM images clearly showed that all four ceramide analogs were incorporated into the bacterial membrane and the azide function was accessible for click reaction with DBCO-Sulfo-Cy5 (Fig. 5). None of the four analogs showed pronounced clustering. In contrast to the results of flow cytometry analysis, the super-resolution images demonstrated the strongest incorporation for the ω–azido-C_{16}-ceramide. In addition, the ω–azido-C_{16}-ceramide exhibited a tendency to accumulate in the contact areas between two bacteria. Control labelling experiments without ceramide treatment showed also non-specific staining of bacteria but at much lower efficiency (Fig. S1).

73
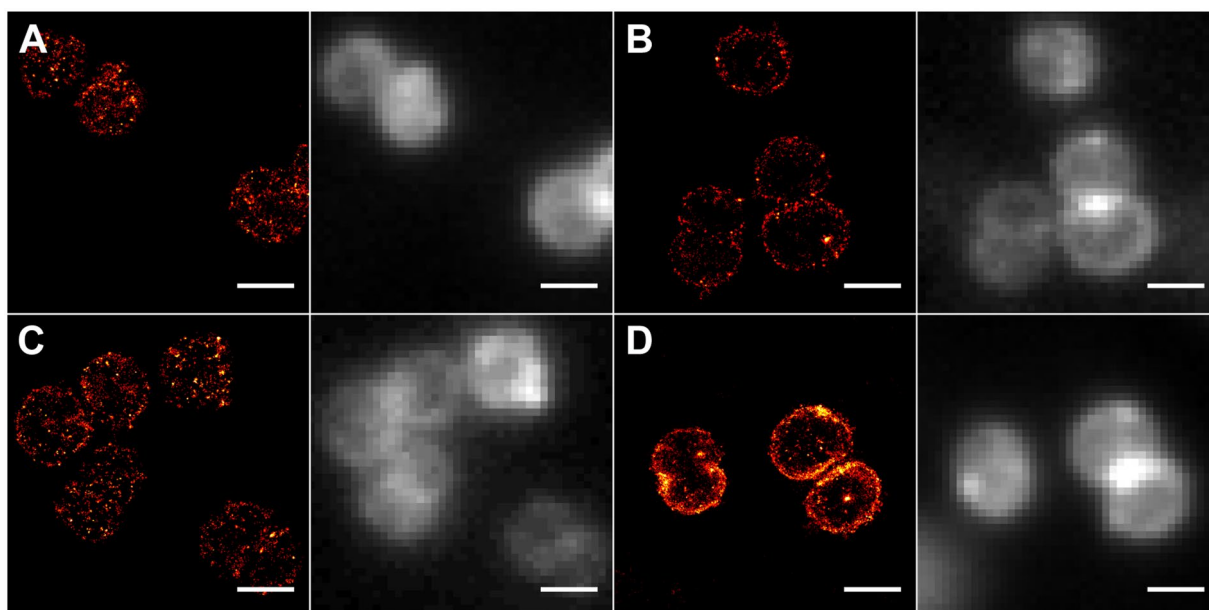
Figure 5. dSTORM and corresponding wide-field fluorescence of *N. meningitidis* after treatment with (**A**) α–azido-C$_6$-ceramide, (**B**) ω–azido-C$_6$-ceramide, (**C**) α–azido-C$_{16}$-ceramide, and (**D**) ω–azido-C$_{16}$-ceramide and clicking with DBCO-Sulfo-Cy5 by copper-free biorthogonal click chemistry. Scale bar, 1 μm.

Effect of sphingosine and functionalized ceramide analogs on bacterial cell physiology.

In order to analyse the mechanism of the antibacterial activity of sphingosine and the functionalized ceramide analogs on bacteria, growing *S. aureus* strain ATCC 29213 or *N. meningitidis* strain MC58 were treated with diethyloxacarbocyanine, a validated indicator of the proton motive force in *S. aureus* and other bacteria[30]. This two-colour flow cytometry assay showed the expected shift in the red:green fluorescence ratio following addition of the proton ionophore carbonyl cyanide-m-chlorophenylhydrazone (CCCP) to the bacteria (Fig. S2): We observed a red:green ratio of about 6 for untreated stained *S. aureus*, which decreased to a red:green ratio of about 2 after incubation with CCCP. A similar decrease of the ratio was observed after treatment of *S. aureus* with sphingosine, indicating the collapse of the proton gradient (Fig. S2A). The red:green ratio for untreated stained *N. meningitidis* was about 1.8. The ratio also decreased significantly when bacteria were treated with sphingosine or ω–azido-C$_6$-ceramide, whereas the red:green ratio was unaltered or even increased after treatment with α–azido-C$_6$-ceramide (Fig. S2B and C). Taken together these preliminary findings indicate that both sphingosine and ω–azido-C$_6$-ceramide dissipate the bacterial cell's membrane potential in *N. meningitidis* and/or *S. aureus*.

Discussion

Previous studies have demonstrated that numerous sphingolipids, extracted and purified from natural sources, can act as bactericidal agents against various microorganisms[4,6–10,31]. Sphingolipids showed growth inhibitory activity against Gram-positive and Gram-negative bacteria, fungi or microalgae[6–8,10,31]. The degree of the antibacterial activity depends on the sphingolipid structure and the microorganism tested. One of the best studied sphingolipids regarding antimicrobial activity is the long chain base sphingosine. Sphingosines form a primary part of sphingolipids, a class of cell membrane lipids that include sphingomyelin, an important phospholipid. Several studies have shown that sphingosine (and dihydrosphingosines and 6-hydroxysphingosines) are potent antimicrobials[4,6,7,14,32,33]. Of note, recent studies demonstrated that sphingosine is also an important first-line defence of healthy airways against *Pseudomonas aeruginosa*[11]. Herein we demonstrated that sphingosine has also a significant antimicrobial activity against the Gram-negative species *N. meningitidis* and *N. gonorrhoeae*.

Ceramides are a structurally heterogeneous and complex group of sphingolipids containing derivatives of sphingosine bases in amide linkage with a variety of fatty acids. Differences in chain length, type and extent of hydroxylation, saturation etc. are responsible for the heterogeneity of sphingolipids. Some of the most structurally complex ceramides are found in the skin, which includes the presence of a very-long-chain fatty acid (C30 to C32) with an ω-hydroxyl group that is esterified to another fatty acid[34–36], and in testis, which contains neutral glycosphingolipids with very-long-chain (C26 to C32) polyunsaturated fatty acids[37,38]. Ceramides with very short fatty acids (C2) have also been found in mammals and are formed by an acetyl transfer from platelet-activating factor to sphingenine[39,40]. In this study we now show that short-chain C$_6$-ceramides and a functionalized ω–azido-C$_6$-ceramide are active against *N. meningitidis* and the related species *N. gonorrhoeae*. Interestingly, they were inactive against *E. coli* and *S. aureus*. Time-killing kinetics revealed a significant decrease in mean viable count of *N. meningitidis* treated with sphingosine or ω–azido-C$_6$-ceramide. *N. meningitidis* was efficiently killed by ω–azido-C$_6$-ceramide within 2 h of treatment.

At present, little is known about the exact mechanism of lipid antimicrobial activity, although recently published findings suggest that sphingosine causes ultrastructural damage in *E. coli* and *S. aureus*[31]. Antimicrobial

lipids may penetrate and disrupt the cell wall layer of bacteria or may alter the cytoplasmic membrane. It is also likely that they might directly penetrate the cell wall and cytoplasmatic membrane and enter the cytoplasm. Herein, bacteria might accumulate them as intracellular inclusion. In order to get insight into the mechanism, we made use of azido-functionalized sphingolipids to visualize lipid uptake and localization in bacteria. We observed that the ceramide analogs are efficiently incorporated into the bacterial membrane within a short time period (Figs 4 and 5).

Recently, it has been shown by dSTORM that ceramides are enriched in ceramide-rich platforms with a size of ~75 nm in the plasma membrane of eukaryotes[41]. In contrast, the ceramide distribution in *N. meningitidis* membranes appears mostly homogeneous. Only the long chain ceramide ω–azido-C_{16}-ceramide accumulated slightly in contact zones to other bacteria (Fig. 5D). However, differences in the incorporation efficiency are difficult to quantify because α and ω-azido groups exhibit a different accessibility for click reaction and the different lengths of the alkyl side chains (C6 and C16) result in different incorporation efficiencies and geometries[22]. Moreover, probe preparation for flow cytometry differed from that for CLSM and dSTORM. Bacteria were incubated for additional 30 min before analyzing by CLSM and/or dSTORM to allow efficient binding of the bacteria to pre-coated chamber slides. It is likely that the additional incubation time probably resulted in damage of the cell wall when ω–azido-C_6-ceramide was used thus resulting in less efficient staining and signal intensity detected by dSTORM compared to treatment with the ω–azido-C_{16}-ceramide analog.

However, localization studies alone do not allow to draw any conclusions about the mode of action of the substance, and a more systematic examination of the effect of sphingosine and short-chain ceramide-analogs on growth and membrane integrity of *N. meningitidis* is needed. In preliminary experiments, we found that treatment of bacteria with both sphingosine and ω–azido-C_{16}-ceramide resulted in depolarization of the membrane potential (unpublished data): growing *S. aureus* and *N. meningitidis* strains were treated with diethyloxacarbocyanine, a validated indicator of the proton motive force in *S. aureus* and other bacteria. This two-color flow cytofluorometry assay showed the expected shift in the red-green fluorescence ratio following the addition of the protonophore carbonyl cyanide-m-chlorophenylhydrazone (CCCP) to growing cells. Treatment of *S. aureus* with sphingosine and of *N. meningitidis* with sphingosine or ω–azido-C_6-ceramide yielded a color ratio shift similar to CCCP treatment (unpublished data), indicating the collapse of the proton gradient.

It is well known that the inoculum size, the type of growth medium, the incubation time and the inoculum preparation method can influence MIC values. Many fastidious bacterial species including *N. gonorrhoeae* and *N. meningitidis* do not grow satisfactorily using standard *in vitro* susceptibility testing approaches with unsupplemented media. Therefore, modifications have been made to the standard CLSI/EUCAST MIC methods to allow laboratories to perform reliable antimicrobial susceptibility testing. Such modifications typically involve the use of test media with supplemental nutrients, prolonged incubation times, and/or incubation in an atmosphere with an increased concentration of carbon dioxide. Herein, we either used proteose peptone medium or the recently described Graver-Wade[23] medium to determine MIC values of sphingosine, ceramides and ceramide analogs. Interestingly, MIC and MBC values were influenced by the type of growth medium and values shifted within 1 to 2 dilutions. The difference might lie in the degree of free and protein-bound ceramides and sphingosine in the different test media solutions.

Infections caused by pathogenic *Neisseriae* are normally treated with antibiotics; however, the increasing occurrence of antibiotic-resistant bacterial strains as seen for *N. gonorrhoeae*[17,42–44] makes it highly desirable to identify new antimicrobials. Short-chain ceramides and their derivatives could prove useful in this regard, since they have high antibacterial activity and low toxicity at a bactericidal concentration. Here, we report for the first time the antimicrobial activity of synthetic ceramide analogs on *N. meningitidis* and the related species *N. gonorrhoeae*. Based on the results represented within this study a systematic functional analysis of the antimicrobial mechanism may enable the development of more efficient synthetic ceramide analogs with potential for therapeutic intervention. However, various hurdles and challenges will have to be overcome in the development of sphingolipid analogs or mimetics as therapeutic agents to treat a bacterial infections in particular avoiding interaction of the compounds with the host cells and preventing host cell cytotoxicity.

Synthetic ceramide analogs have been prepared for a wide range of purposes and are particularly of interest for the development as therapeutic agents in the treatment of cancer[45]. For example, ceramide analogs have been synthesized to explore structure-function relationships in cell signaling[46], or as inhibitors of enzymes of ceramide metabolism[47]. Other analogs have shown activity as potential anticancer agents, such as L-threo-C6-pyridinium-ceramide-bromide[48] or (2S,3R)-(4E,6E)-2-octanoyl-amidoocta-decadiene-1,3-diol (4,6-diene-Cer) with antiproliferative activity in breast cancer cells[49]. Unfortunately, ceramides are highly hydrophobic, poorly water-soluble molecules limiting their potential therapeutic utility. To overcome this hurdle, synthetic ceramide analogs have been developed that offer reduced lipophilicity or near complete water solubility. In recent years, there have been remarkable improvements in the design and delivery of ceramide analogs[45]. Intriguing new approaches have been the generation of water soluble pyridinium-ceramides[48,50] or the delivery of pegylated liposomes[51]. In terms of systemic delivery of ceramide the advent of nanotechnology has shown the greatest promise[45].

Materials and Methods

Bacterial strains, mutants and culture conditions.
Isolate MC58 was used as a representative strain of the species *N. meningitidis*. Strain MC58 is a serogroup (Sg) B strain of the sequence type (ST)-74 (ST-32 clonal complex [cc]), which was isolated in 1983 in the UK and was kindly provided by E. R. Moxon[52]. Isolate FA1090 was used as a representative strain of the species *N. gonorrhoeae*. Strain FA1090 is a porin serotype PIB-3, streptomycin (Sm)-resistant strain, originally isolated in the 1970s from the endocervix of a woman with disseminated gonococcal infection[53] and has been used extensively in experimental human infection studies[54]. *Escherichia coli* ATCC 12759 and *S. aureus* isolates ATCC 29213 were included as control strains and to obtain information about

Gram-negative and Gram-positive susceptibility and resistance. *N. meningitidis* strain MC58 and *N. gonorrhoeae* strain FA1090 were cultured on Columbia Agar with 5% sheep blood (COS; bioMérieux, Lyon, France) and incubated at 37 °C with 5% CO_2 overnight. Liquid culturing was performed in proteose-peptone medium (PPM) plus 1% Kellogg's supplement I and II (PPM$^+$). *E. coli* ATCC 12759 and *S. aureus* ATCC 29213 were grown in Mueller-Hinton broth (Becton Dickinson, Maryland, USA) at 37 °C.

Preparation of lipids. D-*erythro*-Sphingosine (C18) was obtained from Santa Cruz Biotechnology, Heidelberg, Germany. Unmodified C_6-ceramide and C_{16}-ceramide were obtained from Avanti Polar Lipids (Alabama, USA). Lipids were dissolved in ethanol, stored at −20 °C and protected from light. The azido ceramides (Fig. 1B) were synthesized as previously described[22].

Antimicrobial assay. Broth microdilution assays were used to determine the minimal inhibitory concentration (MIC), the MIC$_{50}$, and the minimal bactericidal concentration (MBC) of D-*erythro*-sphingosine, short-chain ceramides or long-chain ceramides and their analogs. Briefly, lipid suspensions were diluted in PPM$^+$, Graver-Wade medium (GW)[23] or cation-supplemented Mueller-Hinton broth (for *E. coli* and *S. aureus*), which meets the requirements of the EUCAST standard, in standard 96 well microtiter plates (Sarstedt, Nuembrecht, Germany). Microdilution plates were prepared using serial twofold dilutions of the lipids (concentration ranging from 64 μg/ml to 0.0625 μg/ml in a total volume of 75 μl) in the respective media. At concentration higher than 64 μg/ml the lipids had an optical density that interfered with the determination of the MIC. To prepare the inoculum, all bacteria cell suspensions were adjusted to McFarland 0.5 ($1–2 × 10^8$ CFU/mL). The suspension was further diluted to provide a final inoculum density of $5 × 10^5$ CFU/ml in the wells of the microdilution panels in a volume of 75 μl equal to the volume of diluted lipid. The plates were incubated for 16 h at 37 °C and 5% CO_2 (for *N. meningitidis* and *N. gonorrhoeae*) and 37 °C (for *S. aureus* and *E. coli*). The optical density of bacterial growth was read at 540 nm in a spectrophotometer (Infinite F200 Pro Reader, Tecan Group, Maennedorf, Switzerland). The MIC was defined as the lowest concentration of an antibacterial agent that prevented visible growth under the test conditions, the MIC$_{50}$ was defined as the lowest concentration of lipid that reduced growth by more than 50%, and the MBC was defined as the concentration of lipid that prevented growth. Quality control was monitored with *E. coli* ATCC 12759 and *S. aureus* isolates ATCC 29213.

Killing kinetic assays. Killing kinetic experiments were performed according to previously published methods[55]. Briefly, freshly prepared colonies were resuspended in 10 ml PPM + medium and incubated in a shaker at 37 °C, 200 rpm for 1 to 2 h. Cultures were then diluted to a 0.5 McFarland standard and further diluted so that the starting inoculum was approximately $1 × 10^6$ CFU/ml. Sphingosine, Avanti Polar unmodified C_6-ceramide and ω–azido-C_6-ceramide was added to the prepared bacterial suspension so that the final concentration was 1 X the MIC of the compounds tested. A growth control with no lipid was also included. The starting inoculum was determined from the growth control tube immediately after dilution and was recorded as the bacterial CFU count at time zero. After addition of the compounds the tubes were incubated in a shaker at 37 °C, 200 rpm and viability counts were estimated at 1, 2, 3, 4, 5, 6, 7, 8, and 24 h by removing 1 mL of the culture, diluting as appropriate, and plating 100 μl on COS agar plates. COS agar plates were incubated at 37 °C with 5% CO_2 overnight. Colonies were counted using a ProtoCOL colony counter (Synbiosis, Cambridge, UK) and the results were recorded as the number CFU/ml. A ≥ 3-log$_{10}$ decrease in the number of CFU/ml was considered bactericidal.

Membrane potential analysis and flow cytometry. Membrane potential was determined by flow cytometry using a BacLight™ bacterial membrane potential kit (Molecular probes). This test is based on a fluorescent membrane-potential indicator dye, 3,3′-diethyloxacarbocyanine iodide (DiOC$_2$(3)), along with a proton ionophore carbonyl cyanide-m-chlorophenylhydrazone (CCCP). DiOC$_2$(3) at low concentrations exhibits green fluorescence in all bacterial cells, but it becomes more concentrated in healthy cells that are maintaining a membrane potential, causing the dye to self-associate and the fluorescence emission to shift to red. *S. aureus* and *N. meningitidis* were grown to mid-logarithmic phase, and $1 × 10^6$ cells per ml were treated with ethanol (solvent), sphingosine, α–azido-C_{16}-ceramide or ω–azido-C_6-ceramide, or incubated in either the presence or absence of 5 μM CCCP (used as a depolarized control) followed by incubation with 30 μM DiOC$_2$(3) for 30 min at 37 °C and then analyzed by flow cytometry. DiOC$_2$(3) was excited with the 488 nm argon laser, and emission was detected as follows: green fluorescence was detected using a 530/30 filter, and red fluorescence was detected with a 585/42 filter. The ratio of red to green fluorescence intensity were calculated using mean fluorescence intensities following the manufacturer's description.

Mammalian cell line. The simian virus 40 large T antigen-transformed human brain microvascular endothelial cells (HBMEC) were cultured as previously described[56–58]. Briefly, HBMECs were cultured in RPMI-1640 medium (Gibco Life Technologies, Karlsruhe, Germany) supplemented with 10% fetal calf serum (FCS, Gibco Life Technologies), 10% Nu serum® IV (Corning, NY, USA 10%; Becton Dickinson), 1% sodium pyruvate (1 mM), 1% L-glutamine (2 mM), 1% non-essential amino acids (all purchased from GE Healthcare, Little Chalfont, UK), 5 U ml^{-1} heparin (Biochrom, Berline, Germany) and 30 μg mL^{-1} endothelial cell growth supplement (ECGS, CellSystems, Troisdorf, Germany). Cultures were incubated in a humid atmosphere at 37 °C with 5% CO_2. Cells between the 10th and 25th passages were used for apoptosis analysis. HBMEC were cultured in T25 flasks (Corning Costar Corporation, Cambridge, MA, USA). The embryonic kidney cell line HEK293T and the hepatocellular carcinoma cell line HepG2 were purchased from the American Type Culture Collection, ATCC® CRL-3216™ and ATCC® HB-8065™, respectively. HEK293T and HepG2 were routinely cultured in Dulbecco's modified Eagle's medium (DMEM) + GlutaMAX™-I (Gibco Life Technologies, Karlsruhe, Germany) supplemented with 10% FCS.

Apoptosis analysis.   HBMEC, HEK293T or HepG2 cells were seeded in 6-well tissue culture plates to a density of 2×10^6 cells/well. The medium was changed and cells were treated with the compounds overnight. Cells were harvested and washed once with 1 x PBS$^{-/-}$ and once with Annexin V binding buffer (BD Biosciences). Cells were resuspended and transferred into a 500 μL siliconized polypropylene tube. Annexin V-Alexa Fluor 488 (Molecular Probes) was added at a 1:20 dilution and cells were incubated for 15 min at RT. Following this, propidium iodide (PI) was added at a final concentration of 1 μg/mL and cells were stained for a further 15 min at RT. After staining, cells were washed twice with PBS$^{-/-}$ and fixed with 2% formaldehyde for 10 min on ice. Following fixation, cells were washed twice with PBS$^{-/-}$ and treated with 50 μg/mL DNase-free RNase (Sigma, R4642) for 15 min at 37 °C. Cells were then washed once with PBS$^{-/-}$ and immediately analyzed using a BD FACSCaliburTM flow cytometer (BD Biosciences) and BD CellQuestTM Pro Software (BD Biosciences). For each measurement, at least 10,000 cells were counted. Cells that stained positive for annexin V represented cells with intact membranes and externalized phosphatidylserine (early apoptosis) and cells positive for annexinV/PI represent cells that had lost membrane integrity (late apoptosis/necrosis). A modified Annexin V/ PI method was used to assess cell death[59].

Flow cytometry and click chemistry reaction.   For detection of ceramide incorporation bacteria were fed with functionalized (α–azido-C$_6$-ceramide, ω–azido-C$_6$-ceramide, α–azido-C$_{16}$-ceramide and ω–azido-C$_{16}$-ceramide) ceramides at a concentration of 5 μM for indicated time points at 37 °C and 5% CO$_2$, washed one time with 1 mL PBS and bacteria were exposed to 5 μM DBCO-Sulfo-Cy5 dye (Jena Bioscience, Jena, Germany) and the click reaction was performed for 15 min at 37 °C and 5% CO$_2$. Bacteria were washed three times with 1 mL PBS, then resuspended in 500 μL FACS buffer (PBS + 5% FCS) and used for flow cytometry analysis.

LSM and *d*STORM.   LSM and dSTORM imaging was performed as previously described[41]. Briefly, bacteria were fed with functionalized ceramide for 15 min as described above, followed by a 15 min click chemistry reaction. Bacteria were washed three times with 1 mL PBS, resuspended in 100 μL RPMI-1640 medium and seeded on precoated chamber slides (Nunc™ Lab-Tek™ II Chamber Slide™, ThermoScientifc Fisher) for 30 min at 37 °C and 5% CO$_2$. Bacteria were fixed with 2% PFA for 15 min at RT and chamber slides were stored overnight at 4 °C before microscopy experiment. For super-resolution microscopy bacteria were covered with switching buffer consisting of 100 mM ß-mercaptoethylamine (MEA, Sigma) in PBS and pH adjusted with potassium hydroxide to 7.4. Super-resolution measurements were performed at an inverted wide-field fluorescence microscope (IX-71; Olympus) with an oil-immersion objective (60x, NA 1.45; Olympus) and suitable excitation and emission filters (ZT405/514/635rpc; Chroma; EM01-R442/514/647-25; Semrock). The organic fluorophores (DBCO-Sulfo-Cy5) were excited with a 640 nm laser (Cube 640–100 C; Coherent). After passing a long- and bandpass filter (LP635; Semrock; HC 679/41; Semrock) photons were detected by an electron-multiplying CCD camera (iXon Ultra DU-897; Andor). The sample was homogenously illuminated with an irradiation intensity of ~ 7 kW/cm^2 and super-resolved images were reconstructed with rapidSTORM 3.3.1[60,61] from 30,000 frames with an exposure time of 20 ms. LSM was performed with a LSM700 (Zeiss, Germany) equipped with a Plan-Apochromat 63×1.4 oil-immersion objective and the PBS-covered sample was excited with a 639 nm solid state laser.

Statistical analysis.   Statistical analysis was performed using unpaired Student *t* test with ****$p < 0.0001$, ***$p < 0.001$, **$p < 0.01$, *$p < 0.05$. The exact Kruskal-Wallis test was performed to detect differences in killing kinetics, utilizing a 5% level of statistical significance. This nonparametric analog to analysis of variance (ANOVA) was used due to modest sample size and violation of the normality assumptions for parametric procedures. Moreover, the trapezoidal area under the curve (AUC) was determined to summarize the measurement of bacterial viability of treatment time course.

References

1. O'Brien, J. S. & Rouser, G. The fatty acid composition of brain sphingolipids: sphingomyelin, ceramide, cerebroside, and cerebroside sulfate. *Journal of lipid research* **5**, 339–342 (1964).
2. Xu, K. & Thornalley, P. J. Antitumour activity of sphingoid base adducts of phenethyl isothiocyanate. *Bioorganic & medicinal chemistry letters* **10**, 53–54 (2000).
3. Pruett, S. T. *et al.* Biodiversity of sphingoid bases ("sphingosines") and related amino alcohols. *Journal of lipid research* **49**, 1621–1639, https://doi.org/10.1194/jlr.R800012-JLR200 (2008).
4. Drake, D. R., Brogden, K. A., Dawson, D. V. & Wertz, P. W. Thematic review series: skin lipids. *Antimicrobial lipids at the skin surface. Journal of lipid research* **49**, 4–11, https://doi.org/10.1194/jlr.R700016-JLR200 (2008).
5. Fischer, C. L. *et al.* The roles of cutaneous lipids in host defense. *Biochim Biophys Acta* **1841**, 319–322, https://doi.org/10.1016/j.bbalip.2013.08.012 (2014).
6. Fischer, C. L. *et al.* Antibacterial activity of sphingoid bases and fatty acids against Gram-positive and Gram-negative bacteria. *Antimicrob Agents Chemother* **56**, 1157–1161, https://doi.org/10.1128/aac.05151-11 (2012).
7. Bibel, D. J., Aly, R. & Shinefield, H. R. Antimicrobial activity of sphingosines. *The Journal of investigative dermatology* **98**, 269–273 (1992).
8. Dongfack, M. D. *et al.* A new sphingolipid and furanocoumarins with antimicrobial activity from Ficus exasperata. *Chemical & pharmaceutical bulletin* **60**, 1072–1075 (2012).
9. El-Amraoui, B., Biard, J. F. & Fassouane, A. Haliscosamine: a new antifungal sphingosine derivative from the Moroccan marine sponge Haliclona viscosa. *SpringerPlus* **2**, 252, https://doi.org/10.1186/2193-1801-2-252 (2013).
10. Possemiers, S., Van Camp, J., Bolca, S. & Verstraete, W. Characterization of the bactericidal effect of dietary sphingosine and its activity under intestinal conditions. *International journal of food microbiology* **105**, 59–70, https://doi.org/10.1016/j.ijfoodmicro.2005.05.007 (2005).
11. Pewzner-Jung, Y. *et al.* Sphingoid long chain bases prevent lung infection by Pseudomonas aeruginosa. *EMBO molecular medicine* **6**, 1205–1214, https://doi.org/10.15252/emmm.201404075 (2014).

77

12. Saied, E. M., Banhart, S., Burkle, S. E., Heuer, D. & Arenz, C. A series of ceramide analogs modified at the 1-position with potent activity against the intracellular growth of Chlamydia trachomatis. *Future medicinal chemistry* **7**, 1971–1980, https://doi.org/10.4155/fmc.15.126 (2015).

13. Del Olmo, E. *et al.* Simple dihydrosphyngosine analogues with potent activity against MDR-Mycobacterium tuberculosis. *Bioorganic & medicinal chemistry letters* **19**, 5764–5768, https://doi.org/10.1016/j.bmcl.2009.07.147 (2009).

14. Bibel, D. J., Aly, R., Shah, S. & Shinefield, H. R. Sphingosines: antimicrobial barriers of the skin. *Acta dermato-venereologica* **73**, 407–411 (1993).

15. Rouphael, N. G. & Stephens, D. S. Neisseria meningitidis: biology, microbiology, and epidemiology. *Methods Mol Biol* **799**, 1–20, https://doi.org/10.1007/978-1-61779-346-2_1 (2012).

16. Caugant, D. A. & Maiden, M. C. J. Meningococcal carriage and disease–Population biology and evolution. *Vaccine* **27**, B64–B70 (2009).

17. Unemo, M. & Shafer, W. M. Antimicrobial resistance in Neisseria gonorrhoeae in the 21st century: past, evolution, and future. *Clin Microbiol Rev* **27**, 587–613, https://doi.org/10.1128/cmr.00010-14 (2014).

18. Prescher, J. A. & Bertozzi, C. R. Chemistry in living systems. *Nature chemical biology* **1**, 13–21, https://doi.org/10.1038/nchembio0605-13 (2005).

19. Heilemann, M. *et al.* Subdiffraction-resolution fluorescence imaging with conventional fluorescent probes. *Angewandte Chemie (International ed. in English)* **47**, 6172–6176, https://doi.org/10.1002/anie.200802376 (2008).

20. van de Linde, S. *et al.* Direct stochastic optical reconstruction microscopy with standard fluorescent probes. *Nature protocols* **6**, 991–1009, https://doi.org/10.1038/nprot.2011.336 (2011).

21. Collenburg, L. *et al.* A Functionalized Sphingolipid Analogue for Studying Redistribution during Activation in Living T Cells. *Journal of immunology (Baltimore, Md. : 1950)* **196**, 3951–3962, https://doi.org/10.4049/jimmunol.1502447 (2016).

22. Walter, T. *et al.* Incorporation studies of clickable ceramides in Jurkat cell plasma membranes. *Chemical communications (Cambridge, England)* **53**, 6836–6839, https://doi.org/10.1039/c7cc01220a (2017).

23. Wade, J. J. & Graver, M. A. A fully defined, clear and protein-free liquid medium permitting dense growth of Neisseria gonorrhoeae from very low inocula. *FEMS Microbiol Lett* **273**, 35–37, https://doi.org/10.1111/j.1574-6968.2007.00776.x (2007).

24. Letschert, S. *et al.* Super-resolution imaging of plasma membrane glycans. *Angewandte Chemie (International ed. in English)* **53**, 10921–10924, https://doi.org/10.1002/anie.201406045 (2014).

25. Mertsch, A., Letschert, S., Memmel, E., Sauer, M. & Seibel, J. Synthesis and application of water-soluble, photoswitchable cyanine dyes for bioorthogonal labeling of cell-surface carbohydrates. *Zeitschrift fur Naturforschung. C, Journal of biosciences* **71**, 347–354, https://doi.org/10.1515/znc-2016-0123 (2016).

26. Seibel, J. *et al.* Investigating infection processes with a workflow from organic chemistry to biophysics: the combination of metabolic glycoengineering, super-resolution fluorescence imaging and proteomics. *Expert review of proteomics* **10**, 25–31, https://doi.org/10.1586/epr.12.72 (2013).

27. Jewett, J. C. & Bertozzi, C. R. Cu-free click cycloaddition reactions in chemical biology. *Chemical Society reviews* **39**, 1272–1279 (2010).

28. Sauer, M. & Heilemann, M. Single-Molecule Localization Microscopy in Eukaryotes. *Chemical reviews* **117**, 7478–7509, https://doi.org/10.1021/acs.chemrev.6b00667 (2017).

29. Mateos-Gil, P., Letschert, S., Doose, S. & Sauer, M. Super-Resolution Imaging of Plasma Membrane Proteins with Click Chemistry. *Frontiers in cell and developmental biology* **4**, 98, https://doi.org/10.3389/fcell.2016.00098 (2016).

30. Silverman, J. A., Perlmutter, N. G. & Shapiro, H. M. Correlation of daptomycin bactericidal activity and membrane depolarization in Staphylococcus aureus. *Antimicrob Agents Chemother* **47**, 2538–2544 (2003).

31. Fischer, C. L. *et al.* Sphingoid bases are taken up by Escherichia coli and Staphylococcus aureus and induce ultrastructural damage. *Skin pharmacology and physiology* **26**, 36–44, https://doi.org/10.1159/000343175 (2013).

32. Bibel, D. J., Aly, R. & Shinefield, H. R. Topical sphingolipids in antisepsis and antifungal therapy. *Clinical and experimental dermatology* **20**, 395–400 (1995).

33. Bibel, D. J. *et al.* Antimicrobial activity of stratum corneum lipids from normal and essential fatty acid-deficient mice. *The Journal of investigative dermatology* **92**, 632–638 (1989).

34. Wertz, P. W. Lipids and barrier function of the skin. *Acta dermato-venereologica. Supplementum* **208**, 7–11 (2000).

35. Wartewig, S. & Neubert, R. H. Properties of ceramides and their impact on the stratum corneum structure: a review. *Part 1: ceramides. Skin pharmacology and physiology* **20**, 220–229, https://doi.org/10.1159/000104420 (2007).

36. Feingold, K. R. Thematic review series: skin lipids. The role of epidermal lipids in cutaneous permeability barrier homeostasis. *Journal of lipid research* **48**, 2531–2546, https://doi.org/10.1194/jlr.R700013-JLR200 (2007).

37. Walden, C. M. *et al.* Accumulation of glucosylceramide in murine testis, caused by inhibition of beta-glucosidase 2: implications for spermatogenesis. *J Biol Chem* **282**, 32655–32664, https://doi.org/10.1074/jbc.M702387200 (2007).

38. Rabionet, M. *et al.* Male germ cells require polyenoic sphingolipids with complex glycosylation for completion of meiosis: a link to ceramide synthase-3. *J Biol Chem* **283**, 13357–13369, https://doi.org/10.1074/jbc.M800870200 (2008).

39. Merrill, A. H. Jr. Sphingolipid and glycosphingolipid metabolic pathways in the era of sphingolipidomics. *Chemical reviews* **111**, 6387–6422, https://doi.org/10.1021/cr2002917 (2011).

40. Van Overloop, H., Denizot, Y., Baes, M. & Van Veldhoven, P. P. On the presence of C2-ceramide in mammalian tissues: possible relationship to etherphospholipids and phosphorylation by ceramide kinase. *Biological chemistry* **388**, 315–324, https://doi.org/10.1515/bc.2007.035 (2007).

41. Burgert, A. *et al.* Characterization of Plasma Membrane Ceramides by Super-Resolution Microscopy. *Angewandte Chemie (International ed. in English)* **56**, 6131–6135, https://doi.org/10.1002/anie.201700570 (2017).

42. Shimuta, K. *et al.* Antimicrobial resistance and molecular typing of Neisseria gonorrhoeae isolates in Kyoto and Osaka, Japan, 2010 to 2012: intensified surveillance after identification of the first strain (H041) with high-level ceftriaxone resistance. *Antimicrob Agents Chemother* **57**, 5225–5232, https://doi.org/10.1128/aac.01295-13 (2013).

43. Unemo, M. Current and future antimicrobial treatment of gonorrhoea - the rapidly evolving Neisseria gonorrhoeae continues to challenge. *BMC infectious diseases* **15**, 364, https://doi.org/10.1186/s12879-015-1029-2 (2015).

44. Ohnishi, M. *et al.* Is Neisseria gonorrhoeae initiating a future era of untreatable gonorrhea?: detailed characterization of the first strain with high-level resistance to ceftriaxone. *Antimicrob Agents Chemother* **55**, 3538–3545, https://doi.org/10.1128/aac.00325-11 (2011).

45. Barth, B. M., Cabot, M. C. & Kester, M. Ceramide-based therapeutics for the treatment of cancer. *Anti-cancer agents in medicinal chemistry* **11**, 911–919 (2011).

46. Bielawska, A., Crane, H. M., Liotta, D., Obeid, L. M. & Hannun, Y. A. Selectivity of ceramide-mediated biology. Lack of activity of erythro-dihydroceramide. *J Biol Chem* **268**, 26226–26232 (1993).

47. Bielawska, A. *et al.* (1S,2R)-D-erythro-2-(N-myristoylamino)-1-phenyl-1-propanol as an inhibitor of ceramidase. *J Biol Chem* **271**, 12646–12654 (1996).

48. Senkal, C. E. *et al.* Potent antitumor activity of a novel cationic pyridinium-ceramide alone or in combination with gemcitabine against human head and neck squamous cell carcinomas *in vitro* and *in vivo*. *The Journal of pharmacology and experimental therapeutics* **317**, 1188–1199, https://doi.org/10.1124/jpet.106.101949 (2006).

78

49. Struckhoff, A. P. *et al.* Novel ceramide analogs as potential chemotherapeutic agents in breast cancer. *The Journal of pharmacology and experimental therapeutics* **309**, 523–532, https://doi.org/10.1124/jpet.103.062760 (2004).

50. Novgorodov, S. A. *et al.* Positively charged ceramide is a potent inducer of mitochondrial permeabilization. *J Biol Chem* **280**, 16096–16105, https://doi.org/10.1074/jbc.M411707200 (2005).

51. Stover, T. C., Sharma, A., Robertson, G. P. & Kester, M. Systemic delivery of liposomal short-chain ceramide limits solid tumor growth in murine models of breast adenocarcinoma. *Clinical cancer research: an official journal of the American Association for Cancer Research* **11**, 3465–3474, https://doi.org/10.1158/1078-0432.ccr-04-1770 (2005).

52. McGuinness, B. T. *et al.* Point mutation in meningococcal por A gene associated with increased endemic disease. *The Lancet* **337**, 514–517 (1991).

53. Nachamkin, I., Cannon, J. G. & Mittler, R. S. Monoclonal antibodies against Neisseria gonorrhoeae: production of antibodies directed against a strain-specific cell surface antigen. *Infect Immun* **32**, 641–648 (1981).

54. Hobbs, M. M. *et al.* Experimental Gonococcal Infection in Male Volunteers: Cumulative Experience with Neisseria gonorrhoeae Strains FA1090 and MS11mkC. *Frontiers in microbiology* **2**, 123, https://doi.org/10.3389/fmicb.2011.00123 (2011).

55. Ruppen, C. & Sendi, P. Time kill assays for _Streptococcus agalactiae_ and synergy testing. (2015).

56. Simonis, A., Hebling, S., Gulbins, E., Schneider-Schaulies, S. & Schubert-Unkmeir, A. Differential activation of acid sphingomyelinase and ceramide release determines invasiveness of Neisseria meningitidis into brain endothelial cells. *PLoS Pathog* **10**, e1004160, https://doi.org/10.1371/journal.ppat.1004160 (2014).

57. Stins, M. F., Badger, J. & Sik Kim, K. Bacterial invasion and transcytosis in transfected human brain microvascular endothelial cells. *Microb Pathog* **30**, 19–28 (2001).

58. Stins, M. F., Gilles, F. & Kim, K. S. Selective expression of adhesion molecules on human brain microvascular endothelial cells. *J Neuroimmunol* **76**, 81–90, doi:S0165-5728(97)00036-2 [pii] (1997).

59. Rieger, A. M., Nelson, K. L., Konowalchuk, J. D. & Barreda, D. R. Modified annexin V/propidium iodide apoptosis assay for accurate assessment of cell death. *Journal of visualized experiments: JoVE*, https://doi.org/10.3791/2597 (2011).

60. Wolter, S. *et al.* Rapidstorm: accurate, fast open-source software for localization microscopy. *Nature methods* **9**, 1040–1041, https://doi.org/10.1038/nmeth.2224 (2012).

61. Wolter, S. *et al.* Real-time computation of subdiffraction-resolution fluorescence images. *Journal of microscopy* **237**, 12–22, https://doi.org/10.1111/j.1365-2818.2009.03287.x (2010).

Acknowledgements

Author Contributions

J.B., J.S. and A.S.U. developed the concept of this work. J.B., A.B. and J.S. performed the experiments. T.W. synthesized the functionalized ceramide analogs. A.S.U., J.S. and M.S. wrote the manuscript.

Additional Information

Supplementary information accompanies this paper at https://doi.org/10.1038/s41598-017-18071-w.

Competing Interests: The authors declare that they have no competing interests.

Publisher's note: Springer Nature remains neutral with regard to jurisdictional claims in published maps and institutional affiliations.

79

3.6   Neisseria meningitidis Type IV Pili Trigger Ca^{2+}-Dependent Lysosomal Trafficking of the Acid Sphingomyelinase to Enhance Surface Ceramide Levels

Abstract

"Acid sphingomyelinase (ASM) is a lipid hydrolase that converts sphingomyelin to ceramide and that can be activated by various cellular stress mechanisms, including bacterial pathogens. Vesicle transportation or trafficking of ASM from the lysosomal compartment to the cell membrane is a prerequisite for its activation in response to bacterial infections; however, the effectors and mechanisms of ASM translocation and activation are poorly defined. Our recent work documented the key importance of ASM for *Neisseria meningitidis* uptake into human brain microvascular endothelial cells (HBMEC). We clearly identified OpcA to be one bacterial effector promoting ASM translocation and activity, though it became clear that additional bacterial components were involved, as up to 80% of ASM activity and ceramide generation was retained in cells infected with an opcA-deficient mutant. We hypothesized that *N. meningitidis* might use pilus components to promote the translocation of ASM into HBMEC. Indeed, we found that both live, piliated *N. meningitidis* and pilus-enriched fractions trigger transient ASM surface display, followed by the formation of ceramide-rich platforms (CRPs). By using indirect immunocytochemistry and *direct* stochastic optical reconstruction microscopy, we show that the overall number of CRPs with a size of $\approx$80 nm in the plasma membrane is significantly increased after exposure to pilus-enriched fractions. Infection with live bacteria as well as exposure to pilus-enriched fractions transiently increased cytosolic Ca^{2+} levels in HBMEC, and this was found to be important for ASM surface display mediated by lysosomal exocytosis, as depletion of cytosolic Ca^{2+} resulted in a significant decrease in ASM surface levels, ASM activity, and CRP formation." [114]

The following manuscript was published on July 23$^{\mathrm{rd}}$, 2019 in Infection and Immunity and permission for legal second publication within this thesis was kindly granted from both the publishers and the co-authors.

Neisseria meningitidis Type IV Pili Trigger Ca²⁺-Dependent Lysosomal Trafficking of the Acid Sphingomyelinase To Enhance Surface Ceramide Levels

Simon Peters,[a] Jan Schlegel,[b] Jérôme Becam,[a] Elita Avota,[c] Markus Sauer,[b] Alexandra Schubert-Unkmeir[a]

[a]Institute of Hygiene and Microbiology, University of Wuerzburg, Wuerzburg, Germany
[b]Department of Biotechnology and Biophysics, Biocenter, University of Wuerzburg, Wuerzburg, Germany
[c]Institute for Virology and Immunobiology, University of Wuerzburg, Wuerzburg, Germany

ABSTRACT Acid sphingomyelinase (ASM) is a lipid hydrolase that converts sphingomyelin to ceramide and that can be activated by various cellular stress mechanisms, including bacterial pathogens. Vesicle transportation or trafficking of ASM from the lysosomal compartment to the cell membrane is a prerequisite for its activation in response to bacterial infections; however, the effectors and mechanisms of ASM translocation and activation are poorly defined. Our recent work documented the key importance of ASM for *Neisseria meningitidis* uptake into human brain microvascular endothelial cells (HBMEC). We clearly identified OpcA to be one bacterial effector promoting ASM translocation and activity, though it became clear that additional bacterial components were involved, as up to 80% of ASM activity and ceramide generation was retained in cells infected with an *opcA*-deficient mutant. We hypothesized that *N. meningitidis* might use pilus components to promote the translocation of ASM into HBMEC. Indeed, we found that both live, piliated *N. meningitidis* and pilus-enriched fractions trigger transient ASM surface display, followed by the formation of ceramide-rich platforms (CRPs). By using indirect immunocytochemistry and direct stochastic optical reconstruction microscopy, we show that the overall number of CRPs with a size of ∼80 nm in the plasma membrane is significantly increased after exposure to pilus-enriched fractions. Infection with live bacteria as well as exposure to pilus-enriched fractions transiently increased cytosolic Ca²⁺ levels in HBMEC, and this was found to be important for ASM surface display mediated by lysosomal exocytosis, as depletion of cytosolic Ca²⁺ resulted in a significant decrease in ASM surface levels, ASM activity, and CRP formation.

KEYWORDS *Neisseria meningitidis*, acid sphingomyelinase, sphingolipids, superresolution microscopy, type IV pili

Acid sphingomyelinase (ASM) is a lipid hydrolase causing sphingomyelin breakdown and the release of ceramides, which associate into small ceramide-enriched membrane domains that fuse to larger ceramide-rich platforms (CRPs), thereby modulating membrane structures and signal transduction (1–3).

Several bacterial pathogens regulate ASM translocation and/or activity to exploit host sphingolipids during their infection processes (4–15). This is reflected by the importance of this enzyme in host defenses (mainly uptake and trafficking in phagocytes), as revealed for *Pseudomonas aeruginosa* (5) and for *Listeria monocytogenes* and *Neisseria gonorrhoeae* (7, 16, 17). In addition, ASM was also found to be crucial for bacterial uptake into nonphagocytic cells, including endothelial cells. In peripheral endothelial cells, *Staphylococcus aureus* infection increased ASM activity, and this contributed to the development of pulmonary edema (18). In brain endothelial cells,

81

ASM translocation and the increased activity caused by OpcA-expressing *Neisseria meningitidis* resulted in enhanced ceramide surface display, which was found to support bacterial uptake by recruitment of the ErbB2 receptor, involved in bacterial uptake into CRPs (6). This observation paralleled the finding obtained with the related species *N. gonorrhoeae* in phagocytic cells (16), where ASM caused the recruitment of CEACAM receptors in CRPs.

ASM localizes in lysosomes or in specialized lysosomal compartments named secretory lysosomes (19). Its activation may occur within this compartment by protein kinase Cδ-mediated phosphorylation (20, 21) or has been suggested to require translocation from the intracellular compartment to the extracellular leaflet of the cell membrane. For example, the application of hydrogen peroxide to mammalian cells induces a rapid Ca^{2+}-dependent ASM translocation by lysosomal exocytosis, followed by its activation (22), and plasmalemmal injury-triggered Ca^{2+} influxes have been shown to induce the fusion of lysosomes with the plasma membrane, resulting in exocytosis and activation of ASM (23).

N. meningitidis (the meningococcus) is a human pathogen that colonizes the upper respiratory tract of approximately 10 to 40% of the healthy population (24, 25). In rare cases the pathogen can cause devastating invasive infections, resulting in sepsis and meningitis, predominantly in young infants and toddlers. Via its outer membrane protein OpcA, *N. meningitidis* is capable of triggering ASM translocation and increasing its activity as well as ceramide release and the formation of CRPs on the surface of brain endothelial cells (6). The ASM translocation elicited by OpcA critically relies on OpcA interaction with heparan sulfate proteoglycans and the subsequent activation of phosphatidylcholine-specific phospholipase C. In addition to OpcA, further meningococcal candidates are likely to contribute to ASM translocation, because infection-induced ASM translocation and ceramide surface display were reduced by only about 20 to 30% with an isogenic mutant lacking *opcA* (6).

As major adhesins, type IV pili (TfP) play key roles in pathogenic *Neisseria* species by mediating the contact with eukaryotic cell surfaces (26). The pilus fiber is composed of a single structural component, the major pilin, PilE. In addition to PilE, several other structural pilin proteins, including PilC, PilD, PilG, and PilF, and the minor pilins PilX, PilV, and ComP contribute to TfP function (27–31), which includes the uptake of DNA for natural transformation and bacterial movement (32, 33) and initiation of signal transduction cascades (34). Purified neisserial pili and pili from the bacterial crude membrane fraction have been shown to induce transient increases of cytosolic Ca^{2+} levels in infected eukaryotic cells (35, 36). Moreover, pilus-induced Ca^{2+} transients trigger lysosomal exocytosis, exposing lysosomal Lamp1 at the host cell surface (36).

In this study, we tested the hypothesis that the pilus-induced Ca^{2+} flux in brain endothelial cells triggers lysosomal exocytosis, exposing ASM at the outer leaflet of the plasma membrane. We found that infection of human brain microvascular endothelial cells (HBMEC) with the highly piliated isolate *N. meningitidis* 8013 but not an isogenic pilus-deficient meningococcal mutant resulted in an increase in the amount of ceramide on the host cell surface in an amitriptyline-sensitive manner. Exposure of HBMEC to pilus-enriched fractions (PeF) also triggered transient ASM surface display, paralleled by increased surface Lamp1 levels. Importantly, inhibition of cytosolic Ca^{2+} levels inhibited pilus-induced Lamp1 as well as ASM surface display and the formation of CRPs, indicating that ASM is delivered to the outer leaflet of the plasma membrane by pilus-induced lysosomal exocytosis.

RESULTS

Exposure of *N. meningitidis* strain 8013 to brain endothelial cells induces ceramide release and the formation of ceramide-enriched platforms. We have recently shown that *N. meningitidis* strain MC58 causes a rapid but transient translocation of the acid sphingomyelinase (ASM) in human brain microvascular endothelial cells (HBMEC). In this system, OpcA interaction with heparan sulfate proteoglycans significantly contributed to ASM translocation and activity (6). The 80% residual cer-
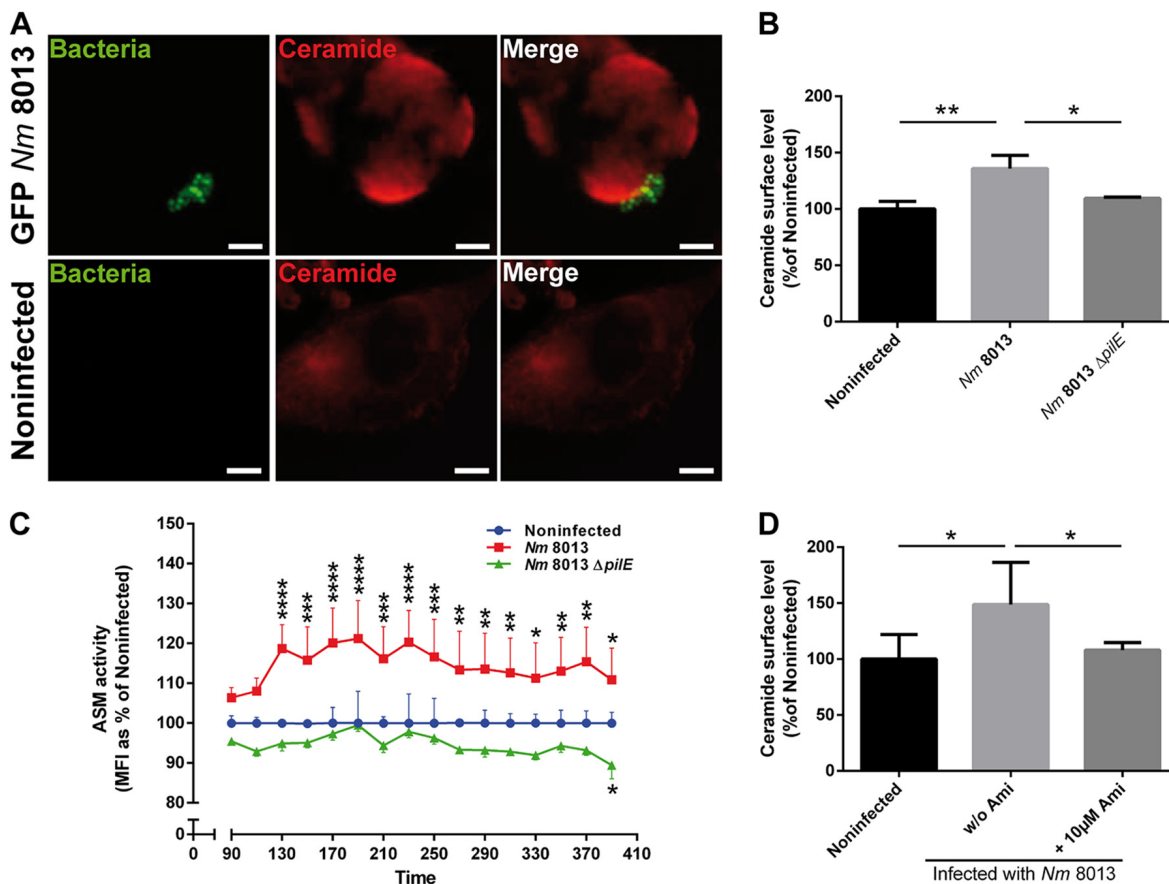
FIG 1 Highly piliated *N. meningitidis* (*Nm*) strain 8013 activates ASM and the formation of CRPs on HBMEC. (A) HBMEC were grown to confluence in 8-well Ibidi μ-slides and were infected with a GFP-expressing variant of *N. meningitidis* strain 8013 for 4 h or were left noninfected. Cells were washed, fixed in paraformaldehyde (FA), and stained with an anticeramide antibody and secondary Cy5-conjugated goat anti-mouse IgM (red). Images were captured using a Nikon Eclipse Ti-E inverted microscope with a 40× objective lens. Bars, 10 μm. (B) HBMEC were infected with wild-type strain *N. meningitidis* 8013 or an isogenic, pilus-deficient mutant (*N. meningitidis* 8013 $\Delta pilE$) or were left noninfected for 4 h. Surface ceramide levels were determined by flow cytometry, and data are represented as the relative levels of ceramides on the host cell surface. Error bars represent the mean $\pm$ SD. One-way ANOVA with Dunnett's *post hoc* test was used to determine significance. *, $P < 0.05$; **, $P < 0.01$. (C) ASM activity was determined on HBMEC by measuring sphingomyelin hydrolysis to phosphorylcholine. Cells were seeded in black 96-well plates to confluence and infected with *N. meningitidis* 8013 or left noninfected (basal activity). Reported is the activity of ASM after infection with bacteria. Values show the mean $\pm$ SD from three independent experiments. MFI, mean fluorescence intensity. Two-way ANOVA was used to determine significance. *, $P < 0.05$; **, $P < 0.01$; ***, $P < 0.001$; ****, $P < 0.0001$. (D) HBMEC were infected with *N. meningitidis* 8013 for 4 h in the presence or absence of the ASM inhibitor amitriptyline (+10 μM Ami and w/o [without] Ami, respectively) or were left noninfected. Surface ceramide levels were determined by flow cytometry, and data are represented as the relative levels of ceramides on the host cell surface compared to that on noninfected cells. Values are expressed as a percentage of the level for noninfected cells $\pm$ SD. One-way ANOVA with Dunnett's *post hoc* test was used to determine significance. *, $P < 0.05$. All experiments were performed at least three times in duplicate.

amide induction by an isogenic *opcA*-deficient mutant suggested that other meningococcal components also contributed to ASM induction (6). To analyze whether the type IV pili (TfP) might be involved, a highly piliated, Opa-negative (Opa⁻), *opcA*-deficient derivative of serogroup C, meningococcal strain 8013 (clone 12, also designated 2C4.3) (37), was applied and tested for its ability to contribute to ASM translocation in HBMEC. In common with *N. meningitidis* isolate MC58, immunofluorescence images demonstrate that a green fluorescent protein (GFP)-expressing variant of strain 8013 induced the formation of and adhered to CRPs (detected by the antibody 15B4) (Fig. 1A). HBMEC were then infected with *N. meningitidis* strain 8013 for 4 h, and surface ceramide levels on infected HBMEC were determined by flow cytometry (Fig. 1B; see also Fig. S1 in the supplemental material). *N. meningitidis* strain 8013 was found to be significantly effective at inducing ceramides on HBMEC (Fig. 1B), while this was not observed with a nonpiliated *pilE*-deficient mutant (*N. meningitidis* 8013 $\Delta pilE$) (Fig. 1B). To analyze whether the surface ceramide release detected relied on ASM, we determined the

activity of the enzyme on living HBMEC after infection with the wild type and the *pilE*-deficient mutant. *N. meningitidis* strain 8013 but not the pilus-deficient mutant caused significant ASM activity, which peaked within 130 min postinfection (p.i.) (Fig. 1C). Corroborating the crucial role of ASM in *N. meningitidis* strain 8013-induced ceramide release, the latter was abrogated in HBMEC exposed to the ASM inhibitor amitriptyline 30 min prior to infection (Fig. 1D).

N. meningitidis recruits lysosomal ASM to the cell surface. Because we detected ASM activity at the cell surface after *N. meningitidis* exposure, we reasoned that the enzyme should be translocated to and therefore be detectable at the outer leaflet of the plasma membrane. At 4 h following *N. meningitidis* treatment, ASM staining was observed in clusters on nonpermeabilized HBMEC close to bacterial microcolonies (Fig. 2A, left) suggesting its surface display. On a quantitative basis, this could be confirmed by flow cytometry (Fig. 2A, right). To test whether the translocation of ASM to the surface level of infected HBMEC might involve lysosomal exocytosis, Lamp1, a lysosomal marker, was detected on the surface of *N. meningitidis* 8013-infected HBMEC and analyzed by immunofluorescence microscopy and flow cytometry. The results revealed an increase in the level of Lamp1 membrane staining and Lamp1 surface levels as well as the codetection of both molecules, ASM and Lamp1, on infected HBMEC (Fig. 2B and C).

N. meningitidis-induced lysosomal exocytosis and ASM translocation to the plasma membrane are Ca^{2+} dependent. Lysosomal exocytosis requires Ca^{2+} elevation for the fusion of predocked lysosomes with the plasma membrane. Because *N. meningitidis* induces Ca^{2+} release from intracellular stores in infected human epithelial and endothelial cells (35, 38), we analyzed whether this would also apply to infection with *N. meningitidis* strain 8013 in our cell culture model system by using the calcium indicator Fluo-8. *N. meningitidis* strain 8013 significantly induced the cytosolic Ca^{2+} concentration in infected cells compared to the uninfected controls (Fig. 3A and B and, for single cell analysis, Fig. 3C). To verify that the increase in calcium levels reflected the release from intracellular stores, Ca^{2+} concentrations were again monitored by real-time immunofluorescence microscopy in cells treated with 50 μM 2-aminoethoxydiphenyl borate (2-APB), a chemical that acts to inhibit both inositol 1,4,5-trisphosphate receptors and transient receptor potential channels, prior to infection with meningococci. The inhibitor diminished calcium efflux in infected cells, supporting the finding that Ca^{2+} was indeed released from the endoplasmic reticulum in HBMEC (Fig. 3A and B, right). If Ca^{2+} mobilization is required for *N. meningitidis*-induced lysosomal exocytosis, 2-APB preexposure of HBMEC should affect the surface display of Lamp1, ASM, and ceramide as well as surface ASM activity. In fact, 2-APB dose dependently reduced the Lamp1 as well as ASM surface levels measured by flow cytometry (Fig. 4A and B). In addition, increased ASM activity and ceramide surface accumulation were not observed after 2-APB treatment (Fig. 4C and D), indicating that ASM translocation to the plasma membrane during meningococcal infection is mediated by Ca^{2+}-dependent lysosomal exocytosis.

N. meningitidis PilC1 is involved in ceramide release. Two PilC alleles that encode two paralogous proteins, PilC1 and PilC2, have been described (27). PilC2 is expressed independently of PilC1 and mediates adhesion to some cell types, not including endothelial cells (27, 39), while the adhesive properties of TfP to endothelial cells depend on PilC1 (27). PilC1-deficient (PilC2 positive) mutants fail to adhere to endothelial cells, and moreover, PilC1-deficient mutants fail to trigger Ca^{2+} release (35). To identify the role of PilC1 and PilC2 in ceramide release, we generated Δ*pilC1* and Δ*pilC2* mutant strains and analyzed their adhesive properties as well as ceramide accumulation on infected HBMEC by a gentamicin protection assay, immunofluorescence microscopy, and flow cytometry analysis. The Δ*pilC1* mutant showed much reduced adherence to HBMEC comparable to that of the nonpiliated Δ*pilE* mutant and was unable to increase ceramide levels or promote the formation of CRPs on infected cells, while these properties were fully retained in the Δ*pilC2* mutant (Fig. 5).
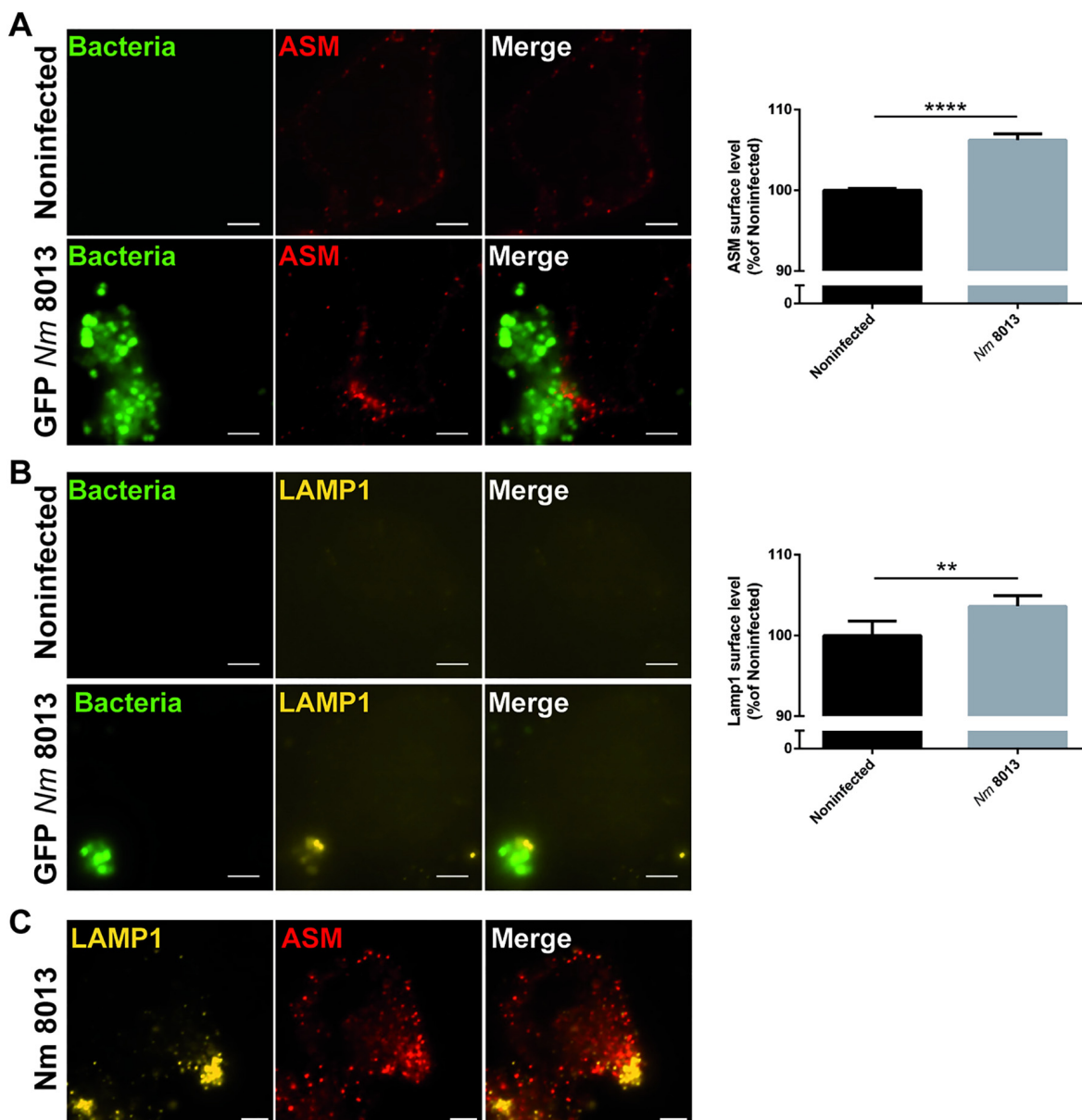
FIG 2 *N. meningitidis* induces the translocation of lysosomal ASM and Lamp1 to the cell surface. HBMEC were grown to confluence in 8-well Ibidi μ-slides and infected with the GFP-expressing *N. meningitidis* 8013 strain for 4 h or were left noninfected, and then ASM translocation as well as Lamp1 exposure on the host cell surface was evaluated. (A) (Left) Cells were washed, stained live on ice with a rabbit IgG anti-ASM antibody and secondary Cy5-conjugated anti-rabbit IgG F(ab')$_2$, and then fixed in FA (red). Bars, 5 μm. (Right) ASM exposure on the plasma membrane was determined by flow cytometry of nonpermeabilized cells. Data show the mean $\pm$ SD from three independent experiments performed in duplicate. ****, $P < 0.0001$ by an unpaired, two-tailed Student's *t* test. (B) (Left) Cells were washed, stained live on ice with a mouse IgG PE-conjugated anti-Lamp1 antibody, and then fixed in FA (yellow). Bars, 5 μm. (Right) Lamp1 exposure to the plasma membrane was determined by flow cytometry of nonpermeabilized cells. Data show the mean $\pm$ SD from three independent experiments performed in duplicate. **, $P < 0.01$ by an unpaired, two-tailed Student's *t* test. (C) Cells were infected with the *N. meningitidis* 8013 strain for 4 h, washed, fixed in FA, and stained with a mouse IgG PE-conjugated anti-Lamp1 antibody (yellow), as well as rabbit IgG anti-ASM antibody and secondary Cy5-conjugated anti-rabbit IgG F(ab')$_2$ (red). Bars, 5 μm.

Depletion of Ca²⁺ levels interferes with bacterial uptake. We previously demonstrated that ASM translocation is of functional importance in meningococcal uptake (6). To corroborate the previous finding of the functional importance of ASM translocation in bacterial uptake, HBMEC were pretreated with 2-APB for 30 min prior to infection, and adhesion and invasion were determined. Indeed, the decrease in Ca²⁺ levels caused by 2-APB affected *N. meningitidis* uptake by HBMEC (Fig. 6), which could also be observed after chelation of intracellular Ca²⁺ by the acetoxymethyl ester of EGTA (EGTA-AM) (Fig. S2).

85
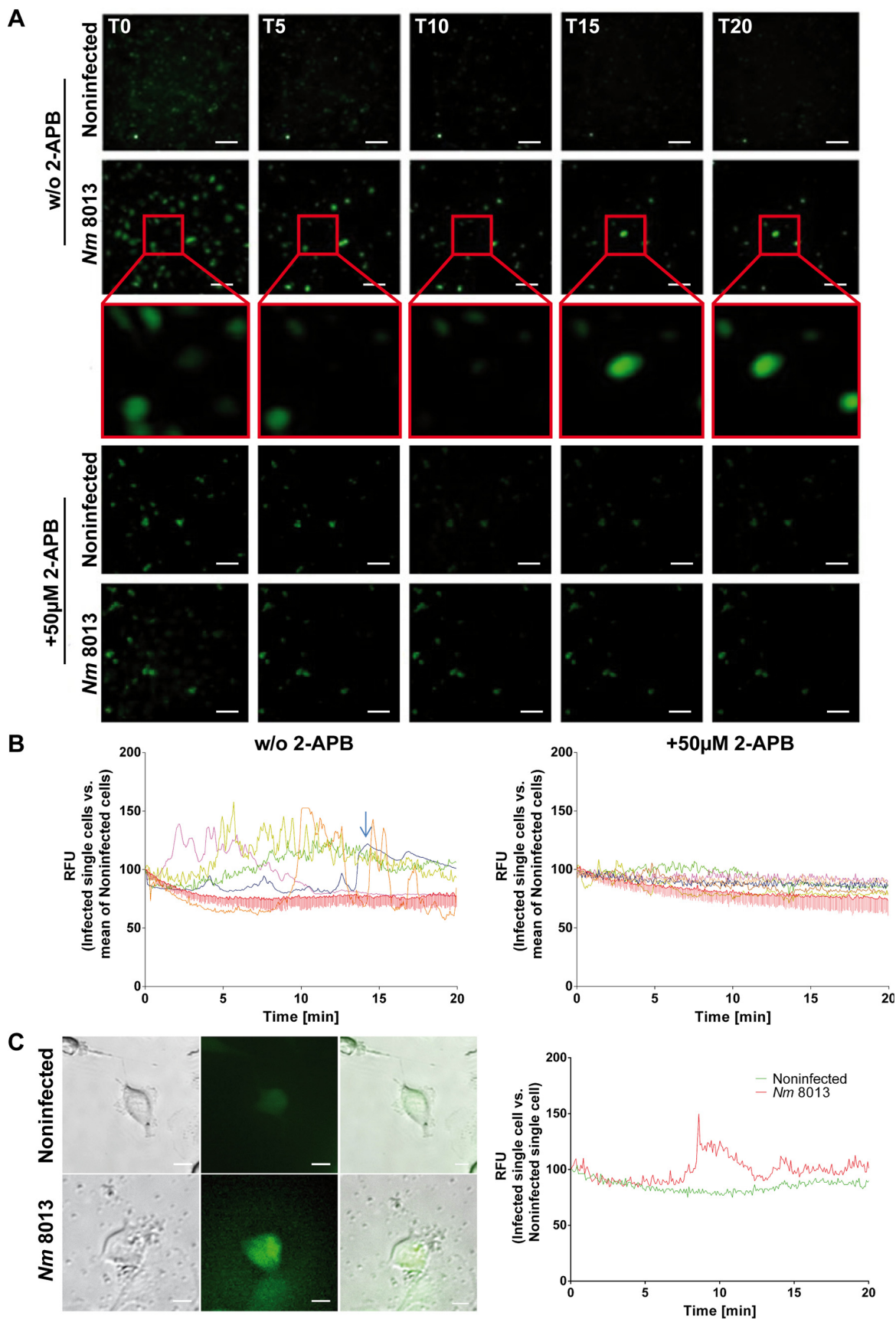
FIG 3 *N. meningitidis* increases cytosolic Ca²⁺ levels in brain endothelial cells derived from the endoplasmic reticulum. Fluo-8-loaded HBMEC were infected with *N. meningitidis* 8013 in the presence or absence of 50 μM 2-APB or were left noninfected, and cytosolic Ca²⁺

(Continued on next page)

86
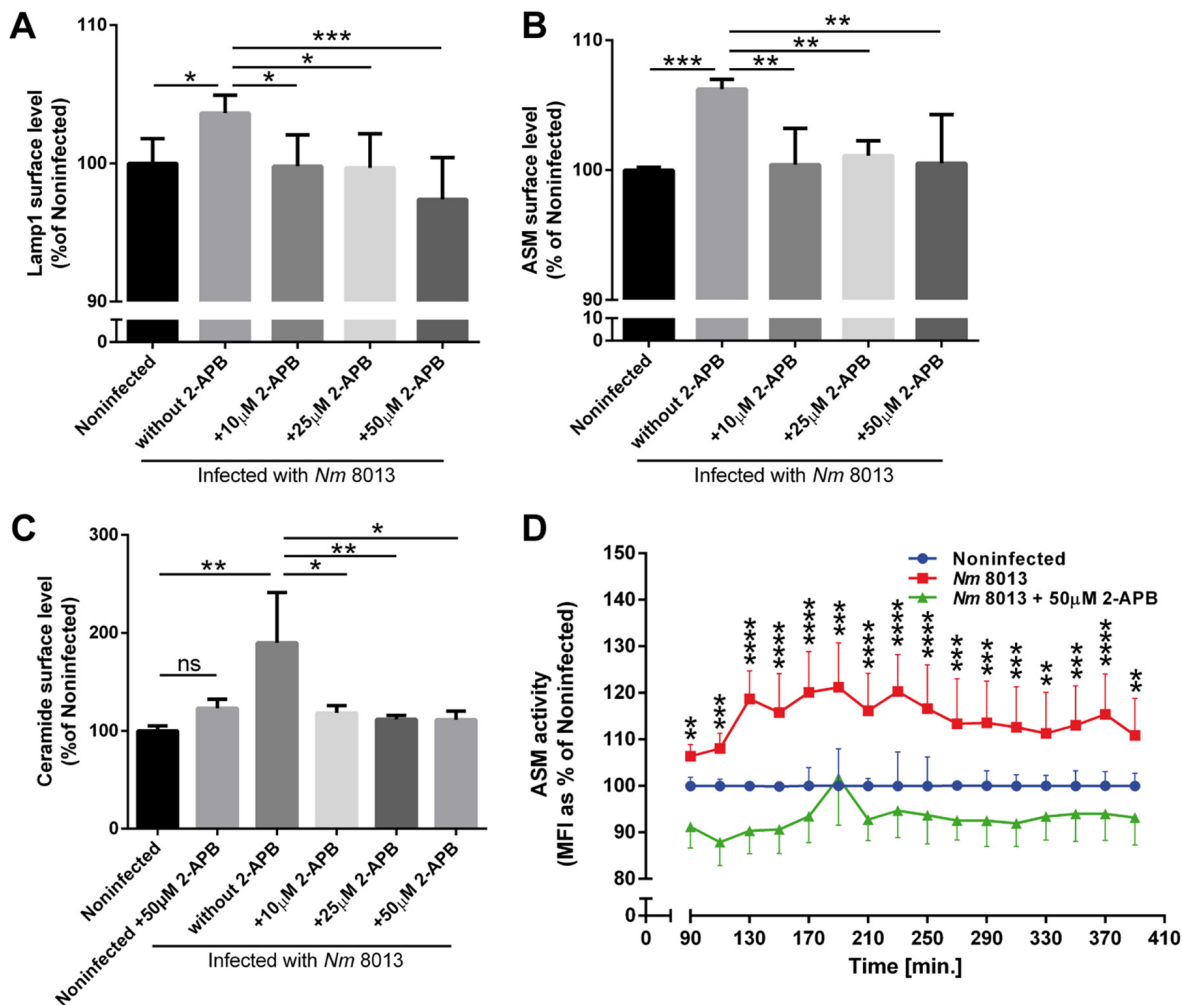
FIG 4 *N. meningitidis*-induced ASM translocation to the plasma membrane is Ca²⁺ dependent. HBMEC were treated with different concentrations of 2-APB (10, 25, 50 μM) for 30 min prior to infection with *N. meningitidis* 8013. *N. meningitidis*-induced Lamp1 exocytosis, ASM translocation, and ceramide surface levels were detected by flow cytometry analysis using a mouse IgG PE-conjugated anti-Lamp1 antibody (A), a mouse IgG2a anti-ASM antibody and secondary Cy3-conjugated anti-mouse IgG F(ab')$_2$ (B), or an anticeramide antibody and secondary Cy5-conjugated goat anti-mouse IgM (C). Data show the mean $\pm$ SD levels as a percentage of those for noninfected cells from three independent experiments performed in duplicate. One-way ANOVA with Dunnett's *post hoc* test was performed to determine significance. *, $P < 0.05$; **, $P < 0.01$; ***, $P < 0.001$. (D) ASM activity after infection with bacteria in the presence (50 μM) or absence of 2-ABP. Values show the mean $\pm$ SD from three independent experiments. Two-way ANOVA was used to determine significance. *, $P < 0.05$; **, $P < 0.01$; ***, $P < 0.001$; ****, $P < 0.0001$.

Pilus-enriched fractions trigger calcium release and ASM translocation in HBMEC. We next aimed at determining the role of pili as effectors in *N. meningitidis*-induced Ca²⁺ release from HBMEC. Pilus-enriched fractions purified from the piliated wild-type meningococcal strain 8013 did not contain detectable levels of porins (a major pathogenicity factor involved in Ca²⁺ influx into the host cell [44]), while the presence of pilin in the preparations was visualized with a monoclonal antibody raised against PilE (Fig. S3). Cytosolic Ca²⁺ concentrations were determined in HBMEC loaded

FIG 3 Legend (Continued)
concentrations were monitored over 20 min. Images were captured using a Nikon Eclipse Ti-E inverted microscope and analyzed using NIS Elements AR software (Nikon). (A) Representative fluorescence images taken at the indicated time points (0, 5, 10, 15, and 20 min [T0, T5, T10, T15, and T20, respectively]) are shown. Images were taken at a $\times$20 magnification. Bars, 100 μm. (B) Fluorescence data from representative cells were exported and are shown as the number of relative fluorescence units (RFU) relative to the start fluorescence intensity value. Images show the results for infected single cells (left) or 2-APB-treated cells (right) versus the mean for noninfected cells. The arrow indicates the results for a single cell which appears at 15 min in the inset in panel A. 2-APB, 2-aminoethoxydiphenyl borate. (C) Representative single-cell analysis results. Pictures (left) show single cells which were analyzed for their fluorescence intensity (right). Bars, 10 μm.

87
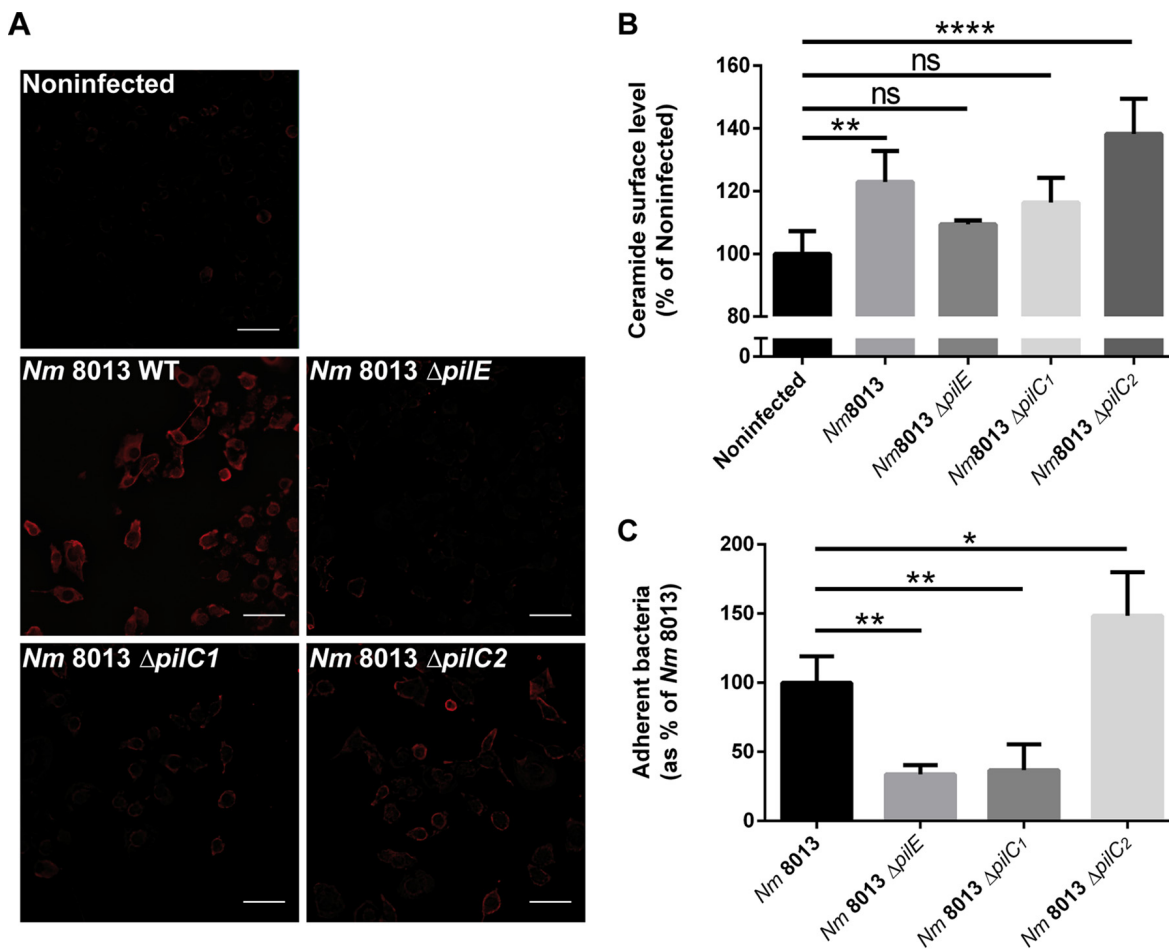
FIG 5 Ceramide release and CRP formation in response to isogenic Δ*pilC1* or Δ*pilC2* meningococcal mutants. (A) HBMEC were grown to confluence in 8-well Ibidi μ-slides and were infected with wild-type (WT) strain *N. meningitidis* 8013 or isogenic meningococcal mutant *N. meningitidis* 8013 Δ*pilE*, *N. meningitidis* 8013 Δ*pilC1*, or *N. meningitidis* 8013 Δ*pilC2* for 4 h or were left noninfected. Cells were washed, fixed in FA, and stained with an anticeramide antibody and secondary Cy5-conjugated goat anti-mouse IgM (red). Images were captured using a Nikon Eclipse Ti-E inverted microscope with a 20× objective lens. Bars, 100 μm. The results of one of three reproducible experiments are shown. (B) HBMEC were infected with wild-type strain *N. meningitidis* 8013 or isogenic mutant *N. meningitidis* 8013 Δ*pilE*, *N. meningitidis* 8013 Δ*pilC1*, or *N. meningitidis* 8013 Δ*pilC2* or were left noninfected for 4 h. Surface ceramide levels were determined by flow cytometry, and data are represented as the relative levels of ceramides on the host cell surface. (C) HBMEC were infected with the *N. meningitidis* 8013 wild-type strain or the indicated mutants (the Δ*pilE*, Δ*pilC1*, or Δ*pilC2* mutant) for 4 h at an MOI of 100. Adhesion was determined by a gentamicin protection assay. Error bars represent the mean ± SD. One-way ANOVA with Dunnett's *post hoc* test was used to determine significance. *, $P < 0.05$; **, $P < 0.01$; ****, $P < 0.0001$; ns, not significant.

with the fluorescent Ca^{2+} indicator Fluo-8 and treated with 2.5 μg/ml of pilus-enriched fractions. Immediately after addition, pilus-enriched fractions (but not control buffer [not shown]) induced a significant cytosolic Ca^{2+} increase within 2 to 5 min, and the levels quickly returned to the baseline levels (Fig. 7A). Lysosomal exocytosis was next monitored in LysoTracker-loaded cells exposed to 2.5 μg/ml of pilus-enriched fractions or medium alone (in the absence of Ca^{2+}). A rapid decrease in the fluorescence signal was observed after treatment with pilus-enriched fractions, indicating that fusion of the lysosomal membrane with the plasma membrane and LysoTracker release occurred (Fig. 7B, pilus-enriched fractions [PeF]). Treatment of HBMEC with 2.5 μg/ml of the pilus-enriched fractions slightly but significantly increased both ASM and ceramide plasma membrane surface display, as determined by flow cytometry at 2 h after exposure (Fig. 7C). In addition, the pilus-enriched fraction induced 2-APB-sensitive ASM surface activity (Fig. 7E).

The pilus-enriched fraction also efficiently induced CRP formation on HBMEC. This was first revealed by standard microscopy (Fig. 7D), and thereafter, the distribution of CRPs was analyzed by single-molecule sensitive superresolution microscopy using
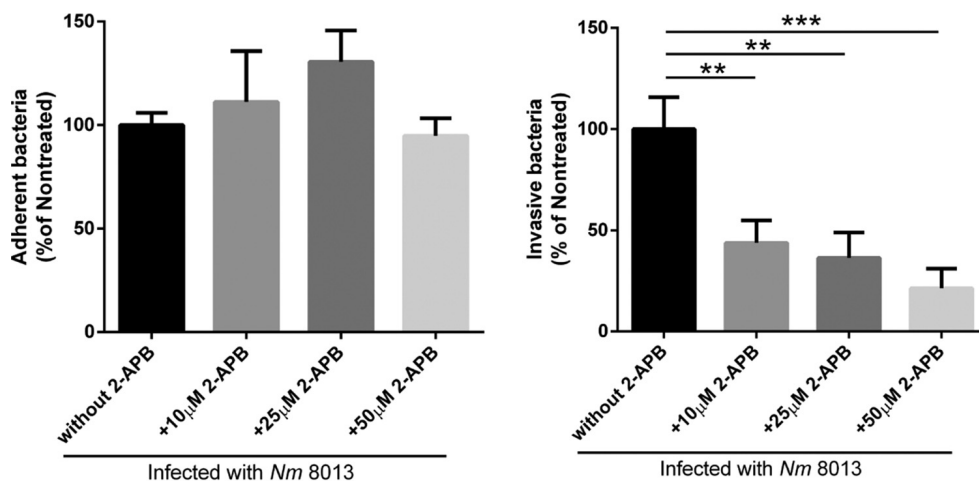
FIG 6 Depletion of the Ca²⁺ level interferes with invasion of *N. meningitidis* strain 8013 into HBMEC. HBMEC were pretreated with different concentrations (10, 25, 50 μM) of the 1,4,5-trisphosphate receptor inhibitor 2-APB. Afterwards, cells were infected for 4 h at an MOI of 100, and adhesion (left) and invasion (right) were determined by a gentamicin protection assay. All results show the mean $\pm$ SD levels as a percentage of the levels for untreated control cells from three independent experiments performed in duplicate. *P* values are relative to the values for untreated control cells and were determined by an ordinary one-way ANOVA with Dunnett's *post hoc* test. **, $P < 0.01$, ***, $P < 0.001$.

indirect immunocytochemistry and direct stochastic optical reconstruction microscopy (*d*STORM) (40, 41) (Fig. 8). The overall number of CRPs with a size of ~80 nm (41) in the plasma membrane was significantly increased in HBMEC after 2 h of exposure to the pilus-enriched fractions, and the formation of CRPs could be prevented by treatment with 2-APB (Fig. 8A to D).

DISCUSSION

ASM has been shown to be an important factor in pathogen infection and survival. Some bacterial pathogens can target ASM and thereby modulate microdomain reorganization, which can alter cellular internalization or cell death (5–8, 11, 16–18, 43). As a prerequisite, lysosomal ASM has to be relocalized at the cell surface and activated; however, the precise mechanism by which this is achieved during bacterial infections remains unknown. In this study, we tested the hypothesis that the meningococcal pilus-induced increase in cytosolic Ca²⁺ triggers lysosomal exocytosis and increases the amount of cell surface ASM, followed by lipid microdomain formation. We demonstrate that the highly piliated *N. meningitidis* isolate 8013 but not an isogenic pilus-deficient mutant was effective at inducing ceramides on HBMEC. Increased ceramide surface levels reflected increased ASM activity and were abrogated in the presence of the ASM inhibitor amitriptyline. We showed that pilus-enriched fractions also triggered the transient translocation of ASM to the host cell surface. We provided microscopic evidence that live, piliated bacteria as well as pilus-enriched fractions induced transient increases in cytosolic Ca²⁺ levels in HBMEC and triggered lysosomal exocytosis, as detected by exposure of Lamp1. Of importance, we finally showed that depletion of cytosolic Ca²⁺ transients with 2-APB, a chemical that acts to inhibit inositol 1,4,5-trisphosphate receptors, abolished not only Lamp1 levels but also ASM translocation and, thus, the formation of CRPs on *N. meningitidis*-infected HBMEC or cells treated with pilus-enriched fractions.

We have recently shown that *N. meningitidis* strains can transiently translocate ASM if they express the OpcA protein and use CRPs as a port of entry into HBMEC (6). However, further meningococcal factors besides OpcA are likely to contribute to ASM translocation and the generation of ceramides, since infection of brain endothelial cells with an isogenic mutant lacking *opcA* resulted in a decrease in the amount of ceramide on the host cell surface of only about 20 to 30% (6). TfP of pathogenic *Neisseria* are essential during the initial stage of infection and are known to initiate a signal
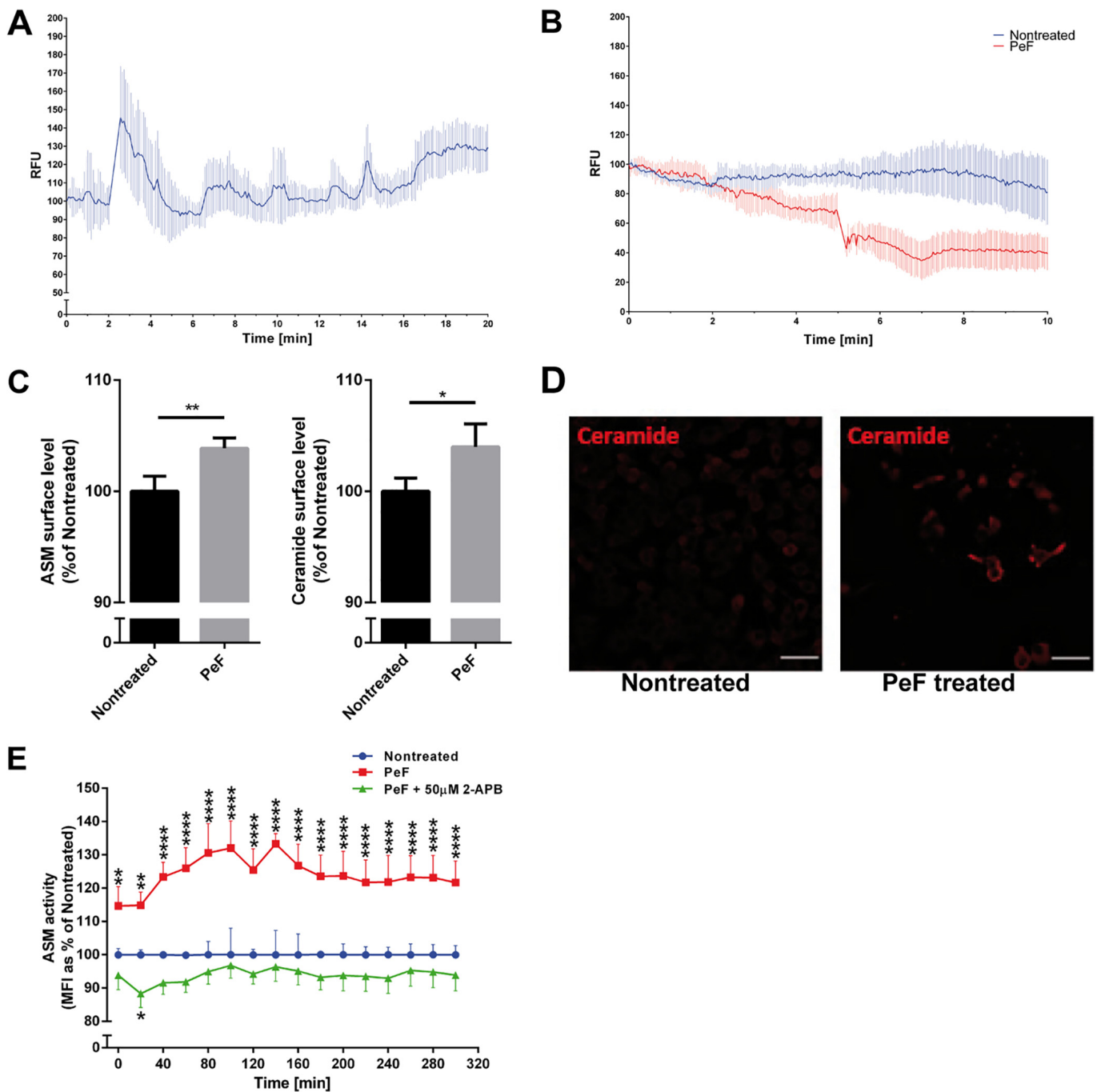
FIG 7 Effect of pilus-enriched fractions on Ca²⁺ fluxes, ASM translocation and activity, and ceramide release. (A) HBMEC were loaded with Fluo-8 and treated with 2.5 μg pilus-enriched fraction (PeF) from *N. meningitidis* 8013 in Ca²⁺-free medium. Cytosolic Ca²⁺ concentrations were monitored over 10 min using a Nikon Eclipse Ti-E inverted microscope and analyzed using NIS Elements AR software (Nikon). Fluorescence data from representative cells were exported and are shown as the mean ± SD number of relative fluorescence units relative to the starting fluorescence intensity value. (B) HBMEC were loaded with LysoTracker green (80 nM) and treated with PeF (2.5 μg) in Ca²⁺-free medium. Fluorescence signals were monitored over 10 min. Fluorescence data from representative cells were exported and are shown as the mean ± SD number of relative fluorescence units relative to the starting fluorescence intensity value. Note the disappearance of the LysoTracker green signal after addition of PeF, indicative of lysosomal exocytosis. (C) Cells were maintained in infection medium and incubated with PeF (2.5 μg) from *N. meningitidis* 8013. The pilus-induced translocation of ASM and ceramide surface levels were detected by flow cytometry analysis. Data show the mean ± SD from three independent experiments performed in duplicate. *P* values were determined by an unpaired, two-tailed Student's *t* test. *, $P < 0.05$; **, $P < 0.01$. (D) Cells were grown to confluence in Ibidi μ-slides and were incubated with PeF (2.5 μg) from *N. meningitidis* 8013 or were left nontreated. Cells were washed, fixed in FA, and stained with an anticeramide antibody and secondary Cy5-conjugated goat anti-mouse IgM (red). Bars, 10 μm. (E) Cells were incubated with PeF or left nontreated, and ASM activity was determined. Reported is the activity of ASM after incubation of the cells with PeF (1 μg) from *N. meningitidis* 8013. Values show the mean ± SD from three independent experiments. A two-way ANOVA was used to determine significance. *, $P < 0.05$; **, $P < 0.01$; ****, $P < 0.0001$.
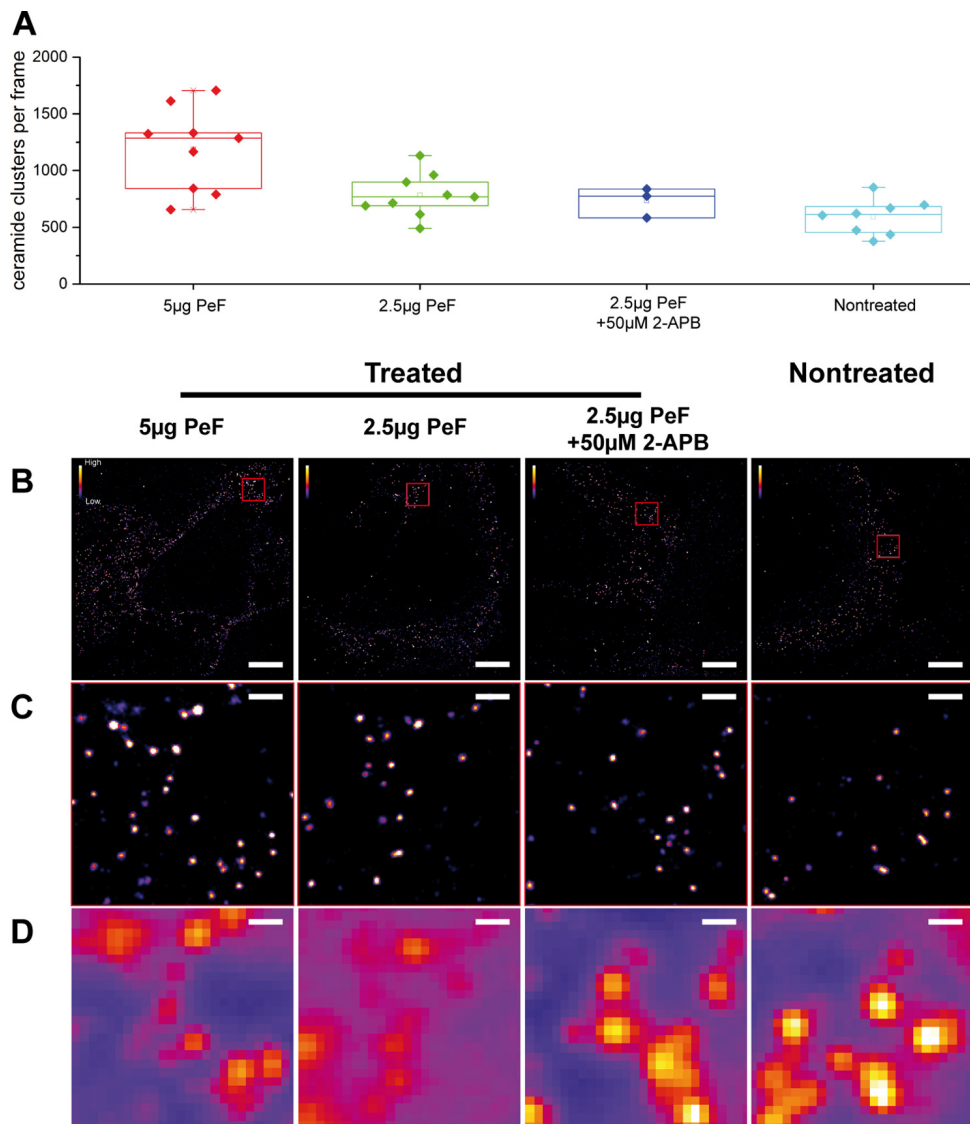
FIG 8 Treatment of HBMEC with pilus-enriched fractions increases the number of plasma membrane-associated CRPs. (A) Quantification of subdiffraction-sized CRPs within the plasma membrane of HBMEC pretreated with different concentrations of the pilus-enriched fraction (PeF) at 5 μg, 2.5 μg, or 2.5 μg or with 50 μM 2-APB or not treated. The superresolution images show a dose-dependent enrichment of sphingolipid nanodomains upon pilus treatment. (B) Representative dSTORM images of HBMEC treated with the indicated concentrations of PeF (as shown in panel A). (C) Images of the corresponding dSTORM insets (red squares) from panel B, illustrating the increase in the number of CRPs induced by the addition of PeF. (D) Conventional diffraction-limited microscopy of the sections shown in panel C. Bars, 5 μm (B) and 500 nm (C and D).

transduction cascade, resulting in tyrosine phosphorylation of cytoskeletal proteins (34). In addition, they induce Ca²⁺ transients in cultures of epithelial cells and monocytes (35, 36, 44). Here, we used real-time fluorescence imaging to examine Ca²⁺ levels in HBMEC during infection with piliated bacteria. Like the purified proteins and as shown for A431 and ME180 cells, live bacteria also triggered changes in cytosolic Ca²⁺ fluxes (35, 36). Besides TfP, the pilus-associated *Neisseria* porins also trigger a transient rise in cytosolic Ca²⁺ levels. In contrast to TfP-induced Ca²⁺ increases, the porin-triggered Ca²⁺ influx is rapid, occurs within 2 min after exposure of the protein, and stimulates endosome exocytosis (45, 46). Pilus-associated porins are supposed to insert into the host membrane to trigger an influx of Ca²⁺ ions from the external environment (44). In our experimental setting, we can exclude the possibility of any effects related to *N. meningitidis* porins, since experiments were performed in Ca²⁺-free medium and we could not detect any porin proteins on our pilus-enriched fraction preparation.

Ca^{2+} transients in cultures of epithelial cells have been thought to be transduced by the proposed pilus receptor, CD46 (35), as it could be blocked by anti-CD46 antibodies (35). However, recent publications have highlighted the specific interaction between the meningococcal ligands PilE and PilV and the cellular host receptor CD147 to be essential for meningococcal adhesion to human brain endothelial cells and colonization of human blood vessels (42). Whether Ca^{2+} transients might be transduced by CD147 needs further investigations.

Ca^{2+} is a highly versatile intracellular signal that can regulate many different cellular functions (49, 50), and the effects of Ca^{2+} fluxes in response to *N. meningitidis* are likely to be various. These transients have, for example, been demonstrated to increase the intracellular survival of the related species *N. gonorrhoeae*. Ca^{2+}-dependent lysosomal exocytosis leads to the redistribution of Lamp1 to the plasma membrane and the release of the luminal content of the vesicle to the extracellular milieu. Lamp1 cleavage at the host cell surface by the secreted neisserial IgA protease finally results in lysosome remodeling and enhanced bacterial survival within cells (36, 45, 51). The data presented in this study now show that the exocytic events resulting from the pilus-induced Ca^{2+} transients also bring ASM to the outer leaflet of the plasma membrane. However, further studies are required to determine the exact mechanism of ASM enzyme activation in response to TfP.

In nonsecretory cells, most lysosomes that undergo Ca^{2+}-regulated exocytosis belong to a peripheral population (52). By this means, calcium is primarily responsible for the fusion rather than the recruitment of lysosomes to the plasma membrane (52). Peripheral lysosomes were subsequently identified to be the major population of intracellular vesicles that respond to Ca^{2+} fluxes by fusing with the plasma membrane and promoting plasma membrane repair (23, 52–54). Restoring membrane integrity is crucial to preclude necrosis and apoptosis and reduce inflammation from necrotic cells. Interestingly, host cell entry by *Trypanosoma cruzi* mimics a process of plasma membrane injury and repair that involves Ca^{2+}-mediated exocytosis of lysosomes and the delivery of ASM to the outer leaflet of the plasma membrane, followed by a rapid form of endocytosis that internalizes membrane lesions (53, 55). A similar mechanism was recently observed during the entry of adenovirus into nonphagocytic cells (56). The viral membrane lytic protein protein VI induces small plasma membrane lesions and stimulates Ca^{2+} influx and lysosomal exocytosis, finally resulting in the release of ASM and the degradation of sphingomyelin to ceramide lipids in the plasma membrane (56). In contrast to the stimulation of lysosomal exocytosis by *T. cruzi* or adenovirus infection, the *N. meningitidis*-mediated increase of Ca^{2+} transients did not involve small plasma membrane lesions or Ca^{2+} influx from the extracellular milieu; instead, Ca^{2+} transients arose from the endoplasmic reticulum.

Besides bacterial or viral infection, ASM is exposed to the host cell surface in response to further stimuli, including CD95 or DR5 ligation, UV irradiation, or membrane damage (5, 57–61). Recently, the application of the reactive oxygen species (ROS) hydrogen peroxide to mammalian cells has been demonstrated to induce a rapid Ca^{2+}-dependent ASM translocation by lysosomal exocytosis (22). In contrast, CD95 or DR5 activation induces ROS-dependent ASM trafficking independently of Ca^{2+} (58). The precise mechanism for Ca^{2+}-independent ASM externalization is not well understood and might involve protein kinase Cδ phosphorylation of ASM and translocation to the plasma membrane (20). Taken together, in this study, we provide experimental evidence supporting the conclusion that ASM, which resides within lysosomes, can be exocytosed from *N. meningitidis*-infected brain endothelial cells in a Ca^{2+}-dependent manner and act on the outer plasma membrane to promote the formation of CRPs.

MATERIALS AND METHODS

Bacterial strains. *N. meningitidis* strain 8013 (clone 12, also designated 2C4.3) is a piliated capsulated Opa- and Opc-negative variant of the serogroup C meningococcal clinical isolate 8013 (sequence type 77 [ST77]/ST8 clonal complex [CC]; Institut Pasteur, 1989) and was kindly provided by M. Taha (37). The characteristics of the wild-type strain and the mutants are summarized in Table S1 in the supplemental material. Bacteria were grown overnight on Columbia blood agar plates (bioMérieux) at 37°C in 5% CO_2

and cultured on the next day in PPM+ medium (proteose-peptone medium supplemented with $1\times$ Kellogg´s supplement, 0.01 M $MgCl_2$, and 0.005 M $NaHCO_3$). Pilus mutants were grown overnight on GC agar plates (37°C, 5% CO_2) with spectinomycin (75 μg/ml) and were cultured in the same medium used for the wild type but supplemented with additional spectinomycin (75 μg/ml).

Cell culture. Immortalized human brain microvascular endothelial cells (HBMEC) were kindly provided by K. S. Kim (62) and were cultured as described previously (63). Briefly, cells were cultured in RPMI 1640 medium supplemented with 1% sodium pyruvate (1 mM), 1% L-glutamine (2 mM), and 1% nonessential amino acids (all purchased from GE Healthcare, Little Chalfont, UK) plus 5 U/ml heparin (Biochrom, Berlin, Germany) and 30 μg/ml endothelial cell growth supplement (ECGS; CellSystems, Troisdorf, Germany). Cells were incubated at 37°C in 5% CO_2 in a humidified atmosphere.

Infection assays. Adhesion and invasion were determined by using gentamicin protection assays. Cells at between the 10th and 25th passages were used for infection assays at a density of 4×10^5 cells/well, with bacteria used at a multiplicity of infection (MOI) of 100, unless indicated otherwise, as described previously (6).

Reagents and antibodies. The following antibodies were used in this study: mouse IgG2a anti-ASM (clone ab74281; Abcam), rabbit IgG anti-ASM (clone H181; Santa Cruz), mouse IgM anticeramide (clone MID 15B4; Enzo Life Science), rabbit IgG anticeramide (kindly provided by E. Bieberich [41]), mouse IgG phycoerythrin (PE)-conjugated anti-Lamp1 (clone H4A3; Santa Cruz), mouse IgG anti-PilE (SM1; M. Virji [66]), polyclonal rabbit anti-PorB (Genosys Biotechnologies), a mouse IgM isotype control (clone ICIGMPU; Immunostep), a mouse IgG1 isotype control (clone PPV-06; Invitrogen), and a normal rabbit IgG isotype control (clone sc-2027; Santa Cruz). The following secondary conjugated antibodies, all of which were purchased from Jackson ImmunoResearch, were used in this study: Cy5-conjugated goat anti-mouse IgM, Cy5-conjugated goat anti-rabbit IgG (H+L), Cy3-conjugated goat anti-rabbit IgG (H+L), Cy3-conjugated rabbit anti-mouse IgG F(ab')₂, and peroxidase-conjugated goat anti-mouse IgG and IgM (H+L). The isotype and secondary antibody controls are shown in Fig. S4. The following reagents were used in this study: 2-aminoethoxydiphenyl borate (2-APB; Tocris Bioscience) was used at a final concentration of 10, 25, or 50 μM and did not affect bacterial growth or fitness when applied under infection conditions. Hoechst 33342 (Invitrogen) was used for nuclear staining at a final concentration of 1 μg/ml, the calcium indicator dye Fluo-8 (Abcam) was used at a final concentration of 4 μM, and LysoTracker green DND-26 (Invitrogen) was used at a concentration of 80 nM. All compounds were dissolved in dimethyl sulfoxide (DMSO), and the final concentration of DMSO in the culture wells never exceeded 0.1%.

Flow cytometry. At 3 days prior to the experiment, 1.25×10^5 cells/ml were seeded in a 24-well plate and were grown to approximately 1×10^6 cells/ml. On the day of the infection experiment, cell medium was replaced by RPMI 1640 medium plus 10% human serum and, if indicated, preincubated for 30 min with different concentrations of 2-APB. Cells were infected with the bacteria for 4 h. After infection, the cells were washed once with phosphate-buffered saline (PBS), trypsinized, and harvested in an Eppendorf tube. After washing with ice-cold fluorescence-activated cell sorting (FACS) buffer (5% fetal calf serum [FCS] in PBS), the cells were incubated with either mouse IgM anticeramide (1:30 in FACS buffer), mouse IgG PE-conjugated anti-Lamp1 (1:20 in FACS buffer), mouse IgG2a anti-ASM (1:250 in FACS buffer), or the corresponding isotype control antibodies (1:100 in FACS buffer) for 1.5 h at 4°C in the dark. After incubation, the cells were washed three times with FACS buffer and incubated with the appropriate secondary antibodies (1:500 in FACS buffer) for 30 min. Then, the cells were washed three times with FACS buffer and were fixed in 3.7% paraformaldehyde (FA; in PBS) for 30 min at 4°C. Afterwards, the cells were washed 3 times with FACS buffer and 500 μl was transferred into a FACS tube for measurement. Ten thousand cells were analyzed using a FACSCalibur flow cytometer (BD Bioscience), and the data were analyzed and graphed using FlowJo (v10) software (FlowJo, LLC).

ASM activity assay. For determination of ASM surface activity, a commercially available acid sphingomyelinase activity assay kit from Echelon was used with some adaptations to the manufacturer's protocol. One day prior to the infection experiment, 0.75×10^4 cells were seeded into a black-walled, black-bottom 96-well plate (Thermo Scientific). On the day of infection, the growth medium was replaced with RPMI 1640 medium plus 10% human serum, and infection assays were carried out for 2 h at 37°C in 5% CO_2. When indicated, cells were pretreated with 50 μM 2-APB for 30 min prior to infection. After infection, cells were washed once with PBS and the ASM substrate was added directly to the cells. For pilus-treated samples, 1 μg of the preparation was added to the cells right after the substrate was added. The activity of ASM was then detected in a spectrophotometer (Infinite F200 Pro Reader; Tecan Group, Maennedorf, Switzerland) at a 360-nm excitation wavelength and a 460-nm emission wavelength every 20 min for 5 h.

Immunofluorescence microscopy. For ceramide staining, 2.5×10^4 cells/well were seeded in 8-well chamber μ-slides (Ibidi) and grown overnight. Cells were infected with bacteria for 4 h, washed with PBS, and fixed for 20 min with 3.7% paraformaldehyde. For the indicated experiments, cells were infected with GFP-expressing *N. meningitidis* strain 8013, a derivative of *N. meningitidis* 8013 expressing GFP from the plasmid pEG2-Ery (64). After fixation, cells were washed two times with PBS and blocked for 5 min in blocking buffer (1% FCS, 2% bovine serum albumin [BSA] in PBS). Then, the cells were washed and incubated with the primary antibody (1:200 dilution in blocking buffer) for 45 min at room temperature (RT), followed by treatment with the appropriate Cy fluorescent dye-labeled secondary antibody (1:200 in blocking buffer) for 45 min. (For ASM and LAMP1, cells were stained live on ice before fixation.) The samples were covered with PBS, and images were taken using a Nikon Eclipse Ti-E inverted microscope equipped with an Okolab incubator set to 37°C. Images were taken at a $\times$40 magnification and processed and analyzed using ImageJ software.

LSM and *d*STORM. Laser scanning microscopy (LSM) and *d*STORM imaging were performed as previously described (42). Briefly, HBMEC were seeded into 0.2% gelatin-coated 8-well plates on coverslip II slides (Sarstedt) at a concentration of 3×10^4 cells per well. After 24 h, the cells were treated with the amounts of pilus-enriched fractions indicated above for 2 h. After washing, the cells were labeled on ice with ~2-μg/ml rabbit anti-C16/24 ceramide IgG antibody for 50 min in cell culture medium and again washed. The cells were then fixed with 3% formaldehyde and 0.3% glutaraldehyde for 15 min on ice and 30 min at RT. After washing and blocking for 30 min with 5% BSA in PBS, staining with a secondary Alexa Fluor 647-conjugated goat anti-rabbit F(ab')$_2$ IgG fragment followed by 1 h in 5% BSA blocking buffer was performed. Cells were washed and again fixed with 2% formaldehyde and 0.2% glutaraldehyde to immobilize the antibodies. *d*STORM imaging was performed in switching buffer, consisting of 100 mM β-mercaptoethylamine (MEA; Sigma) in PBS, adjusted to pH 7.4. An inverted wide-field fluorescence microscope (model IX-71; Olympus) equipped with an oil-immersion objective (60$\times$; numerical aperture, 1.45; Olympus) was used for superresolution measurements. Alexa Fluor 647 fluorophores were excited with a 641-nm diode laser (model Cube 640-100C; Coherent), which was spectrally cleaned by use of a cleanup filter (Laser Clean-up filter 640/10; Chroma). Emission light was filtered by a dichroic mirror (beamsplitter HC560/659; Semrock) and a band- and long-pass filter (bandpass filter HC697/75 and longpass filter LP647; Semrock) before it was projected onto an electron-multiplying charge-coupled-device camera chip (model iXon DU-897; Andor). Additional lenses in the detection path were used to generate a final pixel size of 128 nm. The equatorial plasma membrane slightly above the coverslip was imaged using a highly inclined and laminated optical sheet (Hilo). Thirty thousand images with an exposure time of 20 ms were recorded while using an irradiation intensity of ~7 kW/cm². Data were processed with the ThunderSTORM and rapidSTORM programs and analyzed with Fiji or custom-written Mathematica code. The number of CRPs in the reconstructed superresolved images with a pixel size of 20 nm was determined using the "analyze particles" command in Fiji software. LSM imaging was performed with an LSM700 system (Zeiss, Germany) equipped with a Plan-Apochromat 63$\times$ (numerical aperture, 1.4) oil objective. Cy5 fluorophores were excited with a 639-nm solid-state laser. Images were processed using LSM software Zen system 2012 and Fiji software.

Calcium measurement. Intracellular calcium levels were estimated using a Fluo-8 no-wash calcium assay (Abcam Ltd., Cambridge, UK). The assay was performed according to the manufacturer's protocol with minor modifications. Briefly, 1.5×10^5 cells/well were seeded in 24-well plates and allowed to plate down overnight. Prior to infection, cell culture medium was removed and the cells were washed twice with Hanks' balanced salt solution (HBSS; calcium free; Sigma). Cells were incubated with 4 μM Fluo-8 in HBSS for 30 min at 37°C in 5% CO$_2$. After incubation, the cells were washed three times with HBSS and covered with 300 μl HBSS. Fluo-8-loaded cells were then infected with bacteria in the presence or absence of 50 μM 2-APB or were left uninfected. Changes in intracellular calcium levels were observed over a 20-min period using a Nikon Eclipse Ti-E inverted microscope and evaluated with the time measurement option of Nikon NIS-Elements AR software. For analysis, individual cells were selected for single-cell analysis and tracking of calcium level changes.

Preparation of pilus-enriched fractions. For preparation of pilus-enriched fractions, the bacterial content of 50 blood agar plates was harvested in 40 ml of 0.15 M ethanolamine (in PBS) with a pH of 10.5. Pili were sheared off by intensive vortexing for 2 min, followed by centrifugation at 12,000 $\times$ *g* for 10 min at RT to remove the cellular debris. The supernatant was used for an additional centrifugation step at 21,000 $\times$ *g* for 90 min to remove smaller debris. Then, the supernatant was transferred to an Erlenmeyer flask, ammonium sulfate-saturated 0.15 M ethanolamine was added to a concentration of 10%, and the mixture was incubated under continuous shaking for 30 min at RT. The protein-ammonium sulfate precipitate was then harvested by centrifugation at 21,000 $\times$ *g* for 15 min. The supernatant was then discarded and the pellet was resuspended in 0.05 M Tris-buffered saline (TBS), pH 7.5. Protein solutions were then applied to a 6-ml Viva Spin column with a 7,000-dalton-molecular-weight-cutof (MWCO) and were centrifuged at 4,000 $\times$ *g* at RT until the volume reached 1 ml. To clean the sample, TBS was added again to 6 ml, followed by centrifugation as mentioned above.

Statistical analysis. Statistical analysis was performed with GraphPad Prism (v6) software (GraphPad Software Inc., La Jolla, CA) by an unpaired two-tailed Student's *t* test or analysis of variance (ANOVA) followed by a *post hoc* test. Significance values are indicated in the figure legends.

SUPPLEMENTAL MATERIAL

Supplemental material for this article may be found at https://doi.org/10.1128/IAI .00410-19.

SUPPLEMENTAL FILE 1, PDF file, 0.1 MB.
SUPPLEMENTAL FILE 2, PDF file, 0.1 MB.
SUPPLEMENTAL FILE 3, PDF file, 0.1 MB.
SUPPLEMENTAL FILE 4, PDF file, 0.1 MB.
SUPPLEMENTAL FILE 5, PDF file, 0.1 MB.
SUPPLEMENTAL FILE 6, PDF file, 0.1 MB.
SUPPLEMENTAL FILE 7, PDF file, 0.1 MB.

ACKNOWLEDGMENTS

REFERENCES

1. Kolesnick RN, Goni FM, Alonso A. 2000. Compartmentalization of ceramide signaling: physical foundations and biological effects. J Cell Physiol 184:285–300. https://doi.org/10.1002/1097-4652(200009)184:3<285::AID-JCP2>3.0.CO;2-3.

2. Holopainen JM, Subramanian M, Kinnunen PK. 1998. Sphingomyelinase induces lipid microdomain formation in a fluid phosphatidylcholine/sphingomyelin membrane. Biochemistry 37:17562–17570. https://doi.org/10.1021/bi980915e.

3. Nurminen TA, Holopainen JM, Zhao H, Kinnunen PK. 2002. Observation of topical catalysis by sphingomyelinase coupled to microspheres. J Am Chem Soc 124:12129–12134. https://doi.org/10.1021/ja017807r.

4. Utermohlen O, Karow U, Lohler J, Kronke M. 2003. Severe impairment in early host defense against Listeria monocytogenes in mice deficient in acid sphingomyelinase. J Immunol 170:2621–2628. https://doi.org/10.4049/jimmunol.170.5.2621.

5. Grassme H, Jendrossek V, Riehle A, von Kurthy G, Berger J, Schwarz H, Weller M, Kolesnick R, Gulbins E. 2003. Host defense against Pseudomonas aeruginosa requires ceramide-rich membrane rafts. Nat Med 9:322–330. https://doi.org/10.1038/nm823.

6. Simonis A, Hebling S, Gulbins E, Schneider-Schaulies S, Schubert-Unkmeir A. 2014. Differential activation of acid sphingomyelinase and ceramide release determines invasiveness of Neisseria meningitidis into brain endothelial cells. PLoS Pathog 10:e1004160. https://doi.org/10.1371/journal.ppat.1004160.

7. Grassme H, Gulbins E, Brenner B, Ferlinz K, Sandhoff K, Harzer K, Lang F, Meyer TF. 1997. Acidic sphingomyelinase mediates entry of N. gonorrhoeae into nonphagocytic cells. Cell 91:605–615. https://doi.org/10.1016/S0092-8674(00)80448-1.

8. Esen M, Schreiner B, Jendrossek V, Lang F, Fassbender K, Grassme H, Gulbins E. 2001. Mechanisms of Staphylococcus aureus induced apoptosis of human endothelial cells. Apoptosis 6:431–439. https://doi.org/10.1023/A:1012445925628.

9. McCollister BD, Myers JT, Jones-Carson J, Voelker DR, Vázquez-Torres A. 2007. Constitutive acid sphingomyelinase enhances early and late macrophage killing of Salmonella enterica serovar Typhimurium. Infect Immun 75:5346–5352. https://doi.org/10.1128/IAI.00689-07.

10. Vazquez CL, Rodgers A, Herbst S, Coade S, Gronow A, Guzman CA, Wilson MS, Kanzaki M, Nykjaer A, Gutierrez MG. 2016. The proneurotrophin receptor sortilin is required for Mycobacterium tuberculosis control by macrophages. Sci Rep 6:29332. https://doi.org/10.1038/srep29332.

11. Teichgräber V, Ulrich M, Endlich N, Riethmüller J, Wilker B, De Oliveira-Munding CC, van Heeckeren AM, Barr ML, von Kürthy G, Schmid KW, Weller M, Tümmler B, Lang F, Grassme H, Döring G, Gulbins E. 2008. Ceramide accumulation mediates inflammation, cell death and infection susceptibility in cystic fibrosis. Nat Med 14:382–391. https://doi.org/10.1038/nm1748.

12. Zhang Y, Li X, Carpinteiro A, Gulbins E. 2008. Acid sphingomyelinase amplifies redox signaling in Pseudomonas aeruginosa-induced macrophage apoptosis. J Immunol 181:4247–4254. https://doi.org/10.4049/jimmunol.181.6.4247.

13. Zhang Y, Li X, Grassme H, Doring G, Gulbins E. 2010. Alterations in ceramide concentration and pH determine the release of reactive oxygen species by Cftr-deficient macrophages on infection. J Immunol 184:5104–5111. https://doi.org/10.4049/jimmunol.0902851.

14. Yu H, Zeidan YH, Wu BX, Jenkins RW, Flotte TR, Hannun YA, Virella-Lowell I. 2009. Defective acid sphingomyelinase pathway with Pseudomonas aeruginosa infection in cystic fibrosis. Am J Respir Cell Mol Biol 41:367–375. https://doi.org/10.1165/rcmb.2008-0295OC.

15. Nakatsuji T, Tang DC, Zhang L, Gallo RL, Huang CM. 2011. Propionibacterium acnes CAMP factor and host acid sphingomyelinase contribute to bacterial virulence: potential targets for inflammatory acne treatment. PLoS One 6:e14797. https://doi.org/10.1371/journal.pone.0014797.

16. Hauck CR, Grassme H, Bock J, Jendrossek V, Ferlinz K, Meyer TF, Gulbins E. 2000. Acid sphingomyelinase is involved in CEACAM receptor-mediated phagocytosis of Neisseria gonorrhoeae. FEBS Lett 478:260–266. https://doi.org/10.1016/S0014-5793(00)01851-2.

17. Schramm M, Herz J, Haas A, Kronke M, Utermohlen O. 2008. Acid sphingomyelinase is required for efficient phago-lysosomal fusion. Cell Microbiol 10:1839–1853. https://doi.org/10.1111/j.1462-5822.2008.01169.x.

18. Peng H, Li C, Kadow S, Henry BD, Steinmann J, Becker KA, Riehle A, Beckmann N, Wilker B, Li PL, Pritts T, Edwards MJ, Zhang Y, Gulbins E, Grassme H. 2015. Acid sphingomyelinase inhibition protects mice from lung edema and lethal Staphylococcus aureus sepsis. J Mol Med (Berl) 93:675–689. https://doi.org/10.1007/s00109-014-1246-y.

19. Kornhuber J, Rhein C, Muller CP, Muhle C. 2015. Secretory sphingomyelinase in health and disease. Biol Chem 396:707–736. https://doi.org/10.1515/hsz-2015-0109.

20. Zeidan YH, Hannun YA. 2007. Activation of acid sphingomyelinase by protein kinase Cdelta-mediated phosphorylation. J Biol Chem 282:11549–11561. https://doi.org/10.1074/jbc.M609424200.

21. Zeidan YH, Wu BX, Jenkins RW, Obeid LM, Hannun YA. 2008. A novel role for protein kinase Cdelta-mediated phosphorylation of acid sphingomyelinase in UV light-induced mitochondrial injury. FASEB J 22:183–193. https://doi.org/10.1096/fj.07-8967com.

22. Li X, Gulbins E, Zhang Y. 2012. Oxidative stress triggers Ca-dependent lysosome trafficking and activation of acid sphingomyelinase. Cell Physiol Biochem 30:815–826. https://doi.org/10.1159/000341460.

23. Andrews NW, Almeida PE, Corrotte M. 2014. Damage control: cellular mechanisms of plasma membrane repair. Trends Cell Biol 24:734–742. https://doi.org/10.1016/j.tcb.2014.07.008.

24. Caugant DA, Maiden MCJ. 2009. Meningococcal carriage and disease—population biology and evolution. Vaccine 27(Suppl 2):B64–B70. https://doi.org/10.1016/j.vaccine.2009.04.061.

25. Cartwright KA, Stuart JM, Jones DM, Noah ND. 1987. The Stonehouse survey: nasopharyngeal carriage of meningococci and Neisseria lactamica. Epidemiol Infect 99:591–601. https://doi.org/10.1017/s0950268800066449.

26. Virji M, Saunders JR, Sims G, Makepeace K, Maskell D, Ferguson DJ. 1993. Pilus-facilitated adherence of Neisseria meningitidis to human epithelial and endothelial cells: modulation of adherence phenotype occurs concurrently with changes in primary amino acid sequence and the glycosylation status of pilin. Mol Microbiol 10:1013–1028. https://doi.org/10.1111/j.1365-2958.1993.tb00972.x.

27. Nassif X, Beretti JL, Lowy J, Stenberg P, O'Gaora P, Pfeifer J, Normark S, So M. 1994. Roles of pilin and PilC in adhesion of Neisseria meningitidis to human epithelial and endothelial cells. Proc Natl Acad Sci U S A 91:3769–3773. https://doi.org/10.1073/pnas.91.9.3769.

28. Helaine S, Carbonnelle E, Prouvensier L, Beretti JL, Nassif X, Pelicic V. 2005. PilX, a pilus-associated protein essential for bacterial aggregation, is a key to pilus-facilitated attachment of Neisseria meningitidis to human cells. Mol Microbiol 55:65–77. https://doi.org/10.1111/j.1365-2958.2004.04372.x.

29. Carbonnelle E, Helaine S, Nassif X, Pelicic V. 2006. A systematic genetic analysis in Neisseria meningitidis defines the Pil proteins required for assembly, functionality, stabilization and export of type IV pili. Mol Microbiol 61:1510–1522. https://doi.org/10.1111/j.1365-2958.2006.05341.x.

30. Cehovin A, Simpson PJ, McDowell MA, Brown DR, Noschese R, Pallett M, Brady J, Baldwin GS, Lea SM, Matthews SJ, Pelicic V. 2013. Specific DNA recognition mediated by a type IV pilin. Proc Natl Acad Sci U S A 110:3065–3070. https://doi.org/10.1073/pnas.1218832110.

31. Tonjum T, Freitag NE, Namork E, Koomey M. 1995. Identification and characterization of pilG, a highly conserved pilus-assembly gene in pathogenic Neisseria. Mol Microbiol 16:451–464. https://doi.org/10.1111/j.1365-2958.1995.tb02410.x.

32. Merz AJ, So M, Sheetz MP. 2000. Pilus retraction powers bacterial twitching motility. Nature 407:98–102. https://doi.org/10.1038/35024105.

33. Fussenegger M, Rudel T, Barten R, Ryll R, Meyer TF. 1997. Transformation competence and type-4 pilus biogenesis in Neisseria gonorrhoeae—a review. Gene 192:125–134. https://doi.org/10.1016/S0378-1119(97)00038-3.

34. Hoffmann I, Eugene E, Nassif X, Couraud PO, Bourdoulous S. 2001.

Activation of ErbB2 receptor tyrosine kinase supports invasion of endothelial cells by Neisseria meningitidis. J Cell Biol 155:133–143. https://doi.org/10.1083/jcb.200106148.

35. Kallstrom H, Islam MS, Berggren PO, Jonsson AB. 1998. Cell signaling by the type IV pili of pathogenic Neisseria. J Biol Chem 273:21777–21782. https://doi.org/10.1074/jbc.273.34.21777.

36. Ayala BP, Vasquez B, Clary S, Tainer JA, Rodland K, So M. 2001. The pilus-induced Ca²⁺ flux triggers lysosome exocytosis and increases the amount of Lamp1 accessible to Neisseria IgA1 protease. Cell Microbiol 3:265–275. https://doi.org/10.1046/j.1462-5822.2001.00112.x.

37. Nassif X, Lowy J, Stenberg P, O'Gaora P, Ganji A, So M. 1993. Antigenic variation of pilin regulates adhesion of Neisseria meningitidis to human epithelial cells. Mol Microbiol 8:719–725. https://doi.org/10.1111/j.1365-2958.1993.tb01615.x.

38. Asmat TM, Tenenbaum T, Jonsson AB, Schwerk C, Schroten H. 2014. Impact of calcium signaling during infection of Neisseria meningitidis to human brain microvascular endothelial cells. PLoS One 9:e114474. https://doi.org/10.1371/journal.pone.0114474.

39. Morand PC, Drab M, Rajalingam K, Nassif X, Meyer TF. 2009. Neisseria meningitidis differentially controls host cell motility through PilC1 and PilC2 components of type IV pili. PLoS One 4:e6834. https://doi.org/10.1371/journal.pone.0006834.

40. Heilemann M, van de Linde S, Schuttpelz M, Kasper R, Seefeldt B, Mukherjee A, Tinnefeld P, Sauer M. 2008. Subdiffraction-resolution fluorescence imaging with conventional fluorescent probes. Angew Chem Int Ed 47:6172–6176. https://doi.org/10.1002/anie.200802376.

41. Burgert A, Schlegel J, Becam J, Doose S, Bieberich E, Schubert-Unkmeir A, Sauer M. 2017. Characterization of plasma membrane ceramides by super-resolution microscopy. Angew Chem Int Ed 56:6131–6135. https://doi.org/10.1002/anie.201700570.

42. Bernard SC, Simpson N, Join-Lambert O, Federici C, Laran-Chich MP, Maissa N, Bouzinba-Segard H, Morand PC, Chretien F, Taouji S, Chevet E, Janel S, Lafont F, Coureuil M, Segura A, Niedergang F, Marullo S, Couraud PO, Nassif X, Bourdoulous S. 2014. Pathogenic Neisseria meningitidis utilizes CD147 for vascular colonization. Nat Med 20:725–731. https://doi.org/10.1038/nm.3563.

43. Grassme H, Henry B, Ziobro R, Becker KA, Riethmuller J, Gardner A, Seitz AP, Steinmann J, Lang S, Ward C, Schuchman EH, Caldwell CC, Kamler M, Edwards MJ, Brodlie M, Gulbins E. 2017. β1-Integrin accumulates in cystic fibrosis luminal airway epithelial membranes and decreases sphingosine, promoting bacterial infections. Cell Host Microbe 21:707–718.e8. https://doi.org/10.1016/j.chom.2017.05.001.

44. Ayala P, Wilbur JS, Wetzler LM, Tainer JA, Snyder A, So M. 2005. The pilus and porin of Neisseria gonorrhoeae cooperatively induce Ca(2+) transients in infected epithelial cells. Cell Microbiol 7:1736–1748. https://doi.org/10.1111/j.1462-5822.2005.00586.x.

45. Ayala P, Vasquez B, Wetzler L, So M. 2002. Neisseria gonorrhoeae porin P1.B induces endosome exocytosis and a redistribution of Lamp1 to the plasma membrane. Infect Immun 70:5965–5971. https://doi.org/10.1128/IAI.70.11.5965-5971.2002.

46. Muller A, Gunther D, Dux F, Naumann M, Meyer TF, Rudel T. 1999. Neisserial porin (PorB) causes rapid calcium influx in target cells and induces apoptosis by the activation of cysteine proteases. EMBO J 18:339–352. https://doi.org/10.1093/emboj/18.2.339.

47. Reference deleted.

48. Reference deleted.

49. Berridge MJ, Lipp P, Bootman MD. 2000. The versatility and universality of calcium signalling. Nat Rev Mol Cell Biol 1:11–21. https://doi.org/10.1038/35036035.

50. Carafoli E, Santella L, Branca D, Brini M. 2001. Generation, control, and processing of cellular calcium signals. Crit Rev Biochem Mol Biol 36:107–260. https://doi.org/10.1080/20014091074183.

51. Lin L, Ayala P, Larson J, Mulks M, Fukuda M, Carlsson SR, Enns C, So M. 1997. The Neisseria type 2 IgA1 protease cleaves LAMP1 and promotes survival of bacteria within epithelial cells. Mol Microbiol 24:1083–1094. https://doi.org/10.1046/j.1365-2958.1997.4191776.x.

52. Jaiswal JK, Andrews NW, Simon SM. 2002. Membrane proximal lysosomes are the major vesicles responsible for calcium-dependent exocytosis in nonsecretory cells. J Cell Biol 159:625–635. https://doi.org/10.1083/jcb.200208154.

53. Reddy A, Caler EV, Andrews NW. 2001. Plasma membrane repair is mediated by Ca(2+)-regulated exocytosis of lysosomes. Cell 106:157–169. https://doi.org/10.1016/S0092-8674(01)00421-4.

54. Rodriguez A, Webster P, Ortego J, Andrews NW. 1997. Lysosomes behave as Ca²⁺-regulated exocytic vesicles in fibroblasts and epithelial cells. J Cell Biol 137:93–104. https://doi.org/10.1083/jcb.137.1.93.

55. Fernandes MC, Cortez M, Flannery AR, Tam C, Mortara RA, Andrews NW. 2011. Trypanosoma cruzi subverts the sphingomyelinase-mediated plasma membrane repair pathway for cell invasion. J Exp Med 208:909–921. https://doi.org/10.1084/jem.20102518.

56. Luisoni S, Suomalainen M, Boucke K, Tanner LB, Wenk MR, Guan XL, Grzybek M, Coskun U, Greber UF. 2015. Co-option of membrane wounding enables virus penetration into cells. Cell Host Microbe 18:75–85. https://doi.org/10.1016/j.chom.2015.06.006.

57. Charruyer A, Grazide S, Bezombes C, Muller S, Laurent G, Jaffrezou JP. 2005. UV-C light induces raft-associated acid sphingomyelinase and JNK activation and translocation independently on a nuclear signal. J Biol Chem 280:19196–19204. https://doi.org/10.1074/jbc.M412867200.

58. Dumitru CA, Carpinteiro A, Trarbach T, Hengge UR, Gulbins E. 2007. Doxorubicin enhances TRAIL-induced cell death via ceramide-enriched membrane platforms. Apoptosis 12:1533–1541. https://doi.org/10.1007/s10495-007-0081-9.

59. Grassme H, Jekle A, Riehle A, Schwarz H, Berger J, Sandhoff K, Kolesnick R, Gulbins E. 2001. CD95 signaling via ceramide-rich membrane rafts. J Biol Chem 276:20589–20596. https://doi.org/10.1074/jbc.M101207200.

60. Grassme H, Riehle A, Wilker B, Gulbins E. 2005. Rhinoviruses infect human epithelial cells via ceramide-enriched membrane platforms. J Biol Chem 280:26256–26262. https://doi.org/10.1074/jbc.M500835200.

61. Avota E, Gulbins E, Schneider-Schaulies S. 2011. DC-SIGN mediated sphingomyelinase-activation and ceramide generation is essential for enhancement of viral uptake in dendritic cells. PLoS Pathog 7:e1001290. https://doi.org/10.1371/journal.ppat.1001290.

62. Stins MF, Gilles F, Kim KS. 1997. Selective expression of adhesion molecules on human brain microvascular endothelial cells. J Neuroimmunol 76:81–90. https://doi.org/10.1016/S0165-5728(97)00036-2.

63. Unkmeir A, Latsch K, Dietrich G, Wintermeyer E, Schinke B, Schwender S, Kim KS, Eigenthaler M, Frosch M. 2002. Fibronectin mediates Opc-dependent internalization of Neisseria meningitidis in human brain microvascular endothelial cells. Mol Microbiol 46:933–946. https://doi.org/10.1046/j.1365-2958.2002.03222.x.

64. Lappann M, Haagensen JA, Claus H, Vogel U, Molin S. 2006. Meningococcal biofilm formation: structure, development and phenotypes in a standardized continuous flow system. Mol Microbiol 62:1292–1309. https://doi.org/10.1111/j.1365-2958.2006.05448.x.

65. Reference deleted.

66. Virji M, Heckels JE. 1983. Antigenic cross-reactivity of Neisseria pili: investigations with type- and species-specific monoclonal antibodies. J Gen Microbiol 129:2761–2768. https://doi.org/10.1099/00221287-129-9-2761.

3.7   Super-Resolution Microscopy Reveals Local Accumulation of Plasma Membrane Gangliosides at Neisseria meningitidis Invasion Sites

Abstract

"*Neisseria meningitidis* (meningococcus) is a Gram-negative bacterium responsible for epidemic meningitis and sepsis worldwide. A critical step in the development of meningitis is the interaction of bacteria with cells forming the blood-cerebrospinal fluid barrier, which requires tight adhesion of the pathogen to highly specialized brain endothelial cells. Two endothelial receptors, CD147 and the β2-adrenergic receptor, have been found to be sequentially recruited by meningococci involving the interaction with type IV pilus. Despite the identification of cellular key players in bacterial adhesion the detailed mechanism of invasion is still poorly understood. Here, we investigated cellular dynamics and mobility of the type IV pilus receptor CD147 upon treatment with pili enriched fractions and specific antibodies directed against two extracellular Ig-like domains in living human brain microvascular endothelial cells. Modulation of CD147 mobility after ligand binding revealed by single-molecule tracking experiments demonstrates receptor activation and indicates plasma membrane rearrangements. Exploiting the binding of Shiga (STxB) and Cholera toxin B (CTxB) subunits to the two native plasma membrane sphingolipids globotriaosylceramide (Gb3) and raft-associated monosialotetrahexosylganglioside GM1, respectively, we investigated their involvement in bacterial invasion by super-resolution microscopy. Structured illumination microscopy (SIM) and *direct* stochastic optical reconstruction microscopy (*d*STORM) unraveled accumulation and coating of meningococci with GM1 upon cellular uptake. Blocking of CTxB binding sites did not impair bacterial adhesion but dramatically reduced bacterial invasion efficiency. In addition, cell cycle arrest in G1 phase induced by serum starvation led to an overall increase of GM1 molecules in the plasma membrane and consequently also in bacterial invasion efficiency. Our results will help to understand downstream signaling events after initial type IV pilus-host cell interactions and thus have general impact on the development of new therapeutics targeting key molecules involved in infection." [115]

frontiers
in Cell and Developmental Biology

Super-Resolution Microscopy Reveals Local Accumulation of Plasma Membrane Gangliosides at *Neisseria meningitidis* Invasion Sites

Jan Schlegel[1], Simon Peters[2], Sören Doose[1], Alexandra Schubert-Unkmeir[2] and Markus Sauer[1]*

[1] *Department of Biotechnology and Biophysics, Biocenter, Julius Maximilian University Würzburg, Würzburg, Germany,*
[2] *Institute of Hygiene and Microbiology, Julius Maximilian University Würzburg, Würzburg, Germany*

Neisseria meningitidis (meningococcus) is a Gram-negative bacterium responsible for epidemic meningitis and sepsis worldwide. A critical step in the development of meningitis is the interaction of bacteria with cells forming the blood-cerebrospinal fluid barrier, which requires tight adhesion of the pathogen to highly specialized brain endothelial cells. Two endothelial receptors, CD147 and the β2-adrenergic receptor, have been found to be sequentially recruited by meningococci involving the interaction with type IV pilus. Despite the identification of cellular key players in bacterial adhesion the detailed mechanism of invasion is still poorly understood. Here, we investigated cellular dynamics and mobility of the type IV pilus receptor CD147 upon treatment with pili enriched fractions and specific antibodies directed against two extracellular Ig-like domains in living human brain microvascular endothelial cells. Modulation of CD147 mobility after ligand binding revealed by single-molecule tracking experiments demonstrates receptor activation and indicates plasma membrane rearrangements. Exploiting the binding of Shiga (STxB) and Cholera toxin B (CTxB) subunits to the two native plasma membrane sphingolipids globotriaosylceramide (Gb3) and raft-associated monosialotetrahexosylganglioside GM1, respectively, we investigated their involvement in bacterial invasion by super-resolution microscopy. Structured illumination microscopy (SIM) and *direct* stochastic optical reconstruction microscopy (*d*STORM) unraveled accumulation and coating of meningococci with GM1 upon cellular uptake. Blocking of CTxB binding sites did not impair bacterial adhesion but dramatically reduced bacterial invasion efficiency. In addition, cell cycle arrest in G1 phase induced by serum starvation led to an overall increase of GM1 molecules in the plasma membrane and consequently also in bacterial invasion efficiency. Our results will help to understand downstream signaling events after initial type IV pilus-host cell interactions and thus have general impact on the development of new therapeutics targeting key molecules involved in infection.

Keywords: *Neisseria meningitidis*, sphingolipids, gangliosides and lipid rafts, super-resolution microscopy, single-molecule tracking

98

INTRODUCTION

The obligate human pathogenic Gram-negative bacterium *Neisseria meningitidis* can cause epidemic meningitis and in severe cases sepsis and progressing fatal shock (Stephens et al., 2007). In healthy individuals the meningococci may reside as commensal organisms in the nasopharynx without affecting the host (Yazdankhah and Caugant, 2004). Under certain circumstances, the bacteria can enter the bloodstream and adhere to endothelial cells of blood microvessels, also known as vascular colonization (Melican and Dumenil, 2012) leading to inflammatory processes and disruption of the blood-cerebrospinal fluid barrier, a crucial step in disease progression into meningitis (reviewed in Lemichez et al., 2010). The initial process of bacterial adhesion to brain endothelial cells is mediated by type IV pili and its adhesion receptor CD147 on the host cell (Bernard et al., 2014).

Recently, super-resolution microscopy by *direct* stochastic optical reconstruction microscopy (*d*STORM) (Heilemann et al., 2008) demonstrated that *N. meningitidis* binding to endothelial cells requires CD147/β2-adrenergic receptor clustering at bacterial adhesion sites (Maïssa et al., 2017). Here, the assembly of plasma membrane receptors might serve as platform to support host-pathogen interactions. However, the molecular process of subsequent barrier-crossing is still under debate. Besides the investigated loosening of endothelial tight junctions (Coureuil et al., 2009; Schubert-Unkmeir et al., 2010) there is evidence that meningococci may use transcytotic pathways to enter perivascular tissues (Nikulin et al., 2006; Sutherland et al., 2010). Since signaling and interactions of CD147 is dependent on plasma membrane cholesterol (Wu et al., 2017) and ganglioside-enriched lipid rafts (Li et al., 2013) downstream rearrangement of the plasma membrane might facilitate bacterial invasion of cells.

Indeed, recent data suggests meningococcal type IV pili dependent binding to gangliosides (Mubaiwa et al., 2017), which has already been known for several pathogens colonizing the respiratory tract (Krivan et al., 1988). Glycosphingolipids in general are important host cell targets for a plenitude of pathogens such as fungi, bacteria, and viruses (Nakayama et al., 2018). They are composed of complex, highly variable glycan moieties linked to a lipophilic ceramide backbone with extensive molecular heterogeneity (Lingwood, 2011). Two well studied glycosphingolipids with receptor functions are the monosialotetrahexosylganglioside GM1, a prototype ganglioside, and the globotriaosylceramide Gb3, which both interact with protein receptors within lipid rafts to generate signaling platforms (Mutoh et al., 1995; Ichikawa et al., 2009; Lingwood et al., 2010; Prasanna et al., 2016).

Besides its importance in neuronal plasticity, GM1 can be targeted by Simian virus 40 (Tsai et al., 2003), *Brucella suis* (Naroeni and Porte, 2002), Cholera toxin B subunit (Cuatrecasas, 1973), *Escherichia coli* enterotoxin (Hyun and Kimmich, 1984), and *Vibrio cholerae* enterotoxin (Otnaess et al., 1983). Gb3, also known as CD77, is a marker for B cells entering apoptosis, but is also exploited by the Human Immunodeficiency Virus (HIV), or Shiga Toxin from *Shigella dysenteriae* (Lindberg et al., 1987;

Mangeney et al., 1991; Hammache et al., 1999). Interestingly, the two glycosphingolipids are differentially expressed depending on the cell-cycle with an upregulation of GM1 in G0/G1 phase and increased expression of Gb3 in G2/M phase (Majoul et al., 2002).

Here, we first set out to investigate the mobility of CD147 upon *N. meningitidis* infection by single-molecule tracking experiments. Next, we investigated the role of the two sphingolipids GM1 and Gb3 during infection with *N. meningitidis* using fluorescently labeled CTxB and STxB subunits, respectively. Super-resolution microscopy by structured illumination microscopy (SIM) (Gustafsson, 2000) and *direct* stochastic optical reconstruction microscopy (*d*STORM) (Heilemann et al., 2008; van de Linde et al., 2011) shows GM1 accumulation around meningococci highlighting their significant importance for bacterial invasion.

MATERIALS AND METHODS

Bacterial Strains

Neisseria meningitidis strain MC58 was used in this study as a representative strain. Strain MC58 is a serogroup (Sg) B strain of the sequence type (ST)-74 (ST-32 clonal complex [cc]), which was isolated in 1983 in the United Kingdom and was kindly provided by E. R. Moxon (McGuinness et al., 1991). *N. meningitidis* strain 8013 (clone 12, also designated 2C43) was used for the preparation of the pili enriched fraction (PeF). This strain is a piliated capsulated Opa-, Opc- variant of the serogroup C meningococcal clinical isolate 8013 (ST-77/ST-8 clonal complex (cc), Institut Pasteur, 1989) and was kindly provided by M. Taha (Nassif et al., 1993). *N. meningitidis* strains were grown overnight on Columbia blood agar plates (bioMérieux) at 37°C and 5% CO_2 in a humidity incubator and cultured on the next day in PPM + medium (proteose-peptone medium supplemented with $1\times$ Kellogg's supplement, 0.01 M $MgCl_2$ and 0.005 M $NaHCO_3$).

Cell Culture

Immortalized human brain microvascular endothelial cells (HBMEC) were kindly provided by K. S. Kim (Stins et al., 1997) and were cultured as described previously (Unkmeir et al., 2002). Briefly, cells were cultured in RPMI-1640 medium supplemented with 1% sodium pyruvate (1 mM), 1% L-glutamine (2 mM), 1% non-essential amino acids (all purchased from GE Healthcare, Little Chalfont, United Kingdom), 5 U/ml heparin (Biochrom, Berlin, Germany) and 30 µg/ml endothelial cell growth supplement (ECGS, CellSystems, Troisdorf, Germany). Cells were incubated at 37°C and 5% CO_2 in a humidified atmosphere.

Infection Assays

Adhesion and invasion was determined by using the gentamicin protection assays as described elsewhere (Simonis et al., 2014). Briefly, cells between the 10th and 25th passages were used for infection assays at a density of 4×10^5 cells/well. Cell medium was changed to infection medium [RPMI + 10% human serum (HS)] and cells were infected with MC58 at a multiplicity of infection (MOI) of 100 for 4 h. If indicated, cells were pre-incubated with 6.6 µg/ml CTxB in RPMI for 30 min prior to the

99

medium change. To determine the number of adherent bacteria, cells were washed three times with phosphate buffered saline (PBS), to remove unbound bacteria, and afterward incubated with 1% saponin in RPMI to lyse the cells. Then, the cell-lysates were collected, diluted and plated on blood agar plates. To determine invasive bacteria, cells were handled similar to the adherent set with the exception of an additional incubation of the cells with gentamicin (200 μg/ml) for 2 h prior to the saponin treatment to kill all extracellular bacteria.

Immunofluorescence and Fluorescence Microscopy

HBMEC were seeded onto 0.2% gelatine coated 8-well chamber slides (Sarstedt) at a density of 2×10^4 cells/well and incubated for at least 24 h. To avoid possible interference of labeled CD147 receptors with the coating during single-molecule tracking, HBMEC were seeded onto KOH cleaned 8-well glass instead. Following infection with the indicated bacterial strain, cells were fixed with 2% formaldehyde and 0.2% glutaraldehyde for 15 min and washed. Labeling was performed with CTxB and/or STxB (Sigma-Aldrich, custom conjugated to Alexa Fluor 647 or Alexa Fluor 555) at a concentration of 5 μg/ml for 1 h. Alternatively, cells were incubated over night with Alexa Fluor 488 phalloidin as recommended by standard protocols (Thermo Fisher Scientific). To immobilize the toxin subunits, cells were again fixed by 2% formaldehyde and washed with PBS before *d*STORM imaging. Samples were embedded in prolong glass antifade mountant for SIM (Zeiss Elyra S.1) or covered with switching buffer (100 mM Cysteamine in PBS, pH 7.7) for *d*STORM. Imaging conditions and microscope setups were used as previously described (Burgert et al., 2017). Reconstruction from the raw data was performed with ThunderSTORM (Ovesný et al., 2014) or Zeiss ZEN software for *d*STORM and SIM, respectively. Spatial analysis of localization data was done with custom-made Python software. Ripley's h function was computed and analyzed as described in Burgert et al. (2017). Ripley's h function (Kiskowski et al., 2009) was computed for experimental and simulated data. Synthetic data with a localization density and region equal to the experimental data was prepared from a homogeneous point process of complete spatial randomness and from a clustered Neyman-Scott point process in which parent localizations are homogeneously distributed and accompanied by normal-distributed child localizations. The number of child localizations is Poisson distributed with a mean equal to the number of localizations per cluster as found for the experimental data sets. The standard deviation of the normal distribution is set to 8 nm resembling the localization precision. Ripley's h function was computed 100 times from 200 random data points in order to estimate the variance.

Single-Molecule Tracking

To perform single-molecule tracking, the non-competitive monoclonal CD147 antibody (clone: MEM-M6/1, Biorad) was directly coupled to the amine-reactive dye SeTau-647-NHS (SETA Biomedicals) to obtain a degree of labeling of

1.7. After purification by size-exclusion (Zeba spin desalting columns 40K MWCO Thermo Fisher Scientific) HBMEC were labeled with 0.17 nM antibody solution for 5 min at 37°C and washed twice before imaging in FluoroBrite DMEM media (Thermo Fisher Scientific). If stated, HBMEC were incubated for 30 min with 10 μg/ml MEM-M6/6 CD147 antibody or 2 μg PeF/well before labeling with MEM-M6/1 antibody. Imaging was performed at the setup described in the microscopy methods section with exposure time 20 ms for a total acquisition time of 100 s. Spot detection was performed by fitting with ThunderSTORM (Ovesný et al., 2014) and tracks generated and filtered for minimal track length of 20 frames with the Python implementation of the Crocker-Grier (Crocker and Grier, 1996) algorithm Trackpy (Allan et al., 2016). Mean squared displacements of each measurement were calculated and the resulting ensemble MSD was fit with a power law (Manzo and Garcia-Parajo, 2015; Shen et al., 2017), $MSD(\tau) = \alpha t^n$, yielding the distribution of the generalized diffusion constant [α] and anomalous exponent [n].

G1 Synchronization of HBMEC

G1 synchronization was performed using the method of serum starvation. 24 h prior to the experiment, HBMEC growth medium was removed and cells were washed once with PBS. Afterward, RPMI was added and the cells were further incubated as mentioned bevor. The cell population shift was controlled by propodium iodid (PI) staining. For that, cells were washed once with PBS and harvested in Eppendorf tubes. Afterward cells were washed three times with PBS, fixed in 3.7% formaldehyde for 30 min on ice and permeabilized with 0.25% Triton X-100 in PBS on ice. Cells were then stained with 10 μg/ml PI + 25 μg/ml RNase and incubated for 30 min at room temperature in the dark and immediately analyzed afterward. 10,000 cells were analyzed using the FACSCalibur™ flow cytometer (BD Bioscience) and data were analyzed and graphed using FlowJo v10 (FlowJo, LLC). The gating strategy for G1, S, and G2 phase is shown in **Supplementary Figure S5B**.

Flow Cytometry

Three days prior to the experiment, 1.25×10^5 cells/ml were seeded in a 24-well plate and grown to approximately 1×10^6 cells/ml. On the day of the infection experiment, cell medium was replaced by RPMI + 10% HS. Cells were infected with bacteria for 4 h. After infection, cells were washed once with PBS, trypsinized and harvested in an Eppendorf tube. After washing with ice cold FACS buffer (5% FCS in PBS), cells were incubated with Alexa Fluor 647 labeled CTxB for 30 min at room temperature in the dark. After incubation, cells were washed three times with FACS buffer and fixed in 3.7% paraformaldehyde in PBS for 30 min at 4°C. Afterward, cells were washed three times with FACS buffer and 500 μl were transferred into a FACS-tube for the measurement. 10,000 cells were analyzed using the FACSCalibur™ flow cytometer (BD Bioscience) and data were analyzed and graphed using FlowJo v10 (FlowJo, LLC).

Preparation of Pilus Enriched Fractions (PeF)

Pilus enriched fractions (PeF) were prepared as described previously (Peters et al., 2019). The bacterial content of 50 blood agar plates was harvested in 40 ml of 0.15 M ethanolamine (in PBS) with a pH of 10.5. Pili were sheared of by intensive vortexing for 2 min followed by centrifugation at 12.000 × *g* for 10 min at room temperature to remove cellular debris. The supernatant was used for an additional centrifugation step at 21.000 × *g* for 90 min to remove smaller debris. Then, the supernatant was transferred to an Erlenmeyer flask and ammonium sulfate saturated 0.15 M ethanolamine was added to a concentration of 10% and was incubated under continuous shacking for 30 min at room temperature. The protein-ammonium sulfate precipitate was then harvested by centrifugation at 21.000 × *g* for 15 min. The supernatant was discarded and the pellet was re-suspended in 0.05 M Tris buffer saline (TBS) pH 7.5. Protein solutions were then applied to a 6 ml Viva Spin column with a 7 kDa molecular weight cut of (MWCO) and were centrifuged at 4000 × *g* at room temperature until the volume reaches 1 ml. To clean the sample, TBS was added again to 6 ml followed by centrifugation as mentioned above.

Statistical Analysis and Data Visualization

Statistical analysis was performed by either unpaired two-tailed Student's *t*-test or analysis of variance (ANOVA) test followed by a *post hoc* test. Significance values are indicated by asterisks: $*P < 0.05$; $**P < 0.01$; $***P < 0.001$; $****P < 0.0001$. Normality was tested using the Kolmogorov–Smirnov test. Data was visualized as box plots showing the interquartile range (IQR) of the data with median as line and mean as square. The whiskers represent the lowest and highest value within 1.5 IQR of the lower and upper quartile, respectively. Outliers are shown as filled squares outside the IQR box.

RESULTS

Single-Molecule Tracking Reveals Modulation of CD147 Receptor Mobility Upon Interaction

It has been shown that CD147 and β2-adrenergic receptor (ß2AR) are organized in pre-existing complexes at the plasma membrane of endothelial cells, which accumulate at sites of meningococcal adhesion (Maïssa et al., 2017). This local enrichment of CD147-ß2AR complexes in the plasma membrane possibly allows bacteria to adhere to vascular walls *in vivo* and resist hemodynamic forces of blood flow. Since accumulation of receptors at bacterial adhesion sites requires a high mobility in the plasma membrane we performed live-cell single-molecule tracking experiments of CD147 under various experimental conditions using an N-terminal binding monoclonal antibody (MEM-6/1) directly conjugated to the photostable fluorescent dye SeTau-647 (Tsunoyama et al., 2018). In contrast to the membrane-proximal binding monoclonal antibody MEM-6/6

(**Figure 1A**) MEM-6/1 does not compete with the binding site of type IV pili as demonstrated by single-molecule tracking experiments of human brain microvascular endothelial cells (HBMEC) pretreated with saturating concentrations of pilus enriched fraction (PeF) (**Figure 1A** and **Supplementary Figure S1**; Bernard et al., 2014). Pretreatment with saturating PeF concentration did significantly reduce the number of accessible MEM-M6/1 epitopes during individual single-molecule tracking experiments (**Supplementary Figure S1**).

Using SeTau-647 labeled MEM-6/1 antibodies we followed CD147 on the basal plasma membrane of human brain microvascular endothelial cells (HBMEC) for a duration of 100 s with a time resolution of 20 ms using total internal reflection fluorescence (TIRF) microscopy (**Figure 1B** and **Supplementary Video S1**). For quantification of diffusion dynamics, we analyzed the mean square displacement (MSD) and fitted it with a power law (Manzo and Garcia-Parajo, 2015; Shen et al., 2017):

$$\mathrm{MSD}(\tau) = \alpha \tau^n$$

Treatment of HBMEC with the competitive MEM 6/6 antibody reduced the generalized diffusion constant α (**Figure 1C**) as well as the number of localized CD147 molecules (**Supplementary Figure S1**) whereas the anomalous diffusion exponent *n* remained unaltered (**Figure 1D**). Addition of meningococcal PeF before (pre-treated) and after labeling (post-treated) increased α and *n* only slightly (**Figures 1C,D**) demonstrating that PeF does not significantly change the mobility of the neisserial type IV pili receptor CD147. Still, the slight changes in mobility observed may indicate cytoskeletal rearrangements of the plasma membrane sphingolipid organization. Indeed a recent study revealed an increase in ceramide-rich platforms upon treatment of HBMEC with type IV pili (Peters et al., 2019). Therefore, we investigated the distribution and localization of the native glycosphingolipids GM1 and Gb3 by super-resolution microscopy.

Rearrangement of Plasma Membrane Sphingolipids During Meningococcal Infection

To investigate possible changes in lipid organization upon meningococcal adhesion we visualized the distribution of the two sphingolipids GM1 and Gb3 in the plasma membrane of brain endothelial cells using the cholera toxin B (CTxB) and shiga toxin B (STxB) subunit, respectively. Two-color confocal laser scanning images of HBMEC show that GM1 and Gb3 exhibit cell-cycle dependent expression rates (**Figure 2A**), only in S phase both sphingolipids are expressed and simultaneously detectable in the plasma membrane (Majoul et al., 2002). Corresponding *d*STORM images show that GM1 and Gb3 are homogeneously distributed throughout the plasma membrane of HBMEC (**Figures 2B–D**) without clear indication of clustering (**Supplementary Figure S2**). Analysis of the spatial distribution of localization data by Ripley's h function indicates merely clusters on length scales similar to the *d*STORM localization precision (∼8 nm). These clusters originate from repeated detection of fluorophores on each toxin subunit. The number

101

FIGURE 1 | Single-molecule tracking of CD147 on HBMEC using monoclonal antibodies. **(A)** CD147 is a single pass membrane protein with two extracellular Ig-like domains. The N-terminal IgC2 domain is recognized by the MEM-M6/1 antibody which was conjugated to the photostable dye SeTau-647 (Tsunoyama et al., 2018) and used for single-molecule tracking. The membrane proximal IgI domain is the binding site for MEM-M6/6 and type IV pili of *N. meningitidis*. **(B)** Example of CD147 single-molecule tracks. SeTau-647 coupled MEM-M6/1 is depicted in cyan with corresponding local tracks in yellow. Overlay was created with the Fiji (Schindelin et al., 2012) plugin TrackMate (Tinevez et al., 2017). Scale bar, 1 μm. **(C)** The diffusion coefficient of CD147 is reduced upon pretreatment with 10 μg/ml MEM-M6/6 and hardly affected by PeF treatment. Values represent individual single-molecule tracking experiments. **(D)** The anomalous diffusion exponent is not affected by MEM-M6/6 treatment but increases slightly upon PeF treatment. Significance values are indicated by asterisks: $*P < 0.05$; $**P < 0.01$; $***P < 0.001$; $****P < 0.0001$.

of localizations per cluster (as quantified by the DBSCAN clustering algorithm) follows the degree of labeling of pentameric CTxB (0.9) and STxB (0.5). The same observations were made on toxin subunits unspecifically bound to the glass surface (**Supplementary Figure S3**).

Upon infection of cells with *N. meningitidis* the plasma membrane distribution of Gb3 remained unchanged (**Figures 3A,B**). In contrast GM1 showed a remarkable increase in fluorescence intensity around adhesive meningococci on the plasma membrane of HBMEC (**Figure 4A**). *d*STORM images of CTxB labeled HBMEC in the presence of

meningococci were recorded from an axial plane slightly above the equatorial plane under epi-illumination to ensure imaging of a large part of the cellular plasma membrane with adhesive bacteria (**Figure 4B**). Our data clearly demonstrate strong accumulation of the ganglioside GM1 around adhesive bacteria (**Figure 4B**) whereas uninfected HBMEC show a homogeneous distribution of GM1 in the plasma membrane (**Figure 2**). To exclude non-specific binding of CTxB and STxB to meningococci, bacteria were seeded onto glass without HBMEC, labeled and imaged by *d*STORM. The corresponding images show that the two

102
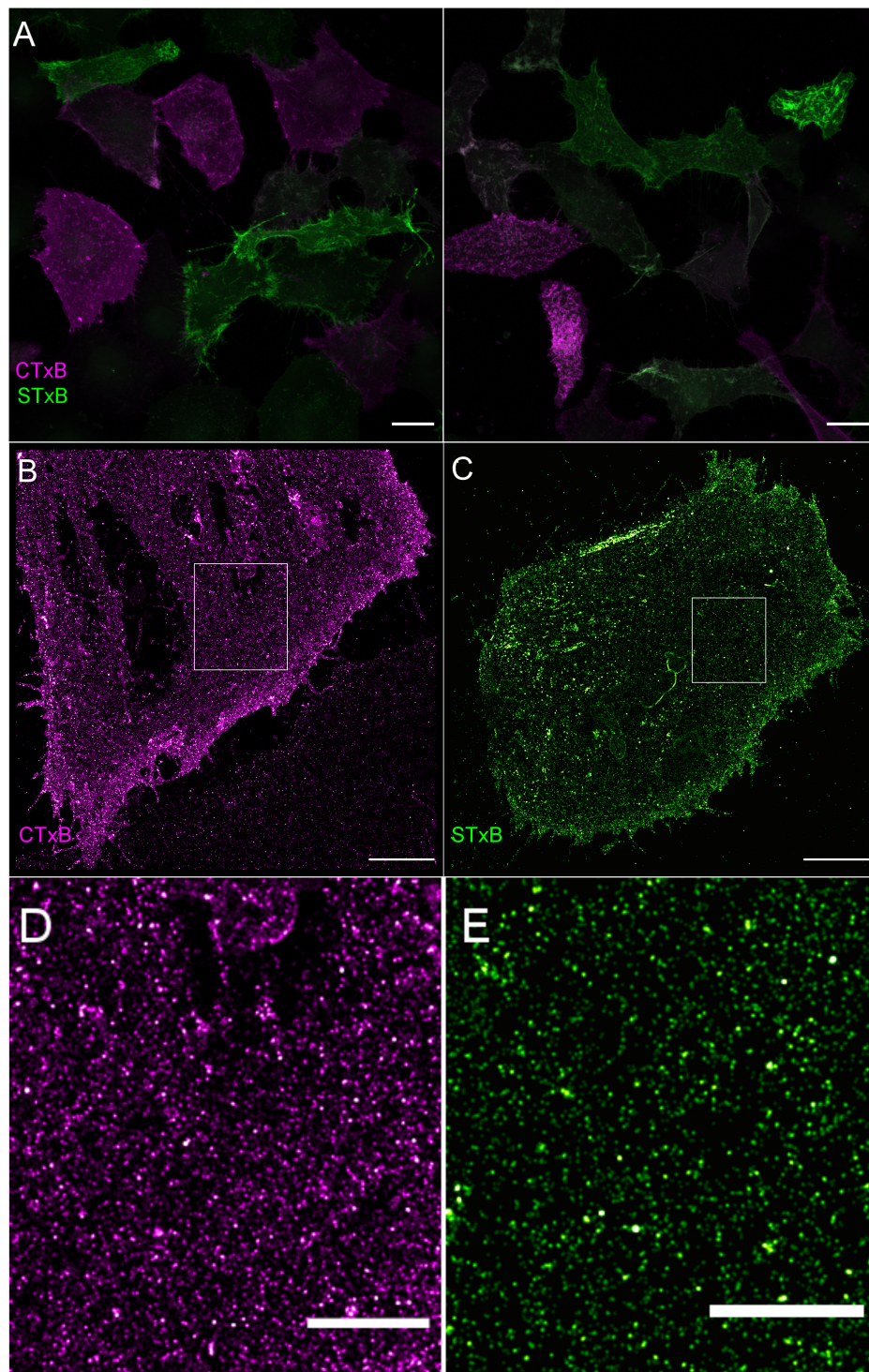
FIGURE 2 | Visualization of sphingolipids GM1 and Gb3 in the plasma membrane of brain endothelial cells. **(A)** Confocal laser scanning microscopy images of GM1 (magenta) and Gb3 (green) labeled with CTxB-Alexa Fluor 647 (magenta) and STxB-Alexa Fluor 555 (green), respectively. Scale bar, 20 μm. **(B)** 2D dSTORM images of GM1 labeled with CTxB-Alexa Fluor 647, and **(C)** Gb3 labeled with STxB-Alexa Fluor 647 showing a homogeneous distribution of the two sphingolipids in the plasma membrane of HBMEC. Scale bar, 5 μm. **(D)** Expanded views of the white boxed regions showing homogeneous distributions of CTxB **(D)** and STxB **(E)**. Both regions are representative areas which were used for cluster analysis by Ripley's h function **(Supplementary Figure S2)**. Scale bar 2 μm.

103

FIGURE 3 | Fluorescence microscopy of Gb3 in the plasma membrane of brain endothelial cells during *N. meningitidis* infection. **(A)** Confocal laser scanning microscopy of HBMEC labeled with STxB-Alexa Fluor 555 (magenta) and infected with GFP expressing *N. meningitidis* (green). No accumulation of Gb3 was observed at invasion sites. Scale bar, 5 μm. **(B)** Super-resolution *d*STORM image showing that the distribution of Gb3 in the plasma membrane of HBMEC does not change upon infection with meningococci (green). Gb3 was labeled with Alexa Fluor 647 conjugated STxB (red). The diffraction limited GFP signal was upscaled for the overlay. Same imaging and analysis parameters were used for the *d*STORM image as in **Figure 2**. Scale bar, 5 μm.

sphingolipids do not bind non-specifically to meningococci (**Supplementary Figure S3**).

Next, we tested if CD147 and actin as highly conserved key cytoskeletal protein involved in organization of the plasma membrane, colocalize with GM1 and accumulate around meningococci adhesion sites on the plasma membrane of HBMEC (Coureuil et al., 2010; Maïssa et al., 2017). However, SIM images show strong colocalization of the adhesion receptor CD147 and actin but no enrichment or morphological change at invasion sites of bacteria (**Supplementary Figure S4**).

Increased Bacterial Invasion Upon G1 Phase Arrest and GM1 Upregulation

Since the expression of GM1 and Gb3 is highest in G1 and G2 phase of the cell cycle, respectively (Majoul et al., 2002) we next investigated cell cycle dependent effects on the adhesion and invasion efficiency of *N. meningitidis*. Serum starvation 24 h before the experiment caused a significant increase of HBMEC

residing in G1 phase as demonstrated by PI staining of the DNA and flow cytometry analysis (**Supplementary Figures S5A,B**). Simultaneously the concentration of ganglioside GM1 present in the plasma membrane in G1 phase increased substantially (**Supplementary Figure S5C**).

Interestingly, infection of G1 phase arrested cells caused an even more pronounced increase of GM1 levels present in the plasma membrane of HBMEC (**Supplementary Figure S5C**). To analyze effects of increased GM1 levels during G1 phase on bacterial adhesion and invasion we performed gentamicin protection assays to estimate the number of adherent or invasive bacteria by counting of residual bacterial colonies. Here, bacterial adhesion was neither influenced by serum starvation of host cells nor blocking of GM1 by unlabeled CTxB (**Figure 5B**). In contrast, invasion of HBMEC by meningococci was significantly increased in synchronized cells and this effect could be abolished by blocking of GM1 (**Figure 5A**).

DISCUSSION

Single-molecule tracking enables the observation of highly dynamic processes from viral cell entry mechanisms (Ruthardt et al., 2011) to ligand-binding (Yanagawa et al., 2018) at high spatiotemporal resolution. Upon ligand-binding and subsequent activation, receptors typically undergo conformational changes and/or changes in oligomerization states, which is often accompanied by reduced mobility resulting in decreased diffusion coefficients (Chung et al., 2010; Yanagawa et al., 2018). In this study, we could show that the presence of a PeF alone did not significantly change the diffusion coefficient of neisserial type IV pilus receptor CD147. Rather, our data indicate a slightly altered type of mobility toward normal diffusion which might indicate cytoskeletal rearrangements or modulation of the plasma membrane lipid environment. Interestingly, addition of the monoclonal M6/6 antibody before single-molecule tracking experiments resulted in a strong decrease in the number of M6/1 antibodies bound on the plasma membrane.

Since both antibodies are capable to bind to monomeric and dimeric CD147 molecules (Koch et al., 1999) M6/6 antibody-induced clustering resulting in a reduced M6/1 antibody epitope accessibility can be excluded as explanation. Instead, the following hypotheses seem to be more plausible. Binding of M6/6 to the membrane proximal Ig-like domain might activate the receptor and induce the local production of matrix metalloproteinases leading to subsequent receptor shedding. Indeed, CD147-induced expression of matrix metalloproteinases results in proteolytic cleavage of membrane-associated CD147 and an increase of its soluble form (Tang et al., 2004). Additionally, the diffusion coefficient of CD147 was significantly reduced upon M6/6 antibody binding indicating that activation of CD147 reduces its mobility in the plasma membrane (**Figure 1C**). Notably, the M6/6 antibody has unique properties and can inhibit OKT3-induced T cell proliferation (Koch et al., 1999) or modulate multidrug resistance (Somno et al., 2016). This implies that CD147 signaling might influence plasma membrane organization and promote immobilization of the receptor. For
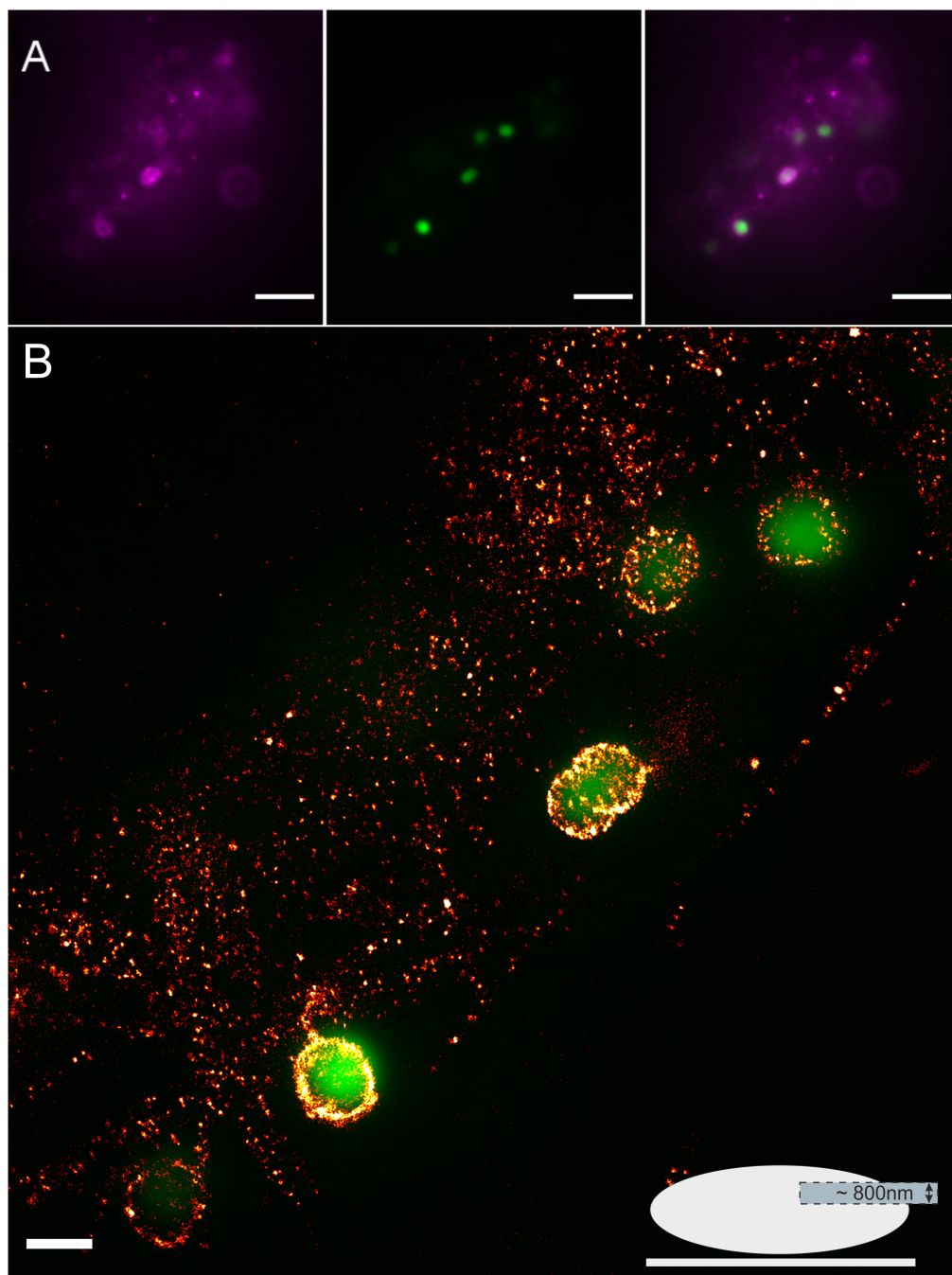
FIGURE 4 | Fluorescence imaging of GM1 in HBMEC upon infection with GFP expressing *N. meningitidis*. **(A)** Widefield fluorescence images of meningococci (green) and GM1 labeled with Alexa Fluor 647 CTxB (magenta). Scale bar, 5 μm. **(B)** *d*STORM image showing strong accumulation of GM1 around infection sites. The lower right corner shows a schematic model illustrating the mode of imaging. Adherent HBMEC were irradiated by epi-illumination. Detection was performed in an axial plane ensuring the imaging of a substantial part of the plasma membrane (light blue area). The axial area captured by the 2D *d*STORM image is determined to approximately 800 nm by the blurring of the point spread function above and below the imaging plane and data analysis parameter. Scale bar 1 μm.

this reason, following studies should dissect effects introduced by specific binding characteristics of the antibodies by using monovalent Fab fragments.

In contrast, addition of PeF did slightly increase the mobility of CD147 receptors (**Figure 1D**) although neisserial type IV pili and the M6/6 antibody compete for the same binding site (Bernard et al., 2014). In general, the affinity of the PilE and PilV monomers to CD147 is low and the need for multimeric organization as type IV pili seems to play an important role in mediating adherence (Bernard et al., 2014).

105

FIGURE 5 | Adhesion and invasion efficacy of *N. meningitidis* upon cell cycle arrest of HBMEC in G1 phase and CTxB pre-treatment. **(A)** The number of invasive meningococci was determined by gentamicin protection assays. Here, all extracellular bacteria were killed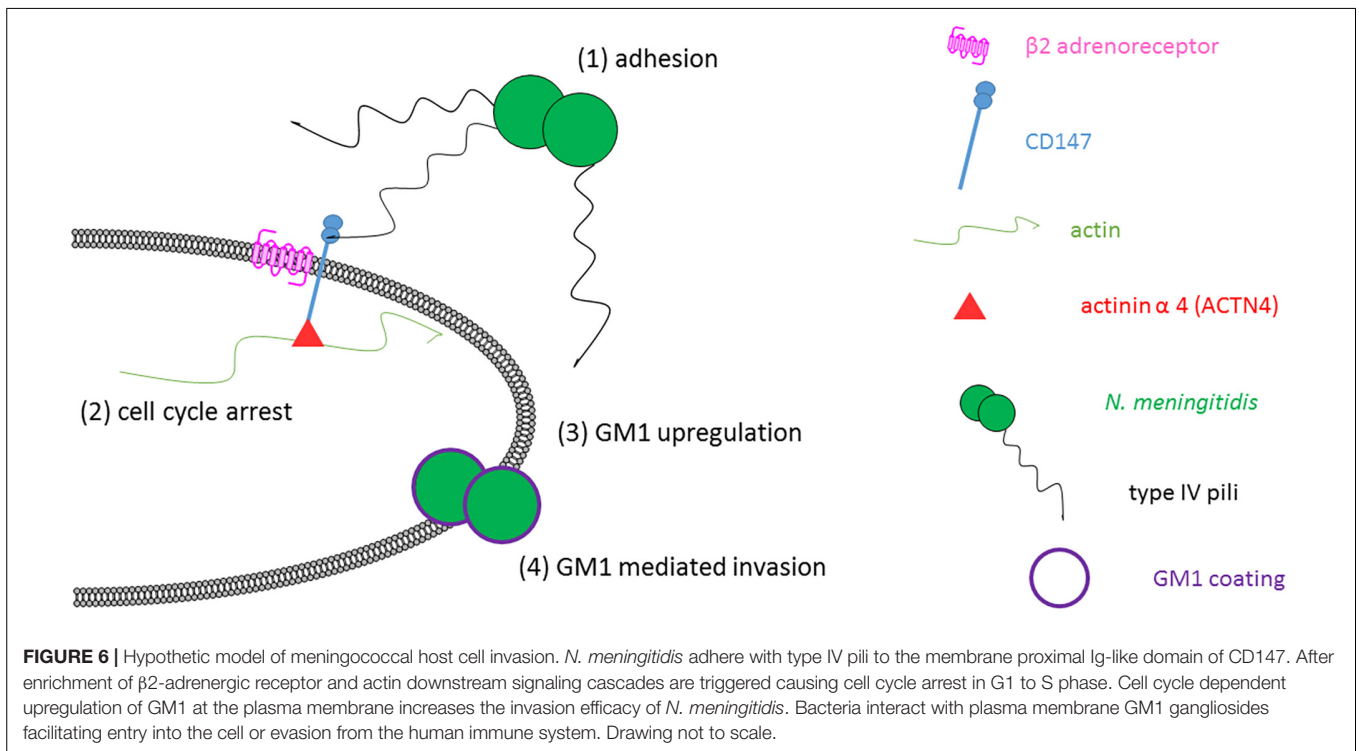 by incubation for 2 h in gentamicin solution and intracellular bacteria counted. Non-synchronized or G1 synchronized cells were preincubated with 6.6 μg/ml CtxB for 30 min at 37°C (if indicated) and afterward infected with MC58 for 4 h with a MOI of 100. **(B)** The number of adhesive bacteria was determined by counting of residual meningococci colonies after thorough washing and lysis of HBMEC.

Since our pili preparation contains mainly monomeric pilin subunits, as shown by Peters et al. (2019), incubation with our PeF preparation might not resemble the native condition where in addition to the multimeric assembly as pilus fibers whole micrometer-sized bacteria are attached to CD147. It seems thus more likely, that binding of the competitive M6/6 antibody reflects the native interaction of

type IV pili with CD147 although this has to be verified in future experiments.

Glycosphingolipids represent important pathogen receptors (Nakayama et al., 2018) with thousands of possible structures. Notably, bacterial lipopolysaccharides are able to mimic host cell glycosphingolipids causing evasion of the immune system or leading to autoimmune diseases (Harvey et al., 2001).

FIGURE 6 | Hypothetic model of meningococcal host cell invasion. *N. meningitidis* adhere with type IV pili to the membrane proximal Ig-like domain of CD147. After enrichment of β2-adrenergic receptor and actin downstream signaling cascades are triggered causing cell cycle arrest in G1 to S phase. Cell cycle dependent upregulation of GM1 at the plasma membrane increases the invasion efficacy of *N. meningitidis*. Bacteria interact with plasma membrane GM1 gangliosides facilitating entry into the cell or evasion from the human immune system. Drawing not to scale.

106

3 RESULTS

Schlegel et al.   Bacterial Invasion Investigated by *d*STORM

Although several possible host glycosphingolipids binding partners have been identified for *N. meningitidis* (Hugosson et al., 1998; Mubaiwa et al., 2017) molecular information about their involvement in pathogen interactions remained elusive. Furthermore, with a bacteria size of approximately 1 μm, the molecular details of host-bacteria interactions are difficult to image with conventional diffraction-limited fluorescence microscopy. Using single-molecule sensitive *d*STORM we could show that gangliosides are important host cell receptors mediating cellular entry of meningococcus by accumulating at bacterial adhesion sites (**Figure 4B**). Here, it has to be considered that CTxB does not exclusively bind to GM1 but possibly also to a plethora of other gangliosides (Kuziemko et al., 1996). Upon binding CTxB can be endocytosed via caveolae and clathrin-independent pathways although clathrin-mediated endocytosis seems to cover the major fraction (Torgersen et al., 2001). Which pathways are used in the context of meningococcal invasion and whether the bacteria are able to locally induce upregulation of GM1 or if this is a passive event triggered by cell cycle modulation is presently unknown and requires further experiments. Of note, pentameric STxB and CTxB possess multiple binding sites for individual glycosphingolipids and binding can be influenced by the chain length and saturation state of the attached fatty acid (Pellizzari et al., 1992; Kiarash et al., 1994). In order to reduce possible effects induced by multivalent toxin binding we fixed the cells before labeling to immobilize the binding partners.

However, our findings demonstrate that cell cycle arrest in G1 phase causes an increase of plasma membrane GM1 molecules leading to enhanced bacterial uptake. Blocking of GM1 strongly reduces infection efficiency implying the importance of plasma membrane gangliosides for bacterial invasion. *N. meningitidis* infection can cause accumulation of brain endothelial cells in S phase (Oosthuysen et al., 2016) and of human epithelial cells in G1 phase (Papen et al., 2016) and both cell cycle phases are positive for CTxB labeling (Majoul et al., 2002). Therefore, we propose a model where meningococci regulate their own uptake by initiating a positive feedback loop (**Figure 6**). The increased invasion efficacy should thus even be more pronounced in human epithelial cells whose gangliosides have already been described to interact with *Pseudomonas aeruginosa* pili (Comolli et al., 1999). We assume that this mechanism might play an important role in the initial uptake from the nasopharynx into the blood. Blocking this interaction could represent a promising method to avoid life-threatening dissemination of meningococci and help to develop therapeutic approaches for bacterial clearance.

DATA AVAILABILITY

The raw data supporting the conclusions of this manuscript will be made available by the authors, without undue reservation, to any qualified researcher.

AUTHOR CONTRIBUTIONS

JS designed and performed the experiments, applied the data analysis, and wrote the manuscript. SP performed the

experiments involving living *N. meningitidis*, analyzed the data, and wrote the manuscript. SD performed the cluster analysis and data simulation, and provided the discussion. AS-U and MS guided the project, developed concepts, and wrote the manuscript.

SUPPLEMENTARY MATERIAL

The Supplementary Material for this article can be found online at: https://www.frontiersin.org/articles/10.3389/fcell.2019.00194/full#supplementary-material

FIGURE S1 | Number of localizations detected during individual CD147 single-molecule tracking experiments on HBMEC. CD147 was labeled with subnanomolar concentrations of monoclonal CD147 MEM-M6/1 antibody conjugated to SeTau647. Localizations were detected by fitting with ThunderSTORM (Ovesný et al., 2014). HBMEC were seeded on KOH cleaned glass and pre-treated with 10 μg/ml MEM-M6/6 CD147 antibody or 2 μg PeF/well before labeling with MEM-M6/1 antibody, if stated.

FIGURE S2 | Spatial distribution analysis of dSTORM data (red line). Ripley's h function was estimated 100 times (gray data curves with mean shown in color) for the dSTORM data representing GM1 labeled with CTxB-Alexa647 (left) and Gb3 labeled with STxB-Alexa647 (right) as shown in **Figures 2C,D**, respectively. For comparisn, Ripley's h function is shown for simulated data that represents a point process of complete spatial randomness (blue) and a clustered point process representing spatial clusters due to repeated localizations per toxin. The data indicates that experimental data is largely controlled by the photophysical clustering showing a homogeneous distribution of the two sphingolipids in the plasma membrane of HBMEC. The peak positions are found at nearly identical positions of (left) 27 nm and 22 nm and of (right) 38 nm and 21 nm for experimental and simulated data, representatively.

FIGURE S3 | *d*STORM images of GM1 and Gb3 of GFP expressing *N. meningitidis* (green) without HBMEC labeled with Alexa Fluor 647 conjugated CTxB or STxB. Both toxins non-specifically bind to the coverslip but do not show any accumulation at bacteria. The diffraction limited GFP signal was upscaled for the overlay. Scale bar, 5 μm.

FIGURE S4 | SIM images of GFP expressing meningococci infected HBMEC. CD147 labeled with monoclonal MEM-M6/1 and secondary F(ab)2-Alexa Fluor 647 (magenta). Actin labeled with phalloidin Atto565 (gray). GFP signal of meningococci (green) and overlay of the three images showing that CD147 and actin colocalize but do not accumulate at bacterial adhesion sites. Scale bar, 10 μm.

FIGURE S5 | Flow cytometry analysis of cell cycle state and average ganglioside GM1 concentration present in the plasma membrane of HMBEC. **(A)** Serum starvation was performed 24 h prior to the experiment by replacing the growth medium with RPMI. On the next day, cells were harvested, fixed, permeabilized and stained with PI (10 μg/ml PI + 25 μg/ml RNase) for 30 min in the dark at

room temperature. Afterward, PI incooperation was estimated via flow cytometry. Histogram of unsynchronized and G1 synchronized cells with the indicated gating strategy shown in **(B)**. **(C)** For the analysis of cell surface GM1, cells were stained with Alexa Fluor 647 conjugated CtxB for 30 min at room temperature in the dark.

Then, cells were fixed for 30 min at 4°C, washed three times with FACS buffer and analyzed by flow cytometry.

VIDEO S1 | Examples of CD147 single-molecule tracks measured from one cell.

REFERENCES

Allan, D., Caswell, T., Keim, N., and van der Wel, C. (2016). *Trackpy: Trackpy V0.3*.2. Zenodo.

Bernard, S. C., Simpson, N., Join-Lambert, O., Federici, C., Laran-Chich, M.-P., Maïssa, N., et al. (2014). Pathogenic *Neisseria meningitidis* utilizes CD147 for vascular colonization. *Nat. Med.* 20, 725–731. doi: 10.1038/nm.3563

Burgert, A., Schlegel, J., Bécam, J., Doose, S., Bieberich, E., Schubert-Unkmeir, A., et al. (2017). Characterization of plasma membrane ceramides by super-resolution microscopy. *Angew. Chem. Int. Ed. Engl.* 56, 6131–6135. doi: 10.1002/anie.201700570

Chung, I., Akita, R., Vandlen, R., Toomre, D., Schlessinger, J., and Mellman, I. (2010). Spatial control of EGF receptor activation by reversible dimerization on living cells. *Nature* 464, 783–787. doi: 10.1038/nature08827

Comolli, J. C., Waite, L. L., Mostov, K. E., and Engel, J. N. (1999). Pili binding to asialo-GM1 on epithelial cells can mediate cytotoxicity or bacterial internalization by *Pseudomonas aeruginosa*. *Infect. Immun.* 67, 3207–3214.

Coureuil, M., Lécuyer, H., Scott, M. G. H., Boularan, C., Enslen, H., Soyer, M., et al. (2010). Meningococcus hijacks a β2-adrenoceptor/β-Arrestin pathway to cross brain microvasculature endothelium. *Cell* 143, 1149–1160. doi: 10.1016/j.cell.2010.11.035

Coureuil, M., Mikaty, G., Miller, F., Lécuyer, H., Bernard, C., Bourdoulous, S., et al. (2009). Meningococcal type IV pili recruit the polarity complex to cross the brain endothelium. *Science* 325, 83–87. doi: 10.1126/science.1173196

Crocker, J. C., and Grier, D. G. (1996). Methods of digital video microscopy for colloidal studies. *J. Colloid Interface Sci.* 179, 298–310. doi: 10.1006/jcis.1996.0217

Cuatrecasas, P. (1973). Gangliosides and membrane receptors for cholera toxin. *Biochemistry* 12, 3558–3566. doi: 10.1021/bi00742a032

Gustafsson, M. G. (2000). Surpassing the lateral resolution limit by a factor of two using structured illumination microscopy. *J. Microsc.* 198, 82–87. doi: 10.1046/j.1365-2818.2000.00710.x

Hammache, D., Yahi, N., Maresca, M., Piéroni, G., and Fantini, J. (1999). Human erythrocyte glycosphingolipids as alternative cofactors for human immunodeficiency virus type 1 (HIV-1) entry: evidence for CD4-induced interactions between HIV-1 gp120 and reconstituted membrane microdomains of glycosphingolipids (Gb3 and GM3). *J. Virol.* 73, 5244–5248.

Harvey, H. A., Swords, W. E., and Apicella, M. A. (2001). The mimicry of human glycolipids and glycosphingolipids by the lipooligosaccharides of pathogenic neisseria and haemophilus. *J. Autoimmun.* 16, 257–262. doi: 10.1006/jaut.2000.0477

Heilemann, M., van de Linde, S., Schüttpelz, M., Kasper, R., Seefeldt, B., Mukherjee, A., et al. (2008). Subdiffraction-resolution fluorescence imaging with conventional fluorescent probes. *Angew. Chem. Int. Ed. Engl.* 47, 6172–6176. doi: 10.1002/anie.200802376

Hugosson, S., Angström, J., Olsson, B. M., Bergström, J., Fredlund, H., Olcén, P., et al. (1998). Glycosphingolipid binding specificities of *Neisseria meningitidis* and *Haemophilus influenzae*: detection, isolation, and characterization of a binding-active glycosphingolipid from human oropharyngeal epithelium. *J. Biochem.* 124, 1138–1152. doi: 10.1093/oxfordjournals.jbchem.a022232

Hyun, C. S., and Kimmich, G. A. (1984). Interaction of cholera toxin and *Escherichia coli* enterotoxin with isolated intestinal epithelial cells. *Am. J. Physiol.* 247, G623–G631. doi: 10.1152/ajpgi.1984.247.6.G623

Ichikawa, N., Iwabuchi, K., Kurihara, H., Ishii, K., Kobayashi, T., Sasaki, T., et al. (2009). Binding of laminin-1 to monosialoganglioside GM1 in lipid rafts is crucial for neurite outgrowth. *J. Cell Sci.* 122, 289–299.doi: 10.1242/jcs.030338

Kiarash, A., Boyd, B., and Lingwood, C. A. (1994).). Glycosphingolipid receptor function is modified by fatty acid content. *Verotoxin* 1 and verotoxin 2c preferentially recognize different globotriaosyl ceramide fatty acid homologues. *J. Biol. Chem.* 269, 11138–11146.

Kiskowski, M. A., Hancock, J. F., and Kenworthy, A. K. (2009). On the use of Ripley's K-function and its derivatives to analyze domain size. *Biophys. J.* 97, 1095–1103. doi: 10.1016/j.bpj.2009.05.039

Koch, C., Staffler, G., Hüttinger, R., Hilgert, I., Prager, E., Cerný, J., et al. (1999). T cell activation-associated epitopes of CD147 in regulation of the T cell response, and their definition by antibody affinity and antigen density. *Int. Immunol.* 11, 777–786. doi: 10.1093/intimm/11.5.777

Krivan, H. C., Roberts, D. D., and Ginsburg, V. (1988). Many pulmonary pathogenic bacteria bind specifically to the carbohydrate sequence GalNAc beta 1-4Gal found in some glycolipids. *Proc. Natl. Acad. Sci. U.S.A.* 85, 6157–6161. doi: 10.1073/pnas.85.16.6157

Kuziemko, G. M., Stroh, M., and Stevens, R. C. (1996). Cholera toxin binding affinity and specificity for gangliosides determined by surface plasmon resonance. *Biochemistry* 35, 6375–6384. doi: 10.1021/bi952314i

Lemichez, E., Lecuit, M., Nassif, X., and Bourdoulous, S. (2010). Breaking the wall: targeting the endothelium by pathogenic bacteria. *Nat. Rev. Microbiol.* 8, 93–104. doi: 10.1038/nrmicro2269

Li, L., Tang, W., Wu, X., Karnak, D., Meng, X., Thompson, R., et al. (2013). HAb18G/CD147 promotes pSTAT3-mediated pancreatic cancer development via CD44s. *Clin. Cancer Res.* 19, 6703–6715. doi: 10.1158/1078-0432.CCR-13-0621

Lindberg, A. A., Brown, J. E., Strömberg, N., Westling-Ryd, M., Schultz, J. E., and Karlsson, K. A. (1987). Identification of the carbohydrate receptor for Shiga toxin produced by *Shigella* dysenteriae type 1. *J. Biol. Chem.* 262, 1779–1785.

Lingwood, C. A. (2011). Glycosphingolipid functions. *Cold Spring Harb. Perspect. Biol.* 3, a004788. doi: 10.1101/cshperspect.a004788

Lingwood, C. A., Binnington, B., Manis, A., and Branch, D. R. (2010). Globotriaosyl ceramide receptor function - where membrane structure and pathology intersect. *FEBS Lett.* 584, 1879–1886. doi: 10.1016/j.febslet.2009.11.089

Maïssa, N., Covarelli, V., Janel, S., Durel, B., Simpson, N., Bernard, S. C., et al. (2017). Strength of *Neisseria meningitidis* binding to endothelial cells requires highly-ordered CD147/β2-adrenoceptor clusters assembled by alpha-actinin-4. *Nat. Commun.* 8:15764. doi: 10.1038/ncomms15764

Majoul, I., Schmidt, T., Pomasanova, M., Boutkevich, E., Kozlov, Y., and Söling, H.-D. (2002). Differential expression of receptors for shiga and cholera toxin is regulated by the cell cycle. *J. Cell Sci.* 115, 817–826.

Mangeney, M., Richard, Y., Coulaud, D., Tursz, T., and Wiels, J. (1991). CD77: an antigen of germinal center B cells entering apoptosis. *Eur. J. Immunol.* 21, 1131–1140. doi: 10.1002/eji.1830210507

Manzo, C., and Garcia-Parajo, M. F. (2015). A review of progress in single particle tracking: from methods to biophysical insights. *Rep. Prog. Phys.* 78:124601. doi: 10.1088/0034-4885/78/12/124601

McGuinness, B. T., Clarke, I. N., Lambden, P. R., Barlow, A. K., Poolman, J. T., Jones, D. M., et al. (1991). Point mutation in meningococcal por a gene associated with increased endemic disease. *Lancet* 337, 514–517. doi: 10.1016/0140-6736(91)91297-8

Melican, K., and Dumenil, G. (2012). Vascular colonization by *Neisseria meningitidis*. *Curr. Opin. Microbiol.* 15, 50–56. doi: 10.1016/j.mib.2011.10.008

Mubaiwa, T. D., Hartley-Tassell, L. E., Semchenko, E. A., Jen, F. E.-C., Srikhanta, Y. N., Day, C. J., et al. (2017). The glycointeractome of serogroup B *Neisseria meningitidis* strain MC58. *Sci. Rep.* 7:5693. doi: 10.1038/s41598-017-05894-w

Mutoh, T., Tokuda, A., Miyadai, T., Hamaguchi, M., and Fujiki, N. (1995). Ganglioside GM1 binds to the Trk protein and regulates receptor function. *Proc. Natl. Acad. Sci. U.S.A.* 92, 5087–5091. doi: 10.1073/pnas.92.11.5087

Nakayama, H., Nagafuku, M., Suzuki, A., Iwabuchi, K., and Inokuchi, J.-I. (2018). The regulatory roles of glycosphingolipid-enriched lipid rafts in immune systems. *FEBS Lett.* 592, 3921–3942. doi: 10.1002/1873-3468.13275

Naroeni, A., and Porte, F. (2002). Role of cholesterol and the ganglioside GM(1) in entry and short-term survival of *Brucella suis* in murine macrophages. *Infect. Immun.* 70, 1640–1644. doi: 10.1128/IAI.70.3.1640-1644.2002

Nassif, X., Lowy, J., Stenberg, P., O'Gaora, P., Ganji, A., and So, M. (1993). Antigenic variation of pilin regulates adhesion of *Neisseria meningitidis* to

108

human epithelial cells. *Mol. Microbiol.* 8, 719–725. doi: 10.1111/j.1365-2958. 1993.tb01615.x

Nikulin, J., Panzner, U., Frosch, M., and Schubert-Unkmeir, A. (2006). Intracellular survival and replication of *Neisseria meningitidis* in human brain microvascular endothelial cells. *Int. J. Med. Microbiol.* 296, 553–558. doi: 10.1016/j.ijmm.2006. 06.006

Oosthuysen, W. F., Mueller, T., Dittrich, M. T., and Schubert-Unkmeir, A. (2016). *Neisseria meningitidis* causes cell cycle arrest of human brain microvascular endothelial cells at S phase via p21 and cyclin G2. *Cell Microbiol.* 18, 46–65. doi: 10.1111/cmi.12482

Otnaess, A. B., Laegreid, A., and Ertresvåg, K. (1983). Inhibition of enterotoxin from *Escherichia coli* and *Vibrio cholerae* by gangliosides from human milk. *Infect. Immun.* 40, 563–569.

Ovesný, M., Křížek, P., Borkovec, J., Svindrych, Z., and Hagen, G. M. (2014). ThunderSTORM: a comprehensive imagej plug-in for PALM and STORM data analysis and super-resolution imaging. *Bioinformatics* 30, 2389–2390. doi: 10. 1093/bioinformatics/btu202

Papen, M., von Oosthuysen, W. F., Becam, J., Claus, H., and Schubert-Unkmeir, A. (2016). Disease and carrier isolates of *Neisseria meningitidis* Cause G1 Cell Cycle Arrest in Human Epithelial Cells. *Infect. Immun.* 84, 2758–2770. doi: 10.1128/IAI.00296-16

Pellizzari, A., Pang, H., and Lingwood, C. A. (1992). Binding of verocytotoxin 1 to its receptor is influenced by differences in receptor fatty acid content. *Biochemistry* 31, 1363–1370. doi: 10.1021/bi00120a011

Peters, S., Schlegel, J., Becam, J., Avota, E., Sauer, M., and Schubert-Unkmeir, A. (2019). *Neisseria meningitidis* type IV pili trigger Ca2+-dependent lysosomal trafficking of the acid sphingomyelinase to enhance surface ceramide levels. *Infect. Immun.* 87:e00410-19. doi: 10.1128/IAI.00410-19

Prasanna, X., Jafurulla, M., Sengupta, D., and Chattopadhyay, A. (2016). The ganglioside GM1 interacts with the serotonin1A receptor via the sphingolipid binding domain. *Biochim. Biophys. Acta* 1858, 2818–2826. doi: 10.1016/j. bbamem.2016.08.009

Ruthardt, N., Lamb, D. C., and Bräuchle, C. (2011). Single-particle tracking as a quantitative microscopy-based approach to unravel cell entry mechanisms of viruses and pharmaceutical nanoparticles. *Mol. Ther.* 19, 1199–1211. doi: 10.1038/mt.2011.102

Schindelin, J., Arganda-Carreras, I., Frise, E., Kaynig, V., Longair, M., Pietzsch, T., et al. (2012). Fiji: an open-source platform for biological-image analysis. *Nat. Methods* 9, 676–682. doi: 10.1038/nmeth.2019

Schubert-Unkmeir, A., Konrad, C., Slanina, H., Czapek, F., Hebling, S., and Frosch, M. (2010). *Neisseria meningitidis* induces brain microvascular endothelial cell detachment from the matrix and cleavage of occludin: a role for MMP-8. *PLoS Pathog.* 6:e1000874. doi: 10.1371/journal.ppat.1000874

Shen, H., Tauzin, L. J., Baiyasi, R., Wang, W., Moringo, N., Shuang, B., et al. (2017). Single particle tracking: from theory to biophysical applications. *Chem Rev.* 117, 7331–7376. doi: 10.1021/acs.chemrev.6b00815

Simonis, A., Hebling, S., Gulbins, E., Schneider-Schaulies, S., and Schubert-Unkmeir, A. (2014). Differential activation of acid sphingomyelinase and ceramide release determines invasiveness of *Neisseria meningitidis* into brain endothelial cells. *PLoS Pathog.* 10:e1004160. doi: 10.1371/journal.ppat.1004160

Somno, A., Anuchapreeda, S., Chruewkamlow, N., Pata, S., Kasinrerk, W., and Chiampanichayakul, S. (2016). Involvement of CD147 on multidrug resistance through the regulation of P-glycoprotein expression in K562/ADR leukemic cell line. *Leuk. Res. Rep.* 6, 33–38. doi: 10.1016/j.lrr.2016.08.001

Stephens, D. S., Greenwood, B., and Brandtzaeg, P. (2007). Epidemic meningitis, meningococcaemia, and *Neisseria meningitidis*. *Lancet* 369, 2196–2210. doi: 10.1016/S0140-6736(07)61016-61012

Stins, M. F., Gilles, F., and Kim, K. S. (1997). Selective expression of adhesion molecules on human brain microvascular endothelial cells. *J. Neuroimmunol.* 76, 81–90. doi: 10.1016/s0165-5728(97)00036-2

Sutherland, T. C., Quattroni, P., Exley, R. M., and Tang, C. M. (2010). Transcellular passage of *Neisseria meningitidis* across a polarized respiratory epithelium. *Infect. Immun.* 78, 3832–3847. doi: 10.1128/IAI.01377-1379

Tang, Y., Kesavan, P., Nakada, M. T., and Yan, L. (2004). Tumor-stroma interaction: positive feedback regulation of extracellular matrix metalloproteinase inducer (EMMPRIN) expression and matrix metalloproteinase-dependent generation of soluble EMMPRIN. *Mol. Cancer Res.* 2, 73–80.

Tinevez, J.-Y., Perry, N., Schindelin, J., Hoopes, G. M., Reynolds, G. D., Laplantine, E., et al. (2017). TrackMate: an open and extensible platform for single-particle tracking. *Methods* 115, 80–90. doi: 10.1016/j.ymeth.2016. 09.016

Torgersen, M. L., Skretting, G., van Deurs, B., and Sandvig, K. (2001). Internalization of cholera toxin by different endocytic mechanisms. *J. Cell Sci.* 114, 3737–3747.

Tsai, B., Gilbert, J. M., Stehle, T., Lencer, W., Benjamin, T. L., and Rapoport, T. A. (2003). Gangliosides are receptors for murine polyoma virus and SV40. *EMBO J.* 22, 4346–4355. doi: 10.1093/emboj/cdg439

Tsunoyama, T. A., Watanabe, Y., Goto, J., Naito, K., Kasai, R. S., Suzuki, K. G. N., et al. (2018). Super-long single-molecule tracking reveals dynamic-anchorage-induced integrin function. *Nat. Chem. Biol.* 14, 497–506. doi: 10.1038/s41589-018-0032-35

Unkmeir, A., Latsch, K., Dietrich, G., Wintermeyer, E., Schinke, B., Schwender, S., et al. (2002). Fibronectin mediates Opc-dependent internalization of *Neisseria meningitidis* in human brain microvascular endothelial cells. *Mol. Microbiol.* 46, 933–946. doi: 10.1046/j.1365-2958.2002.03222.x

van de Linde, S., Löschberger, A., Klein, T., Heidbreder, M., Wolter, S., Heilemann, M., et al. (2011). Direct stochastic optical reconstruction microscopy with standard fluorescent probes. *Nat. Protoc.* 6, 991–1009. doi: 10.1038/nprot.2011. 336

Wu, B., Cui, J., Yang, X.-M., Liu, Z.-Y., Song, F., Li, L., et al. (2017). Cytoplasmic fragment of CD147 generated by regulated intramembrane proteolysis contributes to HCC by promoting autophagy. *Cell Death Dis.* 8:e2925. doi: 10.1038/cddis.2017.251

Yanagawa, M., Hiroshima, M., Togashi, Y., Abe, M., Yamashita, T., Shichida, Y., et al. (2018). Single-molecule diffusion-based estimation of ligand effects on G protein-coupled receptors. *Sci. Signal.* 11:eaao1917. doi: 10.1126/scisignal. aao1917

Yazdankhah, S. P., and Caugant, D. A. (2004). *Neisseria meningitidis*: an overview of the carriage state. *J. Med. Microbiol.* 53, 821–832. doi: 10.1099/jmm.0.45529-45520

109

3.8   Super-Resolution Microscopy of Sphingolipids

Introduction

"Sphingolipids are key players in infection and homeostasis of health and disease. They serve as important structural components of biological membranes and maintain the indispensable heterogeneity of the plasma membrane. Nevertheless, their investigation is hindered by their size well below the diffraction limit of light and their highly dynamic behavior. Emerging single-molecule sensitive superresolution microscopy techniques such as *direct* stochastic optical reconstruction microscopy (*d*STORM) [84] and photoactivated localization microscopy [78] have the potential to provide information about the distribution of plasma membrane components with virtually molecular spatial resolution in health and disease [110, 115, 116]. New powerful techniques, such as STED-FCS, even allow to follow fast lipid nanoscale dynamics in living cells [117–119]. Through the accessibility of commercial instruments, these techniques are nowadays available at many laboratories and broadly applied. However, superresolution imaging of plasma membrane components and particular lipids are error-prone due to their residual mobility even after strong fixation. We provide efficient sample preparation and data acquisition methods enabling artifact-free imaging of sphingolipid microdomains by superresolution microscopy."

The following manuscript was accepted on January 9$^{\text{th}}$, 2020 in Methods in Molecular Biology (Springer) and permission for legal second publication within this thesis was kindly granted from both the publishers and the co-authors.

Chapter 17 1

Superresolution Microscopy of Sphingolipids 2

Jan Schlegel and Markus Sauer 3

Abstract 4

This chapter provides a step-by-step protocol to label and visualize sphingolipids by superresolution 5
microscopy with a special focus on single-molecule localization microscopy by *d*STORM. We provide 6
information on custom fluorophore conjugation to raft-associated toxins and antibodies, and a labeling 7
protocol for appropriate sample treatment. 8

Key words Superresolution microscopy, *d*STORM, Sphingolipids 9

AU1

1 Introduction 10

Sphingolipids are key players in infection and homeostasis of health 11
and disease. They serve as important structural components of 12
biological membranes and maintain the indispensable heterogene- 13
ity of the plasma membrane. Nevertheless, their investigation is 14
hindered by their size well below the diffraction limit of light and 15
their highly dynamic behavior. Emerging single-molecule sensitive 16
superresolution microscopy techniques such as *direct* stochastic 17
optical reconstruction microscopy (*d*STORM) [1] and photoacti- 18
vated localization microscopy [2] have the potential to provide 19
information about the distribution of plasma membrane compo- 20
nents with virtually molecular spatial resolution in health and dis- 21
ease [3–5]. New powerful techniques, such as STED-FCS, 22
even allow to follow fast lipid nanoscale dynamics in living cells 23
[6–8]. Through the accessibility of commercial instruments, these 24
techniques are nowadays available at many laboratories and broadly 25
applied. However, superresolution imaging of plasma membrane 26
components and particular lipids are error-prone due to their resid- 27
ual mobility even after strong fixation. We provide efficient sample 28
preparation and data acquisition methods enabling artifact-free 29
imaging of sphingolipid microdomains by superresolution 30
microscopy. 31

Jan Schlegel and Markus Sauer

2 Materials

2.1 Antibodies and Toxins

1. Dissolve antibodies and toxins as recommended by the supplier and avoid freeze–thaw cycles by preparing appropriate aliquots. Sphingolipid specific antibodies or toxins can be purchased by local suppliers or upon request from corresponding working group. Handle proteins as recommended by the supplier to avoid loss of reactivity (*see* **Note 1**). The following table depicts toxins and antibodies which were successfully used for single-molecule localization microscopy of sphingolipids (Fig. 1):

Molecule	Target	References
Shiga toxin B subunit (STxB)	Globotriaosylceramide (Gb3)	Schlegel et al. [5]
Cholera toxin B subunit (CTxB)	Monosialotetrahexosylganglioside (GM1)	Schlegel et al. [5]
Ceramide IgG antibody	Ceramides with varying chain length	Burgert et al. [3]
θ-Toxin D4	Plasma membrane cholesterol	Mizuno et al. [4]

2.2 Amine Reactive Dyes

1. Amine reactive dyes: 1 mg Alexa Fluor 647 *N*-hydroxysuccinimide (NHS) ester, 1 mg Alexa Fluor 532 NHS ester. For preparation of amine reactive dyes *see* **Note 2**.

2.3 Antibody and Toxin Coupling

1. Cross-linking buffer: 100 mM sodium bicarbonate, pH 8.3. Dilute 10 mL ultrapure water with 84.01 mg sodium bicarbonate to obtain a 100 mM bicarbonate buffer with pH of ~8.3 (*see* **Note 2**). Filter cross-linking buffer by using syringe filters with pore sizes of 0.2 μm.

2. Storage buffer: PBS with 0.02% sodium azide (*see* **Note 3**).

3. The dye of choice functionalized as NHS ester.

4. Size-exclusion spin columns with molecular weight cut off 7 kDa and volume capacity ~100 μL.

5. UV-Vis spectrophotometer for microvolume samples.

2.4 Staining and Superresolution Microscopy by dSTORM

1. Chambered high-precision cover glass with glass bottom suitable for superresolution microscopy.

2. Glass cleaning solution: 1 M KOH sterile filtered.

3. Coating solution: 0.1 mg/mL poly-D-lysine in water. Dilute 5 mg of poly-D-lysine in 50 mL ultrapure water. Sterile filtered and aliquoted solution can be stored for up to 2 years at 2–8 °C.
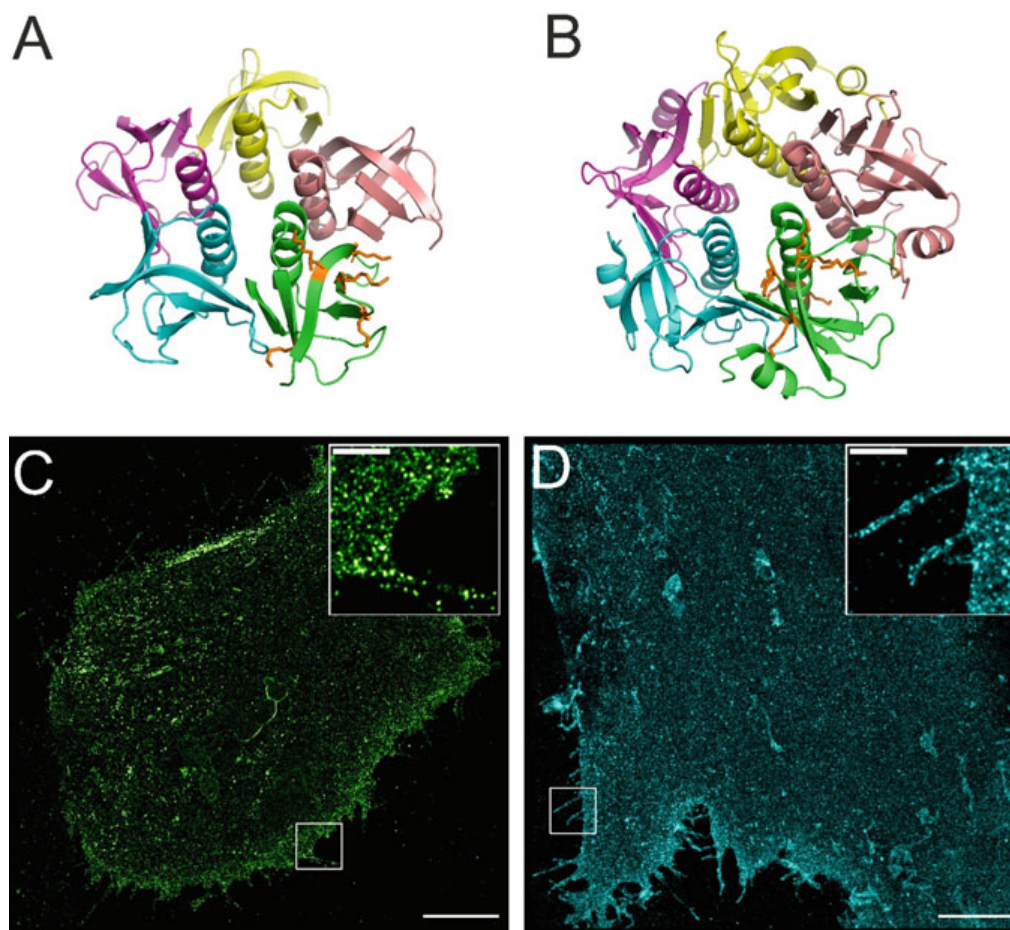
Fig. 1 Molecular structures and dSTORM images of STxB and CTxB. (**a**) Molecular structure of pentameric STxB (PDB: 1C48) [18]. Each monomer is depicted in a different color and all five lysine residues of one monomer are shown in orange. (**b**) Molecular structure of pentameric CTxB (PDB: 1JR0) [19]. Each monomer is depicted in a different color and all eight lysine residues of one monomer are shown in orange. (**c**) dSTORM image of the basal plasma membrane of an eukaryotic cell labeled with STxB Alexa Fluor 647 as described in the abovementioned fixation protocol. (**d**) dSTORM image of the basal plasma membrane of an eukaryotic cell labeled with CTxB Alexa Fluor 647 as described in the abovementioned fixation protocol. Note the fine underlying structure of plasma membrane protrusions highlighted in the insets. Scale bar, 10 μm and 1 μm (insets). (dSTORM images were adapted from [5])

4. Live-cell labeling solution: Hank's Balanced Salt Solution (HBSS) with calcium and magnesium.

5. Fixation solution: 2% Formaldehyde 0.2% glutaraldehyde in PBS.

6. Blocking solution: 5% BSA in PBS.

7. Switching buffer: 100 mM β-mercaptoethylamine (β-MEA) in PBS, pH 7.4–7.7. Always prepare fresh switching buffer just before performing *d*STORM. Dilute 114 mg cysteamine hydrochloride in 10 mL PBS and adjust pH to ~7.5 by addition of ~30 μL 5 M KOH solution (*see* **Note 4**). Always wear gloves and safety glasses when working with high concentrations of KOH.

8. Optical cleaning solution: 85% petroleum ether 15% isopropanol.

2.5 Microscopy Setup

1. To perform *d*STORM we recommend the use of an inverted wide-field TIRF microscope in combination with high NA objectives. Alexa Fluor 647 and Alexa Fluor 532 should be excited with spectrally cleaned laser lines around 640 nm and 530 nm, respectively. The laser powers should be high enough to approach irradiation intensities of ~7 kW/cm^2 at the sample. A corresponding filter cube with excitation and emission filters as well as dichroic mirror should be used to collect as much fluorescence as possible and to block unwanted excitation light in the direction of the camera. Single-photon sensitive EMCCD or sCMOS cameras with high quantum efficiency should be used.

3 Methods

3.1 Antibody and Toxin Coupling

1. Dilute lyophilized antibodies or toxins directly in cross-linking buffer to obtain solutions with concentrations around ~2 mg/mL. Higher concentrations may improve the subsequent cross-linking reaction. If the lyophilized powder already contains primary amines (e.g., Tris) reconstitute the proteins as recommended by the supplier and proceed with **step 2** to exchange the buffer with cross-linking buffer. Otherwise proceed with **step 3**.

2. Follow the protocol provided with the size-exclusion spin columns to exchange the buffer with cross-linking buffer.

3. Dilute the amine reactive NHS-modified dye in high-grade anhydrous DMSO to desired concentration. Usually, concentrations around 5–10 mM are convenient because it is still below the solubility limit of most dyes but high enough to reduce the amount of residual DMSO in the final staining solution. Incubate the dissolved dye for 15 min. at room temperature in the dark and check if it is completely solubilized. Add a 5 to 15-fold molar excess of the dye to the proteins and mix carefully by pipetting up and down a few times. Allow the cross-linking reaction to take place for at least 1 h at room temperature in the dark on a nutating mixer or use other continuous stirring. This reaction can also be performed for 4 h at 4 °C for fragile proteins.

4. Follow the protocol provided with the size-exclusion spin columns to exchange the buffer with storage buffer. Proteins more prone to denaturation can be stabilized by adding BSA at a concentration of 1–10 mg/mL.

5. Determine the degree of labeling (DOL): Measure the absorbance spectrum of the sample from 250 to 800 nm. Use storage buffer as blank and calculate the DOL with the following equation:

$$\text{DOL} = \frac{A_{\max} \times \varepsilon_{\text{prot}}}{(A_{280} - A_{\max} \times C_{280}) \times \varepsilon_{\text{prot}}}$$

where $A_{\max}$ is the absorbance maximum at the maximal absorbance wavelength of the dye. The molar extinction coefficient of the protein $\varepsilon_{\text{prot}}$ in M^{-1} cm^{-1} for a typical IgG antibody is ~210,000 M^{-1} cm^{-1} but varies depending on the protein sequence. If there is no information from the vendor one can compute the theoretical value with the ProtParam tool [9]. The theoretical molar extinction coefficient for the monomeric toxins STxB and CTxB are ~8600 M^{-1} cm^{-1} and ~10,000 M^{-1} cm^{-1}, respectively.

6. Check the functionality of your protein–fluorophore conjugate after conjugation of the dye. Depending on the cross-linking site within the protein, the binding affinity can be influenced. This can be checked by feeding the cells with the commercially available target molecules following the labeling procedure described in the next section.

3.2 Sample Preparation and Labeling

1. Prepare the glass surface for subsequent cell attachment by incubation with glass cleaning solution for at least 1 h. Wash the glass thoroughly with water to remove residual KOH and allow the surface to dry in a sterile environment. Add coating solution onto the glass surface and incubate at 37 °C for 1 h. Add enough volume to get a homogenous distribution and coating. Wash again three times with water and allow the surface to dry (*see* **Note 5**).

2. Seed cells at appropriate density in cell culture medium onto the coated glass surface and incubate for a minimum of 24 h in the incubator. To use the live-cell labeling protocol follow **step 3**. To use the fixation protocol follow **step 6** (*see* **Note 6**).

3. To perform live-cell labeling incubate the cells for 5 min. at room temperature and put them on a smooth scratch-resistant surface on ice. Incubate for 5 min on ice.

4. Wash the cells once with ice-cold live-cell labeling solution and add the conjugated toxin or antibody diluted in HBSS onto the cells. Test different concentrations in initial experiments to estimate the optimal dilution. Usually, concentrations between 1 and 5 μg/mL are sufficient. Incubate for 30 and 60 min. in the dark.

5. Wash three times with ice-cold live-cell labeling solution and fix the cells by addition of ice-cold fixation solution. Incubate for
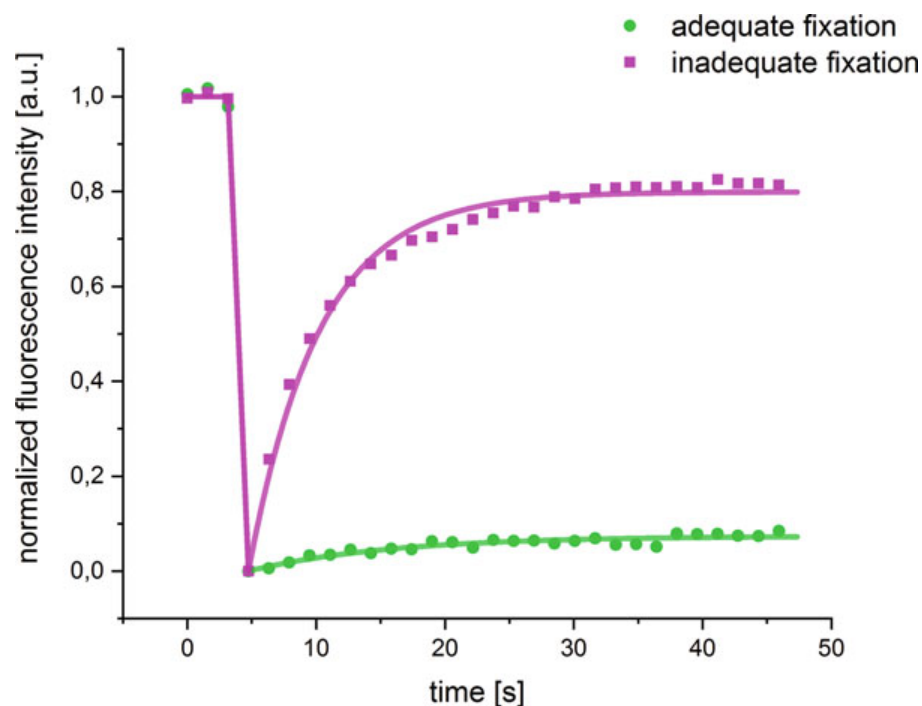
15 min. on ice and 20 min. at room temperature. Wash cells three times with PBS and perform microscopic investigations as soon as possible. 171 172 173

6. If available, perform the following step on a 37 °C prewarmed heating plate in the fume hood. Wash the cells once with 37 °C prewarmed HBSS and add prewarmed fixation solution. Incubate the cells for 20 min at 37 °C. Wash cells three times with PBS. 174 175 176 177 178

7. Add blocking buffer and incubate for 30 min at room temperature. Add the conjugated toxin or antibody diluted in blocking buffer onto the cells. Test different concentrations in initial experiments to estimate the optimal dilution. Usually, concentrations between 1 and 5 μg/mL are sufficient. Incubate for 60 min in the dark and wash three times with PBS. 179 180 181 182 183 184

8. Add fixation solution to immobilize all molecules and incubate for 20 min. Wash three times with PBS and immediately perform microscopic investigations (*see* **Note** 7). 185 186 187 188

3.3 Data Acquisition and Analysis

1. A detailed description of the principle and protocols of performing *d*STORM is provided in the literature [10–12]. The following steps should serve as guideline to perform initial experiments. Add sufficient switching buffer to the cells until they are covered and transfer the sample to the *d*STORM setup. Adjust the objective correction collar to the thickness of the cover glass and clean the glass surface and front lens of the objective by adding a few drops of optical cleaning solution onto delicate task wipes and gentle movement in one direction. Add a drop of immersion fluid on the objective and allow to form contact without introducing air bubbles. Set the focus to the basal membrane of the plasma membrane on the camera and wait for 10 min. to reduce drift. Check again the focus and proceed with the measurement. 189 190 191 192 193 194 195 196 197 198 199 200 201 202

2. Set exposure time to 20 ms and increase the laser power until fluorophores start to switch between a nonfluorescent off- and a fluorescent on-state. It is important to operate the camera in a very sensitive mode while using enough laser power to ensure efficient photoswitching (blinking) of the fluorophores. Start the measurement when single fluorophores can be detected as well separated spots and record 20,000 frames. 203 204 205 206 207 208 209

3. Spot detection and image reconstruction can be performed with several superresolution data analysis packages [13–16] which have been tested and compared recently [17]. 210 211 212 213

4 Notes

1. Some proteins are only stable in specific buffers which are not compatible with the protocol described here. For example buffers containing high amounts of stabilizing proteins or additional primary amines will impede fluorophore conjugation. In this case we recommend to apply classical two-step immunofluorescence labeling with primary and secondary fluorescent antibodies.

2. Amine reactive dyes should be used as fresh as possible and dissolved just before the experiments in anhydrous high-grade DMSO. In general, only ultrapure and sterile filtered solutions should be used. To perform *d*STORM we recommend the use of Alexa Fluor 647 or Alexa Fluor 532 NHS esters.

3. The half-life of hydrolysis of the NHS ester decreases with increasing pH of the buffer and can compete with the primary amine reaction. For less concentrated protein samples HEPES buffers with lower pH around 7.2 should be used in combination with extended cross-linking times. Note that no Tris buffered solutions should be used for cross-linking since any additional primary amines will interfere with the reaction.

4. Sodium azide may be added as a preservative but may interfere with bioorthogonal strain promoted alkyne-azide cycloaddition (SPAAC). We recommend storage in pure PBS when additional SPAAC reactions are performed. Additional information on performing SPAAC experiments in combination with superresolution microscopy are accessible in the literature [20, 21].

5. There are several different protocols for the preparation of convenient switching buffers depending on the blinking characteristics of the dyes. The mentioned switching buffer should work fine in most applications but adaption of the pH value should be considered when performing two-color measurements. Moreover, the addition of an oxygen scavenger system to deplete molecular oxygen may improve blinking characteristics for Alexa Fluor 647. A good overview about fluorophore–buffer combinations is described in the following publication [10].

6. Different cell lines may require different coating procedures to ensure appropriate cell attachment. Cells with strong adhesion capabilities usually grow without any coating and can be seeded onto the pure cleaned glass surface, which can reduce nonspecific background.

215
216
217
218
219
220
221
222
223
224
225
226
227
228
229
230
231
232
233
234
235
236
237
238
239
240
241
242
243
244
245
246
247
248
249
250
251
252
253
254
255

Jan Schlegel and Markus Sauer

Fig. 2 Residual mobility of azido-modified sphingolipid analogs [23] after fixation can be checked by FRAP. (**a**) Region of interest was bleached after three frames and intensity recovery followed over time. Magenta squares represent individual data points of an insufficiently fixed sample and green circles of an adequately fixed sample. Solid lines represent the fitted values with mobile fractions of ~80% (magenta) and ~7% (green), respectively

7. Fixation of the cells before labeling can influence the number of accessible epitopes and lead to weak permeabilization of the plasma membrane. In event of low signal or strong unwanted intracellular staining we recommend to use the live-cell labeling protocol. Since toxin binding can also influence the molecular distribution of sphingolipids in the plasma membrane we recommend to follow the fixation protocol whenever possible. In addition, plasma membrane behavior is strongly temperature dependent and low temperature specific effects might be measured.

8. To check complete immobilization of the proteins fluorescence recovery after photobleaching (FRAP) experiments can be performed on a conventional laser scanning microscope (LSM) (Fig. 2). A detailed review about studying protein dynamics can be found elsewhere [22].

118

Acknowledgments

We thank Prof. Dr. Erhard Bieberich for providing the anti-ceramide IgG antibodies. We thank Lisa Behringer-Pließ, Petra Geßner, Marcus Behringer, and Oliver Reichert for excellent technical assistance. This work was supported by the Deutsche Forschungsgemeinschaft (DFG SA829/16-2) and the IZKF (project N-375).

References

1. Heilemann M, van de Linde S, Schüttpelz M et al (2008) Subdiffraction-resolution fluorescence imaging with conventional fluorescent probes. Angew Chem Int Ed Engl 47 (33):6172–6176. https://doi.org/10.1002/anie.200802376

2. Betzig E, Patterson GH, Sougrat R et al (2006) Imaging intracellular fluorescent proteins at nanometer resolution. Science 313 (5793):1642–1645. https://doi.org/10.1126/science.1127344

3. Burgert A, Schlegel J, Bécam J et al (2017) Characterization of plasma membrane ceramides by super-resolution microscopy. Angew Chem Int Ed Engl 56(22):6131–6135. https://doi.org/10.1002/anie.201700570

4. Mizuno H, Abe M, Dedecker P et al (2011) Fluorescent probes for superresolution imaging of lipid domains on the plasma membrane. Chem Sci 2(8):1548. https://doi.org/10.1039/c1sc00169h

5. Schlegel J, Peters S, Doose S et al (2019) Super-resolution microscopy reveals local accumulation of plasma membrane gangliosides at Neisseria meningitidis invasion sites. Front Cell Dev Biol 7:194. https://doi.org/10.3389/fcell.2019.00194

6. Honigmann A, Mueller V, Ta H et al (2014) Scanning STED-FCS reveals spatiotemporal heterogeneity of lipid interaction in the plasma membrane of living cells. Nat Commun 5:5412. https://doi.org/10.1038/ncomms6412

7. Sezgin E, Schneider F, Galiani S et al (2019) Measuring nanoscale diffusion dynamics in cellular membranes with super-resolution STED-FCS. Nat Protoc 14(4):1054–1083. https://doi.org/10.1038/s41596-019-0127-9

8. Eggeling C, Ringemann C, Medda R et al (2009) Direct observation of the nanoscale dynamics of membrane lipids in a living cell. Nature 457(7233):1159–1162. https://doi.org/10.1038/nature07596

9. Walker JM (2005) The proteomics protocols handbook. Methods in molecular biology. Humana Press Inc, Totowa, NJ

10. van de Linde S, Löschberger A, Klein T et al (2011) Direct stochastic optical reconstruction microscopy with standard fluorescent probes. Nat Protoc 6(7):991–1009. https://doi.org/10.1038/nprot.2011.336

11. Heilemann M, van de Linde S, Mukherjee A et al (2009) Super-resolution imaging with small organic fluorophores. Angew Chem Int Ed Engl 48(37):6903–6908. https://doi.org/10.1002/anie.200902073

12. Endesfelder U, Heilemann M (2015) Direct stochastic optical reconstruction microscopy (dSTORM). Methods Mol Biol 1251:263–276. https://doi.org/10.1007/978-1-4939-2080-8_14

13. Wolter S, Löschberger A, Holm T et al (2012) rapidSTORM: accurate, fast open-source software for localization microscopy. Nat Methods 9(11):1040–1041. https://doi.org/10.1038/nmeth.2224

14. Ovesný M, Křížek P, Borkovec J et al (2014) ThunderSTORM: a comprehensive ImageJ plug-in for PALM and STORM data analysis and super-resolution imaging. Bioinformatics 30(16):2389–2390. https://doi.org/10.1093/bioinformatics/btu202

15. Li Y, Mund M, Hoess P et al (2018) Real-time 3D single-molecule localization using experimental point spread functions. Nat Methods 15(5):367–369. https://doi.org/10.1038/nmeth.4661

16. Franke C, Sauer M, van de Linde S (2017) Photometry unlocks 3D information from 2D localization microscopy data. Nat Methods 14 (1):41–44. https://doi.org/10.1038/nmeth.4073

17. Sage D, Pham T-A, Babcock H et al (2019) Super-resolution fight club: assessment of 2D and 3D single-molecule localization microscopy software. Nat Methods 16(5):387–395.

Jan Schlegel and Markus Sauer

367 https://doi.org/10.1038/s41592-019-0364-
368 4

369 18. Ling H, Bast D, Brunton JL et al. (2000)
370 Mutated Shiga-like toxin B subunit (G62T)

371 19. Merritt EA, Hol WGJ (2002) Cholera toxin
372 B-pentamer with ligand BMSC-0011

373 20. Mateos-Gil P, Letschert S, Doose S et al (2016)
374 Super-resolution imaging of plasma membrane
375 proteins with click chemistry. Front Cell Dev
376 Biol 4:98. https://doi.org/10.3389/fcell.
377 2016.00098

378 21. Letschert S, Goehler A, Franke C et al (2014)
379 Super-resolution imaging of plasma membrane

380 Glycans. Angew Chem Int Ed Engl 53
381 (41):10921–10924. https://doi.org/10.
382 1002/anie.201406045

383 22. Lippincott-Schwartz J, Snapp E, Kenworthy A
384 (2001) Studying protein dynamics in living
385 cells. Nat Rev Mol Cell Biol 2(6):444–456.
386 https://doi.org/10.1038/35073068

387 23. Walter T, Schlegel J, Burgert A et al (2017)
388 Incorporation studies of clickable ceramides in
389 Jurkat cell plasma membranes. Chem Commun
390 (Camb) 53(51):6836–6839. https://doi.org/
391 10.1039/c7cc01220a

3.9   Whole-Cell Imaging of Plasma Membrane Receptors by 3D Lattice Light-Sheet *d*STORM

Abstract

"The molecular organization of receptors in the plasma membrane of cells is paramount for their functionality. We combined lattice light-sheet (LLS) microscopy with three-dimensional (3D) single-molecule localization microscopy (*d*STORM) and single-particle tracking to quantify the expression and distribution, and mobility of CD56 receptors on whole fixed and living cells, finding that CD56 accumulated at cell–cell interfaces. For comparison, we investigated two other receptors, CD2 and CD45, which showed different expression levels and distributions in the plasma membrane. Overall, 3D-LLS-*d*STORM enabled imaging and single-particle tracking of plasma membrane receptors with single-molecule sensitivity unperturbed by surface effects. Our results demonstrate that receptor distribution and mobility are largely unaffected by contact to the coverslip but the measured localization densities are in general lower at the basal plasma membrane due to partial limited accessibility for antibodies." [120]

The following manuscript was published on February 14th, 2020 in Nature Communications and permission for legal second publication within this thesis was kindly granted from both the publishers and the co-authors.

Whole-cell imaging of plasma membrane receptors by 3D lattice light-sheet *d*STORM

Felix Wäldchen[1,3], Jan Schlegel [1,3], Ralph Götz[1], Michael Luciano[2], Martin Schnermann[2], Sören Doose [1] & Markus Sauer [1✉]

The molecular organization of receptors in the plasma membrane of cells is paramount for their functionality. We combined lattice light-sheet (LLS) microscopy with three-dimensional (3D) single-molecule localization microscopy (*d*STORM) and single-particle tracking to quantify the expression and distribution, and mobility of CD56 receptors on whole fixed and living cells, finding that CD56 accumulated at cell–cell interfaces. For comparison, we investigated two other receptors, CD2 and CD45, which showed different expression levels and distributions in the plasma membrane. Overall, 3D-LLS-*d*STORM enabled imaging and single-particle tracking of plasma membrane receptors with single-molecule sensitivity unperturbed by surface effects. Our results demonstrate that receptor distribution and mobility are largely unaffected by contact to the coverslip but the measured localization densities are in general lower at the basal plasma membrane due to partial limited accessibility for antibodies.

---

[1] Department of Biotechnology and Biophysics, Biocenter, University of Würzburg, Am Hubland, 97074 Würzburg, Germany. [2] Chemical Biology Laboratory, Center for Cancer Research, National Cancer Institute, Frederick, MD 21702, USA. [3] These authors contributed equally: Felix Wäldchen, Jan Schlegel. ✉email: m.sauer@uni-wuerzburg.de

Since the beginning of the twentieth century, the role of receptors in modulating cellular processes has been studied extensively worldwide. Numerous drugs that specifically bind to receptors have been developed and are being used in established therapies[1]. To fully exploit the possibilities of receptor-targeted therapies, quantitative information about receptor expression, distribution, and mobility in the plasma membrane is required. Localization microscopy delivers single-molecule information about molecular compositions, spatial distributions, and about absolute numbers of proteins present in subcellular compartments[2]. Thus, important insights into the molecular organization of biological systems, e.g., the expression, distribution, and mobility of therapeutically addressable receptors in the plasma membrane of tumor cells, can be gained[3].

Single-molecule imaging of plasma membrane molecules is commonly performed at the bottom plasma membrane at the coverslip/cell interface (referred to as the basal membrane) based on total internal reflection fluorescence (TIRF) microscopy[4,5]. However, such experiments have also raised questions to which extent the molecular organization and mobility of receptors on the basal plasma membrane is affected by contact to a glass surface. This has led to the use of light-sheet single-molecule microscopy to illuminate non-coverslip contacting regions and study membrane organization of T cells on the upper (apical) membrane[6,7]. Light-sheet illumination uses a separate set of optics to illuminate only a thin volume of the cell that corresponds to the focal plane of the detection objective, thus increasing the signal-to-noise ratio in single-molecule imaging and tracking experiments, and restricting photobleaching of dyes and photodamage of cells to a thin volume[6–8].

The ideal light-sheet configuration enables whole-cell three-dimensional (3D) single-molecule localization and tracking, and excites only those molecules that can be detected at the same time. To fulfill these requirements, we used lattice light-sheet (LLS) microscopy[9–12] in combination with single-molecule localization microscopy (SMLM), by direct stochastic optical reconstruction microscopy (*d*STORM)[13] or photoactivated localization microscopy (PALM)[14] and single-particle tracking for whole-cell 3D imaging of plasma membrane receptors[15,16]. LLS microscopy in combination with SMLM by points accumulation for imaging in nanoscale topography (PAINT) has already produced impressive images from thick samples including dividing cells and at the periphery of small embryos[10]. However, PAINT microscopy often leads to nonlinear swelling due to dye accumulation and requires acquisition times of up to several days, because labels continually bind to the specimen throughout the imaging process[10]. Although LLS-PAINT is suited for the study of densely crowded specimens, receptor imaging on the plasma membrane of whole cells does not exhibit such challenging conditions. Therefore, we use Alexa Fluor 647, the bridged carbocyanine dye Cy5B, and SeTau647-labeled primary antibodies for SMLM imaging and single-particle tracking, respectively, of plasma membrane receptors on fixed and living 293T cells. Although the carbocyanine dye Alexa Fluor 647 is the favorite dye for *d*STORM[17], Cy5B fluorescence can be efficiently recovered from hydride reduction enabling PALM-like SMLM in oxygenated buffer with high localization precision[18]. The squaraine rotaxane dye SeTau647 exhibits a high photostability, enabling recording of long single-molecule trajectories[19]. The 3D whole-cell SMLM images of three different plasma membrane receptors (CD56, CD2, and CD45) show that contact to the coverslip does not induce receptor clustering. Receptor distribution and mobility are largely unaffected by contact to the coverslip. However, our data disclose that localization densities are in general lower at the basal plasma membrane, and CD56 and CD45 accumulate at cell–cell interfaces.

Results and Discussion

3D-LLS-*d*STORM of plasma membrane molecules. The neural cell adhesion molecule (NCAM), also known as CD56, is an important pathogen recognition receptor on human natural killer cells[20,21] and is involved in fundamental biological processes including cell–cell adhesion, learning, and memory. To explore the distribution of CD56 on the plasma membrane of fixed cells unperturbed by coverslip interactions, we used astigmatic 3D-LLS-*d*STORM and Alexa Fluor 647-labeled primary antibodies (Supplementary Fig. 1). Using astigmatic 3D-*d*STORM in combination with cubic spline interpolated point-spread functions (PSFs)[16], the axial detection range fully covers the axial irradiation volume defined by the light-sheet thickness of ~1.4 μm (Supplementary Fig. 2). To localize receptors on the whole plasma membrane of 293T cells, the sample was scanned through the LLS repetitively at 40 nm steps, while continuously acquiring images (Fig. 1, Supplementary Fig. 3, and Supplementary Movies 1 and 2). This resulted in a total acquisition time of 191 min for a volume of $53.1\,\mu m \times 26.6\,\mu m \times 40.0\,\mu m$ (x, y, z), corresponding to a volume perpendicular to the coverslip of $47.5\,\mu m \times 52.5\,\mu m \times 11.7\,\mu m$ in the "biological coordinate system" (x', y', z') (Supplementary Fig. 1). We determined an experimental localization precision from more than 294,000 localizations of Alexa Fluor 647 blinking events of 16 nm in x, 17 nm in y, and 74 nm in z-direction, or when estimated after rotation to the biological coordinate system of 20 nm and 14 nm in the coverslip plane (x', y') and 38 nm in z'-direction (Supplementary Figs. 1, 4, and 5).

The 3D volume rendering of reconstructed localizations of 293T cells showed a heterogeneous distribution of CD56 receptors with a distinct accumulation at cell–cell interfaces (Fig. 1a and Supplementary Fig. 3a). Maximum-intensity projections of membranes illustrated the accumulation of CD56 receptors at cell–cell interfaces. The localization densities of CD56 at cell–cell interfaces of (1234 ± 146) and (2034 ± 350) localizations/μm^2 (median ± median absolute deviation) was approximately twice as dense as it would be expected for two contacting apical membranes with densities of (361 ± 79) and (544 ± 80) localizations/μm^2. The substantially lower localization densities measured at the basal plasma membranes of (138 ± 76) and (189 ± 97) localizations/μm^2 indicate inefficient antibody labeling at basal cell membranes (Fig. 1e and Supplementary Fig. 3b).

For comparison, we measured the surface expression of two other plasma membrane receptors: CD2[22], another cell adhesion molecule found on the surface of T cells, and CD45, the receptor-like transmembrane protein tyrosine phosphatase that is highly expressed on all nucleated hematopoietic cells[23]. The 3D-LLS-SMLM images showed that the expression of CD2 and CD45 on Jurkat T cells is lower than the expression of CD56 on 293T cells and is homogeneously distributed (Supplementary Figs. 6 and 7, and Supplementary Movies 3 and 4). A closer inspection of the localization densities revealed a higher CD2 density at the apical membrane $(134 \pm 25$ localizations/$\mu m^2)$ compared with the densities at the basal membrane $(23 \pm 9$ localizations/$\mu m^2)$ and a lower density at the cell–cell interface $(76 \pm 14$ localizations/$\mu m^2)$ (Supplementary Fig. 6). As measured for the other plasma membrane molecules, CD45 showed localization densities of $(47 \pm 6$ localizations/$\mu m^2)$ on the basal and slightly higher densities on the apical membrane $(63 \pm 8$ localizations/$\mu m^2)$, but in contrast to CD2, a pronounced accumulation at cell–cell interfaces $(218 \pm 25$ localizations/$\mu m^2)$ as also measured for CD56 (Supplementary Fig. 7). Overall, these data demonstrate that the measured localization densities are in general lower at the basal plasma membrane of adherent cells most probably due to inefficient labeling with IgG antibodies.

Strikingly, 3D-LLS-*d*STORM images and movies of CD56, CD2, and CD45 showed some smaller localization clusters that do

123
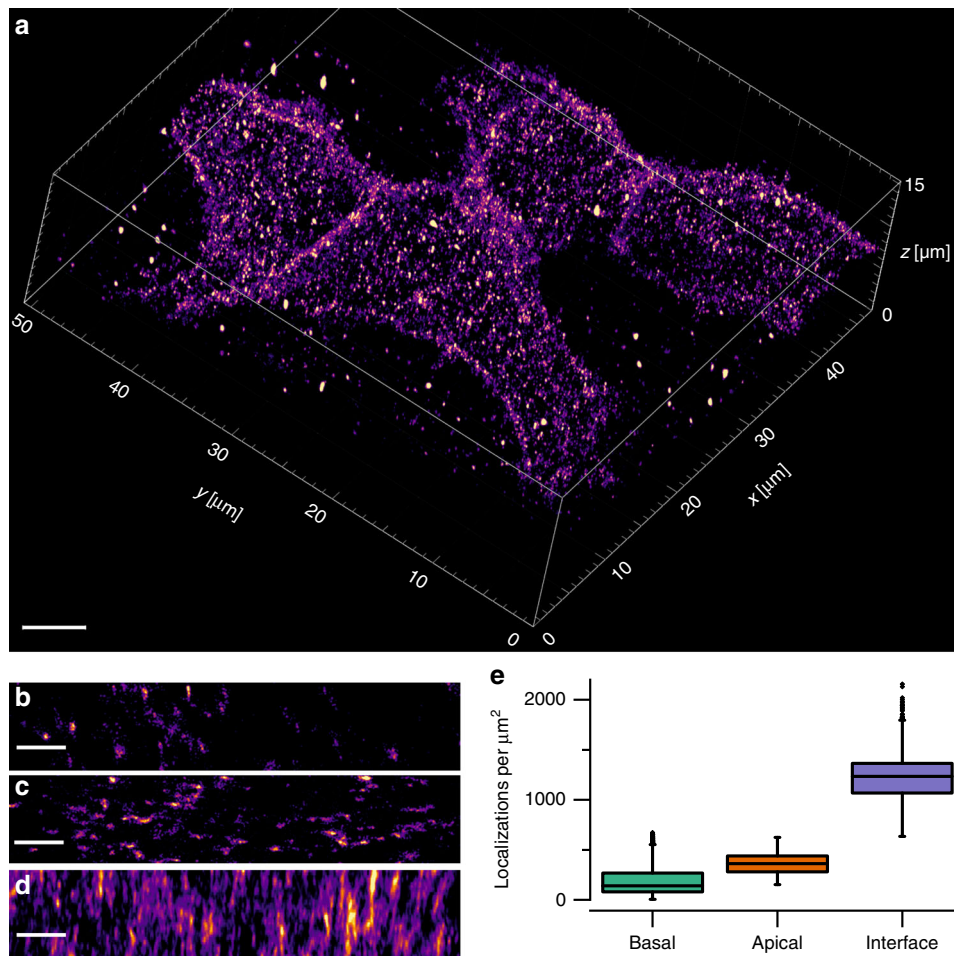
Fig. 1 Visualizing the distribution of CD56 receptors in the plasma membrane of fixed whole 293T cells by 3D-LLS-dSTORM. a Reconstructed volume rendering of single-molecule localizations shows considerable accumulation of CD56 receptors at cell–cell interfaces between the three cells. Representative 2D *xy*-projections of small areas of the basal (**b**) and apical (**c**) plasma membrane. Representative 2D projection perpendicular to the *z*-axis highlighting the increased CD56 density and the cell–cell interface (**d**). Note the lower spatial resolution in *z*-direction. **e** Localization densities (median ± MAD) measured at the basal (139 ± 76 localizations/μm^2) and apical plasma membrane (361 ± 79 localizations/μm^2), and at the cell–cell interface (1234 ± 146 localizations/μm^2) for the shown cell. Boxplot of $n = 7201$ (basal), $n = 854$ (apical), and $n = 628$ (interface) sliding window data points. Boxplots show median (center line), 25th and 75th percentile (box), and 1.5× interquartile range (whiskers). Scale bars, 5 μm (**a**), 1 μm (**b**–**d**).

not appear in 2D-*d*STORM images recorded from the basal plasma membrane by TIRF microscopy (compare Fig. 1 and Supplementary Figs. 3, 6, and 7). In 2D-TIRF-*d*STORM images, the receptors are homogeneously distributed and do not exhibit any sign of accumulation (Supplementary Fig. 8). Cross-sections of the basal, apical, and equatorial planes of CD2-, CD45-, and CD56-labeled cells and a close look at the 3D-LLS-*d*STORM movies showed that receptors are also localized intracellularly (Supplementary Fig. 9 and Supplementary Movies 1, 2, and 4), indicating that antibody binding induced endocytosis of receptors occurs (even though labeling was performed at 4 °C, see Online Methods) or antibodies might penetrate through membrane defects. The appearance of intracellular clusters in 3D-LLS-*d*STORM experiments depends strongly on the receptor investigated and typically varied between different experiments (Supplementary Fig. 9).

Single-particle tracking by 3D-LLS microscopy. Accumulation of receptors at cell–cell interfaces requires a high mobility in the plasma membrane. To investigate the mobility of CD56 in the basal plasma membrane of living 293T cells, we first performed two-dimensional (2D) single-particle tracking experiments using SeTau647[19]-labeled primary antibodies on poly-D-lysine-coated and untreated, cleaned coverslips by TIRF microscopy. In these experiments, the mobility of CD56 receptors showed a dramatic decrease when changing from cleaned coverslips to poly-D-lysine coating (Supplementary Fig. 10), which seriously complicates data analysis and interpretation. To exclude any interference of the measured mobility by surface effects, we used 3D-LLS microscopy to track CD56 receptors on the plasma membrane at 37 °C (Fig. 2). Single particles were tracked in 3D using astigmatic imaging, but without sample scanning. 3D-LLS microscopy allowed us to follow CD56 receptors on the fluid-exposed faces of the plasma membrane unperturbed by glass surface interactions. For quantification of diffusion dynamics, we analyzed the mean square displacement (MSD) $< \Delta x^2 >$ in each dimension[15,24–26]. Although the overall data (Fig. 2) hints at some deviation from the linear time dependence that would be observed for free diffusion, we focused the quantitative analysis on the most reliable first five data points that could be fitted well to a model function for free diffusion. In living 293T cells, individual CD56 signals on the apical and equatorial plasma membranes exhibited a diffusion constant of 0.058, 0.059, and 0.023 μm^2/s in *x*, *y*, and *z*, respectively, and offsets reflecting the localization precision of a few tens of nanometer (Fig. 2). Next, we added CK666 to the imaging buffer, a cell-permeable molecule that binds to the actin-related

124
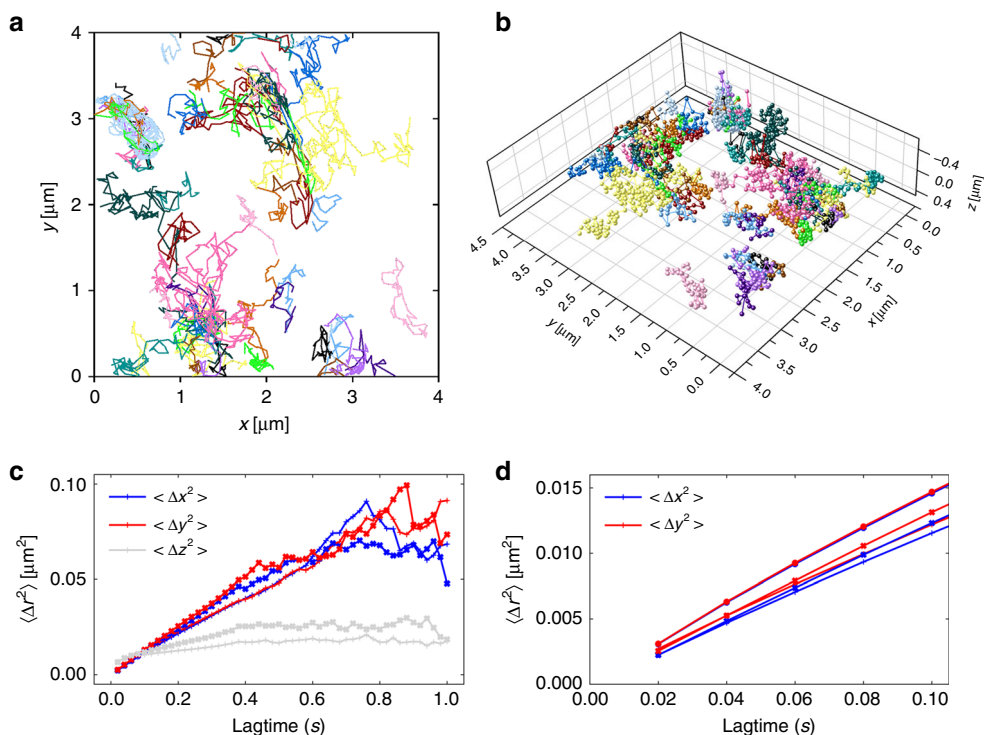
Fig. 2 Single-particle tracking in living cells by LLSM. a Trajectories of CD56 molecules in the plasma membrane of 293T cells measured at 37 °C. **b** Astigmatic detection enables tracking of CD56 receptors in 3D. **c** The ensemble mean square displacement for each dimension $r \in (x, y, z)$ for all trajectories with (cross symbols) and without (plus symbols) actin inhibitor CK666. $n = 7$ different cells were tracked for each condition. Each cell yielded an ensemble of >100 trajectories. **d** Ensemble mean square displacement zoomed to the part from which diffusion constants were determined by fitting a linear function. In addition to the LLS microscopy data ($n = 7$ tracking experiments examined from different cells of one biological sample), 2D-TIRF data are shown for 293T cells ($n = 6$ tracking experiments examined from different cells of one biological sample) adhered on cleaned coverslips (circle symbols).

protein Arp2/3 complex and inhibits actin assembly[27,28], and thus might influence the mobility of CD56 in the plasma membrane. However, we found only slightly increased diffusion constants of 0.06, 0.065, and 0.032 $\mu m^2/s$, respectively, for the fast diffusion component. This effect is consistent with observations from fluorescence recovery after photobleaching (FRAP)[29] experiments. FRAP data measured from cell–cell interfaces also indicated only minor insignificant variation in the measured time constants and the mobile fraction (Supplementary Fig. 11 and Supplementary Movie 5).

Overall, the NCAM CD56 works as a kind of glue that not only mediates cell–cell adhesion but also induces activation of a complex network of intracellular signaling cascades[21,22,30,31]. To fulfill its task, CD56 has to be mobile in the plasma membrane to move efficiently towards cell–cell contact areas and connect the two cells via trans-interactions. Using 3D-LLS microscopy in combination with SMLM (Fig. 1) and single-particle tracking (Fig. 2), we showed that CD56 receptors exhibit diffusional mobility in the plasma membrane and accumulate at cell–cell interfaces.

To summarize, we have demonstrated that 3D-LLS microscopy in combination with SMLM and single-particle tracking offers a unique and robust method to determine the distribution and mobility of plasma membrane receptors on whole cells unperturbed by surface effects. Tracking experiments in a LLS microscope will be helpful when studying cell types that do not adhere strongly on uncoated coverslides. Our results show that the labeling efficiency and mobility of plasma membrane molecules can be influenced by a direct contact to the coverslip (Figs. 1 and 2, and Supplementary Fig. 3) but their distribution in the membrane remains largely unaffected. Epi-fluorescence approaches have successfully demonstrated their potential for

3D SMLM deep within intact tissue using self-interference and active PSF shaping[32,33]; however, they irradiate the whole volume during the entire experiments and thus cause out-of-focus fluorescence background, reduced signals due to photobleaching of fluorophores, and photodamage in live-cell experiments. Hence, a combination of these methods with LLS microscopy will pave the way for quantitative, single-molecule sensitive 3D receptor imaging also within the tissue. Single-molecule sensitive 3D-LLSM approaches might be ideally suited to study the dynamic molecular organization of immunological synapses formed at the interface between antigen-presenting and T cells.

Methods

Cell culture and fluorescence labeling. The 293T cells (German Collection of Microorganisms and Cell Cultures, Braunschweig, Germany; #ACC635) were cultured in Dulbeccos's modified Eagle's medium (DMEM, Sigma-Aldrich, #D5796) with 10% fetal calf serum (FCS) (Sigma-Aldrich, #F7524), 1% L-Glutamine (already in DMEM suppl.), and 1% Pen-Strep (Sigma-Aldrich, #P4333) at 5% CO_2 atmosphere and 37 °C. For single-molecule experiments, ~4×10^4 cells were seeded onto poly-D-lysine-coated 5 mm coverslips the day before staining. The LEAF™ purified monoclonal mouse anti-human CD56 antibody (clone: HCD56, Biolegend, #318324) was conjugated with SeTau-647-NHS (SETA BioMedicals, #K9-4149) in 100 mM $NaHCO_3$ buffer to obtain a degree-of-labeling (DOL) of ~1.7 and was stored in phosphate-buffered saline (PBS) with 0.05% sodium azide. Cells were washed with FluoroBrite™ DMEM (Gibco™ #A1896701) and labeled with 0.33 nM of the SeTau-647-conjugated antibody for 5 min at 37 °C. After two additional washing steps, single-particle tracking was performed in FluoroBrite DMEM supplemented with 170 μM CK666 (Sigma, #SML0006) or DMSO as control. For 3D-dSTORM, cells were grown on poly-D-Lysine-coated 5 mm coverslips for 24 h. The CD56 antibody was conjugated with Alexa Fluor™ 647-NHS ester (Invitrogen™) in 100 mM $NaHCO_3$ to obtain a DOL of ~2.3 as determined by absorption spectroscopy. Cells were washed and stained with 10 μg/ml of the Alexa Fluor™ 647-conjugated antibody in FluoroBrite on ice for 40 min. After two washing steps, cells were fixed with 2% formaldehyde and 0.2% glutaraldehyde for 15 min on ice and additional 15 min at room temperature followed by three additional washing steps. Jurkat T-cells were grown in RPMI 1640 media

supplemented with 10% FCS, 1 mM L-glutamine, 100 U/ml penicillin, and 0.1 mg/ml streptomycin at 37 °C and 5% CO$_2$. For imaging, 1.5×10^5 cells per well were seeded in poly-D-lysine-coated chamber slides (Lab-Tek II, Nunc, Thermo Fisher Scientific) and allowed to adhere at 37 °C at 5% CO$_2$ for 1 h. Fifty micrograms of monoclonal anti-human primary antibodies directed against CD2 (Biolegend; TS1/8, 309202) and CD45 (Biolegend, 2D1; 368502) were incubated in a 5 molar excess of Cy5B-NHS[18] or Alexa Fluor™ 647-NHS (Invitrogen™), respectively, in 100 mM NaHCO$_3$ at room temperature for 3 h in the dark. To remove unreacted dyes and to exchange the buffer to 0.02 NaN$_3$ dissolved in PBS, the antibodies were purified with 0.5 ml 7 kDa Spin Desalting Columns (Thermo Fisher, 89882). Finally, the DOL of the purified antibody was determined by a UV-VIS spectrophotometer (Jasco V-650) to ~3–4. Conjugated antibodies were stored at 4 °C. Live-cell staining was performed on ice (~4 °C) for 45 min using an antibody concentration of 5 µg/ml in PBS. After washing, the cells were fixed for 15 min in 4% formaldehyde and 0.2% glutaraldehyde. Following three more washing steps, the cells were stored in PBS at 4 °C until imaging at room temperature.

Lattice light-sheet microscopy. The LLS microscope was configured and operated similar to the one described in Chen et al.[9] and Legant et al.[10]. To accommodate 3D-*d*STORM measurements and to benefit from commercial components, we made several modifications to the system. First, we used a 2 W 647 nm continuous wave laser (MPB Communications 2RU-VFL-p-2000-647-B1R) to produce an illumination intensity of 3.6 kW/cm^2 at the sample for optimal photoswitching of Alexa Fluor 647[13,17], and photoactivation and localization of Cy5B[18]. The laser was filtered by a clean-up filter (Chroma Technology Corporation ZET642/20×) and expanded to a $1/e^2$ diameter of 2.5 mm with a set of two lenses (Thorlabs C240TME-A and Edmund Optics 47-661). The spatial light modulator (Forth Dimension Displays QXGA-3DM) has smaller pixels (50.7 nm at the sample) and slightly faster switching times. For scanning of the light sheet, we used improved galvanometer mirrors (Cambridge Technology 8315K). The illumination objective (Special Optics, 0.70 numerical aperture (NA), 3.74 mm WD, part number 54-10-7) has a slightly increased NA. On the detection path, the system is equipped with a dichroic mirror (Chroma Technology Corporation ZT405/488/561/640rpc) and quad-band emission filter (Chroma Technology Corporation ZET405/488/561/640m). Single-molecule fluorescence signals were detected using a sCMOS camera (Hamamatsu Orca Flash 4.0 v3) connected to a water cooler (Innovatek AQ240-Pro), to eliminate vibrations. For single-color measurements conducted in this work, a long-pass filter (Chroma Technology Corporation ET655lp) was added directly in front of the camera. The pixel size at the sample was 103.8 nm. To further enhance the stability of the system, we built a custom light-tight enclosure around the whole microscope. Additional parts of the illumination and detection path were shielded with custom-made 3D printed parts to increase laser safety and light tightness. For illumination, a dithered, maximally symmetric fundamental square lattice with a minimum NA of 0.42 and a maximum NA of 0.50 was used, as it confines the excitation best to the depth of field of the detection objective (Nikon CFI Apo LWD 25XW, 1.1 NA), thereby reducing out-of-focus excitation and background fluorescence. At the same time, the light-sheet length of 15 µm, determined by the maximum NA, is ideally suited for the height of typical 293T cells. The light-sheet thickness was measured to 1.4 µm (Supplementary Fig. 2).

3D-*d*STORM imaging and density calculation. For *d*STORM imaging (Fig. 1), 293T cells were labeled as described above. The sample bath was filled with photoswitching buffer: PBS with 100 mM β-mercaptoethylamine (Sigma-Aldrich), 0.4% (w/v) glucose, and 0.4% glucose oxidase, adjusted to pH 7.4[13,17]. 3D-LLS-SMLM imaging of Cy5B-labeled receptors was performed in PBS buffer using solely 647 nm excitation[18]. Before imaging, the sample was reduced for 20–30 min in 26 mM NaBH$_4$ and washed three times with 1× PBS. Upon irradiation at 647 nm, individual Cy5B molecules are spontaneously photoactivated and localized. Photoactivated fluorophores reside in their fluorescent state until they are photobleached[18]. Images were acquired at 50 Hz including the stepping motion, whereas the sample was scanned by 40 nm per frame in a saw tooth motion along *s* (*s* direction; Supplementary Fig. 1a). The stepping motion was performed during read-out of the camera. One thousand and one frames comprise one image stack, after which the acquisition repeats for a total of 573 stacks resulting in $1001 \times 573 = 573{,}573$ frames. SMLM processing was performed using the super-resolution microscopy analysis platform[16] and the corresponding graphics processing unit (GPU)-accelerated Matlab software (available at https://github.com/jries/SMAP-light) after the measurement. Localization coordinates were corrected for sample scanning by subtracting the known shift. For 3D calibration, 100 nm fluorescent beads (TetraSpeck™ T7279, Thermo Fisher) were coated on a coverslip and imaged using the same buffer conditions. In Fig. 1, a total of 3.2×10^6 localizations were detected of which 0.7×10^6 were localized outside the 1.4 µm range illuminated by the light sheet or filtered with a minimum photon threshold and discarded. We did not use track emission to correct for overcounting. To correct for sample scanning during acquisition and to rotate the volume to coverslip plane, custom software was developed in Python. Rendering 2D images and histograms for density analysis was done using ThunderSTORM[34] and FIJI[35]. To measure the densities at different parts of the cell membrane, a sliding window algorithm with a window size of 2 µm × 2 µm and a step size of 0.2 µm was implemented in FIJI. For rendering 3D volumes, Imaris (Bitplane) was used.

Single-particle tracking. For single-particle tracking, cells were labeled as described above. The LLS microscope's sample chamber was heated to 37 °C for at least 24 h before starting the experiments. For capturing single-particle dynamics, image sequences were acquired with 20 ms exposure time in a single plane. The data were fitted with a 3D PSF as already described and the resulting 3D molecule positions were linked to tracks using Trackpy[36], a Python implementation of the popular Crocker–Grier algorithm[37]. For each measurement, the MSDs $<\Delta x^2>$ of all tracks with a length of at least 20 frames were calculated and the resulting ensemble MSD was fit at small lag times with a linear function[15,24–26]

$$<\Delta x^2>(\tau) = o + 2D\tau$$

Here, *o* is an offset resembling the square of the localization precision, *D* is the diffusion constant, and *τ* is the lag time.

FRAP analysis. The 293T cells were seeded into eight-well chambered cover glass (Cellvis, #C8-1.5H-N) and labeled after 24 h with 10 µg/ml Alexa Fluor™ 647-conjugated antibody in FluoroBrite for 10 min at 37 °C. FRAP experiments were performed on a confocal microscope (Zeiss LSM700) using the Plan-Apochromat 63 × 1.4 oil-immersion objective and 2% 639 nm solid-state laser excitation intensity for image acquisition. Every 1.5 s an image was recorded for a total acquisition time of 120 s and after three initial images a bleaching step was performed using 100% laser intensity of the 639 nm and 555 nm laser with a pixel dwell time of 37.6 µs. Frame size, bleaching area, as well as laser intensities and imaging speed was kept constant for all FRAP experiments. All experiments were performed at 37 °C and 5% CO$_2$ using a stage top incubator (Tokai Hit). FRAP data were analyzed with the software Zen system 2012 and custom-made python code.

Statistics and reproducibility. In all boxplots, the middle line is the median and the lower and upper hinges correspond to the first and third quartiles, respectively. The upper (and lower) whisker is drawn up to the largest (and smallest) observed data point within 1.5 times the interquartile range. Individual data points beyond the end of the whiskers represent all outliers. If not stated otherwise, 3D-LLS-*d*STORM data were acquired once from one biological sample, analyzed, and shown. Supplementary Fig. 10 depicts one from six and nine individual 2D single-particle tracking experiments examined from different cells of one biological sample for cleaned glass and poly-D-lysine coating, respectively. Supplementary Fig. 11 shows 1 from 12 individual FRAP experiments examined from different cells of one biological sample.

Reporting summary. Further information on research design is available in the Nature Research Reporting Summary linked to this article.

Data availability
All data that support the findings described in this study are available within the manuscript and the related Supplementary Information, and from the corresponding authors upon reasonable request.

References

1. Overington, J. P., Al-Lazikani, B. & Hopkins, A. L. How many drug targets are there? *Nat. Rev. Drug Discov.* **5**, 993–996 (2006).
2. Sauer, M. & Heilemann, M. Single-molecule localization microscopy in eukaryotes. *Chem. Rev.* **117**, 7478–7509 (2017).
3. Del Paggio, J. C. Immunotherapy: cancer immunotherapy and the value of cure. *Nat. Rev. Clin. Oncol.* **15**, 268–270 (2018).
4. Rossy, J., Owen, D. M., Williamson, D. J., Yang, Z. & Gaus, K. Conformational states of the kinase Lck regulate clustering in early T cell signaling. *Nat. Immun.* **14**, 82–89 (2013).
5. Baumgart, F. et al. Varying label density allows artifact-free analysis of membrane-protein nanoclusters. *Nat. Methods* **13**, 661–664 (2016).
6. Hu, Y. S., Cang, H. & Lillemeier, B. F. Superresolution imaging reveals nanometer- and micrometer-scale spatial distributions of T-cell receptors in lymph nodes. *Proc. Natl Acad. Sci. USA* **113**, 7201–7206 (2016).
7. Ponjavic, A. et al. Single-molecule light-sheet imaging of suspended T cells. *Biophys. J.* **114**, 2200–2211 (2018).
8. Gustavsson, A.-K., Petrov, P. N., Lee, M. Y., Shechtman, Y. & Moerner, W. E. 3D single-molecule super-resolution microscopy with a tilted light sheet. *Nat. Commun.* **9**, 123 (2018).
9. Chen, B.-C. et al. Lattice light-sheet microscopy: imaging molecules to embryos at high spatiotemporal resolution. *Science* **346**, 1257998 (2014).
10. Legant, W. R. et al. High-density three-dimensional localization microscopy across large volumes. *Nat. Methods* **13**, 359–365 (2016).

11. Liu, Z. et al. 3D imaging of Sox2 enhancer clusters in embryonic stem cells. *eLife* **3**, e04236 (2014).
12. Lu, C.-H. et al. Lightsheet localization microscopy enables fast, large-scale, and three-dimensional super-resolution imaging. *Commun. Biol.* **2**, 177 (2019).
13. Heilemann, M. et al. Subdiffraction-resolution fluorescence imaging with conventional fluorescent probes. *Angew. Chem. Int. Ed.* **47**, 6172–6176 (2008).
14. Shroff, H. et al. Dual-color superresolution imaging of genetically expressed probes within individual adhesion complexes. *Proc. Natl Acad. Sci. USA* **104**, 20308–20318 (2008).
15. Shen, H. et al. Single particle tracking: from theory to biophysical applications. *Chem. Rev.* **117**, 7331–7376 (2017).
16. Li, Y. et al. Real-time 3D single-molecule localization using experimental point spread functions. *Nat. Methods* **15**, 367–369 (2018).
17. van de Linde, S. et al. Direct stochastic optical reconstruction microscopy with standard fluorescent probes. *Nat. Protoc.* **6**, 991–1009 (2011).
18. Michie, M. S. et al. Cyanine conformational restraint in the far-red range. *J. Am. Chem. Soc.* **139**, 12406–12409 (2017).
19. Tsunoyama, T. A. et al. Super-long single-molecule tracking reveals dynamic-anchorage-induced integrin function. *Nat. Chem. Biol.* **14**, 497–506 (2018).
20. Van Acker, H. H., Capsomidis, A., Smits, E. L. & Van Tendeloo, V. F. CD56 in the immune system: more than a marker for cytotoxicity? *Front. Immunol.* **8**, 892 (2017).
21. Ziegler, S. et al. CD56 is a pathogen recognition receptor on human natural killer cells. *Sci. Rep.* **7**, 6138 (2017).
22. Murray, A. J., Lewis, S. J., Barclay, A. N. & Brady, R. L. One sequence, two folds: a metastable structure of CD2. *Proc. Natl Acad. Sci. USA* **91**, 7337–7341 (1995).
23. Zamoyska, R. et al. Why is there so much CD45 on T cells? *Immunity* **27**, 421–423 (2007).
24. Manzo, C. & Garcia-Parajo, M. F. Reports on progress in physics. *Phys. Soc. (Gt. Br.)* **78**, 124601 (2015).
25. Wieser, S. & Schütz, G. J. Tracking single molecules in the live cell plasma membrane—do's and don't's. *Methods* **46**, 131–140 (2008).
26. Michalet, X. Mean square displacement analysis of single-particle trajectories with localization error: Brownian motion in an isotropic medium. *Phys. Rev. E Stat. Nonlin. Soft Matter Phys.* **82**, 041914 (2010).
27. Hetrick, B., Hans, M. S., Helgeson, L. A. & Nolen, B. J. Small molecules CK-666 and CK-869 inhibit actin-related protein 2/3 complex by blocking an activating conformational change. *Chem. Biol.* **20**, 701–712 (2013).
28. Firat-Karalar, E. N. & Welch, M. D. New mechanisms and functions of actin nucleation. *Curr. Opin. Cell Biol.* **23**, 4–13 (2011).
29. Reits, E. A. J. & Neefjes, J. J. From fixed to FRAP: measuring protein mobility and activity in living cells. *Nat. Cell Biol.* **3**, E145–E147 (2001).
30. Kulahin, N. et al. Direct demonstration of NCAMcis-dimerization and inhibitory effect of palmitoylation using the BRET2technique. *FEBS Lett.* **585**, 58–64 (2011).
31. Soroka, V. et al. Structure and interactions of NCAM Ig1-2-3 suggest a novel zipper mechanism for homophilic adhesion. *Structure* **11**, 1291–1301 (2003).
32. Bon, P. et al. Self-interference 3D super-resolution microscopy for deep tissue investigations. *Nat. Methods* **15**, 449–454 (2018).
33. Mlodzianoski, M. J. et al. Active PSF shaping and adaptive optics enable volumetric localization microscopy through brain sections. *Nat. Methods* **15**, 583–586 (2018).
34. Ovesný, M., Křížek, P., Borkovec, J., Svindrych, Z. & Hagen, G. M. ThunderSTORM: a comprehensive ImageJ plug-in for PALM and STORM data analysis and super-resolution imaging. *Bioinformatics (Oxf., Engl.)* **30**, 2389–2390 (2014).
35. Schindelin, J. et al. Fiji: an open-source platform for biological-image analysis. *Nat. Methods* **9**, 676–682 (2012).
36. Allan, D., Caswell, T., Keim, N. & van der Wel, C. *Trackpy: Trackpy V0.3.2* (Zenodo, 2016).
37. Crocker, J. C. & Grier, D. G. Methods of digital video microscopy for colloidal studies. *J. Colloid Interface Sci.* **179**, 298–310 (1996).

Acknowledgements

Author contributions

F.W., J.S., and M. Sauer conceived and designed the project. M. Sauer supervised the project. J.S. performed all labeling and 2D tracking experiments. R.G. performed 2D-dSTORM experiments. F.W. built the lattice light-sheet microscope and performed all 3D-dSTORM experiments. F.W., J.S., and S.D. performed data analysis. M.L. and M. Schnermann provided fluorophores. F.W., J.S., S.D., and M. Sauer wrote and commented on the paper.

Competing interests

The authors declare no competing interests.

Additional information

3.10   Reconstituting NK Cells after Allogeneic Stem Cell Transplantation Show Impaired Response to the Fungal Pathogen *Aspergillus fumigatus*

Abstract

"Delayed natural killer (NK) cell reconstitution after allogeneic stem cell transplantation (alloSCT) is associated with a higher risk of developing invasive aspergillosis. The interaction of NK cells with the human pathogen *Aspergillus (A.) fumigatus* is mediated by the fungal recognition receptor CD56, which is relocated to the fungal interface after contact. Blocking of CD56 signaling inhibits the fungal mediated chemokine secretion of MIP-1α, MIP-1β, and RANTES and reduces cell activation, concluding a functional role of CD56 in fungal recognition. We collected peripheral blood of recipients of an allograft on defined time points after alloSCT (day 60, 90, 120, 180). NK cells were isolated, directly challenged with live *A. fumigatus* germ tubes, and cell function was analyzed and compared to healthy individuals. After alloSCT, NK cells displayed a higher percentage of CD56$^{\text{bright}}$CD16$^{\text{dim}}$ cells throughout the time of blood collection. However, CD56 binding and relocalization to the fungal contact side were decreased. We could correlate this deficiency to the administration of corticosteroid therapy that further negatively influenced the secretion of MIP-1α, MIP-1β, and RANTES. As a consequence, the treatment of healthy NK cells *ex vivo* with corticosteroids abrogated chemokine secretion measured by multiplex immunoassay. Furthermore, we analyzed NK cells regarding their actin cytoskeleton by Structured Illumination Microscopy (SIM) and flow cytometry and demonstrate an actin dysfunction of NK cells shown by reduced F-actin content after fungal co-cultivation early after alloSCT. This dysfunction remains until 180 days post-alloSCT, concluding that further actin-dependent cellular processes may be negatively influenced after alloSCT. To investigate the molecular pathomechansism, we compared CD56 receptor mobility on the plasma membrane of healthy and alloSCT primary NK cells by single-molecule tracking. The results were very robust and reproducible between tested conditions which point to a different molecular mechanism and emphasize the importance of proper CD56 mobility."

Reconstituting NK cells after allogeneic stem cell transplantation show impaired response to the fungal pathogen *Aspergillus fumigatus*

Esther Weiss[1][¶], Jan Schlegel[2][¶], Ulrich Terpitz[2], Michael Weber[3], Joerg Linde[3], Anna-Lena Schmitt[1], Kerstin Hünniger[3,4], Lothar Marischen[1], Florian Gamon[1], Joachim Bauer[1], Claudia Löffler[1], Oliver Kurzai[3,4], Charles Oliver Morton[5], Markus Sauer[2], Hermann Einsele[1][&], and Juergen Loeffler[1][&][*]

[1]Department of Internal Medicine II, WÜ4i, University Hospital Wuerzburg, Wuerzburg, Germany
[2]Department of Biotechnology and Biophysics, Biocenter, Julius-Maximilian-University, Wuerzburg, Germany
[3]Leibniz Institute for Natural Product Research and Infection Biology – Hans Knoell Institute, Jena, Germany
[4]Institute for Hygiene and Microbiology, Julius-Maximilian-University, Wuerzburg, Germany
[5]School of Science and Health, Western Sydney University, Campbelltown NSW 2560, Australia

[¶] shared first authorship
[&] shared last authorship
[*] Correspondence: Prof. Dr. Jürgen Löffler (loeffler_j@ukw.de)

Keywords: natural killer cell, Aspergillus fumigatus, stem cell transplantation, corticosteroids, CCL3, CCL4, CCL5

NK-*A. fumigatus* interaction after alloSCT

Abstract

Delayed natural killer (NK) cell reconstitution after allogeneic stem cell transplantation (alloSCT) is associated with a higher risk of developing invasive aspergillosis. The interaction of NK cells with the human pathogen *Aspergillus (A.) fumigatus* is mediated by the fungal recognition receptor CD56, which is relocated to the fungal interface after contact. Blocking of CD56 signaling inhibits the fungal mediated chemokine secretion of MIP-1α, MIP-1β, and RANTES and reduces cell activation, concluding a functional role of CD56 in fungal recognition.

We collected peripheral blood of recipients of an allograft on defined time points after alloSCT (day 60, 90, 120, 180). NK cells were isolated, directly challenged with live *A. fumigatus* germ tubes, and cell function was analyzed and compared to healthy individuals. After alloSCT, NK cells displayed a higher percentage of CD56^{bright}CD16^{dim} cells throughout the time of blood collection. However, CD56 binding and relocalization to the fungal contact side were decreased. We could correlate this deficiency to the administration of corticosteroid therapy that further negatively influenced the secretion of MIP-1α, MIP-1β, and RANTES. As a consequence, the treatment of healthy NK cells *ex vivo* with corticosteroids abrogated chemokine secretion measured by multiplex immunoassay. Furthermore, we analyzed NK cells regarding their actin cytoskeleton by Structured Illumination Microscopy (SIM) and flow cytometry and demonstrate an actin dysfunction of NK cells shown by reduced F-actin content after fungal co-cultivation early after alloSCT. This dysfunction remains until 180 days post-alloSCT, concluding that further actin-dependent cellular processes may be negatively influenced after alloSCT. To investigate the molecular pathomechansism, we compared CD56 receptor mobility on the plasma membrane of healthy and alloSCT primary NK cells by single-molecule tracking. The results were very robust and reproducible between tested conditions which point to a different molecular mechanism and emphasize the importance of proper CD56 mobility.

2

Introduction

Following allogeneic stem cell transplantation (alloSCT), patients are characterized by a period of profound T and B cell deficiency until the completion of immune system reconstitution, which can take up to two years (Corre et al., 2010). During this critical period of T and B cell deficiency, in which a patient is more susceptible to bacterial, viral and fungal infections, cellular components of innate immunity are of major importance as they represent the first line of immune defense. Alveolar macrophages can kill inhaled conidia, but additionally, recruit neutrophils to the site of infection. Phagocytes, such as monocytes and dendritic cells, communicate with the adaptive immune system, thereby modulating inflammatory responses. Through the involvement of pattern recognition receptors that recognize pathogen-associated molecular patterns, cells of the innate immune system distinguish between different pathogens (Steele et al., 2005, Park and Lee, 2013, Kawai and Akira, 2009). Cytokines, chemokines, and chemokine receptors play essential roles in immunity against opportunistic pathogens and may determine the type of effector response. NK cells develop in the bone marrow and secondary lymphoid organs until they reach a defined stage, enter the bloodstream, and seed into peripheral organs (Bjorkstrom et al., 2016).

Interestingly, NK cells are not restricted after migration but can circulate from lung to blood and *vice versa*, as shown in the study by Marquardt *et al.* (Marquardt et al., 2017). NK cells constitute approximately 10% of lymphocytes in blood (Campbell and Hasegawa, 2013) and can be subdivided into CD56^{bright} and CD56^{dim} cells (Caligiuri, 2008). CD56^{bright} NK cells are potent cytokine producers and do not express the Fc receptor CD16, while the latter efficiently lyse target cells (Caligiuri, 2008). There is strong evidence for a gradual differentiation from CD56^{bright} cells into CD56^{dim} NK cells (Romagnani et al., 2007, Moretta, 2010, Chan et al., 2007). Under healthy conditions CD56^{dim} NK cells represent ~90% of blood NK cells (Campbell and Hasegawa, 2013). In allograft recipients CD56^{dim} NK cells are underrepresented compared to healthy controls as the subset ratio of CD56^{bright} NK cells increase to 40-50% (Dulphy et al., 2008). NK cells are potent killers of tumor cells, and once they encounter these cells, NK cells are activated and release the effector molecules granzyme and perforin, leading to target cell lysis (Topham and Hewitt, 2009). In addition to their tumor-killing function, NK cells also interact with several pathogens (Lieke et al., 2008, Vitenshtein et al., 2016, Fauci et al., 2005).

NK cells are essential during fungal infections, which has been shown in mouse models as well as in clinical studies. Morrison *et al.* showed in a neutropenic mouse model that CCL2 depletion inhibited pulmonary NK cell migration and furthermore favored the development of invasive aspergillosis (Morrison et al., 2003). In a later study, NK cell-derived IFN-γ was shown to be essential to control fungal infections in neutropenic mice and depletion of NK cells or IFN-γ resulted in a higher fungal burden (Park et al., 2009). Confirming the importance of NK cells in humans, Stuehler *et al.* monitored recipients of an allograft over 12 months and found a clear correlation between reduced NK cell counts and delayed NK cell reconstitution with a higher risk of developing IA in patients receiving HSCT (Stuehler et al., 2015). These studies highlighted the role of NK cells during fungal infections in immunocompromised hosts and were influential for our study.

Fungal pathogens are recognized by several natural activating receptors, e.g. natural activating receptor NKp46 and NKp30 (Vitenshtein et al., 2016, Li et al., 2013). A recent study demonstrated that the neural cell adhesion molecule (NCAM-1, CD56) on NK cells binds to hyphae of *Aspergillus* species which induces NK cell activation measured by the expression of the activation marker CD69 (Ziegler et al., 2017). Interestingly, blocking of CD56 resulted in reduced secretion of the chemokines macrophage inflammatory protein (MIP)-1α (CCL3), MIP-1β (CCL4), and

3

RANTES (CCL5) after fungal challenge, suggesting inhibited immune cell recruitment to sites of inflammation (Ziegler et al., 2017).

In this study, we describe the individual process of NK cell reconstitution of randomly selected recipients of an allograft and present prospective longitudinal functional data from NK cells collected at defined time points after transplantation. We show that the expression of the fungal recognition receptor CD56 is increased for more than 180 days after alloSCT. Despite the higher expression, fungal binding was inhibited in some NK cells obtained from patients after alloSCT. We excluded that this was due to an actin defect; however, fungal mediated actin induction was dependent on time after alloSCT, concluding NK cell development-related effects. In additional experiments, we could show that corticosteroid treatment reduced the binding of CD56 to fungal pathogens and consecutively diminished downstream chemokine secretion. By treatment of healthy NK cells with corticosteroids *ex vivo*, we confirmed that corticosteroids negatively influence CD56 downstream signaling by inhibition of chemokine secretion. Thus, corticosteroids may influence the development of IA by suppressing NK cell function in addition to effects on other immune cells. Interestingly, CD56 receptor mobility within the plasma membrane of alloSCT NK cells was not influenced as probed by single-molecule tracking experiments which indicates defects in CD56 signaling rather than its mobility.

4

Material and methods

Patient information

Peripheral blood was collected from patients after the successful treatment of AML (acute myeloid leukemia), ALL (acute lymphatic leukemia) or multiple myeloma (MM). Drawing of blood was performed at day 60, 90, 120, and 180 post-alloSCT. Relevant patient information is displayed in Table 1.

Cell culture

NK cells were isolated from EDTA blood obtained from healthy individuals or patients after 60, 90, 120, or 180 days post alloSCT. NK cell isolation was performed using the MACSxpress ® Whole Blood NK Cell Isolation Kit (negative isolation, Miltenyi Biotec). NK cells were frozen in liquid nitrogen. Thawing of NK cells was performed in pre-warmed RPMI 1640 + 10 % fetal calf serum (FCS). Cell recovery was over 90 % after thawing compared to the cell amount before freezing. NK cell viability after thawing was monitored with a cell viability analyzer (VICELL XR, Beckman Coulter) and was consistently over 95 %. NK cells were pre-stimulated with 1000 U/ml interleukin-2 (IL-2, Proleukin ™ Novartis) overnight at a cell concentration of 1×10^6 cells/ml. NK cells were cultured with *A. fumigatus* germ tubes (MOI 0.5) or plain medium (RPMI + 10 % FCS) at a cell concentration of 1×10^6 cells/ml for 6 h. Cell cultures were harvested, centrifuged (300 g, 10 min), and supernatants were frozen at -20 °C for short-term storage (Weiss et al., 2018) for later enzyme-linked-immunosorbent immunoassay.

Fungal strain

The *A. Fumigatus* strain ATCC46645 was plated on malt agar plates. Conidia were harvested and incubated in RPMI 1640 overnight under constant shaking (200 rpm) at 25 °C to generate *A. fumigatus* germ tubes. Germ tubes were centrifuged (5000 g, 10 min) and resuspended in fresh medium supplemented with 10 % FCS.

Flow cytometry

NK cells were treated with the following antibodies to analyze the surface expression: anti-CD56 FITC (BD), anti-NKp46 PE (BD), anti-CD3 PerCP (BD) and anti-CD16 PerCP (Biolegend). NK cell purity was monitored by NKp46+ and CD3- gating and was consistently over 95 % (Ziegler et al., 2017, Weiss et al., 2018). For analysis of actin dynamics in live cells, cells were stained in 1 µM Live Cell Fluorogenic F-actin Labelling Probe (SiR-actin 647, Spirochrome) for 50 min. Relative CD56 and F-actin values were calculated with equations (1) and (2). Flow cytometric analysis was performed with a FACSCalibur (BD), and data were analyzed by FlowJo software (TreeStar).

$$\text{Relative CD56} = \frac{\text{CD56 MFI (NKAF)}}{\text{CD56 MFI (NK)}} \quad (1)$$

$$\text{Relative F-actin} = \frac{\text{SiR-647 MFI (NKAF)}}{\text{SiR-647 MFI (NK)}} \quad (2)$$

5

CD16$^+$ cell isolation

NK cell subsets were separated by CD16 magnetic beads over an MS column (Miltenyi Biotec). CD16$^+$ and CD16$^-$ cells were pre-stimulated with 1000 U/ml Proleukin overnight before co-cultures were set with *A. fumigatus* germ tubes for 6 h at 37 °C. Supernatants were frozen at -20 °C as previously described (Weiss et al., 2018) and were used for later enzyme-linked immunosorbent assay. NK cells were analyzed by flow cytometry, and subset purity was monitored by anti-CD56 antibody staining to discriminate between the CD56^{dim} and the CD56^{bright} subset.

Multiplex immunoassay

Supernatants of NK cells from alloSCT patients and healthy controls treated with *A. fumigatus* germ tubes or non-treated NK cells were analyzed by multiplex immunoassay (eBioscience) regarding the presence of the chemokines MIP-1α, MIP-1β, and RANTES using the BioPlex 200 System (Bio-Rad).

Enzyme-linked immunosorbent assay (ELISA)

Supernatants of healthy NK cells treated with prednisolone *ex vivo* were analyzed regarding the presence of MIP-1α, MIP-1β, and RANTES. MIP-1α, MIP-1β (R&D Systems), and RANTES (Biolegend) ELISA were performed according to the manufacturer's protocol.

Prednisolone treatment

NK cells were incubated in 1000 U/ml IL-2 in the presence of 25 µg/ml Prednisolut ® (prednisolone 21-succinate, mibe GmbH) for 40 h. Prednisolut ® concentrations were comparable to those administered to patients in an acute phase treatment (2 mg/kg). After prednisolone treatment, the medium was exchanged, and NK cells were either co-cultured with *A. fumigatus* germ tubes (MOI 0.5) or alone for 6 h. NK cells were analyzed by flow cytometry, and supernatants were used for ELISA.

Structured illumination microscopy

NK cells were cultured alone or with *A. fumigatus* germ tubes (MOI 0.5) for 6 h at 37 °C on poly-D-lysine coated 8-well Lab-Tek coverglass chambers (Sarstedt). Samples were fixed in 3 % formaldehyde (FA) in RPMI 1640 before staining. CD56 was stained with anti-CD56 Alexa Fluor 647 antibody (1:50, clone HCD56, Biolegend) for 1 h, the actin cytoskeleton with Phalloidin Atto 550 staining solution for 24 h (1:100, Sigma), and the fungal cell wall with Calcofluor for 10 min (500 µg/ml, Sigma). Samples were embedded in ProLong Gold Antifade Mountant (Thermo Fisher Scientific) and analyzed on a Zeiss Elyra S.1 SIM. Using the Plan-Apochromat 63x/1.4 Oil objective in combination with 642 nm (5%), 561 nm (1%), and 405 nm (2%) laser lines, we acquired z-stacks with slice spacings of 300 nm.Exposure times of 100 ms and 3 SIM rotations were used for each individual channel. Emission signals were recorded with a sCMOS PCO Edge 5.5 and analyzed with the ZEN 2.3 SP1 software.For visualization maximum intensity projections of reconstructed z-stacks were used. To quantify the actin signal of each NK cell, z-stacks were

6

projected as summed slices. A constant circular area was moved over each NK cell and the intensity was measured using Fiji (Schindelin et al., 2012).

Single-molecule tracking

Single-molecule tracking was performed as described recently (Schlegel et al., 2019, Wäldchen et al., 2020). In short, CD56 primary antibodies (clone HCD56, Biolegend) were conjugated to the bright and photostable fluorophore SeTau-647-NHS (SETA BioMedicals, #K9-4149) (Tsunoyama et al., 2018) via N-hydroxysuccinimide ester amine crosslinking. Primary NK cells were labelled 5 minutes at 4°C with 0.33 nM antibody solution diluted in colourless RPMI 1640. Cells were washed via centrifugation at 500 xg and seeded onto KOH cleaned 8-well on cover glass (Sarstedt). After 30 minutes, single-molecule trajectories were recorded at room temperature by using a highly inclined and laminated optical sheet (HILO) and a previously described *d*STORM setup (Burgert et al., 2017). To increase signal-to-noise ratio exposure times were set to 50ms and time series with 5000 frames acquired. Individual molecules were detected by ThunderSTORM (Ovesny et al., 2014), filtered and tracks generated with minimal track length of 20 frames with the Python implementation of the Crocker-Grier (Crocker and Grier, 1996) algorithm Trackpy (Allan, 2018, April 21). Mean squared displacementswere calculated and the resulting ensemble MSD was fit with a power law, $MSD(\tau) = 4D_\alpha\tau^\alpha$ resulting in the generalized diffusion coefficient D_α and anomalous exponent α.

Statistical analysis

The normality of the data was tested with D'Agostino & Pearson normality test. Normally distributed data (n=2 groups) were either analyzed with an unpaired t-test with Welch's correction or with a paired t-test. Data not following Gaussian's distribution were analyzed with a Mann-Whitney test. When multiple comparisons were performed, normally distributed data were analyzed by one-way ANOVA with correction for multiple testing by FDR method of Benjamini and Hochberg. Data not following Gaussian's distribution were analyzed with a Kruskal-Wallis test with FDR correction (no data matching) or with a Friedman test with FDR correction (matched data). Statistical analysis was performed with GraphPad Prism 7.

Ethical statement

This study obtained written consent by the ethics committee of the University of Wuerzburg (#34/15).

Data availability

All relevant data supporting the findings of the study are available in this article and its Supplementary Information files, or from the corresponding authors upon request, with restriction of data that would compromise patient confidentiality.

7

Results

Characterization of NK cells from recipients of an allograft and healthy controls

To monitor NK cell counts and subsets in patients after successful treatment of AML (acute myeloid leukemia), ALL (acute lymphatic leukemia) or multiple myeloma (MM) by alloSCT and healthy donors, we analyzed blood at 60, 90, and 120 days after alloSCT and in healthy controls. In line with previous studies (Ullah et al., 2016), total NK cell counts were similar within 60-120 days after transplantation compared to healthy controls (Fig. 1A). Patients after alloSCT experience a period of immune deficiency in which T cells are underrepresented (Corre et al., 2010); thus, the percentage of other cell types in PBMCs increases. When the percentage of NK cells (Fig. 1B) measured in PBMCs was plotted against the percentage of T cells after alloSCT (Fig. 1C), a negative correlation was observed (p <0.0001), confirming that the higher percentage of NK cells in PBMCs was associated with T cell deficiency (Fig. 1D).
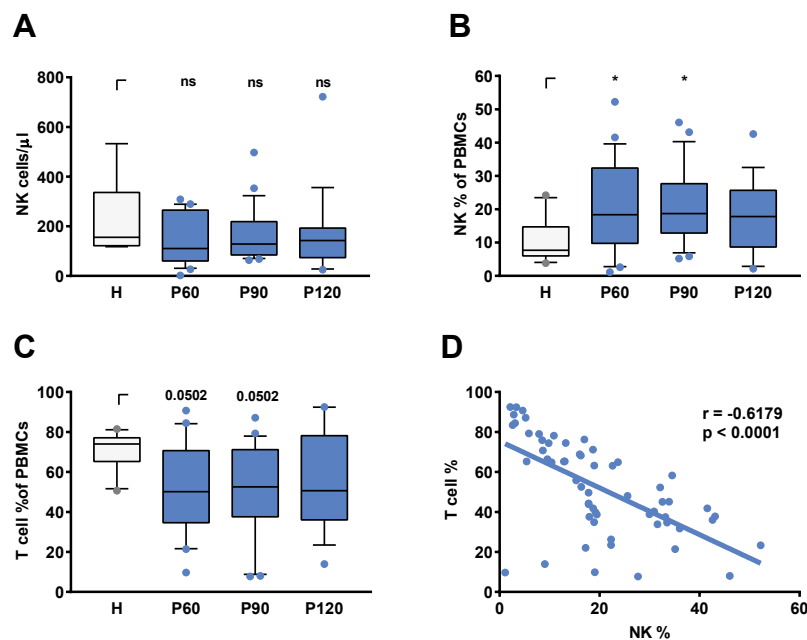
Figure 1: NK and T cell composition in patients after alloSCT and healthy controls. (A) Total NK cell counts per µl, **(B)** NK cell percentages in PBMCs and **(C)** T cell percentages in PBMCs were measured in the peripheral blood from healthy individuals (H) or patients 60, 90, or 120 days post-alloSCT (P60, P90, P120). Statistics were analyzed by (A) Kruskal-Wallis test with FDR correction (Benjamini and Hochberg), **(B, C)** one-way ANOVA with FDR correction (Benjamini and Hochberg, * q < 0.05, F_B[3, 70] = 2.248, F_c [3, 70]= 1.964). Data were acquired from **(A-C)** n = 10 (H), n = 22 (P_60), n = 23 (P_90) and n = 19 (P_120) independent experiments. **(D)** NK/ T cell ratios were calculated by Pearson correlation. Data were obtained from n = 60 different experiments including time points ranging from 60-120 days post-alloSCT patients (n = 26).

8

NK cells obtained from healthy donors or after alloSCT were analyzed for the expression of specific surface markers (Fig. 2). For this purpose, NK cells were stained with anti-CD56 and anti-CD16 antibodies and gated into $CD56^{bright}CD16^-$, $CD56^{bright}CD16^+$, and $CD56^{dim}CD16^{++}$ subsets (Fig. 2A). NK cells derived after alloSCT significantly displayed lower amounts of $CD56^{dim}CD16^{++}$ cells, whereas the proportion of $CD56^{bright}CD16^+$ and $CD56^{bright}CD16^-$ cells was higher (Fig. 2B), which is in accordance with previous findings (Dulphy et al., 2008). In contrast, obviously the phenotypic expression of CD56 and CD16 within subsets remains unchanged after alloSCT, as there were no significant differences detectable when we analyzed the CD56 and CD16 MFI within each subset between healthy donors and recipients of an allograft (Fig. 2C, D). These experiments showed that NK cell recovery after alloSCT is a fast process whereas NK cell subset distribution does not recover even by 180 days post-alloSCT.
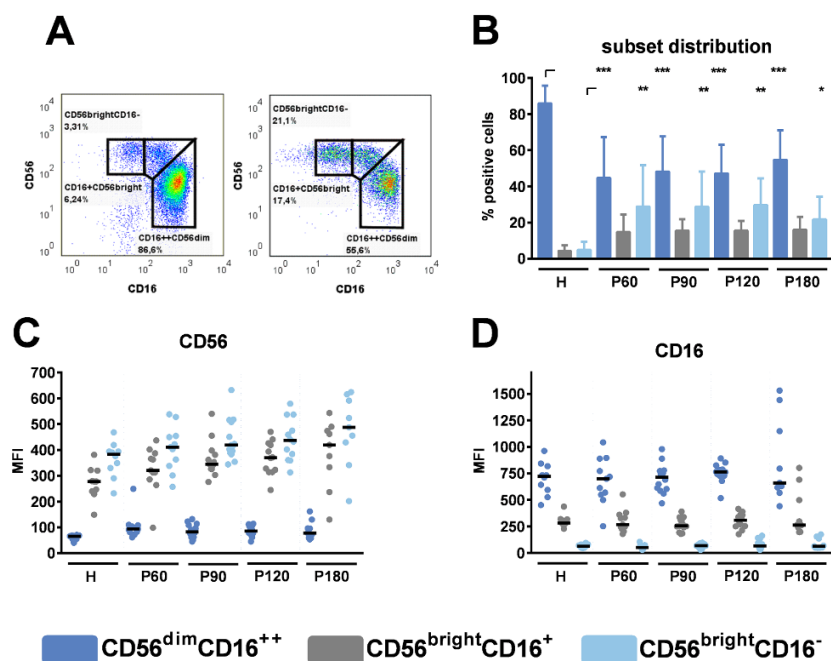
Figure 2: NK cell subsets in reconstituting NK cells. NK cells were pre-stimulated with 1000 U/ml IL-2 overnight. **(A)** Representative gating strategies for healthy individuals (left) and recipients of an allograft (right). **(B)** NK cell subsets were compared between healthy individuals and recipients of an allograft. Data are displayed as mean + SD. **(C)** CD56 MFI and **(D)** CD16 MFI within NK cell subset were analyzed by flow cytometry. Data were acquired from n = 10 (H); n = 11 (P60); n = 14 (P90); n = 12 (P120); n = 9 (P180) different experiments. Medians are displayed. Statistical analysis was performed by **(B)** one-way ANOVA ($CD16^{++}CD56^{dim}$ and $CD16^+CD56^{bright}$, $F[14, 156] = 25.87$) and Kruskal-Wallis test ($CD16^-CD56^{bright}$). Corrections for multiple testing were performed by the FDR method of Benjamini and Hochberg. Statistical significances are marked by asterisks (* $p < 0.05$, ** $p < 0.01$, *** $p < 0.001$).

NK-*A. fumigatus* interaction after alloSCT

NK cell binding to the fungus is inhibited by corticosteroid treatment

As the fraction of CD56^{dim} NK cells was lower in allograft recipients, we investigated the fungal binding capacity of reconstituting, not fully matured NK cells. CD56 is a PRR on human NK cells, and stimulation with *A. fumigatus* germ tubes causes relocalization of the normal homogenously distributed CD56 from the NK cell surface to the fungal interface, resulting in a reduced detection of CD56 by flow cytometry (Ziegler et al., 2017). This reduced detection of CD56 on NK cells that are derived from former NK-*A. fumigatus* co-culture experiments correlates with a remaining CD56 signal on the fungal surface in absence of NK cells (Supplementary Fig. 1), concluding that CD56 stays stuck on the fungus after physical separation of co-cultures.

We investigated the fungal binding capacity by co-culturing NK cells from alloSCT recipients or healthy individuals with *A. fumigatus* germ tubes for 6 h before analyzing the cells by flow cytometry. To analyze the individual NK cell subsets we gated into CD16^{-} and CD16^{+} NK cells. Within CD16^{-} and CD16^{+} cells, we analyzed the fungal binding by CD56 mean fluorescence intensity (MFI). Relative CD56 values were calculated through dividing CD56 MFI after fungal co-culture by CD56 MFI before fungal co-culture. Thus, low relative CD56 values indicated a strong binding of CD56 (Fig. 3).

Healthy CD16^{-} NK cells displayed lower relative CD56 values compared to healthy CD16^{+} NK cells, indicating better fungal binding of the CD16^{-} subset (Fig. 3A). In contrast, there was no detectable difference between CD16^{+} and CD16^{-} cells in alloSCT patients (Fig. 3A). The binding capacity of NK cells obtained after alloSCT did not significantly change over time; however, we detected outliers leading to high standard deviations in each group (Fig. 3A). Next, we analyzed if those outliers correlate with a special treatment after alloSCT, as drugs may impair cell function. Within the CD16^{+} subset, more CD56^{bright} cells were observed in patients after alloSCT compared to healthy individuals (Fig. 1B). This may be the reason why CD16^{+} cells after alloSCT (median = 0.15) displayed a better fungal binding compared to healthy CD16^{+} cells (median = 0.23) (Fig. 3B). This enhanced fungal binding of CD16^{+} cells after alloSCT was abrogated when patients were under corticosteroid therapy during the time of blood collection (Fig. 3B). In addition, a lower capacity in fungal binding was observed in the CD16^{-} subset derived from patients under corticosteroid therapy (CD16^{-} = 0.21) compared to non-corticosteroid treated individuals (CD16^{-} = 0.13) or even healthy individuals (CD16- = 0.14) (Fig. 3B).
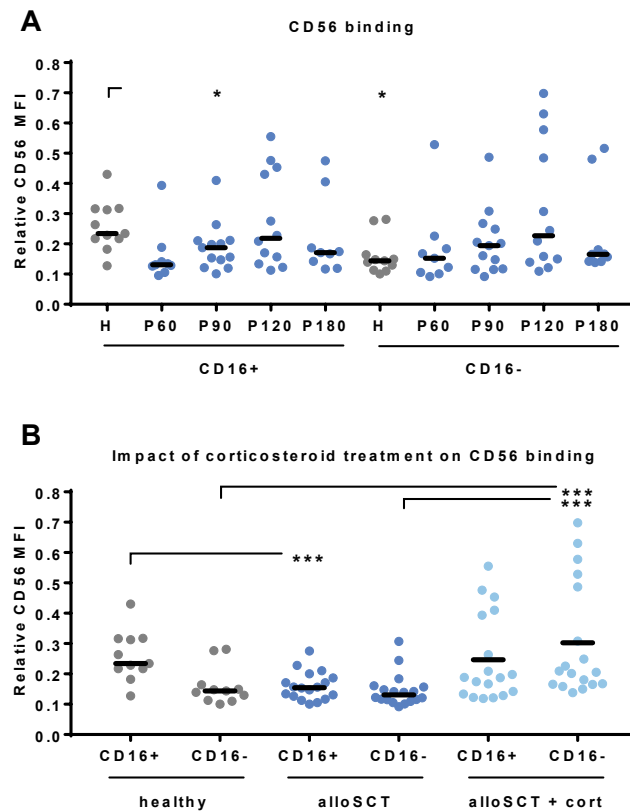
Figure 3: Corticosteroid treatment inhibits CD56 binding to the fungus. NK cells were pre-stimulated with 1000 U/ml IL-2 overnight before NK cells were co-cultured with *A. fumigatus* germ tubes (AF, MOI 0.5) or plain medium at 37 °C for 6 h. NK cells were gated into NKp46+/CD16+ or NKp46+/CD16- cells. CD56 mean fluorescence intensity (MFI) was evaluated by flow cytometry with and without fungal co-culture. Relative CD56 expression was calculated for alloSCT NK cells (P) and healthy controls (H). Values for relative CD56 expression were grouped regarding **(A)** the time after alloSCT and **(B)** corticosteroid treatment. Data were acquired from **(A)** n = 11 (H); n = 9 (P60), n = 13 (P90); n = 12 (P120); n = 9 (P180) and **(B)** n = 11 (healthy) n = 18 (alloSCT and alloSCT + cort) experiments. Medians are displayed. Significant differences were calculated by the Kruskal-Wallis test with correction for multiple testing by the FDR method of Benjamini and Hochberg and are marked by asterisks (* p < 0.05; *** p < 0.001).

11

NK cells derived from patients during corticosteroid therapy display reduced fungal mediated chemokine secretion

After CD56 binding to the fungus, NK cells secrete the chemokines MIP-1α, MIP-1β, and RANTES that are reduced secreted when CD56 is blocked before fungal co-culture (Ziegler et al., 2017). These chemokines are important for immune cell recruitment (Charmoy et al., 2010, Bless et al., 2000, Souto et al., 2003)and are secreted explicitly by CD16$^+$CD56^{dim} NK cells, which are underrepresented early after alloSCT (Fig. 2B) (Fauriat et al., 2010). To specifically analyze CD16$^+$CD56^{dim} NK cells, we separated CD16$^+$ from CD16$^-$ cells by CD16 positive magnetic isolation (Fig. 4A). CD16$^+$ cells derived 90 days after alloSCT secreted significantly lower amounts of MIP-1α and showed a reduced secretion of MIP-1β and RANTES after fungal stimulation compared to healthy controls, indicating functional deficiencies of this subset (Fig. 4B-D).
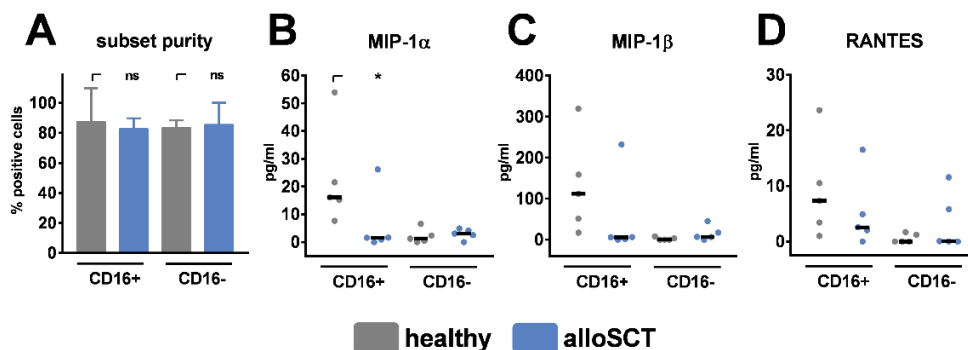
Figure 4: Chemokine secretion is inhibited in CD16+ cells after alloSCT. NK cells were obtained from healthy individuals or 90 days after alloSCT and were pre-stimulated with 1000 U/ml IL-2 overnight. **(A)** NK cell subsets were isolated with CD16 magnetic bead positive isolation, and subset purity was analyzed by flow cytometry. NK cell subsets were co-cultured with *A. fumigatus* germ tubes (AF, MOI 0.5) or plain medium for 6 h at 37 °C. Supernatants were collected, and chemokine levels of **(B)** MIP-1α, **(C)** MIP-1β, and **(D)** RANTES were analyzed. Data are displayed as **(A)** medians + range, **(B-D)** medians and were acquired from n = 5 different experiments. Significant differences were calculated by the Kruskal-Wallis test with correction for multiple testing by the FDR method of Benjamini and Hochberg and marked by an asterisk (* p < 0.05).

Since corticosteroids were negatively influencing CD56 binding to the fungus, which was shown to mediate the secretion of MIP-1α, MIP-1β, and RANTES (Ziegler et al., 2017), we analyzed if corticosteroids were also influencing chemokine secretion *in vivo*. Indeed, NK cells derived from patients after alloSCT that were currently under corticosteroid therapy secreted lower amounts of chemokines compared to NK cells derived from patients without corticosteroid therapy (Fig. 5).
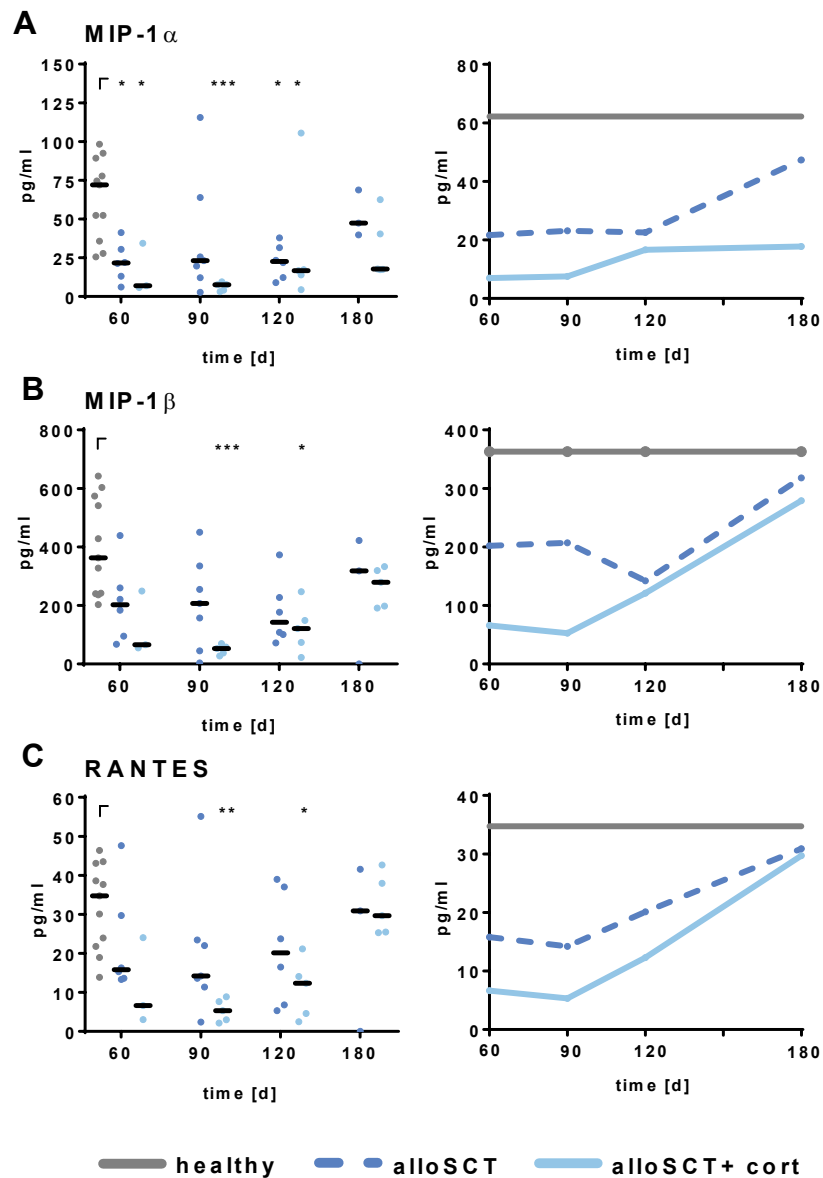
Figure 5: Chemokine secretion by alloSCT NK cells and healthy controls. NK cells were pre-stimulated with 1000 U/ml IL-2 overnight. NK cells obtained after alloSCT with and without corticosteroid treatment (alloSCT + cort) or from healthy controls (H) were co-cultured with *A. fumigatus* germ tubes (AF, MOI 0.5) or plain medium at 37 °C for 6 h. Supernatants were collected, and cytokine and chemokine levels of **(A)** MIP-1α, **(B)** MIP-1β, and **(C)** RANTES were analyzed. Data were acquired from n = 11 (H), n = 6 (alloSCT 60), n = 7 (alloSCT 90), n = 6 (alloSCT 120), n = 3 (alloSCT 180), n = 3 (cort 60), n = 5 (cort 90), n = 120 (cort 120), and n = 5 (cort 180) experiments. Data are displayed as medians. Significant differences were calculated by Kruskal-Wallis test with correction for multiple testing by the FDR method of Benjamini and Hochberg. Statistical significances are marked by asterisks (* $p < 0.05$, ** $p < 0.01$, *** $p < 0.001$).

13

NK cells from healthy individuals treated with prednisolone ex vivo show impaired fungal mediated chemokine secretion

Since we observed defects in CD56 binding and chemokine secretion of NK cells obtained from patients after corticosteroid treatment, we next analyzed the effects of corticosteroids on healthy NK cells *ex vivo*. Therefor we stimulated NK cells for 40 h with physiological levels of prednisolone that are present in patients during an acute phase treatment.

Prednisolone had no effect neither on NK cell viability nor on the cell amount measured by a cell viability analyzer (Fig. 6A). After stimulation, the medium was exchanged, and NK cells were co-cultured with *A. fumigatus* germ tubes for 6 h. Prednisolone induced the down-regulation of CD56 MFI on the NK cell's surface, which made relative CD56 MFI an unreliable readout for analyzing *ex vivo* the effect of prednisolone treatment on CD56 binding to the fungus (Fig. 6B). Notably, NK cells derived from patients during corticosteroid therapy showed no CD56 downregulation compared to the control patient group (Supplement Fig. 2). A corticosteroid mediated down-regulation of activation markers was shown in earlier studies (Ohira et al., 2017). Besides CD56, the NK cell activation markers NKp46 and CD69 were down-regulated on the NK cell surface after prednisolone treatment *ex vivo* (Supplement Fig 3A,B).

Thus, we focused on the secretion of the fungal mediated chemokines MIP-1α, MIP-1β, and RANTES after treatment of healthy NK cells *ex vivo* with prednisolone. Interestingly, prednisolone treatment abrogated the ability to secrete those chemokines in fungal stimulated NK cells (Fig. 6C-E). From these experiments, we concluded that corticosteroids have detrimental effects on the fungal binding and secretion of chemokines.
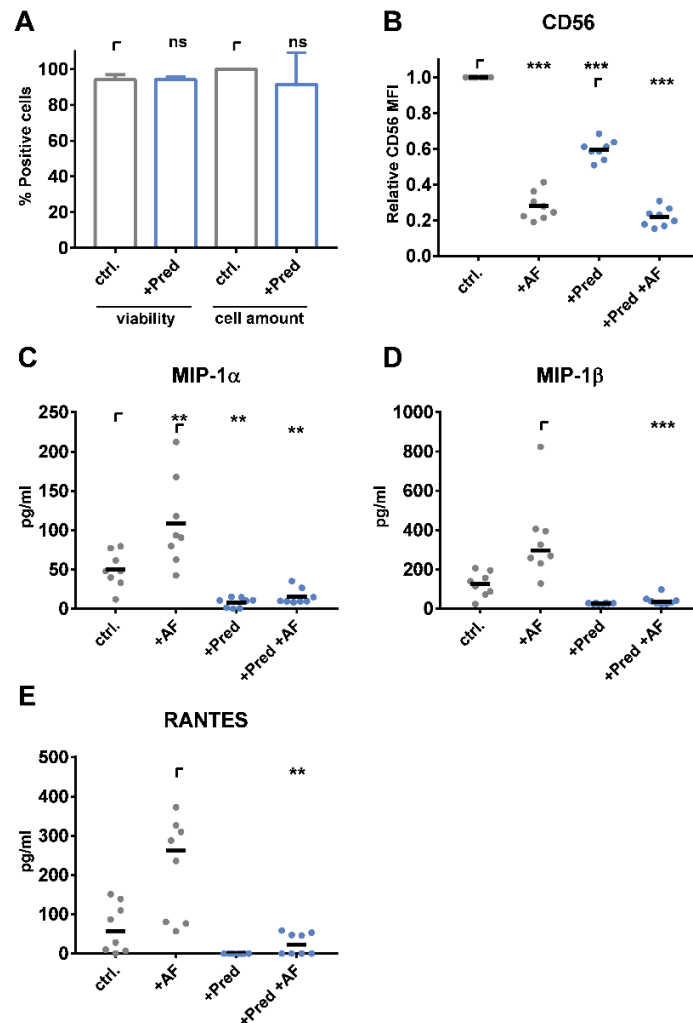
Figure 6: Prednisolone treatment of healthy NK cells reduces CD56 mediated chemokine secretion of MIP-1α, MIP-1β, and RANTES. NK cells were cultured with 1000 U/ml IL-2 in the presence of 25 µg/ml prednisolone for 40 h. **(A)** NK cell viability and cell counts were monitored by trypan blue staining using a cell viability analyzer (Beckman Coulter Vicell XR). NK cell-*A. fumigatus* (MOI 0.5) co-cultures were set for 6 h. **(B)** CD56 mean fluorescence intensity (MFI) was analyzed by flow cytometry. The secretion of **(C)** MIP-1α and **(D)** MIP-1β and **(E)** RANTES was analyzed by multiplex immunoassay. Data were acquired from **(A)** n = 5, **(B-E)** n = 8 different experiments. Data are displayed as **(A)** means + SD, **(B, C)** means, and **(D, E)** medians. Statistics were calculated by **(A)** paired t-test, **(B, C)** one-way ANOVA with FDR correction ($F_B[1.452, 10.16] = 445.2$, $F_C[1.198, 8.385] = 21.46$) and **(D, E)** Friedman test with FDR correction. Statistical significances are marked by asterisks (** $p < 0.01$, *** $p < 0.001$).

NK cells obtained after alloSCT display defects in fungal mediated actin polymerization

Our previous studies demonstrate that CD56 relocalization to the fungal interface is dependent on actin (Ziegler et al., 2017). Since NK cells obtained from patients treated with corticosteroids showed reduced CD56 relocalization (Fig. 3), we hypothesized that this might be due to cytoskeletal defects. Thus, we first analyzed whether fungal stimulation induces actin polymerization by co-culturing NK cells obtained from healthy controls or after alloSCT with *A. fumigatus* germ tubes for 6 h. SIM was used to visualize actin dynamics in NK cells with subdiffraction spatial resolution (Gustafsson, 2000). Indeed, in NK cells from healthy individuals the presence of *A. fumigatus* germ tubes induced actin polymerization as indicated by more intense fluorescent staining of the F-actin binding probe phalloidin (Fig. 7A). In particular, the fluorescence of phalloidin was frequently increased at cell surface areas where the NK cell membrane interacted with the fungal hyphae (marked by arrow), concluding that actin polymerization is induced by fungal hyphae (Fig. 7B). Interestingly, NK cells frequently attached in close proximity to the fungal septae (Supplement Fig. 4A) and distinct actin protrusions were abolished upon *ex vivo* CSA treatment in healthy cells and in several alloSCT patient NK cells (Supplement Fig. 4B).
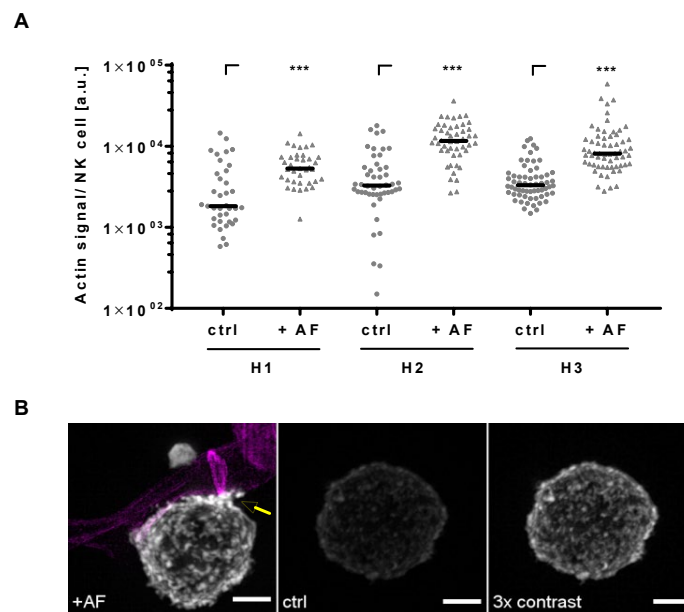
Figure 7: *A. fumigatus* stimulates F-Actin in NK cells. NK cells were pre-stimulated with 1000 U/ml IL-2 overnight. NK cells were co-cultured with (AF, MOI 0.5) or without (ctrl) *A fumigatus* germ tubes for 6 h. Cultures were fixed, and F-actin was stained with phalloidin staining solution for 24 h. Calcofluor was used to visualize the fungal cell wall. **(A)** Quantification of the actin signal per NK cell derived from n = 37 (H1), n = 48 (H2), and n = 62 (H3) SIM z-stacks. Data are displayed in medians and arbitrary units. Statistics were calculated by Wilcoxon test to compare the control samples and the fungal treated samples within each donor. Significant differences are displayed by asterisks (*** p < 0.001). **(B)** Fluorescence intensities were compared between NK cells treated with *A. fumigatus* germ tubes (AF, left) or control cells (ctrl, middle). To better visualize the distribution of F-actin on control cells, we displayed the fluorescence signal of phalloidin with three times higher contrast (right). Increases in F-actin levels by fungal treatment are marked by an arrow. Fungal hyphae are displayed in magenta. Representative data from n = 3 different experiments are shown. Scale bar, 2 μm.

16

Next, we analyzed the actin cytoskeleton with live-cell staining using flow cytometry. NK cells obtained from healthy individuals or patients 60, 90, 120, or 180 days post alloSCT were incubated with *A. fumigatus* germ tubes for 6 h, co-cultures were harvested, and cells were incubated in 1 μM SiR 647 F-actin binding peptides (Fig. 8). The induction of actin was calculated by dividing the actin signal after fungal co-culture by the actin signal before fungal co-culture (Fig. 8). To analyze the dependency of CD56 binding on the actin induction, we plotted relative CD56 values obtained from NK cells after alloSCT against the individual fungal mediated actin induction (Fig. 8A). Indeed, relative CD56 values negatively correlated with the induction of actin ($p = 0.0104$, two-tailed Spearman correlation), indicating that CD56 relocalization is dependent on fungal mediated actin polymerization (Fig. 8A).

Since CD56 binding to the fungus was dependent on fungal mediated actin polymerization (Fig. 8A) and CD56 binding was negatively affected by corticosteroid treatment (Fig. 3B), we next analyzed whether actin polymerization changed during corticosteroid treatment. Therefore, we grouped patients into corticosteroid receiving and non-corticosteroid receiving cohorts and only included samples matching the time after alloSCT and further drug treatment. There were no significant differences in the fungal mediated actin induction observable between corticosteroid-receiving and non-corticosteroid receiving patients (Fig. 8B). Also, *ex vivo* prednisolone treatment of healthy NK cells was not influencing fungal mediated actin induction (Fig. 8C).

However, fungal mediated actin polymerization was dependent on the time point of blood collection after alloSCT. Interestingly, NK cells collected at early time points after alloSCT showed a weaker fungal mediated actin polymerization (mean at day 60: 1.69) in comparison to later time points (mean at day 180: 3.69) or healthy controls (mean: 3.26, Fig. 5b) (Fig. 8D). Notably, CD16$^+$ and CD16$^-$ NK cells showed no differences in actin polymerization after *A. fumigatus* co-culture (Suppl. Fig. 5), concluding that the differences between healthy individuals and patients after alloSCT are not the cause of different NK cell subset contributions.
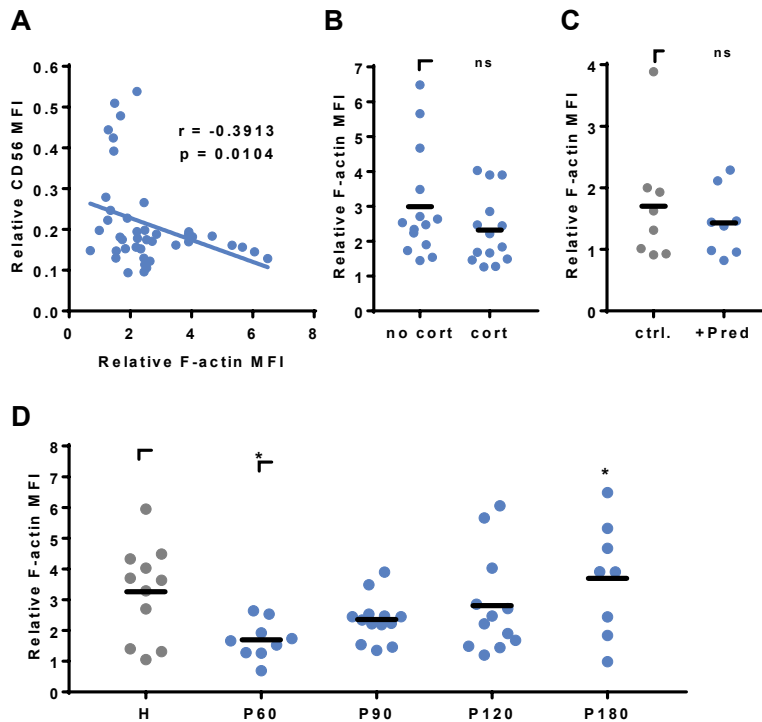
Figure 8: Actin induction following fungal stimulation recovers within 6 months after alloSCT. (A, B, D) NK cells were isolated from patients 60, 90, 120, and 180 days after alloSCT (P) or healthy controls (H). **(B)** NK cells were isolated from healthy controls and stimulated with 25 μg/ml prednisolone *ex vivo* for 40 h. **(A-D)** NK cells were cultured alone or with *A. fumigatus* germ tubes (MOI 0.5) for 6 h. Cells were stained for surface markers, treated with the F-Actin binding probe Sir647 for 50 min, and were analyzed by flow cytometry. Relative actin induction was calculated by the division of Sir647 MFI after fungal co-culture with Sir647 MFI of control cells. Data were acquired from **(A)** n = 44, **(B)** n = 14, **(C)** n = 8 , and **(D)** n = 11 (H); n = 9 (P60), n = 13 (P90); n = 12 (P120); n = 8 (P180) different experiments. Data are displayed as **(B-D)** means. Significant differences were calculated by **(A)** two-tailed Spearman correlation, **(B)** unpaired t-test with Welch's correction, **(C)** Wilcoxon test, and **(D)** One-way ANOVA with FDR correction (F[4, 48] = 3.112), and. Statistical significance is marked by an asterisk (* $p < 0.05$).

To test, whether the impaired fungal clearance in alloSCT derived NK cells might be due to changes in CD56 mobility we performed 2D single-molecule tracking (SMT) experiments of CD56 (Supplementary Video 1) as described previously (Schlegel et al., 2019, Wäldchen et al., 2020). Surprisingly, we could not observe significant differences in the diffusion coefficient (Fig. 9A), anomalous diffusion constant (Fig 9B) and bound fraction (data not shown) (Hansen et al., 2018)between control and alloSCT NK cells. All tested parameters were quite robust and are in good agreement with previously published data (Wäldchen et al., 2020), highlighting the importance of proper CD56 mobility for NK cell physiology.
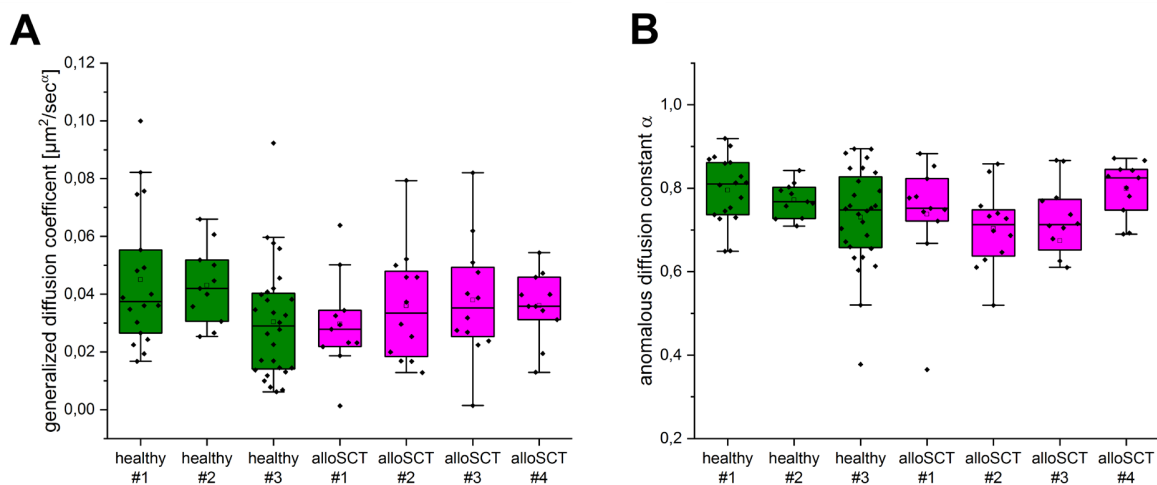
Figure 9: Single-molecule tracking of CD56 on primary NK cells of healthy and alloSCT patients isolated 120 days after alloSCT. (A) No significant differences in the ensemble diffusion coefficents derived from MSD analysis of individual trajectories between healthy (green) and alloSCT (magenta) NK cells. Median diffusion coefficents were between 0.028 and 0.042 $\mu m^2/s^\alpha$. (B) Analysis of anomalous diffusion indicates subdiffusive behaviour of CD56 on healthy (green) and alloSCT (magenta) NK cells with no significant differences between healthy and alloSCT trajectories. We analyzed at least 11 NK cells with numerous trajectories for each condition (healthy #1 n=18, healthy #2 n=11, healthy #3 n=28, alloSCT #1 n=11, alloSCT #2 n=12, alloSCT #3 n=12, alloSCT #4 n=11)

In order to follow single CD56 molecules simultaneously with the underlying actin cytoskeleton we performed SMT experiments in the presence of the fluorogenic far-red F-actin probe SiR700. Since fluorescence emission of labelled CD56 receptors and F-actin was detected by one camera and same filter settings, we had to bleach the strong F-actin signal before both signals had similar intensity regimes. Indeed, CD56 molecules moved along individual actin filaments in the cell periphery (Supplementary Video 2) which is in good agreement with partial colocalization of CD56 and actin observed by SIM (Supplementary Figure 5).

19

Discussion

Patients after alloSCT are at an increased risk of IA due to a long-term state of T/B cell deficiency (Corre et al., 2010). Besides, a lack of innate immune cells such as neutrophils further negatively impacts on the outcome of IA (Muhlemann et al., 2005). Stuehler *et al.* correlated low NK cell counts and NK cell reconstitution with a higher risk of developing IA, which underlined the role of NK cells in the defense against *A fumigatus* (Stuehler et al., 2015). The interaction of NK cells with *A. fumigatus* is mediated by the neuronal cell adhesion molecule (NCAM-1, CD56), which binds to interacting hyphae in an actin- and time-dependent manner. Blocking of CD56 was shown to reduce fungal mediated NK cell activation and the secretion of the immune-recruiting chemokines MIP-1α, MIP-1β, and RANTES (Ziegler et al., 2017).

By comparing CD56 and CD16 expression levels on NK cells obtained after alloSCT and healthy controls, we confirmed the presence of more immature CD16$^-$CD56^{bright} NK cells in the peripheral blood of allograft recipients which persisted in most of the patients until 180 days post-transplant. Nevertheless, we detected no significant differences in CD56 dependent fungal binding between NK cells derived from healthy individuals or alloSCT patients independent from the time point of blood draw. However, CD56 binding after alloSCT was distributed inhomogeneously and showed outliers.

Considering the possibility that different drug treatments of alloSCT recipients might influence NK cell binding to fungal pathogens, we found CD56 binding to be inhibited in blood samples from patients receiving corticosteroid therapy. This therarpy is mainly applied to treat acute or chronic-graft-versus-host disease (GvHD). Interestingly, patients developing acute or chronic GvHD after alloSCT have also an increased risk for IA, especially when receiving corticosteroids (Labbe et al., 2007). Corticosteroids have anti-inflammatory and immunosuppressive effects and are administered to prevent graft rejection after alloSCT (Quellmann et al., 2008). Additionally, several cell functions, e.g., cytotoxicity, cell metabolism, and cytokine production, are suppressed by glucocorticoid treatment (Thum et al., 2008, Scheinman et al., 1995, Elftman et al., 2007).

Indeed, corticosteroid treatment inhibited the fungal mediated secretion of MIP-1α, MIP-1β, and RANTES in NK cells obtained at day 60-120 post-alloSCT. After 180 days, chemokine levels from corticosteroid treated NK cells normalized to that of healthy control levels which may be due to tapering of corticosteroid treatment over time, as corticosteroids are primarily used to treat GvHD after alloSCT (Quellmann et al., 2008, Bacigalupo et al., 2017). Therefore, low-level doses of corticosteroids to later time points may only marginally impact chemokine secretion. The primary corticosteroid agent for treatment of a GvHD is prednisolone, thus we tested the effect of prednisolone on NK cells from healthy individuals *ex vivo*. Prednisolone abrogated the fungal mediated secretion of MIP-1α, MIP-1β, and RANTES in healthy NK cells, confirming detrimental effects on chemokine secretion and immune cell function.

Glucocorticoids intracellularly bind to glucocorticoid receptors which are then transported into the nucleus. GR can either bind to glucocorticoid response elements (GREs), and function as transcriptional inducers or repressors, or interact with other transcription factors, thereby influencing their target gene expression (Jantzen et al., 1987, Beato, 1989, Beato et al., 1996, Nelson et al., 2003). In particular, glucocorticoids can inhibit NF-κB target gene expression by increasing the export rate of the activated p65 (RelA) NF-κB subunit from the nucleus to the cytoplasm (Nelson et al., 2003). MIP-1α, MIP-1β, and RANTES are NF-κB target genes, and their biological function is to recruit leukocytes to sites of inflammation and the initiation of a protective Th1 response (Moriuchi et al., 1997, Grove and Plumb, 1993, Widmer et al., 1993, Schrum et al.,

20

1996, Huang and Levitz, 2000). Since NK cells secrete MIP-1α, MIP-1β, and RANTES after fungal binding by CD56, we hypothesize that CD56 might activate the NF-κB pathway after relocalization to the fungal interaction site.

Former studies report that CD56 relocalization to the fungal interface is abolished after disruption of actin dynamics by cytochalasin D, concluding actin-dependent CD56 relocalization (Ziegler et al., 2017). We supported these findings by showing that a higher fungal mediated actin induction correlated with higher CD56 relocalization. We further demonstrated that the overall potential for fungal mediated actin polymerization was reduced in NK cells obtained after alloSCT. Interestingly, this was a time-dependent effect and actin defects recovered within 180 days post-alloSCT at which time actin induction was similar to healthy controls. Until now, it has not been clear why NK cells obtained early after alloSCT show a lower potential for actin polymerization. Actin polymerization is crucial for NK cell differentiation, activation, and cytotoxicity (Lee and Mace, 2017, Carisey et al., 2018, Watzl and Long, 2003). Interestingly, the recent work from Lee and Mace has revealed that NK cell motility increases with cell maturation, concluding that the actin cytoskeleton may fully develop over time (Lee and Mace, 2017). Since actin dynamics are crucial for several cellular processes, this may impact further functions in NK cells and other cell types post-alloSCT that have to be investigated in future studies. Although CD56 relocalization to the hyphae is dependent on actin dynamics, the overall mobility and diffusion properties of this adhesion receptor in the plasma membrane is not influenced in alloSCT patients even upon corticosteroid treatment 120 days post-alloSCT. Thus, impaired CD56 function during corticosteroid therapy is probably not caused by defects in receptor mobility but rather by other mechanisms, e.g. hindered downstream signalling cascades. By using SMT we randomly observed a small subset of CD56 molecules and did not account for the many CD56 isoforms and their degree of sialylation. Future studies should therefore unravel the role of CD56 isoforms as well as the time course after alloSCT on CD56 diffusion. Interestingly, CD56 mobility was very robust in all tested conditions which might reflect its important function in NK cell physiology.

We demonstrated that CD56 binding and the secretion of chemokines are impaired after corticosteroid treatment, suggesting that CD56 may activate NF-κB signaling after fungal binding. Since it was shown that NK cells have a protective effect on the outcome of IA (Stuehler et al., 2015), our data demonstrated that corticosteroid treatment might favor the development of IA also by suppressing NK cell function in addition to effects on other immune cells.

Author Contribution

E.W. and J.Sch. developed concepts, performed experiments, performed data analyses, and wrote the manuscript. U.T. developed concepts and wrote the manuscript. M.W. performed data analyses and wrote the manuscript. A. S., K.H., and L.M. performed experiments. J.B. and F.G. recruited blood donors and analyzed clinical data. C.L. analyzed clinical data. O.K., M.S., J.Li., and C.O.M. provided discussion and contributed to the manuscript. H. E. and J.Loe. developed concepts, supervised the study, and wrote the manuscript.

Conflict of interest statement

The authors declare that the submitted work was carried out without the presence of any personal, professional or financial relationships that could potentially be construed as a conflict of interest.

Contribution to the field statement

Aspergillus fumigatus is an ubiquitous fungal pathogen mainly found on degrading biomass. The 2-3 μm small spores are disseminated by air, and are small enough to be daily inhaled by human individuals. In healthy persons, the innate immune system is able to clear spores within hours. In contrast, immune suppression enables fungal germination, infiltration of deeper lung tissues, and encountering the bloodstream, which results in severe systemic infections or even death. Invasive aspergillosis (IA) is observed in ~5 % of the patients after allogeneic stem cell transplantation (alloSCT); however, the mortality rate is devastating (>75 %). Delayed NK cell reconstitution after alloSCT and diminished cell numbers were associated with a higher risk of developing IA. NK cells recognize *A. fumigatus* by a surface receptor named CD56, which is binding to hyphal structures and mediating cell activation and secretion of immune recruiting chemokines like MIP-1α, MIP-1β, and RANTES. In this study, we characterized anti-fungal NK cell responses of healthy individuals and patients after alloSCT. CD56 binding to the fungus was decreased during corticosteroid therapy, which was further associated with reduced secretion of MIP-1α, MIP-1β, and RANTES. Treatment of healthy NK cells with corticosteroids *ex vivo* had the same adverse effect on NK cell function, demonstrating inhibitory impact of corticosteroids on anti-fungal NK cell function.

Table 1: Patient characteristics.

ID	Gender	Age (yrs)	Day 60	Day 90	Day 120	Day 180	GvHD with systemic CS treatment	CS treatment duration	CS dosage
2	female	36	CSA	CSA	CSA, pred	CSA, pred	no	>18 weeks	low-dose
4	male	59	CSA, MMF	CSA, MMF	CSA	noT	no	-	-
5	male	62	MMF	pred	pred	noT	skin	~4 weeks	initial high doses
6	female	60	CSA, MMF	CSA, MMF	CSA, hydrocort	CSA, hydrocort	no	>20 weeks	low-dose
7	male	57	MMF	noT	noT	noT	no	-	-
8	female	49	CSA, MMF	CSA	CSA, Rituximab	CSA, pred, rapa	skin, IT	~3 weeks	initial high doses
9	male	55	rapa, MMF, hydrocort, CSA	MMF, CSA	CSA	CSA, pred, rapa	skin, IT	~4 weeks	initial high doses
10	male	63	pred, rapa	pred, rapa	pred, rapa	noT	no	>8 weeks	low-dose
12	female	45	CSA, MMF	n/a	n/a	n/a	no	-	-
14	female	42	CSA, rapa, MMF	rapa, pred	rapa, pred	rapa, pred	skin	>15 weeks	initial high doses
15	male	66	rapa, MMF, pred	rapa, MMF, pred	rapa, MMF, pred	rapa, pred	no	>25 weeks	low-dose
16	female	34	CSA, MMF	CSA, MMF	CSA, MMF, pred	hydrocort	skin	~6 weeks	initial high doses
17	male	58	MMF, CSA, rapa	rapa, MMF	rapa	rapa	no	-	-
18	male	45	CSA, pred, budesonid	rapa, pred	rapa, pred	n/a	liver, IT	>14 weeks	initial high doses
22	male	48	rapa, MMF	rapa, MMF	rapa, MMF	noT	no	-	-
24	male	49	CSA, rapa	CSA, rapa	n/a	n/a	no	-	-
26	male	65	CSA, MMF	CSA, MMF	CSA	CSA	no	-	-

CSA = cyclosporine, rapa = rapamycin, hydrocort = hydrocortisone, pred = prednisolone, MMF = mycophenolate mofetil, CS = corticosteroid, IT = intestinal tract, low-dose (<1 mg/kg), high-dose (>1 mg/kg)

23

Supplementary Information
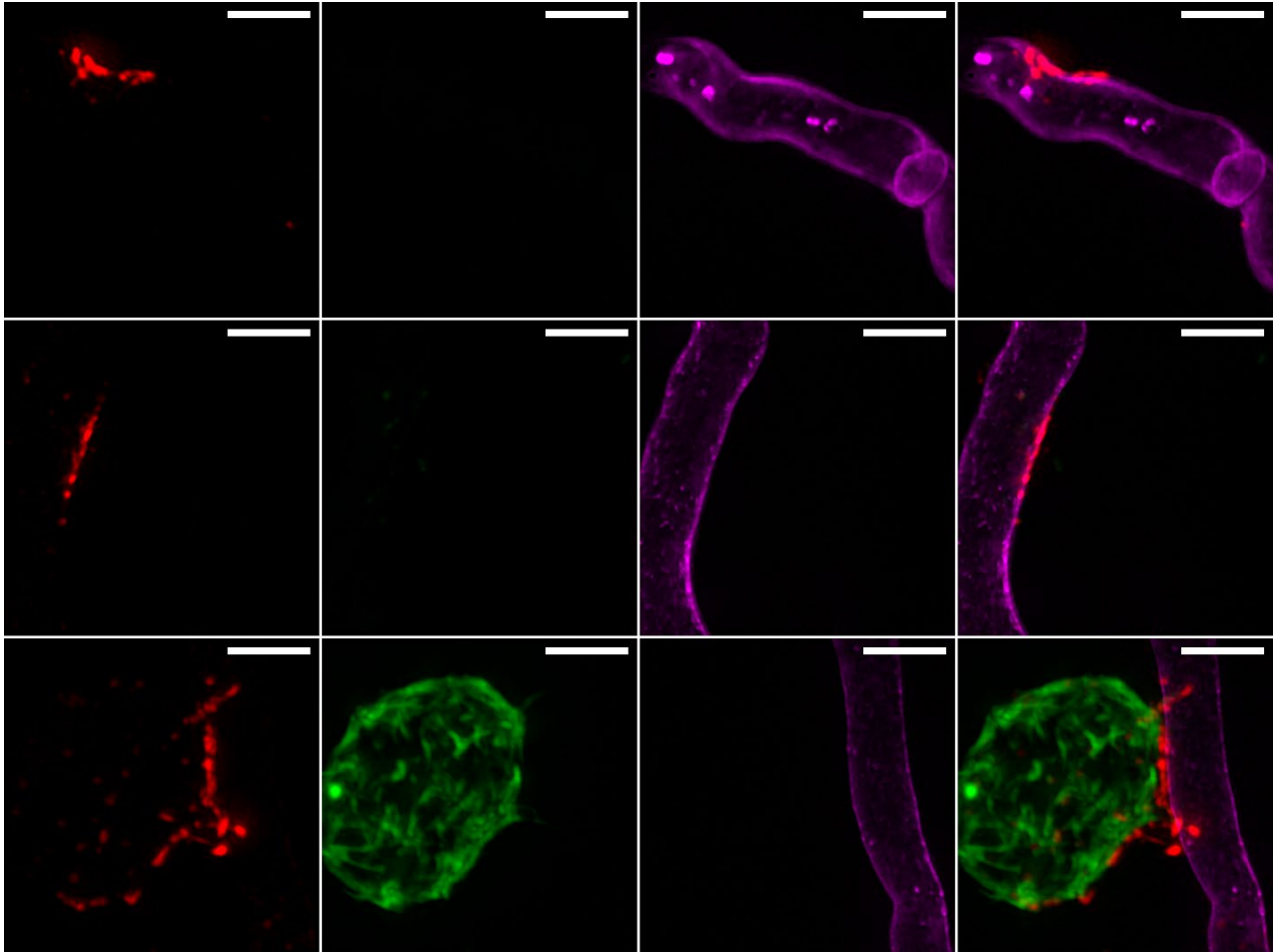
Supplementary Figure 1: The remaining CD56-positive interaction site on the fungal surface after physical separation of co-cultures. First two rows show example images from NK cell CD56 contact sites (red) after physical separation of NK cells (green) from *A. fumigatus* (magenta). Remaining CD56 signal at the hyphae indicates a strong molecular interaction, whereas whole NK cells (green) were washed away. NK cells were labelled with phalloidin and *A. fumigatus* with calcofluor. Scale bar, 3 μm.
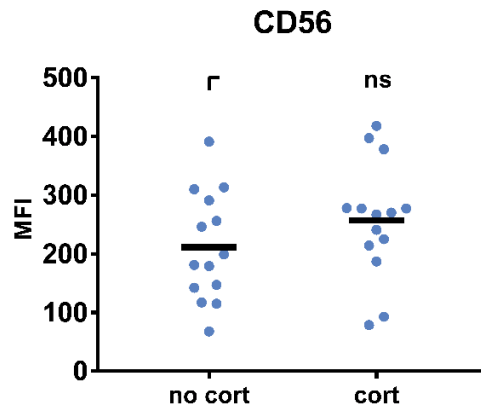
CD56

Supplementary Figure 2: CD56 MFI is not altered on NK cells obtained from corticosteroid recipients. NK cells derived after alloSCT were incubated with 1000 U/ml IL-2 overnight before the medium was exchanged, and NK cells were cultured for 6 h in RPMI + FCS. The surface expression of CD56 was determined by flow cytometry. Mean fluorescence intensities (MFI) of CD56 was determined in NK cells obtained from patients with (cort) or without corticosteroid (no cort) treatment. Samples were matched regarding time after alloSCT and further drug treatment. Data were acquired from n = 14 experiments. Data are displayed as medians. Statistical analysis was performed by unpaired t-test with Welch's correction.
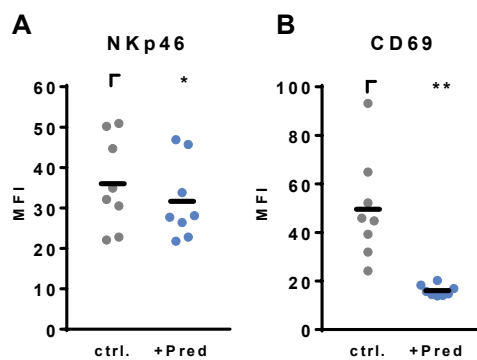
Supplementary Figure 3: Prednisolone treatment of healthy NK cells decreases the expression of the activation markers NKp46 and CD69. NK cells were treated with 25 µg/ml prednisolone in the presence of 1000 U/ml IL-2 for 40 h. The medium was exchanged, and NK cells were either cultured alone or with *A. fumigatus* germ tubes (MOI 0.5) for 6 h. Cells were analyzed regarding the surface expression of **(A)** NKp46 and **(B)** CD69 using flow cytometry. Data are displayed as means. Statistical analyses were performed by paired t-test and significant differences are marked by asterisks (* p < 0.05, ** p < 0.01).
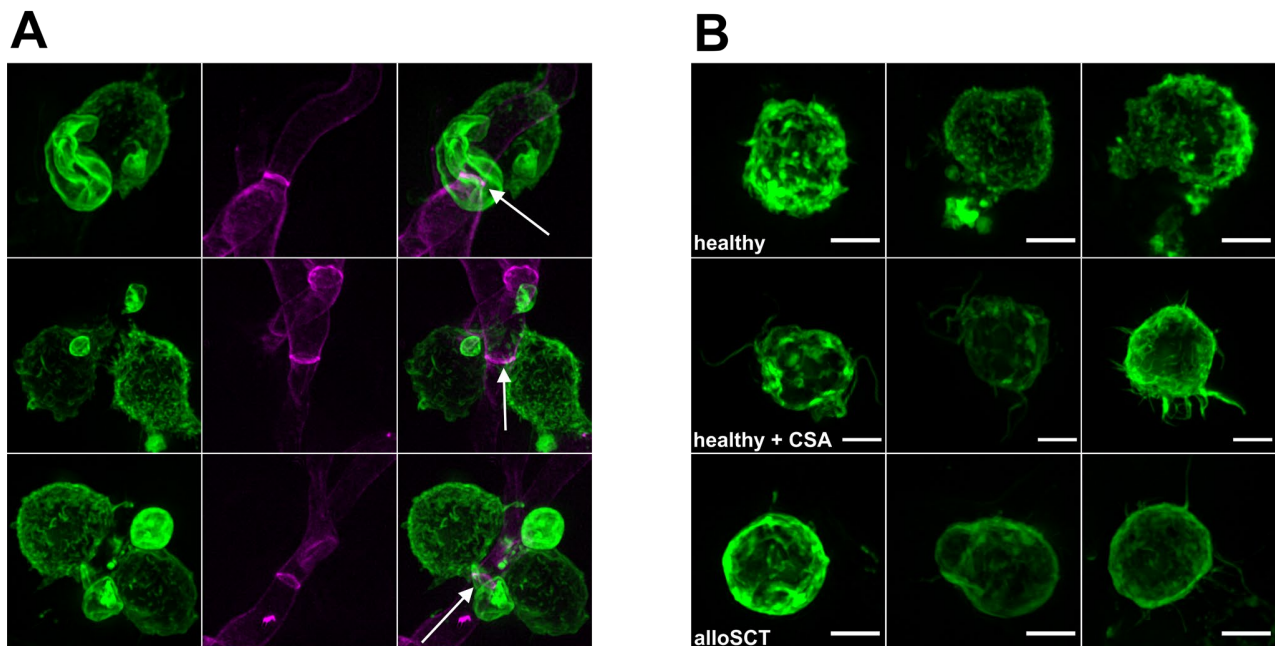
Supplementary Figure 4: NK cells interact at *A. fumigatus* septae and show different actin morphologies upon corticosteroid treatment. NK cells were labelled with phalloidin (green) and *A. fumigatus* with calcofluor (magenta). (A) Frequently, NK cells adhered at fungal septae (white arrow) and showed strong actin induction. (B) Healthy NK cells showed distinct and fine actin protrusions which were abolished upon *ex vivo* cyclosporine treatment or in several alloSCT NK cells. Scale bar, 3µm.
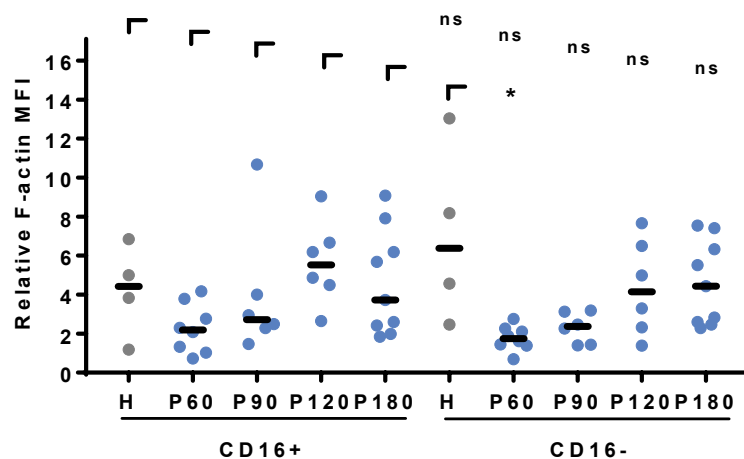
Supplementary Figure 5: NK cells were isolated from patients 60, 90, 120, and 180 days after alloSCT (P) or healthy controls (H). For analysis, NK cells were pre-stimulated with 1000 U/ml IL-2 overnight and afterward co-cultured with *A. fumigatus* germ tubes (MOI 0.5) or alone for 6 h. NK cells were treated with the F-Actin binding probe Sir647 for 50 min before cells were analyzed by flow cytometry. Relative actin induction was calculated by the division of Sir647 MFI after fungal co-culture with Sir647 MFI of control cells. Data were acquired from n = 4 (H); n = 8 (P60); n = 6 (P90); n = 6 (P120); n = 9 (P180) different

experiments. Data are displayed as medians. Significant differences were calculated by Kruskal-Wallis test with FDR correction to compare within NK cell subsets, and Wilcoxon test to compare between NK cell subsets. Statistical significance is marked by an asterisk (* $p < 0.05$).

Supplementary Video 1: Single-molecule tracking of CD56 on human NK cells. NK cells were isolated from patients 120 days after alloSCT or healthy individuals and labelled with anti-CD56 antibodies as described. Example video from one experiment showing CD56 receptors moving on the basal plasma membrane. Single spots are marked by magenta circles and local tracks are shown as yellow lines. The video was generated with the help of the Fiji plugin TrackMate [1,2]. Scale bar, 2 µm.

Supplementary Video 2: Single-molecule tracking of CD56 on human NK cells in combination with actin visualization. NK cells were isolated from patients 120 days after alloSCT or healthy individuals and labelled with anti-CD56 antibodies and SiR700 actin as described. Example video from one experiment showing bright CD56 receptors moving along individual actin filaments in the NK cell periphery.

Corre, Carmagnat, Busson, de Latour, Robin, Ribaud, . . . Socie, Long-term immune deficiency after allogeneic stem cell transplantation: B-cell deficiency is associated with late infections. *Haematologica* 95, 1025-1029 (2010).

Steele, Rapaka, Metz, Pop, Williams, Gordon, . . . Brown, The beta-glucan receptor dectin-1 recognizes specific morphologies of Aspergillus fumigatus. *PLoS pathogens* 1, e42 (2005).

Park, Lee, Recognition of lipopolysaccharide pattern by TLR4 complexes. *Experimental & Molecular Medicine* 45, e66 (2013).

Kawai, Akira, The roles of TLRs, RLRs and NLRs in pathogen recognitionInt Immunol. 21:313. *International Immunology* 21, 317-337 (2009).

Bjorkstrom, Ljunggren, Michaelsson, Emerging insights into natural killer cells in human peripheral tissues. *Nature reviews. Immunology* 16, 310-320 (2016).

Marquardt, Kekalainen, Chen, Kvedaraite, Wilson, Ivarsson, . . . Michaelsson, Human lung natural killer cells are predominantly comprised of highly differentiated hypofunctional CD69-CD56dim cells. *J Allergy Clin Immunol* 139, 1321-1330 e1324 (2017).

Campbell, Hasegawa, Natural killer cell biology: an update and future directions. *J Allergy Clin Immunol* 132, 536-544 (2013).

Caligiuri, Human natural killer cells. *Blood Journal*, (2008).

Romagnani, Juelke, Falco, Morandi, D'Agostino, Costa, . . . Ferlazzo, CD56brightCD16- killer Ig-like receptor- NK cells display longer telomeres and acquire features of CD56dim NK cells upon activation. *J Immunol* 178, 4947-4955 (2007).

Moretta, Dissecting CD56dim human NK cells. *Blood* 116, 3689-3691 (2010).

Chan, Hong, Atzberger, Kollnberger, Filer, Buckley, . . . Bowness, CD56bright human NK cells differentiate into CD56dim cells: role of contact with peripheral fibroblasts. *J Immunol* 179, 89-94 (2007).

Dulphy, Haas, Busson, Belhadj, Peffault de Latour, Robin, . . . Toubert, An Unusual CD56brightCD16low NK Cell Subset Dominates the Early Posttransplant Period following

HLA-Matched Hematopoietic Stem Cell Transplantation. *The Journal of Immunology* 181, 2227-2237 (2008).

Topham, Hewitt, Natural killer cell cytotoxicity: how do they pull the trigger? *Immunology* 128, 7-15 (2009).

Lieke, Nylen, Eidsmo, McMaster, Mohammadi, Khamesipour, . . . Akuffo, Leishmania surface protein gp63 binds directly to human natural killer cells and inhibits proliferation. *Clin Exp Immunol* 153, 221-230 (2008).

Vitenshtein, Charpak-Amikam, Yamin, Bauman, Isaacson, Stein, . . . Mandelboim, NK Cell Recognition of Candida glabrata through Binding of NKp46 and NCR1 to Fungal Ligands Epa1, Epa6, and Epa7. *Cell Host Microbe* 20, 527-534 (2016).

Fauci, Mavilio, Kottilil, NK cells in HIV infection: paradigm for protection or targets for ambush. *Nature reviews. Immunology* 5, 835-843 (2005).

Morrison, Park, Mooney, Mehrad, Chemokine-mediated recruitment of NK cells is a critical host defense mechanism in invasive aspergillosis. *Journal of Clinical Investigation* 112, 1862-1870 (2003).

Park, Hughes, Burdick, Strieter, Mehrad, Early NK cell-derived IFN-{gamma} is essential to host defense in neutropenic invasive aspergillosis. *J Immunol* 182, 4306-4312 (2009).

Stuehler, Kuenzli, Jaeger, Baettig, Ferracin, Rajacic, . . . Khanna, Immune Reconstitution After Allogeneic Hematopoietic Stem Cell Transplantation and Association With Occurrence and Outcome of Invasive Aspergillosis. *J Infect Dis* 212, 959-967 (2015).

Li, Kyei, Timm-McCann, Ogbomo, Jones, Shi, . . . Mody, The NK Receptor NKp30 Mediates Direct Fungal Recognition and Killing and Is Diminished in NK Cells from HIV-Infected Patients. *Cell Host & Microbe* 14, 387-397 (2013).

Ziegler, Weiss, Schmitt, Schlegel, Burgert, Terpitz, . . . Loeffler, CD56 Is a Pathogen Recognition Receptor on Human Natural Killer Cells. *Scientific reports*. 2017 (10.1038/s41598-017-06238-4.).

Weiss, Ziegler, Fliesser, Schmitt, Hünniger, Kurzai, . . . Loeffler, First Insights in NK—DC Cross-Talk and the Importance of Soluble Factors During Infection With Aspergillus fumigatus. *Front Cell Infect Microbiol* 8, (2018).

Schindelin, Arganda-Carreras, Frise, Kaynig, Longair, Pietzsch, . . . Cardona, Fiji: an open-source platform for biological-image analysis. *Nat Methods* 9, 676-682 (2012).

Schlegel, Peters, Doose, Schubert-Unkmeir, Sauer, Super-Resolution Microscopy Reveals Local Accumulation of Plasma Membrane Gangliosides at Neisseria meningitidis Invasion Sites. *Frontiers in Cell and Developmental Biology* 7, (2019).

Wäldchen, Schlegel, Götz, Luciano, Schnermann, Doose, Sauer, Whole-cell imaging of plasma membrane receptors by 3D lattice light-sheet dSTORM. *Nature Communications* 11, 887 (2020).

Tsunoyama, Watanabe, Goto, Naito, Kasai, Suzuki, . . . Kusumi, Super-long single-molecule tracking reveals dynamic-anchorage-induced integrin function. *Nat Chem Biol* 14, 497-506 (2018).

Burgert, Schlegel, Becam, Doose, Bieberich, Schubert-Unkmeir, Sauer, Characterization of Plasma Membrane Ceramides by Super-Resolution Microscopy. *Angew Chem Int Ed Engl* 56, 6131-6135 (2017).

Ovesny, Krizek, Borkovec, Svindrych, Hagen, ThunderSTORM: a comprehensive ImageJ plug-in for PALM and STORM data analysis and super-resolution imaging. *Bioinformatics* 30, 2389-2390 (2014).

Crocker, Grier, Methods of Digital Video Microscopy for Colloidal Studies. *Journal of Colloid and Interface Science* 179, 298-310 (1996).

28

Allan, trackpy: Trackpy v0.4.1 (Version v0.4.1). Zenodo. . (2018, April 21).

Ullah, Hill, Tey, Functional Reconstitution of Natural Killer Cells in Allogeneic Hematopoietic Stem Cell Transplantation. *Frontiers in immunology* 7, 144 (2016).

Charmoy, Brunner-Agten, Aebischer, Auderset, Launois, Milon, . . . Tacchini-Cottier, Neutrophil-Derived CCL3 Is Essential for the Rapid Recruitment of Dendritic Cells to the Site of Leishmania major Inoculation in Resistant Mice. *PLoS pathogens* 6, e1000755 (2010).

Bless, Huber-Lang, Guo, Warner, Schmal, Czermak, . . . Ward, Role of CC chemokines (macrophage inflammatory protein-1 beta, monocyte chemoattractant protein-1, RANTES) in acute lung injury in rats. *J Immunol* 164, 2650-2659 (2000).

Souto, Aliberti, Campanelli, Livonesi, Maffei, Ferreira, . . . Silva, Chemokine production and leukocyte recruitment to the lungs of Paracoccidioides brasiliensis-infected mice is modulated by interferon-gamma. *Am J Pathol* 163, 583-590 (2003).

Fauriat, Long, Ljunggren, Bryceson, Regulation of human NK-cell cytokine and chemokine production by target cell recognition. *Blood* 115, 2167-2176 (2010).

Ohira, Nishida, Tryphonopoulos, Ruiz, Ohdan, Tzakis, Impact of Steroids on Natural Killer Cells Against Cytotoxicity and Hepatitis C Virus Replication. *Transplant Proc* 49, 1160-1164 (2017).

Gustafsson, Surpassing the lateral resolution limit by a factor of two using structured illumination microscopy. *J Microsc* 198, 82-87 (2000).

Hansen, Woringer, Grimm, Lavis, Tjian, Darzacq, Robust model-based analysis of single-particle tracking experiments with Spot-On. *Elife* 7, (2018).

Muhlemann, Wenger, Zenhausern, Tauber, Risk factors for invasive aspergillosis in neutropenic patients with hematologic malignancies. *Leukemia* 19, 545-550 (2005).

Labbe, Su, Laverdiere, Pepin, Patino, Cohen, . . . Roy, High incidence of invasive aspergillosis associated with intestinal graft-versus-host disease following nonmyeloablative transplantation. *Biol Blood Marrow Transplant* 13, 1192-1200 (2007).

Quellmann, Schwarzer, Hubel, Greb, Engert, Bohlius, Corticosteroids for preventing graft-versus-host disease after allogeneic myeloablative stem cell transplantation. *Cochrane Database Syst Rev*, Cd004885 (2008).

Thum, Bhaskaran, Abdalla, Ford, Sumar, Bansal, Prednisolone suppresses NK cell cytotoxicity in vitro in women with a history of infertility and elevated NK cell cytotoxicity. *Am J Reprod Immunol* 59, 259-265 (2008).

Scheinman, Gualberto, Jewell, Cidlowski, Baldwin, Characterization of mechanisms involved in transrepression of NF-kappa B by activated glucocorticoid receptors. *Mol Cell Biol* 15, 943-953 (1995).

Elftman, Norbury, Bonneau, Truckenmiller, Corticosterone impairs dendritic cell maturation and function. *Immunology* 122, 279-290 (2007).

Bacigalupo, Milone, Cupri, Severino, Fagioli, Berger, . . . Gruppo Italiano Trapianto di Midollo, Steroid treatment of acute graft-versus-host disease grade I: a randomized trial. *Haematologica* 102, 2125-2133 (2017).

Jantzen, Strahle, Gloss, Stewart, Schmid, Boshart, . . . Schutz, Cooperativity of glucocorticoid response elements located far upstream of the tyrosine aminotransferase gene. *Cell* 49, 29-38 (1987).

Beato, Gene regulation by steroid hormones. *Cell* 56, 335-344 (1989).

Beato, Truss, Chavez, Control of transcription by steroid hormones. *Ann N Y Acad Sci* 784, 93-123 (1996).

Nelson, Wilde, Spiller, Kennedy, Ray, Sullivan, . . . White, NF-kappaB signalling is inhibited by glucocorticoid receptor and STAT6 via distinct mechanisms. *J Cell Sci* 116, 2495-2503 (2003).

Moriuchi, Moriuchi, Fauci, Nuclear factor-kappa B potently up-regulates the promoter activity of RANTES, a chemokine that blocks HIV infection. *J Immunol* 158, 3483-3491 (1997).

Grove, Plumb, C/EBP, NF-kappa B, and c-Ets family members and transcriptional regulation of the cell-specific and inducible macrophage inflammatory protein 1 alpha immediate-early gene. *Mol Cell Biol* 13, 5276-5289 (1993).

Widmer, Manogue, Cerami, Sherry, Genomic cloning and promoter analysis of macrophage inflammatory protein (MIP)-2, MIP-1 alpha, and MIP-1 beta, members of the chemokine superfamily of proinflammatory cytokines. *J Immunol* 150, 4996-5012 (1993).

Schrum, Probst, Fleischer, Zipfel, Synthesis of the CC-chemokines MIP-1alpha, MIP-1beta, and RANTES is associated with a type 1 immune response. *J Immunol* 157, 3598-3604 (1996).

Huang, Levitz, Stimulation of macrophage inflammatory protein-1alpha, macrophage inflammatory protein-1beta, and RANTES by Candida albicans and Cryptococcus neoformans in peripheral blood mononuclear cells from persons with and without human immunodeficiency virus infection. *J Infect Dis* 181, 791-794 (2000).

Lee, Mace, Acquisition of cell migration defines NK cell differentiation from hematopoietic stem cell precursors. *Molecular biology of the cell* 28, 3573-3581 (2017).

Carisey, Mace, Saeed, Davis, Orange, Nanoscale Dynamism of Actin Enables Secretory Function in Cytolytic Cells. *Curr Biol* 28, 489-502.e489 (2018).

Watzl, Long, Natural killer cell inhibitory receptors block actin cytoskeleton-dependent recruitment of 2B4 (CD244) to lipid rafts. *J Exp Med* 197, 77-85 (2003).

3.11   Nanoscale Imaging of Bacterial Infections by Sphingolipid Expansion Microscopy

Abstract

"Expansion microscopy (ExM) enables super-resolution imaging of proteins and nucleic acids on conventional microscopes. However, imaging of details of the organization of lipid bilayers by light microscopy remains challenging. We introduce an azide- and amino-modified sphingolipid ceramide, which upon incorporation into membranes can be labeled by click chemistry and linked into hydrogels, followed by 4x to 10x expansion. Confocal and structured illumination microscopy (SIM) enabled imaging of sphingolipids and their interactions with proteins in the plasma membrane and membrane of intracellular organelles with a spatial resolution of 10-20 nm. Because sphingolipids accumulated efficiently in pathogens we used sphingolipid ExM to investigate bacterial infections of human HeLa229 cells by *Neisseria gonorrhoeae*, *Chlamydia trachomatis* and *Simkania negevensis* with a resolution so far only provided by electron microscopy. In particular, sphingolipid ExM allowed us to visualize the inner and outer membrane of intracellular bacteria and determine their distance to 27.6 ± 7.7 nm."

The following manuscript was submitted on June 8th, 2020 to an open-access peer-reviewed international journal and permission for legal second publication within this thesis was kindly granted from both the publishers and the co-authors.

Nanoscale imaging of bacterial infections by sphingolipid expansion microscopy

Ralph Götz[1‡], Tobias C. Kunz[2‡], Julian Fink[3], Franziska Solger[2], Jan Schlegel[1], Jürgen Seibel[3], Vera Kozjak-Pavlovic[2], Thomas Rudel[2, †] and Markus Sauer[1, †]

[1]Department of Biotechnology and Biophysics, Biocenter, Julius-Maximilians-Universität Würzburg, Am Hubland, 97074 Würzburg, Germany

[2]Department of Microbiology, Biocenter, Julius-Maximilians-Universität Würzburg, Am Hubland, 97074 Würzburg, Germany

[3]Institute for Organic Chemistry, Julius-Maximilians-Universität Würzburg, Am Hubland, 97074 Würzburg, Germany

[‡]These authors contributed equally: Ralph Götz, Tobias C. Kunz

[†]Corresponding authors: T.R. (thomas.rudel@biozentrum.uni-wuerzburg.de) M.S. (m.sauer@uni-wuerzburg.de)

Abstract

Expansion microscopy (ExM) enables super-resolution imaging of proteins and nucleic acids on conventional microscopes. However, imaging of details of the organization of lipid bilayers by light microscopy remains challenging. We introduce an azide- and amino-modified sphingolipid ceramide, which upon incorporation into membranes can be labeled by click chemistry and linked into hydrogels, followed by 4x to 10x expansion. Confocal and structured illumination microscopy (SIM) enabled imaging of sphingolipids and their interactions with proteins in the plasma membrane and membrane of intracellular organelles with a spatial resolution of 10-20 nm. Because sphingolipids accumulated efficiently in pathogens we used sphingolipid ExM to investigate bacterial infections of human HeLa229 cells by *Neisseria gonorrhoeae, Chlamydia trachomatis* and *Simkania negevensis* with a resolution so far only provided by electron microscopy. In particular, sphingolipid ExM allowed us to visualize the inner and outer membrane of intracellular bacteria and determine their distance to 27.6 ± 7.7 nm.

Introduction

In the last decade, super-resolution microscopy has evolved as a very powerful method for subdiffraction-resolution fluorescence imaging of cells and structural investigations of cellular organelles[1,2]. Super-resolution microscopy methods can now provide a spatial resolution that is well below the diffraction limit of light microscopy, enabling invaluable insights into the spatial organization of proteins in biological samples. However, in particular three-dimensional and multicolor super-resolution microscopy methods require elaborate equipment and experience and are therefore mostly restricted to specialized laboratories.

Expansion microscopy (ExM) provides an alternative approach to bypass the diffraction limit and enable super-resolution imaging on standard fluorescence microscopes. By linking a protein of interest into a dense, cross-linked network of a swellable polyelectrolyte hydrogel, biological specimens can be physically expanded allowing ~70 nm lateral resolution by confocal laser scanning microscopy. Since its introduction by Boyden and co-workers in 2015[3], expansion microscopy (ExM) has shown impressive results including the magnified visualization of pre- or post-expansion labeled proteins and RNAs with fluorescent proteins, antibodies, and oligonucleotides, respectively, in cells, tissues, and human clinical specimen[4]. ExM has been developing at an enormous speed with various protocols providing expansion factors from 4x[3] to 10x[5,6] and even 20x by iterative expansion[7]. In addition, various protocols have been introduced enabling subdiffraction-resolution imaging of proteins, RNA, and bacteria in cultured cells, neurons, and tissues by confocal fluorescence microscopy and in combination with super-resolution microscopy[5-14].

In order to be usable for ExM, the molecule of interest has to exhibit amino groups that can react with glutaraldehyde (GA)[9], MA-NHS[9], AcX[10], or Label-X[11] and be linked into the polyelectrolyte hydrogel. The plasma membrane of cells is mainly composed of glycerophospholipids, sphingolipids, and cholesterol. Due to the lack of primary amino groups, these lipids neither can be fixed by formaldehyde, glutaraldehyde and other chemical fixatives nor expanded using available ExM protocols. To this end, we sought to functionalize a lipid that is compatible with ExM. So far, sphingolipids have only been functionalized as azides to enable fluorescence labeling by click chemistry after incorporation into cellular membranes[15-18]. Therefore, we set out to introduce an azide and primary amino group into sphingolipids to enable fluorescence labeling and chemical fixation as well as linking of the lipid into a swellable hydrogel. Our results demonstrate that the designed bifunctional sphingolipid is efficiently incorporated into membranes of cells and accumulates in bacterial membranes, which allowed us to investigate the distribution of lipids and interactions with proteins in cellular and bacterial membranes with high spatial resolution.

Results

Sphingolipid ExM of cellular membranes

Sphingolipids are natural lipids comprised of the sphingoid base backbone sphingosine, which when N-acylated with fatty acids forms ceramide, a central molecule in sphingolipid biology. Sphingolipid ceramides regulate cellular processes such as differentiation, proliferation, growth arrest and apoptosis. Ceramide-rich membrane areas promote structural changes within the plasma membrane, which segregate membrane receptors and affect the membrane curvature and vesicle formation, fusion and trafficking[19,20].

We selected ω-N$_3$-C$_6$-ceramide, which is efficiently incorporated into cellular membranes and can be click-labeled with DBCO-functionalized dyes for fluorescence imaging[21,22], for further functionalization with a primary amino group (Supplementary **Figs. 1-13**). Therefore, we synthesized α-NH$_2$-ω-N$_3$-C$_6$-ceramide from (*tert*-butoxycarbonyl)-L-lysine (**Fig. 1a**). We first assessed if the synthesized α-NH$_2$-ω-N$_3$-C$_6$-ceramide (**Fig. 1a**) is incorporated into cellular membranes similar to the control ceramide without amino modification and can be labeled by click chemistry with DBCO-dyes. For this, cells were fed for 1 h with the two ceramides, fixed with glutaraldehyde and click-labeled with DBCO-Alexa Fluor 488. Confocal fluorescence images showed that both analogues ω-N$_3$-C$_6$-ceramide and α-NH$_2$-ω-N$_3$-C$_6$-ceramide were incorporated into the plasma membrane and membranes of intracellular organelles of HeLa229 cells with comparable efficiency (**Fig. 1**). Fluorescence recovery after photobleaching (FRAP) experiments with both ceramides indicated that ω-N$_3$-C$_6$-ceramide shows a higher mobility in the plasma membrane after fixation than α-NH$_2$-ω-N$_3$-C$_6$-ceramide (**Fig. 1b**). This finding was corroborated by the treatment of labeled cells with detergents, which wash out unfixed lipids. Upon addition of Triton X-100 or saponine ω-N$_3$-C$_6$-ceramide was efficiently washed out whereas the fluorescence signal of the amino-modified analog α-NH$_2$-ω-N$_3$-C$_6$-ceramide decreased only slightly and was preserved for weeks (**Fig. 1c** and **Supplementary Fig. 14**). These results demonstrate that the crosslinker glutaraldehyde can efficiently fix amino-modified ceramides incorporated into cellular membranes.

Since glutaraldehyde (GA) can link proteins into hydrogels[9] we reasoned that α-NH$_2$-ω-N$_3$-C$_6$-ceramides might be as well suited for membrane expansion. To demonstrate its usefulness for ExM we treated HeLa229 with NH$_2$-ω-N$_3$-C$_6$-ceramide followed by glutaraldehyde fixation, permeabilization, fluorescence labeling with DBCO-Alexa Fluor 488, and gelation. For direct comparison we tested the membrane-binding fluorophore-cysteine-lysine-palmitoyl group (mCling), which labels the plasma membrane and is taken up during endocytosis[23]. Since it carries a primary amine as well, it also remains attached to membranes after fixation and permeabilization and can therefore potentially be used for ExM. In fact, both amino-functionalized membrane probes can be expanded using the GA ExM protocol[9]. 4x and 10x

expanded confocal fluorescence images of ceramide stained cells clearly showed staining of the plasma membrane as well as of membranes of intracellular organelles such as mitochondria, whereas mCling is efficiently incorporated mainly into the cell's plasma membrane (**Fig. 2**). To verify the expansion factor and investigate if sphingolipid ExM distorts membranes we imaged the same cell before and after 4x and 10x expansion and determined effective expansion factors of 4.1x and 9.8x (**Supplementary Fig. 15**). The confocal fluorescence images of 4x and 10x expanded cellular membranes demonstrate that sphingolipid ExM labeling is dense enough to support nanoscale resolution imaging of continuous membrane structures and even thin membrane protrusions (**Fig. 2** and **Supplementary Fig. 15**).

Imaging of expanded lipids and proteins

Furthermore, we tested if the sphingolipid ExM protocol enables imaging of lipids and proteins in the same sample. We therefore immunolabeled the mitochondrial protein Prx3 after permeabilization and click labeling of the bifunctional ceramide. The results obtained clearly showed that the amino-functionalized sphingolipid NH_2-ω-N_3-C_6-ceramide can be used advantageously for super-resolution imaging of cellular membranes and interactions between proteins and ceramides in 4x and 10x expanded samples (**Fig. 2a**). Very recently, Boyden and coworkers introduced an alternative membrane ExM method (mExM) based on a membrane intercalating probe, which enables imaging of 4.5x expanded cellular membranes[24]. The membrane probe contains a chain of lysines for binding to a polymer anchorable handle and a lipid tail on the amine terminus of the lysine chain, with a glycine in between to provide mechanical flexibility. Furthermore, a biotin residue is attached to enable fluorescence staining of the probe with labeled streptavidin. Both methods, mExM and sphingolipid ExM allow for joint imaging of proteins and lipid membrane structures at nanoscale resolution.

Sphingolipid ExM of bacterial infections

In addition to the regulation of cellular processes, ceramides play an essential role in infections with pathogenic bacteria[8,25,26]. These include *Neisseria gonorrhoeae*[27], *Simkania negevensis*[28] and *Chlamydia trachomatis*[29,30]. *C. trachomatis* is by far the best investigated example for an interaction of pathogenic bacterium and host sphingolipid metabolism. This obligate intracellular Gram-negative bacterium is the most frequent cause of bacterial sexually transmitted diseases[31]. It resides in a membrane-bound vacuole (the inclusion) inside their host cells and undergoes a complex developmental cycle between infectious non-replicating elementary bodies (EB) and non-infectious replicating reticulate bodies (RB). During infection, *Chlamydia* manipulate a plethora of cellular processes, among them the sphingolipid

metabolism[15,16,32]. The ceramide transporter CERT seems to play a key role in ceramide uptake as it strongly localizes in infected cells at the inclusion membrane recruited by the bacterial inclusion protein IncD instead of mediating golgi-ER-trafficking[33].

To study ceramide uptake by pathogens during infection in more detail we first fed cells with NH_2-ω-N_3-C_6-ceramide for 5 to 60 min 24 h post infection with *C. trachomatis*. The cells were then GA fixed and click-labeled with DBCO-Alexa Fluor 488 for fluorescence imaging. Confocal fluorescence images demonstrated rapid integration of the ceramide into the membrane of *C. trachomatis* already after 5 min and further increasing for longer incubation times (**Supplementary Fig. 16**). This indicates a highly effective and fast ceramide uptake by *C. trachomatis*. Additionally, we applied the specific CERT inhibitor HPA-12 to impede ceramide integration into the bacterial membrane. Fluorescence images recorded after application of HPA-12 showed that HPA-12 efficiently inhibits ceramide uptake by *C. trachomatis* at higher concentrations for short ceramide incubation times of 5 and 15 min (**Supplementary Fig. 16**). For longer ceramide incubation times the influence of HPA-12 treatment on ceramide uptake by bacteria was negligible, suggesting the involvement of different lipid uptake pathways such as vesicle trafficking from the Golgi apparatus[34].

Next, we investigated if the uptake of ceramides by intracellular pathogens enables ExM of infected cells. Therefore, we fed NH_2-ω-N_3-C_6-ceramide to HeLa229 cells post-infection with *C. trachomatis* and *S. negevensis,* another member of the order *Chlamydiales* (**Fig. 3**). Cells were then fixed with GA, permeabilized, click-labeled with DBCO-Alexa Fluor 488 and expanded using two different ExM protocols. Confocal fluorescence images of the same cells recorded before and after 10x expansion revealed a good quality agreement of bacterial membrane shapes and numbers of bacteria (**Supplementary Fig. 17**). In addition, the post-expansion images clearly showed that the ceramides accumulate strongly in bacterial membranes after infection (**Supplementary Fig. 17**).

Cells infected with a high number of *S. negevensis* required 10x expansion to distinguish individual bacteria (**Figs. 3a-c**). On the other hand, already 4x expansion was sufficient to distinguish between the two forms of *C. trachomatis,* RBs and EBs as has already been shown previously by ExM (**Figs. 3d,e**)[8]. Higher expansion (10x ExM) demonstrated that the ceramide signal accumulates in the membranes of the two pathogens *C. trachomatis* and *S. negevensis* (**Figs. 3c,f**). The fluorescence signals of host cell membranes appeared comparably dim (compare **Fig. 2** and **Fig. 3**) indicating an extremely efficient ceramide uptake by bacteria. Corresponding control experiments with ω-N_3-C_6-ceramide and DBCO-Alexa Fluor 488 alone showed only very weak background staining (**Supplementary Fig. 18**). These results clearly show that sphingolipid ExM enables very dense and continuous membrane staining of

intracellular bacteria and thus imaging of bacterial membranes with a resolution hitherto only provided by electron microscopy.

So far, we focused our investigations on bacterial infections and demonstrated the fast and efficient incorporation of NH_2-ω-N_3-C_6-ceramide into *C. trachomatis* and *S. negevensis* and their 4x and 10x expansion (**Fig. 3**). The introduced method can be highly valuable for studying not only host pathogen interactions but also lipid metabolism. It would be very interesting to investigate the interaction of Inc proteins involved in ceramide transport like IncD, CERT, as well as Golgi and ER proteins to further elucidate the uptake and incorporation of ceramides into the membrane of *C. trachomatis*. Furthermore, we tested if the ceramide underlying structure sphingosine can be used successfully for ExM. The sphingoid base backbone sphingosine carries a natural amino group and plays a central role in infections with *N. gonorrhoeae* among other bacterial pathogens[34]. Addition of ω-N_3-sphingosine to infected Chang cells followed by GA fixation, permeabilization, click labeling with DIBO-Alexa Fluor 488 and gelation demonstrated the general applicability of the method. Details of intracellular *N. gonorrhoeae* can be clearly visualized by sphingolipid ExM (**Supplementary Fig. 19**).

Imaging interactions of bacteria and intracellular proteins

To demonstrate the compatibility of sphingolipid ExM for investigations of pathogen interactions with intracellular proteins, we investigated chlamydial interactions with mitochondria. It is known that *C. trachomatis* reorganizes the host organelles. However, so far all investigations have been performed by confocal fluorescence imaging or electron microscopy[35]. Hence, we immunolabeled the mitochondrial matrix protein Prx3 and incorporated ceramides in *C. trachomatis* infected cells before gelation. The corresponding confocal fluorescence images of 10x expanded samples showed the mitochondrial rearrangement after infection with *C. trachomatis* as mitochondria localized around the inclusion (**Fig. 3g**). To highlight details of this interaction by a higher spatial resolution we used structured illumination microscopy (SIM)[36], which allowed us to uncover direct interactions between mitochondria and *C. trachomatis* (**Fig. 3h**). In some cases, Prx3 signals appeared to be located in bacteria indicating unspecific protein uptake. Similar experiments performed in the absence of primary antibodies demonstrated that the signals detected in bacteria are not caused by nonspecific binding of the used secondary antibody (**Supplementary Fig. 20**). Albeit ceramides accumulate strongly in bacterial membranes the labeling density of intracellular membranes is still high enough to enable nanoscale imaging of protein-pathogen interactions in infected cells.

Interestingly, we could often detect individual Chlamydia within close proximity to the inclusion membrane after feeding with NH_2-ω-N_3-C_6-ceramides, possibly indicating an active docking to

the inclusion membrane and an absorption of nutrition by *C. trachomatis* (**Supplementary Fig. 21** and **Supplementary Movie 1**) as has been hypothesized earlier[37] and reported in electron microscopy studies[35,38]. This behavior has previously been proposed as a mechanism by which RBs acquire nutrients including host lipids[39] and as an essential step in chlamydial development[37]. However, previous attempts to localize chlamydial particles in the inclusion required highly laborious techniques such as Serial block-face scanning electron microscopy[35]. Using sphingolipid ExM with clickable probes, the three-dimensional structure of lipid interfaces can be imaged at a lateral resolution of ~20 nm by confocal fluorescence microscopy. This enables to investigate metabolite acquisition like highly efficient ceramide transfer from the host to bacterial membranes at higher resolution and even in three dimensions.

10x Sphingolipid ExM-SIM resolves the double membrane of intracellular bacteria

Whereas transport of ceramide to the *Chlamydia* inclusion has been reported earlier[29], one of the unanswered questions is whether ceramides form parts of the bacterial outer (OM) or inner membrane (IM) or of both these membranes. Indeed, SIM images of 10x expanded chlamydia demonstrated that NH_2-ω-N_3-C_6-ceramides are efficiently incorporated into the IM and OM of intracellular *Chlamydia* (**Figs. 4a,b**). The high labeling efficiency in combination with the high spatial resolution of 10-20 nm of 10x expanded samples provided by SIM allowed us to resolve the IM and OM. We investigated three different infected cells and selected those bacteria whose orientation allowed us to visualize spatially separated OM and IM (i.e. frontal views of bacteria) and determine the distance between the two membranes to 27.6 ± 7.7 nm (s.d.) from 23 cross sectional intensity profiles (**Supplementary Figs. 22** and **23**). This value is typical for the separation of OM and IM of gram-negative bacteria and in agreement with electron microscopy data[40]. Since the mechanism of bacterial membrane biogenesis from host-derived lipids is currently unknown, our findings of the ceramide incorporation in both bacterial membranes suggest an active process rather than only the fusion of lipid vesicles with the surface and exclusive integration into the outer membrane of *Chlamydia*.

The high spatial resolution provided by sphingolipid ExM may also be used to study mechanisms of antibiotic resistance. Infections with multidrug-resistant gram-negative bacteria are difficult to treat because of the double membrane that is impermeable for most antibiotics[41]. Hence, being able to visualize the double membrane might promote the development of antibiotics with improved membrane permeability. Furthermore, sphingolipid ExM can also be used advantageously to investigate various ceramide pathways related to apoptosis, proliferation, cancer, inflammation, and neurodegeneration[34,42].

Discussion

ExM has facilitated super-resolution imaging of cells and tissues with standard fluorescence microscopes available in most research facilities, yet it has been limited to the expansion of proteins and nucleic acids due to the lack of primary amino groups in lipids. We have developed the double-functionalized sphingolipid NH_2-ω-N_3-C_6-ceramide that incorporates efficiently into cellular and bacterial membranes and can be fixed, fluorescently labeled by click chemistry, and linked into polyelectrolyte hydrogels by GA treatment. The mechanism by which GA fixes and crosslinks amino-modified ceramides into hydrogels is less obvious but most probably associated with the existence of multimeric forms of GA containing aldehyde and alkene groups, which both can potentially be covalently linked to the acrylamide polymer[9]. Sphingolipid ExM allows for simultaneous super-resolution imaging of membranes and associated proteins in 4x and 10x expanded samples. In combination with SIM, sphingolipid ExM enables 10-20 nm spatial resolution, approaching that of electron microscopy and has allowed us to resolve details of sphingolipid-protein interactions. Such high spatial resolutions are difficult to achieve using pre-expansion immunolabeling with primary and secondary antibodies but feasible using small membrane incorporated ceramides that are linked into the polymer and fluorescently labeled with minimal linkage error. For clarification, pre-expansion immunolabeling introduces a linkage error of ~ 17.5 nm[7], which translates into a linkage error of ~ 175 nm after 10x expansion. Such large linkage errors in expanded samples severely blur the underlying structure and impede super-resolution imaging with high spatial resolution. We hypothesize that our approach of introducing a primary amino group for fixation and linkage into acrylamide polymers by GA can be broadly used to enable ExM of other lipids and thus far inaccessible molecule classes including carbohydrates.

Materials and Methods

Chemical Synthesis of *α*-Amino-*ω*-Azido-C$_6$-Ceramide

Starting from *N*-Boc-protected L-lysine (1) the introduction of the azide-functionality was accomplished *via* catalytic diazotransfer reaction to obtain azido-acid 2 in 85 % yield. For that, triflyl azide was prepared based on a method of *Yan et al.* with a reduced amount of highly toxic sodium azide and triflyl anhydride compared to previous protocols[43]. Subsequent amide coupling of 2 with sphingosine was performed in DMF under basic conditions using HATU as coupling reagent. The resulting Boc-protected azido-ceramide analogue 3 was isolated in 48 % yield. In the last step the amine group was deprotected by the treatment with TFA in dichloromethane. After basic workup, followed by column chromatography, the target ceramide analogue 4 was successfully isolated in 39% yield. Details on the experimental procedures can be found in the Supporting Information. All isolated compounds were characterized by a combination of HRMS, NMR and IR spectroscopy (**Supplementary Figs. 1-13**).

Cell lines and bacteria

Human HeLa229 cells (ATCC CCL-2.1tm) and human epithelial conjunctival cells (Chang) were cultured in 10 % (v/v) heat inactivated FBS (Sigma-Aldrich) RPMI1640 + GlutaMAXtm medium (Gibcotm) and were grown in a humidified atmosphere containing 5 % (v/v) CO$_2$ at 37 °C. HeLa229 cells were used for infection with *Chlamydia trachomatis* and *Simkania negevensis*, Chang cells for infection with *Neisseria gonorrhoeae.* For this study, *C. trachomatis* serovar L2/434/Bu (ATCC VR-902B^{tm}), *S. negevensis* and *N. gonorrhoeae* (strain MS11, derivative N927) were used. *C. trachomatis* and *S. negevensis* were cultivated as previously described[8,28] .For this, the bacteria were propagated in HeLa229 cells at a multiplicity of infection (MOI) of 1 for 48 h for *C. trachomatis* and 72 h for *S. negevensis*. The cells were then detached and lysed using glass beads (3 mm, Roth). Low centrifugation supernatant (10 min at 2000 g at 4 °C for *C. trachomatis* and 10 minutes at 600 g at 4 °C for *S. negevensis*) was transferred to high speed centrifugation (30 min at 30.000 g at 4 °C for *C. trachomatis* and 30 min at 20.000 g at 4 °C for *S. negevensis*) to pellet the bacteria. Afterwards, the pellet was washed and resuspended in 1x SPG buffer (7.5 % sucrose, 0.052 % KH$_2$PO$_4$, 0.122 % NaHPO$_4$, 0.072 % L-glutamate). The resuspended bacteria were then stored at -80 °C and titrated for an MOI of 1 for further experimentation. Infected cells were incubated in a humidified atmosphere with 5 % (v/v) CO$_2$ at 35 °C. The cell lines as well as the Chlamydia used in this study were tested to be free of Mycoplasma *via* PCR. Neisseria were cultivated on gonococci (GC) agar (ThermoScientific, Waltham, USA) plates supplemented with 1 % vitamin mix at 37 °C and 5 % CO$_2$ for 16 h. On the day of infection, liquid culture was performed in protease-peptone medium (PPM) supplemented with 1 % vitamin mix and 0.5 % sodium bicarbonate 8.4 % solution (PPM+) at 37 °C and 120 rpm. Gonococci were grown to an OD$_{550}$

0.4 to 0.6. Before infecting the cells, the medium of the liquid culture was changed to 4-(2-Hydroxyethyl)piperazine-1-ethanesulfonic acid (HEPES buffer) medium by centrifugation with 4000 rpm for 5 min. After the indicated time of 4 h, the infection was stopped by washing the cells three times with Hepes medium.

Click-Chemistry and Immunolabeling

For immunostaining, cells were seeded on 15 mm coverslips. α-Amino-ω-Azido-C$_6$-Ceramide, ω-Azido-C$_6$-Ceramide, as well as ω-Azido-Sphingosine were fed with 10 μM final concentration for 1 h at 37 °C. For chlamydial infection, the cells were fed with ceramide-analogues 23 h post infection and for infection with *Simkania* for 72 h and for neisserial infection, the cells were fed with the sphingosine analogue immediately before infection. Afterwards, the cells were fixed in 4 % PFA and 0.1 % GA for 15 min, washed 3x in 1xPBS and then permeabilized for 15 min in 0.2 % Triton X-100 in PBS. The cells were then washed again 3x in 1xPBS and then incubated with 5 μM DBCO-488 (Jena Bioscience, CLK-1278-1) at 37 °C for 30 min or 5 μM Click-IT Alexa Fluor® 488 DIBO alkyne dye (ThermoScientific, Waltham, USA) at 37 °C for 30 min. For staining with antibodies, the cells were washed, blocked using 2 % FCS in 1xPBS for 1 h and then incubated in primary antibody diluted in blocking buffer for 1 h in a humid chamber. The primary antibodies used in this study were: anti-HSP60 ms (Santa Cruz, sc-57840, dilution 1:200), anti-*Neisseria gonorrhoeae* primary antibody rb (US biological, dilution 1:200), anti-Prx3 (Origene, TA322470, dilution 1:100) and anti-CERT (Abcam, ab72536, 1:100). After that, the cells were washed 3x in 1xPBS and then incubated in the corresponding secondary antibody diluted in blocking buffer for 1 h and then washed 3x with 1xPBS. The secondary antibodies used were: ATTO 647N ms (Rockland, 610-156-121S, dilution 1:200) and ATTO 647N rb (Sigma, 40839, dilution 1:200).

mCling

mCling (Biosyntan) was labeled using the following procedure[23]: 150 nmol mCling was incubated in 3 molar excess of ATTO 643-Maleimide (ATTO-TEC, AD 643-45) in 100 mM TCEP overnight at RT under continuous shaking. The label product was purified by HPLC (JASCO) and the concentration was determined using a UV-vis spectrophotometer (Jasco V-650). Staining with mCling was performed by the incubation of living cells in 0.5 μM mCling dissolved in media for 10 min at 37°C.

Expansion Microscopy

Stained cells were treated according to Kunz *et al.*[8] for 10 min with 0.25 % GA at RT and gelated after three washing steps. In case of 4x expansion a monomer solution consisting of 8.625 % sodium acrylate (Sigma, 408220), 2.5 % acrylamide (Sigma, A9926), 0.15 % N,N'-methylenbisacrylamide (Sigma, A9926), 2 M NaCl (Sigma, S5886) and 1xPBS and 0.2 % freshly added ammonium persulfate (APS, Sigma, A3678) and tetramethylethylenediamine

(TEMED, Sigma, T7024) was used. Here gelation was performed for 1 h at RT followed by proteinase digestion. In case of 10x expansion 1 ml of the monomer solution containing 0.267 g DMAA (Sigma, 274135) and 0.064 g sodium acrylate (Sigma, 408220) dissolved in 0.57 g ddH$_2$O was degassed for 45 min on ice with nitrogen followed by the addition of 100 µl KPS (0.036 g/l, Sigma, 379824). After another 15 min of degassing and the addition of 4 µl TEMED per ml monomer solution, gelation was performed for 30 min at RT followed by an incubation of 1.5 h at 37 °C. Hereafter the samples were digested for 3 h – overnight in digestion buffer (50 mM Tris pH 8.0, 1 mM EDTA (Sigma, ED2P), 0.5 % Triton X-100 (Thermo Fisher, 28314) and 0.8 M guanidine HCl (Sigma, 50933)), supplied with 8 U/ml protease K (Thermo Fisher, AM2548) and for expansion of Neisseria additional 1 mg/ml Lysozyme according to Lim *et al.*[44]. Digested gels were expanded in hourly changed ddH$_2$O until the expansion saturated. The expansion factor was determined by the gel size using calipers directly after gelation and by the gel size of the digested and expanded samples. We achieved experimental expansion factors of 4.1 for the 4x monomer solution and 10 for the 10x monomer solution, and the expansion factor remained constant for the used monomer solutions. Expanded and chopped gels were stored at 4°C in ddH$_2$O immobilized prior to imaging on PDL-coated glass chambers (Merck, 734-2055).

Confocal Microscopy and SIM

Confocal imaging was performed on an inverted microscope (Zeiss LSM700) or on a Leica TCS SP5 confocal microscope (Leica Biosystems) and SIM-imaging on a Zeiss ELYRA S.1 SR-SIM structured illumination platform using a 63x water-immersion objective (C-Apochromat, 63x 1.2 NA, Zeiss, 441777-9970). Reconstruction of SIM-images was performed using the ZEN image-processing platform with a SIM module. Z-stacks were processed using Imaris 8.4.1 and FIJI 1.51n[45].

FRAP

HeLa229 cells were seeded in an 8-well chambered high precision coverglass (Sarstedt 8-well on coverglass II) and incubated for 24 h at 37 °C and 5 % CO$_2$. The cells were fed with 10 µM of the corresponding azido-ceramide analogue for 30 min in cell culture media. Afterwards, the cells were washed with HBSS with magnesium and calcium and fixed with 4 % formaldehyde and 0.1 % glutaraldehyde in HBSS for 15 min at room temperature and washed. Ceramides were labelled by strain-promoted alkyne-azide cycloaddition (SPAAC) with 10 µM DBCO-Alexa Fluor 488 in HBSS for 30 min at 37 °C and washed. FRAP-imaging was performed at a confocal laser scanning microscope (CLSM) LSM700 (Zeiss, Germany) using the Plan-Apochromat 63x 1.4 oil objective. Using the 488 nm laser line as excitation, a time series with 30 frames every 1.5 s was recorded. After three frames, a circular region of interest with diameter 1.8 µm was bleached and fluorescence recovery followed over time.

References

1.   Sauer, M. & Heilemann, M. Single-Molecule Localization Microscopy in Eukaryotes. *Chem Rev* **117**, 7478-7509 (2017).

2.   Schermelleh, L. *et al.* Super-resolution microscopy demystified. *Nat Cell Biol* **21**, 72-84 (2019).

3.   Chen, F., Tillberg, P.W. & Boyden, E.S. Optical imaging. Expansion microscopy. *Science* **347**, 543-548 (2015).

4.   Wassie, A.T., Zhao, Y. & Boyden, E.S. Expansion microscopy: principles and uses in biological research. *Nature methods* **16**, 33-41 (2019).

5.   Truckenbrodt, S. *et al.* X10 expansion microscopy enables 25-nm resolution on conventional microscopes. *EMBO Rep* **19** (2018).

6.   Truckenbrodt, S., Sommer, C., Rizzoli, S.O. & Danzl, J.G. A practical guide to optimization in X10 expansion microscopy. *Nat Protoc* **14**, 832-863 (2019).

7.   Chang, J.B. *et al.* Iterative expansion microscopy. *Nature methods* **14**, 593-599 (2017).

8.   Kunz, T.C., Gotz, R., Sauer, M. & Rudel, T. Detection of Chlamydia Developmental Forms and Secreted Effectors by Expansion Microscopy. *Front Cell Infect Microbiol* **9**, 276 (2019).

9.   Chozinski, T.J. *et al.* Expansion microscopy with conventional antibodies and fluorescent proteins. *Nature methods* **13**, 485-488 (2016).

10.   Tillberg, P.W. *et al.* Protein-retention expansion microscopy of cells and tissues labeled using standard fluorescent proteins and antibodies. *Nat Biotechnol* **34**, 987-992 (2016).

11.   Chen, F. *et al.* Nanoscale imaging of RNA with expansion microscopy. *Nature Methods* **13**, 679-684 (2016).

12.   Gambarotto, D. *et al.* Imaging cellular ultrastructures using expansion microscopy (U-ExM). *Nature Methods* **16**, 71-74 (2019).

13.   Halpern, A., Alas, G. C. M. Chozinski, T. J., Paredez, A. R. Vaughan, J. C. Hybrid structured illumination expansion microscopy reveals microbial cytoskeleton organization. *ACS Nano* **11**, 12677-12686 (2017).

14.   Sheard, T. M. D., Hurley, M. E., Colyer, J. White, E., Norman, R., Pervolaraki, E., Narayanasamy, K. E., Hou, Y., Kirton, H. M., Yang, Z., Hunter, L. Shim, J.-U., Clowsley, A., Smith, A. D., Baddeley, Soeller, C., Colman, M. A., Jayasinghe, I. Three-dimensional and chemical mapping of intracellular signaling nanodomains in health and disease with enhanced expansion microscopy. *ACS Nano* **13**, 2143-2157 (2019).

15.   Koch-Edelmann, S. *et al.* The cellular ceramide transport protein CERT promotes Chlamydia psittaci infection and controls bacterial sphingolipid uptake. *Cell Microbiol* **19** (2017).

16.   Derre, I., Swiss, R. & Agaisse, H. The lipid transfer protein CERT interacts with the Chlamydia inclusion protein IncD and participates to ER-Chlamydia inclusion membrane contact sites. *PLoS Pathog* **7**, e1002092 (2011).

17.   Fink, J. & Seibel, J. Click reactions with functional sphingolipids. *Biol Chem* **399**, 1157-1168 (2018).

18.   Bécam, J., Burgert, A., Schlegel, J., Sauer, M., Seibel, J., Schubert-Unkmeir, A. Antibacterial activity of ceramide and ceramide analogs against pathogenic Neisseria. *Sci. Rep.* **7**, 17627 (2017).

19   Hannun, Y. A., Obeid, L. M. The Ceramide-centric universe of lipid-mediated cell regulation: stress encounters of the lipid kind. *J. Biol. Chem.* **277**, 25847-25850 (2002).

20.   Burgert, A., Bécam, J., Doose, S., Bieberich, E., Schubert-Unkmeier, A., Sauer, M. Characterization of Plasma Membrane Ceramides by Super-Resolution Microscopy. *Angew. Chem. Int. Ed. Engl.* **56**, 6131-6135 (2017).

21.   Walter, T., Collenburg, L., Japtok, L., Kleuser, B., Schneider-Schaulies, S., Müller, N., Bécam, J., Schubert-Unkmeir, A., Kong, J. N., Bieberich, E., Seibel, J. Incorporation and visualization of azido-functionalized N-oleoyl serinol in Jurkat cells, mouse brain astrocytes, 3T3 fibroblasts and human brain microvascular endothelial cells. *Chem. Commun.* **52**, 8612-8614 (2016).

22.   Collenburg, L., Walter, T., Burgert, A., Müller, N., Seibel, J., Japtok, L., Kleuser, B., Sauer, M., Schneider-Schaulies, S. A. Functionalized Sphingolipid Analogue for Studying Redistribution during Activation in Living T Cells. *J. Immunol.* **196**, 3951-3962 (2016).

23.   Revelo, N. H., Kamin, D., Truckenbrodt, S., Wong, A. B., Reuter-Jessen, K., Reisinger, E., Moser, T., Rizzoli, S. O. A new probe for super-resolution imaging of membranes elucidates trafficking pathways. *J. Cell Biol.* **205**, 591-606 (2014).

24.   Karagiannis, E. D., Kang, J. S., Shin, T. W., Emenari, A., Asano, S., Lin, L., Costa, E. K. IMAXT Grand Chellenge Consortium, Marblestone, A. H., Kasthuri, N., Boyden, E. S. Expansion Microscopy of Lipid Membranes. Preprint at *bioRxiv* doi.org/10.1101/829903 (2019).

25.   Grassme, H., Riethmuller, J., Gulbins, E. Biological aspects of ceramide-enriched membrane domains. *Prog. Lipid Res.* **46**, 161-170 (2007).

26.   Gulbins, E., Dreschers, S., Wilker, B., Grassme, H. Ceramide, membrane rafts and infections. *J. Mol. Med.* **82**, 357-363 (2004).

27.   Faulstich, M., Hagen, F., Avota, E., Kozjak-Pavlovic, V., Winkler, A. C., Xian, Y., Schneider-Schaulies, S., Rudel, T. Neutral sphingomyelinase 2 is a key factor for PorB-dependent invasion of Neisseria gonorrhoeae. *Cell Microbiol.* **17**, 241-253 (2015).

28.   Herweg, J. A., Pons, V., Becher, D., Hecker, M., Krohne, G., Barbier, J., Berger, H., Rudel, T., Mehlitz, A. Proteomic analysis of the Simkania-containing vacuole: the central role of retrograde transport. *Mol. Microbiol.* **99**, 151-171 (2016).

29.   Hackstadt, T., Rockey, D. D., Heinzen, R. A., Scidmore, A. Chlamydia trachomatis interrupts an exocytic pathway to acquire endogenously synthesized sphingomyelin in transit from the Golgi apparatus to the plasma membrane. *EMBO J* **15**, 964-977 (1996).

30.   Kunz, T. C., Kozjak-Pavlovic, V. Diverse Facets of Sphingolipid Involvement in Bacterial Infections. *Front. Cell Dev. Biol.* **7**, 203 (2019).

31.   Belland, R., Ojcius, D. M., Byrne, G. I. Chlamydia. *Nat. Rev. Microbiol.* **2**, 530-531 (2004).

32.   Banhart, S., Schafer, E. K., Gensch, J. M., Heuer, D. Sphingolipid Metabolism and Transport in Chlamydia trachomatis and Chlamydia psittaci Infections. *Front. Cell Dev. Biol.* **7**, 223 (2019).

33.   Hanada, K. Intracellular trafficking of ceramide by ceramide transfer protein. *Proc. Jpn. Acad. Ser. B Phys. Biol. Sci.* **86**, 426-437 (2010).

34.   Zeidan, Y. H., Hannun, Y. A. Translational aspects of sphingolipid metabolism. *Trends Mol. Med.* **13**, 327-336 (2007).

35.   Lee, J. K., Enciso, G. A., Boassa, D., Chander, C. N., Lou, T. K., Pairawan, S. S., Guo, M. C., Wan, F. Y. M., Ellisman, M. H., Sütterlin, C., Tan, M. Replication-dependent size reduction precedes differentiation in Chlamydia trachomatis. *Nat. Commun.* **9**, 45 (2018).

36.   Gustafsson, M. G. Surpassing the lateral resolution limit by a factor of two using structured illumination microscopy. *J. Microsc.* **198**, 82-87 (2000).

37.   Hoare, A., Timms, P., Bavoil, P. M., Wilson, D. P. Spatial constraints within the chlamydial host cell inclusion predict interrupted development and persistence. *BMC Microbiol.* **8**, 5 (2008).

38.   Auer, D., Hugelschaffer, S. D., Fischer, A. B., Rudel, T. The chlamydial deubiquitinase Cdu1 supports recruitment of Golgi vesicles to the inclusion. *Cell. Microbiol.* **22,** e13136 (2019).

39.   Elwell, C. A., Jiang, S., Kim, J. H., Lee, A., Wittmann, T., Hanada, K., Melancon, P., Engel, J. N. Chlamydia trachomatis co-opts GBF1 and CERT to acquire host sphingomyelin for distinct roles during intracellular development. *PLoS Pathog.* **7**, e1002198 (2011).

40.   Asmar, A. T., Ferreira, J. L., Cohen, E. J., Cho, S. H., Beeby, M., Hughes, K. T., Collet, J. F. Communication across the bacterial cell envelope depends on the size of the periplasm. *PLoS Biol.* **15**, e2004303 (2017).

41.   Ghai, S. Understanding antibiotic resistance via outer membrane permeability. *Infect. Drug Resist.* **11**, 523-530 (2018).

42.   Wu, D., Ren, Z., Pae, M., Guo, W., Cui, W. X., Merrill, A. H., Meydani, S. N. Aging up-regulates expression of inflammatory mediators in mouse adipose tissue. *J. Immunol.* **179**, 4829-4839 (2007).

43.   Yan, R.-B., Yang, F., Wu, Y., Zhang, L.-H., Ye, X.-S. An efficient and improved procedure for preparation of triflyl azide and application in catalytic diazotransfer reaction. *Tetrahedron Lett.* **46**, 8993-8995 (2005).

44.   Lim, Y., Shiver, A. L., Khariton, M., Lane, K. M., Ng, K. M., Bray, S. R., Qin, J., Huang, K. C., Wang, B. Mechanically resolved imaging of bacteria using expansion microscopy. *PLoS Biol.* **17**, e3000268 (2019).

45.   Schindelin, J., Arganda-Carreras, I., Frise, E., Kaynig, V., Longair, M., Pietzsch, T., Preibisch, S., Rueden, C., Saalfeld, S., Schmid, B., Tinevez, J. Y., White, D. J., Hartenstein, V., Eliceiri, K., Tomancak, P., Cardona, A. Fiji: an open-source platform for biological-image analysis. *Nat. Methods* **9**, 676-682 (2012).

Acknowledgments

Author contributions: The manuscript was written through contributions of all authors. R.G. and T.C.K. designed and performed experiments, analyzed data and wrote the manuscript. J.F. and J.S. synthesized α-Amino-ω-Azido-C6-Ceramide, J.Sch., F.S. and V.K-P. performed experiments. T.R. and M.S. designed the experiments and wrote the manuscript. All authors have given approval to the final version of the manuscript. ‡These authors contributed equally.

Competing interests: The authors declare no competing financial interests.

Data and materials availability: The raw data that support the findings of this study are available from the corresponding authors upon reasonable request.

Figures
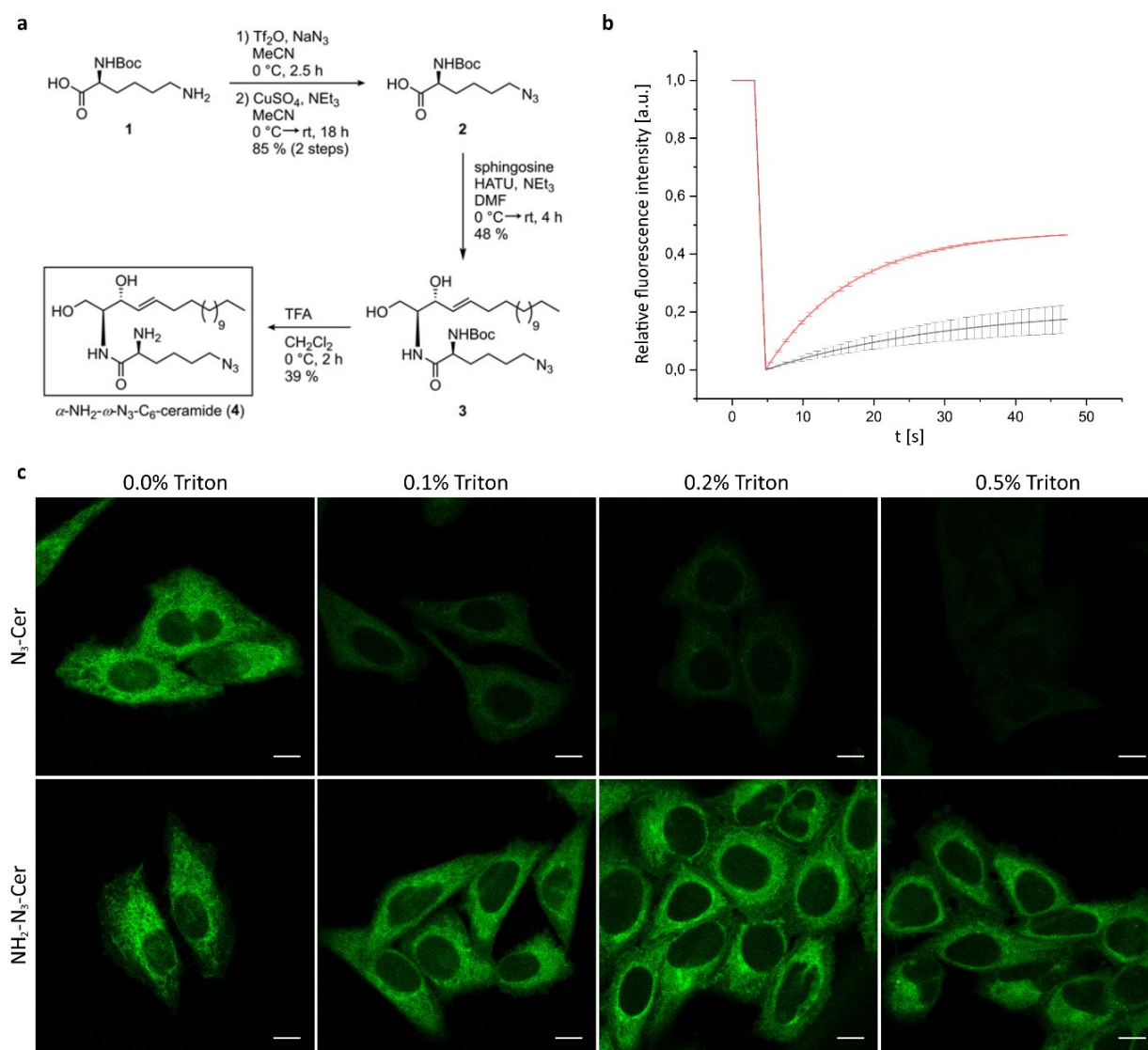
**Figure 1**. **Amino- and azido-functionalized sphingolipids enable fixation and fluorescence labeling of lipids.** (**a**) Schematic overview of the synthesis of α-NH$_2$-ω-N$_3$-C$_6$-Ceramide (for synthesis details see Supporting Information). To investigate the mobility of membrane-incorporated functional sphingolipids HeLa229 cells were fed with 10 µM α-NH$_2$-ω-N$_3$-C$_6$-ceramide or ω-N$_3$-C$_6$-Ceramide, fixed, permeabilized and stained with DBCO-Alexa Fluor 488. (**b**) FRAP experiments with the two incorporated ceramide analogues. After three confocal fluorescence imaging frames, a circular region of interest with a diameter 1.8 µm was bleached and fluorescence recovery followed over time. The α-NH$_2$-ω-N$_3$-C$_6$-ceramide (black) shows a lower mobility (mean mobile fraction of 22.2 %) than the ω-N$_3$-C$_6$-ceramide (red) lacking the primary amino group (mobile fraction of 48.1 %). (**c**) Confocal fluorescence images of fixed and labeled cells in the presence of increasing concentrations of the detergent Triton-X100. With increasing Triton-X100 concentration ω-N$_3$-C$_6$-ceramide is efficiently washed out while the α-NH$_2$-ω-N$_3$-C$_6$-ceramide signal remains preserved. Scale bars, 10 µm.
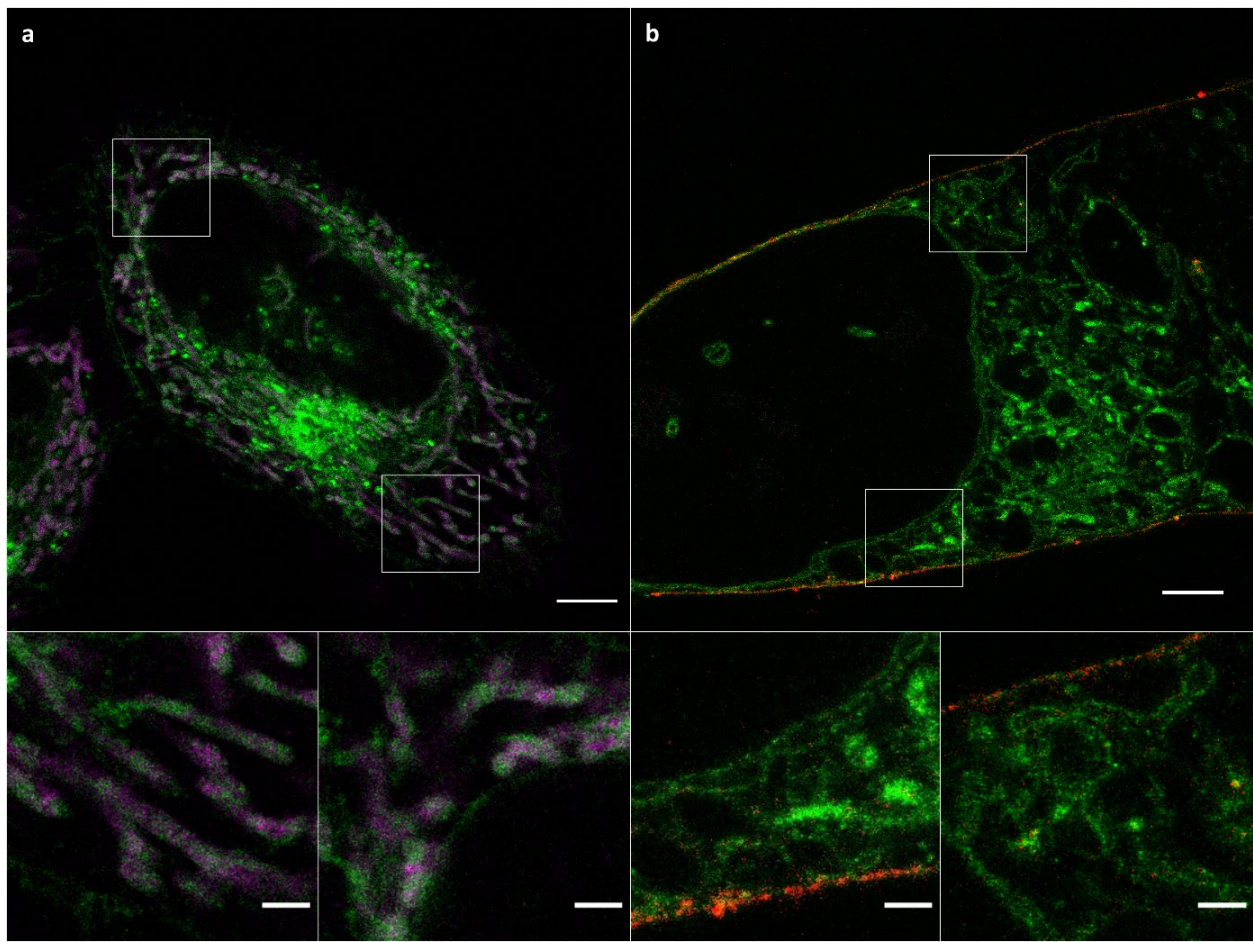
Figure 2. **Sphingolipid ExM enables super-resolution imaging of cellular membranes and protein interactions.** (**a**) Confocal fluorescence image of 4x expanded HeLa229 cells. Cells were fed with α-NH$_2$-ω-N$_3$-C$_6$-ceramide, fixed, permeabilized, and labeled with DBCO-Alexa Fluor 488 (green). In addition, Prx3 (magenta), which is located in the mitochondrial matrix was stained by immunolabeling using ATTO 647N labeled secondary antibodies. (**b**) Confocal fluorescence image of a 10x expanded HeLa229 cell fed with ATTO643-mCling (red) and α-NH$_2$-ω-N$_3$-C$_6$-ceramide clicked with DBCO-Alexa Fluor 488 (green). Scale bars, 20 μm. The images at the bottom show magnified views of the regions outlined by the white boxes in the main images. Scale bars, 5 μm.
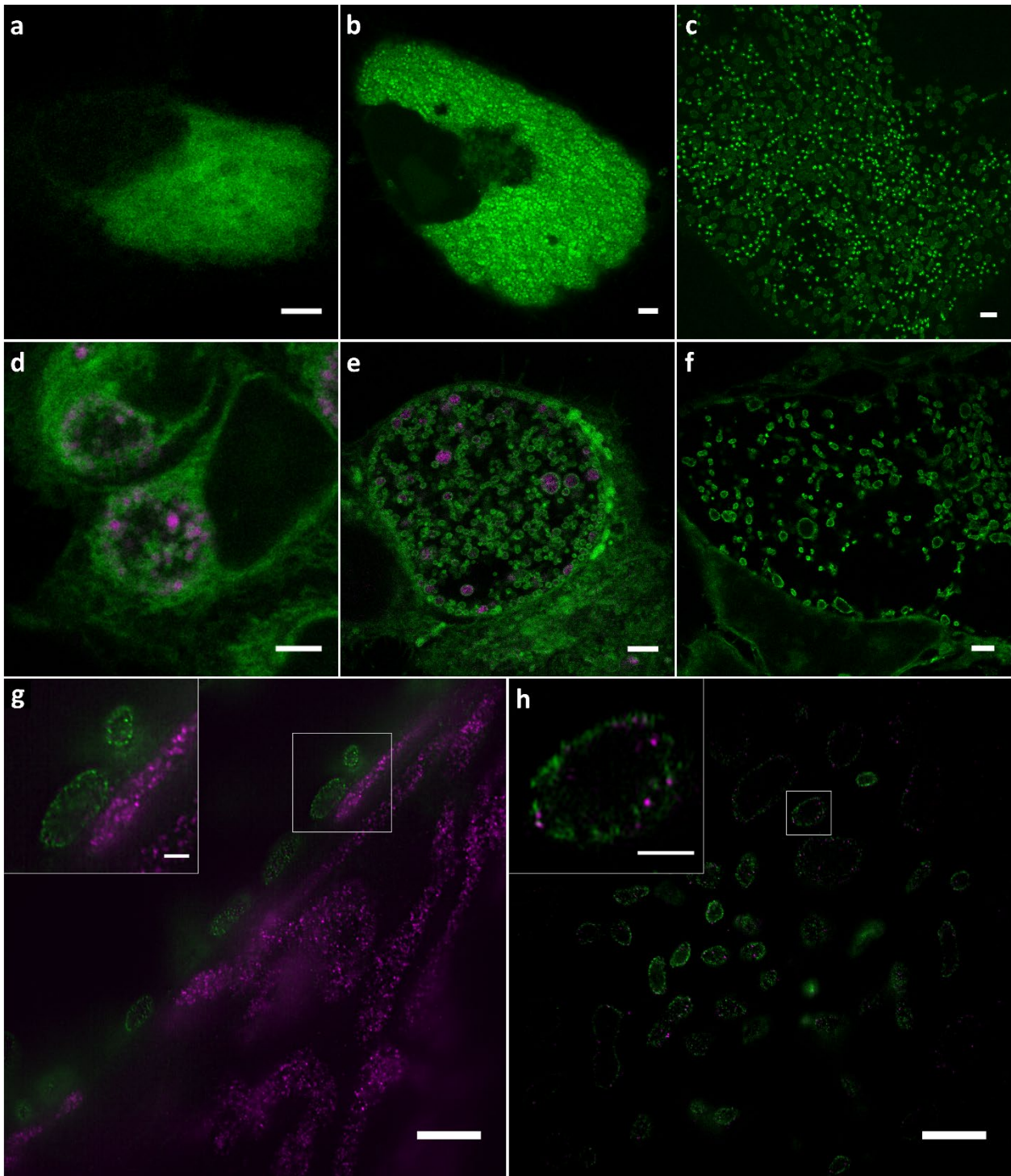
Figure 3. **Sphingolipid ExM visualizes intracellular pathogens and their interactions with mitochondrial proteins**. (**a-c**) Cells were infected with *Simkania negevensis* for 96 h, fed with α-NH$_2$-ω-N$_3$-C$_6$-ceramide, fixed, permeabilized and stained with DBCO-Alexa Fluor 488 (green), and then imaged. The images show different cells before expansion (**a**), after 4x expansion (**b**), and 10x expansion (**c**) recorded by confocal microscopy. (**d-f**) Cells were infected with *Chlamydia trachomatis* for 24 h, fed with α-NH$_2$-ω-N$_3$-C$_6$-ceramide, fixed, permeabilized and stained with DBCO-Alexa Fluor 488 (green). Different cells were imaged before expansion (**d**), after 4x expansion (**e**), and 10x expansion (F) by confocal microscopy. In the unexpanded (**d**) and 4x expanded image (**e**) chlamydial HSP60 was immulabeled with ATTO647N secondary antibody (magenta). (**g**) The mitochondrial marker protein Prx3 was stained by immunolabeling with an ATTO 647N secondary antibody (magenta). The confocal fluorescence image of 10x expanded samples revealed a close contact between Chlamydia

and mitochondria at the inclusion membrane. (**h**) SIM images of 10x expanded samples uncover that some Prx3 molecule are inserted into the bacterial membrane. Scale bars, 5 µm (unexpanded images a,d), 10 µm (4x and 10x expanded images b,c,e,f,g,h), and 2 µm (magnified views in images g,h).
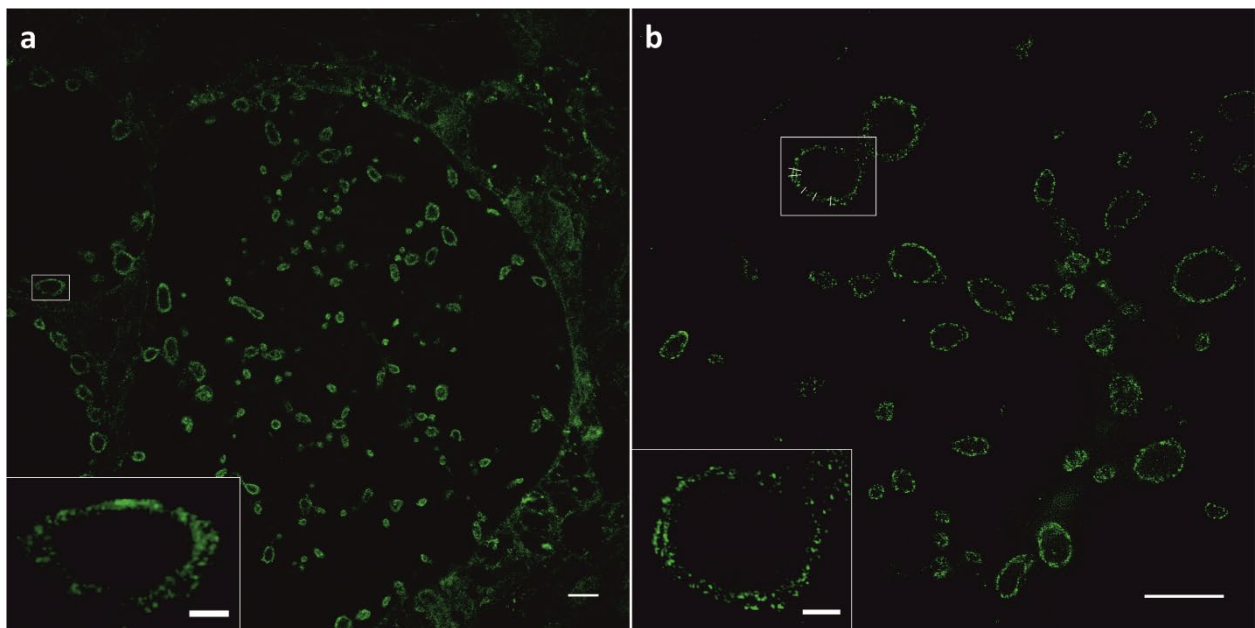
Figure 4. 10x Sphingolipid ExM in combination with SIM resolves the distance between the OM and IM of gram-negative bacteria. HeLa229 cells infected with *Chlamydia trachomatis* for 24 h, fed with α-NH$_2$-ω-N$_3$-C$_6$-ceramide, fixed, permeabilized and click-labeled with DBCO-Alexa Fluor 488 (green). Confocal (**a**) and SIM images (**b**) disclose that ceramides are incorporated into the OM and IM. Fitting intensity cross sectional profiles at different positions by a bimodal Gaussian fit resulted in a peak-to-peak distance of 27.6 ± 7.7 nm (s.d.) (**Supplementary Figs. 22**, **23**). Scale bars 10 µm (a,b), 2 µm (white boxes).

4   Discussion

This thesis aimed to close the gap between the many labeling and imaging modalities available for proteins in contrast to lipids. The discussion will be divided into three parts, depending on the respective labeling procedure, which all have their advantages and disadvantages. First, in section 4.1 the classical approach of immunofluorescence will be discussed. In the following section 4.2, I will give an overview of labeling sphingolipids using click-chemistry. Finally, in section 4.3 the results obtained by exploiting the binding characteristics of toxins will be discussed with regard to the literature.

4.1   Super-Resolution Microscopy of Sphingolipids with Antibodies

One of the first methods, to tag cellular molecules of interst relies on the specific binding characteristics of antibodies [90]. To date the classical approach of using primary and secondary fluorophore coupled antibodies is still often used and the number of available antibodies seems to be endless. *In vivo*, antibodies are generated by terminally differentiated B cells, also known as plasma cells or plasmablast, that are part of our adaptive immune system. Commercial antibodies come in many different flavors and can be divided into monoclonal versus polyclonal production. Production is initiated by injection of the immunogen (immunization) into an appropriate animal, such as rabbit, goat, guinea pig, rat, mouse, donkey or chicken. After several immunization events, to boost the amount of polyclonal antibodies, they can be purified from the blood serum and represent many molecules from different B cells. On the other side, monoclonal antibodies are generated by a single B cell clone which is fused with a myeloma cell line in order to obtain an immortalized B cell myeloma hybridoma. Monoclonal antibodies therefore recognize only one specific antigen in contrast to polyclonal antibodies. Although uncontrolled production of lipid reactive antibodies is hallmark of many auto immune diseases, such as APLS [20] and multiple sclerosis (MS) [538], commercially available antibodies for immunofluorescence are rare. Recent work showed, that CD1 on the surface of antigen presenting cells is able to bind different kind of lipids, and initiate human T cell autoreactivity causing different autoimmune diseases [539, 540].

Since most commercial available ceramide antibodies are large pentameric immunoglobulin M (IgM) molecules with an average weight of 990 kDa, I was interested in the use of smaller IgG antibodies for super-resolution microscopy. In 2007, the group of Prof. Dr. Erhard Bieberich (University of Kentucky, College of Medicine) described the development and characterization of polyclonal anti-ceramide IgG antibodies generated by the immunization of rabbits which outperformed a commercial IgM antibody under different tested conditions [188]. In contrast to the commercial available monoclonal IgM ceramide

antibody (clone MID 15B4), the polyclonal IgG antibodies showed a more homogenous cellular staining pattern [114] which is in agreement with previously published data [188]. Using conventional wide field microscopy and CLSM, individual diffraction limited CRPs are visible which are distributed along the plasma membrane of different cell lines and showed no residual mobility after fixation with formaldehyde and glutaraldehyde. Since several groups reported residual mobility of lipids and glycosylphosphatidylinositol (GPI)-anchored proteins, even after long fixation times in the presence of formaldehyde and glutaraldehyde [199, 200], I also tested different fixation conditions and did not observe any significant changes in CRP morphology nor mobility. Interestingly, there were several smaller CRPs within one diffraction limited ceramide fluorescence cluster with individual diameter of about $\approx 75\,\mathrm{nm}$. The diameter was a robust value among all tested different cell lines at the basal and apical side of the cell. The results indicate that we developed a robust protocol for sub-diffraction quantification and visualization of ceramides using IgG antibodies.

I applied this protocol to study CRP rearrangements in the context of *Neisseria meningitidis* infection of host human brain microvascular endothelial cells (HBMECs). It is reported that several bacterial species are able to modulate host cell ceramide production and subsequently use CRPs to enter the cell [541]. In this context, acid sphingomyelinase (ASM) is a key enzyme involved in the local production of ceramides at the plasma membrane. Under physiological condition the ASM is localized at the lysosomes responsible for permanent turnover of sphingomyelin to ceramide. ASM dysfunction leads to the human lysosomal storage disorder Niemann-Pick disease characterized by uncontrolled accumulation of sphingomyelin. The gram-negative bacterium *Neisseria meningitidis* uses special extension, called type IV pili, to move, adhere and trespass the blood brain barrier [542]. Therefore, the first interaction of the bacteria with HBMECs is mediated via their type IV pili and subsequently ASM is activated to locally generate ceramides at the outer leaflet of the cells [177]. It was not clear, whether the interaction of type IV pili with the host cells is sufficient to stimulate ceramide display at the target cell. For this reason, pili enriched fractions of *Neisseria meningitidis* were purified and incubated with HBMEC followed by *d*STORM with the previously described protocol. I could indeed observe a dose-dependent increase in the number of CRPs upon pili enriched fraction incubation, suggesting that the interaction is sufficient for host cell ceramide generation. Interestingly, I did not observe great differences in size or morphological appearance which is in good agreement and comparable with exogenous treatment by *Bacillus cereus* sphingomyelinase [110] and indicates activation of cellular ASM. In summary, I was able to develop a robust labeling protocol based on IgG binding characteristics which is suited for SMLM and can be used to address biological questions, such as the interaction of human cells with pathogens. Next, I aimed to decrease the linkage error which is introduced by labeling with both, primary and secondary antibodies, and can displace the fluorophores

tens of nanometers away from the structure of interest.

4.2   Super-Resolution Microscopy of Sphingolipids with Click-Chemistry

Application of click-chemistry certainly results in one of the smallest possible linkage errors. Here, direct covalent attachment of a fluorophore of choice to a target structure is achieved by introduction of bioorthogonal reactive groups. As discussed in section 1.2.2, I used mainly the SPAAC reaction with a combination of DBCO moiety at the fluorophore and azide group at the sphingolipid. The distance of the resulting stable triazole complex is less than 1 nm which is sufficient and neglectable for most super-resolution imaging techniques.

Several α- and ω-azide-functionalized ceramide analogs were synthesized from the group of Prof. Dr. Jürgen Seibel (Institute for Organic Chemistry, Würzburg) with fatty acid chain length of either C6 or C16. I fed different cell lines with these analogs and after addition of DBCO modified dyes the localization could be readily visualized. But in contrast to the antibody labeling approach, these lipid derivates were hardly prone to chemical fixation procedures and showed considerable residual mobility. Additionally, they adhered very efficiently onto the glass surface despite extensive testing of different coatings which hampered characterization by dSTORM. For this reason, I started to evaluate their incorporation efficiency as well as their plasma membrane orientation in living Jurkat cells by CLSM and fluorescence anisotropy measurements.

When ceramide analogs were clicked with the membrane impermeable dye DBCO-Sulfo-Cy5, before incubated with cells (pre-clicked), a strong signal in the plasma membrane was observed indicating good incorporation efficiency. Interestingly, when the click reaction was performed after incorporation into the cells (post-clicked) the analogs with longer fatty acid side chain length C16 showed much less signal intensity. Especially, the signal of the α modified variant was as low as for the control cells which were only incubated with the DBCO-Sulfo-Cy5 dye. Assuming similar reaction kinetics between the different analogs and the clickable dye I came to the conclusion that the azide group of the C16 ceramides is stuck deeper within the plasma membrane and inaccessible for the dye. To confirm this hypothesis, I also performed ensemble fluorescence anisotropy experiments of labeled Jurkat cells in a cuvette. I assumed, that azide groups residing deeper within the plasma membrane will also cause higher fluorescence anisotropy values since the rotational mobility of the dye will be limited by interactions with the hydrophobic core of the lipid bilayer. Indeed, the longer pre-clicked C16 azide-modified sphingolipid analogs showed higher fluorescence anisotropy values indicating that the azide group and the dye after click reaction is localized closer to the plasma membrane bilayer. Since the fluorescence

signal was low for post-clicked C16 molecules we only interpreted data obtained from experiments with pre-clicked lipids. Of note, the C6 chained analog with azide group at the α position exhibited higher fluorescence anisotropy values as the one with ω-configuration. Accordingly, fluorophores at the end of the short C6 alkyl chain are able to flip out of the membrane whereas, when localized at the head group or at the end of longer alkyl chains, are trapped in the plasma membrane. It seems, that there is a certain threshold where the increase in hydrophobicity of longer fatty acyl chains overcomes the hydrophilic nature of charged dye molecules to localize within the polar water environment outside of the membrane. Considering the coexistence of liquid ordered (L_o) and liquid disordered (L_d) phase within lipid membranes, our results also fit into the contemporary understanding of plasma membrane organization. That is, the ceramide analogs with longer saturated side chains should partition preferentially into the L_o domain which is thicker, highly ordered, more viscous and enriched in cholesterol. In contrast, the short chained analogs should partition into the L_d phase which is characterized by irregular packing, the presence of kinks, unhindered lateral mobility and decreased Van der Waals interactions. Therefore, it seems plausible that the extracellular clickable dye molecules may penetrate deeper into the membrane of L_d phase and react more easily with the azide groups of short chained or poly-unsaturated lipids. Subsequently, the hydrophilic dye molecul may overcome the lower hydrophobic interactions and flip out of the membrane. In summary, I was able to characterize the localization and accessibility of clickable ceramide analogs in the cellular context and devloped a protocol to investigate their interaction with the plasma membrane.

Major drawbacks of the clickable sphingolipid analogs were their resistance to chemical fixation and strong adherence with the glass surface which made super-resolution microscopy by dSTORM challenging. For this reason, we sought to synthesize new azide-modified variants which are susceptible to chemical aldehyde-based fixation methods. Classical immunocytochemistry starts with fixation of cells by aldehyde containing crosslinkers such as paraformaldehyde or glutaraldehyde. Besides, alcohol based fixatives, oxidizing agents and a metallic group of fixatives can be used to "freeze" and immobilize biological samples [543]. Concentrated formaldehyde in solution will spontaneously react with itself via condensation to form water-insoluble paraformaldehyde polymers. Therefore, commercially available formaldehyde solutions are often stabilzed by the addition of methanol. Additionally, paraformaldehyde can be depolymerized to formaldehyde by heating. When diluted, formaldehyde predominantly exists in its monohydrate form which is methylene glycol [544]. Methylene glycol preferentially reacts with the amino acid side chains of lysine, arginine, cysteine and histidine but is also able to react with the hydroxyl groups of serine, threonine and tyrosine to form reactive hydroxymethyl side chains [545]. Subsequently, these reactive groups may combine to form stable methylene bridges and crosslink the proteins. Glutaraldehyde works in a similar manner, but since it is a bifunc-

tional aledehyde it exhibits stronger crosslinking capability. Moreover, glutaraldehyde crosslinking is faster but can introduce substantial background fluorescence which can be reduced by sodium borohydride treatment [546]. Since many lipids do not contain free amino groups they are not accessible for fixation, but it was reported that phospholipids with amine groups can be fixed by glutaraldehyde [547]. For this reason, we designed a α-amino-ω-azido-C6-ceramide, since its amine-free variant showed good membrane incorporation and labeling efficiency. Residual mobility after different fixation procedures was compared between these two ceramide analogs by fluorescence recovery after photobleaching (FRAP). Indeed, the mobile fractions of all tested conditions were decreased in the α-amino-ω-azido-C6-ceramide, indicating improved chemical fixation by treatment with a combination of formaldehyde and glutaraldehyde. Advantageously, targeting the amino group by aldehyde-based crosslinkers or N-hydroxysuccinimide esters (NHSs) enabled its usage for expansion microscopy where the target of interest is linked into a hydrogel. Subsequently, the sample is isotropically physically expanded by the addition of water and structures previously inaccessible due to the diffraction limit of light can be visualized by convential microscopy [505]. Besides several other factors, the quality is dependent on the covalent linkage of the target structure into the hydrogel and the label density. The linkage can be achieved by introducing polymer-linkable groups such as methacryloyls but also to a certain amount by glutaraldehyde fixation [511]. We could use this new ceramide analog to label efficently eukaryotic and prokaryotic cells and expand them several fold by expansion microscopy.

Finally, I investigated the antibacterial effect of sphingolipids and the previously described azide-modified analogs. It was shown, that sphingolipids exert a detrimental effect on the growth of fungi, microalgae and different Gram-positive and negative bacteria [280–284] although the mechanism is not fully understood. We observed antibacterial activity against *Neisseria meningitidis* and *Neisseria gonorrhoeae* exerted by sphingosine, short-chain C6 ceramide and ω-azido-C6-ceramide. Interestingly, changing the localization of the azide group from the ω to the α position alleviated the antibacterial effects. Assuming that the ω-azide group of the C6 ceramide is also able to flip out of the membrane, as observed for Jurkat cells, it might mediate bactericidal effects at the membrane whereas it may be shielded in the plasma membrane when localized at the α position. Unfortunately, I was not able to discriminate whether the ceramides incorporated into both, the outer and inner membrane, of *Neisseria meningitidis*. Moreover, immobilization by chemical aldehyde-based fixation of amine-free ceramide analogs was possible in *Neisseria meningitidis* in contrast to mammalian cells. Thus, exogenously added ceramides probably interact with an unknown bacterial molecule which enables their immobilization through fixation. It might also be possible, that the ceramides stick within the mesh-like peptidoglycan layer of the bacteria which is rich in sugars and amino acids. It is formed by two alternating amino sugars, N-acetylglucosamine (GlcNAc) and N-acetylmuramic

acid (MurNAc), and each MurNAc is attached to a tetrapeptide consisting of the amino acids L-alanine, D-glutamic acid, meso-diaminopimelic acid and D-alanine. Such, this structure is rich in amide bonds and hydroxyl groups which could be modified by aldehyde-based fixation and which could trap adjacent sphingolipid molecules. As a result, I was able to perform *d*STORM of DBCO-Sulfo-Cy5 clicked ceramide analogs and investigate their distribution within *Neisseria meningitidis*.

4.3   Super-Resolution Microscopy of Sphingolipids with Toxins

In nature, many different toxins evolved with specific binding properties and mode of action. Of particular importance, lipid-binding toxins can be coupled to stable organic dyes and used as reporters or detected via an additional toxin-specific antibody. This approach has several advantages as compared to antibody labeling or the use of click-able lipid analogs. On the one hand, many toxins are much smaller than IgGs and can be genetically encoded and fused to fluorescent proteins or small tags to visualize their binding partners even in living cells. Structural insights allow to get rid of unnecessary or even toxic parts and to use only the lipid-binding domain. On the other hand, they can be used to detect endogenous molecules without the need for exogenous addition of lipid derivatives which might perturb cellular signaling. For labeling of sphingolipids or cholesterol the following toxins are described:

- **Cholera toxin:** Cholera toxin belongs to the class of AB_5 toxins which consists of five B subunits ($M_W \approx 12\,kDa$) and one A subunit ($M_W \approx 27\,kDa$). The $\approx 87\,$kDa holotoxin is expressed by the Gram-negative bacterium *Vibrio cholerae* and causes characteristic watery diarrhea during cholera infection. Seven cholera pandemics are reported for the last 200 years which were responsible for large numbers of deaths [548]. The monomeric A subunit is responsible for the toxic effects by activating adenylate cyclases and the stable pentameric cholera toxin B subunits (CTxBs) for binding to cellular monosialotetrahexosylganglioside (GM1) [549]. Since the A and B subunits are structurally independent it is possible to exploit the binding characteristics of the non-toxic CTxBs to detect GM1. Each B subunit exhibits 8 lysine residues which enables efficient conjugation by NHS-modified dyes although commercial biotin and his tagged variants are available. Pentameric CTxB may bind up to five GM1 molecules and cause one of the strongest known protein-carbohydrate interactions [395]. Of note, CTxB can also bind to blood group antigens on glyco-proteins or glycolipids such as Lewis^X [550, 551] and other gangliosides [395] with lower affinity.

- **Shiga toxin:** Shiga toxin belongs to the class of AB_5 toxins which consists of five B subunits ($M_W \approx 7.7\,kDa$, 69 amino acids) and one A subunit ($M_W \approx 30\,kDa$, 293 amino acids). The $\approx 70\,$kDa holotoxin is expressed by the Gram-negative

bacterium *Shigella dysenteriae* and causes dysentery during *Shigella* infection. It is one of the most potent bacterial toxins and the toxic effect is mediated by the A subunit which stops protein synthesis at the eukaryotic ribosomes. Binding and uptake is mediated by the pentameric shiga toxin B subunit (STxB) which binds to the sphingolipid Gb3. Shiga toxins are also produced by some *Escherichia coli* serogroups which are now classified into subtype Shiga toxin 2a [552]. Interestingly, the subtypes also show different binding affinities, for example Shiga toxin 2e binds preferentially to globotetrahexosylceramide (Gb4) even in the presence of Gb3 [553, 554]. Althoug STxBs bind to the sugar moiety, the binding affinity also depends on the fatty acid chain length, degree of saturation and the presence of cholesterol [391, 414, 555]. STxB contains up to three potential Gb3 binding sites per subunit which would allow to bind 18 molecules per pentamer. The polyvalent binding of STxB can induce tubular membrane invaginations which increase its uptake [556]. Each B subunit exhibits 5 lysine residues which enables efficient conjugation by NHS-modified dyes in addition to the commercially available antibodies and his tagged variants. Of note, Gb3 also represents the P^K substance and Gb4 the P substance in the blood group P system [59, 557] which are detected by STxB in platelets [558] and erythrocytes [559].

- **Lysenin:** Lysenin is composed of 297 amino acids resulting in a $33\,kDa$ pore-forming toxin found in the earthworm *Eisenia fetida* and binds to sphingomyelin [560]. The monomer consists of an N-terminal pore-forming domain and a C-terminal β-trefoil lectin type domain responsible for interaction with sphingomyelin. In contact with sphingomyelin-rich membranes lysenin forms a cytotoxic nonameric pore through the plasma membrane with an inner diameter of $\approx 2\,nm$ [561]. Lysenin can be used to label sphingomyelin in fixed cells by immunofluorescence [562] and Alexa 647-conjugated lysenin enabled dSTORM of sphingomyelin-rich domains [563]. In particular, the group of Toshihide Kobayashi characterized a non-toxic truncated version [564] consisting only of the C-terminal binding domain ($\approx 16\,kDa$, amino acids 161-297) for super-resolution microscopy [116, 563].

- **Equinatoxin II:** Equinatoxin II is a $\approx 20\,kDa$ pore-forming toxin found in tentacle extract of the sea anemone *Actinia equina* which binds to sphingomyelin [565]. It is a potent hemolytic toxin which causes death within 5 minutes in mice at a lethal dose 50% (LD$_{50}$) of $23 - 83\,\frac{\mu g}{kg}$ [566]. In membranes, 3 - 4 monomers oligomerize to form a cation-selective pore with inner diameter of $\approx 2\,nm$. When fused with GFP, intracellular sphingomyelin distribution can be followed in living cells [567] although it preferentially binds to sphingomyelin in the L_d phase in contrast to lysenin which labels clustered sphingomyelin [568].

- **Ostreolysin A:** Ostreolysin A is a $\approx 15\,kDa$ pore-forming toxin found in the

edible oyster mushroom *Pleurotus ostreatus*. Interestingly, wildtype ostreolysin A detects sphingomyelin only in the presence of cholesterol [569] but a point mutation (E69A) has been described which can bind sphingomyelin independent of cholesterol [570]. Fusions with the fluorescent protein mCherry were purified and used for labeling [571] or the protein was conjugated to stable organic fluorophores to visualize endogenous sphingomyelin in cells [29]. In contrast to perfringolysin O D4 and anthrolysin O D4 it can detect sphingomyelin-sequestered cholesterol below a threshold of $\approx 30\,mol\,\%$ of total plasma membrane lipids [570].

- **Perfringolysin O:** Perfringolysin O (θ toxin) is a $\approx 53\,kDa$ pore-forming toxin secreted by the anaerobic Gram-positive bacterium *Clostridium perfringens* which binds to cellular cholsterol. It consists of 4 domains (D1-D4) and domain D4 is responsible for cholesterol recognition and binding [572, 573]. Wildtype toxin induces membrane permeabilization at 37°C and 4°C but a less toxic version for labeling at 4°C has been described with mutations Y181A and C459A [574, 575]. Nevertheless, non-toxic domain D4 with a size of $\approx 13\,kDa$ is sufficient to bind cholesterol and can be used as a helpful tool for fluorescence microscopy [116, 563, 576]. Perfringolysin cannot detect inaccessible cholesterol below a threshold level of $\approx 30\,mol\,\%$ of total plasma membrane lipids. Above $\approx 30\,mol\,\%$ cholesterol becomes accessible [29].

- **Anthrolysin O:** Anthrolysin O shares high homology (87%) and identity (74%) with perfringolysin O [577] and is a $\approx 53\,kDa$ pore-forming toxin secreted by the Gram-positive bacterium *Bacillus anthracis* which binds to cellular cholesterol. Again, non-toxic domain D4 can be used as probe to follow cellular cholesterol distribution [29, 578]. It can be used in combination with ostreolysin A to simultaneously visualize free and sphingomyelin-sequestered cholesterol, respectively, in living cells [29, 579].

- **Filipin III:** Filipin ($M_W = 654.8\,\frac{g}{mol}$) is a cholesterol-binding polyene macrolide antibiotic first isolated from the Gram-positive bacterium *Streptomyces filipinensis* found in the soil on the Philippines [580]. Filipin is a mixture of 4 different components Filipin I - IV which all are fluorescent and show characteristic absorption peaks at 322, 338, and 355 nm. It is routinely used to detect cholesterol in fixed cells, for example in the diagnosis of the sphingolipidose Niemann-Pick type C disease [581, 582]. Nevertheless, it is prone to photobleaching and perturbs plasma membranes probably through permeabilization which impedes its application for live-cell experiments.

- **Theonellamide A:** Theonellamides are 3β-sterol-binding cytotoxic bicyclic dodecapeptides found in the marine sponge *Theonella swinhoei*. Interestingly, the peptide is not produced by the sponge itself but rather by its filamentous, multicellular

symbiont "*Candidatus* Entotheonella serta" [583]. Theonellamides show antifungal activity caused by interactions with ergosterol [584].

I used the specific binding characteristics of STxB and CTxB to investigate the frequency and distribution of Gb3 and GM1, respectively, by *d*STORM in the context of *Neisseria meningitidis* infection. First, I developed robust protocols for conjugation of the toxins with organic dyes, fixation and labeling of cells. Then, I analyzed the nanoscale plasma membrane distribution before and during infection of HBMECs with *Neisseria meningitidis*. Before infection, both sphingolipids were distributed homogenously within the basal plasma membrane but showed opposite cell-cycle dependent expression with upregulation of Gb3 in G2/M and GM1 in G0/G1 phase. Upon infection, distinct accumulation of CTxB-positive gangliosides could be observed around adhesive meningococci but no enrichment of STxB-positive globosides. Moreover, cell-cycle arrest of HBMECs in G1 phase by serum starvation 24 h before the experiment substantially increased the amount of GM1 on the cell surface accompanied by an increased number of invasive bacteria. If accessible GM1 epitopes were blocked by pretreatment with CTxB, the increase in invasive bacteria was abolished. For this reason, I concluded that gangliosides on host cells could represent important molecules for the entry of human pathogens, such as *Neisseria meningitidis*.

4.4   Outlook

Based on the discussed three different labeling methods, I was able to visualize and quantifiy cellular sphingolipid domains below the diffraction limit of light. Nevertheless, each method has its distinct pros and cons which are illustrated in the following Table 2:

	Antibody Labeling	Click Chemistry	Toxin Labeling
Linkage Error	-	+	0
Endogenous Labeling	+	-	+
Binding Induced Clustering	-	+	-
Live Cell	-	+	0
Background on Glass	0	-	+
SMLM Compatibility	+	0	+
Chemical Fixation	+	0	+

Table 2: Pros and cons of the three labeling techniques used in this work to visualize and quantify sphingolipids by super-resolution microscopy. The performance of different paramters of each method was classified into one of three categories. Descending from good to bad: green(+) > yellow(0) > red(-).

I would like to give an outlook, how future directions could improve the bottlenecks of each method. For practical reasons, I will first discuss antibody labeling and toxin labeling simultaneously, since both technqiues fall into the category of peptide-based labeling techniques. As introduced in section 1.2.1, the development and improvement of nanobody-based technologies will decrease the linkage error of antibody labeling step-by-step (see

Figure 7). In addition, the size of an antibody can be reduced to the antigen-binding fragments by cleavage with pepsin and/or papain to generate $(F(ab)_2)$ or (Fab), respectively. In a similar way, the size of many toxins could be reduced to their non-toxic binding domain which also will reduce the displacement of the fluorophores from the target site. These approaches will also help to reduce binding induced clustering, since polyvalent binding events are shifted to monovalent binding events. Structure-guided protein refinement was already successfull for some toxins and allows to use them even for live-cell imaging [29, 574, 575, 579]. Especially in the light of emerging tools to facilitate transit through the plasma membrane, such as peptide vehicles [585] or protein transfection methods, these new tools could also be used to label intracellular targets.

One of the major drawbacks when using clickable sphingolipid analogs is the fact, that they have to be added exogenously to the cells. This will shift the physiological lipid homeostasis and could influence signaling cascades leading to artificial readout. For this reason, a combination of metabolic labeling and click-chemistry would be of interest. In this scenario, clickable sphingolipid precursors are added to the cells and metabolized from the native cellular enzymes to generate a plethora of complex sphingolipids which can be localized via conjugation to a clickable dye. Unfortunately, by using only fluorescence microscopy the species information would be lost and therefore this approach should be coupled with mass spectrometry to identify the actual sphingolipid composition. Of note, several groups already showed the feasability of this approach albeit only for a small subset of metabolites [586–588]. Another issue with the clickable probes is their strong glass interaction which generates high background signal and complicates analysis by total internal reflection fluorescence (TIRF) microscopy. Although I tested several different coatings (lysine, glycine, DBCO-amine, bovine serum albumin (BSA)) which did not reduce the non-specific signal on the glass there might be a coating procedure for that purpose. In particular, expansion microscopy proved to be a promising way since the expansion process drastically reduced background and imaging is not restricted to the glass surface. Another challenge represents the chemical fixation of clickable sphingolipid analogs which was already discussed in section 4.2. Here, introduction of a primary amine improved the immobilization of lipids and enabled their use for expansion microscopy. Another approach is the introduction of photo-crosslinkable groups, such as diazirines. Upon irradiation with UV-light they form highly reactive carbene species which covalently react with nearby molecules. These probes are widely used in photoreactive crosslinking experiments to identify proximal interaction partners of receptors [589]. Indeed, I also tested a diazirine- and azide-modified ceramide analog (bifunctional ceramide) for its suitability in super-resolution microscopy. The following Figure 10 shows an example dSTORM image of Jurkat cells incubated with this analog:
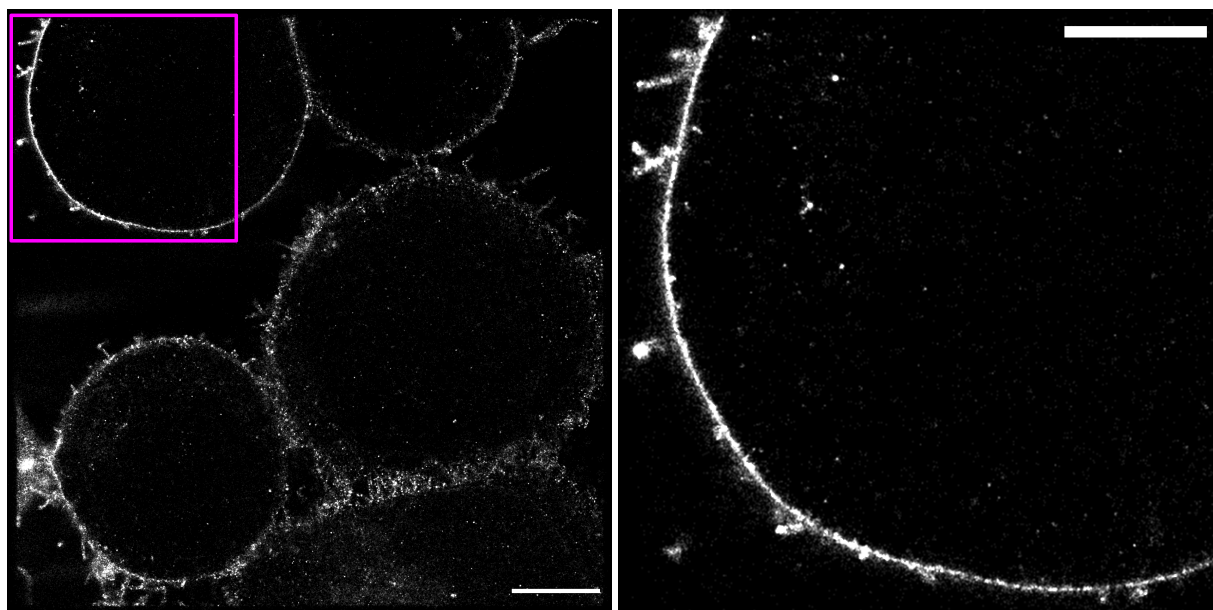
Figure 10: *d*STORM of Jurkat cells incubated with an UV-crosslinkable diazirine- and azide-modified ceramide. Following ceramide incubation cells were fixed at room temperature with formaldehyde and glutaraldehyde and simultaneously irradiated with 350 nm UV-light to enable efficient crosslinking. Subsequently, cells were clicked with the membrane impermeable dye DBCO-Sulfo-Cy5 and analyzed by *d*STORM. Reconstruction was performed with ThunderSTORM [412] from a raw movie of 40 000 images with 20 ms exposure time. Left image shows an overview with scalebar 5 μm and right image an enlargement of the magenta boxed region with scalebar 3 μm. Distinct plasma membrane accumulation could be observed enabling visualization of fine plasma membrane protrusions.

Of note, the bifunctional ceramide showed less signal as compared with the azido-modified ceramide analogs. This might be due to the kink introduced by the diazirine group at the C4-position at the end of a short C5 fatty acid side chain. I also adapted the protocol to reduce background on the glass surface by feeding Jurkat cells in a tube. This allowed us, to wash them thoroughly by centrifugation steps before they attached to the glass surface which drastically reduced background signal on the glass surface. Moreover, this probe was completely immobilized after fixation as analyzed by FRAP (data not shown) and we believe it might also be a convenient probe for expansion microscopy.

In summary, I was able to use all three labeling procedures to characterize and visualize sphingolipid nanodomains in the plasma membrane of different cell lines. I highlighted their pros and cons and showed ways how to avoid common bottlenecks of each technique. These results and techniques will help to understand the complex nature of biological membranes and their nanoscale interaction with proteins.

A   Abbreviations

A ABBREVIATIONS

ChR-2 channelrhodopsin-2 18

GPCR G protein-coupled receptor 18

SDF-1 stromal cell-derived factor 1 18

HBSS Hank's Balanced Salt Solution 19

PBS phosphate-buffered solution 19

FCS fetal calf serum 19

MS multiple sclerosis 180

IgM immunoglobulin M 180

CRP ceramide-rich platform IV

GPI glycosylphosphatidylinositol 181

HBMEC human brain microvascular endothelial cell 181

ASM acid sphingomyelinase 181

L_d liquid disordered 183

L_o liquid ordered 183

FRAP fluorescence recovery after photobleaching 184

NHS N-hydroxysuccinimide esther 184

GlcNAc N-acetylglucosamine 184

MurNAc N-acetylmuramic acid 184

CTxB cholera toxin B subunit IV

STxB shiga toxin B subunit IV

GM1 monosialotetrahexosylganglioside 185

Gb3 globotriaosylceramide 9

Gb4 globotetrahexosylceramide 186

LD$_{50}$ lethal dose 50% 186

TIRF total internal reflection fluorescence 189

BSA bovine serum albumin 189

B List of Publications

Publication #1:

Jan Schlegel, Simon Peters, Sören Doose, Alexandra Schubert-Unkmeir, Markus Sauer: "Super-Resolution Microscopy Reveals Local Accumulation of Plasma Membrane Gangliosides at Neisseria meningitidis Invasion Sites" *Frontiers in cell and developmental biology.* 2019;7:194. doi: 10.3389/fcell.2019.00194. PubMed PMID: 31572726

Publication #2:

Katrin Feldbauer *, Jan Schlegel *, Juliane Weissbecker, Frank Sauer, Phillip G. Wood, Ernst Bamberg, Ulrich Terpitz: „Optochemokine Tandem for Light-Control of Intracellular Ca2" *PLoS ONE.* 2016;11(10):e0165344. doi: 10.1371/journal.pone.0165344. PubMed PMID: 27768773. * shared first authorship

---

Publication #3:

Jan Schlegel, Markus Sauer: "Super-resolution microscopy of sphingolipids" Accepted in *Methods in Molecular Biology* (Springer). 2020

Publication #4:

Tim Walter *, Jan Schlegel *, Anne Burgert, Andreas Kurz, Jürgen Seibel, Markus Sauer: "Incorporation studies of clickable ceramides in Jurkat cell plasma membranes" *Chemical Communications.* 2017;53(51):6836–9. doi: 10.1039/c7cc01220a. PubMed PMID: 28597878. * shared first authorship

---

Publication #5:

Esther Weiss *, Jan Schlegel *, Ulrich Terpitz, Michael Weber, Joerg Linde, Anna-Lena Schmitt, Kerstin Hünniger, Lothar Marischen, Joachim Bauer, Claudia Löffler, Oliver Kurzai, Charles Oliver Morton, Markus Sauer, Hermann Einsele #, and Juergen Loeffler #. „Reconstituting NK cells after allogeneic stem cell transplantation reveal impaired recognition of Aspergillus fumigatus mediated by corticosteroids". * shared first authorship, # shared last authorship

---

Publication #6:

Felix Wäldchen *, Jan Schlegel *, Ralph Götz, Michael Luciano, Martin Schnermann, Sören Doose, Markus Sauer: "Whole-cell imaging of plasma membrane receptors by 3D lattice light-sheet dSTORM" *Nature Communications.* 2020 * shared first authorship

---

Publication #7:

Simon Peters, Jan Schlegel, Jérôme Becam, Elita Avota, Markus Sauer, Alexandra Schubert-Unkmeir: "Neisseria meningitidis Type IV Pili Trigger Ca^{2+}-Dependent Lysosomal Trafficking of the Acid Sphingomyelinase To Enhance Surface Ceramide Levels." *Infection and Immunity.* 2019. doi: 10.1128/IAI.00410-19. PubMed PMID: 31160362.

Publication #8:

Jérôme Becam, Tim Walter, Anne Burgert, <u>Jan Schlegel</u>, Markus Sauer, Jürgen Seibel, Alexandra Schubert-Unkmeir: "Antibacterial activity of ceramide and ceramide analogs against pathogenic Neisseria" *Scientific Reports.* 2017. doi: 10.1038/s41598-017-18071-w.

Publication #9:

Anne Burgert, <u>Jan Schlegel</u>, Jérôme Becam, Sören Doose, Erhard Bieberich, Alexandra Schubert-Unkmeir, Markus Sauer: "Characterization of Plasma Membrane Ceramides by Super-Resolution Microscopy" *Angewandte Chemie.* 2017;56(22):6131–5. doi: 10.1002/anie.201700570. PubMed PMID: 28379629.

Publication #10:

Sabrina Ziegler*, Esther Weiss*, Anna-Lena Schmitt, <u>Jan Schlegel</u>, Anne Burgert, Ulrich Terpitz, Markus Sauer, Lorenzo Moretta, Simona Sivori, Ines Leonhardt, Oliver Kurzai, Hermann Einsele & Juergen Loeffler: "CD56 is a pathogen recognition receptor on human natural killer cells" *Scientific Reports,* volume 7, Article number: 6138 (2017) *equal contribution

---

Publication #11:

Ralph Götz*, Tobias C. Kunz*, Julian Fink, Franziska Solger, <u>Jan Schlegel</u>, Jürgen Seibel, Vera Kozjak-Pavlovic, Thomas Rudel, Markus Sauer: "Nanoscale imaging of cellular and bacterial membranes by sphingolipid expansion microscopy" 2020, Under Revision, *equal contribution

---

C   Approval: "Dissertation Based on Several Published Manuscripts"

Approval of a "Dissertation Based on Several Published Manuscripts" for the doctoral researcher:

Jan Schlegel

who has accomplished a publication record significantly above average as documented in section B.

The **Section Speakers and the Thesis Committee** therefore approve a "Dissertation Based on Several Published Manuscripts".

The **Thesis Committee** additionally confirms that the doctoral researcher has fulfilled all requirements of the GSLS program "life science".

. . . .

Place, Date   Signature

1st Supervisor: Prof. Dr. Markus Sauer

D   Statement of Individual Author Contributions

Publication #1:					
Jan Schlegel, Simon Peters, Sören Doose, Alexandra Schubert-Unkmeir, Markus Sauer: "Super-Resolution Microscopy Reveals Local Accumulation of Plasma Membrane Gangliosides at Neisseria meningitidis Invasion Sites" *Frontiers in cell and developmental biology.* 2019;7:194. doi: 10.3389/fcell.2019.00194. PubMed PMID: 31572726					
Participated in	**Author Initials** Responsibility decreasing from left to right				
Study Design Methods Development	J.S. J.S.	S.P. S.P.	S.D.; A.S.U.; M.S.		
Data Collection	J.S.; S.P.		S.D.; A.S.U.; M.S.		
Data Analysis and Interpretation	J.S.; S.P.		S.D.; A.S.U.; M.S.		
Manuscript Writing Writing Introduction	J.S.; S.P. J.S.; S.P.		S.D.; A.S.U.; M.S.		
Writing of Materials & Methods	J.S.	S.P.	S.D.; A.S.U.; M.S.		
Writing of Discussion	J.S.	S.P.	S.D.; A.S.U.; M.S.		
Writing of First Draft	J.S.	S.P.	S.D.; A.S.U.; M.S.		

Publication #2:				
Katrin Feldbauer *****, <u>Jan Schlegel</u> *****, Juliane Weissbecker, Frank Sauer, Phillip G. Wood, Ernst Bamberg, Ulrich Terpitz: „Optochemokine Tandem for Light-Control of Intracellular Ca2" *PLoS ONE.* 2016;11(10):e0165344. doi: 10.1371/journal.pone.0165344. PubMed PMID: 27768773. ***** shared first authorship				
Participated in	**Author Initials**			
	Responsibility decreasing from left to right			
Study Design Methods Development	P.G.W.; U.T. J.S.; K.F.	E.B.; J.S.; K.F. U.T.; F.S.; J.W.	F.S.; J.W. P.G.W.; E.B.		
Data Collection	J.S.; K.F.	J.W.; F.S.	U.T.	P.G.W.; E.B.	
Data Analysis and Interpretation	J.S.; K.F.; U.T.	E.B.; P.G.W.; F.S.; J.W.			

Manuscript Writing
  Writing Introduction
 	
  Writing of Materials & Methods
 	
  Writing of Discussion
 	
  Writing of First Draft
	
	U.T.
	
	J.S.; U.T.
	
	U.T.
	
	U.T.
		
		J.S.; K.F.
		
		K.F.;
		J.W.;
		F.S.
		J.S.; K.F.
		
		J.S.; K.F.
			
			J.W.;
			F.S.
			E.B.;
			P.G.W.
			
			J.W.;
			F.S.
			J.W.;
			F.S.
				
				E.B.;
				P.G.W.
				
				E.B.;
				P.G.W.
				E.B.;
				P.G.W.	

Publication #3:				
Jan Schlegel, Markus Sauer: "Super-resolution microscopy of sphingolipids" Accepted in *Methods in Molecular Biology* (Springer). 2020					
Participated in	**Author Initials**				
	Responsibility decreasing from left to right				
Study Design	J.S.	M.S.			
Methods Development	J.S.	M.S.			
Data Collection	J.S.	M.S.			
Data Analysis and Interpretation	J.S.	M.S.			
Manuscript Writing					
Writing Introduction	J.S.	M.S.			
Writing of Materials & Methods	J.S.	M.S.			
Writing of Discussion	J.S.	M.S.			
Writing of First Draft	J.S.	M.S.			

Publication #4:					
Tim Walter *, <u>Jan Schlegel</u> *, Anne Burgert, Andreas Kurz, Jürgen Seibel, Markus Sauer: "Incorporation studies of clickable ceramides in Jurkat cell plasma membranes" *Chemical Communications.* 2017;53(51):6836–9. doi: 10.1039/c7cc01220a. PubMed PMID: 28597878. * shared first authorship					
Participated in	**Author Initials**				
	Responsibility decreasing from left to right				
Study Design	M.S.; J.S.; T.W.	J.Se.; A.B.	A.K.		
Methods Development	J.S.; T.W.; A.K.	A.B.	J.Se.; M.S.		
Data Collection	J.S.; T.W.; A.K.	A.B.	J.Se.; M.S.		
Data Analysis and Interpretation	J.S.; T.W.; A.K.	A.B.; J.Se.; M.S.			
Manuscript Writing					
Writing Introduction	T.W.; J.Se.	J.S.; M.S.	A.B.; A.K.		
Writing of Materials & Methods	J.S.; T.W.; A.K.	A.B.	M.S.; J.Se.		
Writing of Discussion	T.W.; J.Se.	J.S.; M.S.	A.B.; A.K.		
Writing of First Draft	T.W.; J.Se.	J.S.; M.S.	A.B.; A.K.		

Publication #5:

Esther Weiss *, <u>Jan Schlegel</u> *, Ulrich Terpitz, Michael Weber, Joerg Linde, Anna-Lena Schmitt, Kerstin Hünniger, Lothar Marischen, Joachim Bauer, Claudia Löffler, Oliver Kurzai, Charles Oliver Morton, Markus Sauer, Hermann Einsele #, and Juergen Loeffler #. „Reconstituting NK cells after allogeneic stem cell transplantation reveal impaired recognition of Aspergillus fumigatus mediated by corticosteroids". * shared first authorship, # shared last authorship

Participated in	Author Initials				
	Responsibility decreasing from left to right				
Study Design Methods Development	J.S.; E.W.; J.L.; H.E.; A.S.	U.T.	M.S.; L.M.	J.B.; C.L.	K.H.; M.W.; J.Li.; O.K.; C.M.
Data Collection	J.S.; E.W.	A.S.	L.M.; K.H.	J.B.; C.L.	J.L.; M.W.; J.Li.; O.K.; C.M.; U.T.; M.S.; H.E.
Data Analysis and Interpretation	J.S.; E.W.	M.W.	L.M.; U.T.	J.L.; M.S.; H.E.	A.S.; K.H.; C.M.; O.K.; J.Li.; C.L.; J.B.
Manuscript Writing	E.W.	J.S.; J.L.	C.M.; H.E.; K.H.; U.T.; L.M.	M.S.	A.S.; J.B.; C.L.; M.W.; J.Li.; O.K.

Publication #6:

Felix Wäldchen *****, <u>Jan Schlegel</u> *****, Ralph Götz, Michael Luciano, Martin Schnermann, Sören Doose, Markus Sauer: "Whole-cell imaging of plasma membrane receptors by 3D lattice light-sheet dSTORM" *Nature Communications.* 2020 ***** shared first authorship

Participated in	Author Initials				
	Responsibility decreasing from left to right				
Study Design Methods Development	J.S.; F.W.	R.G.; S.D.; M.S.	M.L.; M.Sc.		
Data Collection	J.S.; F.W.	R.G.; S.D.; M.S.	M.L.; M.Sc.		
Data Analysis and Interpretation	J.S.; F.W.; S.D.	R.G.; M.S.	M.L.; M.Sc.		
Manuscript Writing Writing Introduction	F.W.; M.S.	J.S.; S.D.	R.G.; M.L.; M.Sc.		
Writing of Materials & Methods	J.S.; F.W.	R.G.; S.D.	M.S.; M.L.; M.Sc.		
Writing of Discussion	F.W.; M.S.	S.D.; J.S.	R.G.; M.L.; M.Sc.		
Writing of First Draft	F.W.; M.S.	S.D.; J.S.	R.G.; M.L.; M.Sc.		

Publication #7:
Simon Peters, <u>Jan Schlegel</u>, Jérôme Becam, Elita Avota, Markus Sauer, Alexandra Schubert-Unkmeir: "Neisseria meningitidis Type IV Pili Trigger Ca^{2+}-Dependent Lysosomal Trafficking of the Acid Sphingomyelinase To Enhance Surface Ceramide Levels." *Infection and Immunity.* 2019. doi: 10.1128/IAI.00410-19. PubMed PMID: 31160362.

Participated in	Author Initials				
	Responsibility decreasing from left to right				
Study Design Methods Development	J.S.; S.P.; A.S.U.	J.B.; E.A.; M.S.			
Data Collection	J.S.; S.P.	J.B.	E.A.; A.S.U.; M.S.		
Data Analysis and Interpretation	J.S.; S.P.	A.S.U.; M.S.	J.B.; E.A.		
Manuscript Writing Writing Introduction	S.P.	A.S.U.; J.S.	E.A.; J.B.; M.S.		
Writing of Materials & Methods	J.S.; S.P.	J.B.	E.A.; A.S.U.; M.S.		
Writing of Discussion	S.P.; A.S.U.	J.S.; E.A.	M.S.; J.B.		
Writing of First Draft	S.P.; A.S.U.	J.S.; E.A.	M.S.; J.B.		

Publication #8:

Jérôme Becam, Tim Walter, Anne Burgert, <u>Jan Schlegel</u>, Markus Sauer, Jürgen Seibel, Alexandra Schubert-Unkmeir: "Antibacterial activity of ceramide and ceramide analogs against pathogenic Neisseria" *Scientific Reports.* 2017. doi: 10.1038/s41598-017-18071-w.

Participated in	Author Initials				
	Responsibility decreasing from left to right				
Study Design Methods Development	J.S.; T.W.; J.B.; A.S.U.	A.B.	M.S.; J.Se.		
Data Collection	J.B.	J.S.; A.B.; T.W.	M.S.; J.Se.; A.S.U.		
Data Analysis and Interpretation	J.S.; J.B.; T.W.; A.S.U.	A.B.; M.S.; J.Se.			
Manuscript Writing Writing Introduction	J.B.; A.S.U.	T.W.; J.S.; A.B.	M.S.; J.Se.		
Writing of Materials & Methods	J.S.; J.B.; T.W.	A.B.	M.S.; A.S.U.; J.Se.		
Writing of Discussion	J.B.; A.S.U.	T.W.; J.S.; A.B.	M.S.; J.Se.		
Writing of First Draft	J.B.; A.S.U.	T.W.; J.S.; A.B.	M.S.; J.Se.		

Publication #9:					
Anne Burgert, <u>Jan Schlegel</u>, Jérôme Becam, Sören Doose, Erhard Bieberich, Alexandra Schubert-Unkmeir, Markus Sauer: "Characterization of Plasma Membrane Ceramides by Super-Resolution Microscopy" *Angewandte Chemie.* 2017;56(22):6131–5. doi: 10.1002/anie.201700570. PubMed PMID: 28379629.					
Participated in	**Author Initials**				
	Responsibility decreasing from left to right				
Study Design Methods Development	A.B.; M.S.; J.S.	J.B.; S.D.	E.B.; A.S.U.		
Data Collection	J.S.; A.B.; J.B.	S.D.	E.B.; A.S.U.; M.S.		
Data Analysis and Interpretation	J.S.; A.B.; S.D.	M.S.; A.S.U.	E.B.; J.B.		
Manuscript Writing					
Writing Introduction	A.B.; M.S.	J.S.; S.D.	J.B.; A.S.U.	E.B.	
Writing of Materials & Methods	A.B.; J.S.; J.B.	S.D.	A.S.U.; M.S.	E.B.	
Writing of Discussion	A.B.; M.S.; J.S.	S.D.	A.S.U.; J.B.	E.B.	
Writing of First Draft	A.B.; M.S.	S.D.; J.S.	J.B.; A.S.U.	E.B.	

Publication #10:

Sabrina Ziegler *, Esther Weiss *, Anna-Lena Schmitt, <u>Jan Schlegel</u>, Anne Burgert, Ulrich Terpitz, Markus Sauer, Lorenzo Moretta, Simona Sivori, Ines Leonhardt, Oliver Kurzai, Hermann Einsele & Juergen Loeffler: "CD56 is a pathogen recognition receptor on human natural killer cells" *Scientific Reports,* volume 7, Article number: 6138 (2017) * equal contribution

Participated in	Author Initials				
	Responsibility decreasing from left to right				
Study Design Methods Development	S.Z.; E.W.; H.E.; J.L.	J.S.; A.B.; U.T.; M.S.	A.S.	S.S.; I.L.	O.K.; L.M.
Data Collection	S.Z.; E.W.	J.S.; A.B.; A.S.	I.L.	S.S.	O.K.; L.M.; J.L.; H.E.; U.T.; M.S.
Data Analysis and Interpretation	S.Z.; E.W.	J.S.; A.B.	M.S.; J.L.; H.E.; U.T.	I.L.; O.K.; A.S.	S.S.; L.M.
Manuscript Writing	S.Z.; E.W.	J.S.; A.B.	J.L.; M.S.; U.T.; H.E.	I.L.; O.K.	S.S.; L.M.; A.S.

Publication #11: Ralph Götz *, Tobias C. Kunz *, Julian Fink, Franziska Solger, <u>Jan Schlegel</u>, Jürgen Seibel, Vera Kozjak-Pavlovic, Thomas Rudel, Markus Sauer: "Nanoscale imaging of cellular and bacterial membranes by sphingolipid expansion microscopy" 2020, Under Revision, * equal contribution					
Participated in	**Author Initials** Responsibility decreasing from left to right				
Study Design Methods Development	R.G.; T.K.; J.F.; J.S.	F.S.	J.Se.; T.R.; M.S.; V.K.P.		
Data Collection	R.G.; T.K.	F.S.; J.S.; J.F.	J.Se.; T.R.; M.S.; V.K.P.		
Data Analysis and Interpretation	R.G.; T.K.	F.S.; J.S.; J.F.	J.Se.; T.R.; M.S.; V.K.P.		
Manuscript Writing	R.G.; T.K.	F.S.; J.S.; J.F.	J.Se.; T.R.; M.S.; V.K.P.		

The doctoral researcher confirms that he has obtained permission from both the publishers and the co-authors for legal second publication.
The doctoral researcher and the primary supervisor confirm the correctness of the above mentioned assessment.

....
Place, Date   Signature
                                                                Doctoral Researcher: Jan Schlegel

....
Place, Date   Signature
                                                      1st Supervisor: Prof. Dr. Markus Sauer

E   Bibliography

[1]   Robert Hooke. *Micrographia, or, Some physiological descriptions of minute bodies made by magnifying glasses: With observations and inquiries thereupon.* London: Printed by Jo. Martyn and Ja. Allestry, 1665.

[2]   J. Loeb. "The Recent Development of Biology". In: *Science (New York, N.Y.)* 20.519 (1904), pp. 777–786.

[3]   Georg Quincke. *Über periodische Ausbreitung an Flüssigkeits-Oberflächen und dadurch hervorgerufene Bewegungserscheinungen.*

[4]   Robert Chambers. "A Micro Injection Study on the Permeability of the Starfish Egg". In: *The Journal of General Physiology* 5.2 (1922), pp. 189–193. DOI: 10.1085/jgp.5.2.189.

[5]   Walther Nernst. "Die elektromotorische Wirksamkeit der Ionen." In: *Physikalische Chemie* 4 (1889), pp. 129–181.

[6]   Rudolf Höber. "Messungen der inneren Leitfähigkeit von Zellen". In: *Pflüger's Archiv für die Gesammte Physiologie des Menschen und der Tiere* 150.1-2 (1913), pp. 15–45. DOI: 10.1007/BF01681047.

[7]   G. B. Chapman and J. Hillier. "Electron Microscopy of Ultra-Thin Sections of Bacteria .1. Cellular Division in Bacillus-Cereus". In: *Journal of Bacteriology* 66.3 (1953), pp. 362–373.

[8]   George B. Chapman. "Electron Microscope Observations on the Behavior of the Bacterial Cytoplasmic Membrane During Cellular Division". In: *The Journal of cell biology* 6.2 (1959), pp. 221–224. DOI: 10.1083/jcb.6.2.221.

[9]   E. Gorter and F. Grendel. "On Bimolecular Layers of Lipoids on the Chromocytes of the Blood". In: *The Journal of experimental medicine* 41.4 (1925), pp. 439–443. DOI: 10.1084/jem.41.4.439.

[10]   *ChemDraw Professional.* 1998-2015.

[11]   Richard Altmann. *Die Elementarorganismen und ihre Beziehungen zu den Zellen.* Leipzig: Veit, 1890.

[12]   Robert V. Farese and Tobias C. Walther. "Lipid Droplets Finally Get a Little R-E-S-P-E-C-T". In: *Cell* 139.5 (2009), pp. 855–860. DOI: 10.1016/j.cell.2009.11.005.

[13]   Sally Martin and Robert G. Parton. "Lipid droplets: A unified view of a dynamic organelle". In: *Nature Reviews Molecular Cell Biology* 7.5 (2006), pp. 373–378. DOI: 10.1038/nrm1912.

[14]   Jeeyun Chung et al. "LDAF1 and Seipin Form a Lipid Droplet Assembly Complex". In: *Developmental cell* 51.5 (2019), 551–563.e7. DOI: 10.1016/j.devcel.2019.10.006.

[15]   Jodi Nunnari and Anu Suomalainen. "Mitochondria: In Sickness and in Health". In: *Cell* 148.6 (2012), pp. 1145–1159. DOI: 10.1016/j.cell.2012.02.035.

[16]   A. S. Reichert and W. Neupert. "Contact sites between the outer and inner membrane of mitochondria - role in protein transport". In: *Biochimica et Biophysica Acta - Molecular Cell Research* 1592.1 (2002), pp. 41–49.

[17]   Laila Cigana Schenkel and Marica Bakovic. "Formation and regulation of mitochondrial membranes". In: *International journal of cell biology* 2014 (2014), p. 709828. DOI: 10.1155/2014/709828.

[18]   Thomas H. Haines and Norbert A. Dencher. "Cardiolipin: A proton trap for oxidative phosphorylation". In: *FEBS letters* 528.1-3 (2002), pp. 35–39. DOI: 10.1016/S0014-5793(02)03292-1.

[19]   Michael Schlame, Stuart Brody, and Karl Y. Hostetler. "Mitochondrial cardiolipin in diverse eukaryotes. Comparison of biosynthetic reactions and molecular acyl species". In: *European Journal of Biochemistry* 212.3 (1993), pp. 727–733. DOI: 10.1111/j.1432-1033.1993.tb17711.x.

[20]   Dan L. Longo, David Garcia, and Doruk Erkan. "Diagnosis and Management of the Antiphospholipid Syndrome". In: *New England Journal of Medicine* 378.21 (2018), pp. 2010–2021. DOI: 10.1056/NEJMra1705454.

[21]   Nikita Ikon and Robert O. Ryan. "Barth Syndrome: Connecting Cardiolipin to Cardiomyopathy". In: *Lipids* 52.2 (2017), pp. 99–108. DOI: 10.1007/s11745-016-4229-7.

[22]   Tammy Ryan et al. "Cardiolipin exposure on the outer mitochondrial membrane modulates α-synuclein". In: *Nature communications* 9.1 (2018), p. 889. DOI: 10.1038/s41467-018-03241-9.

[23]   Giuseppe Paradies. "Oxidative stress, cardiolipin and mitochondrial dysfunction in nonalcoholic fatty liver disease". In: *World Journal of Gastroenterology* 20.39 (2014), p. 14205. DOI: 10.3748/wjg.v20.i39.14205.

[24]   Quan He and Xianlin Han. "Cardiolipin remodeling in diabetic heart". In: *Chemistry and physics of lipids* 179 (2014), pp. 75–81. DOI: 10.1016/j.chemphyslip.2013.10.007.

[25]   Hugh Young. "SYPHILIS". In: *Dermatologic Clinics* 16.4 (1998), pp. 691–698. DOI: 10.1016/S0733-8635(05)70034-6.

[26]   Michael A. Kiebish et al. "Cardiolipin and electron transport chain abnormalities in mouse brain tumor mitochondria: Lipidomic evidence supporting the Warburg theory of cancer". In: *Journal of Lipid Research* 49.12 (2008), pp. 2545–2556. DOI: 10.1194/jlr.M800319-JLR200.

[27]   Manfred Fobker et al. "Accumulation of cardiolipin and lysocardiolipin in fibroblasts from Tangier disease subjects". In: *FEBS letters* 500.3 (2001), pp. 157–162. DOI: 10.1016/S0014-5793(01)02578-9.

[28]   Helgi I. Ingólfsson et al. "Lipid Organization of the Plasma Membrane". In: *Journal of the American Chemical Society* 136.41 (2014), pp. 14554–14559. DOI: 10.1021/ja507832e.

[29]   Kristen A. Johnson et al. "Ostreolysin A and anthrolysin O use different mechanisms to control movement of cholesterol from the plasma membrane to the endoplasmic reticulum". In: *The Journal of biological chemistry* 294.46 (2019), pp. 17289–17300. DOI: 10.1074/jbc.RA119.010393.

[30]   Akash Das et al. "Three pools of plasma membrane cholesterol and their relation to cholesterol homeostasis". In: *eLife* 3 (2014), p. 19316. DOI: 10.7554/eLife.02882.

[31]   Arun Radhakrishnan et al. "Switch-like Control of SREBP-2 Transport Triggered by Small Changes in ER Cholesterol: A Delicate Balance". In: *Cell Metabolism* 8.6 (2008), pp. 512–521. DOI: 10.1016/j.cmet.2008.10.008.

[32]   Neale Ridgway and Roger McLeod, eds. *Biochemistry of lipids, lipoproteins and membranes*. Sixth edition. Amsterdam: Elsevier, 2016.

[33]   Johann Ludwig Wilhelm Thudichum. *A treatise on the chemical constitution of the brain: Based throughout upon original researches*. London, 1884.

[34]   Alfred H. Merrill. "Sphingolipids". In: *Biochemistry of Lipids, Lipoproteins and Membranes*. Ed. by J. E. Vance and Dennis E. Vance. New Comprehensive Biochemistry. s.l.: Elsevier professional, 2008, pp. 363–397. DOI: 10.1016/B978-044453219-0.50015-5.

[35]   Kai Simons and Elina Ikonen. "Functional rafts in cell membranes". In: *Nature* 387.6633 (1997), pp. 569–572. DOI: 10.1038/42408.

[36]   C. A. Lingwood et al. "Globotriaosyl ceramide receptor function - where membrane structure and pathology intersect". In: *FEBS letters* 584.9 (2010), pp. 1879–1886. DOI: 10.1016/j.febslet.2009.11.089.

[37]   Yusuf A. Hannun and Lina M. Obeid. "Principles of bioactive lipid signalling: Lessons from sphingolipids". In: *Nature Reviews Molecular Cell Biology* 9.2 (2008), pp. 139–150. DOI: 10.1038/nrm2329.

[38] G. Han et al. "Identification of small subunits of mammalian serine palmitoyltrans-ferase that confer distinct acyl-CoA substrate specificities". In: *Proceedings of the National Academy of Sciences* 106.20 (2009), pp. 8186–8191. DOI: 10.1073/pnas.0811269106.

[39] F. S. Eichler et al. "Overexpression of the Wild-Type SPT1 Subunit Lowers Des-oxysphingolipid Levels and Rescues the Phenotype of HSAN1". In: *The Journal of Neuroscience* 29.46 (2009), pp. 14646–14651. DOI: 10.1523/JNEUROSCI.2536-09.2009.

[40] Anke Penno et al. "Hereditary Sensory Neuropathy Type 1 Is Caused by the Ac-cumulation of Two Neurotoxic Sphingolipids". In: *Journal of Biological Chemistry* 285.15 (2010), pp. 11178–11187. DOI: 10.1074/jbc.M109.092973.

[41] Kenneth Gable et al. "A Disease-causing Mutation in the Active Site of Ser-ine Palmitoyltransferase Causes Catalytic Promiscuity". In: *Journal of Biological Chemistry* 285.30 (2010), pp. 22846–22852. DOI: 10.1074/jbc.M110.122259.

[42] Kevin Garofalo et al. "Oral l-serine supplementation reduces production of neuro-toxic deoxysphingolipids in mice and humans with hereditary sensory autonomic neuropathy type 1". In: *Journal of Clinical Investigation* 121.12 (2011), pp. 4735–4745. DOI: 10.1172/JCI57549.

[43] Y. Miyake et al. "Serine Palmitoyltransferase Is the Primary Target of a Sphingosine-like Immunosuppressant, ISP-1/Myriocin". In: *Biochemical and bio-physical research communications* 211.2 (1995), pp. 396–403. DOI: 10.1006/bbrc.1995.1827.

[44] Yael Pewzner-Jung, Shifra Ben-Dor, and Anthony H. Futerman. "When Do Lasses (Longevity Assurance Genes) Become CerS (Ceramide Synthases)?" In: *Journal of Biological Chemistry* 281.35 (2006), pp. 25001–25005. DOI: 10.1074/jbc.R600010200.

[45] Krishnan Venkataraman et al. "Upstream of Growth and Differentiation Factor 1 (uog1), a Mammalian Homolog of the Yeast Longevity Assurance Gene 1 (LAG1), Regulates N -Stearoyl-sphinganine (C18-(Dihydro)ceramide) Synthesis in a Fu-monisin B 1 -independent Manner in Mammalian Cells". In: *Journal of Biological Chemistry* 277.38 (2002), pp. 35642–35649. DOI: 10.1074/jbc.M205211200.

[46] Christian Riebeling et al. "Two Mammalian Longevity Assurance Gene (LAG1) Family Members, trh1 and trh4 , Regulate Dihydroceramide Synthesis Using Dif-ferent Fatty Acyl-CoA Donors". In: *Journal of Biological Chemistry* 278.44 (2003), pp. 43452–43459. DOI: 10.1074/jbc.M307104200.

[47] Elad L. Laviad et al. "Characterization of Ceramide Synthase 2". In: *Journal of Biological Chemistry* 283.9 (2008), pp. 5677–5684. DOI: 10.1074/jbc.M707386200.

[48] Bhagirath Chaurasia et al. "Targeting a ceramide double bond improves insulin resistance and hepatic steatosis". In: *Science (New York, N.Y.)* (2019). DOI: 10.1126/science.aav3722.

[49] William L. Holland et al. "Inhibition of Ceramide Synthesis Ameliorates Glucocorticoid-, Saturated-Fat-, and Obesity-Induced Insulin Resistance". In: *Cell Metabolism* 5.3 (2007), pp. 167–179. DOI: 10.1016/j.cmet.2007.01.002.

[50] Monowarul Mobin Siddique et al. "Dihydroceramides: From Bit Players to Lead Actors". In: *Journal of Biological Chemistry* 290.25 (2015), pp. 15371–15379. DOI: 10.1074/jbc.R115.653204.

[51] Anthony H. Futerman and Howard Riezman. "The ins and outs of sphingolipid synthesis". In: *Trends in Cell Biology* 15.6 (2005), pp. 312–318. DOI: 10.1016/j.tcb.2005.04.006.

[52] Kentaro Hanada et al. "CERT-mediated trafficking of ceramide". In: *Biochimica et Biophysica Acta (BBA) - Molecular and Cell Biology of Lipids* 1791.7 (2009), pp. 684–691. DOI: 10.1016/j.bbalip.2009.01.006.

[53] Norio Kudo et al. "Structural basis for specific lipid recognition by CERT responsible for nonvesicular trafficking of ceramide". In: *Proceedings of the National Academy of Sciences* 105.2 (2008), pp. 488–493. DOI: 10.1073/pnas.0709191105.

[54] Cong Ma et al. "Reconstitution of the Vital Functions of Munc18 and Munc13 in Neurotransmitter Release". In: *Science (New York, N.Y.)* 339.6118 (2013), pp. 421–425. DOI: 10.1126/science.1230473.

[55] G. C. Yaney and B. E. Corkey. "Fatty acid metabolism and insulin secretion in pancreatic beta cells". In: *Diabetologia* 46.10 (2003), pp. 1297–1312. DOI: 10.1007/s00125-003-1207-4.

[56] Anthony H. Futerman. "Intracellular trafficking of sphingolipids: Relationship to biosynthesis". In: *Biochimica et Biophysica Acta (BBA) - Biomembranes* 1758.12 (2006), pp. 1885–1892. DOI: 10.1016/j.bbamem.2006.08.004.

[57] Kentaro Hanada. "Ceramide Transport from the Endoplasmic Reticulum to the Trans Golgi Region at Organelle Membrane Contact Sites". In: *Organelle Contact Sites From Molecular Mechanism to Disease Preface.* Ed. by Mitsuo Tagaya and Thomas Simmen. Vol. 997. Advances in Experimental Medicine and Biology. 2017, pp. 69–81. DOI: 10.1007/978-981-10-4567-7_5.

[58] Alfred H. Merrill. "Sphingolipid and Glycosphingolipid Metabolic Pathways in the Era of Sphingolipidomics". In: *Chemical reviews* 111.10 (2011), pp. 6387–6422. DOI: 10.1021/cr2002917.

[59] Helmut Schenkel-Brunner. *Human blood groups: Chemical and biochemical basis of antigen specificity.* Springer, 2013. DOI: 10.1007/978-3-7091-3686-7.

[60]   Annie Laquerrière et al. "Sphingolipidoses and Related Disorders". In: *Developmental Neuropathology*. John Wiley & Sons, Ltd, 2018, pp. 313–367. DOI: 10.1002/9781119013112.ch29.

[61]   Dominik Wigger et al. "Monitoring the Sphingolipid de novo Synthesis by Stable-Isotope Labeling and Liquid Chromatography-Mass Spectrometry". In: *Frontiers in Cell and Developmental Biology* 7 (2019), p. 1235. DOI: 10.3389/fcell.2019.00210.

[62]   J.F.W. Herschel. "On a case of superficial colour presented by a homogeneous liquid internally colourless." In: *Philos. Trans. R. Soc. London* 135 (1845), pp. 143–145.

[63]   G. G. Stokes. "On the change of refractibility of light." In: *Philos Trans R Soc London* 142 (1852), pp. 463–562.

[64]   Hans Lehmann. "Das Lumineszenzmikroskop, seine Grundlagen und seine Anwendungen". In: *Zeitschrift für wissenschaftliche Mikroskopie* 30 (1913), pp. 417–470.

[65]   Oskar Heimstädt. "Das Fluoreszenzmikroskop". In: *Zeitschrift für wissenschaftliche Mikroskopie* 28 (1911), pp. 330–337.

[66]   Joseph R. Lakowicz. *Principles of fluorescence spectroscopy*. Third edition, corrected at 4. printing. New York, NY: Springer, 2010.

[67]   Niccolò Banterle et al. "Fourier ring correlation as a resolution criterion for super-resolution microscopy". In: *Journal of Structural Biology* 183.3 (2013), pp. 363–367. DOI: 10.1016/j.jsb.2013.05.004.

[68]   Robert P. J. Nieuwenhuizen et al. "Measuring image resolution in optical nanoscopy". In: *Nature Methods* 10.6 (2013), pp. 557–562. DOI: 10.1038/nmeth.2448.

[69]   A. Descloux, K. S. Grußmayer, and A. Radenovic. "Parameter-free image resolution estimation based on decorrelation analysis". In: *Nature Methods* 16.9 (2019), pp. 918–924. DOI: 10.1038/s41592-019-0515-7.

[70]   Peter W. Hawkes. "Ernst Ruska". In: *Physics Today* 43.7 (2008), p. 84. DOI: 10.1063/1.2810640.

[71]   F. S. Sjöstrand, Ebba Andersson-Cedergren, and M. M. Dewey. "The ultrastructure of the intercalated discs of frog, mouse and guinea pig cardiac muscle". In: *Journal of Ultrastructure Research* 1.3 (1958), pp. 271–287. DOI: 10.1016/S0022-5320(58)80008-8.

[72]   J. D. Robertson. "The Molecular Structure and Contact Relationships of Cell Membranes". In: *Progress in biophysics and molecular biology* 10 (1960).

[73]   J. D. Robertson. "The Ultrastructure of Cell Membranes and Their Derivatives". In: *Biochemical Society symposium* 16 (1959).

[74] W. Lukosz. "Optical Systems with Resolving Powers Exceeding the Classical Limit*". In: *JOSA* 56.11 (1966), pp. 1463–1471. DOI: 10.1364/JOSA.56.001463.

[75] W. E. Moerner and L. Kador. "Optical Detection and Spectroscopy of Single Molecules in a Solid". In: *Physical Review Letters* 62.21 (1989). DOI: 10.1103/PhysRevLett.62.2535.

[76] M. Orrit and J. Bernard. "Single Pentacene Molecules Detected by Fluorescence Excitation in a P-Terphenyl Crystal". In: *Physical Review Letters* 65.21 (1990). DOI: 10.1103/PhysRevLett.65.2716.

[77] E. Brooks Shera et al. "Detection of single fluorescent molecules". In: *Chemical Physics Letters* 174.6 (1990), pp. 553–557. DOI: 10.1016/0009-2614(90)85485-U.

[78] Eric Betzig et al. "Imaging intracellular fluorescent proteins at nanometer resolution". In: *Science (New York, N.Y.)* 313.5793 (2006), pp. 1642–1645. DOI: 10.1126/science.1127344.

[79] Samuel T. Hess, Thanu P. K. Girirajan, and Michael D. Mason. "Ultra-High Resolution Imaging by Fluorescence Photoactivation Localization Microscopy". In: *Biophysical journal* 91.11 (2006), pp. 4258–4272. DOI: 10.1529/biophysj.106.091116.

[80] Osamu Shimomura, Frank H. Johnson, and Yo Saiga. "Extraction, Purification and Properties of Aequorin, a Bioluminescent Protein from the Luminous Hydromedusan, Aequorea". In: *Journal of Cellular and Comparative Physiology* 59.3 (1962), pp. 223–239. DOI: 10.1002/jcp.1030590302.

[81] M Chalfie et al. "Green fluorescent protein as a marker for gene expression". In: *Science* 263.5148 (1994), pp. 802–805. DOI: 10.1126/science.8303295.

[82] Mats Ormö et al. "Crystal Structure of the Aequorea victoria Green Fluorescent Protein". In: *Science* 273.5280 (1996), pp. 1392–1395. DOI: 10.1126/science.273.5280.1392.

[83] G. H. Patterson and J. Lippincott-Schwartz. "A Photoactivatable GFP for Selective Photolabeling of Proteins and Cells". In: *Science (New York, N.Y.)* 297.5588 (2002). DOI: 10.1126/science.1074952.

[84] Mike Heilemann et al. "Subdiffraction-Resolution Fluorescence Imaging with Conventional Fluorescent Probes". In: *Angewandte Chemie International Edition* 47.33 (2008), pp. 6172–6176. DOI: 10.1002/anie.200802376.

[85] Michael J. Rust, Mark Bates, and Xiaowei Zhuang. "Sub-diffraction-limit imaging by stochastic optical reconstruction microscopy (STORM)". In: *Nature methods* 3.10 (2006), pp. 793–795. DOI: 10.1038/nmeth929.

[86]   Stefan W. Hell and Jan Wichmann. "Breaking the diffraction resolution limit by stimulated emission: Stimulated-emission-depletion fluorescence microscopy". In: *Optics Letters* 19.11 (1994), p. 780. DOI: 10.1364/ol.19.000780.

[87]   T. A. Klar et al. "Fluorescence microscopy with diffraction resolution barrier broken by stimulated emission". In: *Proceedings of the National Academy of Sciences* 97.15 (2000), pp. 8206–8210.

[88]   Rainer Heintzmann and Christoph G. Cremer. "Laterally modulated excitation microscopy: Improvement of resolution by using a diffraction grating". In: International Society for Optics and Photonics, 1999, pp. 185–196. DOI: 10.1117/12.336833.

[89]   M. G. L. Gustafsson. "Surpassing the lateral resolution limit by a factor of two using structured illumination microscopy. Short Communication". In: *Journal of microscopy* 198.2 (2000), pp. 82–87. DOI: 10.1046/j.1365-2818.2000.00710.x.

[90]   Albert H. Coons, Hugh J. Creech, R. Norman Jones and Ernst Berliner. "The Demonstration of Pneumococcal Antigen in Tissues by the Use of Fluorescent Antibody". In: *The Journal of Immunology* 45.3 (1942), pp. 159–170.

[91]   Yongdeng Zhang et al. "Nanoscale subcellular architecture revealed by multicolor three-dimensional salvaged fluorescence imaging". In: *Nature Methods* 17.2 (2020), pp. 225–231. DOI: 10.1038/s41592-019-0676-4.

[92]   Z. Zhang et al. "Structure-based Engineering of anti-GFP Nanobody Tandems as Ultra-High-Affinity Reagents for Purification". In: *Scientific reports* 10.1 (2020). DOI: 10.1038/s41598-020-62606-7.

[93]   L. J. Harris et al. "Refined structure of an intact IgG2a monoclonal antibody". In: *Biochemistry* 36.7 (1997), pp. 1581–1597.

[94]   Howard C. Hang et al. "A metabolic labeling approach toward proteomic analysis of mucin-type O-linked glycosylation". In: *Proceedings of the National Academy of Sciences* 100.25 (2003), pp. 14846–14851. DOI: 10.1073/pnas.2335201100.

[95]   Kathrin Lang and Jason W. Chin. "Cellular incorporation of unnatural amino acids and bioorthogonal labeling of proteins". In: *Chemical reviews* 114.9 (2014), pp. 4764–4806. DOI: 10.1021/cr400355w.

[96]   Jan Dommerholt, Floris P. J. T. Rutjes, and Floris L. van Delft. "Strain-Promoted 1,3-Dipolar Cycloaddition of Cycloalkynes and Organic Azides". In: *Topics in Current Chemistry (Cham)* 374.2 (2016). DOI: 10.1007/s41061-016-0016-4.

[97]   Mark R. Karver, Ralph Weissleder, and Scott A. Hilderbrand. "Bioorthogonal Reaction Pairs Enable Simultaneous, Selective, Multi-Target Imaging**". In: *Angewandte Chemie (International ed. in English)* 51.4 (2012), pp. 920–922. DOI: 10.1002/anie.201104389.

[98] Antoine Adamantidis et al. "Optogenetics: 10 years after ChR2 in neurons—views from the community". In: *Nature neuroscience* 18.9 (2015), pp. 1202–1212. DOI: 10.1038/nn.4106.

[99] Jan Schlegel. "Analysis of the Internalization and Optogenetic Activation of a Rhodopsin-Tandemprotein in NG108-15 Cells by means of Fluorescence Microscopy". Master Thesis. Wuerzburg: Julius-Maximilians-University, 2015.

[100] Georg Nagel et al. "Channelrhodopsin-2, a directly light-gated cation-selective membrane channel". In: *Proceedings of the National Academy of Sciences of the United States of America* 100.24 (2003), pp. 13940–13945. DOI: 10.1073/pnas.1936192100.

[101] Edward S. Boyden et al. "Millisecond-timescale, genetically targeted optical control of neural activity". In: *Nature neuroscience* 8.9 (2005), pp. 1263–1268. DOI: 10.1038/nn1525.

[102] Anding Bi et al. "Ectopic Expression of a Microbial-Type Rhodopsin Restores Visual Responses in Mice with Photoreceptor Degeneration". In: *Neuron* 50.1 (2006), pp. 23–33. DOI: 10.1016/j.neuron.2006.02.026.

[103] Toru Ishizuka et al. "Kinetic evaluation of photosensitivity in genetically engineered neurons expressing green algae light-gated channels". In: *Neuroscience Research* 54.2 (2006), pp. 85–94. DOI: 10.1016/j.neures.2005.10.009.

[104] G. Nagel et al. "Light Activation of channelrhodopsin-2 in Excitable Cells of Caenorhabditis Elegans Triggers Rapid Behavioral Responses". In: *Current biology : CB* 15.24 (2005). DOI: 10.1016/j.cub.2005.11.032.

[105] Xiang Li et al. "Fast noninvasive activation and inhibition of neural and network activity by vertebrate rhodopsin and green algae channelrhodopsin". In: *Proceedings of the National Academy of Sciences* 102.49 (2005), pp. 17816–17821. DOI: 10.1073/pnas.0509030102.

[106] Andreas Reiner and Ehud Y. Isacoff. "The Brain Prize 2013: The optogenetics revolution". In: *Trends in Neurosciences* 36.10 (2013), pp. 557–560. DOI: 10.1016/j.tins.2013.08.005.

[107] *The Shaw Prize*. 2020.

[108] J. Small et al. "Visualising the Actin Cytoskeleton". In: *Microscopy research and technique* 47.1 (1999). DOI: 10.1002/(SICI)1097-0029(19991001)47:1<3::AID-JEMT2>3.0.CO;2-2.

[109] Katrin Feldbauer et al. "Optochemokine Tandem for Light-Control of Intracellular Ca2". In: *PloS one* 11.10 (2016), e0165344. DOI: 10.1371/journal.pone.0165344.

[110] Anne Burgert et al. "Characterization of Plasma Membrane Ceramides by Super-Resolution Microscopy". In: *Angewandte Chemie International Edition* 56.22 (2017), pp. 6131–6135. DOI: `10.1002/anie.201700570`.

[111] T. Walter et al. "Incorporation studies of clickable ceramides in Jurkat cell plasma membranes". In: *Chemical communications (Cambridge, England)* 53.51 (2017), pp. 6836–6839. DOI: `10.1039/c7cc01220a`.

[112] Sabrina Ziegler et al. "CD56 Is a Pathogen Recognition Receptor on Human Natural Killer Cells". In: *Scientific reports* 7.1 (2017). DOI: `10.1038/s41598-017-06238-4`.

[113] Jerome Becam et al. "Antibacterial activity of ceramide and ceramide analogs against pathogenic Neisseria". In: *Scientific reports* 7 (2017). DOI: `10.1038/s41598-017-18071-w`.

[114] Simon Peters et al. "Neisseria meningitidis Type IV Pili Trigger Ca2+-Dependent Lysosomal Trafficking of the Acid Sphingomyelinase To Enhance Surface Ceramide Levels". In: *Infection and immunity* 87.8 (2019). DOI: `10.1128/iai.00410-19`.

[115] Jan Schlegel et al. "Super-Resolution Microscopy Reveals Local Accumulation of Plasma Membrane Gangliosides at Neisseria meningitidis Invasion Sites". In: *Frontiers in cell and developmental biology* 7 (2019), p. 194. DOI: `10.3389/fcell.2019.00194`.

[116] Hideaki Mizuno et al. "Fluorescent probes for superresolution imaging of lipid domains on the plasma membrane". In: *Chemical Science* 2.8 (2011), p. 1548. DOI: `10.1039/c1sc00169h`.

[117] Alf Honigmann et al. "Scanning STED-FCS reveals spatiotemporal heterogeneity of lipid interaction in the plasma membrane of living cells". In: *Nature communications* 5 (2014), p. 5412. DOI: `10.1038/ncomms6412`.

[118] Erdinc Sezgin et al. "Measuring nanoscale diffusion dynamics in cellular membranes with super-resolution STED-FCS". In: *Nature protocols* 14.4 (2019), pp. 1054–1083. DOI: `10.1038/s41596-019-0127-9`.

[119] Christian Eggeling et al. "Direct observation of the nanoscale dynamics of membrane lipids in a living cell". In: *Nature* 457.7233 (2009), pp. 1159–1162. DOI: `10.1038/nature07596`.

[120] Felix Waldchen et al. "Whole-cell imaging of plasma membrane receptors by 3D lattice light-sheet dSTORM". In: *Nature communications* 11.1 (2020), p. 887. DOI: `10.1038/s41467-020-14731-0`.

[121] V. Busskamp et al. "Optogenetic therapy for retinitis pigmentosa". In: *Gene Therapy* 19.2 (2011), pp. 169–175. DOI: `10.1038/gt.2011.155`.

[122] Yuexin Xu et al. "Optogenetic control of chemokine receptor signal and T-cell migration". In: *Proceedings of the National Academy of Sciences of the United States of America* 111.17 (2014), pp. 6371–6376. DOI: 10.1073/pnas.1319296111.

[123] Brook T. Chernet et al. "Use of genetically encoded, light-gated ion translocators to control tumorigenesis". In: *Oncotarget* 7.15 (2016), pp. 19575–19588. DOI: 10.18632/oncotarget.8036.

[124] Tomohiro Ishii et al. "Light generation of intracellular Ca(2+) signals by a genetically encoded protein BACCS". In: *Nature communications* 6 (2015), p. 8021. DOI: 10.1038/ncomms9021.

[125] Taeyoon Kyung et al. "Optogenetic control of endogenous Ca2+ channels in vivo". In: *Nature biotechnology* 33.10 (2015), pp. 1092–1096. DOI: 10.1038/nbt.3350.

[126] Xiang Li, Erich Gulbins, and Yang Zhang. "Oxidative Stress Triggers Ca2+-Dependent Lysosome Trafficking and Activation of Acid Sphingomyelinase". In: *Cellular Physiology and Biochemistry* 30.4 (2012), pp. 815–826. DOI: 10.1159/000341460.

[127] Marisa Brini et al. *Intracellular Calcium Homeostasis and Signaling*. 2012. DOI: 10.1007/978-94-007-5561-1_5.

[128] Juan A. Gilabert. *Cytoplasmic Calcium Buffering*. 2012. DOI: 10.1007/978-94-007-2888-2_20.

[129] Emyr Lloyd-Evans et al. "Endolysosomal calcium regulation and disease". In: *Biochemical Society Transactions* 38.6 (2010), pp. 1458–1464. DOI: 10.1042/bst0381458.

[130] Sonja Kleinlogel et al. "Ultra light-sensitive and fast neuronal activation with the Ca^2+-permeable channelrhodopsin CatCh". In: *Nature neuroscience* 14.4 (2011), pp. 513–518. DOI: 10.1038/nn.2776.

[131] Sonja Kleinlogel et al. "A gene-fusion strategy for stoichiometric and co-localized expression of light-gated membrane proteins". In: *Nature methods* 8.12 (2011), pp. 1083–1088. DOI: 10.1038/nmeth.1766.

[132] Kenneth Lundstrom. *An Overview on GPCRs and Drug Discovery: Structure-Based Drug Design and Structural Biology on GPCRs*. 2009. DOI: 10.1007/978-1-60327-317-6_4.

[133] Adriano Marchese. "Endocytic trafficking of chemokine receptors". In: *Current opinion in cell biology* 27 (2014), pp. 72–77. DOI: 10.1016/j.ceb.2013.11.011.

[134] Christian B.F. Andersen and Søren K. Moestrup. "How calcium makes endocytic receptors attractive". In: *Trends in biochemical sciences* 39.2 (2014), pp. 82–90. DOI: 10.1016/j.tibs.2013.12.003.

[135] Bungo Furusato et al. "CXCR4 and cancer". In: *Pathology international* 60.7 (2010), pp. 497–505. DOI: 10.1111/j.1440-1827.2010.02548.x.

[136] Kathleen L. Arnolds and Juliet V. Spencer. "CXCR4: A virus's best friend?" In: *Infection, Genetics and Evolution* 25 (2014), pp. 146–156. DOI: 10.1016/j.meegid.2014.04.018.

[137] Robert T. Dorsam and J. Silvio Gutkind. "G-protein-coupled receptors and cancer". In: *Nature Reviews Cancer* 7.2 (2007), pp. 79–94. DOI: 10.1038/nrc2069.

[138] Sigrid Hatse et al. "Chemokine receptor inhibition by AMD3100 is strictly confined to CXCR4". In: *FEBS letters* 527.1-3 (2002), pp. 255–262. DOI: 10.1016/s0014-5793(02)03143-5.

[139] Johannes Schindelin et al. "Fiji: An open-source platform for biological-image analysis". In: *Nature methods* 9.7 (2012), pp. 676–682. DOI: 10.1038/nmeth.2019.

[140] Katrin Feldbauer et al. "Channelrhodopsin-2 is a leaky proton pump". In: *Proceedings of the National Academy of Sciences of the United States of America* 106.30 (2009), pp. 12317–12322. DOI: 10.1073/pnas.0905852106.

[141] Jorge García-Martínez et al. "The CarO rhodopsin of the fungus Fusarium fujikuroi is a light-driven proton pump that retards spore germination". In: *Scientific reports* 5.1 (2015). DOI: 10.1038/srep07798.

[142] D. Zimmermann et al. "Effects on capacitance by overexpression of membrane proteins". In: *Biochemical and biophysical research communications* 369.4 (2008), pp. 1022–1026. DOI: 10.1016/j.bbrc.2008.02.153.

[143] Michel Ronjat et al. "Nuclear life of the voltage-gated Cacnb4 subunit and its role in gene transcription regulation". In: *Channels* 7.2 (2013), pp. 119–125. DOI: 10.4161/chan.23895.

[144] Peter R. C. Gascoyne et al. "Correlations between the dielectric properties and exterior morphology of cells revealed by dielectrophoretic field-flow fractionation". In: *Electrophoresis* 34.7 (2013), pp. 1042–1050. DOI: 10.1002/elps.201200496.

[145] Marino Zerial and Heidi McBride. "Rab proteins as membrane organizers". In: *Nature Reviews Molecular Cell Biology* 2.2 (2001), pp. 107–117. DOI: 10.1038/35052055.

[146] Jennifer L. Seachrist and Stephen S.G Ferguson. "Regulation of G protein-coupled receptor endocytosis and trafficking by Rab GTPases". In: *Life Sciences* 74.2-3 (2003), pp. 225–235. DOI: 10.1016/j.lfs.2003.09.009.

[147] Philip Aisen. "Transferrin receptor 1". In: *The International Journal of Biochemistry & Cell Biology* 36.11 (2004), pp. 2137–2143. DOI: 10.1016/j.biocel.2004.02.007.

[148]   Miroslaw Janowski. "Functional diversity of SDF-1 splicing variants". In: *Cell Adhesion & Migration* 3.3 (2009), pp. 243–249. DOI: 10.4161/cam.3.3.8260.

[149]   Frank Scholz et al. "Tuning the Primary Reaction of Channelrhodopsin-2 by Imidazole, pH, and Site-Specific Mutations". In: *Biophysical journal* 102.11 (2012), pp. 2649–2657. DOI: 10.1016/j.bpj.2012.04.034.

[150]   A. Dawydow et al. "Channelrhodopsin-2-XXL, a powerful optogenetic tool for low-light applications". In: *Proceedings of the National Academy of Sciences* 111.38 (2014), pp. 13972–13977. DOI: 10.1073/pnas.1408269111.

[151]   Futwan A. Al-Mohanna, Keith W. T. Caddy, and Stephen R. Bolsover. "The nucleus is insulated from large cytosolic calcium ion changes". In: *Nature* 367.6465 (1994), pp. 745–750. DOI: 10.1038/367745a0.

[152]   Jatta Huotari and Ari Helenius. "Endosome maturation". In: *The EMBO journal* 30.17 (2011), pp. 3481–3500. DOI: 10.1038/emboj.2011.286.

[153]   J Hesselgesser. "Identification and characterization of the CXCR4 chemokine receptor in human T cell lines: Ligand binding, biological activity, and HIV-1 infectivity". In: *J Immunol* 160 (1998), p. 877.

[154]   Bettina Tilton et al. "Signal Transduction by Cxc Chemokine Receptor 4". In: *Journal of Experimental Medicine* 192.3 (2000), pp. 313–324. DOI: 10.1084/jem.192.3.313.

[155]   Ken Abe and Rosa Puertollano. "Role of TRP Channels in the Regulation of the Endosomal Pathway". In: *Physiology* 26.1 (2011), pp. 14–22. DOI: 10.1152/physiol.00048.2010.

[156]   Julia V. Gerasimenko et al. "Calcium uptake via endocytosis with rapid release from acidifying endosomes". In: *Current Biology* 8.24 (1998), pp. 1335–1338. DOI: 10.1016/S0960-9822(07)00565-9.

[157]   Tobias Albrecht et al. "Fluorescent biosensors illuminate calcium levels within defined beta-cell endosome subpopulations". In: *Cell calcium* 57.4 (2015), pp. 263–274. DOI: 10.1016/j.ceca.2015.01.008.

[158]   Sarah J. Swanson et al. "In Vivo Imaging of Ca2+, pH, and Reactive Oxygen Species Using Fluorescent Probes in Plants". In: *Annual Review of Plant Biology* 62.1 (2011), pp. 273–297. DOI: 10.1146/annurev-arplant-042110-103832.

[159]   Beverly A. Teicher and Simon P. Fricker. "CXCL12 (SDF-1)/CXCR4 pathway in cancer". In: *Clinical cancer research : an official journal of the American Association for Cancer Research* 16.11 (2010), pp. 2927–2931. DOI: 10.1158/1078-0432.CCR-09-2329.

[160] A. G. Obukhov et al. "Direct activation of trpl cation channels by G alpha11 subunits". In: *The EMBO journal* 15.21 (1996), pp. 5833–5838. DOI: 10.1002/j.1460-2075.1996.tb00970.x.

[161] Azzam A. Maghazachi. "Role of the Heterotrimeric G Proteins in Stromal-Derived Factor-1α-Induced Natural Killer Cell Chemotaxis and Calcium Mobilization". In: *Biochemical and biophysical research communications* 236.2 (1997), pp. 270–274. DOI: 10.1006/bbrc.1997.6937.

[162] Melanie P. Wescott et al. "Signal transmission through the CXC chemokine receptor 4 (CXCR4) transmembrane helices". In: *Proceedings of the National Academy of Sciences* 113.35 (2016), pp. 9928–9933. DOI: 10.1073/pnas.1601278113.

[163] Benjamin R. Rost et al. "Optogenetic acidification of synaptic vesicles and lysosomes". In: *Nature neuroscience* 18.12 (2015), pp. 1845–1852. DOI: 10.1038/nn.4161.

[164] Geneviève Dupont and Laurent Combettes. "Fine tuning of cytosolic Ca2+ oscillations". In: *F1000Research* 5 (2016), p. 2036. DOI: 10.12688/f1000research.8438.1.

[165] Mark P. Mattson and Sic L. Chan. "Calcium orchestrates apoptosis". In: *Nature cell biology* 5.12 (2003), pp. 1041–1043. DOI: 10.1038/ncb1203-1041.

[166] Guang-Yu LI, Bin FAN, and Yong-Chen ZHENG. "Calcium Overload Is A Critical Step in Programmed Necrosis of ARPE-19 Cells Induced by High-Concentration H2O2". In: *Biomedical and Environmental Sciences* 23.5 (2010), pp. 371–377. DOI: 10.1016/s0895-3988(10)60078-5.

[167] Yusuf A. Hannun and Lina M. Obeid. "The Ceramide-centric Universe of Lipid-mediated Cell Regulation: Stress Encounters of the Lipid Kind". In: *Journal of Biological Chemistry* 277.29 (2002), pp. 25847–25850. DOI: 10.1074/jbc.r200008200.

[168] E. Gulbins and P. L. Li. "Physiological and Pathophysiological Aspects of Ceramide". In: *American journal of physiology. Regulatory, integrative and comparative physiology* 290.1 (2006). DOI: 10.1152/ajpregu.00416.2005.

[169] Félix M. Goñi, Jesús Sot, and Alicia Alonso. "Biophysical properties of sphingosine, ceramides and other simple sphingolipids". In: *Biochemical Society Transactions* 42.5 (2014), pp. 1401–1408. DOI: 10.1042/bst20140159.

[170] Bruno M. Castro et al. "Cholesterol-rich Fluid Membranes Solubilize Ceramide Domains". In: *Journal of Biological Chemistry* 284.34 (2009), pp. 22978–22987. DOI: 10.1074/jbc.m109.026567.

[171] Eduard B. Babiychuk, Katia Monastyrskaya, and Annette Draeger. "Fluorescent Annexin A1 Reveals Dynamics of Ceramide Platforms in Living Cells". In: *Traffic* 9.10 (2008), pp. 1757–1775. DOI: 10.1111/j.1600-0854.2008.00800.x.

[172] Branka Stancevic and Richard Kolesnick. "Ceramide-rich platforms in transmembrane signaling". In: *FEBS letters* 584.9 (2010), pp. 1728–1740. DOI: 10.1016/j.febslet.2010.02.026.

[173] Mary L. Kraft. "Sphingolipid Organization in the Plasma Membrane and the Mechanisms That Influence It". In: *Frontiers in cell and developmental biology* 4 (2017). DOI: 10.3389/fcell.2016.00154.

[174] Claudia R. Bollinger, Volker Teichgräber, and Erich Gulbins. "Ceramide-enriched membrane domains". In: *Biochimica et Biophysica Acta (BBA) - Molecular Cell Research* 1746.3 (2005), pp. 284–294. DOI: 10.1016/j.bbamcr.2005.09.001.

[175] Stefania Luisoni et al. "Co-option of Membrane Wounding Enables Virus Penetration into Cells". In: *Cell Host & Microbe* 18.1 (2015), pp. 75–85. DOI: 10.1016/j.chom.2015.06.006.

[176] Maria Cecilia Fernandes et al. "Trypanosoma cruzi subverts the sphingomyelinase-mediated plasma membrane repair pathway for cell invasion". In: *The Journal of experimental medicine* 208.5 (2011), pp. 909–921. DOI: 10.1084/jem.20102518.

[177] Alexander Simonis et al. "Differential Activation of Acid Sphingomyelinase and Ceramide Release Determines Invasiveness of Neisseria meningitidis into Brain Endothelial Cells". In: *PLoS pathogens* 10.6 (2014), e1004160. DOI: 10.1371/journal.ppat.1004160.

[178] Michaela Faulstich et al. "Neutral sphingomyelinase 2 is a key factor for PorB-dependent invasion ofNeisseria gonorrhoeae". In: *Cellular microbiology* 17.2 (2014), pp. 241–253. DOI: 10.1111/cmi.12361.

[179] M. E. Miller et al. "Ebolavirus Requires Acid Sphingomyelinase Activity and Plasma Membrane Sphingomyelin for Infection". In: *Journal of virology* 86.14 (2012), pp. 7473–7483. DOI: 10.1128/jvi.00136-12.

[180] Masahiro Nagahama et al. "Cellular Uptake of Clostridium botulinum C2 Toxin Requires Acid Sphingomyelinase Activity". In: *Infection and immunity* 85.4 (2017). DOI: 10.1128/iai.00966-16.

[181] Niklas Beyersdorf and Nora Müller. "Sphingomyelin breakdown in T cells: Role in activation, effector functions and immunoregulation". In: *Biological chemistry* 396.6-7 (2015), pp. 749–758. DOI: 10.1515/hsz-2014-0282.

[182] Sokratis A. Apostolidis et al. "Phosphatase PP2A is requisite for the function of regulatory T cells". In: *Nature immunology* 17.5 (2016), pp. 556–564. DOI: 10.1038/ni.3390.

[183]   Juha M. Holopainen, Marappan Subramanian, and Paavo K. J. Kinnunen. "Sphingomyelinase Induces Lipid Microdomain Formation in a Fluid Phosphatidylcholine/Sphingomyelin Membrane†". In: *Biochemistry* 37.50 (1998), pp. 17562–17570. DOI: `10.1021/bi980915e`.

[184]   Salvatore Chiantia, Nicoletta Kahya, and Petra Schwille. "Raft Domain Reorganization Driven by Short- and Long-Chain Ceramide: A Combined AFM and FCS Study". In: *Langmuir* 23.14 (2007), pp. 7659–7665. DOI: `10.1021/la7010919`.

[185]   Anders Björkbom et al. "Effect of Sphingomyelin Headgroup Size on Molecular Properties and Interactions with Cholesterol". In: *Biophysical journal* 99.10 (2010), pp. 3300–3308. DOI: `10.1016/j.bpj.2010.09.049`.

[186]   Ira and Linda J. Johnston. "Sphingomyelinase generation of ceramide promotes clustering of nanoscale domains in supported bilayer membranes". In: *Biochimica et Biophysica Acta (BBA) - Biomembranes* 1778.1 (2008), pp. 185–197. DOI: `10.1016/j.bbamem.2007.09.021`.

[187]   Abo Bakr Abdel Shakor, Katarzyna Kwiatkowska, and Andrzej Sobota. "Cell Surface Ceramide Generation Precedes and Controls FcγRII Clustering and Phosphorylation in Rafts". In: *Journal of Biological Chemistry* 279.35 (2004), pp. 36778–36787. DOI: `10.1074/jbc.m402170200`.

[188]   Kannan Krishnamurthy, Somsankar Dasgupta, and Erhard Bieberich. "Development and characterization of a novel anti-ceramide antibody". In: *Journal of Lipid Research* 48.4 (2007), pp. 968–975. DOI: `10.1194/jlr.d600043-jlr200`.

[189]   Aida E. Cremesti, Felix M. Goni, and Richard Kolesnick. "Role of sphingomyelinase and ceramide in modulating rafts: Do biophysical properties determine biologic outcome?" In: *FEBS letters* 531.1 (2002), pp. 47–53. DOI: `10.1016/s0014-5793(02)03489-0`.

[190]   Ira et al. "Enzymatic generation of ceramide induces membrane restructuring: Correlated AFM and fluorescence imaging of supported bilayers". In: *Journal of Structural Biology* 168.1 (2009), pp. 78–89. DOI: `10.1016/j.jsb.2009.03.014`.

[191]   Lars Kuerschner et al. "Polyene-lipids: A new tool to image lipids". In: *Nature methods* 2.1 (2004), pp. 39–45. DOI: `10.1038/nmeth728`.

[192]   Soumi Mukherjee et al. "Organization and dynamics of N-(7-nitrobenz-2-oxa-1,3-diazol-4-yl)-labeled lipids: A fluorescence approach". In: *Chemistry and physics of lipids* 127.1 (2004), pp. 91–101. DOI: `10.1016/j.chemphyslip.2003.09.004`.

[193]   James E. Shaw et al. "Correlated Fluorescence-Atomic Force Microscopy of Membrane Domains: Structure of Fluorescence Probes Determines Lipid Localization". In: *Biophysical journal* 90.6 (2006), pp. 2170–2178. DOI: `10.1529/biophysj.105.073510`.

[194]   Kai Simons and Mathias J. Gerl. "Revitalizing membrane rafts: New tools and insights". In: *Nature Reviews Molecular Cell Biology* 11.10 (2010), pp. 688–699. DOI: 10.1038/nrm2977.

[195]   Akihiro Kusumi et al. "Dynamic Organizing Principles of the Plasma Membrane that Regulate Signal Transduction: Commemorating the Fortieth Anniversary of Singer and Nicolson's Fluid-Mosaic Model". In: *Annual review of cell and developmental biology* 28.1 (2012), pp. 215–250. DOI: 10.1146/annurev-cellbio-100809-151736.

[196]   V. Mueller et al. "STED Nanoscopy Reveals Molecular Details of Cholesterol- and Cytoskeleton-Modulated Lipid Interactions in Living Cells". In: *Biophysical journal* 101.7 (2011), pp. 1651–1660. DOI: 10.1016/j.bpj.2011.09.006.

[197]   J. F. Frisz et al. "Direct chemical evidence for sphingolipid domains in the plasma membranes of fibroblasts". In: *Proceedings of the National Academy of Sciences* 110.8 (2013), E613–E622. DOI: 10.1073/pnas.1216585110.

[198]   Sebastian van de Linde et al. "Direct stochastic optical reconstruction microscopy with standard fluorescent probes". In: *Nature protocols* 6.7 (2011), pp. 991–1009. DOI: 10.1038/nprot.2011.336.

[199]   Kenji A. K. Tanaka et al. "Membrane molecules mobile even after chemical fixation". In: *Nature methods* 7.11 (2010), pp. 865–866. DOI: 10.1038/nmeth.f.314.

[200]   Tess A. Stanly et al. "Critical importance of appropriate fixation conditions for faithful imaging of receptor microclusters". In: *Biology Open* 5.9 (2016), pp. 1343–1350. DOI: 10.1242/bio.019943.

[201]   Anne Burgert et al. "Artifacts in single-molecule localization microscopy". In: *Histochemistry and cell biology* 144.2 (2015), pp. 123–131. DOI: 10.1007/s00418-015-1340-4.

[202]   Ripley. In: *J. R. Statist. Soc.* 39 (1977), p. 172.

[203]   Sebastian Malkusch and Mike Heilemann. "Extracting quantitative information from single-molecule super-resolution imaging data with LAMA – LocAlization Microscopy Analyzer". In: *Scientific reports* 6.1 (2016). DOI: 10.1038/srep34486.

[204]   Sebastian Letschert et al. "Super-Resolution Imaging of Plasma Membrane Glycans". In: *Angewandte Chemie (International ed. in English)* 53.41 (2014), pp. 10921–10924. DOI: 10.1002/anie.201406045.

[205]   Steve Wolter et al. "rapidSTORM: Accurate, fast open-source software for localization microscopy". In: *Nature methods* 9.11 (2012), pp. 1040–1041. DOI: 10.1038/nmeth.2224.

[206]   Florian Baumgart et al. "Varying label density allows artifact-free analysis of membrane-protein nanoclusters". In: *Nature methods* 13.8 (2016), pp. 661–664. DOI: 10.1038/nmeth.3897.

[207]   Heike Grassmé, Joachim Riethmüller, and Erich Gulbins. "Biological aspects of ceramide-enriched membrane domains". In: *Progress in lipid research* 46.3-4 (2007), pp. 161–170. DOI: 10.1016/j.plipres.2007.03.002.

[208]   Erich Gulbins et al. "Ceramide, membrane rafts and infections". In: *Journal of Molecular Medicine* 82.6 (2004), pp. 357–363. DOI: 10.1007/s00109-004-0539-y.

[209]   N. Lipsky and R. Pagano. "A vital stain for the Golgi apparatus". In: *Science* 228.4700 (1985), pp. 745–747. DOI: 10.1126/science.2581316.

[210]   N. G. Lipsky and R. E. Pagano. "Intracellular translocation of fluorescent sphingolipids in cultured fibroblasts: Endogenously synthesized sphingomyelin and glucocerebroside analogues pass through the Golgi apparatus en route to the plasma membrane". In: *The Journal of cell biology* 100.1 (1985), pp. 27–34. DOI: 10.1083/jcb.100.1.27.

[211]   R. E. Pagano et al. "A novel fluorescent ceramide analogue for studying membrane traffic in animal cells: Accumulation at the Golgi apparatus results in altered spectral properties of the sphingolipid precursor". In: *The Journal of cell biology* 113.6 (1991), pp. 1267–1279. DOI: 10.1083/jcb.113.6.1267.

[212]   Sang-Hyun Son et al. "Syntheses of lactosyl ceramide analogues carrying novel bifunctional BODIPY dyes directed towards the differential analysis of multiplexed glycosphingolipids by MS/MS using iTRAQ". In: *Chem. Commun.* 50.23 (2014), pp. 3010–3013. DOI: 10.1039/c4cc00112e.

[213]   Stéphanie Combemale et al. "A biologically relevant ceramide fluorescent probe to assess the binding of potential ligands to the CERT transfer protein". In: *RSC Advances* 3.41 (2013), p. 18970. DOI: 10.1039/c3ra42395f.

[214]   Jennifer A. Prescher and Carolyn R. Bertozzi. "Chemistry in living systems". In: *Nature chemical biology* 1.1 (2005), pp. 13–21. DOI: 10.1038/nchembio0605-13.

[215]   Alexander Mertsch et al. "Synthesis and application of water-soluble, photoswitchable cyanine dyes for bioorthogonal labeling of cell-surface carbohydrates". In: *Zeitschrift für Naturforschung C* 71.9-10 (2016), pp. 347–354. DOI: 10.1515/znc-2016-0123.

[216]   Arne Homann et al. "Bioorthogonal metabolic glycoengineering of human larynx carcinoma (HEp-2) cells targeting sialic acid". In: *Beilstein Journal of Organic Chemistry* 6 (2010). DOI: 10.3762/bjoc.6.24.

[217]   M. J. Gerl et al. "Sphingosine-1-Phosphate Lyase Deficient Cells as a Tool to Study Protein Lipid Interactions". In: *PloS one* 11.4 (2016). DOI: `10.1371/journal.pone.0153009`.

[218]   Ellen M. Sletten et al. "Difluorobenzocyclooctyne: Synthesis, Reactivity, and Stabilization by β-Cyclodextrin". In: *Journal of the American Chemical Society* 132.33 (2010), pp. 11799–11805. DOI: `10.1021/ja105005t`.

[219]   Ngalle Eric Mbua et al. "Strain-Promoted Alkyne-Azide Cycloadditions (SPAAC) Reveal New Features of Glycoconjugate Biosynthesis". In: *ChemBioChem* 12.12 (2011), pp. 1912–1921. DOI: `10.1002/cbic.201100117`.

[220]   Lena Collenburg et al. "A Functionalized Sphingolipid Analogue for Studying Redistribution during Activation in Living T Cells". In: *The Journal of Immunology* 196.9 (2016), pp. 3951–3962. DOI: `10.4049/jimmunol.1502447`.

[221]   T. Walter et al. "Incorporation and visualization of azido-functionalized N-oleoyl serinol in Jurkat cells, mouse brain astrocytes, 3T3 fibroblasts and human brain microvascular endothelial cells". In: *Chemical Communications* 52.55 (2016), pp. 8612–8614. DOI: `10.1039/c6cc02879a`.

[222]   Joshua C. Vaughan et al. "Phosphine quenching of cyanine dyes as a versatile tool for fluorescence microscopy". In: *Journal of the American Chemical Society* 135.4 (2013), pp. 1197–1200. DOI: `10.1021/ja3105279`.

[223]   Brahm H. Segal. "Aspergillosis". In: *New England Journal of Medicine* 360.18 (2009), pp. 1870–1884. DOI: `10.1056/nejmra0808853`.

[224]   Nina Singh and David L. Paterson. "Aspergillus Infections in Transplant Recipients". In: *Clinical Microbiology Reviews* 18.1 (2005), pp. 44–69. DOI: `10.1128/cmr.18.1.44-69.2005`.

[225]   G. Salmeron et al. "Persistent poor long-term prognosis of allogeneic hematopoietic stem cell transplant recipients surviving invasive aspergillosis". In: *Haematologica* 97.9 (2012), pp. 1357–1363. DOI: `10.3324/haematol.2011.058255`.

[226]   Claudia Stuehler et al. "Immune Reconstitution After Allogeneic Hematopoietic Stem Cell Transplantation and Association With Occurrence and Outcome of Invasive Aspergillosis". In: *Journal of Infectious Diseases* 212.6 (2015), pp. 959–967. DOI: `10.1093/infdis/jiv143`.

[227]   MJ Robertson. "Robertson, M. J. & Ritz, J. Biology and clinical relevance of human natural killer cells. Blood 76, 2421–2438 (1990)". In: *Blood* 76 (1990), p. 2421.

[228]   Megan A. Cooper, Todd A. Fehniger, and Michael A. Caligiuri. "The biology of human natural killer-cell subsets". In: *Trends in Immunology* 22.11 (2001), pp. 633–640. DOI: `10.1016/s1471-4906(01)02060-9`.

[229] Lewis L. Lanier. "Up on the tightrope: Natural killer cell activation and inhibition". In: *Nature immunology* 9.5 (2008), pp. 495–502. DOI: 10.1038/ni1581.

[230] Shu Shun Li et al. "The NK Receptor NKp30 Mediates Direct Fungal Recognition and Killing and Is Diminished in NK Cells from HIV-Infected Patients". In: *Cell Host & Microbe* 14.4 (2013), pp. 387–397. DOI: 10.1016/j.chom.2013.09.007.

[231] Thorsten Lieke et al. "NK Cells Contribute to the Control of Trypanosoma cruzi Infection by Killing Free Parasites by Perforin-Independent Mechanisms". In: *Infection and immunity* 72.12 (2004), pp. 6817–6825. DOI: 10.1128/iai.72.12.6817-6825.2004.

[232] Cherrie-Lee Small et al. "NK Cells Play a Critical Protective Role in Host Defense against Acute Extracellular Staphylococcus aureus Bacterial Infection in the Lung". In: *The Journal of Immunology* 180.8 (2008), pp. 5558–5568. DOI: 10.4049/jimmunol.180.8.5558.

[233] Maria Bouzani et al. "Human NK cells display important antifungal activity against Aspergillus fumigatus, which is directly mediated by IFN-γ release". In: *Journal of immunology (Baltimore, Md. : 1950)* 187.3 (2011), pp. 1369–1376. DOI: 10.4049/jimmunol.1003593.

[234] Elie Mavoungou et al. "A Duffy Binding–Like Domain Is Involved in the NKp30-Mediated Recognition ofPlasmodiumfalciparum–Parasitized Erythrocytes by Natural Killer Cells". In: *The Journal of infectious diseases* 195.10 (2007), pp. 1521–1531. DOI: 10.1086/515579.

[235] Stanislaw Schmidt et al. "Natural killer cell-mediated damage of clinical isolates of mucormycetes". In: *Mycoses* 59.1 (2015), pp. 34–38. DOI: 10.1111/myc.12431.

[236] Stanislaw Schmidt et al. "Human natural killer cells exhibit direct activity against Aspergillus fumigatus hyphae, but not against resting conidia". In: *The Journal of infectious diseases* 203.3 (2011), pp. 430–435. DOI: 10.1093/infdis/jiq062.

[237] Jessica Voigt et al. "Human Natural Killer Cells Acting as Phagocytes Against Candida albicans and Mounting an Inflammatory Response That Modulates Neutrophil Antifungal Activity". In: *The Journal of infectious diseases* 209.4 (2013), pp. 616–626. DOI: 10.1093/infdis/jit574.

[238] Brad E. Morrison et al. "Chemokine-mediated recruitment of NK cells is a critical host defense mechanism in invasive aspergillosis". In: *Journal of Clinical Investigation* 112.12 (2003), pp. 1862–1870. DOI: 10.1172/jci18125.

[239] Stacy J. Park et al. "Early NK Cell-Derived IFN-γ Is Essential to Host Defense in Neutropenic Invasive Aspergillosis". In: *The Journal of Immunology* 182.7 (2009), pp. 4306–4312. DOI: 10.4049/jimmunol.0803462.

[240] Sibylla Braedel et al. "Aspergillus fumigatusantigens activate innate immune cells via toll-like receptors 2 and 4". In: *British Journal of Haematology* 125.3 (2004), pp. 392–399. DOI: 10.1111/j.1365-2141.2004.04922.x.

[241] A. Meier et al. "Toll-like receptor (TLR) 2 and TLR4 are essential for Aspergillus-induced activation of murine macrophages". In: *Cellular microbiology* 5.8 (2003), pp. 561–570. DOI: 10.1046/j.1462-5822.2003.00301.x.

[242] Chad Steele et al. "The Beta-Glucan Receptor Dectin-1 Recognizes Specific Morphologies of Aspergillus fumigatus". In: *PLoS pathogens* 1.4 (2005), e42. DOI: 10.1371/journal.ppat.0010042.

[243] Alon Vitenshtein et al. "NK Cell Recognition of Candida glabrata through Binding of NKp46 and NCR1 to Fungal Ligands Epa1, Epa6, and Epa7". In: *Cell Host & Microbe* 20.4 (2016), pp. 527–534. DOI: 10.1016/j.chom.2016.09.008.

[244] L. L. Lanier et al. "Identity of Leu-19 (CD56) leukocyte differentiation antigen and neural cell adhesion molecule". In: *The Journal of experimental medicine* 169.6 (1989), pp. 2233–2238. DOI: 10.1084/jem.169.6.2233.

[245] Jerome Ritz et al. *Characterization of Functional Surface Structures on Human Natural Killer Cells.* 1988. DOI: 10.1016/s0065-2776(08)60845-7.

[246] Francisco Borrego, José Peña, and Rafael Solana. "Regulation of CD69 expression on human natural killer cells: Differential involvement of protein kinase C and protein tyrosine kinases". In: *European journal of immunology* 23.5 (1993), pp. 1039–1043. DOI: 10.1002/eji.1830230509.

[247] Ana Abad et al. "What makes Aspergillus fumigatus a successful pathogen? Genes and molecules involved in invasive aspergillosis". In: *Revista Iberoamericana de Micología* 27.4 (2010), pp. 155–182. DOI: 10.1016/j.riam.2010.10.003.

[248] Bismarck B. Lozzio and Carmen B. Lozzio. "Properties and usefulness of the original K-562 human myelogenous leukemia cell line". In: *Leukemia Research* 3.6 (1979), pp. 363–370. DOI: 10.1016/0145-2126(79)90033-x.

[249] Jordan S. Orange. "Formation and function of the lytic NK-cell immunological synapse". In: *Nature Reviews Immunology* 8.9 (2008), pp. 713–725. DOI: 10.1038/nri2381.

[250] K. Mortensen and L.-I. Larsson. "Effects of cytochalasin D on the actin cytoskeleton: Association of neoformed actin aggregates with proteins involved in signaling and endocytosis". In: *Cellular and Molecular Life Sciences (CMLS)* 60.5 (2003), pp. 1007–1012. DOI: 10.1007/s00018-003-3022-x.

[251]   R. L. Margolis and L. Wilson. "Addition of colchicine-tubulin complex to micro-tubule ends: The mechanism of substoichiometric colchicine poisoning". In: *Proceedings of the National Academy of Sciences* 74.8 (1977), pp. 3466–3470. DOI: `10.1073/pnas.74.8.3466`.

[252]   J. S. Orange et al. "The mature activating natural killer cell immunologic synapse is formed in distinct stages". In: *Proceedings of the National Academy of Sciences* 100.24 (2003), pp. 14151–14156. DOI: `10.1073/pnas.1835830100`.

[253]   BE Jimenez. "Jimenez, B. E. & Murphy, J. W. In vitro effects of natural killer cells against Paracoccidioides brasiliensis yeast phase. Infection and immunity 46, 552–558 (1984)". In: *Infection and immunity* 46 (1984), p. 552.

[254]   AF Petkus. "Petkus, A. F. & Baum, L. L. Natural killer cell inhibition of young spherules and endospores of Coccidioides immitis. J Immunol 139, 3107–3111 (1987)". In: *J Immunol* 139 (1987), p. 3107.

[255]   SM Levitz. "Levitz, S. M., Dupont, M. P. & Smail, E. H. Direct activity of human T lymphocytes and natural killer cells against Cryptococcus neoformans. Infection and immunity 62, 194–202 (1994)". In: *Infection and immunity* 62 (1994), p. 194.

[256]   S. Diestel et al. "NCAM is ubiquitylated, endocytosed and recycled in neurons". In: *Journal of cell science* 120.22 (2007), pp. 4035–4049. DOI: `10.1242/jcs.019729`.

[257]   Ole Nybroe and Elisabeth Bock. *Structure and Function of the Neural Cell Adhesion Molecules NCAM and L1*. 1990. DOI: `10.1007/978-1-4757-5876-4_18`.

[258]   Iryna Leshchyns'ka and Vladimir Sytnyk. "Intracellular transport and cell surface delivery of the neural cell adhesion molecule (NCAM)". In: *BioArchitecture* 5.3-4 (2015), pp. 54–60. DOI: `10.1080/19490992.2015.1118194`.

[259]   M Nieto. "Nieto, M. et al. Roles of Chemokines and Receptor Polarization in NK-Target Cell Interactions. The Journal of Immunology 161, 3330–3339 (1998)". In: *The Journal of Immunology* 161 (1998), p. 3330.

[260]   TA Fehniger. "Fehniger, T. A. et al. Natural Killer Cells from HIV-1+ Patients Produce C-C Chemokines and Inhibit HIV-1 Infection. The Journal of Immunology 161, 6433–6438 (1998)". In: *The Journal of Immunology* 161 (1998), p. 6433.

[261]   Gary B. Huffnagle and Lisa K. McNeil. "Dissemination ofC. neoformansto the central nervous system: Role of chemokines, Th1 immunity and leukocyte recruitment". In: *Journal of Neurovirology* 5.1 (1999), pp. 76–81. DOI: `10.3109/13550289909029748`.

[262]   Giuliano Bonfá et al. "CCR5 Controls Immune and Metabolic Functions during Toxoplasma gondii Infection". In: *PloS one* 9.8 (2014), e104736. DOI: `10.1371/journal.pone.0104736`.

[263]   Emily M. Mace et al. "Human NK cell development requires CD56-mediated motility and formation of the developmental synapse". In: *Nature communications* 7.1 (2016), p. 132. DOI: 10.1038/ncomms12171.

[264]   T. Lieke et al. "Leishmania surface protein gp63 binds directly to human natural killer cells and inhibits proliferation". In: *Clinical & Experimental Immunology* 153.2 (2008), pp. 221–230. DOI: 10.1111/j.1365-2249.2008.03687.x.

[265]   LL Lanier. "Lanier, L. L. et al. Molecular and functional analysis of human natural killer cell-associated neural cell adhesion molecule (N-CAM/CD56). J Immunol 146, 4421–4426 (1991)". In: *J Immunol* 146 (1991), p. 4421.

[266]   F. Pandolfi et al. "Expression of Cell Adhesion Molecules in Human Melanoma Cell Lines and Their Role in Cytotoxicity Mediated by Tumor-Infiltrating Lymphocytes". In: *Cancer* 69.5 (1992). DOI: 10.1002/cncr.2820690517.

[267]   T. Nitta et al. "Involvement of CD56 (NKH-1/Leu-19 antigen) as an adhesion molecule in natural killer-target cell interaction". In: *The Journal of experimental medicine* 170.5 (1989), pp. 1757–1761. DOI: 10.1084/jem.170.5.1757.

[268]   S. Takasaki. "CD56 Directly Interacts in the Process of NCAM-Positive Target Cell-Killing by NK Cells". In: *Cell Biology International* 24.2 (2000), pp. 101–108. DOI: 10.1006/cbir.1999.0457.

[269]   Charles Oliver Morton et al. "Gene Expression Profiles of Human Dendritic Cells Interacting with Aspergillus fumigatus in a Bilayer Model of the Alveolar Epithelium/Endothelium Interface". In: *PloS one* 9.5 (2014), e98279. DOI: 10.1371/journal.pone.0098279.

[270]   A. Semmlinger et al. "Fever-range temperature modulates activation and function of human dendritic cells stimulated with the pathogenic mould Aspergillus fumigatus". In: *Medical Mycology* 52.4 (2014), pp. 438–444. DOI: 10.1093/mmy/myu005.

[271]   Mirjam Fliesser et al. "Hypoxia-inducible factor 1α modulates metabolic activity and cytokine release in anti- Aspergillus fumigatus immune responses initiated by human dendritic cells". In: *International Journal of Medical Microbiology* 305.8 (2015), pp. 865–873. DOI: 10.1016/j.ijmm.2015.08.036.

[272]   Rut Valgardsdottir et al. "Direct involvement of CD56 in cytokine-induced killer–mediated lysis of CD56+ hematopoietic target cells". In: *Experimental hematology* 42.12 (2014), 1013–1021.e1. DOI: 10.1016/j.exphem.2014.08.005.

[273]   S. Bolte and F. P. Cordelières. "A guided tour into subcellular colocalization analysis in light microscopy". In: *Journal of microscopy* 224.3 (2006), pp. 213–232. DOI: 10.1111/j.1365-2818.2006.01706.x.

[274]   Sven Proppert et al. "Cubic B-spline calibration for 3D super-resolution measurements using astigmatic imaging". In: *Optics Express* 22.9 (2014), p. 10304. DOI: `10.1364/oe.22.010304`.

[275]   JS O'Brien. "O'Brien, J. S. & Rouser, G. The fatty acid composition of brain sphingolipids: Sphingomyelin, ceramide, cerebroside, and cerebroside sulfate. Journal of lipid research 5, 339–342 (1964)". In: *Journal of Lipid Research* 5 (1964), p. 339.

[276]   Ke Xu and Paul J. Thornalley. "Antitumour activity of sphingoid base adducts of phenethyl isothiocyanate". In: *Bioorganic & Medicinal Chemistry Letters* 10.1 (2000), pp. 53–54. DOI: `10.1016/s0960-894x(99)00574-0`.

[277]   Sarah T. Pruett et al. "Thematic Review Series: Sphingolipids.Biodiversity of sphingoid bases ("sphingosines") and related amino alcohols". In: *Journal of Lipid Research* 49.8 (2008), pp. 1621–1639. DOI: `10.1194/jlr.r800012-jlr200`.

[278]   David R. Drake et al. "Thematic Review Series: Skin Lipids. Antimicrobial lipids at the skin surface". In: *Journal of Lipid Research* 49.1 (2007), pp. 4–11. DOI: `10.1194/jlr.r700016-jlr200`.

[279]   Carol L. Fischer et al. "The roles of cutaneous lipids in host defense". In: *Biochimica et Biophysica Acta (BBA) - Molecular and Cell Biology of Lipids* 1841.3 (2014), pp. 319–322. DOI: `10.1016/j.bbalip.2013.08.012`.

[280]   Carol L. Fischer et al. "Antibacterial Activity of Sphingoid Bases and Fatty Acids against Gram-Positive and Gram-Negative Bacteria". In: *Antimicrobial Agents and Chemotherapy* 56.3 (2011), pp. 1157–1161. DOI: `10.1128/aac.05151-11`.

[281]   Debra Jan Bibel, Raza Aly, and Henry R. Shinefield. "Antimicrobial Activity of Sphingosines". In: *Journal of Investigative Dermatology* 98.3 (1992), pp. 269–273. DOI: `10.1111/1523-1747.ep12497842`.

[282]   Marlise Diane Jiofack Dongfack et al. "A New Sphingolipid and Furanocoumarins with Antimicrobial Activity from Ficus exasperata". In: *Chemical and Pharmaceutical Bulletin* 60.8 (2012), pp. 1072–1075. DOI: `10.1248/cpb.c12-00279`.

[283]   Belkassem El-Amraoui, Jean-Fançois Biard, and Aziz Fassouane. "Haliscosamine: A new antifungal sphingosine derivative from the Moroccan marine sponge Haliclona viscosa". In: *SpringerPlus* 2.1 (2013). DOI: `10.1186/2193-1801-2-252`.

[284]   Sam Possemiers et al. "Characterization of the bactericidal effect of dietary sphingosine and its activity under intestinal conditions". In: *International Journal of Food Microbiology* 105.1 (2005), pp. 59–70. DOI: `10.1016/j.ijfoodmicro.2005.05.007`.

[285]   Yael Pewzner-Jung et al. "Sphingoid long chain bases prevent lung infection by Pseudomonas aeruginosa". In: *EMBO Molecular Medicine* 6.9 (2014), pp. 1205–1214. DOI: `10.15252/emmm.201404075`.

[286]   Essa M. Saied et al. "A series of ceramide analogs modified at the 1-position with potent activity against the intracellular growth ofChlamydia trachomatis". In: *Future Medicinal Chemistry* 7.15 (2015), pp. 1971–1980. DOI: 10.4155/fmc.15.126.

[287]   Esther del Olmo et al. "Simple dihydrosphyngosine analogues with potent activity against MDR-Mycobacterium tuberculosis". In: *Bioorganic & Medicinal Chemistry Letters* 19.19 (2009), pp. 5764–5768. DOI: 10.1016/j.bmcl.2009.07.147.

[288]   DJ Bibel. "Bibel, D. J., Aly, R., Shah, S. & Shinefield, H. R. Sphingosines: Antimicrobial barriers of the skin. Acta dermato-venereologica 73, 407–411 (1993)". In: *Acta dermato-venereologica* 73 (1993), p. 407.

[289]   Nadine G. Rouphael and David S. Stephens. *Neisseria meningitidis: Biology, Microbiology, and Epidemiology.* 2011. DOI: 10.1007/978-1-61779-346-2_1.

[290]   Dominique A. Caugant and Martin C.J. Maiden. "Meningococcal carriage and disease—Population biology and evolution". In: *Vaccine* 27 (2009), B64–B70. DOI: 10.1016/j.vaccine.2009.04.061.

[291]   M. Unemo and W. M. Shafer. "Antimicrobial Resistance in Neisseria gonorrhoeae in the 21st Century: Past, Evolution, and Future". In: *Clinical Microbiology Reviews* 27.3 (2014), pp. 587–613. DOI: 10.1128/cmr.00010-14.

[292]   Jeremy James Wade and Michelle Angela Graver. "A fully defined, clear and protein-free liquid medium permitting dense growth ofNeisseria gonorrhoeaefrom very low inocula". In: *FEMS Microbiology Letters* 273.1 (2007), pp. 35–37. DOI: 10.1111/j.1574-6968.2007.00776.x.

[293]   Jürgen Seibel et al. "Investigating infection processes with a workflow from organic chemistry to biophysics: The combination of metabolic glycoengineering, super-resolution fluorescence imaging and proteomics". In: *Expert Review of Proteomics* 10.1 (2013), pp. 25–31. DOI: 10.1586/epr.12.72.

[294]   John C. Jewett and Carolyn R. Bertozzi. "Cu-free click cycloaddition reactions in chemical biology". In: *Chemical Society reviews* 39.4 (2010), p. 1272. DOI: 10.1039/b901970g.

[295]   Markus Sauer and Mike Heilemann. "Single-Molecule Localization Microscopy in Eukaryotes". In: *Chemical reviews* 117.11 (2017), pp. 7478–7509. DOI: 10.1021/acs.chemrev.6b00667.

[296]   Pablo Mateos-Gil et al. "Super-Resolution Imaging of Plasma Membrane Proteins with Click Chemistry". In: *Frontiers in cell and developmental biology* 4 (2016). DOI: 10.3389/fcell.2016.00098.

[297]   Jared A. Silverman, Nancy G. Perlmutter, and Howard M. Shapiro. "Correlation of Daptomycin Bactericidal Activity and Membrane Depolarization in Staphylococcus aureus". In: *Antimicrobial Agents and Chemotherapy* 47.8 (2003), pp. 2538–2544. DOI: `10.1128/aac.47.8.2538-2544.2003`.

[298]   C. L. Fischer et al. "Sphingoid Bases Are Taken Up byEscherichia coliandStaphylococcus aureusand Induce Ultrastructural Damage". In: *Skin Pharmacology and Physiology* 26.1 (2013), pp. 36–44. DOI: `10.1159/000343175`.

[299]   D. J. Bibel, R. Aly, and H. R. Shinefield. "Topical sphingolipids in antisepsis and antifungal therapy". In: *Clinical and Experimental Dermatology* 20.5 (1995), pp. 395–400. DOI: `10.1111/j.1365-2230.1995.tb01356.x`.

[300]   Debra Jan Bibel et al. "Antimicrobial Activity of Stratum Corneum Lipids from Normal and Essential Fatty Acid-Deficient Mice". In: *Journal of Investigative Dermatology* 92.4 (1989), pp. 632–638. DOI: `10.1111/1523-1747.ep12712202`.

[301]   Philip W. Wertz. "Lipids and barrier function of the skin". In: *Acta dermato-venereologica* 80.0 (2000), pp. 7–11. DOI: `10.1080/000155500750042790`.

[302]   S. Wartewig and R.H.H. Neubert. "Properties of Ceramides and Their Impact on the Stratum Corneum Structure: A Review". In: *Skin Pharmacology and Physiology* 20.5 (2007), pp. 220–229. DOI: `10.1159/000104420`.

[303]   Kenneth R. Feingold. "Thematic review series: Skin Lipids. The role of epidermal lipids in cutaneous permeability barrier homeostasis: Fig. 1". In: *Journal of Lipid Research* 48.12 (2007), pp. 2531–2546. DOI: `10.1194/jlr.r700013-jlr200`.

[304]   Charlotte M. Walden et al. "Accumulation of Glucosylceramide in Murine Testis, Caused by Inhibition of β-Glucosidase 2". In: *Journal of Biological Chemistry* 282.45 (2007), pp. 32655–32664. DOI: `10.1074/jbc.m702387200`.

[305]   Mariona Rabionet et al. "Male Germ Cells Require Polyenoic Sphingolipids with Complex Glycosylation for Completion of Meiosis". In: *Journal of Biological Chemistry* 283.19 (2008), pp. 13357–13369. DOI: `10.1074/jbc.m800870200`.

[306]   Helena van Overloop et al. "On the presence of C2-ceramide in mammalian tissues: Possible relationship to etherphospholipids and phosphorylation by ceramide kinase". In: *Biological chemistry* 388.3 (2007). DOI: `10.1515/bc.2007.035`.

[307]   Ken Shimuta et al. "Antimicrobial Resistance and Molecular Typing of Neisseria gonorrhoeae Isolates in Kyoto and Osaka, Japan, 2010 to 2012: Intensified Surveillance after Identification of the First Strain (H041) with High-Level Ceftriaxone Resistance". In: *Antimicrobial Agents and Chemotherapy* 57.11 (2013), pp. 5225–5232. DOI: `10.1128/aac.01295-13`.

[308] Magnus Unemo. "Current and future antimicrobial treatment of gonorrhoea – the rapidly evolving Neisseria gonorrhoeae continues to challenge". In: *BMC Infectious Diseases* 15.1 (2015). DOI: `10.1186/s12879-015-1029-2`.

[309] Makoto Ohnishi et al. "Is Neisseria gonorrhoeae Initiating a Future Era of Untreatable Gonorrhea? Detailed Characterization of the First Strain with High-Level Resistance to Ceftriaxone". In: *Antimicrobial Agents and Chemotherapy* 55.7 (2011), pp. 3538–3545. DOI: `10.1128/aac.00325-11`.

[310] Brian M. Barth, Myles C. Cabot, and Mark Kester. "Ceramide-Based Therapeutics for the Treatment of Cancer". In: *Anti-Cancer Agents in Medicinal Chemistry* 11.9 (2011), pp. 911–919. DOI: `10.2174/187152011797655177`.

[311] Alicja Bielawska et al. "(1S,2R)-D-erythro-2-(N-Myristoylamino)-1-phenyl-1-propanol as an Inhibitor of Ceramidase". In: *Journal of Biological Chemistry* 271.21 (1996), pp. 12646–12654. DOI: `10.1074/jbc.271.21.12646`.

[312] Can E. Senkal et al. "Potent Antitumor Activity of a Novel Cationic Pyridinium-Ceramide Alone or in Combination with Gemcitabine against Human Head and Neck Squamous Cell Carcinomas in Vitro and in Vivo". In: *Journal of Pharmacology and Experimental Therapeutics* 317.3 (2006), pp. 1188–1199. DOI: `10.1124/jpet.106.101949`.

[313] Amanda P. Struckhoff et al. "Novel Ceramide Analogs as Potential Chemotherapeutic Agents in Breast Cancer". In: *Journal of Pharmacology and Experimental Therapeutics* 309.2 (2004), pp. 523–532. DOI: `10.1124/jpet.103.062760`.

[314] Sergei A. Novgorodov et al. "Positively Charged Ceramide Is a Potent Inducer of Mitochondrial Permeabilization". In: *Journal of Biological Chemistry* 280.16 (2005), pp. 16096–16105. DOI: `10.1074/jbc.m411707200`.

[315] T. C. Stover. "Systemic Delivery of Liposomal Short-Chain Ceramide Limits Solid Tumor Growth in Murine Models of Breast Adenocarcinoma". In: *Clinical Cancer Research* 11.9 (2005), pp. 3465–3474. DOI: `10.1158/1078-0432.ccr-04-1770`.

[316] B. T. McGuinness et al. "Point mutation in meningococcal por A gene associated with increased endemic disease". In: *The Lancet* 337.8740 (1991), pp. 514–517. DOI: `10.1016/0140-6736(91)91297-8`.

[317] I Nachamkin. "Nachamkin, I., Cannon, J. G. & Mittler, R. S. Monoclonal antibodies against Neisseria gonorrhoeae: Production of antibodies directed against a strain-specific cell surface antigen. Infect Immun 32, 641–648 (1981)". In: *Infect Immun* 32 (1981), p. 641.

[318] Marcia M. Hobbs et al. "Experimental Gonococcal Infection in Male Volunteers: Cumulative Experience with Neisseria gonorrhoeae Strains FA1090 and MS11mkC". In: *Frontiers in Microbiology* 2 (2011). DOI: `10.3389/fmicb.2011.00123`.

[319]   Parham Sendi and Corinne Ruppen. "Time kill assays for Streptococcus agalactiae and synergy testing". In: (2015). DOI: `10.1038/protex.2015.126`.

[320]   Monique F. Stins, Julie Badger, and Kwang Sik Kim. "Bacterial invasion and transcytosis in transfected human brain microvascular endothelial cells". In: *Microbial Pathogenesis* 30.1 (2001), pp. 19–28. DOI: `10.1006/mpat.2000.0406`.

[321]   Monique F. Stins, Floyd Gilles, and Kwang Sik Kim. "Selective expression of adhesion molecules on human brain microvascular endothelial cells". In: *Journal of neuroimmunology* 76.1-2 (1997), pp. 81–90. DOI: `10.1016/s0165-5728(97)00036-2`.

[322]   Aja M. Rieger et al. "Modified Annexin V/Propidium Iodide Apoptosis Assay For Accurate Assessment of Cell Death". In: *Journal of Visualized Experiments* 50 (2011). DOI: `10.3791/2597`.

[323]   S. WOLTER et al. "Real-time computation of subdiffraction-resolution fluorescence images". In: *Journal of microscopy* 237.1 (2010), pp. 12–22. DOI: `10.1111/j.1365-2818.2009.03287.x`.

[324]   R. N. Kolesnick, F. M. Goñi, and A. Alonso. "Compartmentalization of Ceramide Signaling: Physical Foundations and Biological Effects". In: *Journal of cellular physiology* 184.3 (2000). DOI: `10.1002/1097-4652(200009)184:3<285::AID-JCP2>3.0.CO;2-3`.

[325]   Tuula A. Nurminen et al. "Observation of Topical Catalysis by Sphingomyelinase Coupled To Microspheres". In: *Journal of the American Chemical Society* 124.41 (2002), pp. 12129–12134. DOI: `10.1021/ja017807r`.

[326]   Olaf Utermöhlen et al. "Severe Impairment in Early Host Defense Against Listeria monocytogenes in Mice Deficient in Acid Sphingomyelinase". In: *The Journal of Immunology* 170.5 (2003), pp. 2621–2628. DOI: `10.4049/jimmunol.170.5.2621`.

[327]   H. Grassmé et al. "Host defense against Pseudomonas aeruginosa requires ceramide-rich membrane rafts". In: *Nature medicine* 9.3 (2003), pp. 322–330. DOI: `10.1038/nm823`.

[328]   Heike Grassmé et al. "Acidic Sphingomyelinase Mediates Entry of N. gonorrhoeae into Nonphagocytic Cells". In: *Cell* 91.5 (1997), pp. 605–615. DOI: `10.1016/s0092-8674(00)80448-1`.

[329]   M. Esen et al. In: *APOPTOSIS* 6.6 (2001), pp. 431–439. DOI: `10.1023/a:1012445925628`.

[330]   Bruce D. McCollister et al. "Constitutive Acid Sphingomyelinase Enhances Early and Late Macrophage Killing of Salmonella enterica Serovar Typhimurium". In: *Infection and immunity* 75.11 (2007), pp. 5346–5352. DOI: `10.1128/iai.00689-07`.

[331] Cristina L. Vázquez et al. "The proneurotrophin receptor sortilin is required for Mycobacterium tuberculosis control by macrophages". In: *Scientific reports* 6.1 (2016). DOI: `10.1038/srep29332`.

[332] Volker Teichgräber et al. "Ceramide accumulation mediates inflammation, cell death and infection susceptibility in cystic fibrosis". In: *Nature medicine* 14.4 (2008), pp. 382–391. DOI: `10.1038/nm1748`.

[333] Yang Zhang et al. "Acid Sphingomyelinase Amplifies Redox Signaling in Pseudomonas aeruginosa-Induced Macrophage Apoptosis". In: *The Journal of Immunology* 181.6 (2008), pp. 4247–4254. DOI: `10.4049/jimmunol.181.6.4247`.

[334] Yang Zhang et al. "Alterations in Ceramide Concentration and pH Determine the Release of Reactive Oxygen Species by Cftr-Deficient Macrophages on Infection". In: *The Journal of Immunology* 184.9 (2010), pp. 5104–5111. DOI: `10.4049/jimmunol.0902851`.

[335] Hong Yu et al. "Defective Acid Sphingomyelinase Pathway withPseudomonas aeruginosaInfection in Cystic Fibrosis". In: *American Journal of Respiratory Cell and Molecular Biology* 41.3 (2009), pp. 367–375. DOI: `10.1165/rcmb.2008-0295oc`.

[336] Teruaki Nakatsuji et al. "Propionibacterium acnes CAMP Factor and Host Acid Sphingomyelinase Contribute to Bacterial Virulence: Potential Targets for Inflammatory Acne Treatment". In: *PloS one* 6.4 (2011), e14797. DOI: `10.1371/journal.pone.0014797`.

[337] C. R. Hauck et al. "Acid sphingomyelinase is involved in CEACAM receptor-mediated phagocytosis ofNeisseria gonorrhoeae". In: *FEBS letters* 478.3 (2000), pp. 260–266. DOI: `10.1016/s0014-5793(00)01851-2`.

[338] Michael Schramm et al. "Acid sphingomyelinase is required for efficient phagolysosomal fusion". In: *Cellular microbiology* 10.9 (2008), pp. 1839–1853. DOI: `10.1111/j.1462-5822.2008.01169.x`.

[339] Huiming Peng et al. "Acid sphingomyelinase inhibition protects mice from lung edema and lethal Staphylococcus aureus sepsis". In: *Journal of Molecular Medicine* 93.6 (2015), pp. 675–689. DOI: `10.1007/s00109-014-1246-y`.

[340] Johannes Kornhuber et al. "Secretory sphingomyelinase in health and disease". In: *Biological chemistry* 396.6-7 (2015), pp. 707–736. DOI: `10.1515/hsz-2015-0109`.

[341] Youssef H. Zeidan and Yusuf A. Hannun. "Activation of Acid Sphingomyelinase by Protein Kinase Cδ-mediated Phosphorylation". In: *Journal of Biological Chemistry* 282.15 (2007), pp. 11549–11561. DOI: `10.1074/jbc.m609424200`.

[342]   Youssef H. Zeidan et al. "A novel role for protein kinase Cδ-mediated phosphory-lation of acid sphingomyelinase in UV light-induced mitochondrial injury". In: *The FASEB Journal* 22.1 (2007), pp. 183–193. DOI: 10.1096/fj.07-8967com.

[343]   Dongdong Li et al. "Optogenetic activation of LiGluR-expressing astrocytes evokes anion channel-mediated glutamate release". In: *The Journal of physiology* 590.4 (2012), pp. 855–873. DOI: 10.1113/jphysiol.2011.219345.

[344]   Norma W. Andrews, Patricia E. Almeida, and Matthias Corrotte. "Damage control: Cellular mechanisms of plasma membrane repair". In: *Trends in Cell Biology* 24.12 (2014), pp. 734–742. DOI: 10.1016/j.tcb.2014.07.008.

[345]   K. A. V. Cartwright et al. "The Stonehouse survey: Nasopharyngeal carriage of meningococci and Neisseria lactamica". In: *Epidemiology and Infection* 99.3 (1987), pp. 591–601. DOI: 10.1017/s0950268800066449.

[346]   Mumtaz Virji et al. "Pilus-facilitated adherence of Neisseria meningitidis to hu-man epithelial and endothelial cells: Modulation of adherence phenotype occurs concurrently with changes in primary amino acid sequence and the glycosyla-tion status of pilin". In: *Molecular microbiology* 10.5 (1993), pp. 1013–1028. DOI: 10.1111/j.1365-2958.1993.tb00972.x.

[347]   X. Nassif et al. "Roles of pilin and PilC in adhesion of Neisseria meningitidis to human epithelial and endothelial cells". In: *Proceedings of the National Academy of Sciences* 91.9 (1994), pp. 3769–3773. DOI: 10.1073/pnas.91.9.3769.

[348]   Sophie Hélaine et al. "PilX, a pilus-associated protein essential for bacterial aggre-gation, is a key to pilus-facilitated attachment of Neisseria meningitidis to human cells". In: *Molecular microbiology* 55.1 (2004), pp. 65–77. DOI: 10.1111/j.1365-2958.2004.04372.x.

[349]   Etienne Carbonnelle et al. "A systematic genetic analysis in Neisseria meningitidis defines the Pil proteins required for assembly, functionality, stabilization and export of type IV pili". In: *Molecular microbiology* 61.6 (2006), pp. 1510–1522. DOI: 10.1111/j.1365-2958.2006.05341.x.

[350]   A. Cehovin et al. "Specific DNA recognition mediated by a type IV pilin". In: *Proceedings of the National Academy of Sciences* 110.8 (2013), pp. 3065–3070. DOI: 10.1073/pnas.1218832110.

[351]   Tone Tønjum et al. "Identification and characterization of pilG, a highly con-served pilus-assembly gene in pathogenic Neisseria". In: *Molecular microbiology* 16.3 (1995), pp. 451–464. DOI: 10.1111/j.1365-2958.1995.tb02410.x.

[352]   Alexey J. Merz, Magdalene So, and Michael P. Sheetz. "Pilus retraction powers bacterial twitching motility". In: *Nature* 407.6800 (2000), pp. 98–102. DOI: 10.1038/35024105.

[353]   Martin Fussenegger et al. "Transformation competence and type-4 pilus biogenesis in Neisseriagonorrhoeae – areview". In: *Gene* 192.1 (1997), pp. 125–134. DOI: `10.1016/s0378-1119(97)00038-3`.

[354]   Isabelle Hoffmann et al. "Activation of ErbB2 receptor tyrosine kinase supports invasion of endothelial cells by Neisseria meningitidis". In: *Journal of Cell Biology* 155.1 (2001), pp. 133–144. DOI: `10.1083/jcb.200106148`.

[355]   Helena Källström et al. "Cell Signaling by the Type IV Pili of Pathogenic Neisseria". In: *Journal of Biological Chemistry* 273.34 (1998), pp. 21777–21782. DOI: `10.1074/jbc.273.34.21777`.

[356]   B. Patricia Ayala et al. "The pilus-induced Ca2+ flux triggers lysosome exocytosis and increases the amount of Lamp1 accessible to Neisseria IgA1 protease". In: *Cellular microbiology* 3.4 (2001), pp. 265–275. DOI: `10.1046/j.1462-5822.2001.00112.x`.

[357]   Xavier Nassif et al. "Antigenic variation of pilin regulates adhesion of Neisseria meningitidis to human epithelial cells". In: *Molecular microbiology* 8.4 (1993), pp. 719–725. DOI: `10.1111/j.1365-2958.1993.tb01615.x`.

[358]   Tauseef M. Asmat et al. "Impact of Calcium Signaling during Infection of Neisseria meningitidis to Human Brain Microvascular Endothelial Cells". In: *PloS one* 9.12 (2014), e114474. DOI: `10.1371/journal.pone.0114474`.

[359]   Philippe C. Morand et al. "Neisseria meningitidis Differentially Controls Host Cell Motility through PilC1 and PilC2 Components of Type IV Pili". In: *PloS one* 4.8 (2009), e6834. DOI: `10.1371/journal.pone.0006834`.

[360]   Sandra C. Bernard et al. "Pathogenic Neisseria meningitidis utilizes CD147 for vascular colonization". In: *Nature medicine* 20.7 (2014), pp. 725–731. DOI: `10.1038/nm.3563`.

[361]   Heike Grassmé et al. "β1-Integrin Accumulates in Cystic Fibrosis Luminal Airway Epithelial Membranes and Decreases Sphingosine, Promoting Bacterial Infections". In: *Cell Host & Microbe* 21.6 (2017), 707–718.e8. DOI: `10.1016/j.chom.2017.05.001`.

[362]   Patricia Ayala et al. "The pilus and porin of Neisseria gonorrhoeae cooperatively induce Ca2+ transients in infected epithelial cells". In: *Cellular microbiology* 7.12 (2005), pp. 1736–1748. DOI: `10.1111/j.1462-5822.2005.00586.x`.

[363]   Patricia Ayala et al. "Neisseria gonorrhoeae Porin P1.B Induces Endosome Exocytosis and a Redistribution of Lamp1 to the Plasma Membrane". In: *Infection and immunity* 70.11 (2002), pp. 5965–5971. DOI: `10.1128/iai.70.11.5965-5971.2002`.

[364]   A. Muller. "Neisserial porin (PorB) causes rapid calcium influx in target cells and induces apoptosis by the activation of cysteine proteases". In: *The EMBO journal* 18.2 (1999), pp. 339–352. DOI: `10.1093/emboj/18.2.339`.

[365]   Michael J. Berridge, Peter Lipp, and Martin D. Bootman. "The versatility and universality of calcium signalling". In: *Nature Reviews Molecular Cell Biology* 1.1 (2000), pp. 11–21. DOI: `10.1038/35036035`.

[366]   Ernesto Carafoli et al. "Generation, Control, and Processing of Cellular Calcium Signals". In: *Critical Reviews in Biochemistry and Molecular Biology* 36.2 (2001), pp. 107–260. DOI: `10.1080/20014091074183`.

[367]   Lan Lin et al. "The Neisseria type 2 IgA1 protease cleaves LAMP1 and promotes survival of bacteria within epithelial cells". In: *Molecular microbiology* 24.5 (1997), pp. 1083–1094. DOI: `10.1046/j.1365-2958.1997.4191776.x`.

[368]   Jyoti K. Jaiswal, Norma W. Andrews, and Sanford M. Simon. "Membrane proximal lysosomes are the major vesicles responsible for calcium-dependent exocytosis in nonsecretory cells". In: *Journal of Cell Biology* 159.4 (2002), pp. 625–635. DOI: `10.1083/jcb.200208154`.

[369]   Anita Reddy, Elisabet V. Caler, and Norma W. Andrews. "Plasma Membrane Repair Is Mediated by Ca2+-Regulated Exocytosis of Lysosomes". In: *Cell* 106.2 (2001), pp. 157–169. DOI: `10.1016/s0092-8674(01)00421-4`.

[370]   Ana Rodríguez et al. "Lysosomes Behave as Ca2+-regulated Exocytic Vesicles in Fibroblasts and Epithelial Cells". In: *Journal of Cell Biology* 137.1 (1997), pp. 93–104. DOI: `10.1083/jcb.137.1.93`.

[371]   Alexandra Charruyer et al. "UV-C Light Induces Raft-associated Acid Sphingomyelinase and JNK Activation and Translocation Independently on a Nuclear Signal". In: *Journal of Biological Chemistry* 280.19 (2005), pp. 19196–19204. DOI: `10.1074/jbc.m412867200`.

[372]   Claudia Alexandra Dumitru et al. "Doxorubicin enhances TRAIL-induced cell death via ceramide-enriched membrane platforms". In: *APOPTOSIS* 12.8 (2007), pp. 1533–1541. DOI: `10.1007/s10495-007-0081-9`.

[373]   Heike Grassmé et al. "CD95 Signaling via Ceramide-rich Membrane Rafts". In: *Journal of Biological Chemistry* 276.23 (2001), pp. 20589–20596. DOI: `10.1074/jbc.m101207200`.

[374]   Heike Grassmé et al. "Rhinoviruses Infect Human Epithelial Cells via Ceramide-enriched Membrane Platforms". In: *Journal of Biological Chemistry* 280.28 (2005), pp. 26256–26262. DOI: `10.1074/jbc.m500835200`.

[375]   Elita Avota, Erich Gulbins, and Sibylle Schneider-Schaulies. "DC-SIGN Mediated Sphingomyelinase-Activation and Ceramide Generation Is Essential for Enhancement of Viral Uptake in Dendritic Cells". In: *PLoS pathogens* 7.2 (2011), e1001290. DOI: 10.1371/journal.ppat.1001290.

[376]   Alexandra Unkmeir et al. "Fibronectin mediates Opc-dependent internalization of Neisseria meningitidis in human brain microvascular endothelial cells". In: *Molecular microbiology* 46.4 (2002), pp. 933–946.

[377]   Martin Lappann et al. "Meningococcal biofilm formation: Structure, development and phenotypes in a standardized continuous flow system". In: *Molecular microbiology* 62.5 (2006), pp. 1292–1309. DOI: 10.1111/j.1365-2958.2006.05448.x.

[378]   M. Virji and J. E. Heckels. "Antigenic Cross-reactivity of Neisseria Pili: Investigations with Type- and Species-specific Monoclonal Antibodies". In: *Microbiology* 129.9 (1983), pp. 2761–2768. DOI: 10.1099/00221287-129-9-2761.

[379]   Daniel Allan et al. *Trackpy: Trackpy V0.3.2.* 2016. DOI: 10.5281/zenodo.60550.

[380]   Inhee Chung et al. "Spatial control of EGF receptor activation by reversible dimerization on living cells". In: *Nature* 464.7289 (2010), pp. 783–787. DOI: 10.1038/nature08827.

[381]   J. C. Comolli et al. "Pili binding to asialo-GM1 on epithelial cells can mediate cytotoxicity or bacterial internalization by Pseudomonas aeruginosa". In: *Infection and immunity* 67.7 (1999), pp. 3207–3214.

[382]   Mathieu Coureuil et al. "Meningococcus Hijacks a β2-Adrenoceptor/β-Arrestin Pathway to Cross Brain Microvasculature Endothelium". In: *Cell* 143.7 (2010), pp. 1149–1160. DOI: 10.1016/j.cell.2010.11.035.

[383]   Mathieu Coureuil et al. "Meningococcal type IV pili recruit the polarity complex to cross the brain endothelium". In: *Science (New York, N.Y.)* 325.5936 (2009), pp. 83–87. DOI: 10.1126/science.1173196.

[384]   John C. Crocker and David G. Grier. "Methods of Digital Video Microscopy for Colloidal Studies". In: *Journal of Colloid and Interface Science* 179.1 (1996), pp. 298–310. DOI: 10.1006/jcis.1996.0217.

[385]   Pedro Cuatrecasas. "Gangliosides and membrane receptors for cholera toxin". In: *Biochemistry* 12.18 (1973), pp. 3558–3566. DOI: 10.1021/bi00742a032.

[386]   D. Hammache et al. "Human erythrocyte glycosphingolipids as alternative cofactors for human immunodeficiency virus type 1 (HIV-1) entry: Evidence for CD4-induced interactions between HIV-1 gp120 and reconstituted membrane microdomains of glycosphingolipids (Gb3 and GM3)". In: *Journal of virology* 73.6 (1999), pp. 5244–5248.

[387] H.A Harvey, W.E Swords, and M.A Apicella. "The Mimicry of Human Glycolipids and Glycosphingolipids by the Lipooligosaccharides of Pathogenic Neisseria andHaemophilus". In: *Journal of autoimmunity* 16.3 (2001), pp. 257–262. DOI: `10.1006/jaut.2000.0477`.

[388] S. Hugosson et al. "Glycosphingolipid binding specificities of Neisseria meningitidis and Haemophilus influenzae: Detection, isolation, and characterization of a binding-active glycosphingolipid from human oropharyngeal epithelium". In: *Journal of biochemistry* 124.6 (1998), pp. 1138–1152. DOI: `10.1093/oxfordjournals.jbchem.a022232`.

[389] C. S. Hyun and G. A. Kimmich. "Interaction of cholera toxin and Escherichia coli enterotoxin with isolated intestinal epithelial cells". In: *The American journal of physiology* 247.6 Pt 1 (1984), G623–31. DOI: `10.1152/ajpgi.1984.247.6.G623`.

[390] N. Ichikawa et al. "Binding of laminin-1 to monosialoganglioside GM1 in lipid rafts is crucial for neurite outgrowth". In: *Journal of cell science* 122.2 (2008), pp. 289–299. DOI: `10.1242/jcs.030338`.

[391] A. Kiarash, B. Boyd, and C. A. Lingwood. "Glycosphingolipid receptor function is modified by fatty acid content. Verotoxin 1 and verotoxin 2c preferentially recognize different globotriaosyl ceramide fatty acid homologues". In: *Journal of Biological Chemistry* 269.15 (1994), pp. 11138–11146.

[392] Maria A. Kiskowski, John F. Hancock, and Anne K. Kenworthy. "On the Use of Ripley's K-Function and Its Derivatives to Analyze Domain Size". In: *Biophysical journal* 97.4 (2009), pp. 1095–1103. DOI: `10.1016/j.bpj.2009.05.039`.

[393] Christian Koch et al. "T cell activation-associated epitopes of CD147 in regulation of the T cell response, and their definition by antibody affinity and antigen density". In: *International immunology* 11.5 (1999), pp. 777–786. DOI: `10.1093/intimm/11.5.777`.

[394] H. C. Krivan, D. D. Roberts, and V. Ginsburg. "Many pulmonary pathogenic bacteria bind specifically to the carbohydrate sequence GalNAc beta 1-4Gal found in some glycolipids". In: *Proceedings of the National Academy of Sciences* 85.16 (1988), pp. 6157–6161. DOI: `10.1073/pnas.85.16.6157`.

[395] Geoffrey M. Kuziemko, Mark Stroh, and Raymond C. Stevens. "Cholera Toxin Binding Affinity and Specificity for Gangliosides Determined by Surface Plasmon Resonance†". In: *Biochemistry* 35.20 (1996), pp. 6375–6384. DOI: `10.1021/bi952314i`.

[396] Emmanuel Lemichez et al. "Breaking the wall: Targeting of the endothelium by pathogenic bacteria". In: *Nature reviews. Microbiology* 8.2 (2010), pp. 93–104. DOI: `10.1038/nrmicro2269`.

[397] L. Li et al. "HAb18G/CD147 Promotes pSTAT3-Mediated Pancreatic Cancer Development via CD44s". In: *Clinical Cancer Research* 19.24 (2013), pp. 6703–6715. DOI: 10.1158/1078-0432.ccr-13-0621.

[398] A. A. Lindberg et al. "Identification of the carbohydrate receptor for Shiga toxin produced by Shigella dysenteriae type 1". In: *Journal of Biological Chemistry* 262.4 (1987), pp. 1779–1785.

[399] Clifford A. Lingwood. "Glycosphingolipid functions". In: *Cold Spring Harbor perspectives in biology* 3.7 (2011). DOI: 10.1101/cshperspect.a004788.

[400] Nawal Maïssa et al. "Strength of Neisseria meningitidis binding to endothelial cells requires highly-ordered CD147/β2-adrenoceptor clusters assembled by alpha-actinin-4". In: *Nature communications* 8.1 (2017). DOI: 10.1038/ncomms15764.

[401] Irina Majoul et al. "Differential expression of receptors for Shiga and Cholera toxin is regulated by the cell cycle". In: *Journal of cell science* 115.Pt 4 (2002), pp. 817–826.

[402] Marianne Mangeney et al. "CD77: An antigen of germinal center B cells entering apoptosis". In: *European journal of immunology* 21.5 (1991), pp. 1131–1140. DOI: 10.1002/eji.1830210507.

[403] Carlo Manzo and Maria F. Garcia-Parajo. "A review of progress in single particle tracking: From methods to biophysical insights". In: *Reports on Progress in Physics* 78.12 (2015), p. 124601. DOI: 10.1088/0034-4885/78/12/124601.

[404] Keira Melican and Guillaume Dumenil. "Vascular colonization by Neisseria meningitidis". In: *Current opinion in microbiology* 15.1 (2012), pp. 50–56. DOI: 10.1016/j.mib.2011.10.008.

[405] Tsitsi D. Mubaiwa et al. "The glycointeractome of serogroup B Neisseria meningitidis strain MC58". In: *Scientific reports* 7.1 (2017). DOI: 10.1038/s41598-017-05894-w.

[406] T. Mutoh et al. "Ganglioside GM1 binds to the Trk protein and regulates receptor function". In: *Proceedings of the National Academy of Sciences* 92.11 (1995), pp. 5087–5091. DOI: 10.1073/pnas.92.11.5087.

[407] Hitoshi Nakayama et al. "The regulatory roles of glycosphingolipid-enriched lipid rafts in immune systems". In: *FEBS letters* 592.23 (2018), pp. 3921–3942. DOI: 10.1002/1873-3468.13275.

[408] Aroem Naroeni and Françoise Porte. "Role of Cholesterol and the Ganglioside GM1 in Entry and Short-Term Survival of Brucella suis in Murine Macrophages". In: *Infection and immunity* 70.3 (2002), pp. 1640–1644. DOI: 10.1128/iai.70.3.1640-1644.2002.

[409] Joanna Nikulin et al. "Intracellular survival and replication of Neisseria meningitidis in human brain microvascular endothelial cells". In: *International Journal of Medical Microbiology* 296.8 (2006), pp. 553–558. DOI: `10.1016/j.ijmm.2006.06.006`.

[410] Wilhelm F. Oosthuysen et al. "Neisseria meningitidis causes cell cycle arrest of human brain microvascular endothelial cells at S phase via p21 and cyclin G2". In: *Cellular microbiology* 18.1 (2016), pp. 46–65. DOI: `10.1111/cmi.12482`.

[411] A. B. Otnaess, A. Laegreid, and K. Ertresvåg. "Inhibition of enterotoxin from Escherichia coli and Vibrio cholerae by gangliosides from human milk". In: *Infection and immunity* 40.2 (1983), pp. 563–569.

[412] Martin Ovesný et al. "ThunderSTORM: A comprehensive ImageJ plug-in for PALM and STORM data analysis and super-resolution imaging". In: *Bioinformatics* 30.16 (2014), pp. 2389–2390. DOI: `10.1093/bioinformatics/btu202`.

[413] Michael von Papen et al. "Disease and Carrier Isolates of Neisseria meningitidis Cause G1Cell Cycle Arrest in Human Epithelial Cells". In: *Infection and immunity* 84.10 (2016), pp. 2758–2770. DOI: `10.1128/iai.00296-16`.

[414] A. Pellizzari, H. Pang, and C. A. Lingwood. "Binding of verocytotoxin 1 to its receptor is influenced by differences in receptor fatty acid content". In: *Biochemistry* 31.5 (1992), pp. 1363–1370. DOI: `10.1021/bi00120a011`.

[415] Xavier Prasanna et al. "The ganglioside GM1 interacts with the serotonin 1A receptor via the sphingolipid binding domain". In: *Biochimica et Biophysica Acta (BBA) - Biomembranes* 1858.11 (2016), pp. 2818–2826. DOI: `10.1016/j.bbamem.2016.08.009`.

[416] Nadia Ruthardt, Don C. Lamb, and Christoph Bräuchle. "Single-particle Tracking as a Quantitative Microscopy-based Approach to Unravel Cell Entry Mechanisms of Viruses and Pharmaceutical Nanoparticles". In: *Molecular Therapy* 19.7 (2011), pp. 1199–1211. DOI: `10.1038/mt.2011.102`.

[417] Alexandra Schubert-Unkmeir et al. "Neisseria meningitidis Induces Brain Microvascular Endothelial Cell Detachment from the Matrix and Cleavage of Occludin: A Role for MMP-8". In: *PLoS pathogens* 6.4 (2010), e1000874. DOI: `10.1371/journal.ppat.1000874`.

[418] Hao Shen et al. "Single Particle Tracking: From Theory to Biophysical Applications". In: *Chemical reviews* 117.11 (2017), pp. 7331–7376. DOI: `10.1021/acs.chemrev.6b00815`.

[419] Aoranit Somno et al. "Involvement of CD147 on multidrug resistance through the regulation of P-glycoprotein expression in K562/ADR leukemic cell line". In: *Leukemia research reports* 6 (2016), pp. 33–38. DOI: `10.1016/j.lrr.2016.08.001`.

[420] David S. Stephens, Brian Greenwood, and Petter Brandtzaeg. "Epidemic meningitis, meningococcaemia, and Neisseria meningitidis". In: *The Lancet* 369.9580 (2007), pp. 2196–2210. DOI: 10.1016/S0140-6736(07)61016-2.

[421] Thomas C. Sutherland et al. "Transcellular passage of Neisseria meningitidis across a polarized respiratory epithelium". In: *Infection and immunity* 78.9 (2010), pp. 3832–3847. DOI: 10.1128/IAI.01377-09.

[422] Yi Tang et al. "Tumor-stroma interaction: Positive feedback regulation of extracellular matrix metalloproteinase inducer (EMMPRIN) expression and matrix metalloproteinase-dependent generation of soluble EMMPRIN". In: *Molecular cancer research : MCR* 2.2 (2004), pp. 73–80.

[423] Jean-Yves Tinevez et al. "TrackMate: An open and extensible platform for single-particle tracking". In: *Methods (San Diego, Calif.)* 115 (2017), pp. 80–90. DOI: 10.1016/j.ymeth.2016.09.016.

[424] M. L. Torgersen et al. "Internalization of cholera toxin by different endocytic mechanisms". In: *Journal of cell science* 114.Pt 20 (2001), pp. 3737–3747.

[425] Billy Tsai et al. "Gangliosides are receptors for murine polyoma virus and SV40". In: *The EMBO journal* 22.17 (2003), pp. 4346–4355. DOI: 10.1093/emboj/cdg439.

[426] Taka A. Tsunoyama et al. "Super-long single-molecule tracking reveals dynamic-anchorage-induced integrin function". In: *Nature chemical biology* 14.5 (2018), pp. 497–506. DOI: 10.1038/s41589-018-0032-5.

[427] Bo Wu et al. "Cytoplasmic fragment of CD147 generated by regulated intramembrane proteolysis contributes to HCC by promoting autophagy". In: *Cell death & disease* 8.7 (2017), e2925–e2925. DOI: 10.1038/cddis.2017.251.

[428] Masataka Yanagawa et al. "Single-molecule diffusion-based estimation of ligand effects on G protein–coupled receptors". In: *Science signaling* 11.548 (2018), eaao1917. DOI: 10.1126/scisignal.aao1917.

[429] Siamak P. Yazdankhah and Dominique A. Caugant. "Neisseria meningitidis: An overview of the carriage state". In: *Journal of medical microbiology* 53.Pt 9 (2004), pp. 821–832. DOI: 10.1099/jmm.0.45529-0.

[430] John M. Walker, ed. *The Proteomics Protocols Handbook*. Methods in Molecular Biology. Totowa, NJ: Humana Press Inc, 2005. DOI: 10.1385/1592598900.

[431] Mike Heilemann et al. "Super-resolution imaging with small organic fluorophores". In: *Angewandte Chemie (International ed. in English)* 48.37 (2009), pp. 6903–6908. DOI: 10.1002/anie.200902073.

[432] Ulrike Endesfelder and Mike Heilemann. "Direct stochastic optical reconstruction microscopy (dSTORM)". In: *Methods in molecular biology (Clifton, N.J.)* 1251 (2015), pp. 263–276. DOI: 10.1007/978-1-4939-2080-8_14.

[433] Yiming Li et al. "Real-time 3D single-molecule localization using experimental point spread functions". In: *Nature methods* 15.5 (2018), pp. 367–369. DOI: 10.1038/nmeth.4661.

[434] Christian Franke, Markus Sauer, and Sebastian van de Linde. "Photometry unlocks 3D information from 2D localization microscopy data". In: *Nature methods* 14.1 (2017), pp. 41–44. DOI: 10.1038/nmeth.4073.

[435] Daniel Sage et al. "Super-resolution fight club: Assessment of 2D and 3D single-molecule localization microscopy software". In: *Nature methods* 16.5 (2019), pp. 387–395. DOI: 10.1038/s41592-019-0364-4.

[436] H. Ling et al. *Mutated Shiga-Like Toxin B Subunit (G62T)*. 2000. DOI: 10.2210/pdb1c48/pdb.

[437] E. A. Merritt and W.G.J. Hol. *Cholera Toxin B-Pentamer with Ligand BMSC-0011*. 2002. DOI: 10.2210/pdb1jr0/pdb.

[438] J. Lippincott-Schwartz, E. Snapp, and A. Kenworthy. "Studying protein dynamics in living cells". In: *Nature Reviews Molecular Cell Biology* 2.6 (2001), pp. 444–456. DOI: 10.1038/35073068.

[439] John P. Overington, Bissan Al-Lazikani, and Andrew L. Hopkins. "How many drug targets are there?" In: *Nature Reviews Drug Discovery* 5.12 (2006), pp. 993–996. DOI: 10.1038/nrd2199.

[440] Joseph C. Del Paggio. "Cancer immunotherapy and the value of cure". In: *Nature Reviews Clinical Oncology* 15.5 (2018), pp. 268–270. DOI: 10.1038/nrclinonc.2018.27.

[441] Jérémie Rossy et al. "Conformational states of the kinase Lck regulate clustering in early T cell signaling". In: *Nature immunology* 14.1 (2012), pp. 82–89. DOI: 10.1038/ni.2488.

[442] Ying S. Hu, Hu Cang, and Björn F. Lillemeier. "Superresolution imaging reveals nanometer- and micrometer-scale spatial distributions of T-cell receptors in lymph nodes". In: *Proceedings of the National Academy of Sciences* 113.26 (2016), pp. 7201–7206. DOI: 10.1073/pnas.1512331113.

[443] Aleks Ponjavic et al. "Single-Molecule Light-Sheet Imaging of Suspended T Cells". In: *Biophysical journal* 114.9 (2018), pp. 2200–2211. DOI: 10.1016/j.bpj.2018.02.044.

[444] Anna-Karin Gustavsson et al. "3D single-molecule super-resolution microscopy with a tilted light sheet". In: *Nature communications* 9.1 (2018). DOI: 10.1038/s41467-017-02563-4.

[445] Bi-Chang Chen et al. "Lattice light-sheet microscopy: Imaging molecules to embryos at high spatiotemporal resolution". In: *Science* 346.6208 (2014), p. 1257998. DOI: 10.1126/science.1257998.

[446] Wesley R. Legant et al. "High-density three-dimensional localization microscopy across large volumes". In: *Nature methods* 13.4 (2016), pp. 359–365. DOI: 10.1038/nmeth.3797.

[447] Zhe Liu et al. "3D imaging of Sox2 enhancer clusters in embryonic stem cells". In: *eLife* 3 (2014). DOI: 10.7554/elife.04236.

[448] Chieh-Han Lu et al. "Lightsheet localization microscopy enables fast, large-scale, and three-dimensional super-resolution imaging". In: *Communications biology* 2.1 (2019). DOI: 10.1038/s42003-019-0403-9.

[449] H. Shroff et al. "Dual-color superresolution imaging of genetically expressed probes within individual adhesion complexes". In: *Proceedings of the National Academy of Sciences* 104.51 (2007), pp. 20308–20313. DOI: 10.1073/pnas.0710517105.

[450] Megan S. Michie et al. "Cyanine Conformational Restraint in the Far-Red Range". In: *Journal of the American Chemical Society* 139.36 (2017), pp. 12406–12409. DOI: 10.1021/jacs.7b07272.

[451] Heleen H. van Acker et al. "CD56 in the Immune System: More Than a Marker for Cytotoxicity?" In: *Frontiers in immunology* 8 (2017), p. 892. DOI: 10.3389/fimmu.2017.00892.

[452] A. J. Murray et al. "One sequence, two folds: A metastable structure of CD2". In: *Proceedings of the National Academy of Sciences* 92.16 (1995), pp. 7337–7341. DOI: 10.1073/pnas.92.16.7337.

[453] Rose Zamoyska. "Why Is There so Much CD45 on T Cells?" In: *Immunity* 27.3 (2007), pp. 421–423. DOI: 10.1016/j.immuni.2007.08.009.

[454] Stefan Wieser and Gerhard J. Schütz. "Tracking single molecules in the live cell plasma membrane-Do's and Don't's". In: *Methods (San Diego, Calif.)* 46.2 (2008), pp. 131–140. DOI: 10.1016/j.ymeth.2008.06.010.

[455] Xavier Michalet. "Mean square displacement analysis of single-particle trajectories with localization error: Brownian motion in an isotropic medium". In: *Physical Review E* 82.4 (2010). DOI: 10.1103/physreve.82.041914.

[456] Byron Hetrick et al. "Small Molecules CK-666 and CK-869 Inhibit Actin-Related Protein 2/3 Complex by Blocking an Activating Conformational Change". In: *Chemistry & biology* 20.5 (2013), pp. 701–712. DOI: 10.1016/j.chembiol.2013.03.019.

[457]   Elif Nur Firat-Karalar and Matthew D. Welch. "New mechanisms and functions of actin nucleation". In: *Current opinion in cell biology* 23.1 (2011), pp. 4–13. DOI: 10.1016/j.ceb.2010.10.007.

[458]   Eric A.J. Reits and Jacques J. Neefjes. "From fixed to FRAP: Measuring protein mobility and activity in living cells". In: *Nature cell biology* 3.6 (2001), E145–E147. DOI: 10.1038/35078615.

[459]   Nikolaj Kulahin et al. "Direct demonstration of NCAMcis-dimerization and inhibitory effect of palmitoylation using the BRET2technique". In: *FEBS letters* 585.1 (2010), pp. 58–64. DOI: 10.1016/j.febslet.2010.11.043.

[460]   Vladislav Soroka et al. "Structure and Interactions of NCAM Ig1-2-3 Suggest a Novel Zipper Mechanism for Homophilic Adhesion". In: *Structure* 11.10 (2003), pp. 1291–1301. DOI: 10.1016/j.str.2003.09.006.

[461]   Pierre Bon et al. "Self-interference 3D super-resolution microscopy for deep tissue investigations". In: *Nature methods* 15.6 (2018), pp. 449–454. DOI: 10.1038/s41592-018-0005-3.

[462]   Michael J. Mlodzianoski et al. "Active PSF shaping and adaptive optics enable volumetric localization microscopy through brain sections". In: *Nature methods* 15.8 (2018), pp. 583–586. DOI: 10.1038/s41592-018-0053-8.

[463]   Elise Corre et al. "Long-term immune deficiency after allogeneic stem cell transplantation: B-cell deficiency is associated with late infections". In: *Haematologica* 95.6 (2010), pp. 1025–1029. DOI: 10.3324/haematol.2009.018853.

[464]   B. S. Park and J. O. Lee. "Recognition of Lipopolysaccharide Pattern by TLR4 Complexes". In: *Experimental & molecular medicine* 45.12 (2013). DOI: 10.1038/emm.2013.97.

[465]   T. Kawai and S. Akira. "The Roles of TLRs, RLRs and NLRs in Pathogen Recognition". In: *International immunology* 21.4 (2009). DOI: 10.1093/intimm/dxp017.

[466]   N. K. Björkström, H. G. Ljunggren, and J. Michaëlsson. "Emerging Insights Into Natural Killer Cells in Human Peripheral Tissues". In: *Nature reviews. Immunology* 16.5 (2016). DOI: 10.1038/nri.2016.34.

[467]   N. Marquardt et al. "Human Lung Natural Killer Cells Are Predominantly Comprised of Highly Differentiated Hypofunctional CD69 - CD56 dim Cells". In: *The Journal of allergy and clinical immunology* 139.4 (2017). DOI: 10.1016/j.jaci.2016.07.043.

[468]   K. S. Campbell and J. Hasegawa. "Natural Killer Cell Biology: An Update and Future Directions". In: *The Journal of allergy and clinical immunology* 132.3 (2013). DOI: 10.1016/j.jaci.2013.07.006.

[469]   Michael A. Caligiuri. "Human natural killer cells". In: *Blood* 112.3 (2008), pp. 461–469. DOI: 10.1182/blood-2007-09-077438.

[470]   C. Romagnani et al. "CD56brightCD16- Killer Ig-like Receptor- NK Cells Display Longer Telomeres and Acquire Features of CD56dim NK Cells Upon Activation". In: *Journal of immunology (Baltimore, Md. : 1950)* 178.8 (2007). DOI: 10.4049/jimmunol.178.8.4947.

[471]   L. Moretta. "Dissecting CD56dim Human NK Cells". In: *Blood* 116.19 (2010). DOI: 10.1182/blood-2010-09-303057.

[472]   A. Chan et al. "CD56bright Human NK Cells Differentiate Into CD56dim Cells: Role of Contact With Peripheral Fibroblasts". In: *Journal of immunology (Baltimore, Md. : 1950)* 179.1 (2007). DOI: 10.4049/jimmunol.179.1.89.

[473]   N. Dulphy et al. "An Unusual CD56(bright) CD16(low) NK Cell Subset Dominates the Early Posttransplant Period Following HLA-matched Hematopoietic Stem Cell Transplantation". In: *Journal of immunology (Baltimore, Md. : 1950)* 181.3 (2008). DOI: 10.4049/jimmunol.181.3.2227.

[474]   Nicola J. Topham and Eric W. Hewitt. "Natural killer cell cytotoxicity: How do they pull the trigger?" In: *Immunology* 128.1 (2009), pp. 7–15. DOI: 10.1111/j.1365-2567.2009.03123.x.

[475]   A. S. Fauci, D. Mavilio, and S. Kottilil. "NK Cells in HIV Infection: Paradigm for Protection or Targets for Ambush". In: *Nature reviews. Immunology* 5.11 (2005). DOI: 10.1038/nri1711.

[476]   Esther Weiss et al. "First Insights in NK-DC Cross-Talk and the Importance of Soluble Factors During Infection With Aspergillus fumigatus". In: *Frontiers in cellular and infection microbiology* 8 (2018), p. 288. DOI: 10.3389/fcimb.2018.00288.

[477]   Daniel B. Allan et al. *trackpy: Trackpy v0.4.1*. 2018. DOI: 10.5281/zenodo.1226458.

[478]   M. A. Ullah, G. R. Hill, and S. K. Tey. "Functional Reconstitution of Natural Killer Cells in Allogeneic Hematopoietic Stem Cell Transplantation". In: *Frontiers in immunology* 7 (2016). DOI: 10.3389/fimmu.2016.00144.

[479]   M. Charmoy et al. "Neutrophil-derived CCL3 Is Essential for the Rapid Recruitment of Dendritic Cells to the Site of Leishmania Major Inoculation in Resistant Mice". In: *PLoS pathogens* 6.2 (2010). DOI: 10.1371/journal.ppat.1000755.

[480]   N. M. Bless et al. "Role of CC Chemokines (Macrophage Inflammatory protein-1 Beta, Monocyte Chemoattractant protein-1, RANTES) in Acute Lung Injury in Rats". In: *Journal of immunology (Baltimore, Md. : 1950)* 164.5 (2000). DOI: 10.4049/jimmunol.164.5.2650.

[481]   J. T. Souto et al. "Chemokine Production and Leukocyte Recruitment to the Lungs of Paracoccidioides Brasiliensis-Infected Mice Is Modulated by Interferon-Gamma". In: *The American journal of pathology* 163.2 (2003). DOI: `10.1016/s0002-9440(10)63686-3`.

[482]   C. Fauriat et al. "Regulation of Human NK-cell Cytokine and Chemokine Production by Target Cell Recognition". In: *Blood* 115.11 (2010). DOI: `10.1182/blood-2009-08-238469`.

[483]   M. Ohira et al. "Impact of Steroids on Natural Killer Cells Against Cytotoxicity and Hepatitis C Virus Replication". In: *Transplantation proceedings* 49.5 (2017). DOI: `10.1016/j.transproceed.2017.03.018`.

[484]   Anders S. Hansen et al. "Robust model-based analysis of single-particle tracking experiments with Spot-On". In: *eLife* 7 (2018). DOI: `10.7554/eLife.33125`.

[485]   K. Mühlemann et al. "Risk Factors for Invasive Aspergillosis in Neutropenic Patients With Hematologic Malignancies". In: *Leukemia* 19.4 (2005). DOI: `10.1038/sj.leu.2403674`.

[486]   A. C. Labbé et al. "High Incidence of Invasive Aspergillosis Associated With Intestinal Graft-Versus-Host Disease Following Nonmyeloablative Transplantation". In: *Biology of blood and marrow transplantation : journal of the American Society for Blood and Marrow Transplantation* 13.10 (2007). DOI: `10.1016/j.bbmt.2007.06.013`.

[487]   S. Quellmann et al. "Corticosteroids for Preventing Graft-Versus-Host Disease After Allogeneic Myeloablative Stem Cell Transplantation". In: *The Cochrane database of systematic reviews* 3 (2008). DOI: `10.1002/14651858.CD004885.pub2`.

[488]   M. Y. Thum et al. "Prednisolone Suppresses NK Cell Cytotoxicity in Vitro in Women With a History of Infertility and Elevated NK Cell Cytotoxicity". In: *American journal of reproductive immunology (New York, N.Y. : 1989)* 59.3 (2008). DOI: `10.1111/j.1600-0897.2007.00574.x`.

[489]   R. I. Scheinman et al. "Characterization of Mechanisms Involved in Transrepression of NF-kappa B by Activated Glucocorticoid Receptors". In: *Molecular and Cellular Biology* 15.2 (1995). DOI: `10.1128/mcb.15.2.943`.

[490]   M. D. Elftman et al. "Corticosterone Impairs Dendritic Cell Maturation and Function". In: *Immunology* 122.2 (2007). DOI: `10.1111/j.1365-2567.2007.02637.x`.

[491]   Andrea Bacigalupo et al. "Steroid treatment of acute graft-versus-host disease grade I: A randomized trial". In: *Haematologica* 102.12 (2017), pp. 2125–2133. DOI: `10.3324/haematol.2017.171157`.

[492] H. M. Jantzen et al. "Cooperativity of Glucocorticoid Response Elements Located Far Upstream of the Tyrosine Aminotransferase Gene". In: *Cell* 49.1 (1987). DOI: `10.1016/0092-8674(87)90752-5`.

[493] M. Beato. "Gene Regulation by Steroid Hormones". In: *Cell* 56.3 (1989). DOI: `10.1016/0092-8674(89)90237-7`.

[494] Miguel Beato, Mathias Truss, and Sebastián Chávez. "Control of Transcription by Steroid Hormonesa". In: *Annals of the New York Academy of Sciences* 784.1 (1996), pp. 93–123. DOI: `10.1111/j.1749-6632.1996.tb16231.x`.

[495] G. Nelson et al. "NF-kappaB Signalling Is Inhibited by Glucocorticoid Receptor and STAT6 via Distinct Mechanisms". In: *Journal of cell science* 116.Pt 12 (2003). DOI: `10.1242/jcs.00461`.

[496] H. Moriuchi, M. Moriuchi, and A. S. Fauci. "Nuclear Factor-Kappa B Potently Up-Regulates the Promoter Activity of RANTES, a Chemokine That Blocks HIV Infection". In: *Journal of immunology (Baltimore, Md. : 1950)* 158.7 (1997).

[497] M. Grove and M. Plumb. "C/EBP, NF-kappa B, and c-Ets family members and transcriptional regulation of the cell-specific and inducible macrophage inflammatory protein 1 alpha immediate-early gene". In: *Molecular and Cellular Biology* 13.9 (1993), pp. 5276–5289.

[498] U. Widmer et al. "Genomic Cloning and Promoter Analysis of Macrophage Inflammatory Protein (MIP)-2, MIP-1 Alpha, and MIP-1 Beta, Members of the Chemokine Superfamily of Proinflammatory Cytokines". In: *Journal of immunology (Baltimore, Md. : 1950)* 150.11 (1993).

[499] S. Schrum et al. "Synthesis of the CC-chemokines MIP-1alpha, MIP-1beta, and RANTES Is Associated With a Type 1 Immune Response". In: *Journal of immunology (Baltimore, Md. : 1950)* 157.8 (1996).

[500] C. Huang and S. M. Levitz. "Stimulation of Macrophage Inflammatory protein-1alpha, Macrophage Inflammatory protein-1beta, and RANTES by Candida Albicans and Cryptococcus Neoformans in Peripheral Blood Mononuclear Cells From Persons With and Without Human Immunodeficiency Virus Infection". In: *The Journal of infectious diseases* 181.2 (2000). DOI: `10.1086/315250`.

[501] B. J. Lee and E. M. Mace. "Acquisition of Cell Migration Defines NK Cell Differentiation From Hematopoietic Stem Cell Precursors". In: *Molecular biology of the cell* 28.25 (2017). DOI: `10.1091/mbc.E17-08-0508`.

[502] A. F. Carisey et al. "Nanoscale Dynamism of Actin Enables Secretory Function in Cytolytic Cells". In: *Current biology : CB* 28.4 (2018). DOI: `10.1016/j.cub.2017.12.044`.

[503]   C. Watzl and E. O. Long. "Natural Killer Cell Inhibitory Receptors Block Actin Cytoskeleton-Dependent Recruitment of 2B4 (CD244) to Lipid Rafts". In: *The Journal of experimental medicine* 197.1 (2003). DOI: 10.1084/jem.20020427.

[504]   Lothar Schermelleh et al. "Super-resolution microscopy demystified". In: *Nature Cell Biology* 21.1 (2019), pp. 72–84. DOI: 10.1038/s41556-018-0251-8.

[505]   F. Chen, P. W. Tillberg, and E. S. Boyden. "Optical Imaging. Expansion Microscopy". In: *Science (New York, N.Y.)* 347.6221 (2015). DOI: 10.1126/science.1260088.

[506]   A. T. Wassie, Y. Zhao, and E. S. Boyden. "Expansion Microscopy: Principles and Uses in Biological Research". In: *Nature methods* 16.1 (2019). DOI: 10.1038/s41592-018-0219-4.

[507]   S. Truckenbrodt et al. "X10 Expansion Microscopy Enables 25-nm Resolution on Conventional Microscopes". In: *EMBO reports* 19.9 (2018). DOI: 10.15252/embr.201845836.

[508]   Sven Truckenbrodt et al. "A practical guide to optimization in X10 expansion microscopy". In: *Nature protocols* 14.3 (2019), pp. 832–863. DOI: 10.1038/s41596-018-0117-3.

[509]   Jae-Byum Chang et al. "Iterative expansion microscopy". In: *Nature methods* 14.6 (2017), pp. 593–599. DOI: 10.1038/nmeth.4261.

[510]   T. C. Kunz and V. Kozjak-Pavlovic. "Diverse Facets of Sphingolipid Involvement in Bacterial Infections". In: *Frontiers in cell and developmental biology* 7 (2019). DOI: 10.3389/fcell.2019.00203.

[511]   Tyler J. Chozinski et al. "Expansion microscopy with conventional antibodies and fluorescent proteins". In: *Nature methods* 13.6 (2016), pp. 485–488. DOI: 10.1038/nmeth.3833.

[512]   Paul W. Tillberg et al. "Protein-retention expansion microscopy of cells and tissues labeled using standard fluorescent proteins and antibodies". In: *Nature biotechnology* 34.9 (2016), pp. 987–992. DOI: 10.1038/nbt.3625.

[513]   Fei Chen et al. "Nanoscale imaging of RNA with expansion microscopy". In: *Nature Methods* 13.8 (2016), pp. 679–684. DOI: 10.1038/nmeth.3899.

[514]   Davide Gambarotto et al. "Imaging cellular ultrastructures using expansion microscopy (U-ExM)". In: *Nature Methods* 16.1 (2019), pp. 71–74. DOI: 10.1038/s41592-018-0238-1.

[515]   A. R. Halpern et al. "Hybrid Structured Illumination Expansion Microscopy Reveals Microbial Cytoskeleton Organization". In: *ACS Nano* 11.12 (2017). DOI: 10.1021/acsnano.7b07200.

[516]   T. M.D. Sheard et al. "Three-Dimensional and Chemical Mapping of Intracellular Signaling Nanodomains in Health and Disease With Enhanced Expansion Microscopy". In: *ACS Nano* 13.2 (2019). DOI: `10.1021/acsnano.8b08742`.

[517]   S. Koch-Edelmann et al. "The Cellular Ceramide Transport Protein CERT Promotes Chlamydia Psittaci Infection and Controls Bacterial Sphingolipid Uptake". In: *Cellular microbiology* 19.10 (2017). DOI: `10.1111/cmi.12752`.

[518]   I. Derré, R. Swiss, and H. Agaisse. "The Lipid Transfer Protein CERT Interacts With the Chlamydia Inclusion Protein IncD and Participates to ER-Chlamydia Inclusion Membrane Contact Sites". In: *PLoS pathogens* 7.6 (2011). DOI: `10.1371/journal.ppat.1002092`.

[519]   Julian Fink and Jürgen Seibel. "Click reactions with functional sphingolipids". In: *Biological chemistry* 399.10 (2018), pp. 1157–1168. DOI: `10.1515/hsz-2018-0169`.

[520]   Natalia H. Revelo et al. "A new probe for super-resolution imaging of membranes elucidates trafficking pathways". In: *The Journal of cell biology* 205.4 (2014), pp. 591–606. DOI: `10.1083/jcb.201402066`.

[521]   Emmanouil D. Karagiannis et al. "Expansion Microscopy of Lipid Membranes". In: *bioRxiv* (2019), p. 829903. DOI: `10.1101/829903`.

[522]   Jo-Ana Herweg et al. "Proteomic analysis of the Simkania-containing vacuole: The central role of retrograde transport". In: *Molecular microbiology* 99.1 (2016), pp. 151–171. DOI: `10.1111/mmi.13222`.

[523]   T. Hackstadt et al. "Chlamydia trachomatis interrupts an exocytic pathway to acquire endogenously synthesized sphingomyelin in transit from the Golgi apparatus to the plasma membrane". In: *The EMBO journal* 15.5 (1996), pp. 964–977. DOI: `10.1002/j.1460-2075.1996.tb00433.x`.

[524]   Tobias C. Kunz et al. "Detection of Chlamydia Developmental Forms and Secreted Effectors by Expansion Microscopy". In: *Frontiers in Cellular and Infection Microbiology* 9 (2019), p. 276. DOI: `10.3389/fcimb.2019.00276`.

[525]   R. Belland, D. M. Ojcius, and G. I. Byrne. "Chlamydia". In: *Nature reviews. Microbiology* 2.7 (2004). DOI: `10.1038/nrmicro931`.

[526]   S. Banhart et al. "Sphingolipid Metabolism and Transport in Chlamydia trachomatis and Chlamydia psittaci Infections". In: *Frontiers in cell and developmental biology* 7 (2019). DOI: `10.3389/fcell.2019.00223`.

[527]   Kentaro Hanada. "Intracellular trafficking of ceramide by ceramide transfer protein". In: *Proceedings of the Japan Academy. Series B, Physical and Biological Sciences* 86.4 (2010), pp. 426–437. DOI: `10.2183/pjab.86.426`.

[528]   Y. H. Zeidan and Y. A. Hannun. "Translational Aspects of Sphingolipid Metabolism". In: *Trends in molecular medicine* 13.8 (2007). DOI: `10.1016/j.molmed.2007.06.002`.

[529]   J. K. Lee et al. "Replication-dependent Size Reduction Precedes Differentiation in Chlamydia Trachomatis". In: *Nature communications* 9.1 (2018). DOI: `10.1038/s41467-017-02432-0`.

[530]   Alexander Hoare et al. "Spatial constraints within the chlamydial host cell inclusion predict interrupted development and persistence". In: *BMC Microbiology* 8.1 (2008), pp. 1–9. DOI: `10.1186/1471-2180-8-5`.

[531]   Daniela Auer et al. "The chlamydial deubiquitinase Cdu1 supports recruitment of Golgi vesicles to the inclusion". In: *Cellular microbiology* 22.5 (2020). DOI: `10.1111/cmi.13136`.

[532]   C. A. Elwell et al. "Chlamydia Trachomatis Co-Opts GBF1 and CERT to Acquire Host Sphingomyelin for Distinct Roles During Intracellular Development". In: *PLoS pathogens* 7.9 (2011). DOI: `10.1371/journal.ppat.1002198`.

[533]   A. T. Asmar et al. "Communication Across the Bacterial Cell Envelope Depends on the Size of the Periplasm". In: *PLoS biology* 15.12 (2017). DOI: `10.1371/journal.pbio.2004303`.

[534]   Ishan Ghai and Shashank Ghai. "Understanding antibiotic resistance via outer membrane permeability". In: *Infection and Drug Resistance* 11 (2018), pp. 523–530. DOI: `10.2147/IDR.S156995`.

[535]   D. Wu et al. "Aging Up-Regulates Expression of Inflammatory Mediators in Mouse Adipose Tissue". In: *Journal of immunology (Baltimore, Md. : 1950)* 179.7 (2007). DOI: `10.4049/jimmunol.179.7.4829`.

[536]   Ri-Bai Yan et al. "An efficient and improved procedure for preparation of triflyl azide and application in catalytic diazotransfer reaction". In: *Tetrahedron Letters* 46.52 (2005), pp. 8993–8995. DOI: `10.1016/j.tetlet.2005.10.103`.

[537]   Youngbin Lim et al. "Mechanically resolved imaging of bacteria using expansion microscopy". In: *PLOS Biology* 17.10 (2019), e3000268. DOI: `10.1371/journal.pbio.3000268`.

[538]   Francisco J. Quintana et al. "Lipids and lipid-reactive antibodies as biomarkers for multiple sclerosis". In: *Journal of neuroimmunology* 248.1 (2012), pp. 53–57. DOI: `10.1016/j.jneuroim.2012.01.002`.

[539]   Adam Shahine et al. "A molecular basis of human T cell receptor autoreactivity toward self-phospholipids". In: *Science Immunology* 2.16 (2017). DOI: `10.1126/sciimmunol.aao1384`.

[540] Ildiko Van Rhijn et al. "Lipid and small-molecule display by CD1 and MR1". In: *Nature Reviews Immunology* 15.10 (2015), pp. 643–654. DOI: 10.1038/nri3889.

[541] Monica Rolando and Carmen Buchrieser. "A Comprehensive Review on the Manipulation of the Sphingolipid Pathway by Pathogenic Bacteria". In: *Frontiers in Cell and Developmental Biology* 7 (2019), p. 168. DOI: 10.3389/fcell.2019.00168.

[542] Subramania Kolappan et al. "Structure of the Neisseria meningitidis Type IV pilus". In: *Nature communications* 7 (2016). DOI: 10.1038/ncomms13015.

[543] Rooban Thavarajah et al. "Chemical and physical basics of routine formaldehyde fixation". In: *Journal of Oral and Maxillofacial Pathology : JOMFP* 16.3 (2012), pp. 400–405. DOI: 10.4103/0973-029X.102496.

[544] C. H. Fox et al. "Formaldehyde Fixation". In: *Journal of Histochemistry & Cytochemistry* 33.8 (1985), pp. 845–853. DOI: 10.1177/33.8.3894502.

[545] Isam Eltoum et al. "Introduction to the Theory and Practice of Fixation of Tissues". In: *Journal of Histotechnology* 24.3 (2001), pp. 173–190. DOI: 10.1179/his.2001.24.3.173.

[546] B. Clancy and L. J. Cauller. "Reduction of Background Autofluorescence in Brain Sections Following Immersion in Sodium Borohydride". In: *Journal of neuroscience methods* 83.2 (1998). DOI: 10.1016/s0165-0270(98)00066-1.

[547] M. A. Hayat, ed. *Principles and techniques of electron microscopy: Biological applications*. 4. ed. Cambridge: Cambridge Univ. Press, 2000.

[548] David A. Sack et al. "Cholera". In: *The Lancet* 363.9404 (2004), pp. 223–233. DOI: 10.1016/S0140-6736(03)15328-7.

[549] Jan Holmgren, Ivar Lönnroth, and Lars Svennerholm. "Fixation and Inactivation of Cholera Toxin by GM1 Ganglioside". In: *Scandinavian Journal of Infectious Diseases* 5.1 (1973), pp. 77–78. DOI: 10.3109/inf.1973.5.issue-1.15.

[550] Julie Elisabeth Heggelund et al. "High-Resolution Crystal Structures Elucidate the Molecular Basis of Cholera Blood Group Dependence". In: *PLOS Pathogens* 12.4 (2016), e1005567. DOI: 10.1371/journal.ppat.1005567.

[551] Joel B. Heim et al. "Crystal structures of cholera toxin in complex with fucosylated receptors point to importance of secondary binding site". In: *Scientific Reports* 9.1 (2019), pp. 1–14. DOI: 10.1038/s41598-019-48579-2.

[552] Angela R. Melton-Celsa. "Shiga Toxin (Stx) Classification, Structure, and Function". In: *Microbiology spectrum* 2.4 (2014), EHEC-0024–2013. DOI: 10.1128/microbiolspec.EHEC-0024-2013.

[553] S DeGrandis et al. "Globotetraosylceramide is recognized by the pig edema disease toxin". In: *Journal of Biological Chemistry* 264.21 (1989), pp. 12520–12525.

[554]   J. E. Samuel et al. "Comparison of the Glycolipid Receptor Specificities of Shiga-like Toxin Type II and Shiga-like Toxin Type II Variants". In: *Infection and immunity* 58.3 (1990).

[555]   H. Nakajima et al. "Kinetic Analysis of Binding Between Shiga Toxin and Receptor Glycolipid Gb3Cer by Surface Plasmon Resonance". In: *The Journal of biological chemistry* 276.46 (2001). DOI: `10.1074/jbc.M106015200`.

[556]   Winfried Römer et al. "Shiga toxin induces tubular membrane invaginations for its uptake into cells". In: *Nature* 450.7170 (2007), pp. 670–675. DOI: `10.1038/nature05996`.

[557]   L. J. Bruce. "Molecular Mechanism of P1 Antigen Expression". In: *Blood* 131.14 (2018). DOI: `10.1182/blood-2018-02-833657`.

[558]   Laura L. W. Cooling et al. "Shiga Toxin Binds Human Platelets via Globotriaosyl-ceramide (Pk Antigen) and a Novel Platelet Glycosphingolipid". In: *Infection and immunity* 66.9 (1998), pp. 4355–4366.

[559]   M. Bitzan et al. "Evidence That Verotoxins (Shiga-like Toxins) From Escherichia Coli Bind to P Blood Group Antigens of Human Erythrocytes in Vitro". In: *Infection and immunity* 62.8 (1994).

[560]   N. Yilmaz et al. "Molecular Mechanisms of Action of Sphingomyelin-Specific Pore-Forming Toxin, Lysenin". In: *Seminars in cell & developmental biology* 73 (2018). DOI: `10.1016/j.semcdb.2017.07.036`.

[561]   Marjetka Podobnik et al. "Crystal structure of an invertebrate cytolysin pore reveals unique properties and mechanism of assembly". In: *Nature Communications* 7.1 (2016), pp. 1–10. DOI: `10.1038/ncomms11598`.

[562]   Akiko Yamaji et al. "Lysenin, a Novel Sphingomyelin-specific Binding Protein". In: *Journal of Biological Chemistry* 273.9 (1998), pp. 5300–5306. DOI: `10.1074/jbc.273.9.5300`.

[563]   Mitsuhiro Abe et al. "A Role for Sphingomyelin-Rich Lipid Domains in the Accumulation of Phosphatidylinositol-4,5-Bisphosphate to the Cleavage Furrow during Cytokinesis". In: *Molecular and Cellular Biology* 32.8 (2012), pp. 1396–1407. DOI: `10.1128/MCB.06113-11`.

[564]   Etsuko Kiyokawa et al. "Spatial and Functional Heterogeneity of Sphingolipid-rich Membrane Domains". In: *Journal of Biological Chemistry* 280.25 (2005), pp. 24072–24084. DOI: `10.1074/jbc.M502244200`.

[565]   Alekos Athanasiadis et al. "Crystal Structure of the Soluble Form of Equinatoxin II, a Pore-Forming Toxin from the Sea Anemone Actinia equina". In: *Structure* 9.4 (2001), pp. 341–346. DOI: `10.1016/S0969-2126(01)00592-5`.

[566]   Dušan Šuput. "Equinatoxins: A Review". In: *Marine and Freshwater Toxins*. Ed. by P. Gopalakrishnakone et al. Toxinology. Dordrecht: Springer Netherlands, 2020, pp. 1–17. DOI: `10.1007/978-94-007-6650-1_1-1`.

[567]   Biserka Bakrač et al. "A Toxin-based Probe Reveals Cytoplasmic Exposure of Golgi Sphingomyelin". In: *Journal of Biological Chemistry* 285.29 (2010), pp. 22186–22195. DOI: `10.1074/jbc.M110.105122`.

[568]   Takuma Kishimoto, Reiko Ishitsuka, and Toshihide Kobayashi. "Detectors for evaluating the cellular landscape of sphingomyelin- and cholesterol-rich membrane domains". In: *Biochimica et biophysica acta* 1861.8 Pt B (2016), pp. 812–829. DOI: `10.1016/j.bbalip.2016.03.013`.

[569]   K. Sepcić et al. "Ostreolysin, a Pore-Forming Protein From the Oyster Mushroom, Interacts Specifically With Membrane Cholesterol-Rich Lipid Domains". In: *FEBS letters* 575.1-3 (2004). DOI: `10.1016/j.febslet.2004.07.093`.

[570]   Shreya Endapally et al. "Molecular Discrimination between Two Conformations of Sphingomyelin in Plasma Membranes". In: *Cell* 176.5 (2019), 1040–1053.e17. DOI: `10.1016/j.cell.2018.12.042`.

[571]   Matej Skočaj et al. "Tracking cholesterol/sphingomyelin-rich membrane domains with the ostreolysin A-mCherry protein". In: *PloS one* 9.3 (2014), e92783. DOI: `10.1371/journal.pone.0092783`.

[572]   A. P. Heuck et al. "Mechanism of Membrane Insertion of a Multimeric Beta-Barrel Protein: Perfringolysin O Creates a Pore Using Ordered and Coupled Conformational Changes". In: *Molecular cell* 6.5 (2000). DOI: `10.1016/s1097-2765(00)00119-2`.

[573]   R. Ramachandran et al. "Structural Insights Into the Membrane-Anchoring Mechanism of a Cholesterol-Dependent Cytolysin". In: *Nature structural biology* 9.11 (2002). DOI: `10.1038/nsb855`.

[574]   A. Das et al. "Use of Mutant 125I-perfringolysin O to Probe Transport and Organization of Cholesterol in Membranes of Animal Cells". In: *Proceedings of the National Academy of Sciences of the United States of America* 110.26 (2013). DOI: `10.1073/pnas.1309273110`.

[575]   E. M. Hotze et al. "Arresting Pore Formation of a Cholesterol-Dependent Cytolysin by Disulfide Trapping Synchronizes the Insertion of the Transmembrane Beta-Sheet From a Prepore Intermediate". In: *The Journal of biological chemistry* 276.11 (2001). DOI: `10.1074/jbc.M009865200`.

[576]   Mélanie Carquin et al. "Cholesterol segregates into submicrometric domains at the living erythrocyte membrane: Evidence and regulation". In: *Cellular and Molecular Life Sciences* 72.23 (2015), pp. 4633–4651. DOI: `10.1007/s00018-015-1951-x`.
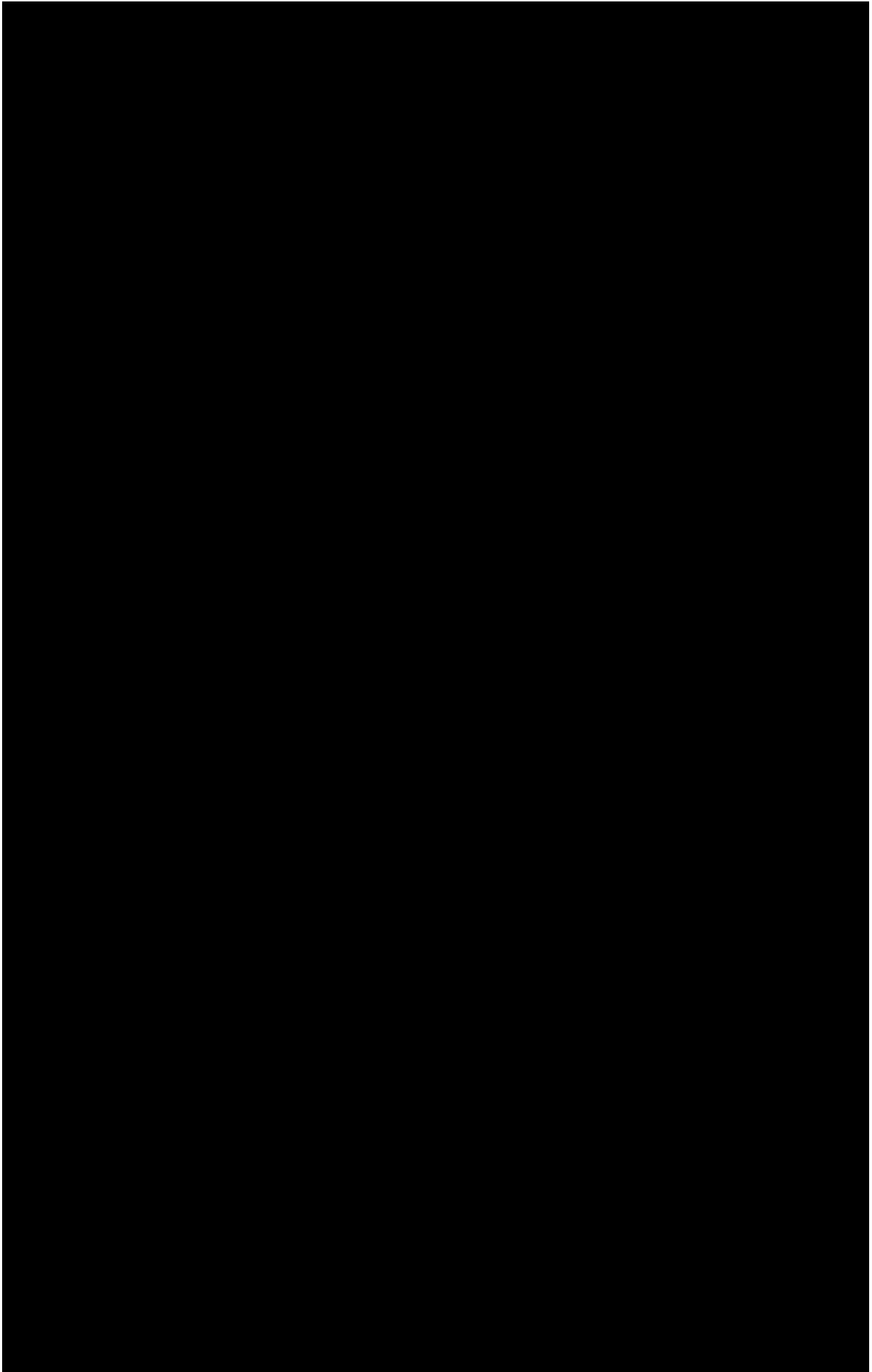
[577]   Jeffrey G. Shannon et al. "Characterization of Anthrolysin O, the Bacillus an-
        thracis Cholesterol-Dependent Cytolysin". In: *Infection and immunity* 71.6 (2003),
        pp. 3183–3189. DOI: 10.1128/IAI.71.6.3183-3189.2003.

[578]   C. He et al. "High-resolution Imaging and Quantification of Plasma Membrane
        Cholesterol by NanoSIMS". In: *Proceedings of the National Academy of Sciences
        of the United States of America* 114.8 (2017). DOI: 10.1073/pnas.1621432114.

[579]   K. A. Johnson and A. Radhakrishnan. "Accessibility of Cholesterol at Cell Sur-
        faces". In: *Journal of Lipid Research* (2020). DOI: 10.1194/jlr.ILR120000836.

[580]   George B. Whitfield et al. "Filipin, an Antifungal Antibiotic: Isolation and Prop-
        erties". In: *Journal of the American Chemical Society* 77.18 (1955), pp. 4799–4801.
        DOI: 10.1021/ja01623a032.

[581]   Frances Platt and Nick Platt, eds. *Methods in Cell Biology : Lysosomes and Lyso-
        somal Diseases*. Academic Press, 2015.

[582]   Y. Mely and G. Duportail. *Fluorescent Methods to Study Biological Membranes.*
        Springer Series on Fluorescence. Springer Berlin Heidelberg, 2012.

[583]   Tetsushi Mori et al. "Single-bacterial genomics validates rich and varied specialized
        metabolism of uncultivated Entotheonella sponge symbionts". In: *Proceedings of the
        National Academy of Sciences* 115.8 (2018), pp. 1718–1723. DOI: 10.1073/pnas.
        1715496115.

[584]   Cheuk Hei Ho et al. "A molecular barcoded yeast ORF library enables mode-
        of-action analysis of bioactive compounds". In: *Nature Biotechnology* 27.4 (2009),
        pp. 369–377. DOI: 10.1038/nbt.1534.

[585]   Meng Zhang et al. "Simple and efficient delivery of cell-impermeable organic fluo-
        rescent probes into live cells for live-cell superresolution imaging". In: *Light: Science
        & Applications* 8.1 (2019), pp. 1–11. DOI: 10.1038/s41377-019-0188-0.

[586]   M. Garrido et al. "Azide-tagged Sphingolipids: New Tools for Metabolic Flux Anal-
        ysis". In: *Chembiochem : a European journal of chemical biology* 16.4 (2015). DOI:
        10.1002/cbic.201402649.

[587]   Hyun Joon Kim et al. "A fluorescent assay for ceramide synthase activity". In:
        Journal of Lipid Research 53.8 (2012), pp. 1701–1707. DOI: 10.1194/jlr.D025627.

[588]   Ingrid Nieves et al. "Chemical Probes of Sphingolipid Metabolizing Enzymes". In:
        Bioactive Sphingolipids in Cancer Biology and Therapy. Ed. by Yusuf A. Hannun
        et al. Cham and s.l.: Springer International Publishing, 2015, pp. 437–469. DOI:
        10.1007/978-3-319-20750-6_19.

[589]   T. Kinoshita et al. "Binding of Brassinosteroids to the Extracellular Domain
        of Plant Receptor Kinase BRI1". In: *Nature* 433.7022 (2005). DOI: 10.1038/
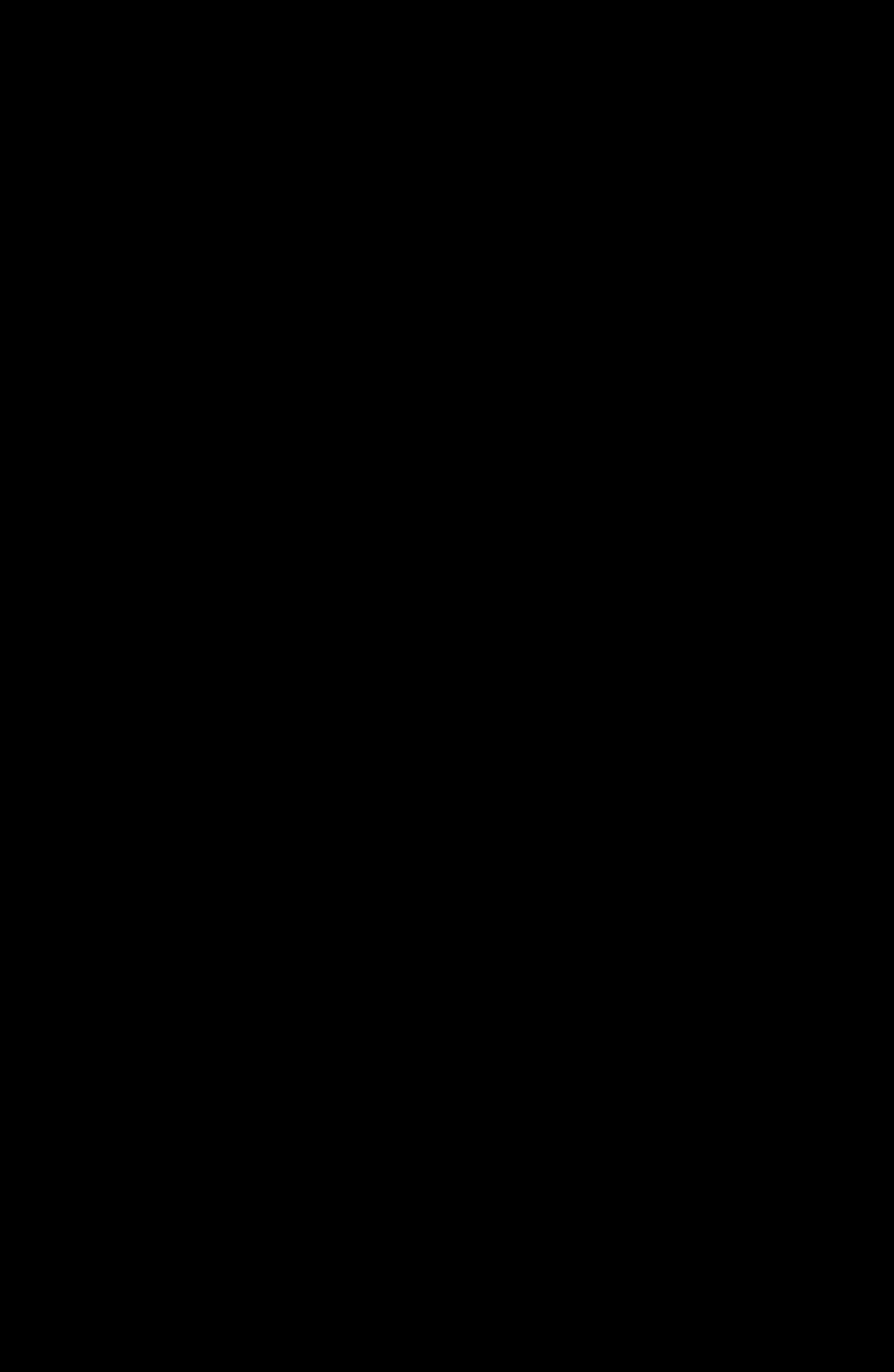   nature03227.

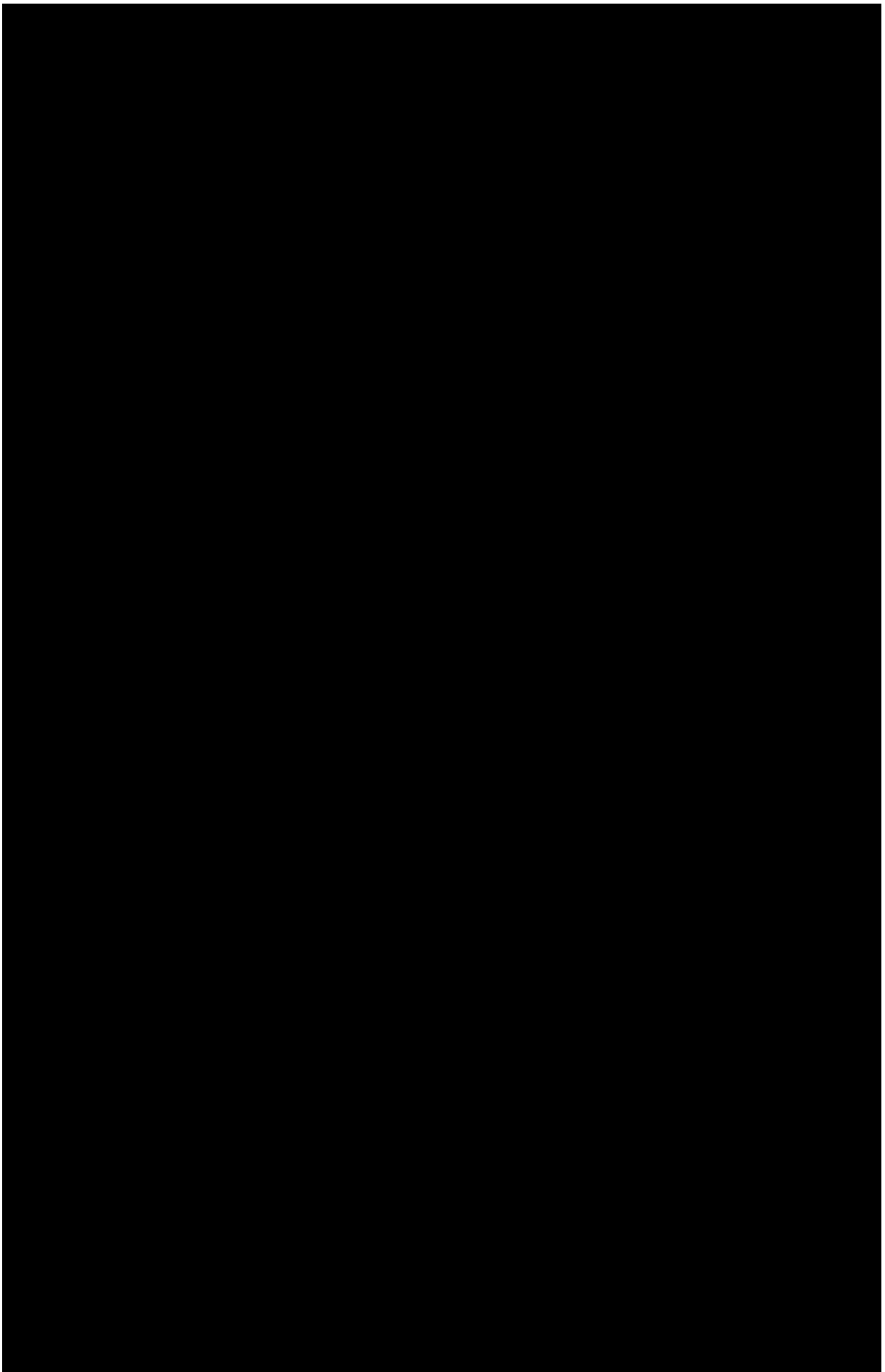# F Acknowledgements

I would like to thank ...

- Prof. Dr. Markus Sauer for being an extraordinary brilliant mentor who allowed me to develop and always supported me and my ideas. The experiences I could make during my PhD and the remarkable environment you created were decisive for my scientific development. I want to thank you in particular for scientific discussions at the Majorcan beach and between horseshoe crabs at the beach of Cold Spring Harbor Laboratory on Long Island as well as for numerous ski seminars in the swiss and french alps.

- my family for constant support and the freedom to let me follow my interests and passion. Your are the best family in the world and I will always know where I belong.

- Nora for being by my side, for taking me as I am and for always supporting me. You are wonderful!

- Prof. Dr. Jürgen Seibel for great collaboration and inspiring and visionary discussions about and beyond sphingolipids.

- Prof. Dr. Sibylle Schneider-Schaulies for introducing me to the world of sphingolipids and organizing excellent SphingoFOR 2123 meetings. I always enjoyed the well-organized and relaxed meetings with the Forschergruppe.

- Prof. Dr. Nurcan Üçeyler for a great collaboration and the freedom to apply our techniques and ideas to your great and fascinating *Morbus Fabry* iPSC cell system.

- Dr. Ulrich Terpitz for introducing me to the world of electrophysiologoy, optogenetics and fungi. I'm thankful for the opportunity to perform my master thesis in your lab and the chance to perform an internship at the Max-Planck-Institute for Biophysics in Frankfurt.

- Prof. Dr. Alexandra Schubert-Unkmeir for a great collaboration within the SphingoFOR 2123 and the opportunity to work with these little fascinating *Neisseria meningitidis* bacteria.

- my thesis commitee for good advice during my annual reports and the constant support.

- the organizers of the Klosters Winter Seminar - it was always a great time with fruitful discussions and constructive teambuilding.

H   Affidavit

Affidavit

I hereby confirm that my thesis entitled "Super-Resolution Microscopy of Sphingolipids and Protein Nanodomains" is the result of my own work. I did not receive any help or support from commercial consultants. All sources and/or materials applied are listed and specified in the thesis.

Furthermore, I confirm that this thesis has not yet been submitted as part of another examination process neither in identical nor in similar form.

....

Place, Date   Signature

Eidesstattliche Erklärung

Hiermit erkläre ich an Eides statt, die Dissertation "Hochaufgelöste Mikroskopie von Sphingolipiden und Protein Nanodomänen" eigenständig, d.h. insbesondere selbständig und ohne Hilfe eines kommerziellen Promotionsberaters, angefertigt und keine anderen als die von mir angegebenen Quellen und Hilfsmittel verwendet zu haben.

Ich erkläre außerdem, dass die Dissertation weder in gleicher noch in ähnlicher Form bereits in einem anderen Prüfungsverfahren vorgelegen hat.

....

Ort, Datum   Unterschrift